

Universiteit
Leiden
The Netherlands

Protostellar jets and planet-forming disks: Witnessing the formation of Solar System analogues with interferometry

Tychoniec, Ł.

Citation
Tychoniec, Ł. (2021, March 9). *Protostellar jets and planet-forming disks: Witnessing the formation of Solar System analogues with interferometry*. Retrieved from https://hdl.handle.net/1887/3147349

Version:	Publisher's Version
License:	Licence agreement concerning inclusion of doctoral thesis in the Institutional Repository of the University of Leiden
Downloaded from:	https://hdl.handle.net/1887/3147349

Note: To cite this publication please use the final published version (if applicable).

Cover Page



Universiteit Leiden



The handle http://hdl.handle.net/1887/3147349 holds various files of this Leiden University dissertation.

Author: Tychoniec, Ł.
Title: Protostellar jets and planet-forming disks: Witnessing the formation of Solar System analogues with interferometry
Issue date: 2021-03-09

Protostellar jets and planet-forming disks: Witnessing the formation of Solar System analogues with interferometry

Proefschrift

ter verkrijging van
de graad van Doctor aan de Universiteit Leiden,
op gezag van Rector Magnificus prof.dr.ir. H. Bijl,
volgens besluit van het College voor Promoties
te verdedigen op dinsdag 9 maart 2021
klokke 16:15 uur
door

Łukasz Tychoniec

geboren te Nowogard, Polen
in 1992

Promotiecommissie

Promotores:	Prof. dr. E. F. van Dishoeck	Universiteit Leiden
	Prof. dr. M. R. Hogerheijde	Universiteit Leiden, Universiteit van Amsterdam
Co-Promotor	Dr. J. J. Tobin	National Radio Astronomy Observatory
Overige leden:	Prof. dr. H. J. A. Röttgering	Universiteit Leiden
	Prof. dr. S. Viti	Universiteit Leiden
	Prof. dr. J. K. Jørgensen	University of Copenhagen
	Dr. M. Tafalla	Observatorio Astronómico Nacional, Madrid
	Dr. M. Ansdell	NASA Headquarters, Washington DC

ISBN: 978-94-6419-137-0

Front cover and chapter title illustrations by Marta Paula Tychoniec

And whether or not it is clear to you,
no doubt the universe is unfolding as it should.

Max Ehrmann
Desiderata, 1924

For Marta,
thank you for convincing me that it was worth it

Contents

1 Introduction **1**
- 1.1 Origin of solar-like stars . . . 2
  - 1.1.1 Collapse of a molecular cloud . . . 2
  - 1.1.2 Protostellar classification . . . 3
  - 1.1.3 Observations of protostars . . . 4
- 1.2 Molecules as tracers of protostellar systems . . . 5
- 1.3 Protostellar jets and outflows . . . 8
  - 1.3.1 Jet launching and observations . . . 8
  - 1.3.2 Entrained outflow . . . 9
  - 1.3.3 Radio jets . . . 9
- 1.4 From embedded to planet-hosting disks . . . 10
  - 1.4.1 Formation of an embedded disk . . . 10
  - 1.4.2 Determination of embedded disk masses . . . 11
- 1.5 Formation of planets . . . 12
- 1.6 This thesis . . . 13

2 The VLA nascent disk and multiplicity survey of Perseus protostars (VANDAM). IV. Free-free emission from protostars: links to infrared properties, outflow tracers, and protostellar disk masses **17**
- 2.1 Introduction . . . 19
  - 2.1.1 The sample . . . 20
- 2.2 Observations and analysis . . . 20
- 2.3 Results . . . 22
  - 2.3.1 Detections . . . 22
  - 2.3.2 Flux densities from protostars . . . 23
  - 2.3.3 Spectral indices . . . 24
  - 2.3.4 Multiple systems . . . 26
  - 2.3.5 Non-detections . . . 29
  - 2.3.6 Updating radio and bolometric luminosity correlations . . . 29
- 2.4 Correlations with molecular outflow tracers . . . 30
  - 2.4.1 Far-infrared line emission . . . 30
  - 2.4.2 Molecular outflow force . . . 32
- 2.5 Mass of the protostellar disks . . . 34
  - 2.5.1 Calculating the mass . . . 34
  - 2.5.2 Evolutionary trend in dust mass . . . 38
- 2.6 Conclusions . . . 39

Appendix . . . 43
- 2.A Tables . . . 43

2.B Additional correlations . . . 73
2.C Interesting sources . . . 74
2.D Free-free and dust slopes . . . 75
2.E Protostars of the VANDAM survey in Ka-band and C-band . . . 87

3 Dust masses of young disks: constraining the initial solid reservoir for planet formation 107
3.1 Introduction . . . 109
3.2 Observations and analysis . . . 110
3.2.1 Observations . . . 110
3.2.2 Gaussian fitting . . . 111
3.3 Dust disk masses . . . 112
3.3.1 Comparison of the integrated fluxes between 1 and 9 mm . . . 112
3.3.2 Disk mass measurements . . . 114
3.3.3 ALMA Class 0/I disk masses for different star-forming regions . . . 116
3.4 Exoplanetary systems and young disks - a comparison of their solid content . 117
3.4.1 Exoplanet sample selection . . . 118
3.4.2 Comparison of young disk dust masses with the solids in exoplanetary systems . . . 118
3.4.3 The context of planet formation models . . . 121
3.5 Conclusions . . . 122
Appendix . . . 127
3.A Additional plots . . . 127

4 Chemical and kinematic structure of extremely high-velocity molecular jets in the Serpens Main star-forming region 133
4.1 Introduction . . . 135
4.2 Observations . . . 137
4.3 Results . . . 138
4.3.1 Images of outflows . . . 138
4.3.2 Velocity regimes . . . 140
4.3.3 Chemical abundances in velocity components . . . 142
4.3.4 Outflow force . . . 146
4.4 Discussion . . . 149
4.4.1 Jet and wind kinematics. The driving force of outflows. . . . 149
4.4.2 Relations with temperature and velocity components from HIFI . . . 151
4.4.3 The case of Ser-emb 8 (N): a pristine outflow-jet system . . . 152
4.4.4 Chemistry of the velocity components . . . 154
4.5 Summary . . . 157
Appendix . . . 159
4.A Relations with temperature and velocity components from HIFI . . . 159
4.B Additional figures . . . 162
4.C Tables . . . 165

5 Which molecule traces what: chemical diagnostics of protostellar sources 171
5.1 Introduction . . . 173
5.2 Physical components of a protostellar system . . . 175
5.3 Observations . . . 177
5.3.1 Datasets . . . 177

5.3.2 Spectral setup of the observations . . . 178
5.4 Protostellar envelope . . . 179
5.4.1 Continuum emission from protostars . . . 179
5.4.2 Molecular lines . . . 181
5.5 Outflows and jets . . . 183
5.5.1 Extremely high-velocity jet . . . 184
5.5.2 Low-velocity outflow . . . 186
5.5.3 Shock sputtering products . . . 188
5.6 Outflow cavity walls . . . 190
5.6.1 Maps . . . 190
5.6.2 Spectral profiles - cavity walls or entrained outflow . . . 192
5.7 Inner envelope . . . 193
5.7.1 Compact emission . . . 193
5.7.2 Embedded disks . . . 196
5.8 Discussion . . . 197
5.8.1 COMs in outflow versus hot core . . . 198
5.8.2 Carbon-chains and other hydrocarbons vs COMs . . . 200
5.8.3 Class 0 vs Class I in different components . . . 201
5.9 Conclusions . . . 202
Appendix . . . 204
5.A Continuum images . . . 204
5.B Envelope tracers . . . 205
5.C Outflow . . . 207
5.D Cavity walls . . . 210
5.E Additional plots . . . 211
5.F Tables . . . 211

Bibliography **215**

Nederlandse samenvatting **233**

English summary **239**

Podsumowanie w języku polskim **245**

Publications **251**

Curriculum Vitae **253**

Acknowledgements **255**



1
Introduction

How did the Earth, Jupiter, the Sun, and the whole Solar System form? This basic curiosity has been a driver for philosophers, scientists, and astronomers for centuries. Limited to observations with the naked eye, ancient Greek philosophers commonly argued that the Earth was at the center of the Universe with the Sun and planets orbiting around her (e.g., Aristotle 370 B.C.; Ptolemei 120).

Copernicus (1543) and others refocused our perception of the Universe with the realization that the Earth is revolving around the Sun. With the progress in understanding of the laws of gravity, ideas about the beginnings of the Solar System were on the right track with the so-called "nebular hypothesis" (Swedenborg 1734; Kant 1755; Laplace 1796).

The emergence of modern astronomy with more and more powerful optical telescopes revealed stunning images of nebulosities across the sky, the most prominent catalogued in Messier catalog. Their nature – are they inside our Galaxy or are they galaxies on their own right – was famously debated by Harlow Shapley and Heber Curtis in 1920. The latter was proven right as the distance to the Andromeda galaxy by Opik (1922) was measured by observing its rotational movement. When Hubble (1929), measured distance to even more galaxies using the Cepheid method developed by Henrietta Leavitt, dimensions of the Universe were pushed almost to infinity. Not all of those nebulae are located millions of light years away. Some of the bright molecular clouds turned out to be located in our Galaxy, and identified as stellar nurseries, such as Orion Molecular Cloud. Those clouds are the primary spots to study the first stages of stars and planet formation. In the days of Hubble and Leavitt, however, the only evidence that planets can be formed around stars was our own Solar System.

End of twentieth century brought a new breakthrough, the discovery of planets around other stars. First planet was found around exotic pulsars (Wolszczan & Frail 1992), but soon after, planets orbiting much more familiar Sun-like stars were detected (Mayor & Queloz 1995). As of today, there are 4370 confirmed exoplanets detected (after exoplanet.eu database, as of 29th October 2020; Schneider et al. 2011). With those numerous detections it became clear that most planetary systems are very different from our own (Madhusudhan 2012; Winn & Fabrycky 2015); for example containing gas giants on a very close orbit, called hot Jupiters, or with many rocky planets closer to their star than Mercury is to the Sun. By pushing the limits of our understanding of the Universe, new questions arose: What is the origin of planetary systems and their diversity? How unique is the Solar System?

At the center of the question about the origin of our Solar System lies the understanding of the beginnings of stars and planets in general. Knowledge about star and planet forma-

tion is gained through astronomical observations of regions where star formation is currently ongoing, along with theoretical models and computational simulations that describe the process of making stars and planets. This thesis is an observational effort to characterize the early phases of star formation with a special focus on two crucial aspects of this process: **protostellar jets** and **embedded disks**. Special attention is paid to links between young protostars and the exoplanetary systems observed in the Milky Way. To understand the importance of jets and disk formation for the star formation process, a general overview of our current knowledge is provided.

1.1 Origin of solar-like stars

1.1.1 Collapse of a molecular cloud

Stars form in molecular clouds that consist predominantly of gas in which the main component by four orders of magnitude is molecular hydrogen (H_2). A small fraction of mass of such clouds (1%) is deposited in solid dust particles built out of refractory material, such as silicates and carbonaceous material; dust grains are often coated with ice mantles consisting of volatile material, such as water (H_2O), methanol (CH_3OH), and carbon monoxide (CO).

Molecular clouds are cold (10-20 K) and dense (10^3–10^6 particles per cm^3) and have ages up to tens of millions of years. Their relative youth compared with the age of the Milky Way has been one of the first arguments for the fact that the star formation is currently ongoing in our Galaxy (Ambartsumian 1947). Stars are predominantly formed in clustered environments (Lada & Lada 2003; Krumholz et al. 2014), however, those birthplaces can vary in terms of density and size (Ward-Thompson et al. 2007); large molecular clouds are observed to form dense filaments and fibers in which prestellar cores can form (André et al. 2010, 2014; Hacar et al. 2013; Tafalla & Hacar 2015). Many physical phenomena such as turbulence and magnetic fields are of importance at this stage (Goodman et al. 1998; McKee & Ostriker 2007).

Eventually cores begin to collapse under their own gravity. Such a core needs to be cold and dense enough for the collapse to satisfy the Jeans criterion (Jeans 1928). On cloud scale, star formation is not a very efficient process, with between 2–4% of gas and dust converted into stars; on the other hand, prestellar cores have up to 30% of star formation efficiency (Alves et al. 2007; Evans et al. 2009; Offner & Arce 2014).

Collapsing clouds form central dense cores, which become optically thick. As pressure and temperature rise, the accretion is halted. Such a core is called a First Hydrostatic Stellar Core (FHSC), it heats up until it reaches the temperature needed to dissociate molecular hydrogen; this process causes the imbalance of equilibrium allowing it to collapse further – a protostar is born (Larson 1969).

Models and evolutionary schemes of star formation are simplified in a sense that they often describe an isolated, single star in the making. However, it should be noted that around 50% of mature solar-mass stars are found in multiple systems (Raghavan et al. 2010), and the multiplicity fraction is even larger in the early stages (Tobin et al. 2016).

Table 1.1: Observational markers of protostellar evolution

Class	$\alpha_{\rm IR}$	$L_{\rm submm}/L_{\rm bol}$	$T_{\rm bol}$ [K]
0	-	$\geq 0.5\%$	≤ 70
I	≥ 0.3	$< 0.5\%$	$70 - 650$
Flat	$0.3 - -0.3$	–	–
II	$-0.3 - -1.6$	–	$650 - 2800$
III	≤ -1.6	–	≥ 2800

1.1.2 Protostellar classification

Low-mass protostars are divided into phenomenological *Classes*, which employ different observational characteristics of young stars and their surroundings. The infrared spectral index

$$\alpha_{\rm IR} = \frac{d\ \log \lambda F_\lambda}{d\ \log \lambda}, \tag{1.1}$$

with λ between 2 and 20 μm, has been the first method of defining the evolutionary stage of a protostar, with redder sources (i.e. brighter emission at longer wavelengths and positive $\alpha_{\rm IR}$) corresponding to younger evolutionary stages (Lada & Wilking 1984). The bolometric temperature associated with the protostellar spectral energy distribution (SED) is the temperature of a blackbody having the same mean frequency. This temperature is an alternative method to classify protostars in different observational classes (Myers & Ladd 1993; Chen et al. 1995). Following the discovery of even redder, Class 0 protostars (André et al. 1993), the submillimeter luminosity as a fraction of total luminosity has been introduced as another border between Class 0 and Class I. Fig. 1.1 presents the overview of protostellar classes along with typical SED for each of them (summarized in Tab. 5.1).

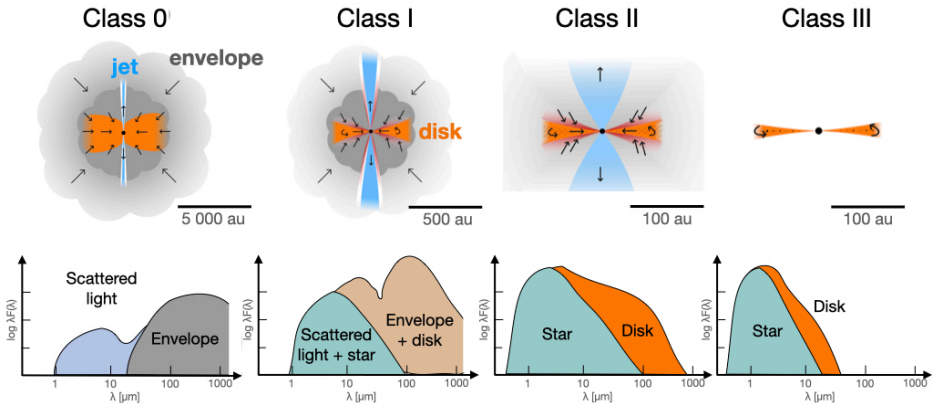


Figure 1.1: *Top*: Schematic view of the protostellar systems at different stages of evolution. *Bottom:* Sketch of mid-infrared SED protostellar classes. Adapted from figure by M. Persson.

Class 0 protostellar systems are deeply embedded in their parent cloud and most of the mass is residing in this natal envelope. Accretion rates are at their highest in this stage and the molecular jet and outflow are most prominent. Due to the conservation of angular momentum, disks already form in this stage (Tobin et al. 2012; Murillo et al. 2013; Maury

et al. 2019), although it is often difficult to disentangle them from a surrounding envelope. Measurements of disk masses in the Class 0 phase show that their disks typically contain 1–10% of the mass of the envelope. These sources are also associated with the richest molecular complexity, as high temperatures of the inner regions of Class 0 systems allow for thermal desorption of ices in so-called hot cores (Herbst & van Dishoeck 2009).

Class I systems are physically characterized as sources with most of their masses already transferred from the envelope to the disk and protostar. Outflows are much weaker and usually they have much wider opening angles compared with Class 0 sources (Arce & Sargent 2006). Less chemical complexity is seen as the gas temperature decreases, except for cases of outbursting sources (van 't Hoff et al. 2018c; Lee et al. 2019b). Disks are clearly observed at this stage with masses between 20–60% of the envelope; this value reaches 70–98% in disks with confirmed Keplerian rotation (Jørgensen et al. 2009). First examples of rings and gaps in those disks can be observed (ALMA Partnership et al. 2015; Segura-Cox et al. 2020; Sheehan & Eisner 2017, 2018; Sheehan et al. 2020), suggesting that planet formation can already start at this early stage. Flat Spectrum sources are sometimes also designated as a transition between Class I and Class II (Greene et al. 1994).

Class II systems are characterized by optically visible pre-main sequence stars, which already begin fusion of deuterium and show rich atomic line emission spectra at visible and near-IR light. These sources are often called T-Tauri stars, named after the prototypical object of this group. In Class II systems, disks can be clearly observed at submillimeter wavelengths (Williams & Cieza 2011), often with rings and gaps (Andrews et al. 2018; Huang et al. 2018), that can be signs of ongoing planet formation. Typical Class II disks are an order of magnitude less massive than Class 0/I disks (Tychoniec et al. 2018b).

Class III systems have only residual emission from a disk as most of their dust is either accreted or assembled in planetesimals and planets. Continuing contraction of the pre-main sequence star causes its temperature to rise high enough so that hydrogen fusion can commence and the star becomes a main sequence star.

Protostellar *Stages* describe the physical properties of the system, resulting from the interpretation and modeling of the observational properties of evolutionary classes. The properties inferred from observations can be the relative masses of the protostar, disk and envelope, or the accretion rate onto the protostar (e.g., van Kempen et al. 2009b). In Stage 0 the mass of the system is dominated by the envelope, while in Stage I, the most mass is already accumulated in the disk and the protostar. Stage II is characterized by decreased accretion rates compared with the previous ones, and the almost negligible mass of the envelope. In Stage III the disk almost disappears and consists mostly of dust, and the accretion stops (Shu et al. 1987; Whitney et al. 2003; Robitaille et al. 2006). The distinction between Stages and Classes is made as some observational properties can be altered by environment, for example, extincted or edge-on Stage II sources can masquerade as Class I systems or Flat Spectrum sources (van Kempen et al. 2009b; Crapsi et al. 2008; Hatchell et al. 2007).

1.1.3 Observations of protostars

From the described properties of Class 0 and I protostars it is clear that studies of the youngest systems are challenging. Low temperatures and high extinctions mean that the bulk of the emission occurs at mid-infrared and longer wavelengths (Fig. 1.1).

Most infrared wavelengths are efficiently blocked by the Earth's atmosphere. That is why progress in infrared astronomy requires space-borne telescopes. ISO and *Spitzer*, among other facilities, revealed the importance of infrared observations of protostars, especially for

their classification and studying the ice content of protostellar envelopes and disks (Boogert et al. 2008). The *Herschel Space Obseratory*, with its large 3.5m dish, revolutionized our view of protostars in the far-IR, by observing water in star-forming regions (van Dishoeck et al. 2011; Hogerheijde et al. 2011); quantifying the heating and cooling mechanisms in protostars (van Kempen et al. 2010; Kristensen et al. 2012; Green et al. 2013; Karska et al. 2018) and mapping molecular clouds with dust continuum emission (André et al. 2014).

Astronomical observations at radio wavelengths are possible from the ground, however, at very dry conditions. Additionally to achieve high angular resolution, interferometry needs to be employed to combine the signal from multiple radio dishes to achieve a spatial resolution competing with optical telescopes. Early studies with single-dish telescopes, before interferometry became available, provided a wealth of information about the star-formation process on scales of 0.05 pc. They revealed the stunning chemical complexity of young protostars, such as IRAS 16293-2422 (van Dishoeck et al. 1995). Single-dish studies are especially useful in probing envelope and cloud-scale emission (e.g., Blake et al. 1994; Jørgensen et al. 2002; Maret et al. 2005; Murillo et al. 2018). The advent of interferometric observations that boost the spatial resolution and collecting power of the submillimeter observations, with facilities such as OVRO, BIMA/CARMA, SMA, and IRAM-PdBI, allowed the protostellar systems to be resolved at this crucial part of spectra, where most of the action happens for the young protostars,

The big leap forward in studying star formation on Solar System scales was made possible by the Atacama Large Millimeter/submillimeter Array (ALMA) on the Chajnantor Plateau in Chile. It has fantastic conditions to observe millimeter universe, at 5000 meters above the sea level, at one of the driest places on Earth. ALMA has been able to resolve the thermal emission from cold dust in protoplanetary disks providing stunning images (van der Marel et al. 2013; ALMA Partnership et al. 2015; Andrews et al. 2018). Its remarkable sensitivity also allowed for unprecedented studies of chemical complexity associated with protostars (Jørgensen et al. 2016). The Very Large Array (VLA) in New Mexico, USA, provides insight into longer wavelengths at subarcsecond resolution. Centimeter wavelengths are a window to observe different physical processes such as ionized and synchrotron emission from young stars. This thesis utilizes the capabilities of ALMA and VLA to probe young Class 0 and Class I protostars. It also aims to pave the way with interferometric observations to new frontiers of studies of star-forming regions that will be made available by the *James Webb Space Telescope* (JWST), set to launch in late 2021.

1.2 Molecules as tracers of protostellar systems

Rotational transitions of molecules allows the protostellar system to be dissected into physical components. Molecular tracers are also a powerful tool to probe densities, temperatures, UV fields, chemical abundances and kinematics (e.g., van Dishoeck & Blake 1998; van Dishoeck & Hogerheijde 1999; Evans 1999). The different components of protostellar systems vary significantly in their physical conditions. We divide the protostellar system into its key components that are illustrated in Fig. 5.1.

Envelope. The envelope surrounding a protostar contains the material that fuels in the accretion process onto the star and disk. The physical conditions in the outer envelope on scales of a few 1000 au are reminiscent of those of starless cores, and their chemical composition is directly inherited from the cloud out of which the star is being born (Caselli & Ceccarelli 2012). Systematic motions such as infall or expansion can occur but otherwise they have low turbulence and narrow line profiles indicative of quiescent gas. Observations

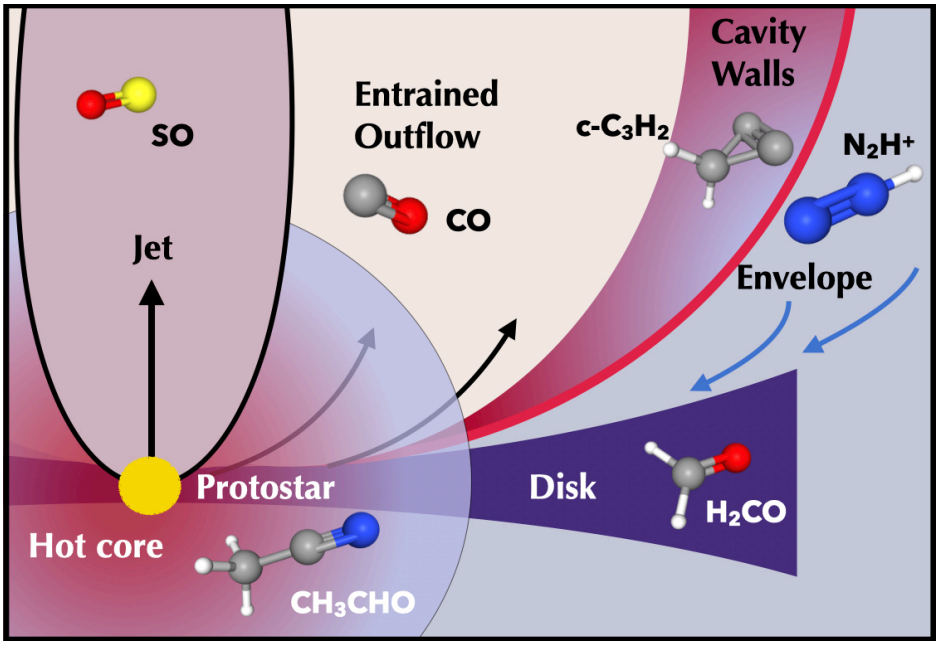


Figure 1.2: Cartoon illustrating the physical components of a protostellar system. Arrows indicate the direction of material in motion; the protostellar jet emerges from the innermost region of the system, but not exclusively from the protostar itself. The size of the envelope with respect to the disk can vary depending on the disk size and temperature profile of the system. Example molecule used is showed in frame, which color correspond to a respective physical component that the molecule is tracing. Molecule images from: https://pubchem.ncbi.nlm.nih.gov/.

with interferometers are challenging because most of the envelope material is resolved out at subarcsecond resolution. Single-dish studies have been very useful in probing the entirety of the envelope emission and pointing to the importance of molecular tracers and line ratios in understanding the physics on large scales (e.g., Blake et al. 1994; van Dishoeck et al. 1995; Ceccarelli et al. 2000; Jørgensen et al. 2002; Maret et al. 2004; Jørgensen et al. 2004b; Emprechtinger et al. 2009; Tobin et al. 2013; Carney et al. 2016; Murillo et al. 2018). Interferometric observations showed a complex geometry of the envelope, and revealed the chemical sensitivity to its temperature profile (Jørgensen et al. 2004a; Tobin et al. 2011). The envelope can be probed by cold and dense gas tracers such as CO isotopologues ^{13}CO and C^{18}O, or ions like N_2H^+, $H^{13}CO^+$ and their deuterated counterparts N_2D^+ and DCO^+ (e.g., Chen et al. 2007; Tobin et al. 2013; van 't Hoff et al. 2018a; Hsieh et al. 2019b). Deuterium fractionation is especially enhanced in cold environments (Caselli et al. 1999).

Outflows. As the material is accreting from the envelope onto the disk and protostar, excess angular momentum is released by means of collimated high-velocity jets which originate from the innermost star-disk interface regions of the protostellar system. In the earliest stages when the mass loss is at its peak, the densities are high enough to form molecules in the internal shocks in the jet (Bachiller & Gomez-Gonzalez 1992; Tafalla et al. 2010). Jets consist initially of mostly molecular material, but undergo significant chemical evolution along

the protostellar lifetime (Nisini et al. 2015). In the molecular stage of the jet, molecules that are enhanced by grain-destruction such as SiO and SO can be observed (Tafalla et al. 2010; Tychoniec et al. 2019; Tabone et al. 2020; Lee 2020).

Much slower (<20 km s^{-1}) and less collimated gas moving away from the protostar is called an outflow. It consists mostly of envelope material, and CO as the most abundant molecule after H_2 is abundantly seen in the entrained gas and wide-angle wind launched from the disk (e.g., Arce & Sargent 2006; Plunkett et al. 2013; Bjerkeli et al. 2016). Temperatures in shocks are much higher than in the surrounding envelope, up to a few thousand K, and sputtering of grain cores and ice mantles can further result in unique chemical signatures from molecules like CH_3OH, C_2H_5OH, CH_3CHO (e.g., Arce et al. 2008; Rodríguez et al. 2017; Lefloch et al. 2017; Codella et al. 2020).

Outflow cavity walls. These are the narrow zones in between the cold dense quiescent envelope material and the lower-density warm cone where outflows are propagating at large velocities. Cavity walls are exposed to UV radiation from the accreting star-disk boundary layer, which can escape through the outflow cavity without being extincted (Spaans et al. 1995). This creates conditions similar to those found in Photon Dominated Regions (PDRs), which occur throughout the interstellar medium near sources of intense UV radiation (Hollenbach & Tielens 1997). In units of the interstellar radiation field (ISRF, Draine 1978), typical values of 10^2–10^3 are found on scales of ~ 1000 au (van Kempen et al. 2009a; Yıldız et al. 2012; Benz et al. 2016; Karska et al. 2018), which is comparable to Horsehead Nebula PDR region (Abergel et al. 2003), while in more energetic regions such as Orion nebula the radiation field exceeds 10^4 times the interstellar value (Marconi et al. 1998). C_2H and c-C_3H_2 are observed in this layer, likely formed from abundant carbon atoms, dissociated out of CO molecules by the UV (Jørgensen et al. 2013; Oya et al. 2017)

Young disk. In the inner envelope, a protoplanetary disk starts to form as the natural outcome of a rotating collapsing core (Cassen & Moosman 1981; Terebey et al. 1984). At early stages it is difficult to identify kinematically whether the so-called embedded disk is rotationally-supported, since any molecular emission from the disk is readily overwhelmed by that from the envelope. In recent years several embedded disks have been identified to have Keplerian rotational structure on scales of ~100 au with tracers such as H_2CO and $C^{18}O$ (Tobin et al. 2012; Murillo et al. 2013; Codella et al. 2014; Yen et al. 2017). Molecular tracers in young disks, apart from providing the kinematic information, can probe their temperature structure as well (van 't Hoff et al. 2018b). Hydrodynamical models of disk formation also predict an accretion shock as envelope material falls onto the disk (Neufeld & Hollenbach 1994; Li et al. 2011). Some molecules, notably SO and SO_2, are proposed as tracers of such shocks (Yen et al. 2014; Sakai et al. 2014b, 2017; Artur de la Villarmois et al. 2019).

Hot core. In the innermost part of the envelope on scales of the disk, temperatures rise above 100 K, so any water and complex organic molecules (COMs) contained in ices are released from the grains back into the gas where they are readily observed at submillimeter wavelengths. This region with its unique chemical richness is called the hot core, or to distinguish it from its high-mass counterpart, hot corino (Herbst & van Dishoeck 2009). High signal-to-noise and high resolution spectra, especially with ALMA and IRAM-PdBI of low-mass protostars revealed that inner envelopes of young protostars are chemically rich, showing prominent emission from e.g., CH_3CHO, CH_3OCHO (e.g., Sakai et al. 2014a; Jørgensen et al. 2016; López-Sepulcre et al. 2017; Codella et al. 2018; Manigand et al. 2020; van Gelder et al. 2020; Bianchi et al. 2020).

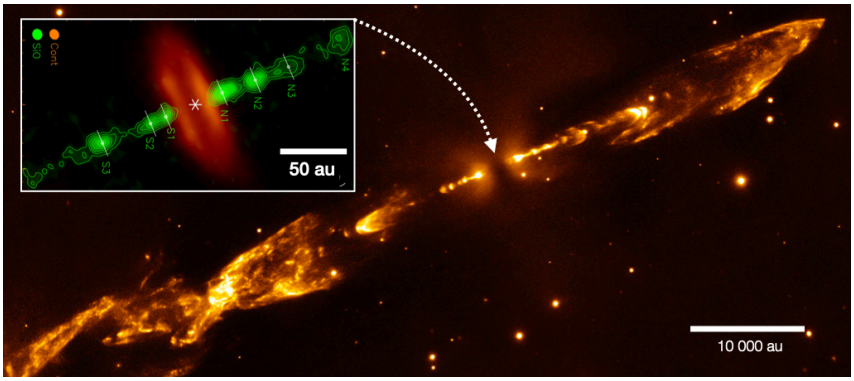


Figure 1.3: Image of the protostellar outflow toward HH212 protostar, through 2.12 μm shocked H_2 observations with VLT (McCaughrean 1994). Inset shows the molecular jet seen in SiO 5–4 transition at 1.3 mm and the continuum emission from the disk at 1.3 mm (Lee et al. 2017).

1.3 Protostellar jets and outflows

Outflows from protostars are a staggering emanation of stars being born. They were first observed in optical light as Herbig-Haro objects rich in spectral lines (Herbig 1950); then with the emergence of radio astronomy, observations of CO line profiles revealed that velocities of these objects are consistent with outflowing, entrained gas from protostars (Snell et al. 1980). Ever since our understanding of their importance to the star formation process has been increasing. Jets and winds from protostars are invoked to release excess angular momentum from the star plus disk system, allowing the accretion to continue (Ferreira et al. 2006). Substantial amounts of material from the envelope are removed from the system by means of outflows. Fig. 1.3 shows the outflow from the HH212-mm protostar in the mid-IR, which traces the shocks with the envelope material. In the submillimeter wavelengths the jet directly launched from the innermost regions can be observed with molecular tracers.

1.3.1 Jet launching and observations

The mechanism of the outflow launching process is still debated. The general consensus is that magnetohydrodynamical (MHD) winds are launched from the innermost regions of the system: either from the protostar-disk interface (X-wind; Shu et al. 1994, 2000) or at larger radii of the disk (disk wind; Pudritz & Norman 1983; Ferreira 1997). This jet entrains the envelope material that can be observed as the low-velocity molecular outflow (Raga et al. 1993).

The launching of the jet is strongly linked to the accretion process. These jets are expected to consist of material directly released from the launching regions, as opposed to the low-velocity outflows which consist mostly of entrained material.

The jet component is observed primarily as so-called *bullets* of concentrated emission, in often symmetric separations, ejected from the central source at high velocities (Guilloteau et al. 1992; Bachiller et al. 1994; Santiago-García et al. 2009; Hirano et al. 2010; Plunkett et al. 2015). Resolved high-velocity bullets show a kinematic structure that is consistent with sideways ejection (Tafalla et al. 2017). The systematically displaced bullets of material

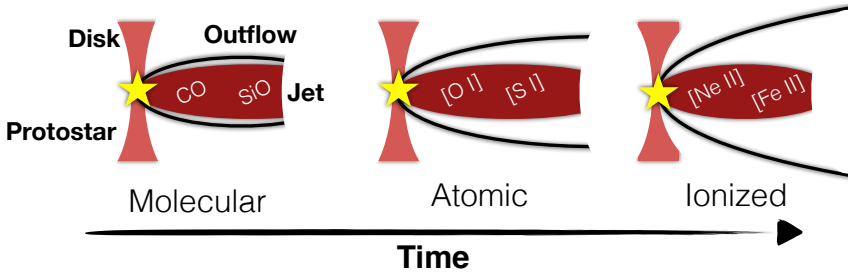


Figure 1.4: Cartoon presenting the chemical evolution of the jet based on the scheme described by Nisini et al. (2015). Young Class 0 jet is mostly molecular, with high mass-loss rates creating conditions for molecule formation; as the mass-loss rate decreases, so does the density in the jet, and photodissociation results in more atomic material; in the late stages the ionized component becomes more prominent.

are explained by the variability of an accretion process. Thus, jets are proposed to provide a record of past episodic accretion events (Raga et al. 1993; Lee 2020).

The jet composition is observed to evolve from mostly molecular, through atomic to ionized material (Nisini et al. 2015). Fig. 1.4 illustrates this process. This evolution is attributed to the change in physical conditions in the jet: lower mass flux results in lower density of material on the way, making the formation of molecules in the bullet less favorable. Moreover, the bullets can be efficiently penetrated by the energetic radiation from the protostar.

1.3.2 Entrained outflow

Surrounding the high-velocity jet is a low-velocity outflow, which consists mostly of entrained envelope material. The properties of outflows are strongly dependent on the evolutionary stage. There is an observed link between the bolometric luminosity of the protostar and its outflow force (Cabrit & Bertout 1992; Bontemps et al. 1996; Mottram et al. 2017). Probing outflows at the earliest stages, when they are most prominent, offers best insight into their properties and interactions with the surrounding envelope.

Shocks, violent encounters between the supersonic jet and outflow with the ambient material, are an important manifestation of the star formation process. Shocks can reveal rich chemistry as high-temperatures created in the shocked regions can lead to formation of some key molecules such as H_2O (Draine et al. 1983; Neufeld & Kaufman 1993; Herczeg et al. 2012; Karska et al. 2014a). Mechanical interactions between the outflows and the envelope can result in sputtering of the ices from the grain, revealing their composition (Arce et al. 2008).

1.3.3 Radio jets

Highly ionized material in shocks can produce thermal emission at radio wavelengths, which is characterized by spectral index $\alpha > -0.1$, where $F_\nu \sim \nu^\alpha$. Free-free emission (*bremsstrahlung*) is produced in ionized medium where free electrons are slowed down, releasing photons at radio wavelengths with typical spectral index of $\alpha = 0.5$. The most important evidence for the link between free-free emission and jets is that the free-free luminosity is related to the outflow force (Cabrit & Bertout 1992) and that, if resolved, such radio emission is observed to

be elongated along the outflow direction (Rodríguez & Reipurth 1989; Anglada et al. 1996; Tychoniec et al. 2018c). It is important to highlight that for studying dust continuum at longer wavelengths, free-free emission can contribute to this flux, which needs to be corrected for.

In a handful of protostars the radio emission shows negative spectral indices $\alpha < -0.1$. at >4 cm wavelengths which is a sign of non-thermal emission (Ainsworth et al. 2014; Tychoniec et al. 2018c). It originates from gyrosynchrotron radiation. Such a mechanism can occur even in low-velocity shocks, where protons may be accelerated to relativistic velocities (Padovani et al. 2016). This process can be relevant as a source of cosmic rays in protostellar envelopes which are otherwise attenuated (Padovani et al. 2013).

1.4 From embedded to planet-hosting disks

Disks of gas and dust surrounding protostars play a central role in understanding the origin of planets as their birthplaces (e.g., Lissauer 1993). The chemical composition of planets depends on that of the disk (Öberg et al. 2011; Madhusudhan 2019) and the physical conditions in the disks are of crucial importance to the mechanism of planet formation.

1.4.1 Formation of an embedded disk

Disk formation starts in the early stages of the star formation, when due to the conservation of the angular momentum, a flattened, rotating structure is created around a protostar (Cassen & Moosman 1981; Terebey et al. 1984). The disk plays a central role in transport of the material from the envelope to the protostar. Observations show that disks are formed rapidly and that the bulk of the mass reservoir is accreted early onto the disk from the envelope, within a few 10^5 yrs after the cloud collapse (Hueso & Guillot 2005; Jørgensen et al. 2009; Williams & Cieza 2011). The observed compact continuum flux due to the dust emission decreases with time, with dust either accreted onto the star or grown into larger bodies that are not detected at submillimeter wavelengths.

Disks surrounding a Class 0/I protostars are called the *embedded disks* as they are still deeply covered in their natal envelope. As protostar enters pre-main sequence (Class II onwards), a well-defined disk around it is called a *protoplanetary disks*, however, emerging paradigm of early planet formation suggest that a name *planet-hosting* disk is more accurate.

Early theoretical models of disk formation suggested that magnetic fields would inhibit the formation of the embedded disks larger than 10 au, due to magnetic braking (Mellon & Li 2008). While majority of embedded disks are indeed small (< 50 au dust size), protostellar disks are now routinely observed (Tobin et al. 2012; Murillo et al. 2013; Segura-Cox et al. 2016; Maury et al. 2019; Tobin et al. 2020), and the magnetic braking might not be as problematic to disk formation as previously thought.

Single-dish observations show that there are large grains in young disks (Weintraub et al. 1989), but only with interferometric studies can resolved disk images at millimeter wavelengths be observed. Early observations with first radio interferometers such as BIMA, OVRO/CARMA, Nobeyama Array, IRAM-PdBI and SMA offered moderate resolution observations of protostellar envelopes, and only with visibility analysis it became possible to distinguish embedded disk from the envelope and show evidence for grain growth (Kawabe et al. 1993; Looney et al. 2000; Jørgensen et al. 2004a, 2009; Kwon et al. 2015).

The interplay of the solid and gas content of disks is fundamental for disk evolution and planet formation. Large grains are drifting inwards due to the drag they experience from the surrounding gas. Young disks are warm, which means that molecular species such as CO

are present in the gas phase even out to large radii (Harsono et al. 2015a; van 't Hoff et al. 2018a, 2020). As the disk cools down, molecules settle onto the grains at the distance from the protostar where the freeze-out temperature of a molecule is reached, at their *iceline*. This results in molecular depletion in the gas phase. As the ice composition of grains changes, their physical properties are altered too, especially freeze-out of H_2O enhances grain growth by coagulation (Stevenson & Lunine 1988). The composition of planetary atmospheres is largely dependent on the location of planetary embryos with respect to the icelines (Öberg et al. 2011; Cridland et al. 2019; Eistrup et al. 2018; Notsu et al. 2020).

However, before we can start discussing factors that determine the composition of atmospheres and cores of planets, there needs to be enough material to produce planets in the first place. Due to the depletion and optical thickness of gas, dust is the most common mass tracer in the disks. This thesis is concerned with dust masses of embedded disks. It is without doubt that gas also plays a crucial role and future observations at high-resolution and sensitivity with ALMA will allow to further constrain also the gas masses.

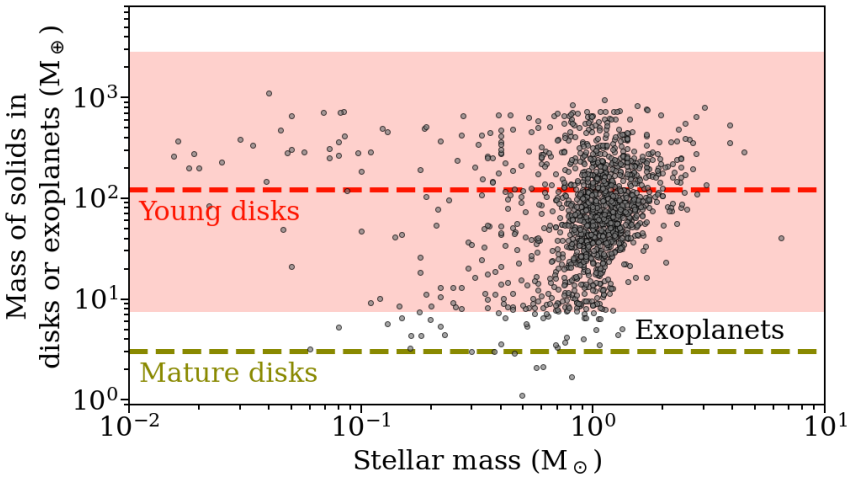


Figure 1.5: Plot showing the distribution of masses of exoplanetary systems obtained from the exoplanet.eu catalog (Schneider et al. 2011), for the planets around main sequence stars with the measured masses. Shaded areas mark the range of the best estimation of the dust disk masses in Perseus from (Tychoniec et al. 2020) young disks (Class 0 and Class I) calculated from the VLA fluxes. Median is indicated with dashed line. The median mass of the Class II disks in Lupus, 3 $M_\oplus$ (Ansdell et al. 2016) is showed in yellow. The masses of the solids in exoplanetary systems are plotted against the stellar mass of the host star.

1.4.2 Determination of embedded disk masses

Submillimeter continuum observations of protostellar systems at high-resolution can be utilized to calculate the dust mass of disks following the equation from Hildebrand (1983):

$$M = \frac{D^2 F_\nu}{\kappa_\nu B_\nu(T_{\rm dust})}, \tag{1.2}$$

with D as the distance to the source, B_ν the Planck function for a temperature $T_{\rm dust}$, and κ_ν the dust opacity (dust mass absorption coefficient) with the assumption of optically thin

emission. Typically the dust temperature is assumed to be 30 K for young disks, similar to protostellar envelopes (Whitney et al. 2003), while more evolved Class II disks are presumably colder at 20 K (Andrews & Williams 2005).

The classic value for κ_ν is based on the Ossenkopf & Henning (1994) calculation $\kappa_{1.3\mathrm{mm}} = 0.9\ \mathrm{cm^2\ g^{-1}}$. The dust opacity is a major source of uncertainty in the dust mass estimation. Panić et al. (2008) summarize a range of literature values between 0.1 and 2 $\mathrm{cm^2\ g^{-1}}$ at 1.3 mm. Higher values are possible if grains have more amorphous carbon than typically assumed (Birnstiel et al. 2018).

The spectral index at millimeter wavelengths α ($F_\nu \sim \nu^\alpha$) can be used to estimate the grain size distribution. The dust emissivity index $\beta = 2 - \alpha$ is defined to indicate the dependence of the dust opacity on frequency ($\kappa_\nu \sim \nu^\beta$). In the interstellar medium the value of β is estimated to be ~1.8 (Draine 2006). In the optically thin limit, a low value of β can point to dust growth (e.g., Natta & Testi 2004; Ricci et al. 2010; Testi et al. 2014).

Masses of embedded disks are difficult to measure, as the envelope is still bright during early stages of evolution. With interferometric observations the envelope is resolved out and the disk can be directly observed. However, the dust tends to be optically thick at submillimeter wavelengths. VLA Ka-band data (9 mm) promise to overcome those limitations, by being sensitive only to larger grains in the densest part of the embedded disk and being optically thin. The major limitation of Ka-band observations is the contamination from free-free emission at those wavelengths.

1.5 Formation of planets

Planets materialize in disks of gas and dust surrounding young stars. Surveys of mature protoplanetary (planet-hosting) disks enabled by ALMA show that their masses are low; in fact so low that formation of currently observed exoplanetary systems would not be possible from the available reservoir of dust (Ansdell et al. 2017; Manara et al. 2018). ALMA and VLA synergy enabled surveys of embedded disks showing that their masses are 5 to 10 times larger than in Class II sources. (Tychoniec et al. 2018c; Tobin et al. 2020). Tychoniec et al. (2020) show that if planet formation starts early, in Class 0/I disks, the dust reservoir is sufficient (Fig. 1.5). Here we present a brief overview of the current concepts on how planets are formed.

The two leading models of the formation of planets are *core accretion* (Mizuno 1980; Pollack et al. 1996) and *gravitational instability* (Kuiper 1951; Cameron 1978; Boss 1997). In the core accretion scenario, dust is first accumulated into larger bodies (planetesimals), through, for example, the streaming instability (Youdin & Goodman 2005). Those planetesimals can attract more and more dust. Models distinguish *pebble accretion*, where parent planetesimal accretes small dust grains, called pebbles (Ormel & Klahr 2010; Lambrechts & Johansen 2012; Johansen & Lambrechts 2017) and *planetesimal accretion* where planetesimals grow through collisions with each other (Mousis et al. 2009). Regardless of the formation route, if a core grows to the size of 10 $\mathrm{M_\oplus}$, it can accrete gas to form a gas giant.

Both planetesimal and pebble accretion have their shortcomings. Planetesimal accretion appears to take too much time, and by the time the core could grow to the size it attracts the gas, there is not much gas left in the disk (Goldreich et al. 2004). On the other hand, planetesimal accretion is very efficient, and eventually most of the planetesimals could be merged into planets (Alibert et al. 2013). Pebble accretion is very fast but not efficient with a maximum efficiency of converting dust disk mass to planets of 10% (Ormel 2017), or up to 30% if multiple planets are produced (Bitsch et al. 2019). This means that while planets can

form early, massive disks are required to produce massive systems. Also there is the need for a large planetesimal that would accrete pebbles needs to start with.

In the gravitational instability scenario, a massive disk becomes gravitationally unstable quickly and collapses with gas and dust to form a giant planet. The main problem with this formation route is the prediction of comparable chemical composition between a planet and a host star which is typically not observed (Thorngren et al. 2016). Another question is whether disks can become unstable.

Both core accretion and gravitational instability scenarios have limitations and the problem of planet formation is far from being solved. Large eccentricities and close orbits observed toward exoplanetary systems are difficult to reproduce with either models, however, this is usually explained by the post-formation dynamical evolution of the systems (Winn & Fabrycky 2015; Dawson & Johnson 2018).

An important input parameter for models of planet formation is the mass reservoir available for the process. This is strongly dependent on the timescale of planet formation. In this thesis, strong evidence is provided that planet formation starts early (Tychoniec et al. 2020). There are several other premises of early planet formation: (i) distribution of populations of meteorites in Solar System (Kruijer et al. 2014), (ii) observed rapid grain growth in Class 0/I (Harsono et al. 2018), (iii) deficiency of masses in mature disks (Williams 2012; Ansdell et al. 2017), (iv) substructures in Class I disks (Sheehan et al. 2020; Segura-Cox et al. 2020).

1.6 This thesis

This thesis presents observational insight into the earliest stages of star and planet formation. With the aid of the ALMA and VLA interferometers, protostellar jets and disks are characterized, setting the stage for future JWST–MIRI observations. The content of the thesis is as follows:

Chapter 2 presents results from the VLA Nascent Disk and Multiplicity Survey (VANDAM) of all Class 0/I protostars in the Perseus molecular cloud, with 4.1 and 6.4 cm (C-band) observations. Toward a hundred protostars we investigated the correlation between free-free emission and protostellar properties, showing a significant dependence of free-free emission on stellar properties. We also found that free-free emission is weakly correlated with J-type shock tracers. A very important outcome of this study was to use our measurements of the free-free component to correct the flux at 9 mm. With this correction we were able to compare the Class 0/I disk masses with those Class II systems for an unbiased sample for the first time. This provided important clues that there is much more dust available for planet formation at the early stages of star formation.

Chapter 3 is the continuation of the work from Chapter 2. We collected ALMA observations of all embedded disks in Perseus, to compare with VLA measurements. Using measurements between 1 and 9 mm we derive an average spectral index $\alpha = 2.5$, showing that significant grain growth occurs in the early stages. We also compare the revised masses of embedded disks with the masses of available exoplanets to find that dust masses of Class 0/I sources in Perseus are sufficient to explain the solid content of the currently observed population of gas giants with efficiency of 10–30%. We also point out that most massive exoplanetary systems might require a higher efficiency of planet formation than single-planet systems.

Chapter 4 presents ALMA observations of high-velocity molecular jets in Serpens. The high detection rate of those jets suggests that they are likely more common than previously thought. The chemical differentiation between the low and high-velocity gas proves the

different physical origin of the two: the former being entrained material and the latter being the gas directly launched from the inner regions of the star-disk system. Our data indicate that the C/O ratio in the EHV gas is lower than in the entrained outflow. A detection of H_2CO in one of the molecular bullets tentatively suggests that dust is launched with the jet.

Chapter 5 is an effort to pinpoint chemical tracers to the physical components of the young protostellar systems at the Solar System scales (50 au) . Cold gas tracers like $C^{18}O$, DCO^+ and N_2D^+, associated with the freeze-out of CO are tracing quiescent envelope material. Shock tracers such as SiO and SO are seen in the outflow; additionally ice-mantle products released with the shock are also detected. SiO, SO and occasionally H_2CO are detected in the high-velocity molecular jet. The cavity walls show tracers of UV-irradiation such as hydrocarbons C_2H and c-C_3H_2 as well as CN. The hot inner envelope, apart from complex organic molecules (COMs), also presents compact emission from small molecules like H_2S, SO, OCS and $H^{13}CN$, most likely related to thermal ice sublimation or accretion shocks.

This thesis can be summarized as follows: Planet formation must start early (< 0.5 Myr), Class 0 and Class I protostars are massive enough to make planets. Therefore characterization of young protostars is essential. Protostellar jets are an important component of the star formation process, it seems that molecular jets are ubiquitous and they may allow to study the composition of the inner regions directly.

The main conclusions of this thesis are:

- Free-free emission from protostars is well correlated with bolometric luminosity and outflow force. The nature of radio emission does not evolve from Class 0 to Class I
- Embedded Class 0 and I disks are more massive than Class II disks, by an order of magnitude. Class 0 disk masses are larger than Class I by a factor of 3, if the same dust temperature is assumed, which suggests that the disk mass is set rapidly.
- Planet formation must start already in the Class 0 systems at $\sim$ 0.1 Myr in order to explain the solid content of currently observed exoplanets.
- Extremely high-velocity jets are more ubiquitous in young protostars than previously thought.
- Molecular tracers observed with interferometers are a powerful tool to discern the physical components of the protostellar systems.

The future is bright for interferometric observations of protostars. With ALMA in full swing we expect many high-resolution observations of young disks, revealing structures showing signs of planet formation in earliest stages. Multi-wavelengths studies of disks will be able to probe the properties of dust in those disks. Observations of molecular jets with many transitions of molecules will enable characterization of physical conditions and will be able to provide constraints on the atomic abundances of the gas launched with the jet and its dust content.

The unique spectral coverage of JWST-MIRI instrument at 5-28 μm, virtually unreachable from the ground, will unveil the ice composition of the protostellar systems. Simultaneously, the gas content will be mapped with the MIRI IFU unit at up to 0.2" resolution. Figure 1.6 illustrates the synergy between ALMA and JWST on the example of one of the guaranteed targets for Cycle 1 JWST observations. Information on the high temperature processes in

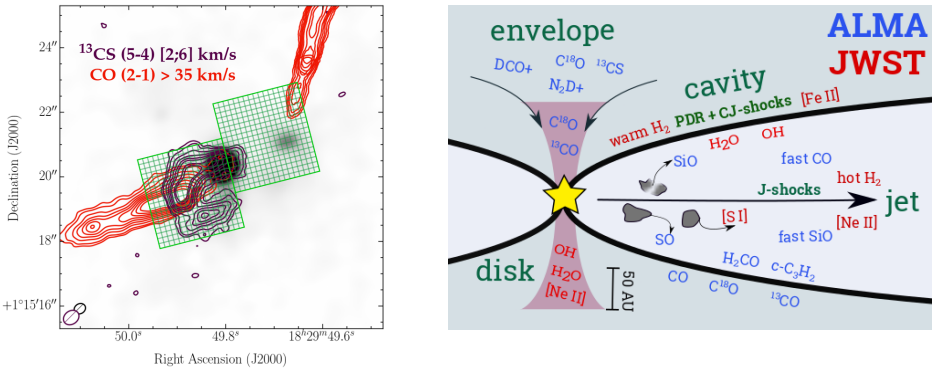
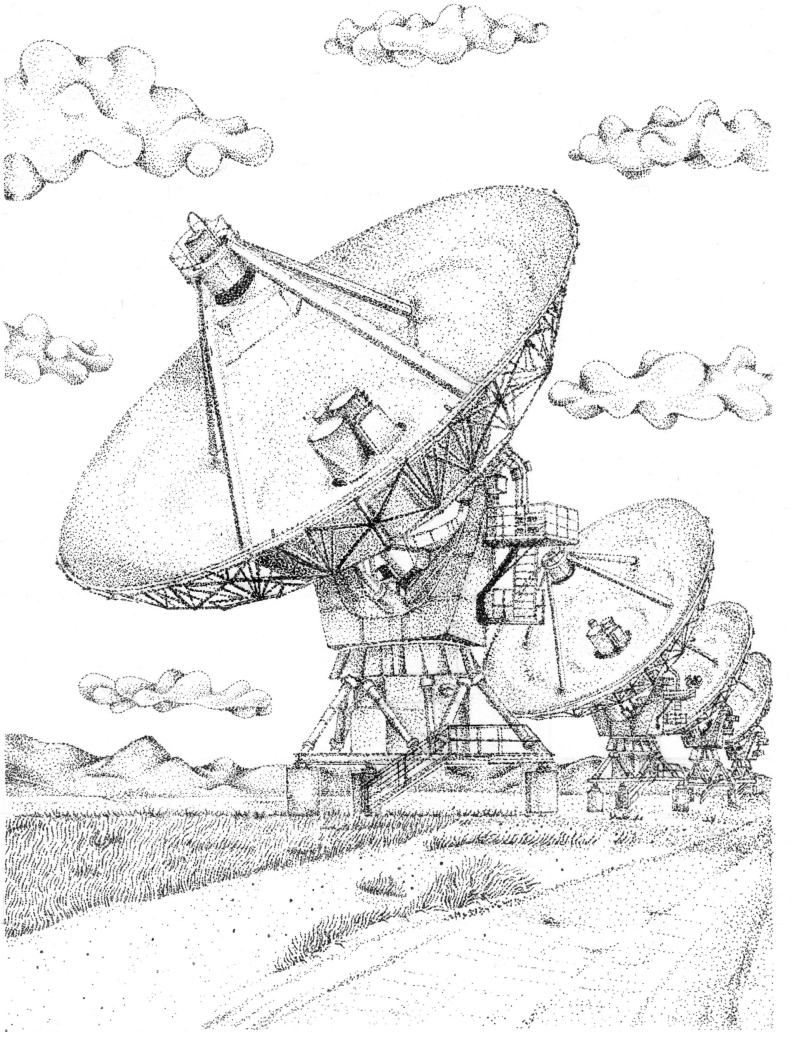


Figure 1.6: *Left:* Serpens SMM1 protostellar system, one of the guaranteed time targets for the JWST/MIRI observations. Map shows ALMA observations from Hull et al. (2016) of dense gas tracer ^{13}CS in purple and the molecular jet mapped by high-velocity CO emission in red contours. 1.3 mm continuum shown in grayscale. Overlaid in green is the MIRI-MRS footprint at its highest resolution which will provide R~3000 spectra from each of the IFU pixels at maximum resolution of 0.2". *Right:* Cartoon image of the various emission components observable with ALMA (in blue) and with JWST/MIRI (red). ALMA probes the molecular part of the jet and entrained outflow material, and delineates the disk and envelope. The mid-IR lines are diagnostics of the hot currently shocked gas but their emission has so far been spatially unresolved. The combination of ALMA and JWST/MIRI will be able to resolve the physical components for the first time.

young stars coupled with ALMA observations of colder molecular gas with kinematic information are going to revolutionize the field of star and planet formation on Solar System scales and inspire new generations of astronomers.



2

The VLA nascent disk and multiplicity survey of Perseus protostars (VANDAM). IV. Free-free emission from protostars: links to infrared properties, outflow tracers, and protostellar disk Masses

Tychoniec Ł., Tobin J.J., Karska A., Chandler C., Dunham M. M., Harris R. J., Kratter K. M., Li Z., Looney, L. W., Melis C., Pérez L. M., Sadavoy S. I., Segura-Cox, D., van Dishoeck E. F.,
Published in Astrophysical Journal Supplement Series, 2018.

Abstract

Emission from protostars at centimeter radio wavelengths has been shown to trace the free-free emission arising from ionizing shocks as a result of jets and outflows driven by protostars. Therefore, measuring properties of protostars at radio frequencies can provide valuable insights into the nature of their outflows and jets. We present a C-band (4.1 cm and 6.4 cm) survey of all known protostars (Class 0 and Class I) in Perseus as part of the VLA Nascent Disk and Multiplicity (VANDAM) Survey. We examine the known correlations between radio flux density and protostellar parameters such as bolometric luminosity and outflow force, for our sample. We also investigate the relationship between radio flux density and far-infrared line luminosities from *Herschel*. We show that free-free emission originates most likely from J-type shocks; however, the large scatter indicates that those two types of emission probe different time and spatial scales. Using C-band fluxes, we removed an estimation of free-free contamination from the corresponding Ka-band (9 mm) flux densities that primarily probe dust emission from embedded disks. We find that the compact ($< 1''$) dust emission is lower for Class I sources (median dust mass 96 $M_\oplus$) relative to Class 0 (248 $M_\oplus$), but several times higher than in Class II (5-15 $M_\oplus$). If this compact dust emission is tracing primarily the embedded disk, as is likely for many sources, this result provides evidence for decreasing disk masses with protostellar evolution, with sufficient mass for forming giant planet cores primarily at early times.

2.1 Introduction

Stars are born through a collapse of cold cores of dust and gas, usually within molecular clouds. A significant fraction of the parental core material is, however, dispersed by powerful outflows and jets rather than incorporated into the protostar (e.g., Arce & Sargent 2006; Offner & Arce 2014). Both outflows and jets are key features observed in star-forming regions toward most young stellar objects (Frank et al. 2014). Outflow properties are expected to reflect the age and activity of the embedded protostar. For example, studies have shown that outflows decrease in force with protostellar evolution (e.g., Bontemps et al. 1996; Yıldız et al. 2015) and outflow ejection rates correlate with accretion onto the central protostar (e.g., Shu et al. 1994; Mottram et al. 2017). Those characteristics suggest that the earliest stages of star formation are essential to investigate because this is the period where stars accumulate most of their mass and are interacting most vigorously with the core and cloud by means of outflows.

Ejecta from the protostar can have different forms. Fast, supersonic jets are well collimated and they interact with cold gas around the protostar in shock events. While likely consisting of atomic gas, it is observed that they can also be composed of high-velocity molecular gas, especially in very young sources (e.g., Bachiller et al. 1990; Tafalla et al. 2004; Hirano et al. 2010). Molecules, however, are most frequently observed in the much wider, and slower outflow, which contains more mass than a jet. The relationship between the outflow and the jet is still strongly debated, but there is a growing body of evidence, both from observations (e.g., Nisini et al. 2015; Dionatos & Güdel 2017) and simulations (e.g., Machida 2014) suggesting that the collimated jet is also powering the wide molecular outflow.

Radio continuum emission from protostars is a unique tracer of the ionized component of the protostellar jet. Radio emission from protostars often appears as an unresolved and compact counterpart to the infrared and submillimeter detections. With high-resolution observations, extended radio emission is often elongated along the direction of the large-scale jets (e.g., Curiel et al. 1989; Anglada et al. 1995), suggesting it is tracing the base of the collimated jet. The radio jets from protostars are most often found toward those in the intermediate and high-mass regime (e.g., Rodríguez & Reipurth 1989; Curiel et al. 1993; Girart et al. 2002), but examples of low-mass protostars with radio jets are known as well (e.g., Rodríguez et al. 1997; Tychoniec et al. 2018c).

Emission at centimeter wavelengths can track various processes in the protostellar environment. The radio spectral index (α; where $F_\nu \sim \nu^\alpha$) can be used to distinguish between different types of emission. Thermal dust emission usually has a steep spectrum with $\alpha = 2+\beta$ where $\beta \lesssim 1$ for dense disks with large grains (Kwon et al. 2009; Testi et al. 2014). Dust emission is still detectable at $\sim$ 1 cm, but is not expected to contribute significantly at C-band. The free-free emission from ionized gas has a spectral index with typical values from -0.1 to 2.0 (Panagia & Felli 1975; Rodríguez et al. 2003). Spectral indices below -0.1 are indicative of non-thermal emission generally associated with synchrotron emission resulting from high-velocity electrons interacting with magnetic fields (e.g., Rybicki & Lightman 1979). This mechanism has been verified as a possibility since polarization in a protostellar radio jet with a negative spectral index has been detected (Carrasco-González et al. 2010). More evolved pre-main sequence stars can exhibit the negative spectral indices due to the gyrosynchrotron emission from the stellar coronae (e.g., Dzib et al. 2013).

Understanding the contribution of different mechanisms of emission at radio wavelengths is essential not only to analyze ionized jets but also to analyze the dust emission at radio wavelengths. The free-free emission can significantly contribute to the continuum at

shorter wavelengths thereby increasing the measured flux densities. Any free-free contamination must be removed to obtain accurate measurements of dust properties and masses of the youngest protostellar disks.

To date, numerous studies have examined radio emission from protostars. Several authors have compiled existing observations and identified general trends between radio emission and protostellar properties (e.g., Anglada et al. 1995; Furuya et al. 2003; Shirley et al. 2007; Wu et al. 2004), while others conducted surveys of molecular clouds. However, the surveys so far lacked sensitivity, resolution and/or sample size (e.g., Reipurth et al. 2004; AMI Consortium: Scaife et al. 2011; Dzib et al. 2013; Pech et al. 2016).

The VLA Nascent Disk and Multiplicity Survey (VANDAM) (Tobin et al. 2015a) is able to overcome previous limitations by targeting the largest homogeneous sample of protostars at 0.8, 1.0, 4.1, and 6.4 cm observing wavelengths. The VANDAM survey targeted all known Class 0 and Class I protostars in the Perseus molecular cloud, providing unbiased observations of the radio jets from those sources. Perseus is a natural choice for this survey, hosting not only the greatest number of young stellar objects among the nearby clouds but also the largest fraction of Class 0 and Class I protostars (Evans et al. 2009). The distance to Perseus (235 pc; Hirota et al. 2011) guarantees high spatial resolution observations.

In this paper, we present C-band observations (4.1 and 6.4 cm) from the NSF's Karl G. Jansky Very Large Array of all known protostars in the Perseus molecular cloud, including flux densities and derived spectral indices. We also calculate masses of compact dust emission at 9 mm from Ka-band observations, taking into account the free-free contributions based on the C-band data. Furthermore, we compare those parameters with protostellar properties such as bolometric luminosity and temperature, molecular and atomic far-infrared line luminosities, and outflow force.

2.1.1 The sample

A total of 95 protostars were targeted by the VANDAM survey in C-band, summarized in Table 3.1. The sample was selected using *Spitzer*, *Herschel*, and Bolocam observations (Enoch et al. 2009; Evans et al. 2009; Sadavoy et al. 2014). The sources have bolometric luminosities between 0.1 $L_\odot$ and 33 $L_\odot$, spanning the low-mass regime. For a detailed description of the source sample selection, see Tobin et al. (2016). The non-detection of three Class II sources in Ka-band: EDJ2009-161, EDJ2009-333, and EDJ2009-268 resulted in them being excluded from the C-band observations. On the other hand, serendipitous Ka-band detections of the Class II sources: EDJ2009-233, EDJ2009-173, EDJ2009-235, and the pre-main sequence binary system SVS3, are included in the C-band sample.

2.2 Observations and analysis

We conducted C-band observations with the VLA in A-configuration between 2014 February 28 and 2014 April 12. The C-band data (4.1 and 6.4 cm) were taken in 8-bit mode, yielding 2 GHz of bandwidth divided into sixteen 128 MHz sub-bands with 2 MHz channels and full polarization products.

We centered 1 GHz basebands at 4.7 and 7.4 GHz avoiding some persistent radio frequency interference in these bands. The observations in two different frequencies allow the measurement of the spectral index which is crucial in the characterization of the sources and discriminating between protostars and extragalactic sources. The radio source 3C48 was both the absolute flux density and bandpass calibrator and J0336+3218 was the complex

gain calibrator. The estimated absolute flux calibration uncertainty is ~ 5% and is not included in the reported flux density errors. This error will not influence the spectral index, as it is obtained from observations at the two ends of the same band, and thus limited only by the uncertainty of the flux calibrator model (~2%; Perley & Butler 2017). Further details of the calibration and data reduction of the C-band observations are described in the previous VANDAM papers (Tobin et al. 2015a; Tychoniec et al. 2018c)

The large primary beam of the C-band observations - 5′ and 7.2′ FWHM for 4.1 and 6.4 cm, respectively - means that fewer pointings are necessary, as compared to Ka-band observations and 38 fields were observed in total. Due to the overlap of the fields, some sources have multiple detections. In those cases, the detection with the lowest distance to the primary beam center was used in the analysis. The typical size of the synthesized beam was 0.″3-0.″4 with a typical RMS noise of 4-6 μJy. Separate characteristics of each field are provided in Table 3.2. We used the AEGEAN source finder version r903 (Hancock et al. 2012) to identify sources in all the fields with a specific *seed* threshold, defining the lowest peak value for the source to be claimed real, set to 6σ. With the CASA (version 4.2.2; McMullin et al. 2007) *imstat* procedure we obtained RMS over the whole image and we used it as an input in the source finder code. Field C15, C16, and C21, have prominent radio galaxies that created artifacts in the maps. For these fields, we measured the noise value manually in an area unaffected by the bright sources. Frames were also cross-checked manually for the protostars not detected by the source finder code and detections over 3σ at protostellar positions were added to the sample.

Based on the method described above, the list of objects was created and we performed 2D Gaussian fitting with the CASA task *imfit* to measure flux densities and corresponding errors. Unresolved sources with relatively faint emission (below 15σ) were fit using Gaussians with position angle and sizes that matched the synthesized beam to avoid unrealistic fit parameters. For sources with extended emission, the source finder code provided multiple peaks of emission that were subsequently used in the *imfit* task as the Gaussian peaks. For these sources, the resulting flux density is the sum of all components. Finally, we corrected fluxes for the primary beam attenuation.

In this work, we explore correlations between measured flux densities and protostellar properties. Due to a large number of non-detections of known protostars, proper accounting of upper limits enables us to derive more accurate correlations from the data. For correlations, we use The Space Telescope Data Analysis System (STSDAS) *statistics* package, that allows one to analyze datasets with upper and/or lower limits. To estimate the correlation strengths, we use Spearman's rank correlation coefficient (ρ), obtained with STSDAS *spearman* procedure which also provides the probability of no correlation (P). The Expectation-Maximization algorithm (EM) is used to obtain parameters of the best linear fit to the data with the procedure *emmethod*. For equations and implementation of the data censoring, see Isobe et al. (1986). To determine if two sets of values are statistically different, we use log-rank test and a Kaplan-Meier (KM) estimator to produce cumulative distribution functions. Both procedures are implemented within the LIFELINES package for Python (Davidson-Pilon 2017) which takes upper limits into account.

2.3 Results

2.3.1 Detections

From the targeted protostars in Table 3.1, we report detections in C-band for 60 out of 95 systems (63%) in either 4.1 or 6.4 cm. Specifically, 31 out of 46 Class 0 (67%) and 21 out of 37 Class I (56%) protostars were detected. We detect 9 of 12 (75%) of targeted Class II systems, but this sample is smaller and biased towards more embedded sources. Out of all systems, 23 have multiple stellar components (21 binary and 2 triple systems) as identified by Tobin et al. (2016); three of those are unresolved in C-band, which results in 117 targeted individual protostars. We detect 11 components of multiple systems (6 Class 0, 3 Class I, and 2 Class II). Thus, the total number of protostars with measured flux in at least one of the wavelengths in C-band is 71, making a detection rate of 61% with 37/57 (65%) Class 0, 24/45 (53%) Class I, and 10/15 (75%) Class II protostars. For known protostars that were not detected, we used 3σ upper limits based on the RMS of the field, corrected for the primary beam attenuation.

For binary systems, we additionally calculated the combined flux of all components together for comparison with parameters that were obtained for unresolved systems. For example, when comparing with outflow force, it is not possible to determine which of the close companions is the outflow driving source, and the same applies to the bolometric luminosity. Far-infrared observations have lower resolution than available with interferometry, so one obtains the luminosity of both components. However, when comparing with bolometric temperature, we compare the flux densities separately for each component of the multiple system, assuming that both companions are at the same evolutionary stage, which is generally a good assumption (Murillo et al. 2016). The summary of measured flux densities and spectral indices is presented in Table 2.3.

Apart from the targeted protostars, we serendipitously detected a plethora of radio sources within the large C-band primary beam. All of them were compared with the SIMBAD catalog. Some of them were detected previously and 17 sources from this sample were marked by various authors as YSO candidates. Due to their tentative classification, they are not considered in the further analysis. However, we note that 8 of them have positive radio spectral indices in C-band as expected for protostars. The more evolved pre-main sequence stars may exhibit negative indices (e.g., Dzib et al. 2013), and distinguishing them from extragalactic sources is difficult by means of spectral index, thus making cross-matched catalogs important. The summary of the sources with possible protostellar nature is presented in Table 2.4.

In Table 2.5 we present 59 previously detected sources of various nature, including 16 stars (2 T-Tauri stars), 27 radio, 8 X-ray, 4 infrared unclassified radio sources, 1 brown dwarf, and 3 associated with starless cores. Negative spectral indices prevail in this sample, indicating non-thermal processes. For stars, the non-thermal emission is probably related to coronal activity, while for unclassified sources it would point to their extragalactic nature. For 12 sources, Pech et al. (2016) reported new detections, and we list them in Table **??**.

Across the entire sample we detect 490 new sources. Table 2.7 lists these new detections. We assume that most of them are extragalactic. To test this, we estimate the expected amount of extragalactic sources based on the equations from Anglada et al. (1998) (see their Appendix) derived from number counts of radio sources (Condon 1984; Rodríguez et al. 1989b). For a detection threshold F_λ, the expected number of extragalactic sources per primary beam is:

$$\mathrm{N}_{6.4} = 1.15\ F_{6.4}^{-0.75} \tag{2.1}$$

$$N_{4.1} = 0.40\ F_{4.1}^{-0.75} \tag{2.2}$$

With the 6 σ threshold used in the source finder we obtain values of:

$$N_{6.4} \sim 16, \text{ for } F_{6.4} \geq 30\ \mu\text{Jy}, \tag{2.3}$$

$$N_{4.1} \sim 7, \text{ for } F_{4.1} \geq 24\ \mu\text{Jy}, \tag{2.4}$$

For the new detections, we find average numbers of $N_{6.4} \sim 15$ and $N_{4.1} \sim 11$ per field. These average values are broadly consistent with the expected number of extragalactic sources, although 4.1 cm value is a bit high. This estimate depends on an assumed spectral index of the extragalactic sources ($\alpha = -0.7$). If some of the sources have flatter indices, we would expect even more of them to be detected at 4.1 cm than predicted.

2.3.2 Flux densities from protostars

Figure 2.1 shows histograms of flux densities at 4.1 and 6.4 cm from the known protostars. We use the log-rank test to estimate probabilities for Class 0 and Class I fluxes to be drawn from the same sample. We obtain high probabilities of 64% and 54% for 4.1 cm and 6.4 cm respectively, consistent with no difference between the two samples. This result, combined with no significant difference between the fraction of detected protostars (65% for Class 0 and 53% for Class I) indicates that the radio emission mechanism should not differ between the two evolutionary classes. This result might indicate that the thermal radio jets are not driven by the release of accretion energy, which is expected to decrease from Class 0 to Class I (Fischer et al. 2017). This is in agreement with Pech et al. (2016), who show for a smaller sample of protostars consistent fluxes between Class 0 and Class I. However, other sample-limited studies suggest that the radio emission mechanisms could be different for Class 0 and Class I protostars (AMI Consortium: Scaife et al. 2011).

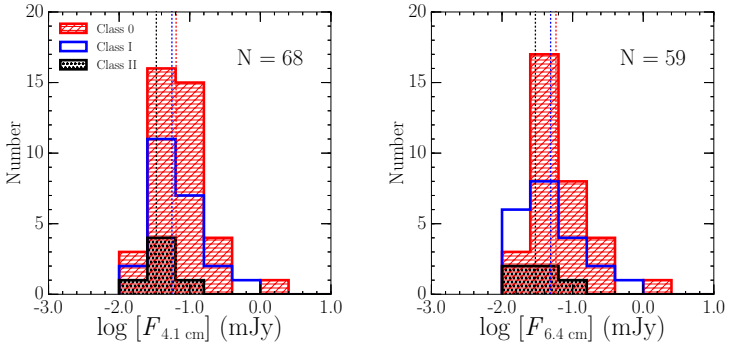


Figure 2.1: Distribution of flux densities for 4.1 cm (left) and 6.4 cm (right). Dashed lines show the median for each evolutionary class. The median values for 4.1 cm flux are 0.064 mJy, 0.056 mJy, and 0.034 mJy, for Class 0, Class I, and Class II. The median values for 6.4 cm flux are 0.058 mJy, 0.048 mJy, and 0.033 mJy for Class 0, Class I, and Class II

Figure 2.2 compares the C-band flux densities corrected for distance (radio luminosities: $L_\lambda = F_\lambda \times D^2$) with the bolometric luminosity and temperature of protostars. The bolometric luminosity is a marker of the protostellar mass and the current accretion rate, and the bolometric temperature is often used to infer protostellar evolutionary status. The values used

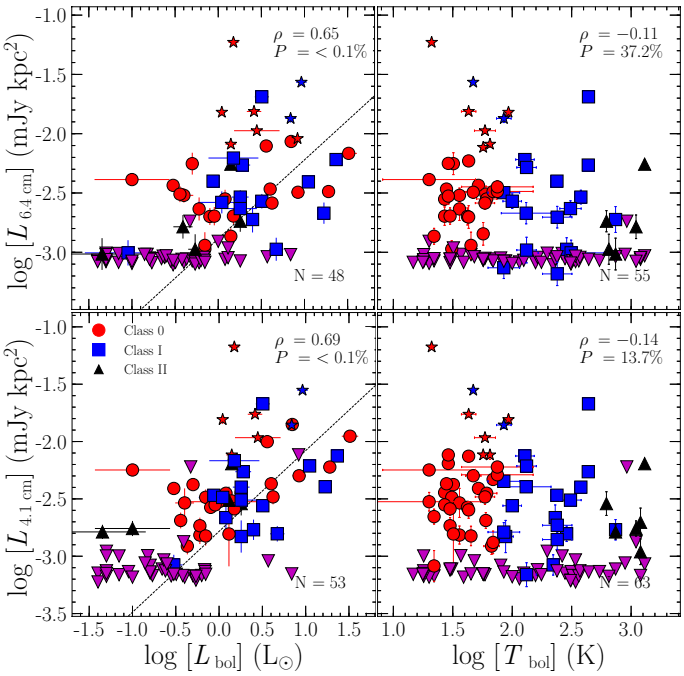


Figure 2.2: Luminosity at 4.1 cm (bottom) and 6.4 cm (top) compared with bolometric luminosity (left) and temperature (right). Spearman's rank correlation coefficient and probability of no correlation is shown in the top-right corner. Sources with resolved radio jets are marked as stars and upper limits as magenta triangles.

here are taken from multiple works analyzing spectral energy distribution of protostars in Perseus (Enoch et al. 2009; Sadavoy et al. 2014; Young et al. 2015; Murillo et al. 2016). We find no correlation with the bolometric temperature, suggesting that the radio emission is independent of the evolutionary class. Previous studies (Dzib et al. 2013, 2015; Pech et al. 2016) are consistent with this result at least for the Class 0 to Class II regime. On the other hand, the radio luminosity shows a weak correlation with the bolometric luminosity. The EM algorithm provides following fitting parameters:

$$\log(L_{4.1\,\mathrm{cm}}) = (-2.78 \pm 0.07) + (0.70 \pm 0.10)\ \log(L_{\mathrm{bol}}), \rho = 0.69 \tag{2.5}$$

$$\log(L_{6.4\,\mathrm{cm}}) = (-2.89 \pm 0.06) + (0.67 \pm 0.10)\ \log(L_{\mathrm{bol}}), \rho = 0.65 \tag{2.6}$$

2.3.3 Spectral indices

With the two C-band fluxes, we calculate the radio spectral index, which is a reliable tool to discriminate between thermal and non-thermal emission processes. We measure the spectral index following:

$$\alpha = \frac{\ln(F_{\nu_1}/F_{\nu_2})}{\ln(\nu_1/\nu_2)} \tag{2.7}$$

To calculate the spectral index errors we use a standard propagation of error (Chiang et al. 2012).

Figure 2.3 shows histograms of the spectral indices for each evolutionary stage. The median values for each distribution are 0.52 for Class 0, 0.41 for Class I, and 0.99 for Class II; the overall median is 0.52. The result from log-rank test for Class 0 and Class I is a 58% probability of these two being drawn from the same sample, thus there is no evidence for evolutionary trend in radio spectral indices. The median value for the total sample is in very good agreement with Shirley et al. (2007) who analyzed a sample of sources with wider range of luminosities, and obtained a median index of 0.5. The median value is also similar to the expected spectral index of ~ 0.6 from an unresolved collimated wind (Reynolds 1986). The spectral index is also consistent with the value of 0.6 obtained for spherical winds of stars Panagia & Felli (1975). Thus, with a median value of $\alpha = 0.52$ we cannot determine the origin of the radio emission from the spectral index alone. Nevertheless, we can rule out some mechanisms from the radio emission. Rodríguez et al. (1993) conclude that highly negative spectral indices like $\alpha < -0.1$ are explained solely by synchrotron emission and cannot arise from free-free emission. Thus, it is important to list those protostellar sources which fall below the free-free regime. The sources with highly negative spectral indices are Per-emb-9 (-0.92 ± 0.63), and Per-emb-19 (-0.91 ± 0.49); they are Class 0 objects with low bolometric luminosity ($L_{\rm bol} < 0.6$ L$_\odot$). The emission from these protostars is compact, but as their signal to noise ratio is low, indicated by the high error of the spectral index measurement, they remain consistent with $\alpha > -0.1$ within 2σ uncertainty.

Figure 2.4 compares the observed spectral index with the radio luminosity for the known protostars in our sample. It is important to note that the most luminous radio sources (> 0.01 mJy kpc^2) have spectral indices below the median for the whole sample, near the optically thin limit for the free-free emission which is -0.1. We conclude that it is caused by the emission from optically thin regions of a jet. Interestingly, most of those sources exhibit resolved radio jets (Tychoniec et al. 2018c) so lower spectral indices come most likely from the outflow positions where the emission is optically thin or non-thermal emission might contribute. Lower spectral indices from resolved jets were theoretically predicted by Reynolds (1986). The most luminous sources exhibit significantly less scatter than the lower luminosity sources. This can be explained by shock ionization dominating the emission of the bright sources, while other, less prominent processes can contribute at low radio luminosities.

We also show the spectral index compared with bolometric luminosity and temperature, in Figure 2.4. We find no correlation between bolometric temperature and spectral index, which suggests that the radio spectral index does not change systematically with protostellar evolution. We found a similar result as in Figure 2.3. A trend in spectral indices with increasing bolometric luminosity can be noted by eye. Removing the four outliers and ignoring upper and lower limits seems to give more hints for correlation (ρ =0.49, P=0.2%; see Figure 2.B.1 in the Appendix 2.B). On the other hand including upper and lower limits in the statistical analysis casts doubt on any relation between the two values (ρ =0.12, P=50%). This relation was also investigated by Shirley et al. (2007) with the conclusion that the optical depth of the emission is not dependent on the source luminosity. Their sample of sources with obtained spectral indices included only three sources with $L_{\rm bol} > 100\ L_\odot$. Even if the relation is unclear, we suggest this requires further study. The enhanced capabilities of VLA demonstrated in this work, can be used in a more massive cloud, where protostars with wider range of bolometric luminosity are present. This could show if the free-free emission becomes optically thick for sources with more ionizing radiation.

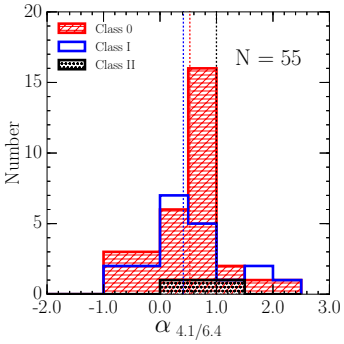


Figure 2.3: Distribution of spectral indices. Dashed lines show the median values for each evolutionary class. Median values are 0.52, 0.41, 0.99, 0.51 for Class 0, Class I, Class II, and total sample respectively. The statistical probability of Class 0 and Class I spectral indices to be drawn from the same sample is 58%.

2.3.4 Multiple systems

The VANDAM survey detected a large number of multiple systems in the Perseus molecular cloud. Due to the superior Ka-band resolution, a detailed analysis of multiplicity was performed with the 8 mm and 1 cm VLA observations (Tobin et al. 2016). A total of 13 new systems with separations below 500 au were detected. Here we examine the emission at longer wavelengths toward these close multiples.

Comments on systems below 30 au:

The VLA Ka-band data showed multiplicity on ~ 30 au scales toward 3 sources: Per-emb-2, Per-emb-5, and Per-emb-18. C-band observations offer lower resolution than Ka-band, which makes detection of the closest binaries impossible. We describe the C-band emission properties of those sources below.

Per-emb-2 appears slightly extended along the direction of the binary at 4.1 cm. The 6.4 cm map, however, is unresolved and peaks at the position of the Per-emb-2-B source. The spectral index map shows steeper values toward the Per-emb-2-A source similar to the Ka-band resolved maps. Tobin et al. (2016) found a similarly steeper spectral index toward Per-emb-2-A from Ka-band data, and suggested that 2-B source is more affected by free-free emission. While unresolved, it appears that most of the C-band flux is aligned with 2-B source but the S/N is low. Per-emb-5 is clearly detected only at 4.1 cm. Its emission is centered on the position of Per-emb-5-B, and its C-band spectral index is consistent with the flat values obtained in the Ka-band.

Per-emb-18 has a steep spectral index in the Ka-band, suggesting that the free-free emission is significantly contributing to the flux at the source position. This source has been identified as a resolved radio jet by VLA C-band observations with a position angle consistent with a large-scale H_2 outflow (Davis et al. 2008) and perpendicular to the position angle of the binary system Tychoniec et al. (2018c).

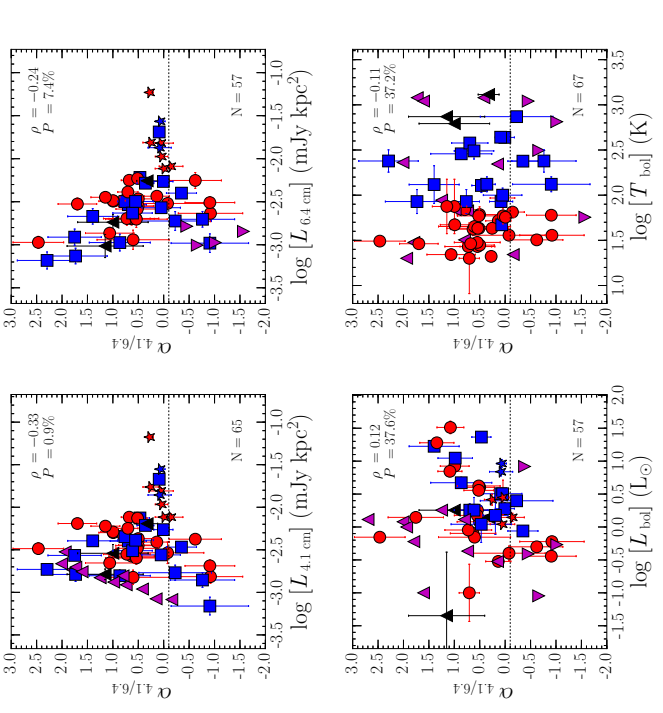


Figure 2.4: Spectral indices between 4.1 cm and 6.4 cm compared with luminosity at 4.1 cm (top left) and 6.4 cm (top right) and with bolometric luminosity (bottom left) and temperature (bottom right). The dashed line indicates minimum value of the spectral index for the free-free emission (α = -0.1). Sources with resolved radio jets are marked as stars, upper limits as magenta triangles facing down, and lower limits as magenta triangles facing up.

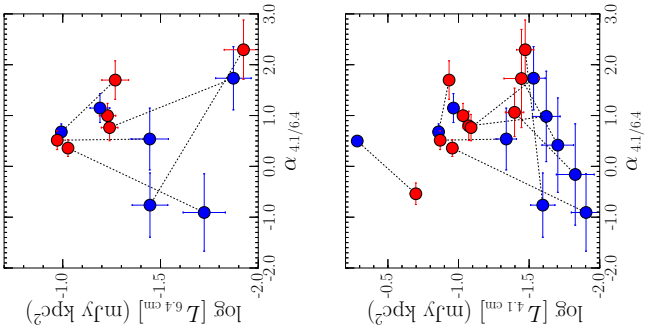


Figure 2.5: Plots showing 6.4 cm (top) and 4.1 cm (bottom) luminosity of the binary systems compared with the spectral index. Red bullet represents the more luminous component of the binary in Ka-band observations Tobin et al. (2016). Dashed lines are connecting components of the same system.

The extended dust structure to the east of Per-emb-18 is seen only in the low-resolution Ka-band image as noted by Tobin et al. (2016) and it is not detected in C-band, further suggesting that this clump is not hosting a protostar nor powering a strong outflow.

Comments on possible close multiples from VANDAM:

Tobin et al. (2016) reported four sources with marginally resolved structures, but not significant enough to report a new detection. The Ka-band maps for EDJ2009-183 from Tobin et al. (2016) shows extended emission that could be attributed to a protostellar component. This emission is marginally detected in the 4.1 cm map, indicating that it might a be faint thermal jet which is also supported by the C-band flat spectral index (0.05 ± 0.38). EDJ2009-156-B is completely unresolved in C-band, but the spectral index suggests a significant contribution of free-free emission to the Ka-band. Per-emb-25 is slightly extended in 4.1 cm map. Interestingly it is peaked at the position of the possible companion, not at the well-detected primary source, making it a strong candidate for a binary. A steep spectral slope in the C-band does not indicate a large contribution from free-free emission Per-emb-52 is a non-detection, preventing further interpretation of the Ka-band data.

Systems with separation > 30 - 500 au:

Tobin et al. (2016) found 19 systems with sources separated by 30 au to 500 au. We detect 10 (50%) of these systems in at least one of the C-band sub-bands. We also identify an additional source in SVS3 that was not detected in Ka-band. A comparison of their fluxes, spectral indices and dust masses is presented in Table **??**. Among detected multiples, some of them have very similar fluxes while for others one of the companions dominates the radio emission. There is no dependence between flux differences and separation. We also find variations in spectral index between the companions. While most of the compact dust differences are moderate, there is the notable example of Per-emb-12 where the A component has a mass ~ 17 times greater than the B component. In the case of Per-emb-12, the B source has greater flux in C-band while in Ka-band the A companion is an order of magnitude brighter. Figure 2.5 illustrates the differences in flux densities and spectral index between the multiple systems.

2.3.5 Non-detections

Radio emission coincident with protostars is well established as a common phenomenon. In this section, we investigate the nature of protostellar sources where we note the absence of the emission at C-band. The most natural explanation for the non-detection arise from the sensitivity of our observations. Even though our sensitivity is quite good ~ 5 μJy RMS, we still may miss the lowest luminosity protostars. The correlation between radio and bolometric luminosity shows that sources with low bolometric luminosities should have lower C-band fluxes (Anglada et al. 1995; Shirley et al. 2007). Indeed, most of our non-detections (except Per-emb-29 and Per-emb-21) have bolometric luminosities below 0.7 $L_\odot$. On the other hand, many of the sources below that threshold have significant radio flux. All the First Hydrostatic Starless Core (FHSC) candidates and Very Low Luminosity Objects (VeLLOs): B1-bN (Hirano et al. 1999; Pezzuto et al. 2012; Gerin et al. 2015), Per-bolo-58 (Enoch et al. 2010), L1451-MMS (Pineda et al. 2011), Per-bolo-45 (Schnee et al. 2012), and L1448IRS2E (Chen et al. 2010), were not detected, probably due to their low luminosity. In contrast, Per-emb-29 and Per-emb-21 are not detected in our C-band observations. Per-emb-21 has $L_\odot$ = 6.9 and Per-emb-29 $L_\odot$=3.7

and we would expect them to have a significant radio flux. It is possible that moderate long-term variability of the free-free emission is tightly connected to the episodic nature of the outflow/accretion events.

2.3.6 Updating radio and bolometric luminosity correlations

Radio emission from low-mass protostars cannot be explained by photoionization because the ionizing flux from the stars is too low (Rodríguez et al. 1989a; Cabrit & Bertout 1992; Anglada et al. 1995). Instead radio emission is attributed to shocks from the jets, which is supported by similar position angles between radio and molecular emission from the outflows (Anglada et al. 1995, and references therein). Correlation of the radio flux and the bolometric luminosity also supports this hypothesis, as more luminous sources are expected to power more energetic outflows (Bontemps et al. 1996; Wu et al. 2004), therefore producing stronger ionizing shocks.

The most up-to-date and complete comparison of the radio flux and bolometric luminosity was provided by Shirley et al. (2007), who compiled data from various works (Anglada et al. 1995, 1998; Furuya et al. 2003; Eiroa et al. 2005). We are able to improve upon this characterization using both the VANDAM sample alone, and by combining it with Shirley et al. (2007) data. The VANDAM observations include lower luminosity protostars than those used in Shirley et al. (2007), hence we can extend the analysis of the bolometric and radio luminosity correlation.

We updated the distances and scaled the bolometric luminosities from the Shirley et al. (2007) consisting of 45 sources at 3.6 cm and 34 at 6 cm. We merged the samples with the 4.1 cm and 6.4 cm sources from VANDAM which resulted in a sample size of 98 and 82 for each wavelength respectively (detections only). For merged VANDAM and Shirley sample we found stronger correlations, with the following linear fitting parameters:

$$\log(L_{4.1\ \mathrm{cm}}) = (-2.66 \pm 0.06) + (0.91 \pm 0.06)\ \log(L_{\mathrm{bol}}), \rho = 0.82 \tag{2.8}$$

$$\log(L_{6.4\ \mathrm{cm}}) = (-2.80 \pm 0.07) + (1.00 \pm 0.07)\ \log(L_{\mathrm{bol}}), \rho = 0.79 \tag{2.9}$$

The correlation for the merged sample appears robust and does not differ significantly from the correlation from Shirley et al. (2007). On the other hand, the linear fit parameters to the VANDAM data are different than for the merged sample, even considering the errors. The somewhat weak correlation in the VANDAM sample alone (see Equations 2.5 and 2.6) results from the scatter within the sample that can be explained by the variable nature of free-free emission. Moreover, a small contribution from the synchrotron emission can cause additional scatter (e.g., Tychoniec et al. 2018c). Only by analyzing protostars spanning several orders of magnitude in luminosity can one derive a robust trend. For example, extended thermal jets can give a temporal rise to the flux. The Perseus results fill out the low-luminosity end of the overall distribution significantly better than before. Morata et al. (2015) analyzed a sample of proto-brown dwarfs showing that they have radio fluxes higher than expected from their bolometric luminosities. This possibly suggests that correlation is flatter at the very low luminosities, but it is not evident with our data.

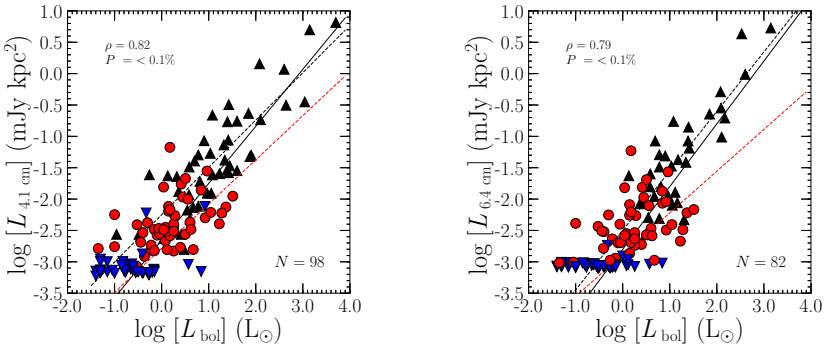


Figure 2.6: Radio luminosities plotted against bolometric luminosities of the sources. Red circles represent VANDAM sources, black triangles are the sources from Shirley et al. (2007), and blue triangles are upper limits of the VANDAM data. Red and black dashed lines show the linear fits to the VANDAM and (Shirley et al. 2007) samples, respectively. The solid line represents fit to the merged sample. Spearman's rank correlation coefficient and the probability of no correlation for the merged sample is shown in the left top corner.

2.4 Correlations with molecular outflow tracers

2.4.1 Far-infrared line emission

To characterize the relationship between radio emission and outflows, we use tracers of jets and outflows from observations of far-infrared molecular and atomic lines. The far-infrared regime is crucial to understand the cooling processes of gas in star-forming clouds; since it predominantly traces warm gas, emission at these wavelengths is expected to probe the currently shocked material (e.g., Nisini et al. 2002; Karska et al. 2013; Manoj et al. 2013, 2016). Thus, we expect to observe a correlation between far-infrared line luminosities and radio luminosity which is likely tracing the shock-ionized gas.

We compare the VANDAM observations with data obtained by The Photoconductor Array Camera and Spectrometer (PACS) instrument (Poglitsch et al. 2010) onboard the *Herschel Space Observatory* (Pilbratt et al. 2010). The data come from two *Herschel* key programs: WISH (van Dishoeck et al. 2011) and DIGIT (Green et al. 2013), as well as from an open time program WILL (Mottram et al. 2017). The PACS spectrometer is an Integral Field Unit (IFU) instrument with 25 spatial pixels (so-called spaxels) a field of view of ~ 50″; each spaxel is 9.″4 x 9.″4, corresponding to a physical resolution of about 2200 au at the distance to Perseus. The wavelength coverage of the PACS instrument (55 - 210 μm) allows one to study some of the key far-IR cooling agents of the shocked gas e.g., CO, H_2O, OH, [O I]. Almost half of the sources analyzed within the sample shows extended emission on the scales of ~ 10^4 au, most commonly in [O I] (Karska et al. 2018). By contrast, VLA observations in C-band primarily trace the emission from the inner 60 au. Comparing such different scales as represented by radio and infrared observations can be challenging. PACS observations trace the outflow history averaged over the past $10^2 - 10^3$ yr while the VLA gives insight on timescales as short as a few years (e.g., Hull et al. 2016). We can then analyze how the nature of the outflow varies in time.

In Figure 2.7 we compare the radio luminosity at 4.1 cm with far-infrared luminosities

of carbon monoxide (CO; J_{up} >14), water vapor (H_2O), oxygen [O I] and hydroxyl radical (OH). Similar figures with 6.4 cm luminosities are given in the Appendix 2.B (Fig 2.B.2). The line luminosities are calculated by co-adding fluxes of the lines detected within the PACS wavelength range, and scaled with distance. We generally see very weak correlations or no evidence of correlations between radio luminosity and far-IR line luminosities. Nevertheless, we explore possible relations. The radio luminosity at 4.1 cm is weakly correlated with OH (ρ = 0.41, P= 2.9%), with a stronger relation for Class I (ρ = 0.64, P = 7.0%); and with [O I] (ρ = 0.34, P = 6.4%), also showing a stronger dependence for Class I (ρ = 0.52, P= 13.9%). For 6.4 cm we can only see a weak correlation with OH (ρ = 0.43, P= 2.1%), and [O I] (ρ = 0.33, P= 8.0%). No correlation with ρ > 0.4 is observed for H_2O and CO line luminosities and radio luminosity. Correlation coefficients are summarized in Table **??**.

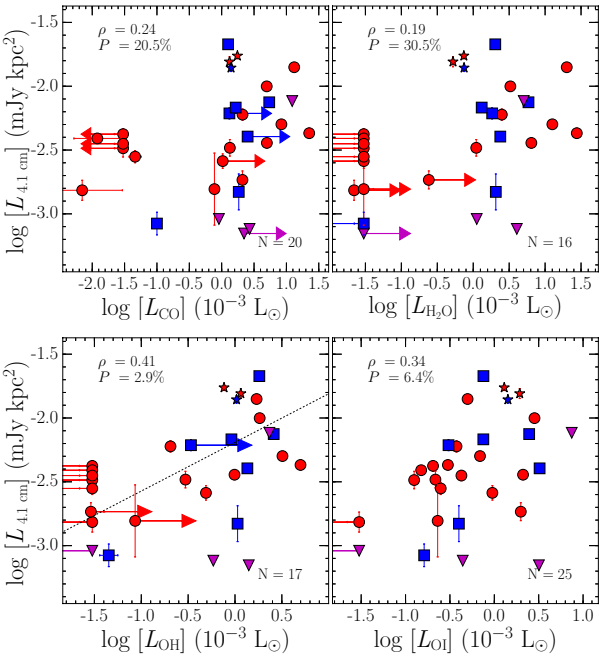


Figure 2.7: Luminosity at 4.1 cm compared with CO (top left), H_2O (top right), [O I] (bottom left) and OH (bottom right) far-IR line luminosity. Upper limits for radio luminosities are plotted as magenta triangles, and lower or upper limits for *Herschel* line luminosities are indicated with arrows. Spearman's rank correlation coefficient and the probability of no correlation is shown in the right top corner (for a combined sample of Class 0 and Class I protostars).

The correlation between radio luminosity and the far-IR line luminosities may be linked to the correlations of those quantities with bolometric luminosity. Karska et al. (2013) show that the correlation of bolometric luminosity and far-IR lines are relatively weak (e.g., r = 0.63 for CO, r = 0.53 for [O I]); the extension over many orders of magnitude in source luminosity shows that the correlation is significant (r>0.92 for CO San José-García et al. 2013). Accordingly, on the scale of one cloud, and with a narrow range of protostellar luminosities, many other phenomena, such as long-term variability of both radio and far-IR emission can

result in a large scatter.

Moderate correlation of radio luminosity with OH and [O I], together with none for CO and H_2O is interesting, as it informs us about the physical origin of the emission. As discussed above, ionization that produces free-free emission is expected to come from shocks. Shocks are divided into two main types: J-type (jump) shocks, with a sharp jump in conditions between pre- and post-shock gas and C-type (continuous) shocks where the change in temperature and density is less dramatic and occurs in a continuous manner (e.g., Draine et al. 1983; Neufeld & Dalgarno 1989; Hollenbach & McKee 1989).

Observations of OH and [O I] with *Herschel* are interpreted as arising in dissociative J-type shocks (van Kempen et al. 2010; Wampfler et al. 2013); up to 50% of CO emission may result from them as well, and less than 10% of the H_2O (Karska et al. 2014b, Mottram et al. 2014). Comparing this to our results, we can infer that ionization that results in free - free emission is likely caused by J - type shocks. Alternatively, UV radiation from accretion shocks or central protostar can explain some of the ionization. In that case, C - type shocks with significant UV contribution could cause the observed ionization.

The observed scatter and weak correlations between far-infrared line and radio continuum fluxes suggest that the ionized collimated jet close to the protostar is not directly related to the large-scale outflow. This is most likely related to the different physical scales compared here - far-IR lines observed with *Herschel* trace material excited in multiple ejection events, while the free-free emission probed by the VLA corresponds only to the most recent ejection. This could potentially be related to the accretion activity, however, a correlation of radio emission and accretion bursts observed through infrared variability has not yet been established (Galván-Madrid et al. 2015).

2.4.2 Molecular outflow force

The discovery of correlations between the outflow force and the radio luminosity was crucial for linking the free-free emission from the protostars to the jet/outflow (e.g., Cabrit & Bertout 1992; Anglada et al. 1995). We examine this relation for the protostars in Perseus, and we add this subset to the sample of known protostellar radio sources with calculated outflow forces to solidify the correlation.

Outflow forces for Perseus protostars were taken from Mottram et al. (2017) and Hatchell et al. (2007) who used CO 3-2 James Clerk Maxwell Telescope (JCMT) observations to measure them. We present a comparison of the radio luminosity and outflow force in Figure 2.8. No significant correlation is observed in these comparisons. When using different observations for outflow forces there is a caveat of introducing additional error through different scales observed and different methods used. This issue can introduce even an order of magnitude errors (van der Marel et al. 2013).

The lack of correlations of radio luminosity with outflow force/momentum differs with a number of other studies (e.g., Cabrit & Bertout 1992; Anglada et al. 1995; Shirley et al. 2007) but all those works used a much wider range of protostellar luminosities in order to derive their correlations. It is important to keep in mind that the molecular outflow force is probed over much greater scales than radio emission, as noted above. It means that while radio emission probes very recent ejection activity, the molecular outflow is averaged over much longer timescales.

To determine if the relation remains valid for a wider range of luminosities, we combine the VANDAM sample with data collected by Shirley et al. (2007), and plot them together in Figure 2.9. We updated distances to the sources included in the sample based on the most

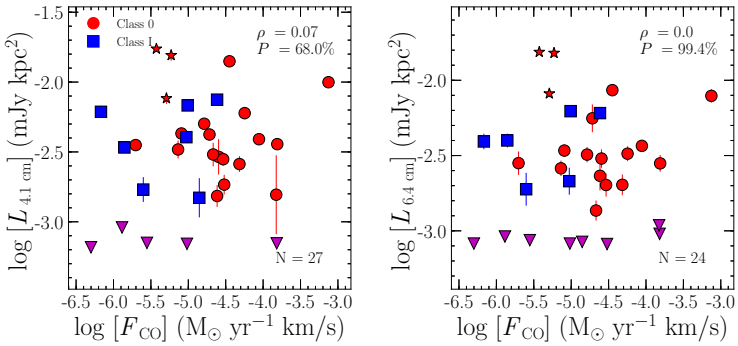


Figure 2.8: Radio luminosity at 4.1 cm (left) and 6.4 cm (right) compared with outflow force from various observations of CO. Upper limits are marked as magenta triangles. The Spearman's rank correlation coefficient and the probability of no correlation are shown in the top-right corner.

recent observations. We again find that the merged sample produces a correlation consistent with that of Shirley et al. (2007). As we noted for bolometric luminosity, the correlations are more clear when spanning more orders of magnitude in source luminosity. For the merged VANDAM and Shirley et al. (2007) sample we fit linear functions with the EM algorithm:

$$\log(L_{4.1\text{ cm}}) = (0.62 \pm 0.45) + (0.58 \pm 0.09)\ \log(F_{\rm CO}), \rho = 0.52 \tag{2.10}$$

$$\log(L_{6.4\text{ cm}}) = (0.54 \pm 0.49) + (0.58 \pm 0.11)\ \log(F_{\rm CO}), \rho = 0.48 \tag{2.11}$$

The AMI Consortium: Scaife et al. (2011, 2012) observed a weaker correlation between the 1.8 cm radio luminosity and the outflow force. Those authors checked if the outflow force is sufficient to produce observed radio flux by calculating the minimum outflow force needed for ionization based on an equation from Curiel et al. (1989):

$$\log L_\nu = 4.24 + \log[F_{\rm out} f(5{\rm GHz}/\nu)] \tag{2.12}$$

where f is the ionization efficiency factor. The AMI Consortium: Scaife et al. (2011) concluded that their sample had outflow forces that were too small to produce the observed radio flux, although the emission at 1.8 cm is likely to have contributions from dust. Here we perform a similar analysis, and the minimum outflow force necessary to produce the observed C-band fluxes is plotted in Figure 2.9. The f=1 case is shown by the dotted line. This case represents the upper limit of the expected C-band fluxes based on 100% outflow efficiency. Thus, we find that the outflow force can easily produce the observed C-band radio emission for both the VANDAM and the Shirley et al. (2007) samples. We note that the energy produced by the outflow is enough to generate the observed radio flux for all the sources, both from Perseus as well as the Shirley et al. (2007) sample.

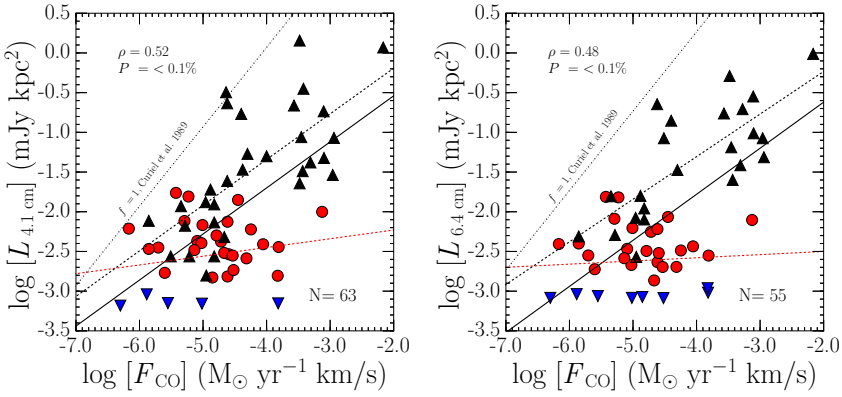


Figure 2.9: Radio luminosity at 4.1 cm (left) and 6.4 cm (right) plotted against outflow force from CO observations. Red and black dashed lines shows linear fits to the VANDAM and Shirley et al. (2007) samples respectively. Solid lines represent fits to the merged sample. Black dash-dot line represent the expected C-band fluxes from the outflow force alone, assuming 100% efficiency following Curiel et al. (1989). This line correspond to the maximum C-band fluxes that can be produced from the CO outflows.

2.5 Mass of the protostellar disks

2.5.1 Calculating the mass

Some of the key questions in star formation are (1) how early do disks form and (2) how do they evolve and form planets. The properties of the youngest disks are still not very well defined. The VANDAM survey in the Ka-band with unprecedented resolution (15 au) found several resolved disk candidates (Tobin et al. 2016; Segura-Cox et al. 2016), but follow-up kinematic data are needed to determine whether or not these structures are rotationally-supported disks. The 9 mm Ka-band emission comes from < 0.″5 scales and likely originates from a disk or compact inner envelope. The observations of the most point-like disk candidates are not consistent with envelope profiles (D. Segura-Cox et al. 2018, in preparation). Therefore compact dust emission at 9 mm is likely tracing genuine disks. Calculating disk masses for an unbiased sample of very young protostars can provide important insights on the early stages of their evolution.

Disk mass can be estimated from the thermal dust emission, assuming the dust is optically thin. Ka-band observations are sensitive to radiation coming from cold and large grains in regions with high densities, which is most likely a direct progenitor of the disk, if not the disk itself. However, continuum emission in the Ka-band may also include a substantial thermal free - free component which can contribute to the emission even at wavelengths shorter than those measured by Ka-band (e.g., Choi 2009). Thus, to accurately estimate the disk mass one needs to remove any free-free contamination from the Ka-band fluxes. For the VANDAM survey we expect free-free emission to contribute significantly to the Ka-band emission for many sources, because the median spectral indices for the sample between 8 mm and 1 cm are below 2 (Tobin et al. 2016). These values are lower than the typical spectral

indices expected for dust, $\alpha = 2 + \beta$, where $\beta < 1$ is expected for dense disks (e.g., Draine 2006; Kwon et al. 2009; Testi et al. 2014). In this section, we assess the contribution of free-free emission on the Ka-band flux to subtract it and hence derive dust-only flux densities to calculate the masses of the embedded disks.

We fit a linear function to C-band logarithmic fluxes and then assumed that the value of this function at 9 mm is the free - free contribution to the total 9 mm flux. We use the Ka-band 9 mm flux density taken in the B configuration, because the beam size is comparable to that of C-band observations taken in the A configuration. Figure 2.10 represents each of the cases in our sample. In case (a), both C-band fluxes are well-detected and we determined the free-free contribution in the Ka-bands from the C-band spectral index; in case (b), the source is detected at one C-band wavelength. To calculate the free-free contribution in case (b) we use the detected C-band flux and assume a free-free spectral index of 0. For case (c), we find a steeper slope for the C-band fluxes than the Ka-band fluxes, which can arise if the free-free emission is optically thick (Ghavamian & Hartigan 1998). Since we expect any free-free emission at Ka-band to be optically thin, we use the 4.1 cm fluxes and an assumed spectral index of zero. In case (d) neither of the C-band fluxes are detected and we assume there is no free-free contamination at Ka-band for these sources. In case (e) we have non-detections in both C-band and Ka-band and we calculate upper limits of these disk masses assuming no free-free contamination. For case (f), we obtain a negative or flat spectral index in Ka-band, which suggests the radio emission is not tracing dust even at 9 mm, and we provide an upper limit.

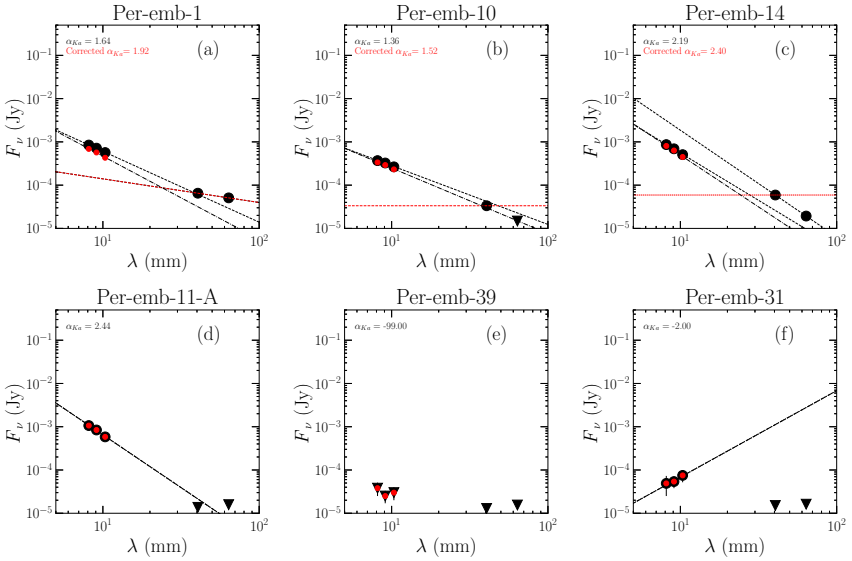


Figure 2.10: Example radio spectral energy distributions for our disk candidates. Each panel shows a different case in how we corrected the Ka-band data for free-free contamination. See text for details. Black bullets represent Ka-band and C-band flux densities, and triangles are upper limits. Red bullets mark the corrected Ka-band flux densities. Dotted lines are linear fits to the original data, and the red line represents the function from which the free-free contribution was estimated. Dash-dot line marks fit to the corrected Ka-band flux densities.

We consider the disk masses from these sources as upper limits and remove no free-free emission. Radio spectra for all of the sources are presented in the Appendix 2.D. For close binaries, unresolved by C-band (Per-emb-2, Per-emb-5, Per-emb-18), we assume they share a common disk and we treat them as single protostars. This analysis is subject to many uncertainties. Free-free emission with a positive slope should turnover at wavelengths shorter than 4 cm, which would decrease the amount of the actual contribution. Ka-band and C-band observations were taken at different epochs (8 months later) and variability of the free-free emission can affect the analysis. The contribution of synchrotron emission can also affect the spectral index. Finally, measured disk masses from Ka-band observations should be considered lower limits because the emission at the 8 mm and 1 cm is sensitive to the largest dust grains in the innermost parts of the disk (Segura-Cox et al. 2016). Nevertheless, we can still compare the disk properties across the VANDAM sample and identify trends with evolution, given that they are observed uniformly.

After correcting the Ka-band fluxes for free-free contamination, we calculate the mass of the disk, following the equation from Hildebrand (1983):

$$M = \frac{D^2 F_\lambda}{\kappa_\lambda B_\lambda(T_{\rm dust})} \tag{2.13}$$

where D is the distance to the protostar ($\sim$ 235 pc), F_λ is the flux density from thermal dust emission, κ_λ is the dust opacity, $B(T_{\rm dust})$ is the Planck blackbody function for an assumed dust temperature of 30 K, typical temperature assumed for cold dust (Whitney et al. 2003). The value of κ_λ is based on the Ossenkopf & Henning (1994) dust opacity models:

$$\kappa_\lambda = 0.00899\Big(\frac{1.3\ {\rm mm}}{\lambda}\Big)^\beta {\rm cm^2 g^{-1}} \tag{2.14}$$

which for λ = 9 mm and β = 1 (Andrews et al. 2009) typical for disks, assuming a gas to dust mass ratio of 100:1, gives a value: $\kappa_{\rm 9\ mm} = 0.00128 {\rm cm^2 g^{-1}}$. Table 2.9 lists the calculated disk masses for the VANDAM sources.

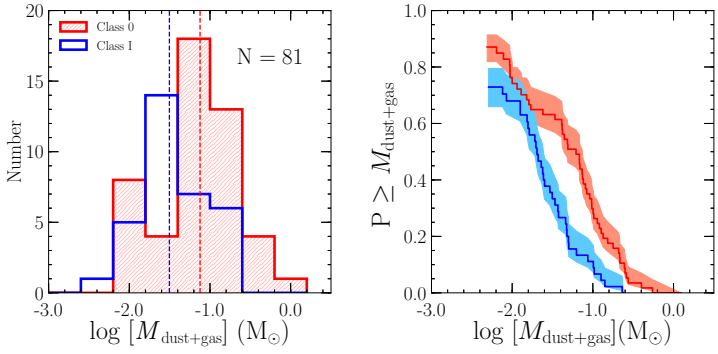


Figure 2.11: Left: Histogram of disk masses for each evolutionary class, obtained with a fixed temperature of dust, T=30 K. Medians are shown with dashed lines, with respective colors. Median values are 0.075 $M_\odot$, 0.031 $M_\odot$, and 0.049 $M_\odot$ for Class 0, Class I, and total sample respectively. The statistical probability of Class 0 and Class I values of the disk mass to be drawn from the same sample is 2.5%. Right: Cumulative distribution obtained with K-M method with 1σ errors shown.

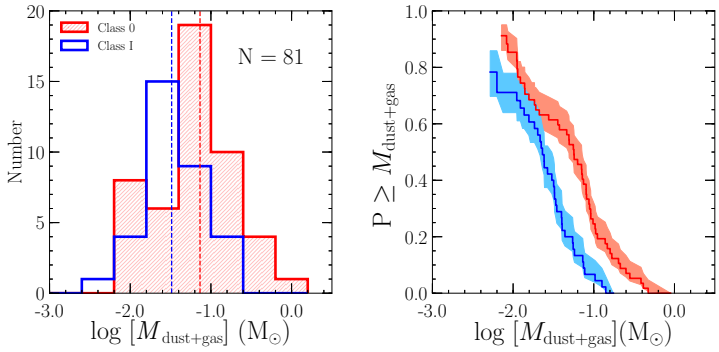


Figure 2.12: Similar to Figure 2.11 but for masses calculated using temperatures determined $T_{\rm dust}$ = 30[K] × $(L_{\rm bol}/{\rm L}\odot)^{1/4}$. Median values are 0.073 $M_\odot$, 0.033 $M_\odot$, 0.055 $M_\odot$ for Class 0, Class I and total sample respectively. We find the statistical probability of 1.5% that the Class 0 and Class I disk masses are drawn from the same sample.

The calculated masses are consistent with those obtained by Segura-Cox et al. (2016) for seven sources from the VANDAM sample. Segura-Cox et al. (2016) used the same Ka-band data to model the disk structure and removed free-free contamination using a point-source model of free-free emission. For Per-emb-8, however, Segura-Cox et al. (2016) modeled a higher disk mass of 0.12-0.24 $M_\odot$, where we obtained a value of 0.097 ± 0.006 $M_\odot$ with our free-free correction. This source exhibits particularly strong, extended free-free emission with a resolved radio jet (Tychoniec et al. 2018c), such that the free-free emission contributes roughly 43% of the Ka-band continuum. For Per-emb-12-A (IRAS 4A) Cox et al. (2015) obtained 2.3 $M_\odot$ from uncorrected VANDAM data (they used β = 1.3, which further increases the estimated mass). With our corrected Ka-band fluxes, we find a mass of 1.2 $M_\odot$, which is still remarkably large, but more consistent with the typical masses (< 1$M_\odot$) of the low-mass protostellar disks (e.g., Jørgensen et al. 2009; Enoch et al. 2011).

Figure 2.11 shows the distribution of mass for each evolutionary stage and the cumulative distribution obtained with the Kaplan-Meier estimator, for Class 0 and Class I only. We notice a clear decrease in mass between Class 0 and Class I with median values of 0.075 $M_\odot$ and 0.031 $M_\odot$ respectively. The log-rank test was used to test the probability of drawing Class 0 and Class I datasets from the same sample. We find the probability of only 2.5%, indicating that Class 0 and Class I mass distributions are statistically different. The sample size of Class II sources is too small to draw statistical conclusions (the median mass is 0.036 $M_\odot$). The median mass for the Class 0 and I sample together is 0.049 $M_\odot$.

As a constant dust temperature for all the sources is a very simplistic assumption, we also tried to account for the source luminosity by scaling the assumed dust temperature with the bolometric luminosity following: $T_{\rm dust}$ = 30[K] × $(L_{\rm bol}/{\rm L}_\odot)^{1/4}$. Figure 2.12 shows the mass distribution in this case. Obtained values are still consistent with an evolutionary decrease of masses, with log-rank test indicating a 1.5 % chance of Class 0 and Class I distributions being drawn from the same sample. Taking into account the inescapable limitations, it is clear that disk mass does not grow between Class 0 and Class I, which suggests that disks form early during the star formation process and have the highest masses at an early age.

Figure 2.13 shows disk masses compared with bolometric temperature and luminosity. We observe a weak correlation (ρ = 0.60, P <0.01%) between the disk mass and the bolometric

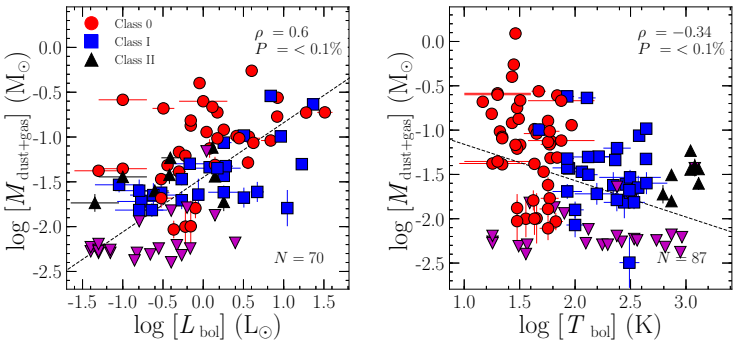


Figure 2.13: Disk mass compared with bolometric luminosity (left) and temperature (right). Upper limits are marked as magenta triangles. Spearman's rank correlation coefficient and the probability of no correlation are shown in the top-right corner. Dashed lines represents the EM algorithm fit to the data. Note that for bolometric luminosity all multiple systems are combined together, while for bolometric temperature each component is considered separately but with the same bolometric temperature, which results in different sample sizes.

luminosity (Figure 2.13). As the latter is used as a proxy of protostellar mass (with many caveats), this result is reminiscent of the correlation between the disk mass and stellar mass observed for the more evolved disks (Natta et al. 2000; Williams & Cieza 2011; Ansdell et al. 2017). The noticeable decrease of disk mass with bolometric temperature is seen, hinting at a dependency between disk mass and evolution (ρ = −0.34, P <0.1%), as already apparent from the distributions of disk masses for Class 0 and Class I discussed above.

Finally, we assess the impact of the free-free emission on the calculated disk masses and spectral indices in Ka-band. Figure 2.14 presents the distributions of masses and spectral indices with and without correction. When the correction is not applied, the spectral indices between 8 mm and 1 cm are flatter (median spectral index drops from 2.04 to 1.69) and the disk masses increase (from 0.048 $M_\odot$ to 0.067 $M_\odot$). The spectral index change is statistically significant, with log-rank: 0.6% while mass change is less robust (log-rank: 37%). Thus, the free-free contribution can to some extent explain the shallower than expected spectral indices observed in the Ka-band Tobin et al. (2016), and it seems that without correcting for the free-free contribution the masses of the disks are slightly overestimated.

2.5.2 Evolutionary trend in dust mass

The advent of the Atacama Large Millimeter/submillimeter Array (ALMA) has made possible studying the gas and dust content of protoplanetary disks with unprecedented sensitivity. Surveys of Class II disks at different mean ages show that the disk dust mass consistently decreases with age within the Class II population (Ansdell et al. 2016; Ansdell et al. 2017; Barenfeld et al. 2016). The other outstanding conclusion from those pioneering surveys was that there is not enough dust content to form gas giant planet cores even in the youngest Class II disks (e.g., Ansdell et al. 2016). Studying even younger embedded disks can answer important questions: does the decrease of the dust mass with age happen as early as from Class 0 to Class I, so in the first 0.5 Myr; is the dust mass in the embedded disks high enough

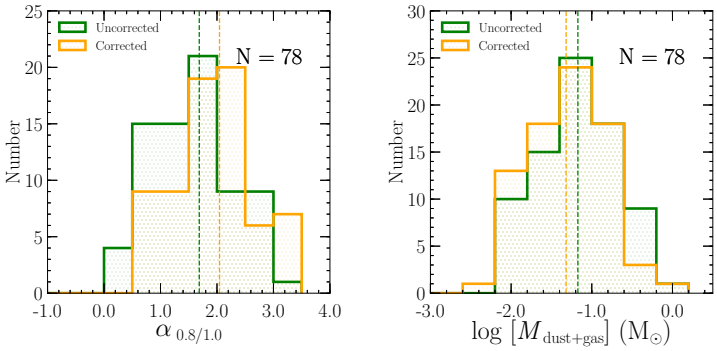


Figure 2.14: Histograms of Ka-band spectral index (left) and disk masses (right). Values not corrected for free-free contribution are shown in green and corrected in yellow. Median values and log-rank probabilities of being drawn from the same sample are: 1.69 (uncorrected), 2.04 (corrected), and 0.6% for the spectral index distributions and 0.067 $M_\odot$ (uncorrected), 0.048 $M_\odot$ (corrected), and 37% for the disk masses.

to allow the formation of the cores of gas giants?

Tobin et al. (2015b) find a median mass of ~ 0.05 $M_\odot$ for 9 Class 0 protostars in Perseus. They note that the value is about an order of magnitude higher than the disk masses for Class II objects by Andrews & Williams (2005), and about 5 times larger than the median mass for Class I disks from Jørgensen et al. (2009). With the much greater sample of VANDAM sources, we confirm a decrease in disk mass with evolutionary class. However, Jørgensen et al. (2009) pointed out that some of the assumptions used to derive mass, such as constant opacity and temperature could confuse the real picture. They considered models provided by Visser et al. (2009) which suggest that dust temperature decreases from Class 0 to Class I due to the systematic decrease in the luminosity between Class 0 and Class I. After applying factors to simulate the evolutionary effects, Jørgensen et al. (2009) find that the apparent trend between Class 0 and Class I masses becomes insignificant. Fischer et al. (2017) recently show a decrease in bolometric luminosity for a large sample of protostars in Orion, which might occur due to the decrease of the envelope emission, while protostellar luminosity still increases. Dunham et al. (2014c) suggest using different temperatures for Class 0 and Class I disks based on pure hydrodynamical simulations. However, our attempt to take into account the possible difference in luminosity between the two evolutionary classes still yields a statistically significant difference between disk masses of Class 0 and Class I protostars.

Figure 2.15 shows a comparison between VANDAM results and Class II surveys presented in Ansdell et al. (2017). The observed decrease of mass between Class 0 and Class I protostars, and further to Class II, shows that a significant fraction of dust is dispersed or incorporated into larger bodies. If the latter scenario is considered, the amount of dust-only mass available for planet formation (248 $M_\oplus$[1]) is enough to form solid cores of the giant planets. The further decrease in mass to 96 $M_\oplus$ in Class I shows that significant grain growth could occur at those early stages (Miotello et al. 2014; Sheehan & Eisner 2017). Recent ALMA surveys of Class II disks yield masses of 5-15 $M_\oplus$ for different star-forming regions (e.g., Barenfeld et al. 2016; Pascucci et al. 2016; Ansdell et al. 2016). It shows that if the core accretion is considered as

[1]values converted to Earth masses and without multiplying by 100 to exclude gas mass

a planet formation route, it may begin very early in Class 0, and the physical conditions at those early stages should be considered in planet formation models.

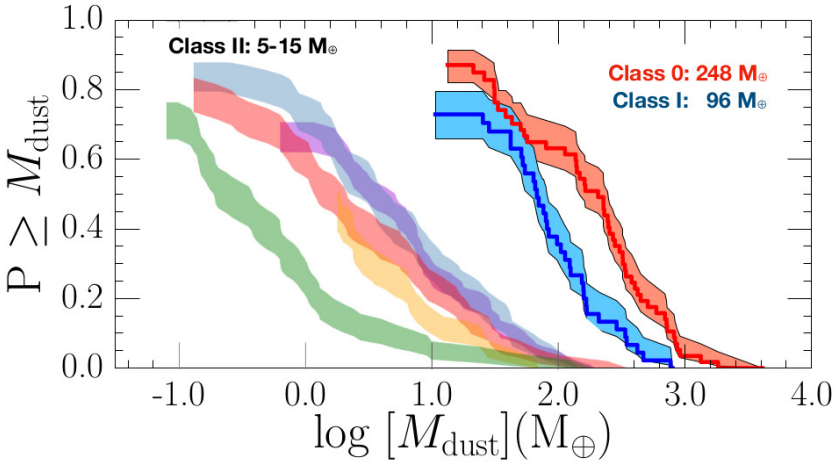


Figure 2.15: Cumulative distributions of disk masses in units of Earth mass. Class II distributions for four regions adapted from Ansdell et al. (2017). Different Class II star forming regions are presented: Taurus (purple, Andrews et al. 2013), Lupus (blue, Ansdell et al. 2016), Chamaeleon I (red, Pascucci et al. 2016), σ Orionis (yellow, Ansdell et al. 2017), and Upper Sco (green, Barenfeld et al. 2016).

2.6 Conclusions

We observed all known (84) Class 0 and I protostellar systems in the Perseus molecular cloud with the VLA at C-band (4.1 cm and 6.4 cm). The major conclusions of this work are as follows:

1. The detection rate is 61% for Class 0 and 53% for Class I protostars. Both flux densities and spectral indices do not show a significant difference between the two evolutionary stages indicating that strength and nature of the emission is independent of evolution at least through the protostellar phase.

2. The spectral index from 4.1 cm to 6.4 cm for the detected protostars has a median value of α_{median} = 0.51, consistent with moderately optically thick thermal free - free emission. The C-band spectral index shows no correlation with protostellar bolometric luminosity and temperature. Sources with resolved thermal jets have typically lower spectral indices consistent with optically thin emission from the jet, in addition to being the brightest free-free objects.

3. We detect all components in half of the close (< 500 au) binary systems present in a sample. Protostellar companions within the same system can have very different flux densities and spectral indices. There are also examples of systems where brighter Ka-band component appears fainter in C-band.

4. We greatly extended the group of the protostars characterized at centimeter wavelengths especially in the low-luminosity end. However, the radio luminosity from the protostars only in Perseus is weakly correlated with bolometric luminosity, by combining these data with previous observations spanning a larger range of $L_{\rm bol}$ we obtained a good correlation. The linear fit for the Perseus-only sample shows a flatter relation between radio and bolometric luminosity than for the merged sample.

5. We investigate correlations between the radio luminosity and molecular and atomic far-IR line luminosity from *Herschel*. We obtain moderate correlations for OH and [O I]. Comparing this result with shock models we conclude that the ionization observed as free-free emission is predominantly a result of J - type shocks. Extending this analysis to a sample of high-mass protostars can provide further insight.

6. We update the correlation between the radio luminosity and outflow force from protostars. Within the range of luminosities in Perseus there is no correlation, but inclusion of a greater range of radio luminosities and outflow forces results in a moderate correlation, consistent with previous studies. We find that the molecular outflow forces are sufficient to produce the obtained radio fluxes in our sample. It shows that while generally shock ionization is a viable explanation of free-free emission, molecular outflows have different characteristics than a thermal radio jet, likely due to the different scales probed.

7. We calculate the disk masses around protostars, using Ka-band (9 mm) flux densities corrected for free-free contribution from the C-band. A statistically significant difference is observed between Class 0 and Class I disk masses with the median disk mass being more than a factor of two higher for Class 0 protostars median dust mass 248 $M_\oplus$ in Class 0). By the Class II phase, the median disk dust mass has dropped by an order of magnitude. This result suggests that protoplanetary disks have their highest masses at early times - with a dust mass reservoir sufficient to form giant planet cores - and that grains can grow rapidly in the embedded phase. The C-band contribution lowers between 8 mm and 1 cm, while the measured disk mass is not significantly changed.

Acknowledgements: The authors thank the anonymous referee, whose comments enhanced the quality of the manuscript. The authors wish to thank Y. Shirley and J. Mottram for sharing data from their previous works, and G. Anglada for insightful comments on the draft. ŁT thanks S. van Terwisga and A. Bosman for stimulating discussions. Astrochemistry in Leiden is supported by the Netherlands Research School for Astronomy (NOVA), by a Royal Netherlands Academy of Arts and Sciences (KNAW) professor prize, and by the European Union A-ERC grant 291141 CHEMPLAN. ŁT is supported by Leiden/ESA Astrophysics Program for Summer Students (LEAPS). J.J.T. acknowledges support from the Homer L. Dodge endowed chair, and J.J.T. and Ł.T. acknowledge support from grant 639.041.439 from the Netherlands Organisation for Scientific Research (NWO). J.J.T. acknowledges past support provided by NASA through Hubble Fellowship grant #HST-HF-51300.01-A awarded by the Space Telescope Science Institute, which is operated by the Association of Universities for Research in Astronomy, Inc., for NASA, under contract NAS 5-26555. AK acknowledges support from the Polish National Science Center grant
2016/21/D/ST9/01098. ŁT and AK acknowledge support from the HECOLS International Associated Laboratory, supported in part by the Polish NCN grant DEC-2013/08/M/ST9/00664. ZYL is supported in part by NASA NNX 14AB38G, NSF AST-1313083 and AST-1716259. The

National Radio Astronomy Observatory is a facility of the National Science Foundation operated under cooperative agreement by Associated Universities, Inc. This research made use of NASA's Astrophysics Data System.

Facilities: VLA

Software: Astropy (Astropy Collaboration et al. 2013), APLpy (Robitaille & Bressert 2012), Matplotlib (Hunter 2007), MPFIT (Markwardt 2009), lifelines (Davidson-Pilon 2017), AEGEAN (Hancock et al. 2012), CASA (McMullin et al. 2007), STSDAS, ds9

Appendix

2.A Tables

Table 2.1: Protostars of the VANDAM survey

Name[a]	RA[b] J2000	Dec[b] J2000	Field[c]	Detected 6.4 cm	Detected 4.1 cm	Class	L_{bol}[d] $L_\odot$)	T_{bol}[d] K
Per-emb-1	03:43:56.805	+32:00:50.201	PerC31	Y	Y	0	1.8±0.1	27.0±1.0
Per-emb-2	03:32:17.927	+30:49:47.825	PerC23	Y	Y	0	0.9±0.1	27.0±1.0
Per-emb-3	03:29:00.574	+31:12:00.204	PerC37	Y	Y	0	0.5±0.1	32.0±2.0
Per-emb-4	03:28:39.101	+31:06:01.800	PerC12	-	-	0	0.2±0.0	31.0±3.0
Per-emb-5	03:31:20.938	+30:45:30.273	PerC24	-	Y	0	1.3±0.1	32.0±2.0
Per-emb-6	03:33:14.404	+31:07:10.714	PerC38	Y	Y	0	0.3±0.0	52.0±3.0
Per-emb-7	03:30:32.681	+30:26:26.480	PerC15	-	-	0	0.1±0.1	37.0±4.0
Per-emb-8	03:44:43.981	+32:01:35.210	PerC25	Y	Y	0	2.6±0.5	43.0±6.0
Per-emb-9	03:29:51.831	+31:39:05.904	PerC6	Y	Y	0	0.6±0.1	36.0±2.0
Per-emb-10	03:33:16.424	+31:06:52.063	PerC38	-	Y	0	0.6±0.1	30.0±2.0
Per-emb-11	03:43:57.064	+32:03:04.788	PerC2	Y	Y	0	1.5±0.1	30.0±2.0
Per-emb-12	03:29:10.536	+31:13:30.933	PerC35	Y	Y	0	7.0±0.7	29.0±2.0
Per-emb-13	03:29:12.015	+31:13:08.031	PerC35	Y	Y	0	4.0±0.3	28.0±1.0
Per-emb-14	03:29:13.547	+31:13:58.150	PerC35	Y	Y	0	0.7±0.1	31.0±2.0
Per-emb-15	03:29:04.054	+31:14:46.236	PerC8	Y	Y	0	0.4±0.1	36.0±4.0
Per-emb-16	03:43:50.978	+32:03:24.101	PerC2	-	-	0	0.4±0.0	39.0±2.0
Per-emb-17	03:27:39.104	+30:13:03.067	PerC20	Y	Y	0	4.2±0.1	59.0±11.0
Per-emb-18	03:29:11.258	+31:18:31.072	PerC37	Y	Y	0	2.8±1.7	59.0±12.0
Per-emb-19	03:29:23.497	+31:33:29.172	PerC4	Y	Y	0	0.4±0.1	60.0±3.0
Per-emb-20	03:27:43.276	+30:12:28.780	PerC20	Y	Y	0	1.4±0.2	65.0±3.0
Per-emb-21	03:29:10.668	+31:18:20.191	PerC18	-	-	0	6.9±1.9	45.0±12.0
Per-emb-22	03:25:22.409	+30:45:13.257	PerC13	Y	Y	0	3.6±0.5	43.0±2.0
Per-emb-23	03:29:17.211	+31:27:46.302	PerC7	Y	Y	0	0.8±0.1	42.0±2.0
Per-emb-24	03:28:45.297	+31:05:41.693	PerC12	-	Y	0	0.4±0.0	67.0±10.0
Per-emb-25	03:26:37.510	+30:15:27.805	PerC21	Y	Y	0	1.2±0.0	61.0±12.0
Per-emb-26	03:25:38.874	+30:44:05.283	PerC29	Y	Y	0	8.4±1.5	47.0±7.0
Per-emb-27	03:28:55.569	+31:14:37.025	PerC8	Y	Y	0	19.0±0.4	69.0±1.0
Per-emb-28	03:43:51.007	+32:03:08.042	PerC2	Y	Y	0/I	0.7±0.1	45.0±2.0
Per-emb-29	03:33:17.877	+31:09:31.816	PerC38	-	-	0/I	3.7±0.4	48.0±1.0
Per-emb-30	03:33:27.303	+31:07:10.159	PerC38	Y	Y	0/I	1.1±0.0	93.0±6.0
Per-emb-31	03:28:32.547	+31:11:05.151	PerC11	-	-	0/I	0.2±0.0	80.0±13.0
Per-emb-32	03:44:02.403	+32:02:04.734	PerC31	-	-	0/I	0.3±0.1	57.0±10.0
Per-emb-33	03:25:36.379	+30:45:14.727	PerC29	Y	-	0	8.3±0.8	57.0±3.0
Per-emb-34	03:30:15.162	+30:23:49.232	PerC28	-	Y	I	1.8±0.1	88.0±13.0
Per-emb-35	03:28:37.090	+31:13:30.787	PerC11	Y	Y	I	11.1±0.3	85.0±26.0
Per-emb-36	03:28:57.373	+31:14:15.772	PerC8	Y	Y	I	6.9±1.0	85.0±12.0
Per-emb-37	03:29:18.964	+31:23:14.304	PerC5	-	-	0	0.5±0.1	22.0±1.0
Per-emb-38	03:32:29.197	+31:02:40.759	PerC22	-	-	I	0.5±0.0	115.0±21.0
Per-emb-39	03:33:13.781	+31:20:05.204	PerC3	-	-	I	0.0±0.1	125.0±47.0
Per-emb-40	03:33:16.669	+31:07:54.901	PerC38	Y	Y	I	1.5±1.0	132.0±25.0
Per-emb-41	03:33:20.341	+31:07:21.354	PerC38	-	-	I	0.2±0.4	157.0±72.0
Per-emb-42	03:25:39.135	+30:43:57.908	PerC29	-	-	I	0.7±0.8	163.0±51.0
Per-emb-43	03:42:02.160	+31:48:02.080	PerC39	-	-	I	0.1±0.1	176.0±42.0
Per-emb-44	03:29:03.763	+31:16:03.808	PerC8	Y	Y	0/I	32.5±7.1	75.0±52.0
Per-emb-45	03:33:09.569	+31:05:31.192	PerC38	-	-	I	0.1±0.1	197.0±93.0
Per-emb-46	03:28:00.414	+30:08:01.013	PerC16	-	Y	I	0.3±0.1	221.0±7.0
Per-emb-47	03:28:34.507	+31:00:50.990	PerC19	-	Y	I	1.2±0.1	230.0±17.0
Per-emb-48	03:27:38.268	+30:13:58.448	PerC20	Y	Y	I	0.9±0.0	238.0±14.0
Per-emb-49	03:29:12.956	+31:18:14.306	PerC18	Y	Y	I	1.1±0.7	239.0±68.0
Per-emb-50	03:29:07.768	+31:21:57.128	PerC10	Y	Y	I	23.2±3.0	128.0±23.0
Per-emb-51	03:28:34.536	+31:07:05.520	PerC12	-	-	I	0.1±0.1	263.0±115.0
Per-emb-52	03:28:39.699	+31:17:31.882	PerC9	-	-	I	0.2±0.2	278.0±119.0
Per-emb-53	03:47:41.591	+32:51:43.672	PerC26	Y	Y	I	4.7±0.9	287.0±8.0
Per-emb-54	03:29:01.548	+31:20:20.497	PerC10	Y	Y	I	16.8±2.6	131.0±63.0
Per-emb-55	03:44:43.298	+32:01:31.235	PerC25	Y	Y	I	1.8±0.8	309.0±64.0
Per-emb-56	03:47:05.450	+32:43:08.239	PerC27	-	-	I	0.5±0.1	312.0±1.0
Per-emb-57	03:29:03.331	+31:23:14.573	PerC10	Y	-	I	0.1±0.5	313.0±200.0
Per-emb-58	03:28:58.422	+31:22:17.480	PerC10	-	-	I	0.6±0.5	322.0±88.0
Per-emb-59	03:28:35.039	+30:20:09.884	PerC17	-	-	I	0.0±0.1	341.0±179.0
Per-emb-60	03:29:20.068	+31:24:07.488	PerC5	-	-	I	0.3±1.1	363.0±240.0

Table 2.1: continued.

Name[a]	RA[b] J2000	Dec[b] J2000	Field[c]	Detected 6.4 cm	Detected 4.1 cm	Class	L_{bol}[d] $L_\odot$)	T_{bol}[d] K
Per-emb-61	03:44:21.357	+31:59:32.514	PerC1	-	-	I	0.2±0.2	371.0±107.0
Per-emb-62	03:44:12.976	+32:01:35.412	PerC1	Y	Y	I	1.8±0.4	378.0±29.0
Per-emb-63	03:28:43.270	+31:17:32.930	PerC9	Y	Y	I	1.9±0.4	436.0±9.0
Per-emb-64	03:33:12.851	+31:21:24.020	PerC3	Y	Y	I	3.2±0.6	438.0±8.0
Per-emb-65	03:28:56.315	+31:22:27.797	PerC10	-	-	I	0.2±0.2	440.0±191.0
Per-emb-66	03:43:45.149	+32:03:58.607	PerC2	-	-	I	0.7±0.2	542.0±110.0
Per-bolo-58	03:29:25.463	+31:28:14.880	PerC7	-	-	0	0.1±0.5	18.0±18.0
Per-bolo-45	03:29:07.699	+31:17:16.800	PerC8	-	-	0	0.1±0.1	18.0±18.0
L1451-MMS	03:25:10.244	+30:23:55.058	PerC14	-	-	0	0.1±0.1	18.0±18.0
L1448IRS2E	03:25:25.660	+30:44:56.695	PerC13	-	-	0	0.1±0.1	18.0±18.0
B1-bN	03:33:21.209	+31:07:43.665	PerC38	-	-	0	0.3±0.1	14.7±1.0
B1-bS	03:33:21.355	+31:07:26.372	PerC38	-	-	0	0.7±0.1	17.7±1.0
L1448IRS1	03:25:09.448	+30:46:21.932	PerC36	Y	Y	I	—	—
L1448NW	03:25:35.670	+30:45:34.192	PerC29	Y	Y	0	1.4±0.1	22.0±1.0
L1448IRS3A	03:25:36.499	+30:45:21.880	PerC29	Y	Y	I	9.2±1.3	47.0±2.0
SVS13C	03:29:01.970	+31:15:38.053	PerC8	Y	Y	0	1.5±0.2	21.0±1.0
SVS13B	03:29:03.077	+31:15:51.739	PerC18	-	Y	0	1.0±1.0	20.0±20.0
IRAS03363+3207	03:39:25.546	+32:17:07.088	PerC33	Y	Y	I?	—	—
EDJ2009-263	03:30:27.161	+30:28:29.613	PerC15	-	-	Flat	0.2±0.1	340.0±18.0
EDJ2009-285	03:32:46.942	+30:59:17.797	PerC22	-	-	II	0.5±0.1	920.0±18.0
IRAS03295+3050	03:32:34.066	+31:00:55.620	PerC22	-	-	II	0.2±0.1	1300.0±18.0
L1455IRS2	03:27:47.689	+30:12:04.314	PerC20	Y	Y	Flat	2.5±0.1	740.0±18.0
EDJ2009-385	03:44:18.168	+32:04:56.907	PerC34	-	-	II	0.4±0.1	1200.0±18.0
EDJ2009-366	03:43:59.650	+32:01:54.007	PerC31	Y	Y	II	1.8±0.1	620.0±18.0
EDJ2009-269	03:30:44.013	+30:32:46.812	PerC32	-	Y	II	1.3±0.1	1200.0±18.0
EDJ2009-183	03:28:59.294	+31:15:48.407	PerC8	Y	Y	Flat	3.2±0.1	100.0±18.0
EDJ2009-164	03:28:53.961	+31:18:09.349	PerC9	-	-	II	0.1±0.1	890.0±18.0
EDJ2009-156	03:28:51.028	+31:18:18.409	PerC9	Y	Y	II	0.0±0.1	740.0±18.0
EDJ2009-172	03:28:56.649	+31:18:35.449	PerC18	Y	-	II	0.4±0.1	1100.0±18.0
IRAS4B'	03:29:12.841	+31:13:06.893	PerC35	-	-	0	0.1±0.1	20.0±20.0
EDJ2009-233	03:29:17.675	+31:22:44.922	PerC5	Y	Y	II	1.4±0.1	1300.0±18.0
EDJ2009-235	03:29:18.258	+31:23:19.758	PerC5	Y	-	II	0.5±0.1	650.0±18.0
SVS3	03:29:10.419	+31:21:59.072	PerC10	Y	Y	II	0.5±0.1	—
SVS13A2	03:29:03.386	+31:16:01.622	PerC8	Y	Y	0?	0.1±0.1	20.0±18.0
EDJ2009-173	03:28:56.963	+31:16:22.199	PerC8	-	Y	II	0.1±0.1	1100.0±18.0

Notes. [a] Names: Per-emb-XX (Enoch et al. 2009), EDJ2009-XXX (Evans et al. 2009), SVS-X (Strom et al. 1976) [b] Coordinates from VANDAM Ka-band observations (Tobin et al. 2016) [c] Name of the observational field where source was closest to the peak of the primary beam response. [d] Values from Enoch et al. (2009), Sadavoy et al. (2014) and Young et al. (2015)

Table 2.2: Summary of the observed fields

Name[a]	Extragalactic 6.4 cm	Protostars 6.4 cm	YSOc 6.4 cm mJy/beam	RMS 6.4 cm	Beam size & PA 6.4 cm	Extragalactic 4 cm	Protostars 4 cm mJy/beam	YSOc 4 cm	RMS 4 cm	Beam size & PA 4 cm
PerC1	7	5	0	0.0053	0.36" x 0.52" -76.40	9	3	1	0.0041	0.23" x 0.34" -76.03
PerC2	11	4	0	0.0050	0.34" x 0.48" 79.18	7	4	0	0.0040	0.22" x 0.31" 78.94
PerC3	25	1	0	0.0050	0.35" x 0.38" -82.95	11	1	0	0.0038	0.23" x 0.25" 89.22
PerC4	12	2	0	0.0049	0.35" x 0.36" -84.58	13	1	0	0.0042	0.23" x 0.24" 87.64
PerC5	9	7	1	0.0051	0.35" x 0.39" 62.69	8	5	1	0.0040	0.22" x 0.24" 83.94
PerC6	11	1	0	0.0050	0.35" x 0.50" -76.67	7	1	0	0.0040	0.22" x 0.32" -76.80
PerC7	15	3	0	0.0049	0.35" x 0.37" -83.60	9	1	0	0.0041	0.23" x 0.24" -87.92
PerC8	19	20	0	0.0048	0.35" x 0.41" 86.58	13	20	1	0.0039	0.22" x 0.26" 87.31
PerC9	15	19	0	0.0051	0.34" x 0.38" 88.11	10	15	0	0.0038	0.22" x 0.25" 88.50
PerC10	15	11	2	0.0051	0.35" x 0.38" 57.66	10	7	2	0.0040	0.23" x 0.24" 81.70
PerC11	16	9	0	0.0050	0.36" x 0.39" -64.98	12	3	0	0.0040	0.23" x 0.25" -78.38
PerC12	14	0	0	0.0052	0.34" x 0.44" 81.86	12	1	0	0.0045	0.23" x 0.28" 74.00
PerC13	21	9	0	0.0052	0.36" x 0.42" -83.87	14	8	0	0.0042	0.23" x 0.27" -81.69
PerC14	17	0	0	0.0052	0.35" x 0.52" -75.00	15	0	0	0.0040	0.22" x 0.33" -74.99
PerC15	8	0	0	0.0055	0.35" x 0.56" -74.66	2	0	0	0.0053	0.25" x 0.46" -80.62
PerC16	22	1	0	0.0047	0.36" x 0.42" -65.46	15	1	0	0.0037	0.23" x 0.26" -81.34
PerC17	26	0	0	0.0050	0.36" x 0.41" -63.46	17	0	0	0.0036	0.23" x 0.26" -82.94
PerC18	6	13	1	0.0057	0.34" x 0.39" 87.70	7	13	1	0.0042	0.22" x 0.26" 88.68
PerC19	19	0	0	0.0053	0.34" x 0.46" 80.66	14	1	0	0.0045	0.22" x 0.30" 72.32
PerC20	28	4	0	0.0053	0.35" x 0.38" 86.90	22	4	0	0.0041	0.22" x 0.24" 88.98
PerC21	10	1	0	0.0048	0.35" x 0.49" -76.18	10	1	0	0.0038	0.23" x 0.32" -75.90
PerC22	12	0	0	0.0050	0.35" x 0.37" -82.78	8	0	0	0.0038	0.23" x 0.24" -88.25
PerC23	12	2	0	0.0050	0.34" x 0.39" -86.53	10	2	0	0.0039	0.22" x 0.25" -87.35
PerC24	10	1	0	0.0066	0.34" x 0.38" -83.93	7	2	0	0.0040	0.22" x 0.25" -84.83
PerC25	17	2	0	0.0049	0.34" x 0.36" -78.68	12	2	0	0.0037	0.25" x 0.26" 75.30
PerC26	16	1	0	0.0048	0.34" x 0.36" -65.17	14	1	0	0.0037	0.22" x 0.23" -63.02
PerC27	20	0	0	0.0048	0.34" x 0.36" -75.53	18	0	0	0.0037	0.22" x 0.24" -72.96
PerC28	14	0	0	0.0051	0.36" x 0.40" -32.98	12	1	0	0.0041	0.23" x 0.25" -74.85
PerC29	19	7	0	0.0053	0.36" x 0.45" -86.34	12	7	0	0.0042	0.23" x 0.29" -83.56
PerC31	13	5	0	0.0051	0.34" x 0.50" 77.98	12	5	0	0.0040	0.22" x 0.32" 78.46
PerC32	9	0	0	0.0054	0.35" x 0.53" -75.83	7	2	0	0.0043	0.22" x 0.35" -75.47
PerC33	14	1	0	0.0050	0.35" x 0.53" -75.80	8	1	0	0.0040	0.22" x 0.34" -75.40
PerC34	14	4	0	0.0053	0.35" x 0.50" -76.70	12	2	0	0.0041	0.22" x 0.32" -76.92
PerC35	18	19	0	0.0048	0.35" x 0.42" 84.35	16	18	0	0.0039	0.23" x 0.27" 85.51
PerC36	14	5	0	0.0068	0.38" x 0.59" -67.14	7	3	0	0.0055	0.25" x 0.39" -69.37
PerC37	6	13	0	0.0068	0.38" x 0.56" -67.40	5	12	0	0.0055	0.25" x 0.37" -69.58
PerC38	24	4	0	0.0049	0.34" x 0.37" -84.82	18	5	0	0.0040	0.22" x 0.24" 80.28
PerC39	29	0	0	0.0049	0.35" x 0.37" -84.52	17	0	1	0.0040	0.22" x 0.24" 82.26

Table 2.3: C-band observation results

Name	RA	Dec	F^a_{vint} 6.4 cm	F^b_{vpeak} 6.4 cm	RMS 6.4 cm	F^a_{vint} 4.1 cm	F^b_{vpeak} 4.1 cm	RMS 4.1 cm	Sp. Index Int.[c]	Sp. Index Peak[d]
	J2000	J2000	mJy	mJy/beam	mJy/beam	mJy	mJy/beam	mJy/beam		
Per-emb-1	03:43:56.805	+32:00:50.201	0.0508±0.0065	0.0476	0.0052	0.0651±0.0059	0.0539	0.0043	0.55±0.34	0.27±0.30
Per-emb-2	03:32:17.927	+30:49:47.825	0.0365±0.0065	0.0278	0.0050	0.0508±0.0056	0.0426	0.0039	0.73±0.46	0.94±0.44
Per-emb-2-A	03:32:17.931	+30:49:47.705	0.0365±0.0065	0.0278	0.0050	0.0508±0.0056	0.0426	0.0039	0.73±0.46	0.94±0.44
Per-emb-2-B	03:32:17.926	+30:49:47.750	-77.0±-77.0	-77.0	-77.0	-77.0±-77.0	-77.0	-77.0	—	—
Per-emb-3	03:29:00.574	+31:12:00.204	0.1012±0.0215	0.0784	0.0068	0.0763±0.0073	0.0673	0.0055	-0.62±0.51	-0.33±0.26
Per-emb-4	03:28:39.101	+31:06:01.800	<0.0160±0.0053	<0.0160	0.0053	<0.0140±0.0047	<0.0140	0.0047	—	—
Per-emb-5	03:31:20.938	+30:45:30.273	<0.0197±0.0000	<0.0000	0.0000	0.0283±0.0184	0.0252	0.0040	>0.80±1.44	>-99.00±-99.00
Per-emb-5-A	03:31:20.943	+30:45:30.271	<0.0197±0.0066	<0.0000	0.0066	0.0283±0.0184	0.0252	0.0040	>0.80±1.61	>-99.00±-99.00
Per-emb-5-B	03:31:20.935	+30:45:30.246	-77.0±-77.0	-77.0	-77.0	-77.0±-77.0	-77.0	-77.0	—	—
Per-emb-6	03:33:14.404	+31:07:10.714	0.0664±0.0057	0.0669	0.0050	0.0706±0.0051	0.0691	0.0042	0.14±0.25	0.07±0.21
Per-emb-7	03:30:32.681	+30:26:26.480	<0.0174±0.0058	<0.0174	0.0058	<0.0183±0.0061	<0.0183	0.0061	—	—
Per-emb-8	03:44:43.981	+32:01:35.210	0.2788±0.0122	0.1323	0.0049	0.3132±0.0166	0.1240	0.0037	0.26±0.15	-0.14±0.10
Per-emb-9	03:29:51.831	+31:39:05.904	0.0420±0.0094	0.0324	0.0050	0.0277±0.0050	0.0281	0.0040	-0.92±0.63	-0.31±0.46
Per-emb-10	03:33:16.424	+31:06:52.063	<0.0148±0.0049	<0.0148	0.0049	0.0334±0.0054	0.0312	0.0041	>1.80±0.81	>1.65±0.79
Per-emb-11	03:43:57.064	+32:03:04.788	0.0366±0.0058	0.0376	0.0052	0.0469±0.0061	0.0425	0.0046	0.55±0.45	0.27±0.39
Per-emb-11-A	03:43:57.064	+32:03:04.787	<0.0158±0.0053	<0.0158	0.0053	<0.0137±0.0046	<0.0137	0.0046	—	—
Per-emb-11-B	03:43:56.881	+32:03:02.977	0.0366±0.0058	0.0376	0.0052	0.0469±0.0061	0.0425	0.0046	0.55±0.45	0.27±0.39
Per-emb-11-C	03:43:57.687	+32:03:09.975	<0.0159±0.0053	<0.0159	0.0053	<0.0140±0.0047	<0.0140	0.0047	—	—
Per-emb-12	03:29:10.536	+31:13:30.933	0.1557±0.0144	0.1026	0.0049	0.2550±0.0139	0.1297	0.0039	1.09±0.24	0.52±0.12
Per-emb-12-A	03:29:10.536	+31:13:30.926	0.0539±0.0085	0.0466	0.0049	0.1166±0.0081	0.0917	0.0039	1.70±0.38	1.49±0.25
Per-emb-12-B	03:29:10.427	+31:13:32.098	0.1017±0.0059	0.1026	0.0049	0.1384±0.0057	0.1297	0.0039	0.68±0.16	0.52±0.12
Per-emb-13	03:29:12.015	+31:13:08.031	0.0618±0.0058	0.0590	0.0049	0.0776±0.0070	0.0549	0.0039	0.50±0.29	-0.16±0.24
Per-emb-14	03:29:13.547	+31:13:58.150	0.0193±0.0031	0.0261	0.0049	0.0591±0.0093	0.0357	0.0040	2.47±0.50	0.69±0.48
Per-emb-15	03:29:04.054	+31:14:46.236	0.0547±0.0077	0.0386	0.0050	0.0528±0.0154	0.0217	0.0041	-0.08±0.71	-1.27±0.51
Per-emb-16	03:43:50.978	+32:03:24.101	<0.0149±0.0050	<0.0149	0.0050	<0.0119±0.0040	<0.0119	0.0040	—	—
Per-emb-17	03:27:39.104	+30:13:03.067	0.0471±0.0056	0.0495	0.0054	0.0596±0.0089	0.0582	0.0042	0.52±0.42	0.36±0.29
Per-emb-17-A	03:27:39.104	+30:13:03.078	0.0471±0.0056	0.0495	0.0054	0.0596±0.0089	0.0582	0.0042	0.52±0.42	0.36±0.29
Per-emb-17-B	03:27:39.115	+30:13:02.839	<0.0161±0.0053	<0.0161	0.0053	<0.0125±0.0042	<0.0125	0.0042	—	—
Per-emb-18	03:29:11.258	+31:18:31.072	0.1919±0.0090	0.1326	0.0058	0.1957±0.0059	0.1505	0.0043	0.04±0.12	0.28±0.11
Per-emb-18-A	03:29:11.254	+31:18:31.061	0.1919±0.0090	0.1326	0.0058	0.1957±0.0059	0.1505	0.0043	0.04±0.12	0.28±0.11
Per-emb-18-B	03:29:11.261	+31:18:31.072	-77.0±-77.0	-77.0	-77.0	-77.0±-77.0	-77.0	-77.0	—	—
Per-emb-19	03:29:23.497	+31:33:29.172	0.0560±0.0087	0.0429	0.0049	0.0371±0.0059	0.0321	0.0042	-0.91±0.49	-0.64±0.38
Per-emb-20	03:27:43.276	+30:12:28.780	0.1477±0.0083	0.1093	0.0054	0.1384±0.0124	0.1098	0.0042	-0.14±0.23	0.01±0.14
Per-emb-21	03:29:10.668	+31:18:20.191	<0.0173±0.0057	<0.0173	0.0057	<0.0127±0.0042	<0.0127	0.0042	—	—
Per-emb-22	03:25:22.409	+30:45:13.257	0.1426±0.0147	0.0978	0.0052	0.1806±0.0149	0.0957	0.0042	0.52±0.29	-0.05±0.15
Per-emb-22-A	03:25:22.409	+30:45:13.253	0.1067±0.0069	0.0978	0.0052	0.1348±0.0072	0.0957	0.0042	0.51±0.18	-0.05±0.15
Per-emb-22-B	03:25:22.352	+30:45:13.151	0.0359±0.0079	0.0360	0.0052	0.0459±0.0077	0.0384	0.0042	0.54±0.61	0.14±0.40
Per-emb-23	03:29:17.211	+31:27:46.302	0.0363±0.0060	0.0356	0.0050	0.0483±0.0057	0.0432	0.0043	0.63±0.45	0.43±0.38
Per-emb-24	03:28:45.297	+31:05:41.693	<0.0159±0.0053	<0.0159	0.0053	0.0222±0.0037	0.0266	0.0046	>0.74±0.82	>1.13±0.83
Per-emb-25	03:26:37.510	+30:15:27.812	0.0510±0.0091	0.0326	0.0048	0.0641±0.0059	0.0507	0.0038	0.50±0.44	0.97±0.36

Table 2.3: continued.

Name	RA	Dec	F^a_{vint} 6.4 cm	F^b_{vpeak} 6.4 cm	RMS 6.4 cm	F^a_{vint} 4.1 cm	F^b_{vpeak} 4.1 cm	RMS 4.1 cm	Sp. Index Int.[c]	Sp. Index Peak[d]
	J2000	J2000	mJy	mJy/beam	mJy/beam	mJy	mJy/beam	mJy/beam		
Per-emb-26	03:25:38.874	+30:44:05.283	0.0581±0.0068	0.0557	0.0054	0.0911±0.0049	0.0937	0.0045	0.99±0.28	1.15±0.24
Per-emb-27	03:28:55.569	+31:14:37.025	0.0589±0.0067	0.0527	0.0051	0.1085±0.0110	0.0744	0.0044	1.34±0.34	0.76±0.25
Per-emb-27-A	03:28:55.569	+31:14:37.022	0.0589±0.0067	0.0527	0.0051	0.0846±0.0056	0.0744	0.0044	0.80±0.29	0.76±0.25
Per-emb-27-B	03:28:55.563	+31:14:36.407	<0.0153±0.0051	<0.0153	0.0051	0.0239±0.0054	0.0271	0.0044	>0.98±0.89	>1.26±0.82
Per-emb-28	03:43:51.007	+32:03:08.042	0.0207±0.0053	0.0208	0.0050	0.0272±0.0053	0.0228	0.0040	0.60±0.71	0.20±0.65
Per-emb-29	03:33:17.877	+31:09:31.816	<0.0166±0.0055	<0.0166	0.0055	<0.0165±0.0055	<0.0165	0.0055	—	—
Per-emb-30	03:33:27.303	+31:07:10.159	0.2747±0.0171	0.1542	0.0055	0.2815±0.0254	0.1681	0.0055	0.05±0.24	0.19±0.11
Per-emb-31	03:28:32.547	+31:11:05.151	<0.0162±0.0054	<0.0162	0.0054	<0.0151±0.0050	<0.0151	0.0050	—	—
Per-emb-32	03:44:02.403	+32:02:04.734	<0.0155±0.0052	<0.0155	0.0052	<0.0126±0.0042	<0.0126	0.0042	—	—
Per-emb-32-A	03:44:02.403	+32:02:04.729	<0.0155±0.0052	<0.0155	0.0052	<0.0126±0.0042	<0.0126	0.0042	—	—
Per-emb-32-B	03:44:02.632	+32:01:59.451	<0.0155±0.0052	<0.0155	0.0052	<0.0126±0.0042	<0.0126	0.0042	—	—
Per-emb-33	03:25:36.379	+30:45:14.727	0.1648±0.0139	0.1154	0.0053	0.1386±0.0071	0.1041	0.0042	-0.38±0.22	-0.23±0.13
Per-emb-33-A	03:25:36.380	+30:45:14.722	0.0259±0.0057	0.0282	0.0053	<0.0127±0.0042	<0.0127	0.0042	<-1.57±0.88	<-1.75±0.84
Per-emb-33-B	03:25:36.380	+30:45:14.722	<0.0618±0.0206	<0.0618	0.0206	<1.6581±0.5527	<1.6581	0.5527	—	—
Per-emb-33-C	03:25:36.321	+30:45:14.913	0.1389±0.0082	0.1154	0.0053	0.1386±0.0071	0.1041	0.0042	-0.00±0.17	-0.23±0.13
Per-emb-34	03:30:15.162	+30:23:49.232	<0.0153±0.0051	<0.0153	0.0051	0.0269±0.0087	0.0178	0.0041	>1.25±1.02	>0.34±0.89
Per-emb-35	03:28:37.090	+31:13:30.787	0.0710±0.0084	0.0626	0.0051	0.1109±0.0110	0.0750	0.0043	0.98±0.34	0.40±0.22
Per-emb-35-A	03:28:37.090	+31:13:30.787	0.0576±0.0056	0.0626	0.0051	0.0815±0.0054	0.0750	0.0043	0.76±0.26	0.40±0.22
Per-emb-35-B	03:28:37.219	+31:13:31.751	0.0134±0.0028	0.0240	0.0051	0.0294±0.0056	0.0271	0.0043	1.73±0.62	0.27±0.58
Per-emb-36	03:28:57.373	+31:14:15.772	0.2433±0.0192	0.1267	0.0051	0.2523±0.0169	0.1037	0.0044	0.08±0.23	-0.44±0.13
Per-emb-36-A	03:28:57.373	+31:14:15.764	0.2433±0.0192	0.1267	0.0051	0.2523±0.0169	0.1037	0.0044	0.08±0.23	-0.44±0.13
Per-emb-36-B	03:28:57.370	+31:14:16.072	<0.0152±0.0051	<0.0152	0.0051	<0.0132±0.0044	<0.0132	0.0044	—	—
Per-emb-37	03:29:18.964	+31:23:14.304	<0.0153±0.0051	<0.0153	0.0051	<0.0122±0.0041	<0.0122	0.0041	—	—
Per-emb-38	03:32:29.197	+31:02:40.759	<0.0150±0.0050	<0.0150	0.0050	<0.0115±0.0038	<0.0115	0.0038	—	—
Per-emb-39	03:33:13.781	+31:20:05.204	<0.0155±0.0052	<0.0155	0.0052	<0.0129±0.0043	<0.0129	0.0043	—	—
Per-emb-40	03:33:16.669	+31:07:54.901	0.1129±0.0102	0.0956	0.0049	0.1232±0.0081	0.1014	0.0041	0.19±0.25	0.13±0.14
Per-emb-40-A	03:33:16.669	+31:07:54.902	0.0940±0.0055	0.0956	0.0049	0.1106±0.0051	0.1014	0.0041	0.36±0.17	0.13±0.14
Per-emb-40-B	03:33:16.679	+31:07:55.269	0.0189±0.0047	0.0265	0.0049	0.0125±0.0030	0.0175	0.0041	-0.91±0.76	-0.91±0.66
Per-emb-41	03:33:20.341	+31:07:21.354	<0.0148±0.0049	<0.0148	0.0049	<0.0123±0.0041	<0.0123	0.0041	—	—
Per-emb-42	03:25:39.135	+30:43:57.908	<0.0164±0.0054	<0.0164	0.0054	<0.0138±0.0046	<0.0138	0.0046	—	—
Per-emb-43	03:42:02.160	+31:48:02.080	<0.0149±0.0050	<0.0149	0.0050	<0.0125±0.0042	<0.0125	0.0042	—	—
Per-emb-44	03:29:03.763	+31:16:03.808	0.1236±0.0132	0.0736	0.0050	0.2015±0.0108	0.0958	0.0042	1.08±0.26	0.58±0.18
Per-emb-44-A	03:29:03.766	+31:16:03.810	0.0590±0.0057	0.0736	0.0050	0.0929±0.0048	0.0958	0.0042	1.00±0.24	0.58±0.18
Per-emb-44-B	03:29:03.742	+31:16:03.789	0.0645±0.0075	0.0709	0.0050	0.1086±0.0060	0.0850	0.0042	1.15±0.28	0.40±0.19
Per-emb-45	03:33:09.569	+31:05:31.192	<0.0178±0.0059	<0.0178	0.0059	<0.0200±0.0067	<0.0200	0.0067	—	—
Per-emb-46	03:28:00.414	+30:08:01.013	<0.0142±0.0047	<0.0142	0.0047	0.0152±0.0031	0.0205	0.0037	>0.15±0.86	>0.81±0.84
Per-emb-47	03:28:34.507	+31:00:50.990	<0.0158±0.0053	<0.0158	0.0053	0.0393±0.0100	0.0242	0.0045	>2.01±0.93	>0.94±0.84
Per-emb-48	03:27:38.268	+30:13:58.448	0.0721±0.0076	0.0572	0.0055	0.0616±0.0051	0.0632	0.0045	-0.35±0.30	0.22±0.26
Per-emb-48-A	03:27:38.277	+30:13:58.558	<0.0166±0.0055	<0.0166	0.0055	<0.0135±0.0045	<0.0135	0.0045	—	—
Per-emb-48-B	03:27:38.258	+30:13:58.319	0.0721±0.0076	0.0572	0.0055	0.0616±0.0051	0.0632	0.0045	-0.35±0.30	0.22±0.26

Table 2.3: continued.

Name	RA	Dec	F^a_{vint} 6.4 cm	F^b_{vpeak} 6.4 cm	RMS 6.4 cm	F^a_{vint} 4.1 cm	F^b_{vpeak} 4.1 cm	RMS 4.1 cm	Sp. Index Int.[c]	Sp. Index Peak[d]
	J2000	J2000	mJy	mJy/beam	mJy/beam	mJy	mJy/beam	mJy/beam		
Per-emb-49	03:29:12.956	+31:18:14.306	0.0477±0.0102	0.0284	0.0058	0.0590±0.0096	0.0333	0.0043	0.47±0.59	0.36±0.54
Per-emb-49-A	03:29:12.952	+31:18:14.289	0.0119±0.0027	0.0232	0.0058	0.0337±0.0047	0.0333	0.0043	2.29±0.59	0.80±0.62
Per-emb-49-B	03:29:12.975	+31:18:14.396	0.0358±0.0075	0.0284	0.0058	0.0253±0.0050	0.0256	0.0043	-0.76±0.63	-0.23±0.59
Per-emb-50	03:29:07.768	+31:21:57.128	0.1096±0.0080	0.0899	0.0053	0.1355±0.0061	0.1199	0.0045	0.47±0.19	0.63±0.15
Per-emb-51	03:28:34.536	+31:07:05.520	<0.0177±0.0059	<0.0177	0.0059	<0.0182±0.0061	<0.0182	0.0061	—	—
Per-emb-52	03:28:39.699	+31:17:31.882	<0.0160±0.0053	<0.0160	0.0053	<0.0129±0.0043	<0.0129	0.0043	—	—
Per-emb-53	03:47:41.591	+32:51:43.672	0.0192±0.0043	0.0265	0.0048	0.0284±0.0044	0.0307	0.0037	0.86±0.60	0.33±0.48
Per-emb-54	03:29:01.548	+31:20:20.497	0.0387±0.0080	0.0313	0.0055	0.0730±0.0063	0.0658	0.0049	1.40±0.49	1.64±0.42
Per-emb-55	03:44:43.298	+32:01:31.235	0.0423±0.0064	0.0386	0.0049	0.0559±0.0052	0.0470	0.0037	0.61±0.39	0.44±0.33
Per-emb-55-A	03:44:43.297	+32:01:31.223	<0.0147±0.0049	<0.0147	0.0049	<0.0111±0.0037	<0.0111	0.0037	—	—
Per-emb-55-B	03:44:43.333	+32:01:31.636	0.0423±0.0064	0.0386	0.0049	0.0559±0.0052	0.0470	0.0037	0.61±0.39	0.44±0.33
Per-emb-56	03:47:05.450	+32:43:08.239	<0.0144±0.0048	<0.0144	0.0048	<0.0112±0.0037	<0.0112	0.0037	—	—
Per-emb-57	03:29:03.331	+31:23:14.573	0.0179±0.0044	0.0233	0.0053	<0.0133±0.0044	<0.0133	0.0044	<-0.66±0.91	<-1.24±0.89
Per-emb-58	03:28:58.422	+31:22:17.480	<0.0154±0.0051	<0.0154	0.0051	<0.0123±0.0041	<0.0123	0.0041	—	—
Per-emb-59	03:28:35.039	+30:20:09.884	<0.0151±0.0050	<0.0151	0.0050	<0.0108±0.0036	<0.0108	0.0036	—	—
Per-emb-60	03:29:20.068	+31:24:07.488	<0.0153±0.0051	<0.0153	0.0051	<0.0122±0.0040	<0.0122	0.0040	—	—
Per-emb-61	03:44:21.357	+31:59:32.514	<0.0164±0.0055	<0.0164	0.0055	<0.0135±0.0045	<0.0135	0.0045	—	—
Per-emb-62	03:44:12.976	+32:01:35.419	0.0529±0.0070	0.0503	0.0056	0.0725±0.0067	0.0598	0.0049	0.70±0.36	0.38±0.30
Per-emb-63	03:28:43.270	+31:17:32.930	0.0985±0.0070	0.0844	0.0052	0.0988±0.0047	0.0940	0.0039	0.01±0.19	0.24±0.16
Per-emb-64	03:33:12.851	+31:21:24.020	0.3704±0.0073	0.3086	0.0050	0.3856±0.0061	0.3076	0.0038	0.09±0.06	-0.01±0.04
Per-emb-65	03:28:56.315	+31:22:27.797	<0.0158±0.0053	<0.0158	0.0053	<0.0132±0.0044	<0.0132	0.0044	—	—
Per-emb-66	03:43:45.149	+32:03:58.607	<0.0155±0.0052	<0.0155	0.0052	<0.0133±0.0044	<0.0133	0.0044	—	—
Per-bolo-58	03:29:25.463	+31:28:14.880	<0.0151±0.0050	<0.0151	0.0050	<0.0135±0.0045	<0.0135	0.0045	—	—
Per-bolo-45	03:29:07.699	+31:17:16.800	<0.0173±0.0057	<0.0173	0.0057	<0.0182±0.0061	<0.0182	0.0061	—	—
L1451-MMS	03:25:10.244	+30:23:55.058	<0.0155±0.0052	<0.0155	0.0052	<0.0121±0.0040	<0.0121	0.0040	—	—
L1448IRS2E	03:25:25.660	+30:44:56.695	<0.0157±0.0052	<0.0157	0.0052	<0.0128±0.0043	<0.0128	0.0043	—	—
B1-bN	03:33:21.209	+31:07:43.665	<0.0149±0.0050	<0.0149	0.0050	<0.0126±0.0042	<0.0126	0.0042	—	—
B1-bS	03:33:21.355	+31:07:26.372	<0.0149±0.0050	<0.0149	0.0050	<0.0126±0.0042	<0.0126	0.0042	—	—
L1448IRS1	03:25:09.448	+30:46:21.932	0.0577±0.0078	0.0593	0.0068	0.0742±0.0063	0.0729	0.0055	0.55±0.35	0.45±0.30
L1448IRS1-A	03:25:09.448	+30:46:21.932	0.0577±0.0078	0.0593	0.0068	0.0742±0.0063	0.0729	0.0055	0.55±0.35	0.45±0.30
L1448IRS1-B	03:25:09.409	+30:46:20.603	<0.0205±0.0068	<0.0205	0.0068	<0.0166±0.0055	<0.0166	0.0055	—	—
L1448NW	03:25:35.670	+30:45:34.192	0.0247±0.0038	0.0288	0.0053	0.0549±0.0106	0.0307	0.0043	1.76±0.54	0.14±0.51
L1448NW-A	03:25:35.669	+30:45:34.109	0.0247±0.0038	0.0288	0.0053	0.0401±0.0060	0.0307	0.0043	1.06±0.48	0.14±0.51
L1448NW-B	03:25:35.672	+30:45:34.356	<0.0160±0.0053	<0.0160	0.0053	0.0149±0.0046	0.0268	0.0043	>-0.16±1.00	>1.14±0.82
L1448IRS3A	03:25:36.499	+30:45:21.880	0.4922±0.0149	0.3717	0.0053	0.5074±0.0149	0.3607	0.0043	0.07±0.09	-0.07±0.04
SVS13C	03:29:01.970	+31:15:38.053	1.0676±0.0218	0.6812	0.0049	1.2095±0.0296	0.6753	0.0039	0.28±0.07	-0.02±0.02
SVS13B	03:29:03.077	+31:15:51.739	<0.0224±0.0075	<0.0224	0.0075	0.0541±0.0101	0.0385	0.0084	>1.94±0.84	>1.19±0.88
IRAS03363+3207	03:39:25.546	+32:17:07.088	0.0222±0.0048	0.0230	0.0050	0.0492±0.0049	0.0467	0.0040	1.75±0.52	1.56±0.52
EDJ2009-263	03:30:27.161	+30:28:29.613	<0.0168±0.0056	<0.0168	0.0056	<0.0168±0.0056	<0.0168	0.0056	—	—
EDJ2009-285	03:32:46.942	+30:59:17.797	<0.0331±0.0110	<0.0331	0.0110	<0.1088±0.0362	<0.1088	0.0362	—	—

Table 2.3: continued.

Name	RA	Dec	$F^a_{\nu int}$ 6.4 cm	$F^b_{\nu peak}$ 6.4 cm	RMS 6.4 cm	$F^a_{\nu int}$ 4.1 cm	$F^b_{\nu peak}$ 4.1 cm	RMS 4.1 cm	Sp. Index Int.[c]	Sp. Index Peak[d]
	J2000	J2000	mJy	mJy/beam	mJy/beam	mJy	mJy/beam	mJy/beam		
IRAS03295+3050	03:32:34.066	+31:00:55.620	<0.0169±0.0056	<0.0169	0.0056	<0.0155±0.0052	<0.0155	0.0052	–	–
L1455IRS2	03:27:47.689	+30:12:04.314	0.0342±0.0086	0.0188	0.0057	0.0308±0.0063	0.0288	0.0049	-0.23±0.71	0.94±0.77
EDJ2009-385	03:44:18.168	+32:04:56.907	<0.0158±0.0053	<0.0158	0.0053	<0.0123±0.0041	<0.0123	0.0041	–	–
EDJ2009-366	03:43:59.650	+32:01:54.007	0.0331±0.0068	0.0273	0.0051	0.0521±0.0124	0.0262	0.0040	1.00±0.69	-0.09±0.53
EDJ2009-269	03:30:44.013	+30:32:46.812	<0.0163±0.0054	<0.0163	0.0054	0.0556±0.0153	0.0199	0.0043	>2.70±0.95	>0.44±0.88
EDJ2009-269-A	03:30:44.014	+30:32:46.813	<0.0163±0.0054	<0.0000	0.0054	0.0358±0.0102	0.0199	0.0043	>1.73±0.97	>-99.00±-99.00
EDJ2009-269-B	03:30:43.975	+30:32:46.583	<0.0163±0.0054	<0.0163	0.0054	0.0198±0.0051	0.0199	0.0043	>0.42±0.93	>0.44±0.88
EDJ2009-183	03:28:59.294	+31:15:48.407	0.0488±0.0069	0.0424	0.0049	0.0499±0.0048	0.0498	0.0040	0.05±0.38	0.36±0.31
EDJ2009-183-A	03:28:59.294	+31:15:48.406	0.0488±0.0069	0.0424	0.0049	0.0499±0.0048	0.0498	0.0040	0.05±0.38	0.36±0.31
EDJ2009-183-B	03:28:59.374	+31:15:48.401	<0.0146±0.0049	<0.0146	0.0049	<0.0120±0.0040	<0.0120	0.0040	–	–
EDJ2009-164	03:28:53.961	+31:18:09.349	<0.0174±0.0058	<0.0174	0.0058	<0.0158±0.0053	<0.0158	0.0053	–	–
EDJ2009-156	03:28:51.028	+31:18:18.409	0.0175±0.0054	0.0200	0.0055	0.0295±0.0042	0.0362	0.0046	1.15±0.75	1.31±0.67
EDJ2009-156-A	03:28:51.028	+31:18:18.409	<0.0166±0.0055	<0.0166	0.0055	<0.0140±0.0047	<0.0140	0.0047	–	–
EDJ2009-156-B	03:28:51.111	+31:18:15.443	0.0175±0.0054	0.0200	0.0055	0.0295±0.0042	0.0362	0.0046	1.15±0.75	1.31±0.67
EDJ2009-172	03:28:56.649	+31:18:35.449	0.0297±0.0068	0.0271	0.0074	<0.0242±0.0080	<0.0242	0.0080	<-0.45±0.89	<-0.26±0.95
EDJ2009-173	03:28:56.963	+31:16:22.199	<0.0152±0.0051	<0.0152	0.0051	0.0316±0.0048	0.0352	0.0044	>1.60±0.81	>1.84±0.78
SVS13A2	03:29:03.386	+31:16:01.622	0.0743±0.0056	0.0768	0.0050	0.1023±0.0051	0.0938	0.0041	0.70±0.20	0.44±0.17
IRAS4B'	03:29:12.841	+31:13:06.893	<0.0146±0.0049	<0.0146	0.0049	<0.0119±0.0040	<0.0119	0.0040	–	–
EDJ2009-233	03:29:17.675	+31:22:44.922	0.1002±0.0078	0.0794	0.0052	0.1161±0.0059	0.1004	0.0043	0.33±0.21	0.52±0.17
EDJ2009-235	03:29:18.258	+31:23:19.758	0.0192±0.0056	0.0199	0.0051	<0.0121±0.0040	<0.0121	0.0040	<-1.01±0.97	<-1.10±0.93
SVS3	03:29:10.419	+31:21:59.072	0.6720±0.0136	0.4126	0.0056	0.7219±0.0268	0.4945	0.0051	0.16±0.09	0.40±0.04
SVS3-A	03:29:10.419	+31:21:59.072	0.2562±0.0074	0.2188	0.0056	0.2005±0.0183	0.1700	0.0052	-0.54±0.21	-0.56±0.09
SVS3-B	03:29:10.369	+31:21:58.963	0.4158±0.0062	0.4126	0.0056	0.5213±0.0085	0.4945	0.0051	0.50±0.05	0.40±0.04

Notes. Flag –77 is used when non-detection results from the source being unresolved. [(a)] $F_{\nu,\mathrm{int}}$ - Integrated flux resulting from area under 2D Gaussian fit to the source. [(b)] $F_{\nu,\mathrm{peak}}$ - Peak value of the flux density on the source. [(c)] S p. Index (Int.) - Spectral index calculated with the integrated flux. [(d)] S p. Index (Peak) - Spectral index calculated with the peak flux.

Table 2.4: Young Stellar Object candidates

Name	RA	Dec	F^a_{vint} 6.4 cm	F^b_{vpeak} 6.4 cm	RMS 6.4 cm	F^a_{vint} 4.1 cm	F^b_{vpeak} 4.1 cm	RMS 4.1 cm	Sp. Index	Sp. Index
	J2000	J2000	mJy	mJy/beam	mJy/beam	mJy	mJy/beam	mJy/beam	Int.[c]	Peak[d]
Per-emb-1	03:43:56.805	+32:00:50.201	0.0508±0.0065	0.0476	0.0052	0.0651±0.0059	0.0539	0.0043	0.55±0.34	0.27±0.30
Per-emb-2	03:32:17.927	+30:49:47.825	0.0365±0.0065	0.0278	0.0050	0.0508±0.0056	0.0426	0.0039	0.73±0.46	0.94±0.44
Per-emb-2-A	03:32:17.931	+30:49:47.705	0.0365±0.0065	0.0278	0.0050	0.0508±0.0056	0.0426	0.0039	0.73±0.46	0.94±0.44
Per-emb-2-B	03:32:17.926	+30:49:47.750	-77.0±-77.0	-77.0	-77.0	-77.0±-77.0	-77.0	-77.0	—	—
Per-emb-3	03:29:00.574	+31:12:00.204	0.1012±0.0215	0.0784	0.0068	0.0763±0.0073	0.0673	0.0055	-0.62±0.51	-0.33±0.26
Per-emb-4	03:28:39.101	+31:06:01.800	<0.0160±0.0053	<0.0160	0.0053	<0.0140±0.0047	<0.0140	0.0047	—	—
Per-emb-5	03:31:20.938	+30:45:30.273	<0.0197±0.0000	<0.0000	0.0000	0.0283±0.0184	0.0252	0.0040	>0.80±1.44	>-99.00±-99.00
Per-emb-5-A	03:31:20.943	+30:45:30.271	<0.0197±0.0066	<0.0000	0.0066	0.0283±0.0184	0.0252	0.0040	>0.80±1.61	>-99.00±-99.00
Per-emb-5-B	03:31:20.935	+30:45:30.246	-77.0±-77.0	-77.0	-77.0	-77.0±-77.0	-77.0	-77.0	—	—
Per-emb-6	03:33:14.404	+31:07:10.714	0.0664±0.0057	0.0669	0.0050	0.0706±0.0051	0.0691	0.0042	0.14±0.25	0.07±0.21
Per-emb-7	03:30:32.681	+30:26:26.480	<0.0174±0.0058	<0.0174	0.0058	<0.0183±0.0061	<0.0183	0.0061	—	—
Per-emb-8	03:44:43.981	+32:01:35.210	0.2788±0.0122	0.1323	0.0049	0.3132±0.0166	0.1240	0.0037	0.26±0.15	-0.14±0.10
Per-emb-9	03:29:51.831	+31:39:05.904	0.0420±0.0094	0.0324	0.0050	0.0277±0.0050	0.0281	0.0040	-0.92±0.63	-0.31±0.46
Per-emb-10	03:33:16.424	+31:06:52.063	<0.0148±0.0049	<0.0148	0.0049	0.0334±0.0054	0.0312	0.0041	>1.80±0.81	>1.65±0.79
Per-emb-11	03:43:57.064	+32:03:04.788	0.0366±0.0058	0.0376	0.0052	0.0469±0.0061	0.0425	0.0046	0.55±0.45	0.27±0.39
Per-emb-11-A	03:43:57.064	+32:03:04.787	<0.0158±0.0053	<0.0158	0.0053	<0.0137±0.0046	<0.0137	0.0046	—	—
Per-emb-11-B	03:43:56.881	+32:03:02.977	0.0366±0.0058	0.0376	0.0052	0.0469±0.0061	0.0425	0.0046	0.55±0.45	0.27±0.39
Per-emb-11-C	03:43:57.687	+32:03:09.975	<0.0159±0.0053	<0.0159	0.0053	<0.0140±0.0047	<0.0140	0.0047	—	—
Per-emb-12	03:29:10.536	+31:13:30.933	0.1557±0.0144	0.1026	0.0049	0.2550±0.0139	0.1297	0.0039	1.09±0.24	0.52±0.12
Per-emb-12-A	03:29:10.536	+31:13:30.926	0.0539±0.0085	0.0466	0.0049	0.1166±0.0081	0.0917	0.0039	1.70±0.38	1.49±0.25
Per-emb-12-B	03:29:10.427	+31:13:32.098	0.1017±0.0059	0.1026	0.0049	0.1384±0.0057	0.1297	0.0039	0.68±0.16	0.52±0.12
Per-emb-13	03:29:12.015	+31:13:08.031	0.0618±0.0058	0.0590	0.0049	0.0776±0.0070	0.0549	0.0039	0.50±0.29	-0.16±0.24
Per-emb-14	03:29:13.547	+31:13:58.150	0.0193±0.0031	0.0261	0.0049	0.0591±0.0093	0.0357	0.0040	2.47±0.50	0.69±0.48
Per-emb-15	03:29:04.054	+31:14:46.236	0.0547±0.0077	0.0386	0.0050	0.0528±0.0154	0.0217	0.0041	-0.08±0.71	-1.27±0.51
Per-emb-16	03:43:50.978	+32:03:24.101	<0.0149±0.0050	<0.0149	0.0050	<0.0119±0.0040	<0.0119	0.0040	—	—
Per-emb-17	03:27:39.104	+30:13:03.067	0.0471±0.0056	0.0495	0.0054	0.0596±0.0089	0.0582	0.0042	0.52±0.42	0.36±0.29
Per-emb-17-A	03:27:39.104	+30:13:03.078	0.0471±0.0056	0.0495	0.0054	0.0596±0.0089	0.0582	0.0042	0.52±0.42	0.36±0.29
Per-emb-17-B	03:27:39.115	+30:13:02.839	<0.0161±0.0053	<0.0161	0.0053	<0.0125±0.0042	<0.0125	0.0042	—	—
Per-emb-18	03:29:11.258	+31:18:31.072	0.1919±0.0090	0.1326	0.0058	0.1957±0.0059	0.1505	0.0043	0.04±0.12	0.28±0.11
Per-emb-18-A	03:29:11.254	+31:18:31.061	0.1919±0.0090	0.1326	0.0058	0.1957±0.0059	0.1505	0.0043	0.04±0.12	0.28±0.11
Per-emb-18-B	03:29:11.261	+31:18:31.072	-77.0±-77.0	-77.0	-77.0	-77.0±-77.0	-77.0	-77.0	—	—
Per-emb-19	03:29:23.497	+31:33:29.172	0.0560±0.0087	0.0429	0.0049	0.0371±0.0059	0.0321	0.0042	-0.91±0.49	-0.64±0.38
Per-emb-20	03:27:43.276	+30:12:28.780	0.1477±0.0083	0.1093	0.0054	0.1384±0.0124	0.1098	0.0042	-0.14±0.23	0.01±0.14
Per-emb-21	03:29:10.668	+31:18:20.191	<0.0173±0.0057	<0.0173	0.0057	<0.0127±0.0042	<0.0127	0.0042	—	—
Per-emb-22	03:25:22.409	+30:45:13.257	0.1426±0.0147	0.0978	0.0052	0.1806±0.0149	0.0957	0.0042	0.52±0.29	-0.05±0.15
Per-emb-22-A	03:25:22.409	+30:45:13.253	0.1067±0.0069	0.0978	0.0052	0.1348±0.0072	0.0957	0.0042	0.51±0.18	-0.05±0.15
Per-emb-22-B	03:25:22.352	+30:45:13.151	0.0359±0.0079	0.0360	0.0052	0.0459±0.0077	0.0384	0.0042	0.54±0.61	0.14±0.40
Per-emb-23	03:29:17.211	+31:27:46.302	0.0363±0.0060	0.0356	0.0050	0.0483±0.0057	0.0432	0.0043	0.63±0.45	0.43±0.38
Per-emb-24	03:28:45.297	+31:05:41.693	<0.0159±0.0053	<0.0159	0.0053	0.0222±0.0037	0.0266	0.0046	>0.74±0.82	>1.13±0.83
Per-emb-25	03:26:37.510	+30:15:27.812	0.0510±0.0091	0.0326	0.0048	0.0641±0.0059	0.0507	0.0038	0.50±0.44	0.97±0.36

Table 2.4: continued.

Name	RA	Dec	F^a_{vint} 6.4 cm	F^b_{vpeak} 6.4 cm	RMS 6.4 cm	F^a_{vint} 4.1 cm	F^b_{vpeak} 4.1 cm	RMS 4.1 cm	Sp. Index Int.[c]	Sp. Index Peak[d]
	J2000	J2000	mJy	mJy/beam	mJy/beam	mJy	mJy/beam	mJy/beam		
Per-emb-26	03:25:38.874	+30:44:05.283	0.0581±0.0068	0.0557	0.0054	0.0911±0.0049	0.0937	0.0045	0.99±0.28	1.15±0.24
Per-emb-27	03:28:55.569	+31:14:37.025	0.0589±0.0067	0.0527	0.0051	0.1085±0.0110	0.0744	0.0044	1.34±0.34	0.76±0.25
Per-emb-27-A	03:28:55.569	+31:14:37.022	0.0589±0.0067	0.0527	0.0051	0.0846±0.0056	0.0744	0.0044	0.80±0.29	0.76±0.25
Per-emb-27-B	03:28:55.563	+31:14:36.407	<0.0153±0.0051	<0.0153	0.0051	0.0239±0.0054	0.0271	0.0044	>0.98±0.89	>1.26±0.82
Per-emb-28	03:43:51.007	+32:03:08.042	0.0207±0.0053	0.0208	0.0050	0.0272±0.0053	0.0228	0.0040	0.60±0.71	0.20±0.65
Per-emb-29	03:33:17.877	+31:09:31.816	<0.0166±0.0055	<0.0166	0.0055	<0.0165±0.0055	<0.0165	0.0055	—	—
Per-emb-30	03:33:27.303	+31:07:10.159	0.2747±0.0171	0.1542	0.0055	0.2815±0.0254	0.1681	0.0055	0.05±0.24	0.19±0.11
Per-emb-31	03:28:32.547	+31:11:05.151	<0.0162±0.0054	<0.0162	0.0054	<0.0151±0.0050	<0.0151	0.0050	—	—
Per-emb-32	03:44:02.403	+32:02:04.734	<0.0155±0.0052	<0.0155	0.0052	<0.0126±0.0042	<0.0126	0.0042	—	—
Per-emb-32-A	03:44:02.403	+32:02:04.729	<0.0155±0.0052	<0.0155	0.0052	<0.0126±0.0042	<0.0126	0.0042	—	—
Per-emb-32-B	03:44:02.632	+32:01:59.451	<0.0155±0.0052	<0.0155	0.0052	<0.0126±0.0042	<0.0126	0.0042	—	—
Per-emb-33	03:25:36.379	+30:45:14.727	0.1648±0.0139	0.1154	0.0053	0.1386±0.0071	0.1041	0.0042	-0.38±0.22	-0.23±0.13
Per-emb-33-A	03:25:36.380	+30:45:14.722	0.0259±0.0057	0.0282	0.0053	<0.0127±0.0042	<0.0127	0.0042	<-1.57±0.88	<-1.75±0.84
Per-emb-33-B	03:25:36.380	+30:45:14.722	<0.0618±0.0206	<0.0618	0.0206	<1.6581±0.5527	<1.6581	0.5527	—	—
Per-emb-33-C	03:25:36.321	+30:45:14.913	0.1389±0.0082	0.1154	0.0053	0.1386±0.0071	0.1041	0.0042	-0.00±0.17	-0.23±0.13
Per-emb-34	03:30:15.162	+30:23:49.232	<0.0153±0.0051	<0.0153	0.0051	0.0269±0.0087	0.0178	0.0041	>1.25±1.02	>0.34±0.89
Per-emb-35	03:28:37.090	+31:13:30.787	0.0710±0.0084	0.0626	0.0051	0.1109±0.0110	0.0750	0.0043	0.98±0.34	0.40±0.22
Per-emb-35-A	03:28:37.090	+31:13:30.787	0.0576±0.0056	0.0626	0.0051	0.0815±0.0054	0.0750	0.0043	0.76±0.26	0.40±0.22
Per-emb-35-B	03:28:37.219	+31:13:31.751	0.0134±0.0028	0.0240	0.0051	0.0294±0.0056	0.0271	0.0043	1.73±0.62	0.27±0.58
Per-emb-36	03:28:57.373	+31:14:15.772	0.2433±0.0192	0.1267	0.0051	0.2523±0.0169	0.1037	0.0044	0.08±0.23	-0.44±0.13
Per-emb-36-A	03:28:57.373	+31:14:15.764	0.2433±0.0192	0.1267	0.0051	0.2523±0.0169	0.1037	0.0044	0.08±0.23	-0.44±0.13
Per-emb-36-B	03:28:57.370	+31:14:16.072	<0.0152±0.0051	<0.0152	0.0051	<0.0132±0.0044	<0.0132	0.0044	—	—
Per-emb-37	03:29:18.964	+31:23:14.304	<0.0153±0.0051	<0.0153	0.0051	<0.0122±0.0041	<0.0122	0.0041	—	—
Per-emb-38	03:32:29.197	+31:02:40.759	<0.0150±0.0050	<0.0150	0.0050	<0.0115±0.0038	<0.0115	0.0038	—	—
Per-emb-39	03:33:13.781	+31:20:05.204	<0.0155±0.0052	<0.0155	0.0052	<0.0129±0.0043	<0.0129	0.0043	—	—
Per-emb-40	03:33:16.669	+31:07:54.901	0.1129±0.0102	0.0956	0.0049	0.1232±0.0081	0.1014	0.0041	0.19±0.25	0.13±0.14
Per-emb-40-A	03:33:16.669	+31:07:54.902	0.0940±0.0055	0.0956	0.0049	0.1106±0.0051	0.1014	0.0041	0.36±0.17	0.13±0.14
Per-emb-40-B	03:33:16.679	+31:07:55.269	0.0189±0.0047	0.0265	0.0049	0.0125±0.0030	0.0175	0.0041	-0.91±0.76	-0.91±0.66
Per-emb-41	03:33:20.341	+31:07:21.354	<0.0148±0.0049	<0.0148	0.0049	<0.0123±0.0041	<0.0123	0.0041	—	—
Per-emb-42	03:25:39.135	+30:43:57.908	<0.0164±0.0054	<0.0164	0.0054	<0.0138±0.0046	<0.0138	0.0046	—	—
Per-emb-43	03:42:02.160	+31:48:02.080	<0.0149±0.0050	<0.0149	0.0050	<0.0125±0.0042	<0.0125	0.0042	—	—
Per-emb-44	03:29:03.763	+31:16:03.808	0.1236±0.0132	0.0736	0.0050	0.2015±0.0108	0.0958	0.0042	1.08±0.26	0.58±0.18
Per-emb-44-A	03:29:03.766	+31:16:03.810	0.0590±0.0057	0.0736	0.0050	0.0929±0.0048	0.0958	0.0042	1.00±0.24	0.58±0.18
Per-emb-44-B	03:29:03.742	+31:16:03.789	0.0645±0.0075	0.0709	0.0050	0.1086±0.0060	0.0850	0.0042	1.15±0.28	0.40±0.19
Per-emb-45	03:33:09.569	+31:05:31.192	<0.0178±0.0059	<0.0178	0.0059	<0.0200±0.0067	<0.0200	0.0067	—	—
Per-emb-46	03:28:00.414	+30:08:01.013	<0.0142±0.0047	<0.0142	0.0047	0.0152±0.0031	0.0205	0.0037	>0.15±0.86	>0.81±0.84
Per-emb-47	03:28:34.507	+31:00:50.990	<0.0158±0.0053	<0.0158	0.0053	0.0393±0.0100	0.0242	0.0045	>2.01±0.93	>0.94±0.84
Per-emb-48	03:27:38.268	+30:13:58.448	0.0721±0.0076	0.0572	0.0055	0.0616±0.0051	0.0632	0.0045	-0.35±0.30	0.22±0.26
Per-emb-48-A	03:27:38.277	+30:13:58.558	<0.0166±0.0055	<0.0166	0.0055	<0.0135±0.0045	<0.0135	0.0045	—	—
Per-emb-48-B	03:27:38.258	+30:13:58.319	0.0721±0.0076	0.0572	0.0055	0.0616±0.0051	0.0632	0.0045	-0.35±0.30	0.22±0.26

Table 2.4: continued.

Name	RA	Dec	F^a_{vint} 6.4 cm	F^b_{vpeak} 6.4 cm	RMS 6.4 cm	F^a_{vint} 4.1 cm	F^b_{vpeak} 4.1 cm	RMS 4.1 cm	Sp. Index Int.[c]	Sp. Index Peak[d]
	J2000	J2000	mJy	mJy/beam	mJy/beam	mJy	mJy/beam	mJy/beam		
Per-emb-49	03:29:12.956	+31:18:14.306	0.0477±0.0102	0.0284	0.0058	0.0590±0.0096	0.0333	0.0043	0.47±0.59	0.36±0.54
Per-emb-49-A	03:29:12.952	+31:18:14.289	0.0119±0.0027	0.0232	0.0058	0.0337±0.0047	0.0333	0.0043	2.29±0.59	0.80±0.62
Per-emb-49-B	03:29:12.975	+31:18:14.396	0.0358±0.0075	0.0284	0.0058	0.0253±0.0050	0.0256	0.0043	-0.76±0.63	-0.23±0.59
Per-emb-50	03:29:07.768	+31:21:57.128	0.1096±0.0080	0.0899	0.0053	0.1355±0.0061	0.1199	0.0045	0.47±0.19	0.63±0.15
Per-emb-51	03:28:34.536	+31:07:05.520	<0.0177±0.0059	<0.0177	0.0059	<0.0182±0.0061	<0.0182	0.0061	—	—
Per-emb-52	03:28:39.699	+31:17:31.882	<0.0160±0.0053	<0.0160	0.0053	<0.0129±0.0043	<0.0129	0.0043	—	—
Per-emb-53	03:47:41.591	+32:51:43.672	0.0192±0.0043	0.0265	0.0048	0.0284±0.0044	0.0307	0.0037	0.86±0.60	0.33±0.48
Per-emb-54	03:29:01.548	+31:20:20.497	0.0387±0.0080	0.0313	0.0055	0.0730±0.0063	0.0658	0.0049	1.40±0.49	1.64±0.42
Per-emb-55	03:44:43.298	+32:01:31.235	0.0423±0.0064	0.0386	0.0049	0.0559±0.0052	0.0470	0.0037	0.61±0.39	0.44±0.33
Per-emb-55-A	03:44:43.297	+32:01:31.223	<0.0147±0.0049	<0.0147	0.0049	<0.0111±0.0037	<0.0111	0.0037	—	—
Per-emb-55-B	03:44:43.333	+32:01:31.636	0.0423±0.0064	0.0386	0.0049	0.0559±0.0052	0.0470	0.0037	0.61±0.39	0.44±0.33
Per-emb-56	03:47:05.450	+32:43:08.239	<0.0144±0.0048	<0.0144	0.0048	<0.0112±0.0037	<0.0112	0.0037	—	—
Per-emb-57	03:29:03.331	+31:23:14.573	0.0179±0.0044	0.0233	0.0053	<0.0133±0.0044	<0.0133	0.0044	<-0.66±0.91	<-1.24±0.89
Per-emb-58	03:28:58.422	+31:22:17.480	<0.0154±0.0051	<0.0154	0.0051	<0.0123±0.0041	<0.0123	0.0041	—	—
Per-emb-59	03:28:35.039	+30:20:09.884	<0.0151±0.0050	<0.0151	0.0050	<0.0108±0.0036	<0.0108	0.0036	—	—
Per-emb-60	03:29:20.068	+31:24:07.488	<0.0153±0.0051	<0.0153	0.0051	<0.0122±0.0040	<0.0122	0.0040	—	—
Per-emb-61	03:44:21.357	+31:59:32.514	<0.0164±0.0055	<0.0164	0.0055	<0.0135±0.0045	<0.0135	0.0045	—	—
Per-emb-62	03:44:12.976	+32:01:35.419	0.0529±0.0070	0.0503	0.0056	0.0725±0.0067	0.0598	0.0049	0.70±0.36	0.38±0.30
Per-emb-63	03:28:43.270	+31:17:32.930	0.0985±0.0070	0.0844	0.0052	0.0988±0.0047	0.0940	0.0039	0.01±0.19	0.24±0.16
Per-emb-64	03:33:12.851	+31:21:24.020	0.3704±0.0073	0.3086	0.0050	0.3856±0.0061	0.3076	0.0038	0.09±0.06	-0.01±0.04
Per-emb-65	03:28:56.315	+31:22:27.797	<0.0158±0.0053	<0.0158	0.0053	<0.0132±0.0044	<0.0132	0.0044	—	—
Per-emb-66	03:43:45.149	+32:03:58.607	<0.0155±0.0052	<0.0155	0.0052	<0.0133±0.0044	<0.0133	0.0044	—	—
Per-bolo-58	03:29:25.463	+31:28:14.880	<0.0151±0.0050	<0.0151	0.0050	<0.0135±0.0045	<0.0135	0.0045	—	—
Per-bolo-45	03:29:07.699	+31:17:16.800	<0.0173±0.0057	<0.0173	0.0057	<0.0182±0.0061	<0.0182	0.0061	—	—
L1451-MMS	03:25:10.244	+30:23:55.058	<0.0155±0.0052	<0.0155	0.0052	<0.0121±0.0040	<0.0121	0.0040	—	—
L1448IRS2E	03:25:25.660	+30:44:56.695	<0.0157±0.0052	<0.0157	0.0052	<0.0128±0.0043	<0.0128	0.0043	—	—
B1-bN	03:33:21.209	+31:07:43.665	<0.0149±0.0050	<0.0149	0.0050	<0.0126±0.0042	<0.0126	0.0042	—	—
B1-bS	03:33:21.355	+31:07:26.372	<0.0149±0.0050	<0.0149	0.0050	<0.0126±0.0042	<0.0126	0.0042	—	—
L1448IRS1	03:25:09.448	+30:46:21.932	0.0577±0.0078	0.0593	0.0068	0.0742±0.0063	0.0729	0.0055	0.55±0.35	0.45±0.30
L1448IRS1-A	03:25:09.448	+30:46:21.932	0.0577±0.0078	0.0593	0.0068	0.0742±0.0063	0.0729	0.0055	0.55±0.35	0.45±0.30
L1448IRS1-B	03:25:09.409	+30:46:20.603	<0.0205±0.0068	<0.0205	0.0068	<0.0166±0.0055	<0.0166	0.0055	—	—
L1448NW	03:25:35.670	+30:45:34.192	0.0247±0.0038	0.0288	0.0053	0.0549±0.0106	0.0307	0.0043	1.76±0.54	0.14±0.51
L1448NW-A	03:25:35.669	+30:45:34.109	0.0247±0.0038	0.0288	0.0053	0.0401±0.0060	0.0307	0.0043	1.06±0.48	0.14±0.51
L1448NW-B	03:25:35.672	+30:45:34.356	<0.0160±0.0053	<0.0160	0.0053	0.0149±0.0046	0.0268	0.0043	>-0.16±1.00	>1.14±0.82
L1448IRS3A	03:25:36.499	+30:45:21.880	0.4922±0.0149	0.3717	0.0053	0.5074±0.0149	0.3607	0.0043	0.07±0.09	-0.07±0.04
SVS13C	03:29:01.970	+31:15:38.053	1.0676±0.0218	0.6812	0.0049	1.2095±0.0296	0.6753	0.0039	0.28±0.07	-0.02±0.02
SVS13B	03:29:03.077	+31:15:51.739	<0.0224±0.0075	<0.0224	0.0075	0.0541±0.0101	0.0385	0.0084	>1.94±0.84	>1.19±0.88
IRAS03363+3207	03:39:25.546	+32:17:07.088	0.0222±0.0048	0.0230	0.0050	0.0492±0.0049	0.0467	0.0040	1.75±0.52	1.56±0.52
EDJ2009-263	03:30:27.161	+30:28:29.613	<0.0168±0.0056	<0.0168	0.0056	<0.0168±0.0056	<0.0168	0.0056	—	—
EDJ2009-285	03:32:46.942	+30:59:17.797	<0.0331±0.0110	<0.0331	0.0110	<0.1088±0.0362	<0.1088	0.0362	—	—

Table 2.4: continued.

Name	RA	Dec	F^a_{vint} 6.4 cm	F^b_{vpeak} 6.4 cm	RMS 6.4 cm	F^a_{vint} 4.1 cm	F^b_{vpeak} 4.1 cm	RMS 4.1 cm	Sp. Index Int.[c]	Sp. Index Peak[d]
	J2000	J2000	mJy	mJy/beam	mJy/beam	mJy	mJy/beam	mJy/beam		
IRAS03295+3050	03:32:34.066	+31:00:55.620	<0.0169±0.0056	<0.0169	0.0056	<0.0155±0.0052	<0.0155	0.0052	—	—
L1455IRS2	03:27:47.689	+30:12:04.314	0.0342±0.0086	0.0188	0.0057	0.0308±0.0063	0.0288	0.0049	-0.23±0.71	0.94±0.77
EDJ2009-385	03:44:18.168	+32:04:56.907	<0.0158±0.0053	<0.0158	0.0053	<0.0123±0.0041	<0.0123	0.0041	—	—
EDJ2009-366	03:43:59.650	+32:01:54.007	0.0331±0.0068	0.0273	0.0051	0.0521±0.0124	0.0262	0.0040	1.00±0.69	-0.09±0.53
EDJ2009-269	03:30:44.013	+30:32:46.812	<0.0163±0.0054	<0.0163	0.0054	0.0556±0.0153	0.0199	0.0043	>2.70±0.95	>0.44±0.88
EDJ2009-269-A	03:30:44.014	+30:32:46.813	<0.0163±0.0054	<0.0000	0.0054	0.0358±0.0102	0.0199	0.0043	>1.73±0.97	>-99.00±-99.00
EDJ2009-269-B	03:30:43.975	+30:32:46.583	<0.0163±0.0054	<0.0163	0.0054	0.0198±0.0051	0.0199	0.0043	>0.42±0.93	>0.44±0.88
EDJ2009-183	03:28:59.294	+31:15:48.407	0.0488±0.0069	0.0424	0.0049	0.0499±0.0048	0.0498	0.0040	0.05±0.38	0.36±0.31
EDJ2009-183-A	03:28:59.294	+31:15:48.406	0.0488±0.0069	0.0424	0.0049	0.0499±0.0048	0.0498	0.0040	0.05±0.38	0.36±0.31
EDJ2009-183-B	03:28:59.374	+31:15:48.401	<0.0146±0.0049	<0.0146	0.0049	<0.0120±0.0040	<0.0120	0.0040	—	—
EDJ2009-164	03:28:53.961	+31:18:09.349	<0.0174±0.0058	<0.0174	0.0058	<0.0158±0.0053	<0.0158	0.0053	—	—
EDJ2009-156	03:28:51.028	+31:18:18.409	0.0175±0.0054	0.0200	0.0055	0.0295±0.0042	0.0362	0.0046	1.15±0.75	1.31±0.67
EDJ2009-156-A	03:28:51.028	+31:18:18.409	<0.0166±0.0055	<0.0166	0.0055	<0.0140±0.0047	<0.0140	0.0047	—	—
EDJ2009-156-B	03:28:51.111	+31:18:15.443	0.0175±0.0054	0.0200	0.0055	0.0295±0.0042	0.0362	0.0046	1.15±0.75	1.31±0.67
EDJ2009-172	03:28:56.649	+31:18:35.449	0.0297±0.0068	0.0271	0.0074	<0.0242±0.0080	<0.0242	0.0080	<-0.45±0.89	<-0.26±0.95
EDJ2009-173	03:28:56.963	+31:16:22.199	<0.0152±0.0051	<0.0152	0.0051	0.0316±0.0048	0.0352	0.0044	>1.60±0.81	>1.84±0.78
SVS13A2	03:29:03.386	+31:16:01.622	0.0743±0.0056	0.0768	0.0050	0.1023±0.0051	0.0938	0.0041	0.70±0.20	0.44±0.17
IRAS4B'	03:29:12.841	+31:13:06.893	<0.0146±0.0049	<0.0146	0.0049	<0.0119±0.0040	<0.0119	0.0040	—	—
EDJ2009-233	03:29:17.675	+31:22:44.922	0.1002±0.0078	0.0794	0.0052	0.1161±0.0059	0.1004	0.0043	0.33±0.21	0.52±0.17
EDJ2009-235	03:29:18.258	+31:23:19.758	0.0192±0.0056	0.0199	0.0051	<0.0121±0.0040	<0.0121	0.0040	<-1.01±0.97	<-1.10±0.93
SVS3	03:29:10.419	+31:21:59.072	0.6720±0.0136	0.4126	0.0056	0.7219±0.0268	0.4945	0.0051	0.16±0.09	0.40±0.04
SVS3-A	03:29:10.419	+31:21:59.072	0.2562±0.0074	0.2188	0.0056	0.2005±0.0183	0.1700	0.0052	-0.54±0.21	-0.56±0.09
SVS3-B	03:29:10.369	+31:21:58.963	0.4158±0.0062	0.4126	0.0056	0.5213±0.0085	0.4945	0.0051	0.50±0.05	0.40±0.04

Notes. Flag −77 is used when non-detection results from the source being unresolved.

[(a)] $F_{\nu,\mathrm{int}}$ - Integrated flux resulting from area under 2D Gaussian fit to the source. [(b)] $F_{\nu,\mathrm{peak}}$ - Peak value of the flux density on the source. [(c)] S p. Index (Int.) - Spectral index calculated with the integrated flux. [(d)] S p. Index (Peak) - Spectral index calculated with the peak flux.

Table 2.5: Known non-protostellar sources

Type[a]	Name[b]	RA	Dec	F_{vint}	F_{vpeak}	RMS	F_{vint}	F_{vpeak}	RMS	Sp. Index	Sp. Index
			6.4 cm	6.4 cm	6.4 cm	4.1 cm	4.1 cm	4.1 cm	Int.	Peak	
	J2000	J2000	mJy	mJy/beam	mJy/beam	mJy	mJy/beam	mJy/beam			
*iC	Cl*IC348LRL1888	03:44:19.78	+31:59:18.85	0.0535±0.0073	0.0454	0.0055	0.0507±0.0064	0.0426	0.0045	-0.11±0.41	-0.14±0.35
Rad	FOW2011-7	03:44:31.47	+32:00:39.43	0.3100±0.0455	0.0685	0.0067	0.1292±0.0608	0.0312	0.0077	-1.93±1.08	-1.37±0.59
*	PSZ2003J034436.5	03:44:36.46	+32:03:13.60	0.1227±0.0147	0.1019	0.0108	<0.0910±0.0303	<0.0910	0.0303	<-0.66±0.78	<-0.25±0.77
X	CXOPZ134	03:44:36.90	+32:01:23.30	1.1031±0.0188	0.9293	0.0131	—	—	—	—	—
Rad	RAC97-VLA37	03:28:37.2	+31:21:25.45	0.5419±0.0148	0.4454	0.0121	—	—	—	—	—
X	WMW2010120	03:28:59.66	+31:25:42.88	0.1378±0.0125	0.1207	0.0109	0.1812±0.1133	0.1366	0.0409	0.60±1.39	0.27±0.69
Rad	RAC97-VLA32	03:29:20.70	+31:15:49.69	0.7378±0.0531	0.4459	0.0346	—	—	—	—	—
Rad	FOW201126	03:29:30.93	+31:22:11.85	1.2263±0.0273	0.8864	0.0180	—	—	—	—	—
X	XMMUJ032821.5	03:28:21.39	+31:14:40.26	0.5440±0.0171	0.4205	0.0142	—	—	—	—	—
Rad	RAC97VLA36	03:28:32.79	+31:14:45.71	0.4585±0.0721	0.1196	0.0276	—	—	—	—	—
Rad	RAC97VLA12	03:28:59.85	+31:14:02.89	0.1897±0.0137	0.1609	0.0127	—	—	—	—	—
cor	EYG2006Bolo3	03:25:10.49	+30:44:47.48	<0.0195±0.0065	<0.0195	0.0065	0.0323±0.0082	0.0449	0.0074	>1.11±0.92	>1.84±0.36
Rad	AR2002IRS2VLA1	03:25:18.58	+30:44:36.94	0.3649±0.0296	0.1616	0.0082	0.2773±0.1057	0.0506	0.0139	-0.60±0.86	-1.45±0.77
Rad	AR2002IRS2VLA3	03:25:22.07	+30:46:05.48	1.1928±0.0570	0.0474	0.0073	<0.4628±0.0098	<0.0295	0.0098	<-2.09±0.15	<-2.09±0.06
Rad	AR2002IRS2VLA5	03:25:31.91	+30:44:37.97	0.2020±0.0190	0.1690	0.0155	—	—	—	—	—
Rad	NVSSJ033009+303248	03:30:09.10	+30:32:49.70	62.0973±0.3761	42.6842	0.0252	—	—	—	—	—
IR	SSTc2dJ033046.4	03:30:46.37	+30:32:43.19	0.2872±0.0230	0.2261	0.0191	—	—	—	—	—
Rad	NVSSJ032742+301140-E	03:27:41.49	+30:11:47.14	8.6257±0.3190	1.3899	0.0127	—	—	—	—	—
X	XMMUJ032742.2	03:27:42.25	+30:11:39.84	0.2220±0.0113	0.2241	0.0117	—	—	—	—	—
Rad	NVSSJ032742+301140-W	03:27:42.76	+30:11:33.99	7.2426±0.3638	0.4162	0.0111	—	—	—	—	—
Rad	NVSSJ032744+300717-N	03:27:43.98	+30:07:18.68	12.7310±1.4865	0.5025	0.0155	—	—	—	—	—
Rad	NVSSJ032744+300717-S	03:27:44.16	+30:07:15.02	<0.0210±0.0070	<0.0210	0.0070	0.8259±0.1140	0.5452	0.0104	>8.09±0.79	>7.18±0.04
Rad	NVSSJ032804+300820	03:28:04.86	+30:08:19.65	13.7439±0.1846	8.0450	0.0259	—	—	—	—	—
Rad	NVSSJ032827+302616-N	03:28:27.50	+30:26:18.52	8.5889±1.0183	2.6233	0.0189	—	—	—	—	—
Rad	NVSSJ032827+302616-S	03:28:27.52	+30:26:12.55	19.7856±0.2594	10.7675	0.0181	—	—	—	—	—
Rad	RAC97-VLA23	03:29:07.17	+31:17:08.98	0.0774±0.0078	0.0616	0.0056	0.0611±0.0200	0.0335	0.0057	-0.52±0.76	-1.34±0.43
X	GFT200276	03:29:15.64	+31:18:51.78	0.0585±0.0066	0.0579	0.0060	0.0494±0.0060	0.0398	0.0047	-0.38±0.37	-0.83±0.35
Rad	RAC97-VLA35	03:29:23.89	+31:16:20.68	0.4748±0.0469	0.0463	0.0107	<0.3431±0.0376	<0.1127	0.0376	<-0.72±0.77	<0.50±0.78
IR	2MASSJ03283173+3059158	03:28:31.75	+30:59:15.79	0.0405±0.0072	0.0378	0.0057	0.0446±0.0061	0.0472	0.0055	0.21±0.49	0.49±0.42
Rad	RZP2014JVLA4	03:43:57.08	+32:03:29.64	0.0619±0.0067	0.0595	0.0056	0.0341±0.0052	0.0400	0.0052	-1.31±0.41	-0.88±0.35
Rad	RZP2014JVLA7	03:44:01.66	+32:04:39.53	0.0475±0.0071	0.0502	0.0066	0.0378±0.0200	0.0334	0.0082	-0.50±1.21	-0.90±0.61
Rad	NVSSJ032628+301618	03:26:28.36	+30:16:18.72	24.8228±0.6660	11.3131	0.0055	13.1329±0.2796	5.5648	0.0054	-1.40±0.08	-6.81±0.02
X	XMMUJ032643.8	03:26:43.79	+30:08:23.77	16.2594±0.2031	10.2420	0.0282	—	—	—	—	—
PoC	LMG94Per7C	03:32:29.00	+31:02:12.15	<0.0152±0.0051	<0.0152	0.0051	0.0151±0.0048	0.0242	0.0039	>-0.00±1.02	>1.03±0.36
Rad	NVSSJ033119+304726	03:31:19.07	+30:47:27.70	35.9500±1.8061	8.5635	0.0074	16.6793±0.6315	3.7696	0.0054	-1.69±0.14	-0.33±0.01
TT*	Cl*IC348LRL1939	03:44:52.74	+32:00:56.39	<0.0166±0.0055	<0.0166	0.0055	0.0310±0.0051	0.0331	0.0050	>1.37±0.82	>1.52±0.33
*	PSZ2003J034453.0	03:44:52.98	+32:05:07.62	0.4971±0.0089	0.4573	0.0083	0.4946±0.0173	0.4533	0.0154	-0.01±0.09	-0.02±0.09
*	PSZ2003J034453.9	03:44:53.85	+32:04:36.18	0.2244±0.0096	0.1855	0.0076	0.1542±0.0149	0.1285	0.0120	-0.83±0.23	-0.81±0.22
*iC	IC34818	03:45:07.73	+32:00:27.18	0.1370±0.0142	0.1144	0.0116	—	—	—	—	—
TT*	Cl*IC348LRL11	03:45:07.98	+32:04:01.82	0.3662±0.0187	0.2654	0.0144	—	—	—	—	—

Table 2.5: continued.

Type[a]	Name[b]	RA	Dec	F_{vint}	F_{vpeak}	RMS	F_{vint}	F_{vpeak}	RMS	Sp. Index	Sp. Index
			6.4 cm	6.4 cm	6.4 cm	4.1 cm	4.1 cm	4.1 cm	Int.	Peak	
	J2000	J2000	mJy	mJy/beam	mJy/beam	mJy	mJy/beam	mJy/beam			
Rad	RR98HH366VLA2	03:47:27.68	+32:52:30.57	0.2346±0.0068	0.2518	0.0063	0.1524±0.0079	0.1487	0.0075	-0.95±0.13	-1.16±0.12
PoC	KJT20073	03:47:42.61	+32:52:27.30	<0.0147±0.0049	<0.0147	0.0049	0.0283±0.0047	0.0306	0.0039	>1.45±0.82	>1.61±0.28
Rad	RR98HH366VLA4	03:47:52.55	+32:52:01.11	1.8373±0.0071	1.7049	0.0056	1.3871±0.0075	1.2874	0.0056	-0.62±0.01	-0.62±0.01
X	CXOUJ034426.1	03:44:26.18	+32:01:13.76	0.0797±0.0122	0.0976	0.0145	—	—	—	—	—
Or*	CXOPZ32	03:44:16.76	+32:09:56.66	2.4096±0.0305	1.3464	0.0115	0.5116±0.0591	0.3168	0.0378	-3.41±0.26	-3.19±0.26
Or*	V*V904Per	03:44:21.66	+32:06:24.78	0.0465±0.0062	0.0482	0.0057	0.0323±0.0060	0.0315	0.0050	-0.80±0.50	-0.94±0.44
*iC	Cl*IC348MM42	03:44:21.74	+32:09:18.51	0.4483±0.0198	0.3059	0.0096	0.1984±0.0272	0.1501	0.0213	-1.80±0.32	-1.57±0.32
*iC	Cl*IC348MM41	03:44:22.17	+32:09:23.76	0.4219±0.0197	0.2618	0.0099	0.1928±0.0970	0.0942	0.0234	-1.73±1.11	-2.25±0.55
dS*	V*V705Per	03:44:31.19	+32:06:22.04	0.1957±0.0083	0.1759	0.0071	0.1494±0.0090	0.1577	0.0089	-0.59±0.16	-0.24±0.15
Or*	V*V913Per	03:44:32.57	+32:08:42.44	0.2461±0.0126	0.2164	0.0110	0.2289±0.0929	0.1531	0.0327	-0.16±0.90	-0.76±0.48
Or*	V*V914Per	03:44:32.73	+32:08:37.45	0.2708±0.0136	0.2299	0.0108	0.2905±0.0859	0.1391	0.0313	0.15±0.66	-1.11±0.51
**	Cl*IC348LRL9	03:44:39.14	+32:09:18.40	0.7142±0.0285	0.4445	0.0189	—	—	—	—	—
Rad	RAC97VLA15	03:29:02.55	+31:13:44.37	0.0632±0.0104	0.0659	0.0108	<0.0960±0.0320	<0.0960	0.0320	<0.92±0.82	<0.83±0.82
X	GFT200299	03:29:25.89	+31:13:44.81	0.0370±0.0067	0.0416	0.0063	0.0347±0.0193	0.0350	0.0078	-0.14±1.29	-0.38±0.60
IR	ASR98	03:28:58.54	+31:12:21.00	<0.0205±0.0068	<0.0205	0.0068	0.0242±0.0063	0.0341	0.0057	>0.37±0.93	>1.12±0.37
IR	WISEJ034158.52	03:41:58.45	+31:48:56.35	0.0358±0.0053	0.0334	0.0049	0.0361±0.0046	0.0397	0.0040	0.02±0.43	0.38±0.39
*	MBO184	03:29:13.49	+31:24:40.56	0.0383±0.0062	0.0378	0.0054	0.0381±0.0138	0.0272	0.0047	-0.01±0.87	-0.73±0.50
BD*	2MASSJ03293053	03:29:30.54	+31:27:27.78	0.0799±0.0066	0.0785	0.0056	0.0867±0.0054	0.0988	0.0060	0.18±0.23	0.51±0.21
Rad	RAC97VLA6	03:28:52.50	+31:14:59.49	0.0427±0.0063	0.0440	0.0062	0.0372±0.0149	0.0285	0.0062	-0.30±0.94	-0.95±0.57

Notes. [(a)] Types from the SIMBAD catalog: Rad - radio soruce; *iC - star in cluster; * - star; X - X-ray source; IR - infrared source; PoC - Part of Cloud; TT* - T-Tauri star; Or* - variable Star of Orion Type; dS* - variable Star of delta Sct Type; ** - double or multiple star [(b)] References: Cl*IC348LRL - Luhman et al. (1998), FOW2011 - Forbrich et al. (2011), PSZ2003 - Preibisch et al. (2003), CXOPZ - Preibisch & Zinnecker (2001), RAC97 - Rodríguez et al. (1999), WMW2010 - Winston et al. (2010), XMMU - XMM-Newton data Unregistered, EYG2006 - (Enoch et al. 2006), AR2002 - Anglada & Rodríguez (2002), NVSS - The NRAO VLA Sky Survey (Condon et al. 1998), SSTc2D - Spitzer c2d Legacy (Young et al. 2004), GFT2002 - Getman et al. (2002), 2MASS - 2-Micron All Sky Survey (Cutri et al. 2003), RZP2014 - Rodríguez et al. (2014), LMG94 - Ladd et al. (1994), RR98 - Rodríguez & Reipurth (1998), KJT2007 - Kirk et al. (2007), V*VXXX - General Catalog of Variable Stars (Kukarkin et al. 1971), ASR - Aspin et al. (1994), MBO - Wilking et al. (2004)

Table 2.6: New detections reported in Pech et al. (2016)

Name	RA	Dec	F_{vint} 6.4 cm	F_{vpeak} 6.4 cm	RMS 6.4 cm	F_{vint} 4.1 cm	F_{vpeak} 4.1 cm	RMS 4.1 cm	Sp. Index Int.	Sp. Index Peak
	J2000	J2000	mJy	mJy/beam	mJy/beam	mJy	mJy/beam	mJy/beam		
J032903.14+312752.6	03:29:03.16	+31:27:52.58	0.0885±0.0132	0.0983	0.0151	–	–	–	–	–
J032819.46+311831.0	03:28:19.48	+31:18:31.20	0.7570±0.0345	0.4897	0.0223	–	–	–	–	–
J032825.98+311616.0	03:28:25.99	+31:16:16.07	0.3582±0.0106	0.2967	0.0088	0.1343±0.0193	0.1180	0.0167	-2.16±0.32	-2.03±0.32
J032832.41+311245.3	03:28:32.43	+31:12:45.52	0.1830±0.0213	0.1566	0.0204	–	–	–	–	–
J034327.28+320028.1	03:43:27.31	+32:00:28.34	0.1417±0.0172	0.1319	0.0148	–	–	–	–	–
J034330.40+320758.4	03:43:30.42	+32:07:58.84	0.2882±0.0204	0.2194	0.0172	–	–	–	–	–
J034342.10+320225.2	03:43:42.11	+32:02:25.34	0.1072±0.0094	0.0953	0.0077	0.0733±0.0356	0.0495	0.0120	-0.84±1.09	-1.44±0.56
J034448.89+320125.0	03:44:48.89	+32:01:25.07	0.1212±0.0064	0.1143	0.0051	0.0816±0.0055	0.0670	0.0041	-0.87±0.19	-1.18±0.17
J034459.29+315658.9	03:44:59.26	+31:56:59.22	0.7574±0.0487	0.1376	0.0133	–	–	–	–	–
J034423.11+320956.3	03:44:23.9	+32:09:56.45	1.4929±0.0183	1.1440	0.0119	–	–	–	–	–
J032909.64+311450.5	03:29:09.67	+31:14:50.65	0.0991±0.0167	0.0855	0.0139	–	–	–	–	–
J032907.13+312635.2	03:29:07.14	+31:26:35.32	0.0936±0.0090	0.0820	0.0079	0.1235±0.0368	0.0746	0.0130	0.61±0.69	-0.21±0.44

Table 2.7: New detections from VANDAM survey

Name	RA	Dec	F^a_{vint} 6.4 cm	F^b_{vpeak} 6.4 cm	RMS 6.4 cm	F_{vint} 4.1 cm	F_{vpeak} 4.1 cm	RMS 4.1 cm	Sp. Index Int.	Sp. Index Peak
	J2000	J2000	mJy	mJy/beam	mJy/beam	mJy	mJy/beam	mJy/beam		
034357.31+315858.86	03:43:57.31	+31:58:58.86	0.0604±0.0101	0.0624	0.0100	<0.0850±0.0283	<0.0850	0.0283	<0.75±0.82	<0.68±0.82
034408.82+320020.63	03:44:08.82	+32:00:20.64	0.0439±0.0069	0.0406	0.0060	0.0441±0.0173	0.0286	0.0062	0.01±0.93	-0.77±0.58
034415.23+315749.09	03:44:15.24	+31:57:49.09	0.0747±0.0075	0.0694	0.0065	0.1245±0.0076	0.1177	0.0070	1.13±0.26	1.16±0.24
034422.04+320322.79	03:44:22.05	+32:03:22.79	<0.0208±0.0069	<0.0208	0.0069	0.0446±0.0073	0.0561	0.0084	>1.68±0.82	>2.19±0.33
034425.40+320249.66	03:44:25.41	+32:02:49.66	0.0367±0.0066	0.0421	0.0067	0.0459±0.0181	0.0308	0.0076	0.49±0.96	-0.69±0.65
032846.12+312050.13	03:28:46.12	+31:20:50.13	0.0428±0.0082	0.0442	0.0073	0.0516±0.0293	0.0379	0.0105	0.41±1.32	-0.34±0.71
032848.98+312313.01	03:28:48.98	+31:23:13.02	0.0455±0.0079	0.0392	0.0065	0.0319±0.0232	0.0252	0.0076	-0.78±1.64	-0.97±0.76
032850.33+312101.60	03:28:50.33	+31:21:01.60	0.0551±0.0078	0.0505	0.0062	0.0498±0.0200	0.0334	0.0066	-0.22±0.94	-0.91±0.51
032850.96+312240.94	03:28:50.97	+31:22:40.94	0.0320±0.0059	0.0368	0.0059	<0.0179±0.0060	<0.0179	0.0060	<-1.28±0.84	<-1.59±0.82
032851.64+312341.52	03:28:51.65	+31:23:41.52	<0.0187±0.0062	<0.0187	0.0062	0.0359±0.0078	0.0432	0.0068	>1.44±0.88	>1.85±0.35
032858.78+312300.39	03:28:58.79	+31:23:00.39	<0.0157±0.0052	<0.0157	0.0052	0.0235±0.0052	0.0265	0.0043	>0.89±0.88	>1.15±0.36
032900.39+312209.19	03:29:00.39	+31:22:09.20	<0.0152±0.0051	<0.0152	0.0051	0.0187±0.0047	0.0240	0.0040	>0.46±0.92	>1.01±0.36
032907.79+312301.88	03:29:07.79	+31:23:01.89	0.0235±0.0052	0.0343	0.0055	<0.0145±0.0048	<0.0145	0.0048	<-1.06±0.88	<-1.90±0.81
032914.28+312131.29	03:29:14.28	+31:21:31.30	0.0439±0.0074	0.0397	0.0063	<0.0213±0.0071	<0.0213	0.0071	<-1.59±0.82	<-1.37±0.81
032915.35+312146.28	03:29:15.36	+31:21:46.29	<0.0196±0.0065	<0.0196	0.0065	0.0399±0.0092	0.0480	0.0078	>1.56±0.89	>1.97±0.36
032813.01+311421.76	03:28:13.02	+31:14:21.76	0.5303±0.0131	0.4402	0.0109	0.3736±0.0525	0.2660	0.0382	-0.77±0.31	-1.11±0.32
032817.27+311603.37	03:28:17.27	+31:16:03.37	0.2107±0.0161	0.1475	0.0112	—	—	—	—	—
032833.53+311054.30	03:28:33.54	+31:10:54.31	0.0396±0.0060	0.0423	0.0055	0.0370±0.0138	0.0248	0.0052	-0.15±0.89	-1.17±0.54
032836.53+311230.77	03:28:36.53	+31:12:30.77	<0.0150±0.0050	<0.0150	0.0050	0.0214±0.0051	0.0247	0.0041	>0.79±0.90	>1.10±0.36
032839.07+311507.54	03:28:39.08	+31:15:07.54	0.0517±0.0084	0.0421	0.0060	0.0353±0.0223	0.0225	0.0066	-0.84±1.43	-1.38±0.72
032839.12+310915.81	03:28:39.12	+31:09:15.82	0.0566±0.0078	0.0541	0.0072	0.0540±0.0287	0.0473	0.0109	-0.10±1.21	-0.30±0.59
032841.70+311350.41	03:28:41.70	+31:13:50.41	0.0527±0.0074	0.0423	0.0055	0.0334±0.0152	0.0191	0.0051	-1.00±1.05	-1.76±0.66
032846.27+311140.40	03:28:46.28	+31:11:40.40	0.0275±0.0054	0.0368	0.0060	<0.0201±0.0067	<0.0201	0.0067	<-0.69±0.85	<-1.33±0.82
032852.98+311234.24	03:28:52.98	+31:12:34.25	<0.0231±0.0077	<0.0231	0.0077	0.0701±0.0140	0.0798	0.0129	>2.45±0.86	>2.74±0.36
032819.89+310151.65	03:28:19.90	+31:01:51.66	0.4847±0.0237	0.3864	0.0206	—	—	—	—	—
032830.05+310618.74	03:28:30.06	+31:06:18.74	0.0761±0.0083	0.0682	0.0065	0.0808±0.0121	0.0616	0.0079	0.13±0.41	-0.23±0.35
032833.19+310604.14	03:28:33.20	+31:06:04.14	0.0281±0.0055	0.0379	0.0059	<0.0183±0.0061	<0.0183	0.0061	<-0.95±0.85	<-1.61±0.81
032834.03+310640.30	03:28:34.03	+31:06:40.31	0.0734±0.0075	0.0657	0.0059	0.0475±0.0068	0.0463	0.0059	-0.96±0.39	-0.77±0.34
032837.35+310156.89	03:28:37.36	+31:01:56.89	0.1683±0.0111	0.1402	0.0091	0.0518±0.0562	0.0630	0.0202	-2.60±2.40	-1.76±0.72
032841.50+310642.16	03:28:41.50	+31:06:42.16	<0.0159±0.0053	<0.0159	0.0053	0.0207±0.0056	0.0288	0.0046	>0.58±0.94	>1.31±0.35
032844.12+310434.93	03:28:44.13	+31:04:34.94	0.0269±0.0055	0.0351	0.0056	<0.0158±0.0053	<0.0158	0.0053	<-1.17±0.86	<-1.76±0.81
032845.02+310720.75	03:28:45.02	+31:07:20.76	0.1443±0.0065	0.1307	0.0055	0.1479±0.0061	0.1381	0.0051	0.05±0.14	0.12±0.12
032845.32+310545.15	03:28:45.33	+31:05:45.15	0.0325±0.0060	0.0339	0.0053	<0.0138±0.0046	<0.0138	0.0046	<-1.88±0.84	<-1.98±0.81
032845.83+310202.34	03:28:45.84	+31:02:02.35	0.2738±0.0100	0.2451	0.0086	0.1849±0.0253	0.1329	0.0173	-0.86±0.31	-1.35±0.30
032848.11+310700.09	03:28:48.12	+31:07:00.10	<0.0167±0.0056	<0.0167	0.0056	0.0252±0.0060	0.0324	0.0052	>0.91±0.90	>1.46±0.36
032852.64+310746.57	03:28:52.64	+31:07:46.57	0.0502±0.0086	0.0442	0.0065	0.0308±0.0233	0.0295	0.0079	-1.07±1.71	-0.89±0.67
032852.78+310106.76	03:28:52.78	+31:01:06.77	0.1376±0.0169	0.1052	0.0131	—	—	—	—	—
032853.19+310311.26	03:28:53.20	+31:03:11.27	0.2467±0.0132	0.1965	0.0102	0.2935±0.0358	0.2430	0.0281	0.38±0.29	0.47±0.28
032855.58+310438.29	03:28:55.58	+31:04:38.29	<0.0208±0.0069	<0.0208	0.0069	0.0495±0.0105	0.0570	0.0093	>1.91±0.87	>2.22±0.36
032858.96+310340.59	03:28:58.96	+31:03:40.59	0.1541±0.0183	0.1331	0.0165	—	—	—	—	—

Table 2.7: continued.

Name	RA	Dec	F^a_{vint} 6.4 cm	F^b_{vpeak} 6.4 cm	RMS 6.4 cm	F^a_{vint} 4.1 cm	F^b_{vpeak} 4.1 cm	RMS 4.1 cm	Sp. Index Int.[c]	Sp. Index Peak[d]
	J2000	J2000	mJy	mJy/beam	mJy/beam	mJy	mJy/beam	mJy/beam		
032507.23+304555.46	03:25:07.23	+30:45:55.47	0.0652±0.0095	0.0586	0.0075	0.0528±0.0339	0.0395	0.0109	-0.46±1.45	-0.87±0.67
032512.54+304153.58	03:25:12.55	+30:41:53.59	0.2792±0.0201	0.2277	0.0166	—	—	—	—	—
032514.82+303918.75	03:25:14.83	+30:39:18.75	1.7929±0.0486	1.1486	0.0327	—	—	—	—	—
032516.84+304757.86	03:25:16.84	+30:47:57.86	<0.0205±0.0068	<0.0205	0.0068	0.0477±0.0091	0.0560	0.0085	>1.86±0.85	>2.21±0.34
032519.72+304605.97	03:25:19.72	+30:46:05.98	<0.0162±0.0054	<0.0162	0.0054	0.0195±0.0053	0.0297	0.0046	>0.42±0.95	>1.34±0.34
032522.11+304734.24	03:25:22.11	+30:47:34.24	0.0534±0.0081	0.0442	0.0061	0.0494±0.0204	0.0363	0.0063	-0.17±0.97	-0.43±0.49
032524.25+303955.88	03:25:24.25	+30:39:55.88	1.4241±0.1252	0.2334	0.0146	—	—	—	—	—
032524.31+305057.30	03:25:24.32	+30:50:57.30	0.1866±0.0193	0.1437	0.0149	—	—	—	—	—
032524.28+304000.60	03:25:24.29	+30:40:00.60	0.6858±0.0993	0.4432	0.0380	—	—	—	—	—
032524.72+304657.60	03:25:24.73	+30:46:57.61	0.1266±0.0121	0.1261	0.0095	0.1996±0.0260	0.1715	0.0130	1.00±0.36	-0.26±0.87
032527.71+304641.83	03:25:27.72	+30:46:41.84	0.3825±0.0112	0.3862	0.0109	0.5546±0.0207	0.5626	0.0191	0.82±0.10	0.83±0.10
032529.95+304803.22	03:25:29.96	+30:48:03.22	0.0492±0.0069	0.0571	0.0070	0.0702±0.0102	0.0683	0.0091	0.79±0.44	0.39±0.40
032532.28+304052.00	03:25:32.28	+30:40:52.01	1.9780±0.0714	1.4240	0.0442	—	—	—	—	—
032532.24+304155.30	03:25:32.24	+30:41:55.31	0.2250±0.0090	0.2071	0.0081	0.1256±0.0173	0.0978	0.0135	-1.29±0.32	-1.65±0.32
032534.46+304028.32	03:25:34.47	+30:40:28.33	1.5917±0.0840	1.2729	0.0676	—	—	—	—	—
032536.26+304802.71	03:25:36.26	+30:48:02.71	0.1470±0.0095	0.1310	0.0084	0.1011±0.0153	0.1112	0.0150	-0.83±0.36	-0.36±0.33
032539.58+304656.70	03:25:39.58	+30:46:56.70	0.1251±0.0086	0.1225	0.0082	0.1073±0.0384	0.0803	0.0143	-0.34±0.80	-0.93±0.42
032542.96+304232.33	03:25:42.97	+30:42:32.33	0.1060±0.0130	0.0943	0.0114	<0.1181±0.0394	<0.1181	0.0394	<0.24±0.78	<0.49±0.78
032543.43+304231.00	03:25:43.44	+30:42:31.00	0.1337±0.0126	0.1085	0.0118	—	—	—	—	—
032554.78+304903.17	03:25:54.78	+30:49:03.17	0.7131±0.0524	0.5204	0.0447	—	—	—	—	—
032447.34+302504.40	03:24:47.34	+30:25:04.41	0.2506±0.0139	0.2332	0.0115	<0.1209±0.0403	<0.1209	0.0403	<-1.60±0.74	<-1.45±0.74
032452.06+302221.96	03:24:52.07	+30:22:21.96	0.1000±0.0091	0.0994	0.0089	0.1164±0.0179	0.1303	0.0174	0.33±0.39	0.60±0.35
032452.21+301812.23	03:24:52.21	+30:18:12.23	5.9376±0.1585	3.3477	0.0258	—	—	—	—	—
032456.73+302217.76	03:24:56.74	+30:22:17.76	<0.0216±0.0072	<0.0216	0.0072	0.0512±0.0101	0.0578	0.0096	>1.90±0.85	>2.17±0.37
032458.61+302142.30	03:24:58.62	+30:21:42.31	0.2043±0.0095	0.1704	0.0072	0.1544±0.0115	0.1430	0.0097	-0.62±0.19	-0.39±0.18
032501.03+302510.81	03:25:01.04	+30:25:10.81	0.0475±0.0068	0.0407	0.0061	<0.0183±0.0061	<0.0183	0.0061	<-2.10±0.80	<-1.76±0.80
032502.29+302438.90	03:25:02.29	+30:24:38.91	0.2663±0.0066	0.2559	0.0057	0.1509±0.0055	0.1557	0.0052	-1.25±0.10	-1.09±0.09
032504.11+302428.98	03:25:04.12	+30:24:28.98	0.0604±0.0063	0.0632	0.0055	0.0400±0.0128	0.0270	0.0047	-0.91±0.74	-1.87±0.43
032506.47+302633.46	03:25:06.47	+30:26:33.46	0.0527±0.0074	0.0531	0.0065	0.0517±0.0082	0.0483	0.0072	-0.04±0.46	-0.21±0.42
032507.66+302147.29	03:25:07.67	+30:21:47.30	<0.0179±0.0060	<0.0179	0.0060	0.0353±0.0070	0.0355	0.0058	>1.50±0.85	>1.51±0.36
032508.12+302354.97	03:25:08.13	+30:23:54.97	<0.0156±0.0052	<0.0156	0.0052	0.0232±0.0046	0.0275	0.0041	>0.88±0.86	>1.25±0.33
032508.15+302250.71	03:25:08.16	+30:22:50.72	<0.0161±0.0054	<0.0161	0.0054	0.0205±0.0050	0.0274	0.0045	>0.52±0.91	>1.16±0.36
032508.23+301831.56	03:25:08.24	+30:18:31.56	3.8700±0.0423	2.9394	0.0131	—	—	—	—	—
032509.19+303025.11	03:25:09.20	+30:30:25.12	2.9432±0.0872	1.0030	0.0209	—	—	—	—	—
032511.45+302715.21	03:25:11.45	+30:27:15.22	0.1057±0.0089	0.0943	0.0072	0.0774±0.0277	0.0561	0.0097	-0.69±0.81	-1.14±0.42
032511.54+302353.63	03:25:11.54	+30:23:53.63	<0.0156±0.0052	<0.0156	0.0052	0.0213±0.0048	0.0254	0.0041	>0.69±0.88	>1.08±0.35
032511.63+302249.14	03:25:11.64	+30:22:49.15	0.0651±0.0068	0.0619	0.0054	0.0356±0.0041	0.0459	0.0044	-1.33±0.34	-0.66±0.29
032512.49+302334.88	03:25:12.50	+30:23:34.89	0.1383±0.0059	0.1378	0.0052	0.0896±0.0048	0.0892	0.0042	-0.95±0.15	-0.96±0.13
032516.55+302517.58	03:25:16.56	+30:25:17.58	0.0776±0.0066	0.0789	0.0058	0.1014±0.0053	0.1075	0.0053	0.59±0.22	0.68±0.19
032519.98+302655.82	03:25:19.98	+30:26:55.82	0.1058±0.0085	0.1105	0.0078	0.0646±0.0300	0.0494	0.0119	-1.09±1.04	-1.77±0.55

Table 2.7: continued.

Name	RA	Dec	F^a_{vint} 6.4 cm	F^b_{vpeak} 6.4 cm	RMS 6.4 cm	F^a_{vint} 4.1 cm	F^b_{vpeak} 4.1 cm	RMS 4.1 cm	Sp. Index Int.[c]	Sp. Index Peak[d]
	J2000	J2000	mJy	mJy/beam	mJy/beam	mJy	mJy/beam	mJy/beam		
032526.06+302649.37	03:25:26.07	+30:26:49.37	0.1118±0.0109	0.1042	0.0096	<0.0659±0.0220	<0.0659	0.0220	<-1.17±0.76	<-1.01±0.76
032531.67+302722.89	03:25:31.67	+30:27:22.90	0.4508±0.0180	0.4167	0.0151	—	—	—	—	—
033027.80+303112.27	03:30:27.80	+30:31:12.28	0.1088±0.0127	0.0762	0.0085	<0.0416±0.0139	<0.0416	0.0139	<-2.12±0.78	<-1.33±0.77
033036.63+302452.04	03:30:36.64	+30:24:52.05	0.0641±0.0088	0.0561	0.0074	<0.0353±0.0118	<0.0353	0.0118	<-1.32±0.79	<-1.02±0.79
033042.33+302843.66	03:30:42.33	+30:28:43.66	0.0947±0.0096	0.0756	0.0071	<0.0305±0.0102	<0.0305	0.0102	<-2.49±0.77	<-2.00±0.76
033042.61+302837.23	03:30:42.61	+30:28:37.24	<0.0213±0.0071	<0.0213	0.0071	0.0593±0.0101	0.0639	0.0103	>2.26±0.82	>2.42±0.35
033043.79+302723.80	03:30:43.79	+30:27:23.80	0.2320±0.0203	0.1592	0.0139	—	—	—	—	—
033055.80+302710.73	03:30:55.80	+30:27:10.74	0.1152±0.0171	0.1070	0.0154	—	—	—	—	—
033100.57+302954.57	03:31:00.58	+30:29:54.57	0.5550±0.0354	0.4576	0.0293	—	—	—	—	—
032743.28+300800.16	03:27:43.29	+30:08:00.17	0.2636±0.0211	0.1344	0.0119	—	—	—	—	—
032749.44+300747.59	03:27:49.44	+30:07:47.59	0.0707±0.0069	0.0653	0.0056	0.0574±0.0070	0.0544	0.0057	-0.46±0.34	-0.40±0.30
032751.73+300807.57	03:27:51.74	+30:08:07.57	0.1099±0.0130	0.1023	0.0133	—	—	—	—	—
032755.64+300613.13	03:27:55.65	+30:06:13.13	0.0263±0.0060	0.0323	0.0054	<0.0154±0.0051	<0.0154	0.0051	<-1.18±0.89	<-1.63±0.82
032756.44+301327.54	03:27:56.44	+30:13:27.55	1.2872±0.0260	1.2483	0.0124	—	—	—	—	—
032756.88+300636.34	03:27:56.89	+30:06:36.34	0.1350±0.0055	0.1465	0.0051	0.0825±0.0044	0.0875	0.0045	-1.08±0.15	-1.14±0.14
032757.99+300604.20	03:27:57.100	+30:06:04.21	0.0236±0.0048	0.0350	0.0053	<0.0152±0.0051	<0.0152	0.0051	<-0.98±0.86	<-1.84±0.81
032800.33+300848.99	03:28:00.34	+30:08:48.100	0.1269±0.0052	0.1384	0.0048	0.1019±0.0039	0.1157	0.0039	-0.48±0.12	-0.39±0.11
032800.80+300733.80	03:28:00.80	+30:07:33.80	0.0259±0.0052	0.0300	0.0048	0.0264±0.0098	0.0177	0.0038	0.04±0.93	-1.16±0.59
032801.12+300746.48	03:28:01.13	+30:07:46.49	<0.0143±0.0048	<0.0143	0.0048	0.0218±0.0040	0.0251	0.0038	>0.94±0.84	>1.25±0.33
032805.24+300700.65	03:28:05.24	+30:07:00.66	0.1120±0.0054	0.1198	0.0050	0.0646±0.0055	0.0532	0.0044	-1.21±0.21	-1.79±0.20
032808.49+300850.02	03:28:08.49	+30:08:50.03	0.0436±0.0082	0.0353	0.0053	0.0219±0.0185	0.0188	0.0049	-1.52±1.91	-1.39±0.66
032816.02+300842.69	03:28:16.02	+30:08:42.69	0.0681±0.0084	0.0615	0.0068	0.0666±0.0296	0.0499	0.0095	-0.05±1.02	-0.46±0.48
032820.31+300915.05	03:28:20.31	+30:09:15.06	0.2334±0.0087	0.2553	0.0088	0.1838±0.0213	0.1805	0.0202	-0.53±0.27	-0.76±0.26
032821.53+300625.55	03:28:21.53	+30:06:25.55	0.1986±0.0270	0.0807	0.0098	0.1564±0.1132	0.0922	0.0287	-0.53±1.62	0.04±0.78
032825.33+300555.36	03:28:25.34	+30:05:55.36	0.0782±0.0148	0.0840	0.0139	—	—	—	—	—
032827.28+301129.96	03:28:27.28	+30:11:29.97	0.7435±0.0272	0.6254	0.0220	—	—	—	—	—
032829.14+300729.30	03:28:29.15	+30:07:29.31	0.7220±0.0219	0.6504	0.0169	—	—	—	—	—
032807.13+302019.92	03:28:07.13	+30:20:19.93	0.2067±0.0173	0.1869	0.0163	—	—	—	—	—
032810.98+302058.62	03:28:10.98	+30:20:58.62	0.1291±0.0121	0.1242	0.0120	—	—	—	—	—
032811.19+301608.83	03:28:11.19	+30:16:08.83	0.2607±0.0228	0.2290	0.0283	—	—	—	—	—
032811.22+301653.92	03:28:11.23	+30:16:53.92	0.5204±0.0384	0.3670	0.0351	—	—	—	—	—
032820.10+302153.30	03:28:20.11	+30:21:53.30	0.3451±0.0086	0.3134	0.0075	0.2043±0.0125	0.1777	0.0104	-1.15±0.15	-1.25±0.14
032823.29+301857.93	03:28:23.29	+30:18:57.94	<0.0190±0.0063	<0.0190	0.0063	0.0308±0.0075	0.0399	0.0065	>1.06±0.91	>1.63±0.36
032823.97+301624.68	03:28:23.97	+30:16:24.69	0.3313±0.0095	0.3072	0.0092	0.1271±0.0200	0.1177	0.0189	-2.11±0.35	-2.11±0.36
032824.39+301658.98	03:28:24.40	+30:16:58.99	0.2568±0.0095	0.2245	0.0080	0.1864±0.0162	0.1531	0.0125	-0.71±0.21	-0.84±0.20
032824.40+301653.47	03:28:24.40	+30:16:53.48	2.4658±0.0225	1.0868	0.0082	0.7997±0.0306	0.6312	0.0131	-2.48±0.09	-0.75±0.80
032824.85+301959.54	03:28:24.85	+30:19:59.55	0.0608±0.0080	0.0517	0.0058	0.0374±0.0187	0.0278	0.0051	-1.07±1.14	-1.37±0.48
032825.36+301739.21	03:28:25.37	+30:17:39.22	<0.0207±0.0069	<0.0207	0.0069	0.0372±0.0094	0.0508	0.0082	>1.29±0.92	>1.97±0.36
032826.39+302105.65	03:28:26.40	+30:21:05.66	0.0465±0.0058	0.0518	0.0057	0.0313±0.0130	0.0222	0.0049	-0.87±0.96	-1.86±0.55
032827.65+302608.06	03:28:27.65	+30:26:08.06	0.2569±0.0687	0.1402	0.0175	—	—	—	—	—

Table 2.7: continued.

Name	RA	Dec	F^a_{vint} 6.4 cm	F^b_{vpeak} 6.4 cm	RMS 6.4 cm	F^a_{vint} 4.1 cm	F^b_{vpeak} 4.1 cm	RMS 4.1 cm	Sp. Index Int.[c]	Sp. Index Peak[d]
	J2000	J2000	mJy	mJy/beam	mJy/beam	mJy	mJy/beam	mJy/beam		
032829.85+302304.84	03:28:29.85	+30:23:04.85	0.0344±0.0071	0.0406	0.0067	<0.0229±0.0076	<0.0229	0.0076	<-0.90±0.86	<-1.26±0.82
032834.53+302146.29	03:28:34.54	+30:21:46.29	0.0466±0.0066	0.0399	0.0054	0.0307±0.0143	0.0202	0.0043	-0.92±1.07	-1.50±0.56
032837.67+301401.21	03:28:37.67	+30:14:01.21	0.3629±0.0167	0.3408	0.0174	—	—	—	—	—
032840.68+302208.10	03:28:40.68	+30:22:08.10	<0.0176±0.0059	<0.0176	0.0059	0.0296±0.0063	0.0323	0.0054	>1.14±0.87	>1.33±0.37
032841.09+302328.03	03:28:41.10	+30:23:28.04	<0.0220±0.0073	<0.0220	0.0073	0.0531±0.0108	0.0597	0.0097	>1.94±0.86	>2.20±0.36
032842.00+302447.34	03:28:42.01	+30:24:47.34	0.2318±0.0149	0.1523	0.0105	<0.0846±0.0282	<0.0846	0.0282	<-2.22±0.75	<-1.29±0.75
032842.87+302232.01	03:28:42.88	+30:22:32.02	0.1037±0.0060	0.1054	0.0065	0.0890±0.0083	0.0854	0.0069	-0.34±0.24	-0.46±0.22
032843.47+302031.34	03:28:43.47	+30:20:31.34	0.0483±0.0062	0.0471	0.0056	0.0486±0.0052	0.0513	0.0046	0.01±0.37	0.19±0.33
032844.06+301647.11	03:28:44.06	+30:16:47.11	0.2401±0.0096	0.2071	0.0080	0.1725±0.0117	0.1806	0.0122	-0.73±0.17	-0.30±0.17
032845.43+301641.82	03:28:45.43	+30:16:41.83	0.1333±0.0094	0.1227	0.0084	<0.0435±0.0145	<0.0435	0.0145	<-2.47±0.75	<-2.28±0.75
032846.23+301812.62	03:28:46.23	+30:18:12.62	0.0405±0.0092	0.0407	0.0067	0.0724±0.0154	0.0474	0.0076	1.28±0.69	-1.29±0.82
032847.52+301835.42	03:28:47.52	+30:18:35.42	<0.0201±0.0067	<0.0201	0.0067	0.0451±0.0087	0.0457	0.0076	>1.77±0.85	>1.81±0.37
032848.25+301722.37	03:28:48.25	+30:17:22.38	0.1616±0.0107	0.1284	0.0081	0.0962±0.0131	0.1053	0.0131	-1.14±0.33	-0.44±0.31
032848.70+301903.58	03:28:48.71	+30:19:03.59	<0.0203±0.0068	<0.0203	0.0068	0.0468±0.0082	0.0561	0.0077	>1.84±0.83	>2.24±0.30
032854.42+302202.28	03:28:54.42	+30:22:02.29	2.1450±0.1158	0.1429	0.0096	<1.1111±0.0213	<0.0638	0.0213	<-1.45±0.15	<-1.33±0.06
032901.45+302044.25	03:29:01.45	+30:20:44.26	0.4951±0.0156	0.4234	0.0144	—	—	—	—	—
032905.57+302300.39	03:29:05.58	+30:23:00.39	0.3878±0.0297	0.3397	0.0291	—	—	—	—	—
032803.71+305839.53	03:28:03.71	+30:58:39.54	4.2055±0.4591	0.4978	0.0269	—	—	—	—	—
032807.88+310007.13	03:28:07.88	+31:00:07.13	0.1859±0.0188	0.1505	0.0152	—	—	—	—	—
032826.22+310306.53	03:28:26.23	+31:03:06.53	0.0759±0.0076	0.0753	0.0067	0.0600±0.0090	0.0646	0.0084	-0.52±0.40	-0.34±0.35
032826.45+305833.39	03:28:26.46	+30:58:33.39	0.0374±0.0071	0.0421	0.0067	0.0197±0.0206	0.0277	0.0084	-1.41±2.34	-0.92±0.76
032832.71+310123.59	03:28:32.71	+31:01:23.59	0.0315±0.0060	0.0321	0.0053	0.0278±0.0054	0.0305	0.0046	-0.28±0.60	-0.11±0.50
032838.07+305853.18	03:28:38.08	+30:58:53.18	0.1578±0.0071	0.1502	0.0060	0.0994±0.0080	0.0862	0.0062	-1.02±0.20	-1.22±0.18
032847.09+305835.43	03:28:47.09	+30:58:35.44	0.2256±0.0105	0.1862	0.0076	0.1950±0.0134	0.1771	0.0119	-0.32±0.18	-0.11±0.17
032847.36+310110.31	03:28:47.36	+31:01:10.31	0.0682±0.0085	0.0554	0.0066	0.0755±0.0102	0.0693	0.0081	0.22±0.40	0.49±0.37
032847.45+305706.43	03:28:47.45	+30:57:06.44	0.0833±0.0104	0.0865	0.0103	0.1367±0.0685	0.0926	0.0287	1.09±1.14	0.15±0.73
032851.59+305926.99	03:28:51.60	+30:59:26.99	0.1080±0.0111	0.0812	0.0084	0.1023±0.0490	0.0695	0.0156	-0.12±1.08	-0.34±0.54
032857.65+310044.46	03:28:57.65	+31:00:44.47	0.0704±0.0108	0.0826	0.0113	<0.1184±0.0395	<0.1184	0.0395	<1.14±0.81	<0.79±0.79
032902.44+310127.65	03:29:02.45	+31:01:27.66	0.1014±0.0142	0.1043	0.0170	—	—	—	—	—
034332.91+320210.36	03:43:32.91	+32:02:10.36	0.0530±0.0095	0.0519	0.0081	0.0318±0.0412	0.0469	0.0146	-1.13±2.88	-0.22±0.77
034334.34+320154.97	03:43:34.35	+32:01:54.98	<0.0231±0.0077	<0.0231	0.0077	0.0581±0.0103	0.0837	0.0128	>2.03±0.83	>2.83±0.34
034340.18+320645.63	03:43:40.19	+32:06:45.64	0.0588±0.0088	0.0548	0.0079	<0.0407±0.0136	<0.0407	0.0136	<-0.81±0.80	<-0.65±0.80
034353.59+320117.24	03:43:53.60	+32:01:17.24	0.0395±0.0065	0.0413	0.0058	<0.0178±0.0059	<0.0178	0.0059	<-1.75±0.82	<-1.85±0.80
034402.80+320553.06	03:44:02.81	+32:05:53.07	<0.0213±0.0071	<0.0213	0.0071	0.0467±0.0111	0.0665	0.0102	>1.73±0.90	>2.51±0.34
032717.23+301041.41	03:27:17.24	+30:10:41.42	0.1908±0.0159	0.1599	0.0159	—	—	—	—	—
032719.74+301334.45	03:27:19.74	+30:13:34.46	0.1034±0.0154	0.0837	0.0109	<0.0904±0.0301	<0.0904	0.0301	<-0.30±0.80	<0.17±0.79
032723.71+301542.28	03:27:23.72	+30:15:42.28	0.8664±0.0141	0.7104	0.0106	0.6439±0.0618	0.4759	0.0275	-0.65±0.21	-0.88±0.13
032726.92+300834.19	03:27:26.93	+30:08:34.19	0.0980±0.0143	0.0988	0.0141	—	—	—	—	—
032727.58+301504.08	03:27:27.59	+30:15:04.08	<0.0238±0.0079	<0.0238	0.0079	0.0489±0.0128	0.0495	0.0119	>1.58±0.93	>1.61±0.53
032728.96+301435.03	03:27:28.97	+30:14:35.04	0.1151±0.0121	0.0572	0.0071	<0.0265±0.0088	<0.0265	0.0088	<-3.24±0.77	<-1.70±0.78

Table 2.7: continued.

Name	RA	Dec	F^a_{vint} 6.4 cm	F^b_{vpeak} 6.4 cm	RMS 6.4 cm	F^a_{vint} 4.1 cm	F^b_{vpeak} 4.1 cm	RMS 4.1 cm	Sp. Index Int.[c]	Sp. Index Peak[d]
	J2000	J2000	mJy	mJy/beam	mJy/beam	mJy	mJy/beam	mJy/beam		
032729.43+301439.98	03:27:29.43	+30:14:39.99	0.0754±0.0107	0.0534	0.0071	<0.0258±0.0086	<0.0258	0.0086	<-2.36±0.80	<-1.60±0.79
032729.65+301444.55	03:27:29.66	+30:14:44.55	0.4015±0.0085	0.3685	0.0071	0.2805±0.0169	0.2743	0.0086	-0.79±0.14	-0.65±0.08
032730.19+301454.53	03:27:30.19	+30:14:54.53	1.7027±0.1407	0.2771	0.0071	0.5980±0.1101	0.0850	0.0086	-2.30±0.44	-4.69±0.59
032731.56+301428.51	03:27:31.57	+30:14:28.51	0.1212±0.0081	0.1059	0.0065	0.0541±0.0077	0.0535	0.0068	-1.78±0.35	-1.50±0.31
032731.59+301612.87	03:27:31.60	+30:16:12.87	0.0896±0.0091	0.0824	0.0083	<0.0398±0.0133	<0.0398	0.0133	<-1.79±0.77	<-1.60±0.77
032735.35+301140.36	03:27:35.35	+30:11:40.36	<0.0179±0.0060	<0.0179	0.0060	0.0270±0.0062	0.0273	0.0054	>0.91±0.89	>0.94±0.44
032736.09+301236.68	03:27:36.10	+30:12:36.68	0.0556±0.0067	0.0513	0.0056	0.0398±0.0056	0.0385	0.0046	-0.74±0.41	-0.63±0.36
032741.25+301750.65	03:27:41.25	+30:17:50.66	1.0649±0.0132	0.8821	0.0107	0.5351±0.0569	0.4808	0.0287	-1.52±0.24	-1.34±0.13
032744.74+301430.67	03:27:44.74	+30:14:30.68	<0.0171±0.0057	<0.0171	0.0057	0.0236±0.0056	0.0239	0.0048	>0.71±0.90	>0.74±0.45
032745.19+301105.16	03:27:45.20	+30:11:05.17	<0.0181±0.0060	<0.0181	0.0060	0.0361±0.0060	0.0382	0.0057	>1.52±0.82	>1.64±0.33
032745.36+301425.88	03:27:45.36	+30:14:25.89	0.0883±0.0054	0.0990	0.0057	0.1258±0.0098	0.1235	0.0048	0.78±0.22	0.49±0.15
032745.41+301412.74	03:27:45.42	+30:14:12.75	<0.0168±0.0056	<0.0168	0.0056	0.0195±0.0053	0.0197	0.0046	>0.33±0.95	>0.35±0.52
032747.75+301346.48	03:27:47.75	+30:13:46.49	<0.0169±0.0056	<0.0169	0.0056	0.0246±0.0054	0.0249	0.0047	>0.83±0.88	>0.85±0.42
032748.10+301450.82	03:27:48.11	+30:14:50.83	<0.0184±0.0061	<0.0184	0.0061	0.0287±0.0065	0.0291	0.0058	>0.99±0.89	>1.01±0.44
032748.34+301525.67	03:27:48.34	+30:15:25.68	<0.0198±0.0066	<0.0198	0.0066	0.0415±0.0080	0.0420	0.0071	>1.63±0.85	>1.66±0.37
032748.35+301439.30	03:27:48.36	+30:14:39.30	0.0817±0.0064	0.0824	0.0060	0.0623±0.0074	0.0578	0.0056	-0.60±0.31	-0.78±0.27
032748.54+301339.57	03:27:48.54	+30:13:39.58	0.0365±0.0063	0.0379	0.0057	<0.0145±0.0048	<0.0145	0.0048	<-2.04±0.83	<-2.12±0.80
032751.06+301230.74	03:27:51.06	+30:12:30.74	<0.0180±0.0060	<0.0180	0.0060	0.0339±0.0068	0.0319	0.0055	>1.39±0.86	>1.26±0.38
032754.68+301305.53	03:27:54.69	+30:13:05.54	<0.0199±0.0066	<0.0199	0.0066	0.0313±0.0079	0.0316	0.0072	>0.99±0.92	>1.02±0.50
032800.56+301345.83	03:28:00.56	+30:13:45.83	0.1118±0.0097	0.1023	0.0088	<0.0477±0.0159	<0.0477	0.0159	<-1.88±0.76	<-1.68±0.76
032801.60+301447.05	03:28:01.60	+30:14:47.05	0.1137±0.0108	0.1001	0.0101	<0.0722±0.0241	<0.0722	0.0241	<-1.00±0.76	<-0.72±0.77
032806.28+301508.19	03:28:06.29	+30:15:08.20	0.3160±0.0165	0.2636	0.0147	—	—	—	—	—
032621.90+301524.43	03:26:21.91	+30:15:24.44	0.0321±0.0064	0.0409	0.0067	<0.0278±0.0093	<0.0278	0.0093	<-0.32±0.86	<-0.85±0.82
032622.17+300937.91	03:26:22.18	+30:09:37.92	0.2463±0.0268	0.1892	0.0215	—	—	—	—	—
032626.03+301555.18	03:26:26.04	+30:15:55.18	<0.0173±0.0058	<0.0173	0.0058	0.0304±0.0072	0.0378	0.0061	>1.24±0.90	>1.72±0.36
032627.66+301615.40	03:26:27.66	+30:16:15.40	<0.0167±0.0056	<0.0167	0.0056	0.0305±0.0150	0.0226	0.0056	>1.33±1.31	>0.67±0.55
032627.89+301621.21	03:26:27.89	+30:16:21.22	<0.0167±0.0056	<0.0167	0.0056	0.0294±0.0171	0.0181	0.0056	>1.25±1.48	>0.17±0.68
032628.05+301542.81	03:26:28.06	+30:15:42.81	<0.0163±0.0054	<0.0163	0.0054	0.0377±0.0073	0.0334	0.0052	>1.85±0.85	>1.58±0.34
032629.70+301406.60	03:26:29.71	+30:14:06.61	<0.0165±0.0055	<0.0165	0.0055	0.0282±0.0054	0.0342	0.0054	>1.18±0.85	>1.61±0.35
032635.17+301416.28	03:26:35.18	+30:14:16.29	0.2456±0.0060	0.2553	0.0050	0.1634±0.0055	0.1449	0.0043	-0.90±0.09	-1.25±0.08
032635.33+301705.46	03:26:35.33	+30:17:05.46	0.1046±0.0054	0.1116	0.0052	0.0720±0.0049	0.0754	0.0047	-0.82±0.19	-0.86±0.17
032639.22+301423.01	03:26:39.23	+30:14:23.02	0.0436±0.0072	0.0407	0.0050	0.0248±0.0138	0.0152	0.0042	-1.24±1.28	-2.17±0.67
032639.74+301141.91	03:26:39.74	+30:11:41.92	0.0392±0.0072	0.0458	0.0074	<0.0366±0.0122	<0.0366	0.0122	<-0.15±0.84	<-0.49±0.82
032640.24+301741.92	03:26:40.24	+30:17:41.92	0.0359±0.0060	0.0415	0.0056	<0.0171±0.0057	<0.0171	0.0057	<-1.63±0.82	<-1.95±0.79
032647.82+301518.28	03:26:47.82	+30:15:18.29	0.0484±0.0061	0.0391	0.0056	0.0492±0.0141	0.0234	0.0056	0.04±0.69	-1.13±0.61
032654.25+301608.09	03:26:54.25	+30:16:08.10	0.0365±0.0071	0.0437	0.0072	<0.0340±0.0113	<0.0340	0.0113	<-0.16±0.85	<-0.55±0.82
033204.44+310037.83	03:32:04.45	+31:00:37.83	0.2097±0.0154	0.1878	0.0150	—	—	—	—	—
033206.57+310510.05	03:32:06.57	+31:05:10.06	0.1370±0.0141	0.1169	0.0133	—	—	—	—	—
033212.12+310419.35	03:32:12.12	+31:04:19.35	0.0637±0.0111	0.0518	0.0084	<0.0459±0.0153	<0.0459	0.0153	<-0.72±0.83	<-0.27±0.82
033212.59+305943.66	03:32:12.59	+30:59:43.67	0.0724±0.0104	0.0675	0.0101	<0.0813±0.0271	<0.0813	0.0271	<0.25±0.80	<0.41±0.80

Table 2.7: continued.

Name	RA	Dec	F^a_{vint} 6.4 cm	F^b_{vpeak} 6.4 cm	RMS 6.4 cm	F^a_{vint} 4.1 cm	F^b_{vpeak} 4.1 cm	RMS 4.1 cm	Sp. Index Int.[c]	Sp. Index Peak[d]
	J2000	J2000	mJy	mJy/beam	mJy/beam	mJy	mJy/beam	mJy/beam		
033224.13+310049.22	03:32:24.14	+31:00:49.23	0.0638±0.0081	0.0462	0.0058	0.0508±0.0071	0.0461	0.0056	-0.50±0.42	-0.01±0.39
033224.21+310414.06	03:32:24.21	+31:04:14.07	0.1541±0.0076	0.1297	0.0056	0.1231±0.0063	0.1074	0.0050	-0.50±0.16	-0.42±0.14
033225.22+310516.98	03:32:25.22	+31:05:16.99	<4.3964±0.0062	<0.0187	0.0062	0.5137±0.0589	0.2186	0.0068	>-4.73±0.38	>0.01±0.26
033225.26+310510.13	03:32:25.27	+31:05:10.13	5.9273±0.1285	1.5213	0.0061	2.5193±0.0545	0.5568	0.0064	-1.88±0.07	-2.21±0.03
033228.88+310439.75	03:32:28.88	+31:04:39.75	<0.0168±0.0056	<0.0168	0.0056	0.0271±0.0058	0.0313	0.0051	>1.05±0.87	>1.38±0.36
033231.02+310256.69	03:32:31.03	+31:02:56.70	<0.0151±0.0050	<0.0151	0.0050	0.0210±0.0046	0.0235	0.0039	>0.73±0.88	>0.98±0.36
033237.57+310314.81	03:32:37.58	+31:03:14.81	0.0240±0.0051	0.0339	0.0055	<0.0143±0.0048	<0.0143	0.0048	<-1.13±0.87	<-1.90±0.82
033240.00+305844.00	03:32:40.00	+30:58:44.00	1.1104±0.0141	0.8809	0.0095	1.2312±0.0266	1.0531	0.0221	0.23±0.06	0.39±0.05
033240.94+310835.22	03:32:40.95	+31:08:35.23	1.5869±0.0266	1.1614	0.0186	—	—	—	—	—
033241.52+310410.95	03:32:41.53	+31:04:10.95	0.0573±0.0090	0.0464	0.0064	<0.0218±0.0073	<0.0218	0.0073	<-2.13±0.81	<-1.67±0.79
033205.81+304937.18	03:32:05.82	+30:49:37.19	0.0297±0.0061	0.0385	0.0061	<0.0194±0.0065	<0.0194	0.0065	<-0.94±0.86	<-1.51±0.81
033208.73+304617.42	03:32:08.73	+30:46:17.43	0.0546±0.0087	0.0543	0.0081	0.0832±0.0384	0.0487	0.0144	0.93±1.08	-0.24±0.73
033208.96+304822.03	03:32:08.97	+30:48:22.03	0.0423±0.0070	0.0413	0.0059	0.0301±0.0169	0.0188	0.0059	-0.75±1.29	-1.74±0.76
033212.00+304753.27	03:32:12.01	+30:47:53.27	<0.0174±0.0058	<0.0174	0.0058	0.0343±0.0060	0.0393	0.0057	>1.49±0.83	>1.79±0.32
033212.21+304952.67	03:32:12.22	+30:49:52.68	<0.3224±0.0052	<0.0156	0.0052	0.1300±0.0227	0.0250	0.0043	>-2.00±0.46	>-2.55±0.79
033212.78+305332.23	03:32:12.78	+30:53:32.23	0.0937±0.0096	0.0846	0.0079	0.0663±0.0392	0.0581	0.0132	-0.76±1.32	-0.83±0.54
033216.49+305319.25	03:32:16.50	+30:53:19.25	0.0636±0.0077	0.0643	0.0072	0.0389±0.0282	0.0409	0.0104	-1.08±1.62	-1.00±0.61
033216.88+305112.55	03:32:16.88	+30:51:12.55	0.0468±0.0066	0.0422	0.0053	0.0268±0.0144	0.0202	0.0045	-1.23±1.22	-1.62±0.56
033218.42+304946.01	03:32:18.42	+30:49:46.02	0.0250±0.0053	0.0309	0.0050	0.0066±0.0100	0.0118	0.0039	-2.95±3.40	-2.11±0.80
033219.26+304803.01	03:32:19.27	+30:48:03.02	0.1287±0.0057	0.1341	0.0054	0.1084±0.0056	0.1002	0.0048	-0.38±0.15	-0.64±0.14
033221.26+305006.71	03:32:21.26	+30:50:06.71	<0.0152±0.0051	<0.0152	0.0051	0.0204±0.0044	0.0265	0.0040	>0.65±0.87	>1.23±0.33
033223.53+304946.15	03:32:23.53	+30:49:46.15	1.6400±0.0506	0.2168	0.0052	1.1425±0.0600	0.0775	0.0043	-0.80±0.13	-2.37±0.28
033243.20+304725.08	03:32:43.20	+30:47:25.09	0.2439±0.0156	0.2262	0.0154	—	—	—	—	—
033247.38+305022.57	03:32:47.39	+30:50:22.58	5.0763±0.1041	3.8361	0.0187	—	—	—	—	—
033052.80+304601.76	03:30:52.81	+30:46:01.77	0.6603±0.0190	0.6110	0.0217	—	—	—	—	—
033108.01+304220.68	03:31:08.02	+30:42:20.69	0.1103±0.0104	0.1016	0.0112	0.1394±0.0457	0.0836	0.0174	0.52±0.75	-0.43±0.52
033118.77+304302.48	03:31:18.78	+30:43:02.49	0.0467±0.0067	0.0481	0.0079	0.0419±0.0055	0.0537	0.0065	-0.24±0.43	0.24±0.45
033118.95+305108.08	03:31:18.95	+30:51:08.08	0.8382±0.0194	0.7848	0.0182	—	—	—	—	—
033119.13+304158.84	03:31:19.14	+30:41:58.84	0.0741±0.0097	0.0614	0.0096	0.0555±0.0328	0.0454	0.0109	-0.64±1.34	-0.67±0.63
033125.83+304554.06	03:31:25.84	+30:45:54.07	<0.0204±0.0068	<0.0204	0.0068	0.0199±0.0049	0.0281	0.0044	>-0.06±0.91	>0.71±0.35
033127.08+304007.83	03:31:27.08	+30:40:07.84	0.1279±0.0155	0.1085	0.0173	—	—	—	—	—
033132.02+304657.15	03:31:32.02	+30:46:57.15	0.0826±0.0074	0.0787	0.0082	0.0811±0.0095	0.0650	0.0073	-0.04±0.32	-0.42±0.34
033141.74+304539.04	03:31:41.74	+30:45:39.04	0.2176±0.0090	0.2209	0.0121	0.2383±0.0260	0.2148	0.0216	0.20±0.26	-0.06±0.25
033147.53+304640.93	03:31:47.53	+30:46:40.94	0.2930±0.0160	0.2745	0.0195	—	—	—	—	—
034432.29+320609.61	03:44:32.30	+32:06:09.62	0.0636±0.0104	0.0716	0.0117	—	—	—	—	—
034437.92+320031.98	03:44:37.92	+32:00:31.98	0.0244±0.0048	0.0346	0.0052	<0.0131±0.0044	<0.0131	0.0044	<-1.38±0.85	<-2.15±0.81
034438.07+315940.20	03:44:38.08	+31:59:40.21	0.0749±0.0092	0.0527	0.0056	0.0647±0.0084	0.0392	0.0052	-0.32±0.39	-0.65±0.37
034439.83+320128.51	03:44:39.83	+32:01:28.52	0.0615±0.0057	0.0605	0.0050	0.0772±0.0049	0.0681	0.0039	0.50±0.25	0.26±0.22
034444.08+315855.73	03:44:44.08	+31:58:55.73	<0.0178±0.0059	<0.0178	0.0059	0.0370±0.0064	0.0385	0.0060	>1.61±0.83	>1.70±0.34
034445.01+320200.80	03:44:45.02	+32:02:00.81	0.0366±0.0054	0.0422	0.0050	0.0288±0.0040	0.0325	0.0038	-0.53±0.44	-0.58±0.37

Table 2.7: continued.

Name	RA	Dec	F^a_{vint} 6.4 cm	F^b_{vpeak} 6.4 cm	RMS 6.4 cm	F^a_{vint} 4.1 cm	F^b_{vpeak} 4.1 cm	RMS 4.1 cm	Sp. Index Int.[c]	Sp. Index Peak[d]
	J2000	J2000	mJy	mJy/beam	mJy/beam	mJy	mJy/beam	mJy/beam		
034458.11+320014.50	03:44:58.11	+32:00:14.51	0.0500±0.0083	0.0459	0.0068	0.0635±0.0202	0.0491	0.0088	0.53±0.79	0.15±0.51
034506.10+315944.42	03:45:06.11	+31:59:44.42	0.1070±0.0133	0.0909	0.0111	—	—	—	—	—
034714.72+325217.62	03:47:14.72	+32:52:17.63	0.2123±0.0128	0.2017	0.0134	—	—	—	—	—
034724.76+325058.82	03:47:24.77	+32:50:58.82	0.0839±0.0083	0.0809	0.0071	0.0627±0.0301	0.0516	0.0105	-0.64±1.08	-0.99±0.49
034725.51+325150.88	03:47:25.51	+32:51:50.88	0.0372±0.0069	0.0438	0.0068	0.0463±0.0217	0.0424	0.0091	0.48±1.11	-0.07±0.58
034730.11+325332.10	03:47:30.11	+32:53:32.10	0.0556±0.0079	0.0496	0.0063	<0.0225±0.0075	<0.0225	0.0075	<-1.99±0.80	<-1.74±0.79
034731.60+324854.03	03:47:31.60	+32:48:54.03	0.0688±0.0094	0.0533	0.0070	0.0454±0.0324	0.0378	0.0099	-0.91±1.60	-0.75±0.65
034733.64+325719.98	03:47:33.64	+32:57:19.98	0.0905±0.0156	0.0915	0.0144	—	—	—	—	—
034735.86+325104.48	03:47:35.87	+32:51:04.48	<0.0152±0.0051	<0.0152	0.0051	0.0177±0.0049	0.0262	0.0043	>0.33±0.95	>1.19±0.36
034736.08+325300.15	03:47:36.09	+32:53:00.16	0.0320±0.0061	0.0336	0.0052	0.0180±0.0124	0.0206	0.0046	-1.27±1.57	-1.07±0.60
034737.17+325225.53	03:47:37.17	+32:52:25.53	<0.0150±0.0050	<0.0150	0.0050	0.0219±0.0048	0.0259	0.0041	>0.84±0.88	>1.20±0.35
034744.16+324942.62	03:47:44.16	+32:49:42.62	0.0377±0.0060	0.0415	0.0055	0.0267±0.0138	0.0238	0.0052	-0.76±1.19	-1.22±0.56
034745.36+325329.08	03:47:45.37	+32:53:29.08	0.0241±0.0056	0.0323	0.0054	<0.0148±0.0049	<0.0148	0.0049	<-1.09±0.90	<-1.73±0.82
034745.48+325226.86	03:47:45.48	+32:52:26.86	0.0448±0.0068	0.0355	0.0050	0.0341±0.0134	0.0221	0.0041	-0.60±0.93	-1.04±0.51
034745.48+325308.04	03:47:45.49	+32:53:08.05	0.0802±0.0058	0.0777	0.0052	0.0656±0.0058	0.0618	0.0045	-0.44±0.25	-0.51±0.22
034752.59+324634.11	03:47:52.60	+32:46:34.12	0.1423±0.0160	0.1180	0.0134	—	—	—	—	—
034753.31+324840.83	03:47:53.31	+32:48:40.83	0.0889±0.0082	0.0927	0.0077	0.1004±0.0168	0.0897	0.0130	0.27±0.42	-0.07±0.37
034753.77+325039.07	03:47:53.78	+32:50:39.08	0.0696±0.0071	0.0709	0.0061	0.0495±0.0100	0.0441	0.0067	-0.75±0.50	-1.05±0.39
034648.40+324558.35	03:46:48.40	+32:45:58.36	0.1045±0.0112	0.0930	0.0091	<0.0655±0.0218	<0.0655	0.0218	<-1.03±0.77	<-0.77±0.77
034655.51+324317.73	03:46:55.51	+32:43:17.73	0.5746±0.0077	0.4817	0.0055	0.2920±0.0077	0.2344	0.0052	-1.49±0.07	-1.59±0.05
034657.28+324519.95	03:46:57.29	+32:45:19.95	0.0411±0.0063	0.0425	0.0060	0.0395±0.0173	0.0269	0.0067	-0.09±1.02	-1.00±0.63
034659.31+324441.71	03:46:59.31	+32:44:41.71	<0.0162±0.0054	<0.0162	0.0054	0.0292±0.0058	0.0322	0.0050	>1.29±0.86	>1.51±0.35
034700.23+324334.78	03:47:00.24	+32:43:34.78	0.2019±0.0063	0.1913	0.0050	0.1640±0.0049	0.1546	0.0041	-0.46±0.10	-0.47±0.08
034700.23+324555.02	03:47:00.24	+32:45:55.03	0.0413±0.0071	0.0385	0.0063	<0.0222±0.0074	<0.0222	0.0074	<-1.36±0.83	<-1.21±0.82
034703.78+324520.62	03:47:03.79	+32:45:20.62	0.0273±0.0055	0.0337	0.0056	<0.0162±0.0054	<0.0162	0.0054	<-1.14±0.86	<-1.61±0.82
034703.91+324208.61	03:47:03.91	+32:42:08.61	0.1023±0.0067	0.0886	0.0050	0.0447±0.0046	0.0447	0.0040	-1.83±0.27	-1.51±0.23
034704.82+324309.10	03:47:04.82	+32:43:09.10	<0.0144±0.0048	<0.0144	0.0048	0.0163±0.0046	0.0227	0.0037	>0.27±0.96	>0.99±0.36
034705.57+324605.69	03:47:05.58	+32:46:05.69	0.0258±0.0054	0.0381	0.0062	<0.0219±0.0073	<0.0219	0.0073	<-0.36±0.87	<-1.22±0.82
034705.72+323758.84	03:47:05.72	+32:37:58.85	0.2557±0.0138	0.2059	0.0111	—	—	—	—	—
034706.55+324338.94	03:47:06.55	+32:43:38.94	<0.0146±0.0049	<0.0146	0.0049	0.0186±0.0046	0.0230	0.0038	>0.53±0.92	>1.01±0.37
034707.45+324201.16	03:47:07.46	+32:42:01.16	0.0888±0.0062	0.0884	0.0050	0.0581±0.0049	0.0572	0.0041	-0.93±0.24	-0.96±0.20
034709.11+324116.63	03:47:09.12	+32:41:16.63	0.0381±0.0075	0.0343	0.0054	0.0413±0.0069	0.0363	0.0050	0.18±0.57	0.13±0.46
034709.83+324602.03	03:47:09.84	+32:46:02.03	0.0584±0.0076	0.0547	0.0063	0.0321±0.0211	0.0257	0.0076	-1.32±1.48	-1.66±0.70
034710.32+324334.28	03:47:10.32	+32:43:34.29	0.0198±0.0043	0.0301	0.0050	<0.0123±0.0041	<0.0123	0.0041	<-1.05±0.88	<-1.97±0.82
034711.50+324458.53	03:47:11.51	+32:44:58.53	0.0310±0.0057	0.0343	0.0056	0.0233±0.0129	0.0180	0.0054	-0.63±1.29	-1.42±0.76
034711.55+323826.11	03:47:11.55	+32:38:26.11	0.2523±0.0122	0.2026	0.0101	0.2629±0.0902	0.1657	0.0299	0.09±0.76	-0.44±0.41
034712.12+323925.05	03:47:12.12	+32:39:25.06	0.2323±0.0203	0.0792	0.0078	0.1410±0.0922	0.0502	0.0135	-1.10±1.45	-0.98±0.45
034712.24+324418.90	03:47:12.25	+32:44:18.90	<0.0159±0.0053	<0.0159	0.0053	0.0180±0.0056	0.0291	0.0048	>0.27±1.00	>1.33±0.36
034716.78+324309.03	03:47:16.79	+32:43:09.03	0.0774±0.0074	0.0697	0.0057	0.0510±0.0072	0.0473	0.0057	-0.92±0.38	-0.85±0.32
034717.20+324055.16	03:47:17.20	+32:40:55.16	0.3749±0.0081	0.3519	0.0067	0.3126±0.0107	0.2850	0.0089	-0.40±0.09	-0.46±0.08

Table 2.7: continued.

Name	RA	Dec	F^a_{vint} 6.4 cm	F^b_{vpeak} 6.4 cm	RMS 6.4 cm	F^a_{vint} 4.1 cm	F^b_{vpeak} 4.1 cm	RMS 4.1 cm	Sp. Index Int.[c]	Sp. Index Peak[d]
	J2000	J2000	mJy	mJy/beam	mJy/beam	mJy	mJy/beam	mJy/beam		
034717.81+323859.74	03:47:17.82	+32:38:59.74	0.8787±0.0126	0.7111	0.0101	0.4332±0.0316	0.4230	0.0305	-1.56±0.16	-1.14±0.16
034721.38+324106.02	03:47:21.38	+32:41:06.02	0.0480±0.0071	0.0478	0.0077	0.0765±0.0311	0.0494	0.0130	1.03±0.95	0.08±0.68
032953.62+302710.43	03:29:53.63	+30:27:10.43	0.1305±0.0147	0.1194	0.0145	—	—	—	—	—
032957.68+302331.91	03:29:57.69	+30:23:31.92	0.4356±0.0128	0.3225	0.0078	1.4523±0.0298	0.8592	0.0127	2.65±0.08	2.16±0.06
032959.91+302149.66	03:29:59.91	+30:21:49.66	0.0902±0.0119	0.0699	0.0079	<0.0399±0.0133	<0.0399	0.0133	<-1.80±0.79	<-1.24±0.78
033002.21+302756.85	03:30:02.22	+30:27:56.86	<0.0331±0.0110	<0.0331	0.0110	0.2146±0.0391	0.2212	0.0364	>4.12±0.84	>4.19±0.36
033006.67+302143.44	03:30:06.67	+30:21:43.44	0.0578±0.0075	0.0531	0.0064	0.0381±0.0226	0.0245	0.0073	-0.92±1.34	-1.70±0.71
033010.51+302259.39	03:30:10.51	+30:22:59.40	0.0306±0.0062	0.0342	0.0053	<0.0138±0.0046	<0.0138	0.0046	<-1.76±0.86	<-2.00±0.81
033010.56+302340.01	03:30:10.57	+30:23:40.01	<0.0157±0.0052	<0.0157	0.0052	0.0225±0.0053	0.0266	0.0044	>0.79±0.90	>1.16±0.36
033012.10+302424.04	03:30:12.11	+30:24:24.05	<0.0156±0.0052	<0.0156	0.0052	0.0172±0.0050	0.0259	0.0043	>0.22±0.98	>1.11±0.37
033015.73+302357.34	03:30:15.73	+30:23:57.35	<0.0153±0.0051	<0.0153	0.0051	0.0212±0.0050	0.0249	0.0041	>0.72±0.90	>1.07±0.36
033017.31+302252.32	03:30:17.31	+30:22:52.33	0.0248±0.0048	0.0335	0.0053	<0.0132±0.0044	<0.0132	0.0044	<-1.38±0.85	<-2.04±0.81
033017.43+301722.32	03:30:17.44	+30:17:22.33	0.1347±0.0211	0.1273	0.0202	—	—	—	—	—
033019.22+302231.60	03:30:19.22	+30:22:31.61	0.0418±0.0063	0.0392	0.0055	0.0293±0.0152	0.0204	0.0049	-0.78±1.19	-1.44±0.61
033020.23+302114.50	03:30:20.24	+30:21:14.50	<0.0193±0.0064	<0.0193	0.0064	0.0364±0.0086	0.0451	0.0074	>1.41±0.90	>1.88±0.36
033021.33+302324.69	03:30:21.33	+30:23:24.69	0.0346±0.0067	0.0330	0.0054	<0.0141±0.0047	<0.0141	0.0047	<-1.98±0.85	<-1.88±0.82
033021.43+302220.96	03:30:21.43	+30:22:20.97	0.0463±0.0079	0.0373	0.0057	0.0356±0.0197	0.0223	0.0055	-0.58±1.27	-1.13±0.64
033022.43+302447.99	03:30:22.43	+30:24:47.99	0.0655±0.0068	0.0577	0.0056	0.0367±0.0166	0.0210	0.0052	-1.27±1.02	-2.23±0.59
033022.71+302559.92	03:30:22.72	+30:25:59.93	0.0695±0.0089	0.0547	0.0063	0.0497±0.0265	0.0311	0.0071	-0.74±1.21	-1.24±0.57
033026.88+301931.74	03:30:26.88	+30:19:31.74	0.1195±0.0144	0.0940	0.0111	<0.1103±0.0368	<0.1103	0.0368	<-0.18±0.78	<0.35±0.78
033032.31+302042.69	03:30:32.32	+30:20:42.69	0.4108±0.0163	0.3020	0.0105	0.2459±0.1137	0.1497	0.0312	-1.13±1.02	-1.55±0.47
032519.59+304621.48	03:25:19.60	+30:46:21.48	0.0423±0.0084	0.0505	0.0083	<0.0428±0.0143	<0.0428	0.0143	<0.02±0.85	<-0.36±0.82
032532.42+304358.17	03:25:32.43	+30:43:58.17	0.0307±0.0055	0.0345	0.0055	<0.0142±0.0047	<0.0142	0.0047	<-1.70±0.83	<-1.95±0.81
032533.32+304504.24	03:25:33.32	+30:45:04.24	<0.0160±0.0053	<0.0160	0.0053	0.0235±0.0050	0.0268	0.0043	>0.85±0.87	>1.14±0.36
032553.14+304602.23	03:25:53.15	+30:46:02.24	0.0985±0.0117	0.0788	0.0080	0.0777±0.0377	0.0424	0.0130	-0.52±1.10	-1.37±0.71
032556.36+304717.29	03:25:56.36	+30:47:17.30	<0.0331±0.0110	<0.0331	0.0110	0.2106±0.0334	0.2125	0.0338	>4.07±0.81	>4.09±0.35
033245.64+312452.53	03:32:45.64	+31:24:52.54	0.1786±0.0216	0.1467	0.0232	—	—	—	—	—
033251.28+312308.11	03:32:51.29	+31:23:08.12	1.3834±0.1037	0.4724	0.0106	0.7010±0.2307	0.1625	0.0325	-1.50±0.74	0.59±0.80
033256.34+312555.79	03:32:56.34	+31:25:55.79	0.1048±0.0144	0.0906	0.0145	—	—	—	—	—
033258.53+312642.65	03:32:58.54	+31:26:42.66	0.1597±0.0171	0.1415	0.0173	—	—	—	—	—
033300.47+312303.83	03:33:00.48	+31:23:03.83	0.0431±0.0065	0.0433	0.0066	0.0353±0.0193	0.0252	0.0083	-0.44±1.25	-1.19±0.80
033300.97+311630.55	03:33:00.98	+31:16:30.56	0.1098±0.0156	0.0866	0.0126	—	—	—	—	—
033301.07+312017.97	03:33:01.07	+31:20:17.98	0.9922±0.0904	0.1060	0.0061	0.5288±0.0689	0.0667	0.0066	-1.39±0.35	-2.11±0.23
033301.18+312355.87	03:33:01.19	+31:23:55.87	<0.0219±0.0073	<0.0219	0.0073	0.0629±0.0260	0.0430	0.0107	>2.32±1.17	>1.49±0.55
033305.49+312119.58	03:33:05.49	+31:21:19.58	0.8815±0.0069	0.8232	0.0053	0.6732±0.0061	0.6143	0.0046	-0.59±0.03	-0.64±0.02
033308.46+312223.89	03:33:08.47	+31:22:23.89	0.0307±0.0060	0.0340	0.0052	<0.0133±0.0044	<0.0133	0.0044	<-1.84±0.85	<-2.07±0.81
033309.51+312243.47	03:33:09.51	+31:22:43.48	0.0421±0.0062	0.0440	0.0053	0.0320±0.0053	0.0325	0.0046	-0.60±0.48	-0.66±0.41
033309.88+311938.99	03:33:09.89	+31:19:38.100	0.0273±0.0053	0.0353	0.0054	<0.0145±0.0048	<0.0145	0.0048	<-1.40±0.85	<-1.96±0.81
033310.68+312429.25	03:33:10.68	+31:24:29.26	0.9460±0.0085	0.8524	0.0067	0.6185±0.0109	0.5300	0.0085	-0.94±0.04	-1.05±0.04
033311.68+312244.53	03:33:11.69	+31:22:44.54	0.0536±0.0062	0.0522	0.0053	0.0617±0.0060	0.0541	0.0045	0.31±0.33	0.08±0.29

Table 2.7: continued.

Name	RA	Dec	F^a_{vint} 6.4 cm	F^b_{vpeak} 6.4 cm	RMS 6.4 cm	F^a_{vint} 4.1 cm	F^b_{vpeak} 4.1 cm	RMS 4.1 cm	Sp. Index Int.[c]	Sp. Index Peak[d]
	J2000	J2000	mJy	mJy/beam	mJy/beam	mJy	mJy/beam	mJy/beam		
033311.84+312546.86	03:33:11.85	+31:25:46.87	0.1676±0.0137	0.1079	0.0091	<0.0615±0.0205	<0.0615	0.0205	<-2.21±0.76	<-1.24±0.76
033312.67+312407.59	03:33:12.67	+31:24:07.59	0.1531±0.0109	0.1010	0.0062	0.1208±0.0087	0.1008	0.0070	-0.52±0.22	-0.00±0.20
033312.75+312201.48	03:33:12.76	+31:22:01.49	0.0412±0.0059	0.0458	0.0050	0.0287±0.0101	0.0205	0.0040	-0.80±0.84	-1.78±0.49
033314.86+312654.13	03:33:14.86	+31:26:54.14	4.7995±0.0420	3.5027	0.0135	—	—	—	—	—
033315.44+311815.86	03:33:15.45	+31:18:15.87	0.5455±0.0077	0.5057	0.0066	0.2801±0.0090	0.2702	0.0081	-1.47±0.08	-1.38±0.07
033319.19+312213.82	03:33:19.20	+31:22:13.82	0.0810±0.0057	0.0800	0.0054	0.0601±0.0058	0.0616	0.0047	-0.66±0.26	-0.57±0.22
033319.34+312632.00	03:33:19.35	+31:26:32.01	0.1990±0.0160	0.1428	0.0125	—	—	—	—	—
033319.55+311857.94	03:33:19.55	+31:18:57.94	0.0431±0.0073	0.0379	0.0062	<0.0206±0.0069	<0.0206	0.0069	<-1.63±0.82	<-1.35±0.82
033320.42+312611.73	03:33:20.42	+31:26:11.73	0.0701±0.0102	0.0816	0.0114	—	—	—	—	—
033322.89+312549.06	03:33:22.90	+31:25:49.07	0.0856±0.0125	0.0762	0.0108	<0.1050±0.0350	<0.1050	0.0350	<0.45±0.80	<0.71±0.80
033330.46+311758.07	03:33:30.46	+31:17:58.08	1.4990±0.1072	0.2998	0.0110	<0.1129±0.0376	<0.1129	0.0376	<-5.70±0.75	<-2.15±0.74
033330.79+311758.04	03:33:30.79	+31:17:58.05	2.3267±0.2322	0.3170	0.0112	—	—	—	—	—
034344.43+320159.61	03:43:44.44	+32:01:59.62	0.0435±0.0074	0.0442	0.0068	0.0439±0.0227	0.0266	0.0087	0.02±1.20	-1.12±0.79
034345.99+320028.25	03:43:45.100	+32:00:28.25	0.0375±0.0066	0.0445	0.0067	<0.0247±0.0082	<0.0247	0.0082	<-0.92±0.83	<-1.30±0.81
034351.19+320339.99	03:43:51.20	+32:03:39.99	<0.0186±0.0062	<0.0186	0.0062	0.0326±0.0076	0.0410	0.0068	>1.24±0.90	>1.74±0.36
034351.87+320311.89	03:43:51.88	+32:03:11.89	<0.0175±0.0058	<0.0175	0.0058	0.0299±0.0063	0.0346	0.0057	>1.19±0.87	>1.51±0.36
034352.18+320038.33	03:43:52.18	+32:00:38.34	0.0344±0.0067	0.0386	0.0056	<0.0153±0.0051	<0.0153	0.0051	<-1.78±0.85	<-2.03±0.80
034356.13+320128.92	03:43:56.13	+32:01:28.92	0.0227±0.0053	0.0316	0.0051	<0.0125±0.0042	<0.0125	0.0042	<-1.32±0.89	<-2.05±0.82
034401.14+320138.86	03:44:01.15	+32:01:38.86	0.0502±0.0058	0.0505	0.0051	0.0337±0.0118	0.0210	0.0041	-0.88±0.81	-1.93±0.48
034410.93+320234.41	03:44:10.94	+32:02:34.41	<0.0186±0.0062	<0.0186	0.0062	0.0387±0.0076	0.0443	0.0068	>1.61±0.85	>1.91±0.34
033035.15+303157.63	03:30:35.15	+30:31:57.64	<0.0185±0.0062	<0.0185	0.0062	0.0323±0.0068	0.0375	0.0059	>1.22±0.87	>1.56±0.35
033041.64+303223.05	03:30:41.65	+30:32:23.05	<0.0165±0.0055	<0.0165	0.0055	0.0197±0.0052	0.0271	0.0044	>0.38±0.93	>1.08±0.36
033046.28+303311.53	03:30:46.28	+30:33:11.54	0.0289±0.0061	0.0349	0.0055	<0.0133±0.0044	<0.0133	0.0044	<-1.71±0.87	<-2.13±0.81
033046.93+303317.99	03:30:46.94	+30:33:17.99	0.0619±0.0074	0.0483	0.0056	0.0537±0.0146	0.0239	0.0045	-0.31±0.66	-1.55±0.49
033102.31+303506.66	03:31:02.32	+30:35:06.67	0.3387±0.0128	0.2763	0.0104	0.3187±0.0460	0.1928	0.0255	-0.13±0.33	-0.79±0.30
033103.03+303105.58	03:31:03.04	+30:31:05.59	0.1058±0.0117	0.0945	0.0101	0.1730±0.0678	0.1180	0.0234	1.08±0.90	0.49±0.50
033105.55+303507.84	03:31:05.56	+30:35:07.85	0.1128±0.0138	0.1032	0.0128	—	—	—	—	—
033853.72+321600.77	03:38:53.73	+32:16:00.77	0.3595±0.0294	0.2836	0.0229	—	—	—	—	—
033855.73+321448.41	03:38:55.73	+32:14:48.41	1.1633±0.0531	0.3744	0.0216	—	—	—	—	—
033857.74+322018.28	03:38:57.75	+32:20:18.29	0.4026±0.0317	0.2725	0.0219	—	—	—	—	—
033906.96+321830.89	03:39:06.97	+32:18:30.89	0.1328±0.0124	0.0880	0.0085	0.0769±0.0562	0.0491	0.0161	-1.20±1.62	-1.28±0.75
033909.15+321727.06	03:39:09.16	+32:17:27.07	0.0350±0.0072	0.0429	0.0071	<0.0299±0.0100	<0.0299	0.0100	<-0.35±0.86	<-0.80±0.82
033911.19+321448.29	03:39:11.20	+32:14:48.29	0.4469±0.0093	0.4057	0.0076	0.3135±0.0149	0.2709	0.0121	-0.78±0.11	-0.89±0.11
033915.18+321542.46	03:39:15.18	+32:15:42.47	<0.0182±0.0061	<0.0182	0.0061	0.0330±0.0066	0.0392	0.0064	>1.31±0.86	>1.69±0.36
033919.55+321618.29	03:39:19.55	+32:16:18.30	0.1671±0.0061	0.1637	0.0053	0.1185±0.0055	0.1122	0.0046	-0.76±0.13	-0.83±0.12
033920.38+321436.56	03:39:20.39	+32:14:36.56	0.0582±0.0063	0.0609	0.0062	0.0600±0.0173	0.0405	0.0068	0.07±0.68	-0.90±0.43
033921.29+321345.87	03:39:21.30	+32:13:45.87	0.2081±0.0209	0.0697	0.0071	0.1911±0.0697	0.0373	0.0098	-0.19±0.83	-1.65±0.55
033927.97+321926.27	03:39:27.98	+32:19:26.28	0.0978±0.0077	0.0842	0.0060	0.0667±0.0070	0.0614	0.0063	-0.84±0.29	-0.69±0.27
033932.54+321044.53	03:39:32.55	+32:10:44.53	0.2025±0.0209	0.1876	0.0203	—	—	—	—	—
033932.58+321414.39	03:39:32.58	+32:14:14.40	0.1250±0.0085	0.1067	0.0069	0.0976±0.0116	0.0852	0.0089	-0.55±0.30	-0.50±0.27

Table 2.7: continued.

Name	RA	Dec	F^a_{vint} 6.4 cm	F^b_{vpeak} 6.4 cm	RMS 6.4 cm	F^a_{vint} 4.1 cm	F^b_{vpeak} 4.1 cm	RMS 4.1 cm	Sp. Index Int.[c]	Sp. Index Peak[d]
	J2000	J2000	mJy	mJy/beam	mJy/beam	mJy	mJy/beam	mJy/beam		
033947.90+321315.74	03:39:47.90	+32:13:15.74	0.7021±0.0255	0.5078	0.0170	—	—	—	—	—
033948.66+321859.77	03:39:48.66	+32:18:59.77	0.1263±0.0133	0.1190	0.0123	—	—	—	—	—
034418.42+320159.93	03:44:18.42	+32:01:59.93	<0.0204±0.0068	<0.0204	0.0068	0.0363±0.0087	0.0491	0.0080	>1.27±0.91	>1.93±0.36
034427.94+320345.53	03:44:27.94	+32:03:45.54	0.0483±0.0075	0.0463	0.0063	0.0318±0.0175	0.0228	0.0064	-0.92±1.26	-1.56±0.69
034428.73+320533.75	03:44:28.73	+32:05:33.76	0.0596±0.0068	0.0626	0.0062	0.0305±0.0156	0.0216	0.0063	-1.48±1.15	-2.34±0.67
032902.89+311232.60	03:29:02.89	+31:12:32.60	<0.0166±0.0055	<0.0166	0.0055	0.0280±0.0050	0.0383	0.0055	>1.15±0.83	>1.84±0.32
032904.54+310924.38	03:29:04.54	+31:09:24.38	0.0582±0.0094	0.0576	0.0088	<0.0607±0.0202	<0.0607	0.0202	<0.09±0.82	<0.12±0.81
032907.58+311337.99	03:29:07.59	+31:13:37.99	0.0363±0.0057	0.0412	0.0056	0.0206±0.0142	0.0210	0.0057	-1.25±1.55	-1.49±0.67
032910.61+311109.85	03:29:10.62	+31:11:09.85	<0.0172±0.0057	<0.0172	0.0057	0.0254±0.0070	0.0371	0.0060	>0.85±0.95	>1.69±0.36
032910.84+311311.14	03:29:10.84	+31:13:11.15	<0.0146±0.0049	<0.0146	0.0049	0.0213±0.0048	0.0239	0.0039	>0.84±0.89	>1.09±0.36
032916.61+311104.46	03:29:16.62	+31:11:04.46	0.1022±0.0120	0.1102	0.0124	—	—	—	—	—
032916.99+311133.25	03:29:16.100	+31:11:33.26	<0.0169±0.0056	<0.0169	0.0056	0.0287±0.0065	0.0351	0.0058	>1.16±0.89	>1.61±0.36
032920.28+310647.61	03:29:20.28	+31:06:47.62	0.8522±0.0433	0.5064	0.0255	—	—	—	—	—
032924.71+311119.06	03:29:24.71	+31:11:19.06	0.0500±0.0079	0.0518	0.0071	<0.0317±0.0106	<0.0317	0.0106	<-1.00±0.81	<-1.08±0.79
032925.10+311013.18	03:29:25.10	+31:10:13.18	0.0743±0.0104	0.0694	0.0087	0.1082±0.0524	0.1008	0.0194	0.83±1.11	0.82±0.51
032926.92+310948.99	03:29:26.93	+31:09:48.100	0.1423±0.0115	0.1300	0.0104	0.1827±0.0913	0.1338	0.0337	0.55±1.11	0.06±0.58
032932.96+311219.84	03:29:32.97	+31:12:19.85	0.0611±0.0095	0.0589	0.0095	<0.0767±0.0256	<0.0767	0.0256	<0.50±0.81	<0.58±0.82
032936.62+311013.52	03:29:36.62	+31:10:13.52	0.2257±0.0227	0.1747	0.0175	—	—	—	—	—
032443.81+304713.89	03:24:43.81	+30:47:13.89	0.4943±0.0243	0.3967	0.0185	—	—	—	—	—
032446.50+304219.50	03:24:46.51	+30:42:19.50	0.7285±0.0441	0.4166	0.0262	—	—	—	—	—
032448.25+304939.50	03:24:48.26	+30:49:39.51	0.2051±0.0218	0.1756	0.0188	—	—	—	—	—
032503.78+304353.56	03:25:03.79	+30:43:53.57	<0.0257±0.0086	<0.0257	0.0086	0.0573±0.0099	0.0621	0.0099	>1.77±0.83	>1.95±0.35
032506.34+304959.17	03:25:06.34	+30:49:59.17	0.0840±0.0101	0.0897	0.0103	0.0906±0.0373	0.0631	0.0163	0.17±0.95	-0.77±0.62
032845.50+311217.35	03:28:45.51	+31:12:17.35	<0.0275±0.0092	<0.0275	0.0092	0.0621±0.0123	0.0729	0.0121	>1.80±0.85	>2.15±0.37
032857.91+311355.20	03:28:57.92	+31:13:55.20	<0.0229±0.0076	<0.0229	0.0076	0.0494±0.0079	0.0485	0.0075	>1.70±0.82	>1.66±0.34
033257.37+311031.11	03:32:57.38	+31:10:31.11	0.1096±0.0128	0.0915	0.0118	—	—	—	—	—
033302.00+310708.76	03:33:02.01	+31:07:08.76	<0.0205±0.0068	<0.0205	0.0068	0.0382±0.0104	0.0588	0.0097	>1.38±0.95	>2.32±0.36
033304.48+310411.59	03:33:04.49	+31:04:11.60	0.0620±0.0094	0.0540	0.0086	<0.0561±0.0187	<0.0561	0.0187	<-0.22±0.81	<0.08±0.81
033309.21+310650.69	03:33:09.21	+31:06:50.69	0.0451±0.0062	0.0414	0.0054	0.0482±0.0145	0.0285	0.0052	0.15±0.73	-0.82±0.50
033312.02+310650.54	03:33:12.02	+31:06:50.54	0.0455±0.0062	0.0482	0.0051	0.0384±0.0067	0.0311	0.0046	-0.37±0.49	-0.96±0.40
033312.82+310536.58	03:33:12.83	+31:05:36.59	0.2609±0.0064	0.2525	0.0055	0.1735±0.0064	0.1657	0.0056	-0.90±0.10	-0.93±0.09
033315.07+310827.41	03:33:15.07	+31:08:27.41	<0.0152±0.0051	<0.0152	0.0051	0.0245±0.0051	0.0286	0.0044	>1.06±0.87	>1.40±0.34
033315.52+310640.22	03:33:15.52	+31:06:40.22	0.0265±0.0057	0.0306	0.0050	0.0270±0.0052	0.0276	0.0043	0.04±0.64	-0.23±0.49
033316.32+311415.53	03:33:16.32	+31:14:15.53	0.2143±0.0246	0.1712	0.0230	—	—	—	—	—
033316.87+310627.16	03:33:16.87	+31:06:27.17	0.0176±0.0046	0.0301	0.0050	<0.0130±0.0043	<0.0130	0.0043	<-0.67±0.94	<-1.86±0.82
033317.60+310524.49	03:33:17.60	+31:05:24.50	0.1263±0.0056	0.1342	0.0055	0.1124±0.0065	0.1010	0.0055	-0.26±0.16	-0.63±0.15
033318.35+310242.67	03:33:18.35	+31:02:42.68	0.1366±0.0092	0.1314	0.0098	0.0948±0.0780	0.1222	0.0279	-0.80±1.82	-0.16±0.53
033318.59+310743.82	03:33:18.60	+31:07:43.83	0.0188±0.0043	0.0294	0.0049	0.0123±0.0082	0.0132	0.0040	-0.94±1.55	-1.77±0.77
033318.67+311153.28	03:33:18.67	+31:11:53.28	0.0720±0.0110	0.0615	0.0089	<0.0628±0.0209	<0.0628	0.0209	<-0.30±0.81	<0.04±0.80
033319.16+310233.74	03:33:19.17	+31:02:33.74	0.1086±0.0129	0.0820	0.0103	<0.0989±0.0330	<0.0989	0.0330	<-0.21±0.78	<0.41±0.78

Table 2.7: continued.

Name	RA	Dec	F^a_{vint} 6.4 cm	F^b_{vpeak} 6.4 cm	RMS 6.4 cm	F^a_{vint} 4.1 cm	F^b_{vpeak} 4.1 cm	RMS 4.1 cm	Sp. Index Int.[c]	Sp. Index Peak[d]
	J2000	J2000	mJy	mJy/beam	mJy/beam	mJy	mJy/beam	mJy/beam		
033320.42+310714.36	03:33:20.43	+31:07:14.36	0.0266±0.0061	0.0296	0.0049	0.0272±0.0054	0.0269	0.0041	0.05±0.67	-0.21±0.50
033320.79+310706.72	03:33:20.80	+31:07:06.73	0.0285±0.0056	0.0309	0.0050	0.0291±0.0112	0.0132	0.0042	0.05±0.95	-1.88±0.78
033323.56+310344.34	03:33:23.56	+31:03:44.34	0.0470±0.0078	0.0535	0.0078	<0.0418±0.0139	<0.0418	0.0139	<-0.26±0.82	<-0.54±0.80
033323.67+310421.23	03:33:23.67	+31:04:21.23	0.2093±0.0087	0.1834	0.0068	0.1864±0.0105	0.1801	0.0097	-0.26±0.15	-0.04±0.14
033324.91+310433.30	03:33:24.91	+31:04:33.31	0.1052±0.0084	0.0934	0.0067	0.0515±0.0305	0.0313	0.0093	-1.57±1.32	-2.41±0.68
033327.40+310645.10	03:33:27.40	+31:06:45.11	0.0321±0.0062	0.0344	0.0056	<0.0173±0.0058	<0.0173	0.0058	<-1.37±0.85	<-1.52±0.82
033330.59+310601.92	03:33:30.60	+31:06:01.92	0.0642±0.0074	0.0614	0.0065	0.0285±0.0236	0.0290	0.0085	-1.79±1.84	-1.65±0.69
033331.07+310925.49	03:33:31.08	+31:09:25.50	0.0404±0.0068	0.0440	0.0070	0.0403±0.0232	0.0324	0.0104	-0.01±1.32	-0.68±0.79
033332.24+310417.05	03:33:32.25	+31:04:17.05	0.0883±0.0112	0.0811	0.0090	0.0898±0.0599	0.0722	0.0212	0.04±1.50	-0.26±0.69
033334.12+310504.73	03:33:34.12	+31:05:04.73	0.0788±0.0089	0.0831	0.0085	0.1017±0.0441	0.0643	0.0179	0.56±0.99	-0.57±0.65
033336.13+310849.28	03:33:36.14	+31:08:49.29	0.3109±0.0106	0.2565	0.0083	0.1672±0.0200	0.1485	0.0170	-1.37±0.27	-1.20±0.26
034129.83+314620.22	03:41:29.84	+31:46:20.22	0.1877±0.0197	0.1664	0.0198	—	—	—	—	—
034137.70+314342.95	03:41:37.70	+31:43:42.96	0.1559±0.0165	0.1405	0.0199	—	—	—	—	—
034140.87+314329.60	03:41:40.88	+31:43:29.60	0.2583±0.0182	0.2335	0.0175	—	—	—	—	—
034144.84+315030.13	03:41:44.85	+31:50:30.13	0.0838±0.0082	0.0866	0.0072	0.0716±0.0118	0.0720	0.0112	-0.34±0.42	-0.41±0.39
034145.01+314515.38	03:41:45.02	+31:45:15.39	0.1261±0.0082	0.1256	0.0086	0.1766±0.0523	0.0954	0.0191	0.74±0.67	-0.61±0.47
034147.97+314251.03	03:41:47.97	+31:42:51.03	0.3455±0.0298	0.1741	0.0160	—	—	—	—	—
034149.42+315043.40	03:41:49.43	+31:50:43.40	0.0417±0.0073	0.0440	0.0064	0.0387±0.0212	0.0342	0.0080	-0.16±1.26	-0.55±0.61
034152.83+314506.46	03:41:52.83	+31:45:06.47	0.5444±0.0085	0.4850	0.0071	0.3540±0.0125	0.3338	0.0110	-0.95±0.08	-0.82±0.08
034154.40+314528.55	03:41:54.40	+31:45:28.55	0.0764±0.0077	0.0777	0.0065	0.0827±0.0103	0.0760	0.0085	0.17±0.35	-0.05±0.31
034156.82+314906.48	03:41:56.82	+31:49:06.49	0.0221±0.0045	0.0307	0.0049	<0.0125±0.0042	<0.0125	0.0042	<-1.26±0.86	<-1.99±0.82
034159.54+314842.07	03:41:59.54	+31:48:42.08	<0.0146±0.0049	<0.0146	0.0049	0.0227±0.0050	0.0241	0.0040	>0.97±0.88	>1.11±0.37
034200.17+314706.37	03:42:00.17	+31:47:06.37	0.0249±0.0053	0.0312	0.0051	<0.0137±0.0046	<0.0137	0.0046	<-1.31±0.87	<-1.81±0.82
034200.34+314525.78	03:42:00.35	+31:45:25.78	1.4481±0.0085	1.3249	0.0064	1.2638±0.0103	1.1275	0.0081	-0.30±0.02	-0.36±0.02
034201.16+314801.13	03:42:01.17	+31:48:01.14	0.0606±0.0066	0.0562	0.0049	0.0406±0.0048	0.0405	0.0041	-0.88±0.35	-0.72±0.29
034201.63+314614.53	03:42:01.64	+31:46:14.53	0.0482±0.0088	0.0385	0.0057	0.0318±0.0209	0.0262	0.0059	-0.91±1.50	-0.84±0.59
034202.88+314527.39	03:42:02.89	+31:45:27.39	0.0517±0.0065	0.0564	0.0065	0.0604±0.0212	0.0390	0.0084	0.34±0.82	-0.81±0.54
034208.20+315126.80	03:42:08.21	+31:51:26.81	0.0430±0.0078	0.0456	0.0071	0.0832±0.0293	0.0531	0.0111	1.46±0.87	0.34±0.57
034210.09+315308.57	03:42:10.09	+31:53:08.58	1.0547±0.0555	0.3049	0.0116	—	—	—	—	—
034210.69+314159.66	03:42:10.69	+31:41:59.66	1.3668±0.0373	0.8543	0.0245	—	—	—	—	—
034211.26+315253.09	03:42:11.26	+31:52:53.09	0.1449±0.0147	0.1205	0.0112	—	—	—	—	—
034212.01+314655.38	03:42:12.01	+31:46:55.39	1.1134±0.0086	0.9931	0.0066	0.7876±0.0103	0.7165	0.0088	-0.76±0.03	-0.72±0.03
034212.06+314752.38	03:42:12.06	+31:47:52.39	0.0851±0.0072	0.0765	0.0062	0.0538±0.0089	0.0570	0.0074	-1.01±0.41	-0.65±0.34
034212.56+314650.44	03:42:12.56	+31:46:50.44	0.0786±0.0083	0.0714	0.0068	0.0819±0.0126	0.0744	0.0095	0.09±0.41	0.09±0.35
034214.27+314453.35	03:42:14.28	+31:44:53.36	0.0613±0.0103	0.0612	0.0101	<0.0921±0.0307	<0.0921	0.0307	<0.90±0.82	<0.90±0.82
034214.63+314737.53	03:42:14.63	+31:47:37.53	0.7330±0.0167	0.6662	0.0069	0.7401±0.0829	0.5832	0.0102	0.02±0.25	-6.19±0.56
034215.06+314828.18	03:42:15.07	+31:48:28.19	0.0845±0.0096	0.0660	0.0069	0.0559±0.0327	0.0422	0.0101	-0.91±1.31	-0.98±0.58
034221.08+314954.04	03:42:21.08	+31:49:54.04	0.0772±0.0109	0.0750	0.0104	<0.1025±0.0342	<0.1025	0.0342	<0.62±0.80	<0.69±0.80
034223.35+315043.66	03:42:23.36	+31:50:43.67	0.1002±0.0118	0.0972	0.0136	—	—	—	—	—
034224.49+314733.15	03:42:24.49	+31:47:33.16	0.0847±0.0121	0.0780	0.0128	—	—	—	—	—

Table 2.7: continued.

Name	RA	Dec	F^a_{vint} 6.4 cm	F^b_{vpeak} 6.4 cm	RMS 6.4 cm	F^a_{vint} 4.1 cm	F^b_{vpeak} 4.1 cm	RMS 4.1 cm	Sp. Index Int.[c]	Sp. Index Peak[d]
	J2000	J2000	mJy	mJy/beam	mJy/beam	mJy	mJy/beam	mJy/beam		
032904.53+313417.08	03:29:04.53	+31:34:17.08	0.0863±0.0107	0.0621	0.0082	<0.0498±0.0166	<0.0498	0.0166	<-1.21±0.78	<-0.49±0.79
032908.30+313215.51	03:29:08.31	+31:32:15.52	<0.0211±0.0070	<0.0211	0.0070	0.0498±0.0124	0.0642	0.0107	>1.90±0.92	>2.46±0.37
032909.75+313154.99	03:29:09.75	+31:31:54.100	0.5257±0.0109	0.4718	0.0090	0.1257±0.0626	0.1088	0.0219	-3.15±1.10	-3.23±0.44
032910.68+313155.12	03:29:10.69	+31:31:55.12	1.6641±0.1248	0.1661	0.0066	<0.5272±0.0089	<0.0268	0.0089	<-2.53±0.51	<-2.77±0.44
032916.33+313412.15	03:29:16.34	+31:34:12.16	0.0285±0.0057	0.0321	0.0053	<0.0153±0.0051	<0.0153	0.0051	<-1.37±0.86	<-1.63±0.82
032917.09+313603.73	03:29:17.09	+31:36:03.73	0.0312±0.0066	0.0383	0.0063	<0.0238±0.0079	<0.0238	0.0079	<-0.60±0.87	<-1.05±0.82
032917.38+313030.42	03:29:17.39	+31:30:30.42	0.0951±0.0089	0.0765	0.0067	0.0669±0.0300	0.0503	0.0095	-0.78±1.01	-0.93±0.46
032918.54+313125.90	03:29:18.55	+31:31:25.91	0.0642±0.0076	0.0589	0.0057	0.0402±0.0188	0.0361	0.0062	-1.03±1.06	-1.08±0.43
032918.91+313319.96	03:29:18.91	+31:33:19.96	0.0362±0.0061	0.0339	0.0050	<0.0134±0.0045	<0.0134	0.0045	<-2.20±0.82	<-2.05±0.80
032920.07+313248.56	03:29:20.07	+31:32:48.56	0.0424±0.0073	0.0357	0.0050	0.0336±0.0045	0.0393	0.0045	-0.51±0.48	0.21±0.40
032921.18+313726.00	03:29:21.19	+31:37:26.00	0.0912±0.0085	0.0872	0.0079	0.0314±0.0398	0.0536	0.0149	-2.35±2.80	-1.07±0.65
032925.37+313120.72	03:29:25.37	+31:31:20.73	<0.0169±0.0056	<0.0169	0.0056	0.0399±0.0068	0.0411	0.0059	>1.89±0.82	>1.96±0.32
032926.49+313317.45	03:29:26.50	+31:33:17.45	0.0375±0.0054	0.0451	0.0050	0.0252±0.0049	0.0271	0.0043	-0.88±0.54	-1.12±0.42
032927.19+313411.91	03:29:27.20	+31:34:11.91	0.0370±0.0057	0.0315	0.0051	0.0350±0.0114	0.0212	0.0045	-0.12±0.79	-0.87±0.59
032927.58+313345.53	03:29:27.58	+31:33:45.53	0.0265±0.0053	0.0314	0.0050	<0.0132±0.0044	<0.0132	0.0044	<-1.53±0.86	<-1.90±0.81
032927.89+313420.83	03:29:27.89	+31:34:20.84	<0.0154±0.0051	<0.0154	0.0051	0.0249±0.0057	0.0281	0.0047	>1.05±0.89	>1.32±0.37
032934.70+313044.79	03:29:34.70	+31:30:44.80	<0.0219±0.0073	<0.0219	0.0073	0.0667±0.0138	0.0759	0.0119	>2.45±0.86	>2.74±0.34
032941.74+313345.59	03:29:41.75	+31:33:45.60	0.6332±0.0651	0.3184	0.0294	—	—	—	—	—
032910.16+312554.75	03:29:10.17	+31:25:54.75	<0.0195±0.0065	<0.0195	0.0065	0.0358±0.0081	0.0466	0.0076	>1.34±0.89	>1.91±0.36
032920.95+312513.07	03:29:20.96	+31:25:13.07	0.0259±0.0061	0.0329	0.0055	<0.0143±0.0048	<0.0143	0.0048	<-1.31±0.90	<-1.84±0.82
032924.03+312319.19	03:29:24.04	+31:23:19.19	<0.0158±0.0053	<0.0158	0.0053	0.0224±0.0051	0.0267	0.0044	>0.76±0.89	>1.15±0.36
032927.82+312450.49	03:29:27.83	+31:24:50.50	<0.0175±0.0058	<0.0175	0.0058	0.0310±0.0063	0.0345	0.0057	>1.25±0.86	>1.49±0.36
032929.81+312114.51	03:29:29.82	+31:21:14.52	<0.0214±0.0071	<0.0214	0.0071	0.0476±0.0106	0.0589	0.0098	>1.76±0.88	>2.23±0.37
032934.29+312246.92	03:29:34.29	+31:22:46.93	0.0619±0.0107	0.0507	0.0072	<0.0295±0.0098	<0.0295	0.0098	<-1.63±0.83	<-1.20±0.80
032943.97+313645.09	03:29:43.97	+31:36:45.10	0.0422±0.0065	0.0479	0.0065	0.0275±0.0177	0.0341	0.0075	-0.94±1.45	-0.75±0.57
032945.11+314127.51	03:29:45.11	+31:41:27.51	0.0542±0.0073	0.0523	0.0063	0.0488±0.0092	0.0455	0.0071	-0.23±0.51	-0.31±0.43
032945.90+313832.99	03:29:45.91	+31:38:32.99	0.0528±0.0058	0.0598	0.0053	0.0384±0.0054	0.0367	0.0046	-0.70±0.39	-1.08±0.34
032949.42+314316.14	03:29:49.43	+31:43:16.14	0.0425±0.0073	0.0525	0.0086	<0.0510±0.0170	<0.0510	0.0170	<0.40±0.83	<-0.07±0.82
032953.00+313736.46	03:29:53.01	+31:37:36.47	0.0470±0.0062	0.0464	0.0054	0.0278±0.0049	0.0309	0.0047	-1.15±0.49	-0.90±0.42
032954.95+314314.25	03:29:54.95	+31:43:14.26	1.4983±0.0517	0.6537	0.0086	0.6357±0.1078	0.2551	0.0169	-1.89±0.38	-1.87±0.63
032955.12+314309.12	03:29:55.13	+31:43:09.12	0.3725±0.0347	0.1339	0.0084	0.1707±0.0359	0.0989	0.0159	-1.72±0.51	-0.83±0.78
032959.45+314040.24	03:29:59.45	+31:40:40.25	0.0979±0.0107	0.0283	0.0059	<0.0554±0.0058	<0.0174	0.0058	<-1.25±0.53	<-1.27±0.34
032959.72+314406.86	03:29:59.72	+31:44:06.86	0.9279±0.0162	0.7205	0.0122	—	—	—	—	—
033001.05+313847.18	03:30:01.05	+31:38:47.19	<0.0170±0.0057	<0.0170	0.0057	0.0306±0.0059	0.0345	0.0053	>1.30±0.85	>1.56±0.34
033003.27+313958.49	03:30:03.28	+31:39:58.49	0.1215±0.0059	0.1325	0.0061	0.0766±0.0090	0.0682	0.0066	-1.02±0.28	-1.46±0.24
032909.31+312936.52	03:29:09.31	+31:29:36.52	0.0317±0.0063	0.0394	0.0062	<0.0229±0.0076	<0.0229	0.0076	<-0.72±0.86	<-1.20±0.81
032911.20+312618.77	03:29:11.21	+31:26:18.78	0.0288±0.0060	0.0368	0.0060	0.0376±0.0162	0.0350	0.0071	0.59±1.05	-0.11±0.58
032917.39+312904.20	03:29:17.39	+31:29:04.20	0.0350±0.0059	0.0401	0.0051	0.0251±0.0126	0.0227	0.0046	-0.74±1.17	-1.26±0.52
032919.10+312712.72	03:29:19.11	+31:27:12.73	<0.0150±0.0050	<0.0150	0.0050	0.0210±0.0052	0.0274	0.0044	>0.74±0.91	>1.32±0.35
032923.06+312805.15	03:29:23.07	+31:28:05.16	0.0353±0.0063	0.0310	0.0049	<0.0127±0.0042	<0.0127	0.0042	<-2.26±0.83	<-1.97±0.81

Table 2.7: continued.

Name	RA	Dec	F^a_{vint} 6.4 cm	F^b_{vpeak} 6.4 cm	RMS 6.4 cm	F^a_{vint} 4.1 cm	F^b_{vpeak} 4.1 cm	RMS 4.1 cm	Sp. Index Int.[c]	Sp. Index Peak[d]
	J2000	J2000	mJy	mJy/beam	mJy/beam	mJy	mJy/beam	mJy/beam		
032923.77+312615.01	03:29:23.78	+31:26:15.01	0.0359±0.0067	0.0341	0.0055	<0.0166±0.0055	<0.0166	0.0055	<-1.70±0.84	<-1.59±0.82
032925.45+312809.52	03:29:25.45	+31:28:09.53	0.0517±0.0056	0.0531	0.0050	0.0554±0.0062	0.0478	0.0045	0.15±0.34	-0.23±0.29
032925.86+312747.55	03:29:25.87	+31:27:47.56	<0.0153±0.0051	<0.0153	0.0051	0.0263±0.0055	0.0275	0.0046	>1.20±0.87	>1.30±0.37
032846.09+311701.38	03:28:46.10	+31:17:01.39	<0.0212±0.0071	<0.0212	0.0071	0.0497±0.0114	0.0639	0.0106	>1.88±0.89	>2.43±0.37
032849.10+311625.00	03:28:49.11	+31:16:25.00	0.0551±0.0071	0.0452	0.0060	<0.0204±0.0068	<0.0204	0.0068	<-2.19±0.79	<-1.75±0.79
032854.48+311439.10	03:28:54.48	+31:14:39.10	0.0442±0.0058	0.0460	0.0052	0.0358±0.0120	0.0212	0.0046	-0.46±0.79	-1.71±0.54
032908.09+311600.88	03:29:08.09	+31:16:00.88	0.0245±0.0052	0.0317	0.0053	<0.0144±0.0048	<0.0144	0.0048	<-1.16±0.87	<-1.73±0.82
032909.70+311456.36	03:29:09.71	+31:14:56.37	0.0270±0.0056	0.0341	0.0054	<0.0155±0.0052	<0.0155	0.0052	<-1.23±0.86	<-1.74±0.81
032834.53+311649.82	03:28:34.53	+31:16:49.82	<0.0179±0.0060	<0.0179	0.0060	0.0287±0.0063	0.0353	0.0057	>1.04±0.88	>1.49±0.36
032850.56+311739.92	03:28:50.57	+31:17:39.92	<0.0159±0.0053	<0.0159	0.0053	0.0162±0.0048	0.0255	0.0042	>0.03±0.98	>1.03±0.36

Table 2.8: Binary systems

System	Separation	Separation	$log(F_1/F_2)$	$log(F_1/F_2)$	$\Delta\alpha$	$log(M_{\rm dust,1}/M_{\rm dust,2})$
	"	au	6.4 cm	4.1 cm		
Per-emb-12	1.83	429.40	-0.28	-0.07	1.02	1.22
Per-emb-22	0.75	176.55	0.47	0.47	0.02	0.44
Per-emb-27	0.62	145.74	>0.59	0.55	>0.18	0.68
Per-emb-33 (A+C)	0.98	229.62	-0.73	<-1.04	>1.57	0.66
Per-emb-35	1.91	448.40	0.63	0.44	0.97	-0.17
Per-emb-40	0.39	91.92	0.70	0.95	1.27	0.64
Per-emb-44	0.30	70.53	-0.04	-0.07	0.15	0.51
Per-emb-49	0.31	73.52	-0.48	0.12	3.06	0.55
L1448NW	0.25	58.98	<0.03	0.43	<1.22	-0.01
EDJ2009-269	0.54	127.78	-	0.26	-	-0.10
SVS3	0.65	152.77	-0.21	-0.41	1.04	-

Table 2.9: Protostellar disk masses

Name	F_ν	F_ν	$F_{\rm dust}/F_{\rm 9mm}$	$M_{\rm gas+dust}$	$M_{\rm gas+dust}$	Flag[a]
	9 mm	corrected		9 mm	corrected	
	mJy	mJy	%	$M_\odot$	$M_\odot$	
Per-emb-1	0.72	0.57	79	0.152± 0.004	0.121± 0.004	a
Per-emb-2	2.04	1.89	92	0.432± 0.019	0.400± 0.019	a
Per-emb-2-A	-	-	-	-	-	-
Per-emb-2-B	-	-	-	-	-	-
Per-emb-3	0.35	0.32	91	0.074± 0.004	0.068± 0.004	a
Per-emb-4	< 0.02	< 0.02	-	< 0.005± 0.002	< 0.005± 0.002	e
Per-emb-5	1.05	1.02	97	0.223± 0.007	0.217± 0.007	b
Per-emb-5-A	-	-	-	-	-	-
Per-emb-5-B	-	-	-	-	-	-
Per-emb-6	0.25	0.16	64	0.052± 0.004	0.034± 0.004	a
Per-emb-7	< 0.02	< 0.02	-	< 0.005± 0.002	< 0.005± 0.002	e
Per-emb-8	0.94	0.48	51	0.200± 0.006	0.103± 0.006	a
Per-emb-9	0.05	0.05	86	0.011± 0.005	0.010± 0.005	a
Per-emb-10	0.33	0.29	89	0.069± 0.004	0.062± 0.004	b
Per-emb-11	0.99	0.89	89	0.211± 0.016	0.188± 0.016	a
Per-emb-11-A	0.84	0.84	100	0.178± 0.006	0.178± 0.006	d
Per-emb-11-B	0.09	0.04	48	0.019± 0.005	0.009± 0.005	c
Per-emb-11-C	0.06	0.06	100	0.013± 0.005	0.013± 0.005	d
Per-emb-12	7.98	6.69	83	1.693± 0.021	1.419± 0.021	a
Per-emb-12-A	7.28	5.80	79	1.544± 0.014	1.231± 0.014	a
Per-emb-12-B	0.70	0.32	45	0.149± 0.007	0.068± 0.007	a
Per-emb-13	2.75	2.59	94	0.583± 0.012	0.548± 0.012	a
Per-emb-14	0.69	0.63	91	0.147± 0.006	0.134± 0.006	c
Per-emb-15	0.07	0.02	28	0.014± 0.005	0.004± 0.005	f
Per-emb-16	0.07	0.07	100	0.015± 0.006	0.015± 0.006	f
Per-emb-17	0.54	0.41	75	0.114± 0.006	0.086± 0.006	a
Per-emb-17-A	0.46	0.33	71	0.097± 0.004	0.069± 0.004	a
Per-emb-17-B	0.08	0.08	100	0.017± 0.002	0.017± 0.002	d
Per-emb-18	0.67	0.46	68	0.141± 0.007	0.097± 0.007	a
Per-emb-18-A	-	-	-	-	-	-
Per-emb-18-B	-	-	-	-	-	-
Per-emb-19	0.24	0.23	95	0.051± 0.005	0.048± 0.005	a
Per-emb-20	0.17	0.06	36	0.037± 0.005	0.013± 0.005	f
Per-emb-21	0.43	0.43	100	0.091± 0.005	0.091± 0.005	d
Per-emb-22	0.64	0.24	38	0.135± 0.009	0.052± 0.009	a
Per-emb-22-A	0.49	0.20	40	0.103± 0.004	0.042± 0.004	a
Per-emb-22-B	0.15	0.05	31	0.032± 0.004	0.010± 0.004	a
Per-emb-23	0.12	0.08	61	0.026± 0.004	0.016± 0.004	c
Per-emb-24	0.07	0.04	66	0.014± 0.002	0.009± 0.002	b
Per-emb-25	0.49	0.35	72	0.103± 0.018	0.074± 0.018	a
Per-emb-26	1.69	1.29	76	0.359± 0.005	0.274± 0.005	a
Per-emb-27	1.69	0.88	52	0.359± 0.008	0.187± 0.008	a
Per-emb-27-A	1.44	1.16	80	0.305± 0.004	0.246± 0.004	a
Per-emb-27-B	0.26	0.23	90	0.054± 0.004	0.049± 0.004	b
Per-emb-28	0.07	0.05	63	0.016± 0.007	0.010± 0.007	c
Per-emb-29	0.47	0.47	100	0.101± 0.004	0.101± 0.004	d
Per-emb-30	0.84	0.54	63	0.178± 0.004	0.114± 0.004	a
Per-emb-31	0.05	0.05	100	0.011± 0.005	0.011± 0.005	f
Per-emb-32	0.10	0.10	100	0.021± 0.005	0.021± 0.005	d

Table 2.9: continued.

Name	F_ν 9 mm mJy	F_ν corrected mJy	$F_{\rm dust}/F_{\rm 9mm}$ %	$M_{\rm gas+dust}$ 9 mm $M_\odot$	$M_{\rm gas+dust}$ corrected $M_\odot$	Flag[a]
Per-emb-32-A	0.04	0.04	100	0.008± 0.002	0.008± 0.002	d
Per-emb-32-B	0.06	0.06	100	0.013± 0.003	0.013± 0.003	d
Per-emb-33	0.88	0.80	91	0.186± 0.012	0.169± 0.012	a
Per-emb-33-A	0.62	0.60	95	0.132± 0.007	0.127± 0.007	b
Per-emb-33-B	0.35	0.35	100	0.074± 0.007	0.074± 0.007	d
Per-emb-33-C	0.25	0.11	45	0.053± 0.005	0.024± 0.005	a
Per-emb-34	0.20	0.17	86	0.043± 0.004	0.037± 0.004	b
Per-emb-35	0.56	0.08	13	0.118± 0.007	0.016± 0.007	a
Per-emb-35-A	0.35	0.10	27	0.074± 0.004	0.020± 0.004	a
Per-emb-35-B	0.21	0.18	85	0.044± 0.004	0.037± 0.004	c
Per-emb-36	1.64	1.36	82	0.348± 0.008	0.287± 0.008	a
Per-emb-36-A	1.42	1.13	79	0.300± 0.005	0.240± 0.005	a
Per-emb-36-B	0.23	0.23	100	0.048± 0.003	0.048± 0.003	d
Per-emb-37	0.19	0.19	100	0.041± 0.004	0.041± 0.004	d
Per-emb-38	0.16	0.16	100	0.034± 0.005	0.034± 0.005	d
Per-emb-39	< 0.03	< 0.03	-	< 0.005± 0.002	< 0.005± 0.002	e
Per-emb-40	0.38	0.21	56	0.080± 0.006	0.045± 0.006	a
Per-emb-40-A	0.34	0.15	43	0.071± 0.003	0.031± 0.003	a
Per-emb-40-B	0.04	0.04	91	0.008± 0.003	0.008± 0.003	f
Per-emb-41	0.09	0.09	100	0.019± 0.005	0.019± 0.005	d
Per-emb-42	0.24	0.24	100	0.050± 0.005	0.050± 0.005	d
Per-emb-43	< 0.02	< 0.02	-	< 0.005± 0.002	< 0.005± 0.002	e
Per-emb-44	1.89	0.89	46	0.402± 0.012	0.188± 0.012	a
Per-emb-44-A	1.43	1.01	70	0.302± 0.004	0.215± 0.004	a
Per-emb-44-B	0.47	0.36	76	0.099± 0.007	0.076± 0.007	c
Per-emb-45	< 0.02	< 0.02	-	< 0.005± 0.002	< 0.005± 0.002	e
Per-emb-46	0.13	0.11	88	0.027± 0.008	0.024± 0.008	b
Per-emb-47	0.26	0.22	84	0.054± 0.006	0.046± 0.006	b
Per-emb-48	0.14	0.11	74	0.030± 0.009	0.023± 0.009	a
Per-emb-48-A	0.08	0.08	100	0.016± 0.005	0.016± 0.005	d
Per-emb-48-B	0.07	0.03	45	0.014± 0.004	0.006± 0.004	f
Per-emb-49	0.45	0.33	73	0.094± 0.008	0.069± 0.008	f
Per-emb-49-A	0.33	0.30	89	0.070± 0.004	0.063± 0.004	c
Per-emb-49-B	0.12	0.11	93	0.025± 0.004	0.023± 0.004	f
Per-emb-50	1.36	1.09	79	0.289± 0.007	0.231± 0.007	a
Per-emb-51	< 0.03	< 0.03	-	< 0.005± 0.003	< 0.005± 0.003	e
Per-emb-52	0.07	0.07	100	0.015± 0.006	0.015± 0.006	d
Per-emb-53	0.22	0.12	52	0.046± 0.006	0.024± 0.006	a
Per-emb-54	0.31	0.23	76	0.065± 0.005	0.050± 0.005	c
Per-emb-55	0.17	0.11	67	0.036± 0.004	0.024± 0.004	c
Per-emb-55-A	0.10	0.10	100	0.021± 0.002	0.021± 0.002	d
Per-emb-55-B	0.07	0.02	21	0.015± 0.002	0.003± 0.002	c
Per-emb-56	0.09	0.09	100	0.020± 0.004	0.020± 0.004	d
Per-emb-57	0.16	0.14	88	0.033± 0.006	0.029± 0.006	b
Per-emb-58	0.08	0.08	100	0.016± 0.005	0.016± 0.005	f
Per-emb-59	< 0.03	< 0.03	-	< 0.006± 0.003	< 0.006± 0.003	e
Per-emb-60	< 0.03	< 0.03	-	< 0.006± 0.003	< 0.006± 0.003	e
Per-emb-61	0.11	0.11	100	0.022± 0.007	0.022± 0.007	d
Per-emb-62	0.61	0.41	66	0.130± 0.006	0.087± 0.006	a
Per-emb-63	0.32	0.22	69	0.069± 0.005	0.047± 0.005	a
Per-emb-64	0.93	0.49	52	0.197± 0.006	0.104± 0.006	a
Per-emb-65	0.12	0.12	100	0.025± 0.007	0.025± 0.007	d
Per-emb-66	< 0.03	< 0.03	-	< 0.006± 0.003	< 0.006± 0.003	e
Per-bolo-58	< 0.03	< 0.03	-	< 0.005± 0.003	< 0.005± 0.003	e
Per-bolo-45	< 0.03	< 0.03	-	< 0.005± 0.002	< 0.005± 0.002	e
L1451-MMS	0.20	0.20	100	0.042± 0.004	0.042± 0.004	d
L1448IRS2E	< 0.03	< 0.03	-	< 0.006± 0.003	< 0.006± 0.003	e
B1-bN	0.98	0.98	100	0.209± 0.007	0.209± 0.007	d
B1-bS	0.72	0.72	100	0.153± 0.011	0.153± 0.011	d
L1448IRS1	0.84	0.67	79	0.178± 0.010	0.142± 0.010	a
L1448IRS1-A	0.77	0.60	77	0.162± 0.005	0.126± 0.005	a
L1448IRS1-B	0.07	0.07	100	0.016± 0.004	0.016± 0.004	d
L1448NW	0.99	0.23	23	0.210± 0.010	0.049± 0.010	a
L1448NW-A	0.59	0.40	66	0.126± 0.005	0.084± 0.005	a
L1448NW-B	0.40	0.38	96	0.084± 0.005	0.081± 0.005	b
L1448IRS3A	1.04	0.48	46	0.220± 0.006	0.101± 0.006	a
SVS13C	2.28	0.46	19	0.483± 0.007	0.097± 0.007	a

Table 2.9: continued.

Name	F_ν 9 mm mJy	F_ν corrected mJy	$F_{\rm dust}/F_{\rm 9mm}$ %	$M_{\rm gas+dust}$ 9 mm $M_\odot$	$M_{\rm gas+dust}$ corrected $M_\odot$	Flag[a]
SVS13B	1.24	1.18	95	0.262± 0.007	0.251± 0.007	b
IRAS03363+3207	0.71	0.66	93	0.151± 0.005	0.141± 0.005	c
EDJ2009-263	0.07	0.07	100	0.015± 0.003	0.015± 0.003	d
EDJ2009-285	< 0.03	< 0.03	-	< 0.006± 0.003	< 0.006± 0.003	e
IRAS03295+3050	0.12	0.12	100	0.025± 0.004	0.025± 0.004	d
L1455IRS2	0.05	0.03	58	0.011± 0.004	0.007± 0.004	f
EDJ2009-385	0.18	0.18	100	0.038± 0.009	0.038± 0.009	d
EDJ2009-366	0.14	0.09	63	0.030± 0.004	0.019± 0.004	c
EDJ2009-269	0.42	0.36	86	0.088± 0.012	0.076± 0.012	b
EDJ2009-269-A	0.21	0.18	83	0.045± 0.005	0.037± 0.005	f
EDJ2009-269-B	0.20	0.19	90	0.043± 0.006	0.039± 0.006	b
EDJ2009-183	0.15	0.10	64	0.033± 0.005	0.021± 0.005	a
EDJ2009-183-A	0.11	0.06	52	0.024± 0.003	0.013± 0.003	a
EDJ2009-183-B	0.04	0.04	100	0.009± 0.003	0.009± 0.003	d
EDJ2009-164	< 0.02	< 0.02	-	< 0.004± 0.002	< 0.004± 0.002	e
EDJ2009-156	0.25	0.09	34	0.053± 0.004	0.018± 0.004	a
EDJ2009-156-A	0.15	0.15	100	0.031± 0.002	0.031± 0.002	d
EDJ2009-156-B	0.10	0.07	71	0.022± 0.002	0.016± 0.002	c
EDJ2009-172	0.31	0.28	90	0.065± 0.006	0.059± 0.006	b
EDJ2009-173	0.20	0.17	84	0.043± 0.003	0.036± 0.003	b
SVS13A2	0.31	0.21	67	0.066± 0.006	0.044± 0.006	c
IRAS4B'	1.23	1.23	100	0.260± 0.013	0.260± 0.013	d
EDJ2009-233	0.36	0.17	47	0.076± 0.005	0.036± 0.005	a
EDJ2009-235	0.04	0.02	54	0.009± 0.003	0.005± 0.003	f
SVS3	0.24	0.00	0	0.052± 0.010	0.000± 0.010	f
SVS3-A	0.21	0.13	58	0.046± 0.007	0.027± 0.007	f
SVS3-B	< 0.03	< 0.03	-	< 0.006± 0.003	< 0.000± 0.003	f

Notes.

Flags: a - regular fit; b - one of the C-band channels with non-detection; c - excess of the free-free emission; d - non-detection in both C-band channels; e - non-detection in both Ka- and C-band; f - flat or negative spectral index in Ka-band; Flags d, e, and f, were treated as upper limits in the analysis.

Table 2.10: Correlations between radio flux and disk masses with line luminosities

	CO	H_2O	OH	[O I]
4.1 cm				
Class 0	0.31	0.24	0.3	0.27
Class I	-0.19	-0.10	**0.64**	**0.52**
Class 0+I	0.24	0.19	**0.41**	0.34
6.4 cm				
Class 0	0.26	0.39	**0.43**	0.28
Class I	-0.18	-0.13	**0.52**	**0.54**
Class 0+I	0.16	0.28	**0.43**	0.33

Notes. Spearman's rank correlation coefficient (ρ) is listed. Bold font is for correlations $\rho > 0.4$. Significant correlations ($P < 5\%$) are underlined.

2.B Additional correlations

We show a spectral index plotted against bolometric luminosities, but with upper/lower limits excluded and with four outliers removed: Per-emb-14, EDJ2009-156, SVS13A2, L1448NW.

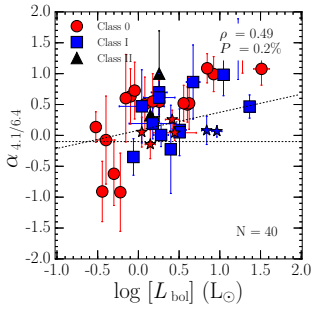


Figure 2.B.1: Left: Spectral index compared with bolometric luminosity with four outliers removed: Per-emb-14, EDJ2009-156, SVS13A2, L1448NW.

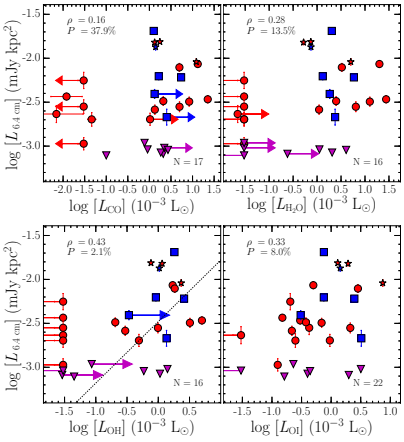


Figure 2.B.2: Luminosity at 6.4 cm compared with CO (top left), H_2O (top right), [O I] (bottom left), and OH (bottom right) line luminosities. Upper limtis for radio luminosities are plotted as magenta triangles, and lower or upper limits for *Herschel* line luminosities are indicated with arrows. Spearman's rank correlation coefficient and probability of no correlation is shown in the right top corner (for combined sample of Class 0 and Class I protostars).

We present in Figure 2.B.2 radio luminosity at 6.4 cm plotted against far-IR line luminosities. The relations at 6.4 cm are similar to those obtained at 4.1 cm.

2.C Interesting sources

We note the serendipitous detection of a few intriguing sources in the C-band observations, although not having protostellar nature. The source SVS3 - also known as IRAS 03260-3111 - is a visible star illuminating the surrounding cloud. It is actually a binary first reported as such by (Connelley et al. 2008). In C-band observations we clearly see both components with SVS3-B being the brighter of the two (Figure 2.C.3). SVS3-A was well detected with Ka-band observations (Tobin et al. 2016) with negative spectral index. It appears to have negative spectral index in C-band observations as well. This altogether points to this star probably being a bright synchrotron source originating from coronal activity, characteristic for more evolved sources and is also supported by X-ray detection (Preibisch 1997; Getman et al. 2002). SVS3-B was not detected in the Ka-band observations indicating that there is very little dust present in this component. Free-free emission associated with the source appears spherical and resolved, consistent with ionized wind from the evolved, luminous star.

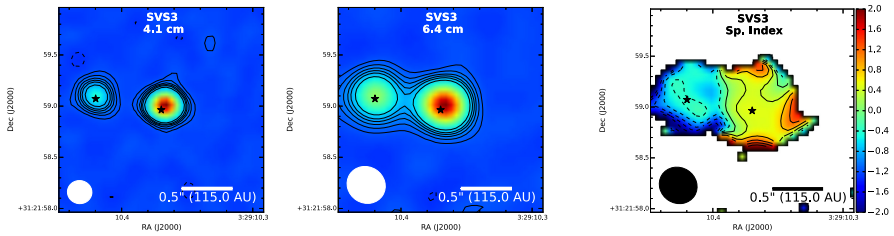


Figure 2.C.3: Maps of SVS3 system centered on a SVS3-B component. From left to right: 4.1 cm, 6.4 cm and spectral index map.

Source BD +30 547 is a visible star with strong variability detected previously (Rodríguez et al. 1999). It also appears variable in our observations. We note a potential transient source appearing about 1" north-west away from BD +30 547 in only one of the maps, from five fields available (Figure 2.C.4).

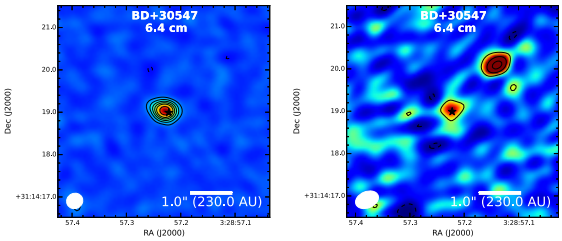


Figure 2.C.4: BD+30 547 maps at 6.4 cm from two different epochs. Significant decrease in brightness of the central source can be observed, as well as the appearance of the new source of emission north-west of the BD+30 547.

We detect source 2MASS J03293053+3127280 reported previously as a brown dwarf (Wilking et al. 2004). Extremely low bolometric luminosity of this source 0.001 $L_{\odot}$ makes explanation of the emission difficult. The source has a positive spectral index, excluding possibility of coronal activity, rather pointing at a surprisingly powerful stellar wind from a brown

dwarf. Recently, Rodríguez et al. (2017) report a detection of brown dwarfs with radio fluxes order-of-magnitude more powerful than expected.

2.D Free-free and dust slopes

Figure 2.D.5 shows the radio spectra for all of the sources from the VANDAM survey. Linear fit to the logarithmic fluxes, applied free-free correction to the dust flux, and the flag used when considering the protostellar disk mass are showed as described in Section 2.5.

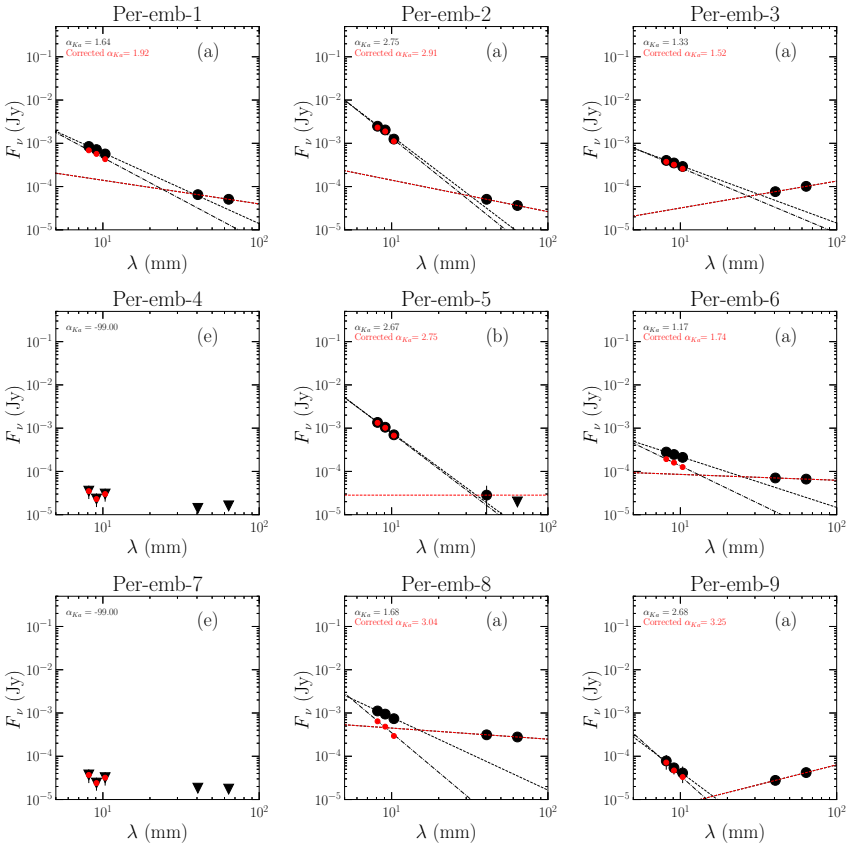


Figure 2.D.5: Radio spectral energy distributions for all protostars in VANDAM survey. Black bullets represent Ka-band and C-band flux densities, and triangles are upper limits. Red bullets mark the corrected Ka-band flux densities. Dotted lines are linear fits to the original data, and the red line represents the function from which the free-free contribution was estimated. Dash-dot line marks fit to the corrected Ka-band flux densities. Labels a-e indicate a different case of correcting Ka-band data for free-free contamination.

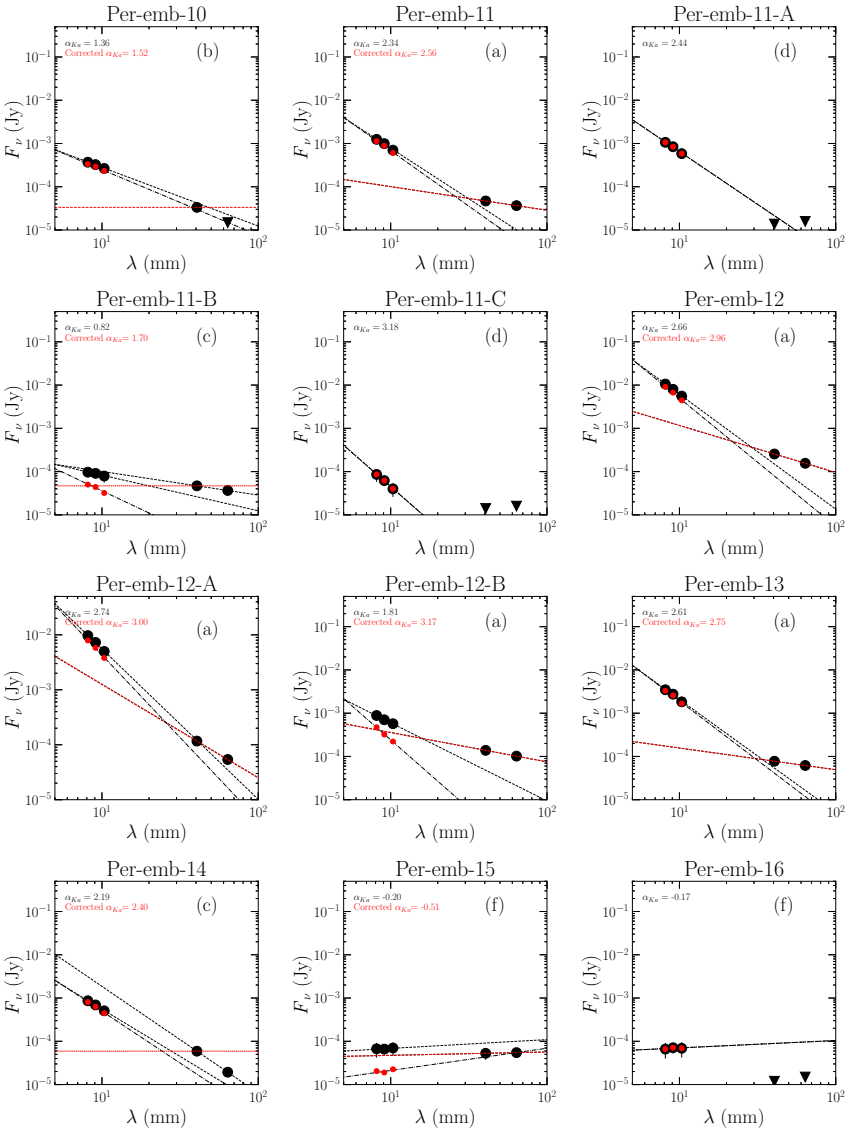


Figure 2.D.5: contd.

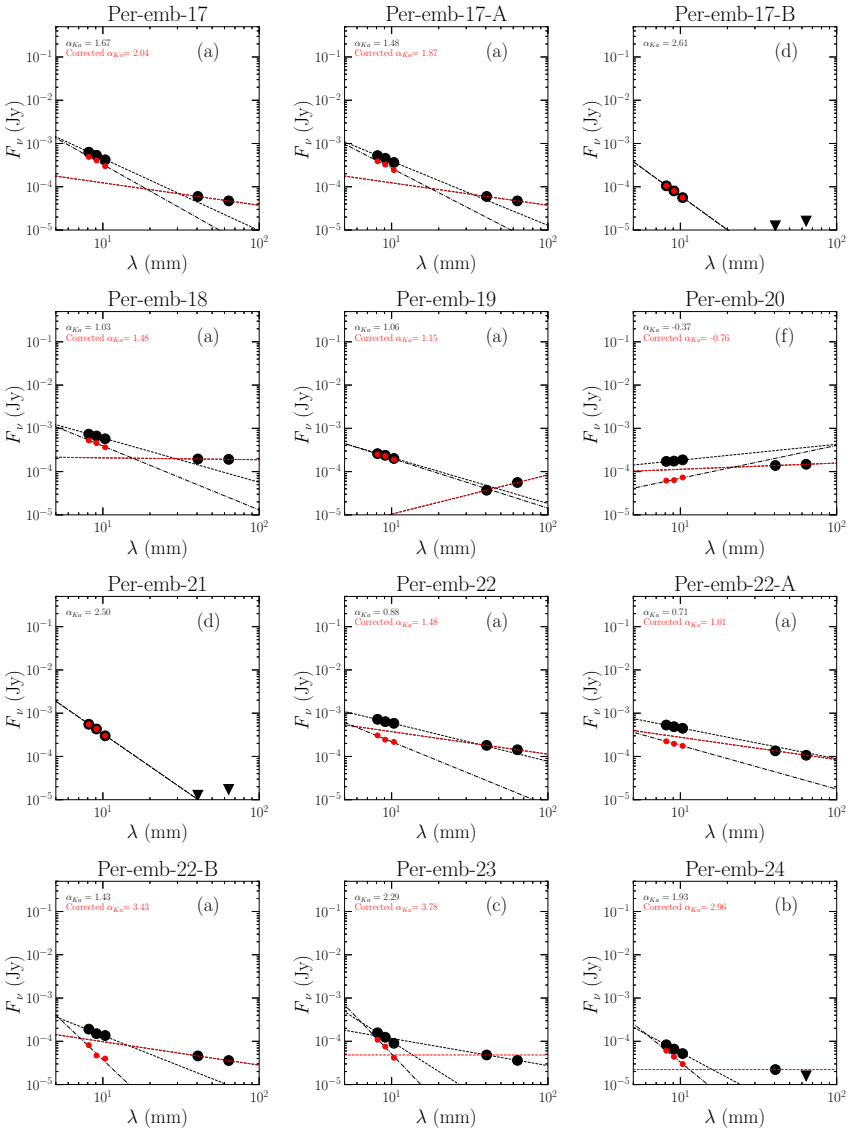


Figure 2.D.5: contd.

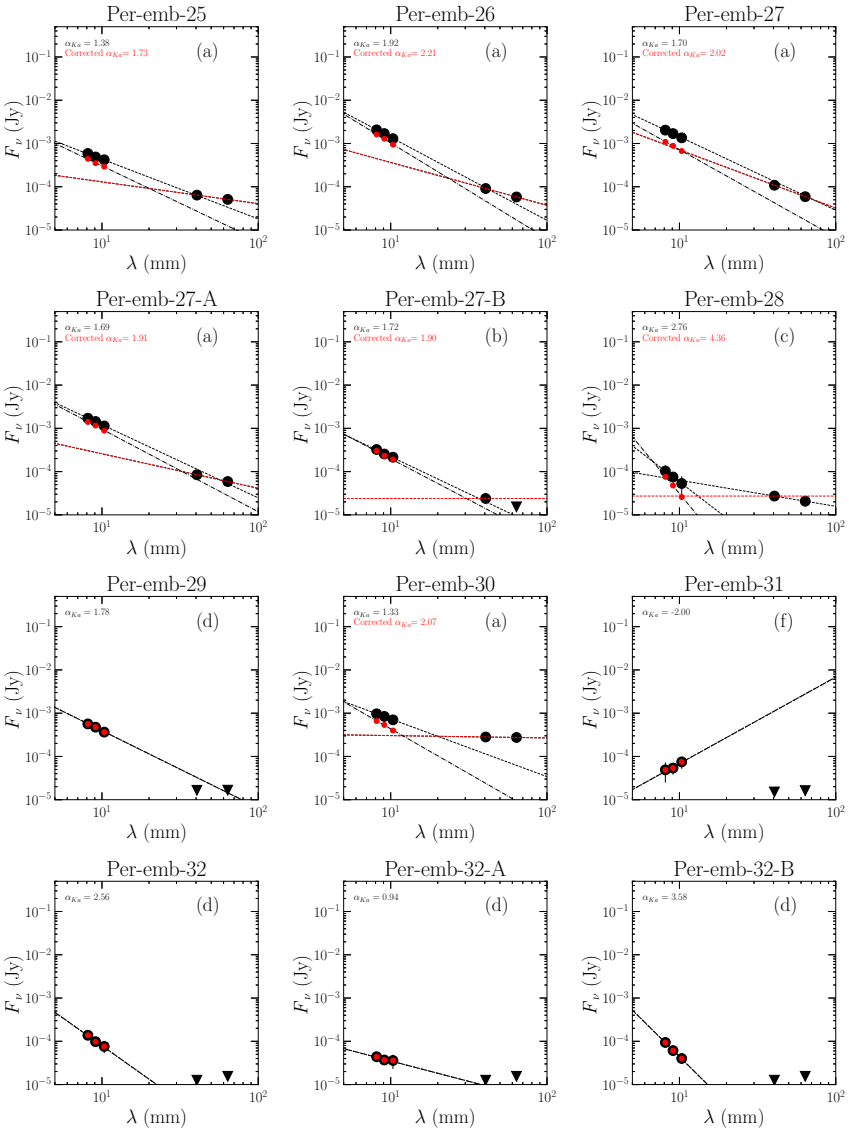


Figure 2.D.5: contd.

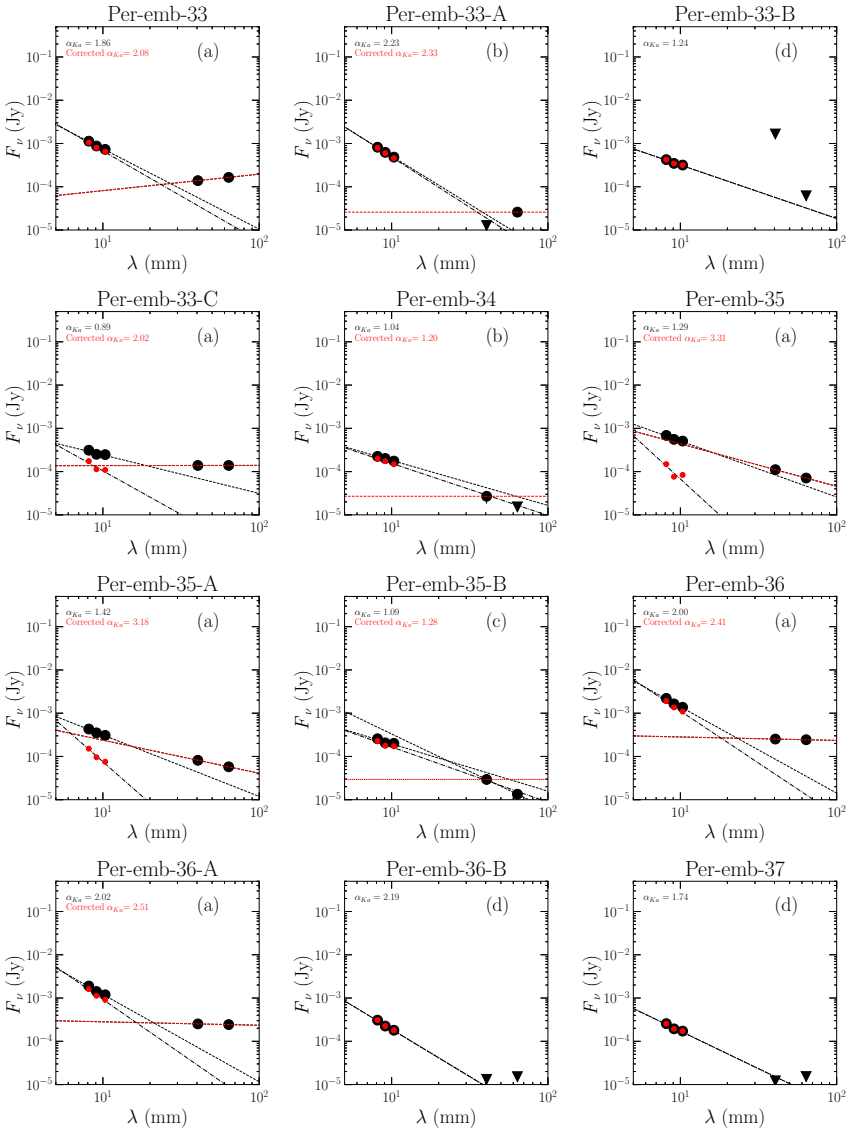


Figure 2.D.5: contd.

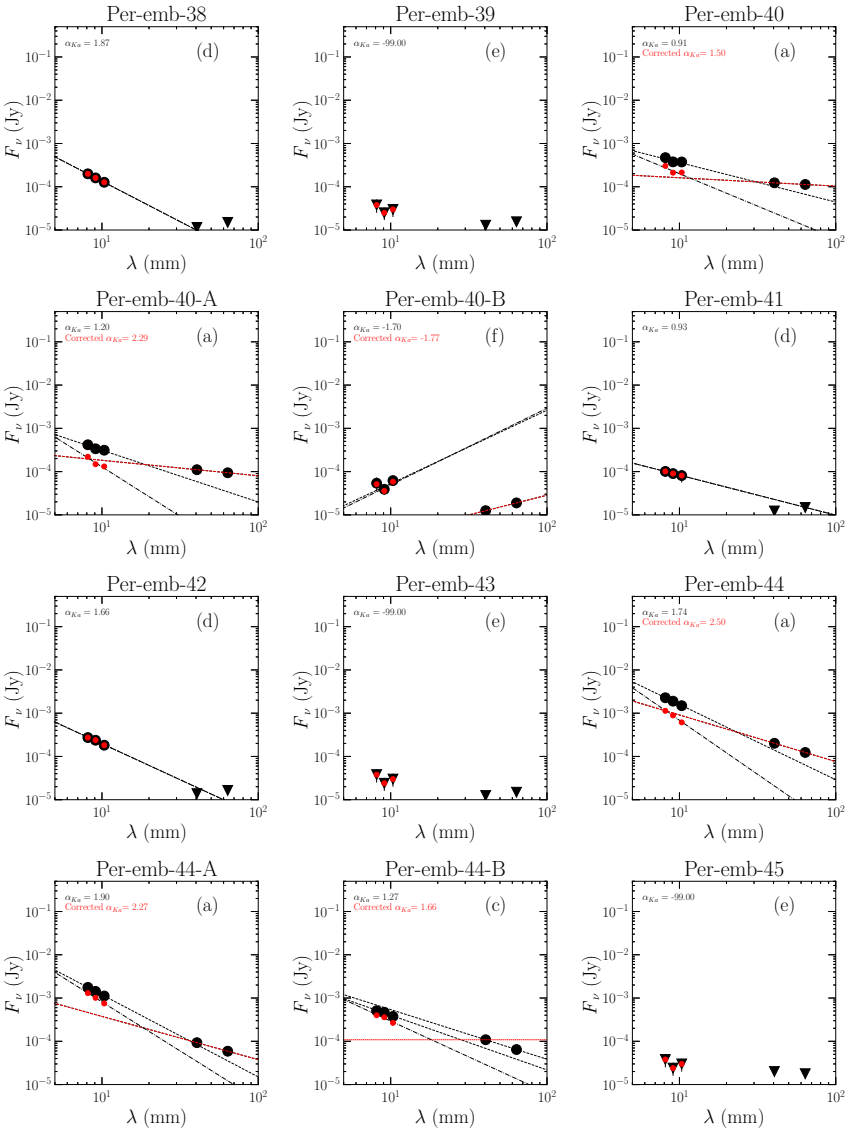


Figure 2.D.5: contd.

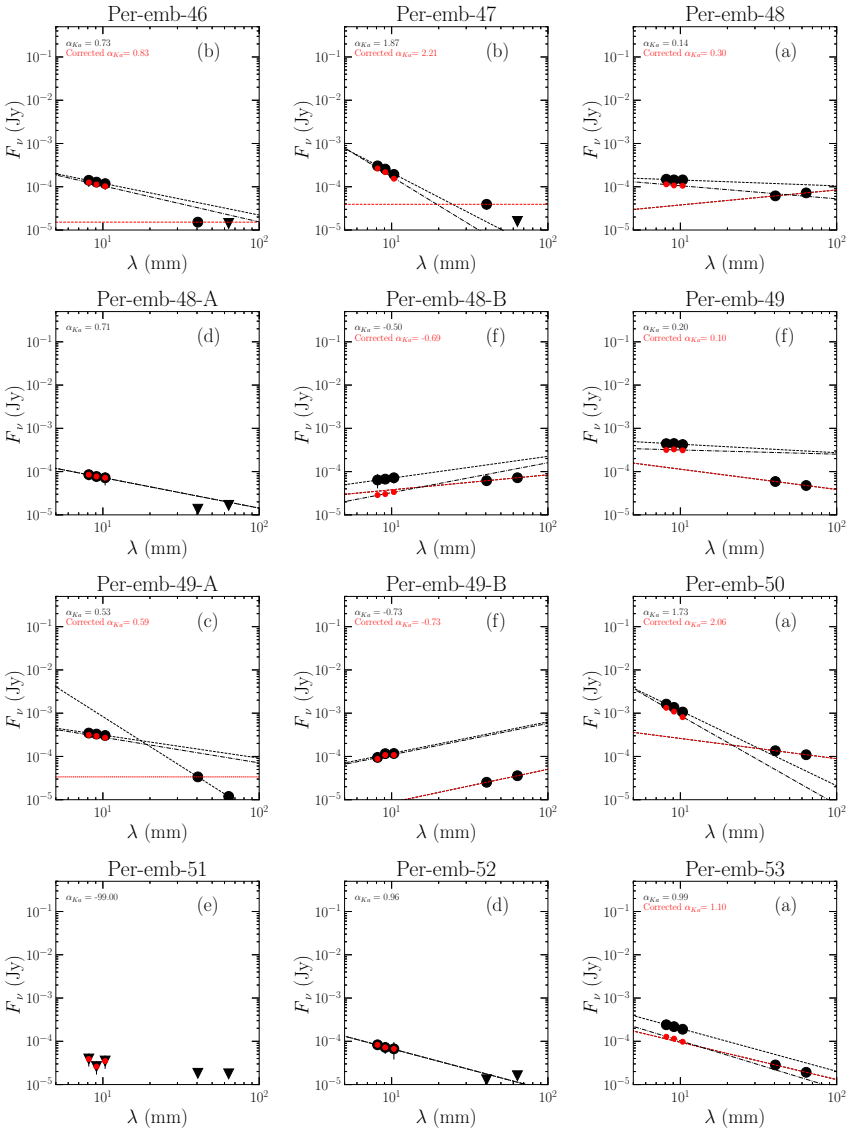


Figure 2.D.5: contd.

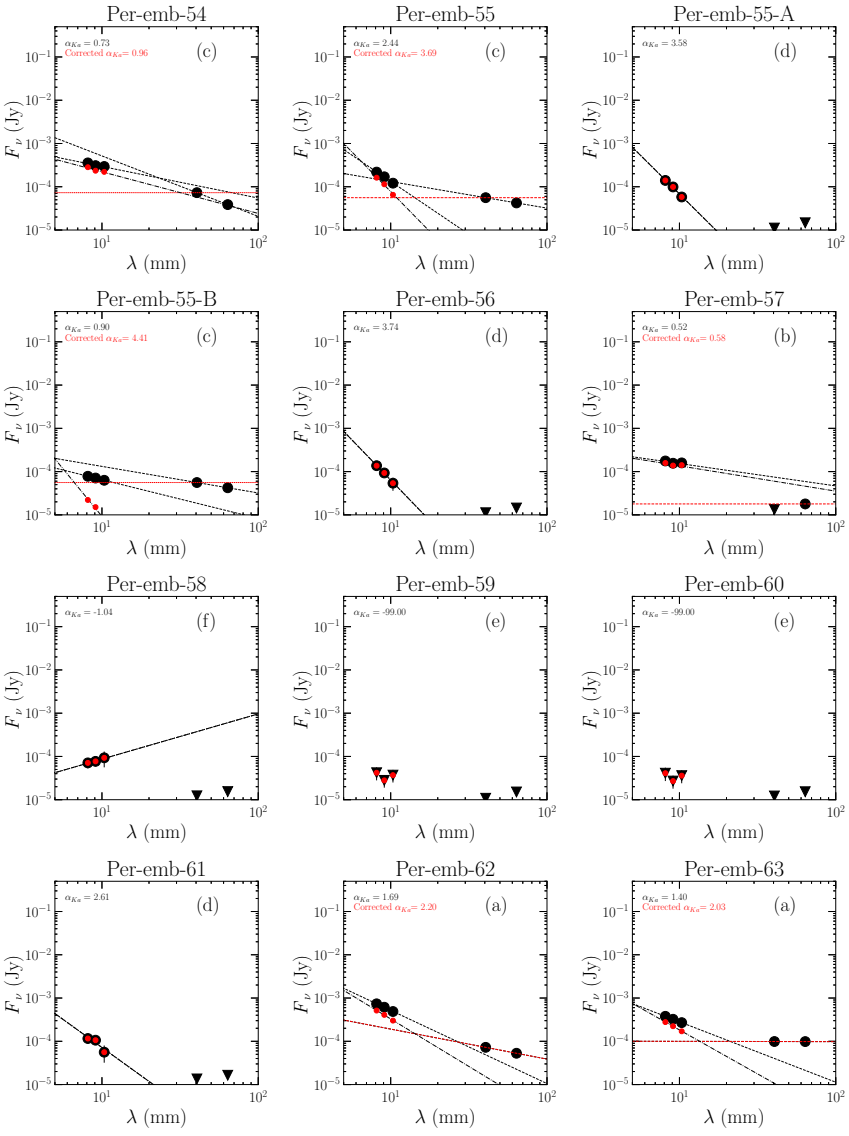


Figure 2.D.5: contd.

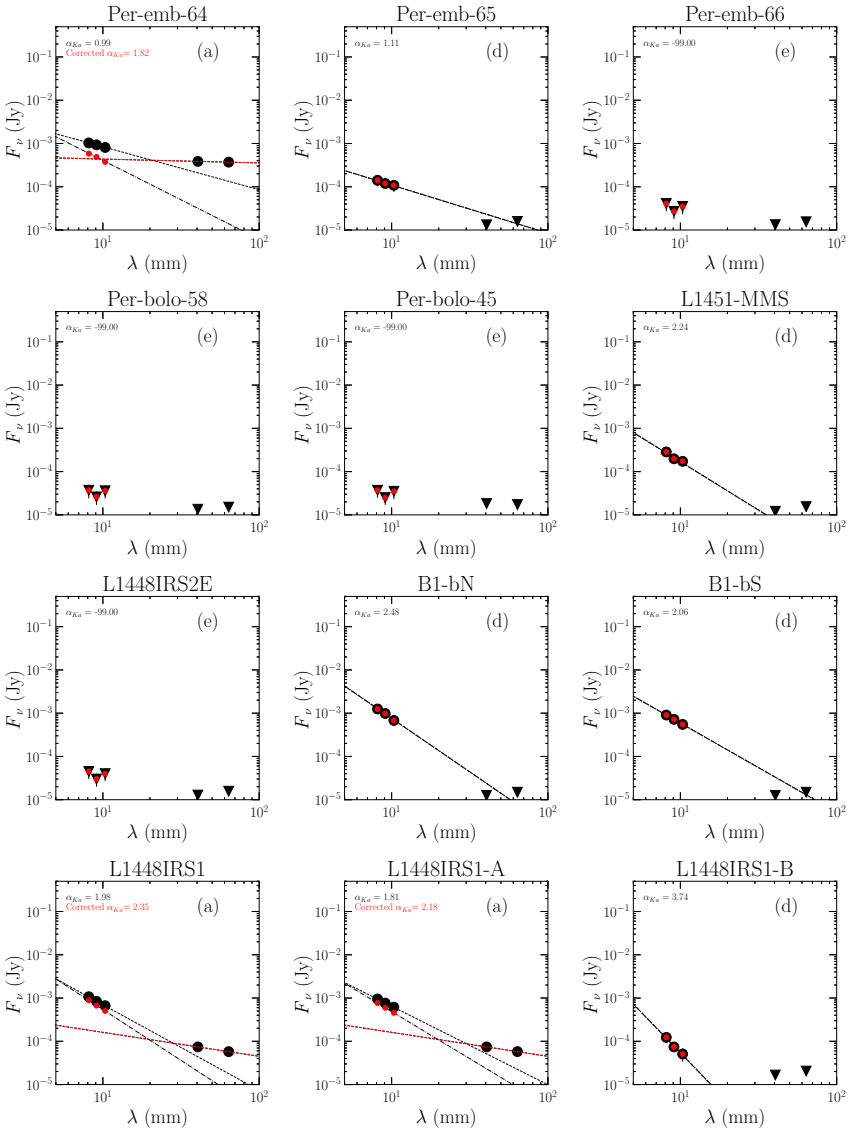


Figure 2.D.5: contd.

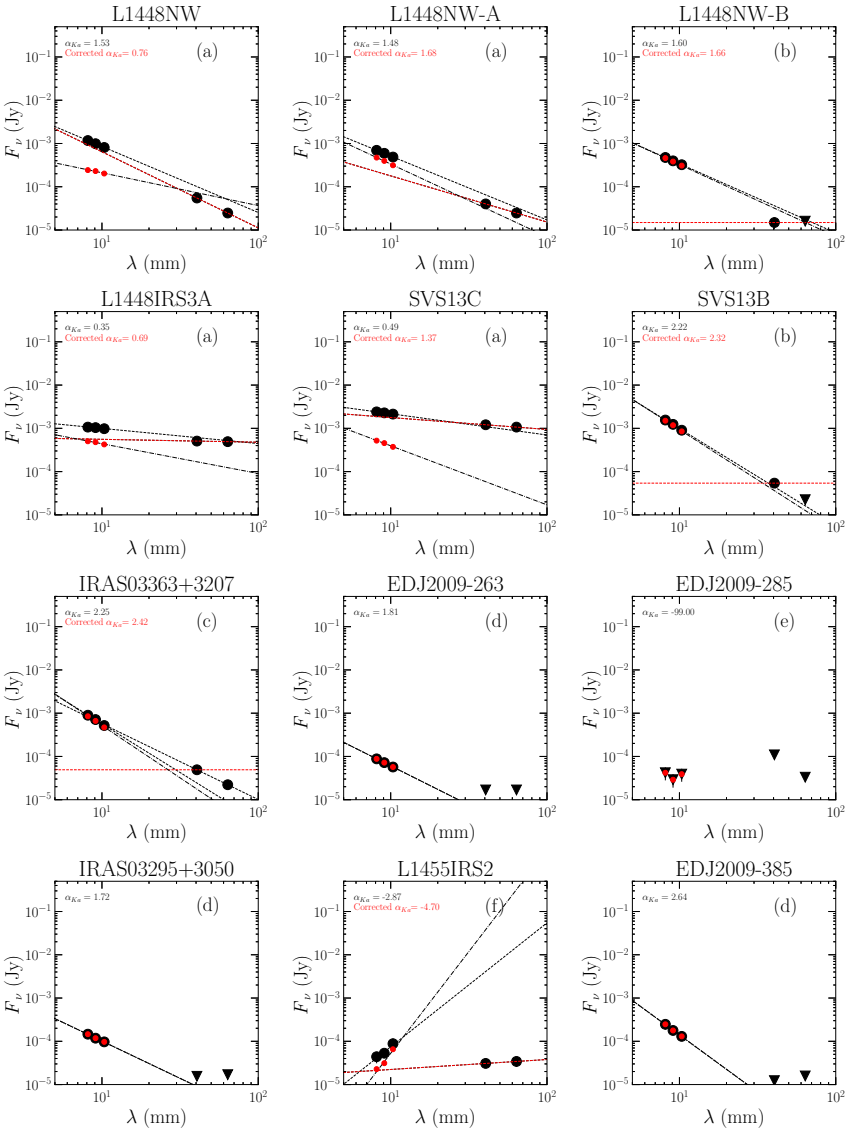


Figure 2.D.5: contd.

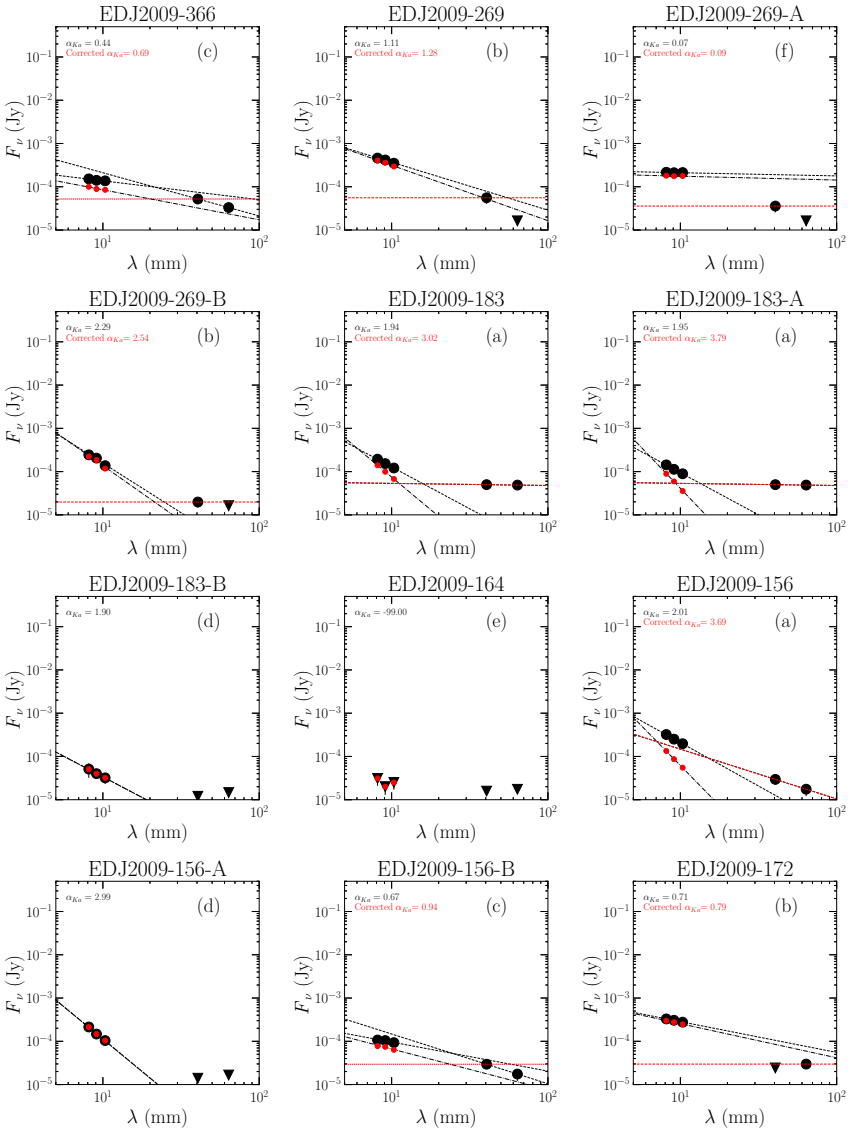


Figure 2.D.5: contd.

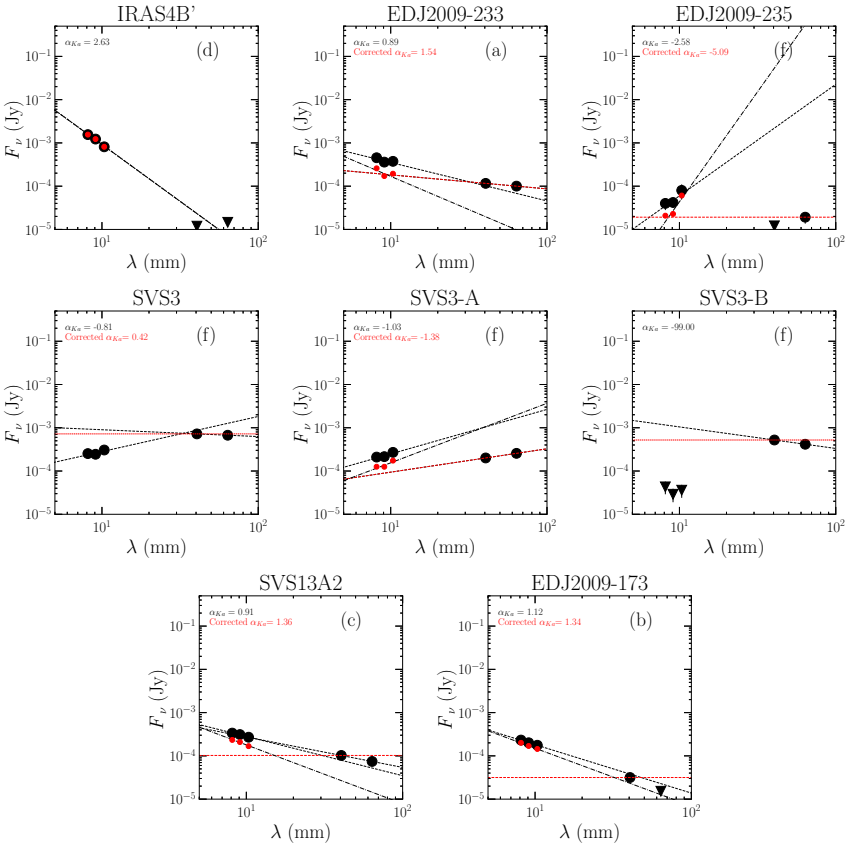


Figure 2.D.5: contd.

2.E Protostars of the VANDAM survey in Ka-band and C-band

Here we present the images of all protostars targeted in VANDAM survey. Figure 2.E.6 shows four images of each protostar obtained in Ka-band (0.8 & 1.0 cm) and in C-band (4.1 & 6.4 cm).

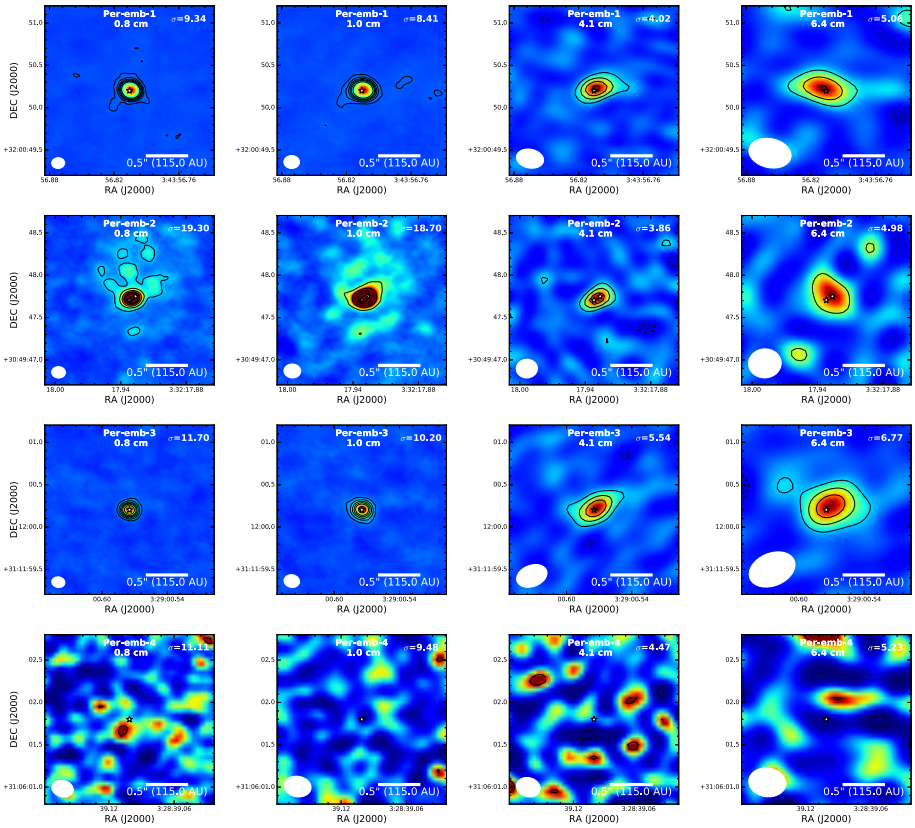


Figure 2.E.6: Images of all protostars targeted by both Ka-band (0.8 & 1.0 cm) and C-band (4.1 & 6.4 cm) observations with increasing wavelength from left to right. The contours are [-3, 3, 6, 9, 12, 15, 20] $\times \sigma$ where σ in mJy for each map is provided in top-right corner.

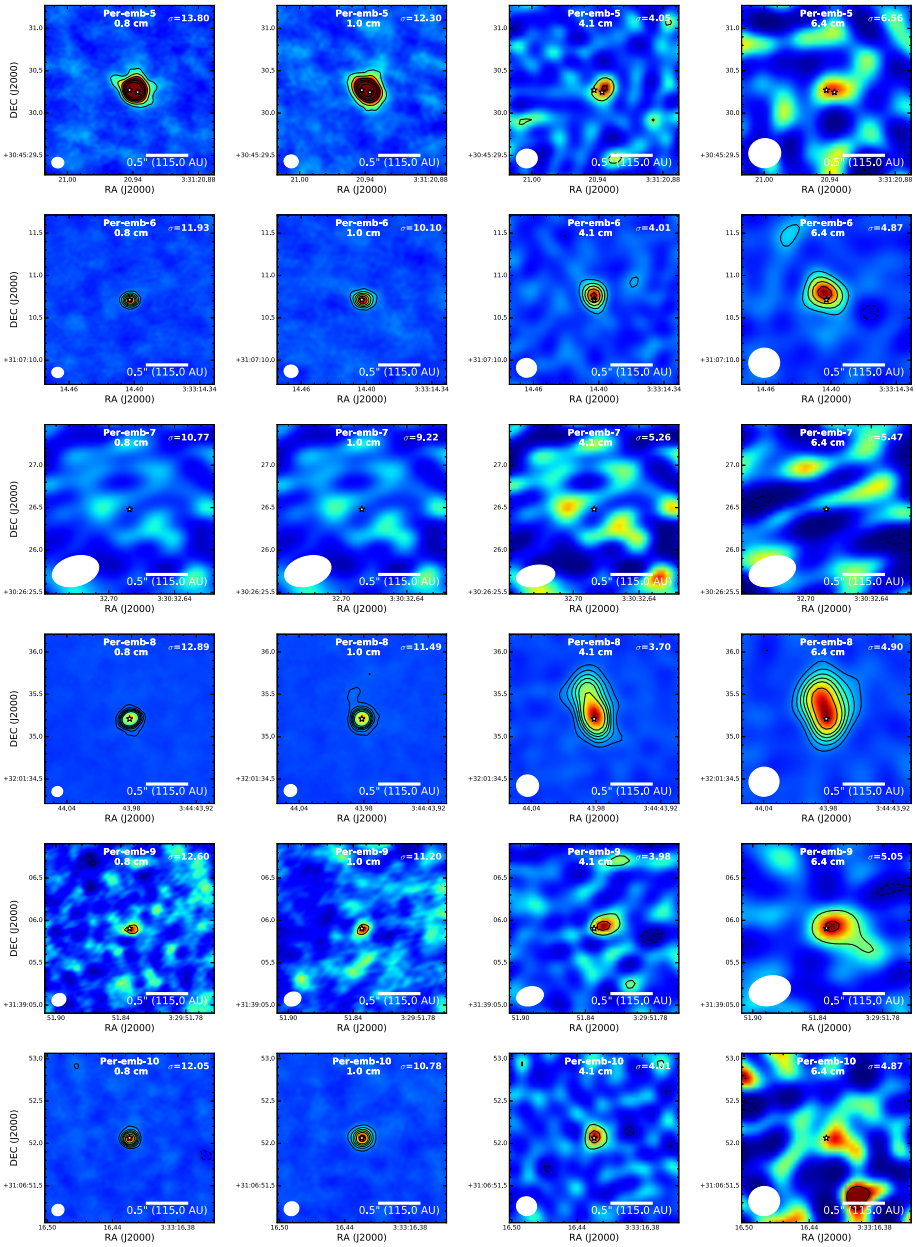


Figure 2.E.6: contd.

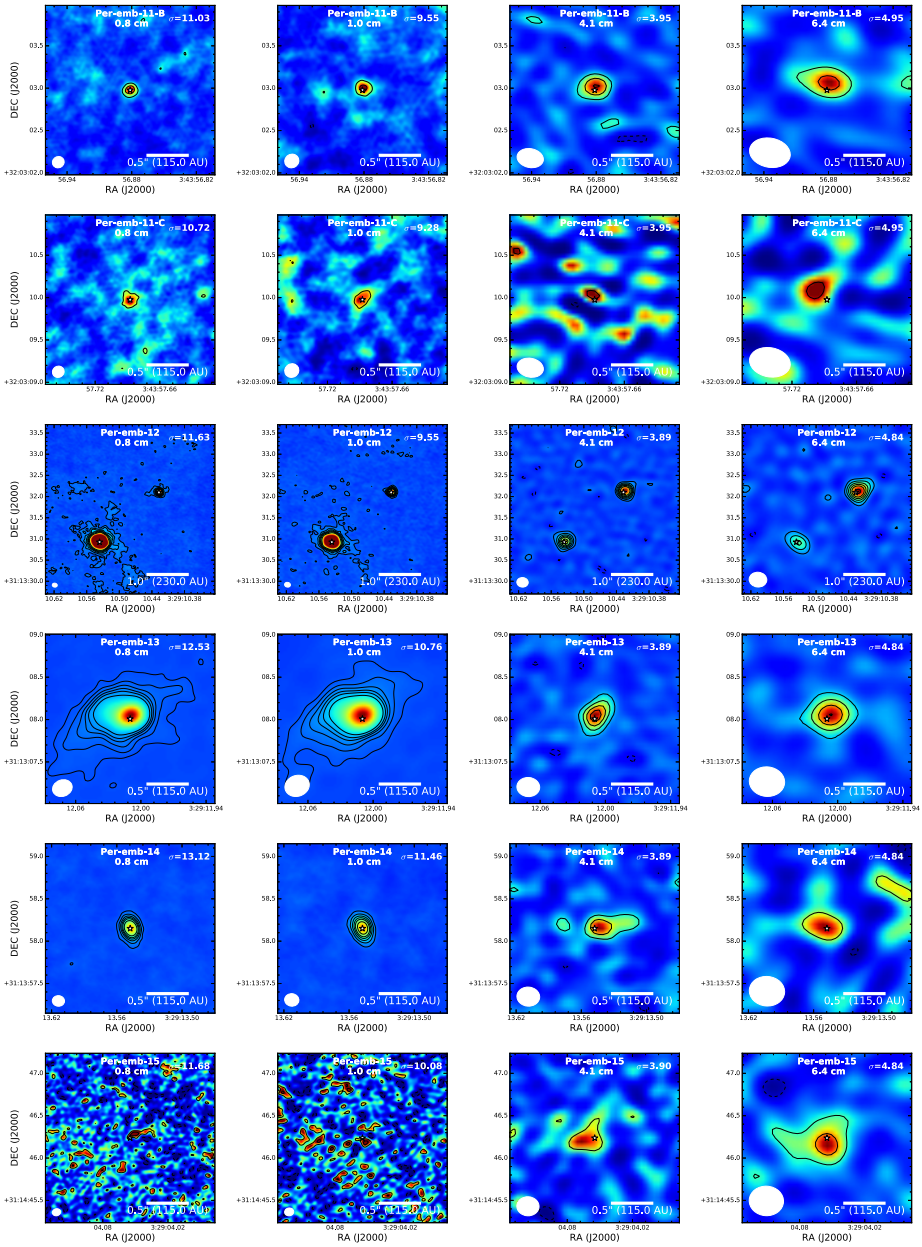


Figure 2.E.6: contd.

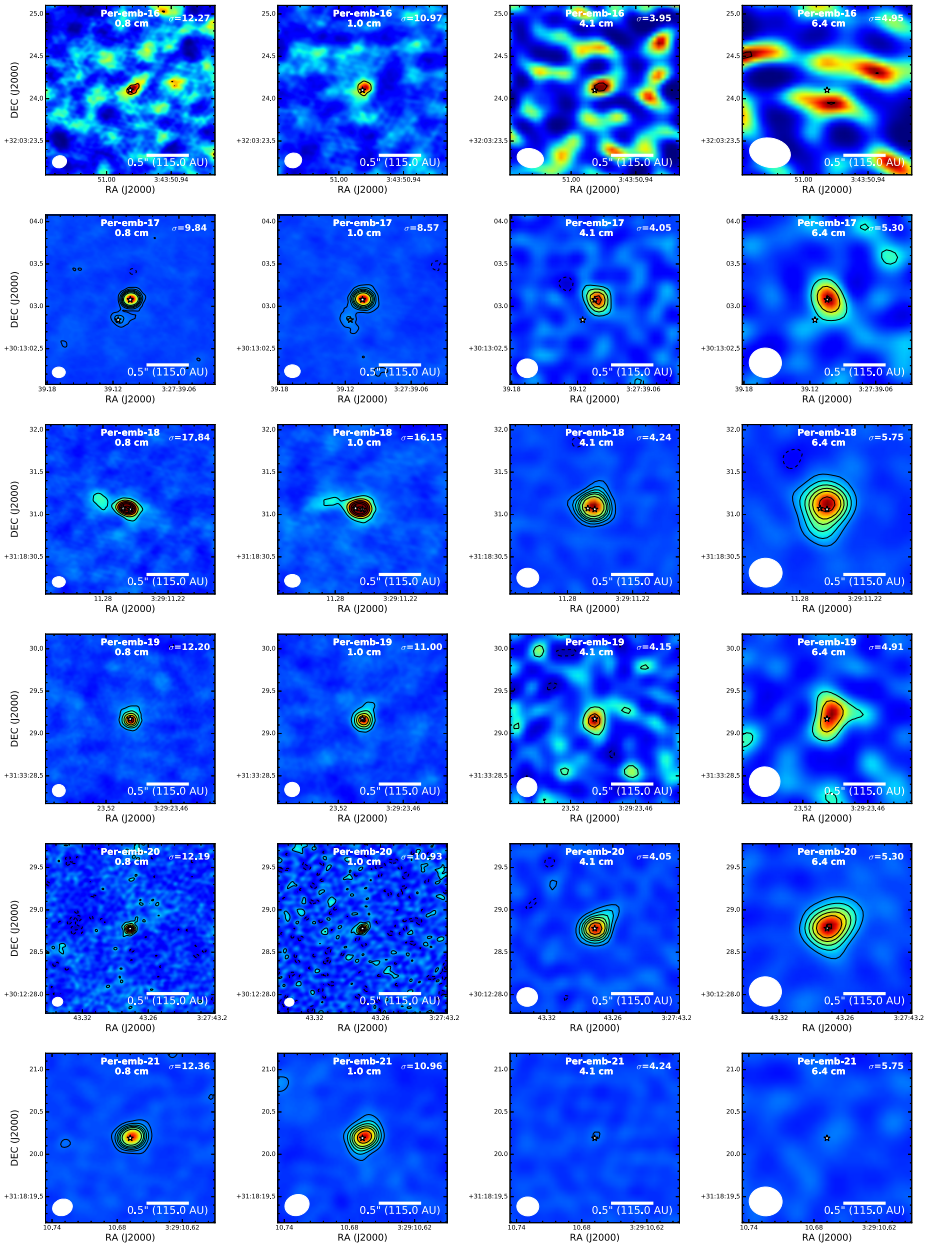


Figure 2.E.6: contd.

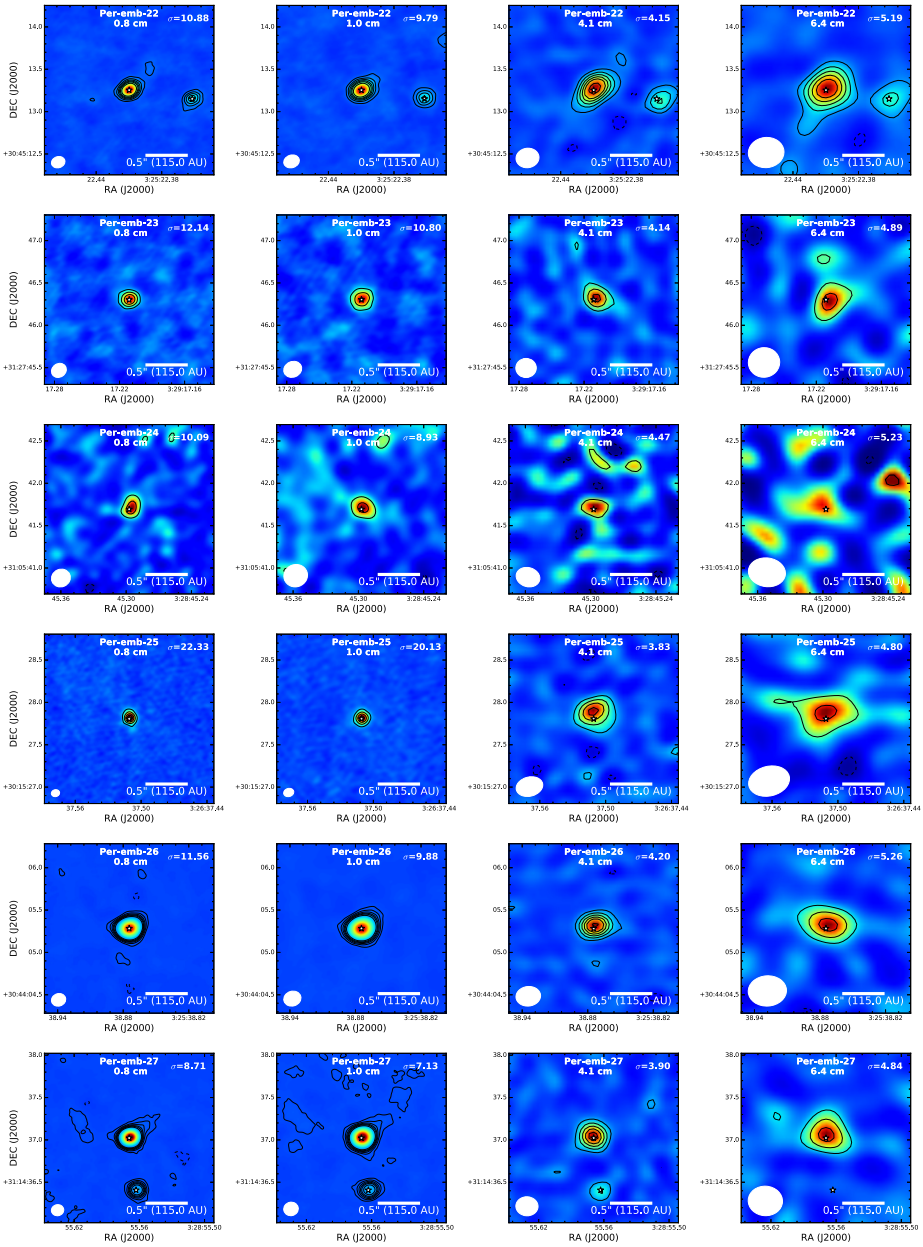


Figure 2.E.6: contd.

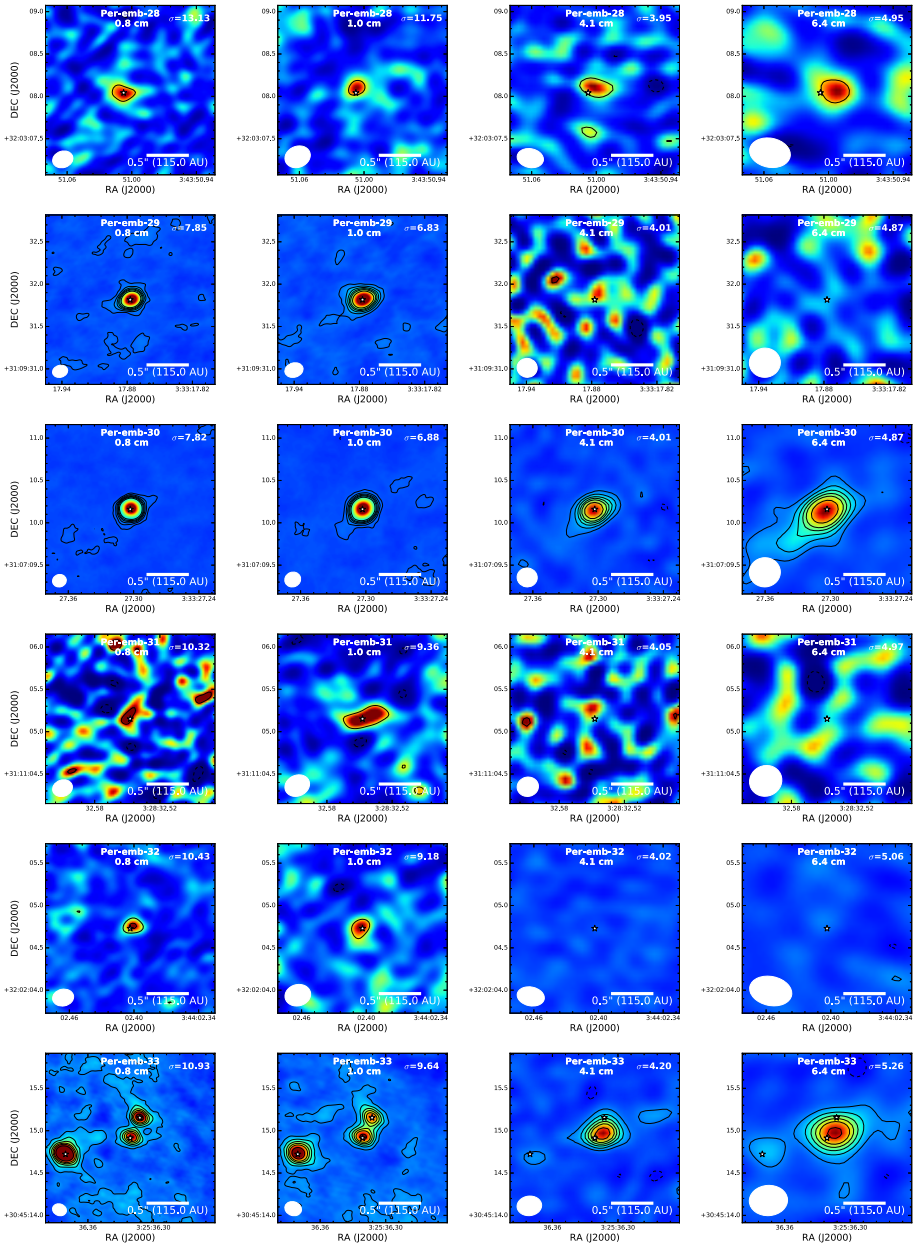


Figure 2.E.6: contd.

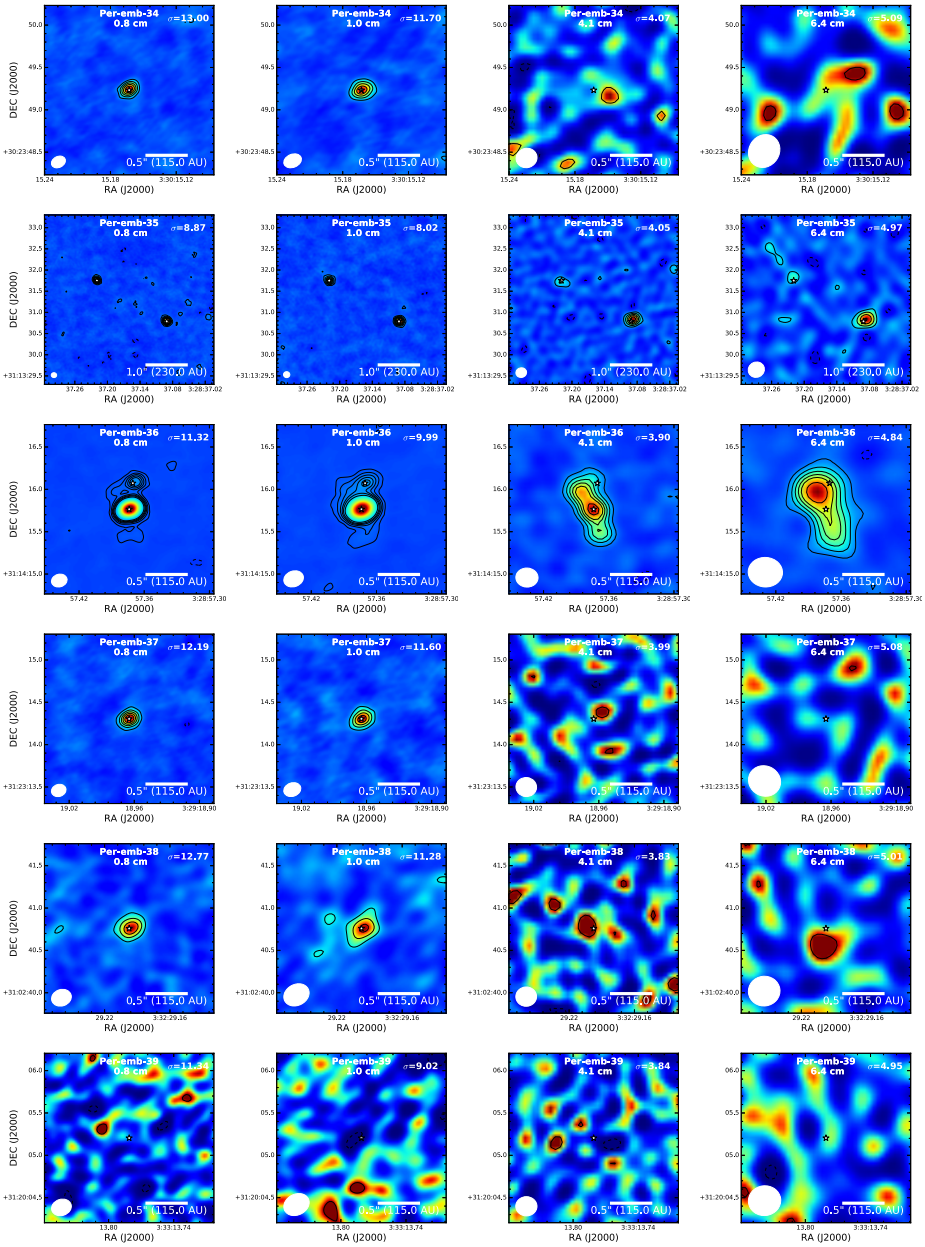


Figure 2.E.6: contd.

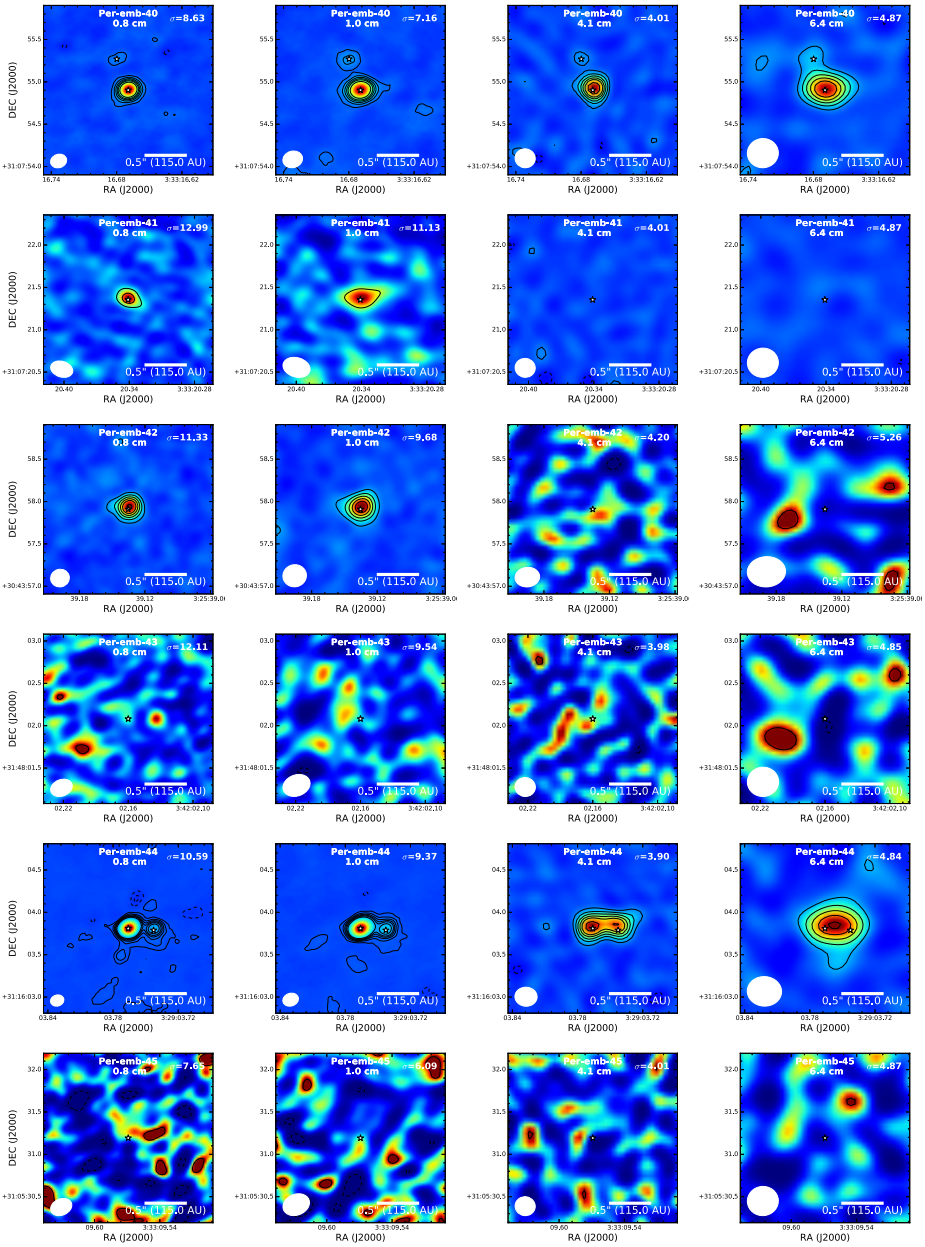


Figure 2.E.6: contd.

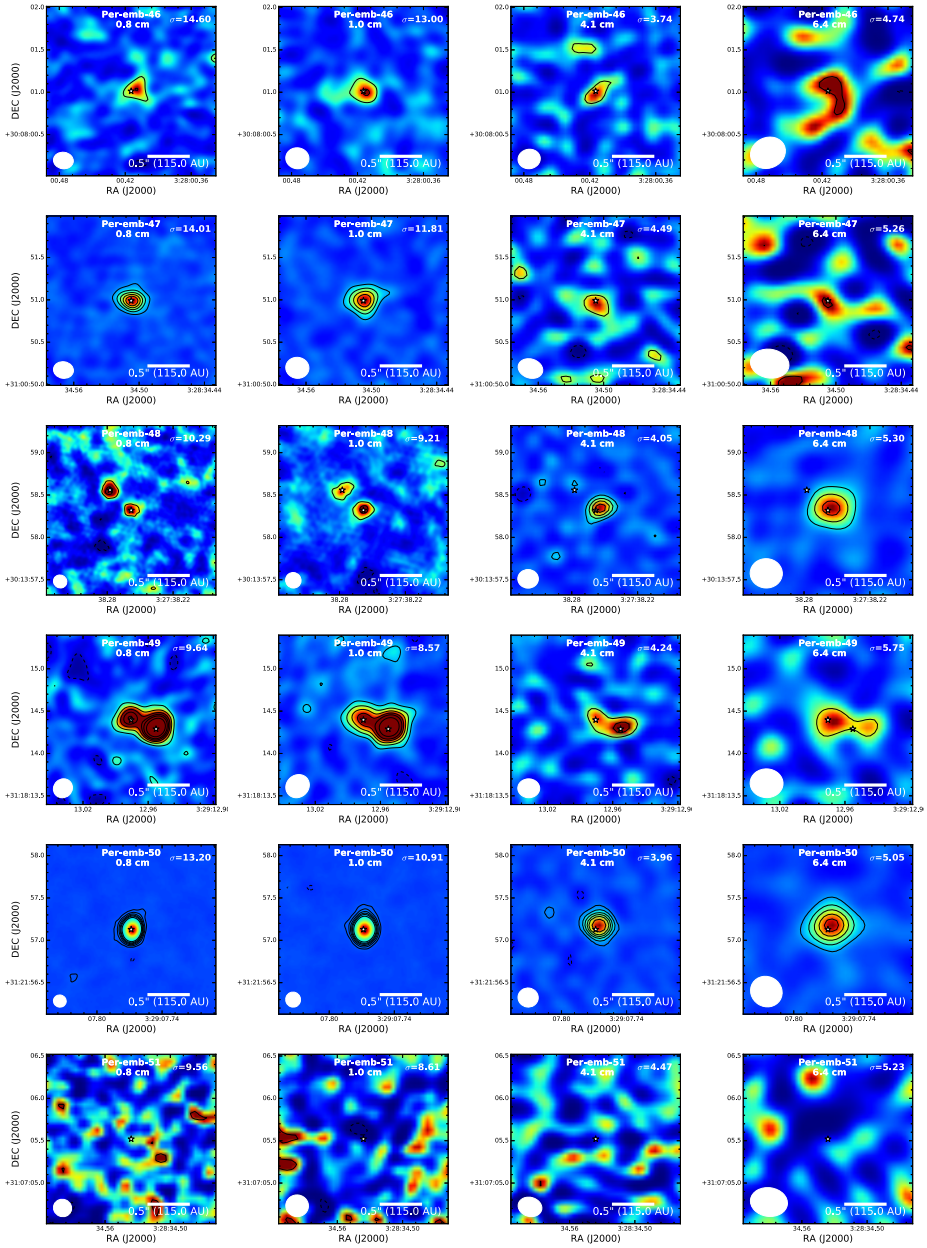


Figure 2.E.6: contd.

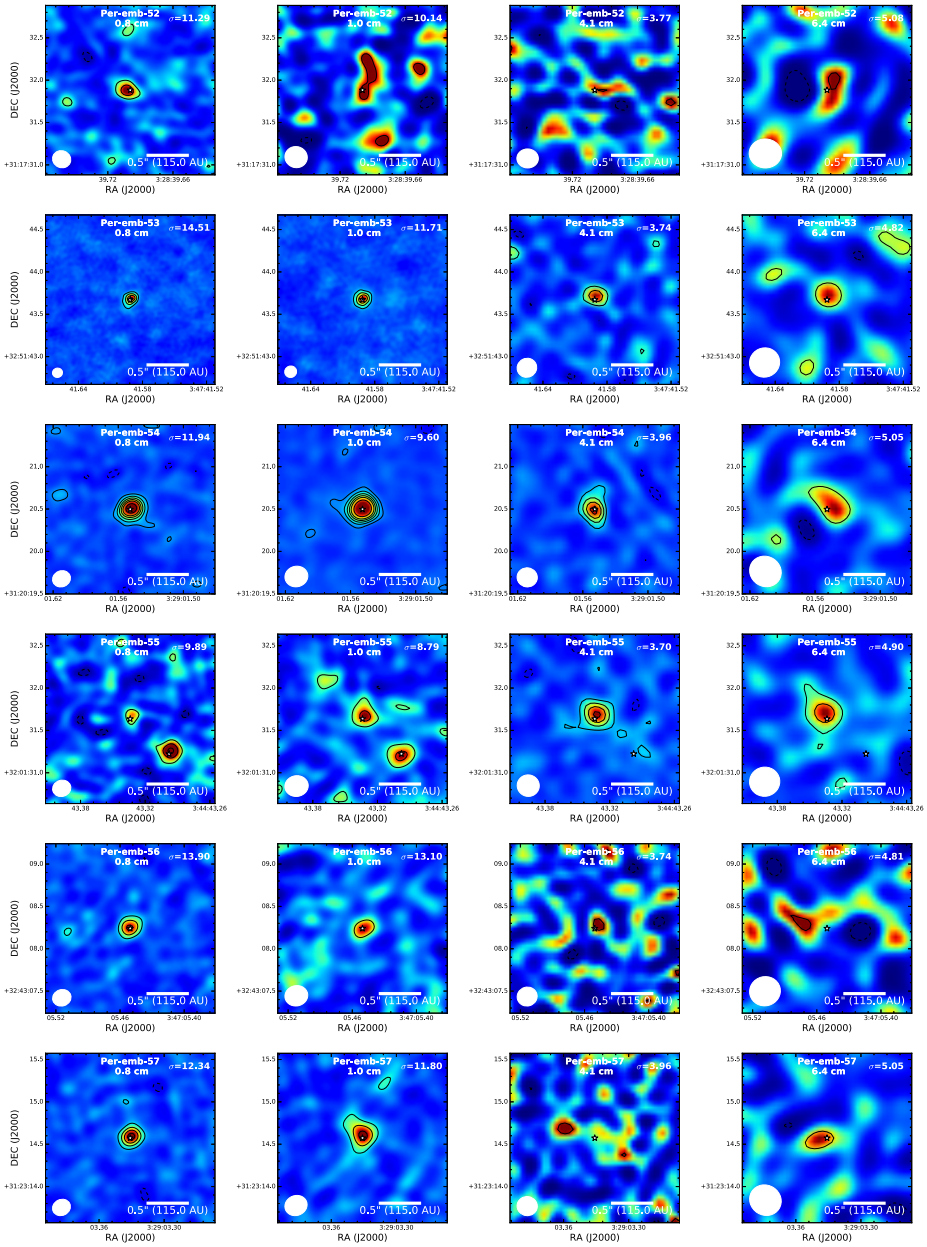


Figure 2.E.6: contd.

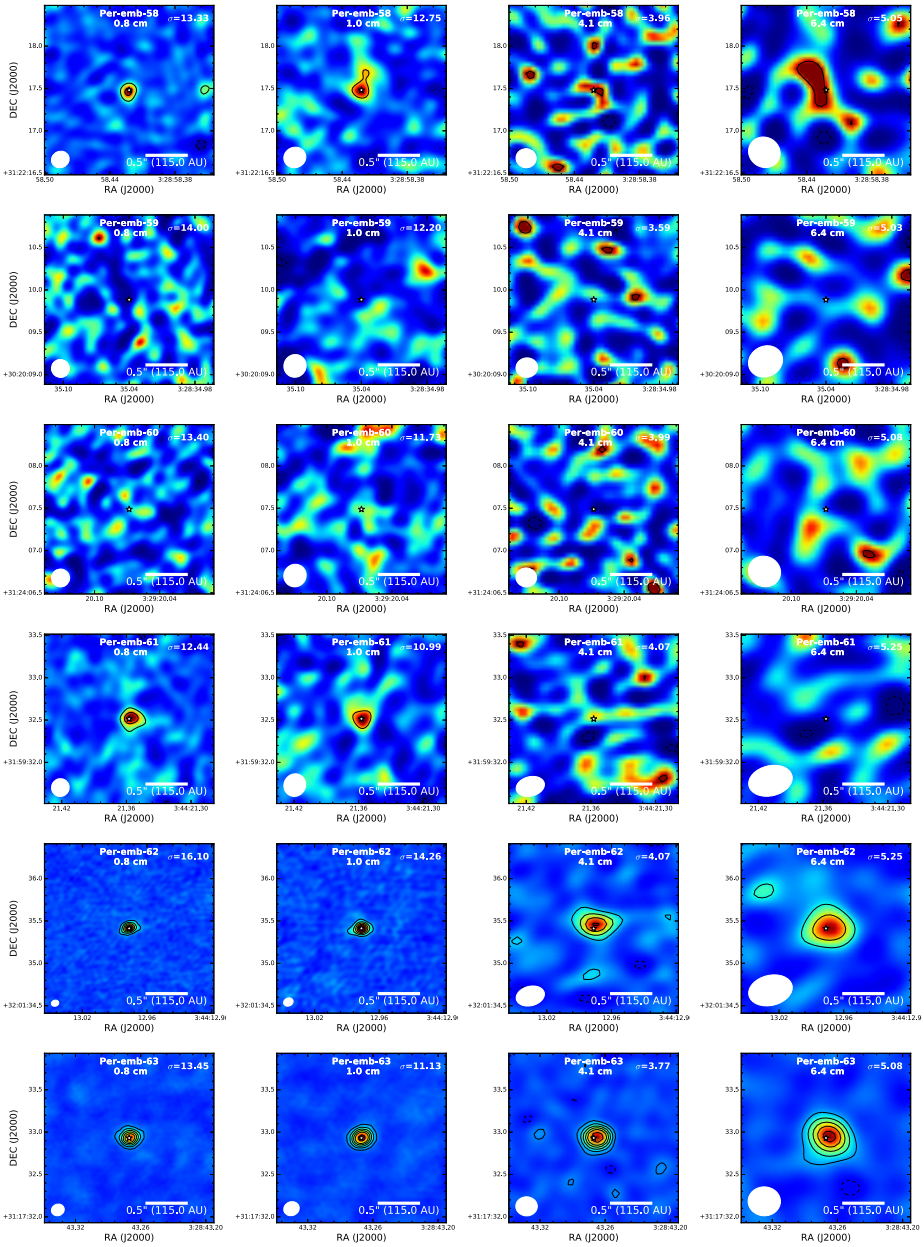


Figure 2.E.6: contd.

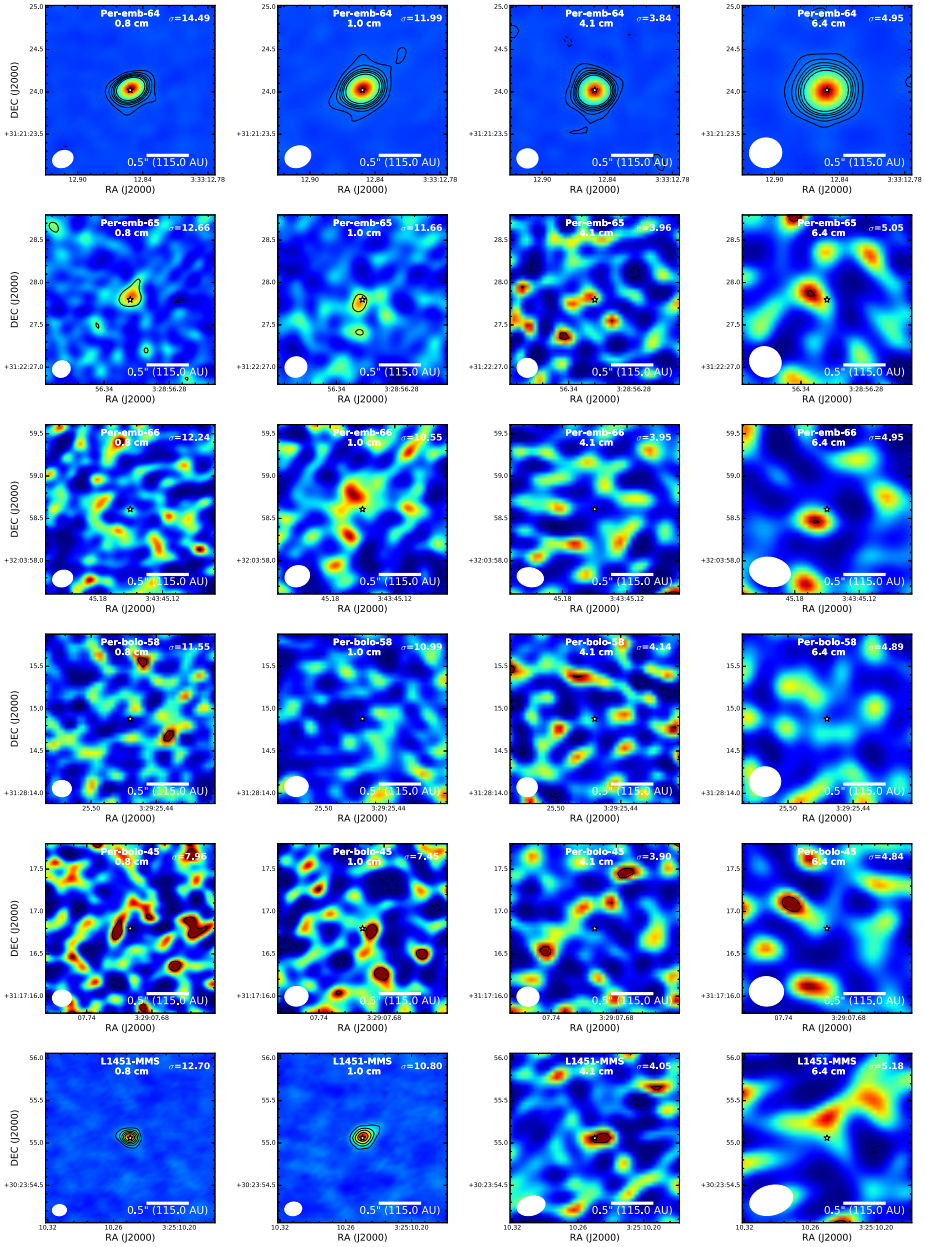


Figure 2.E.6: contd.

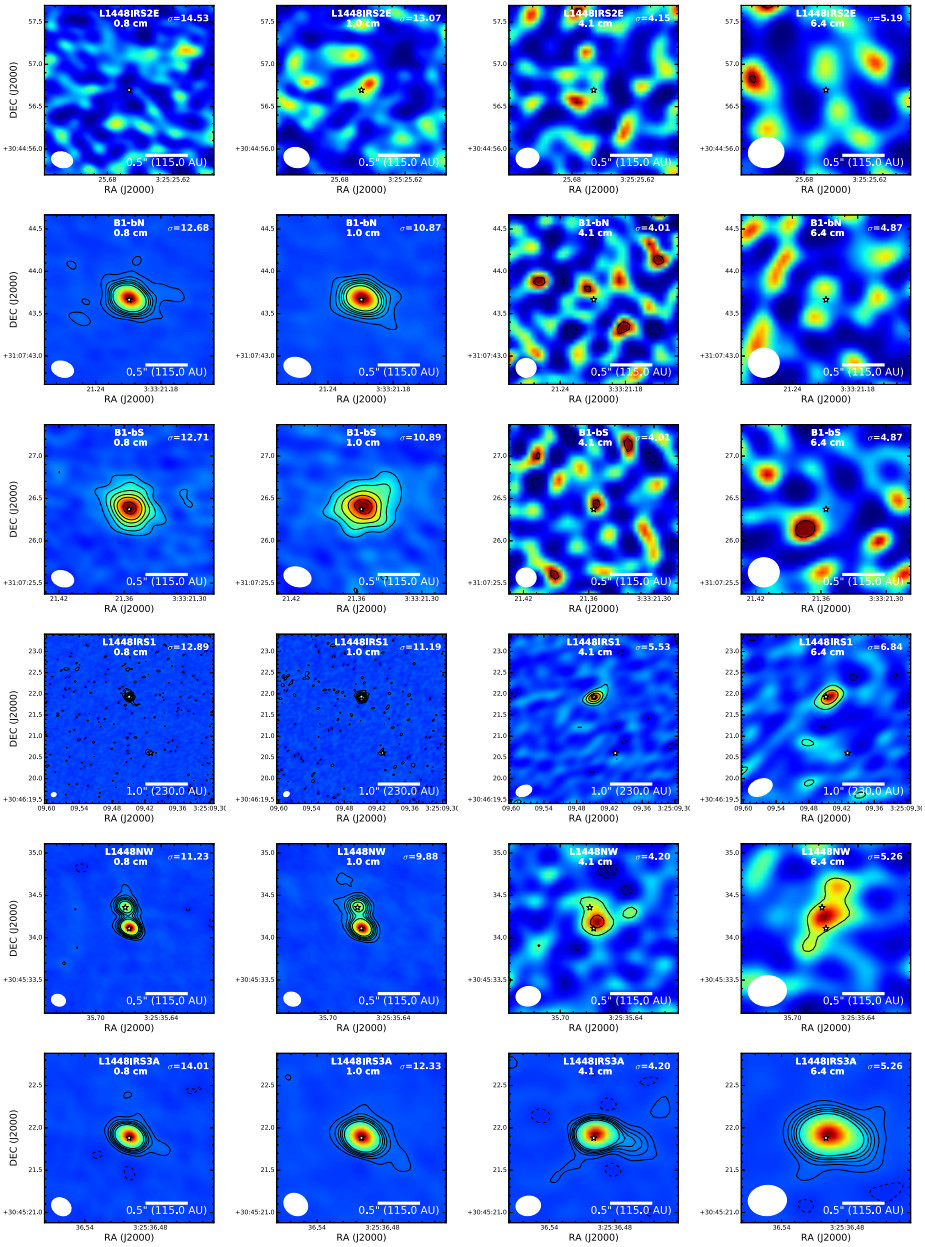


Figure 2.E.6: contd.

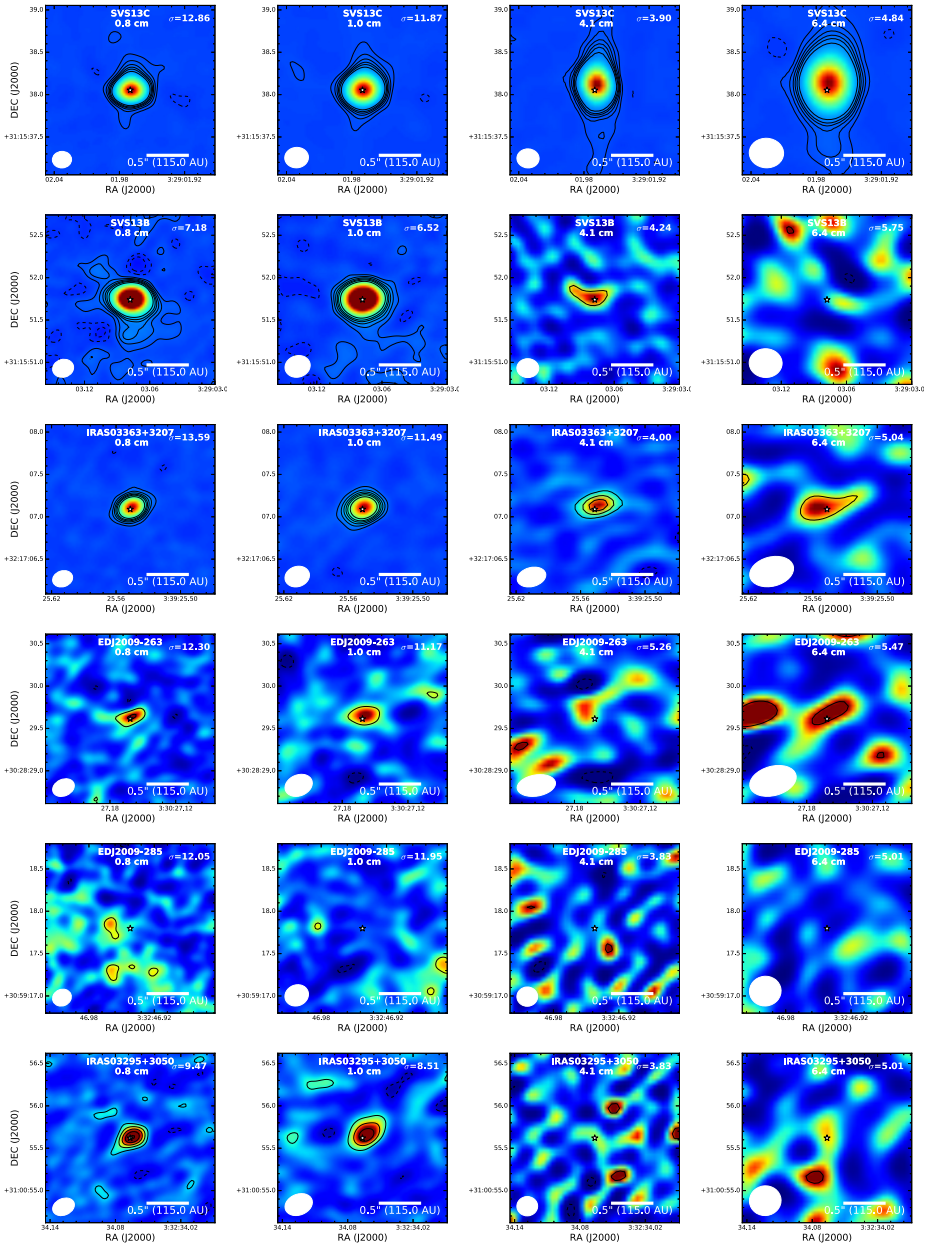


Figure 2.E.6: contd.

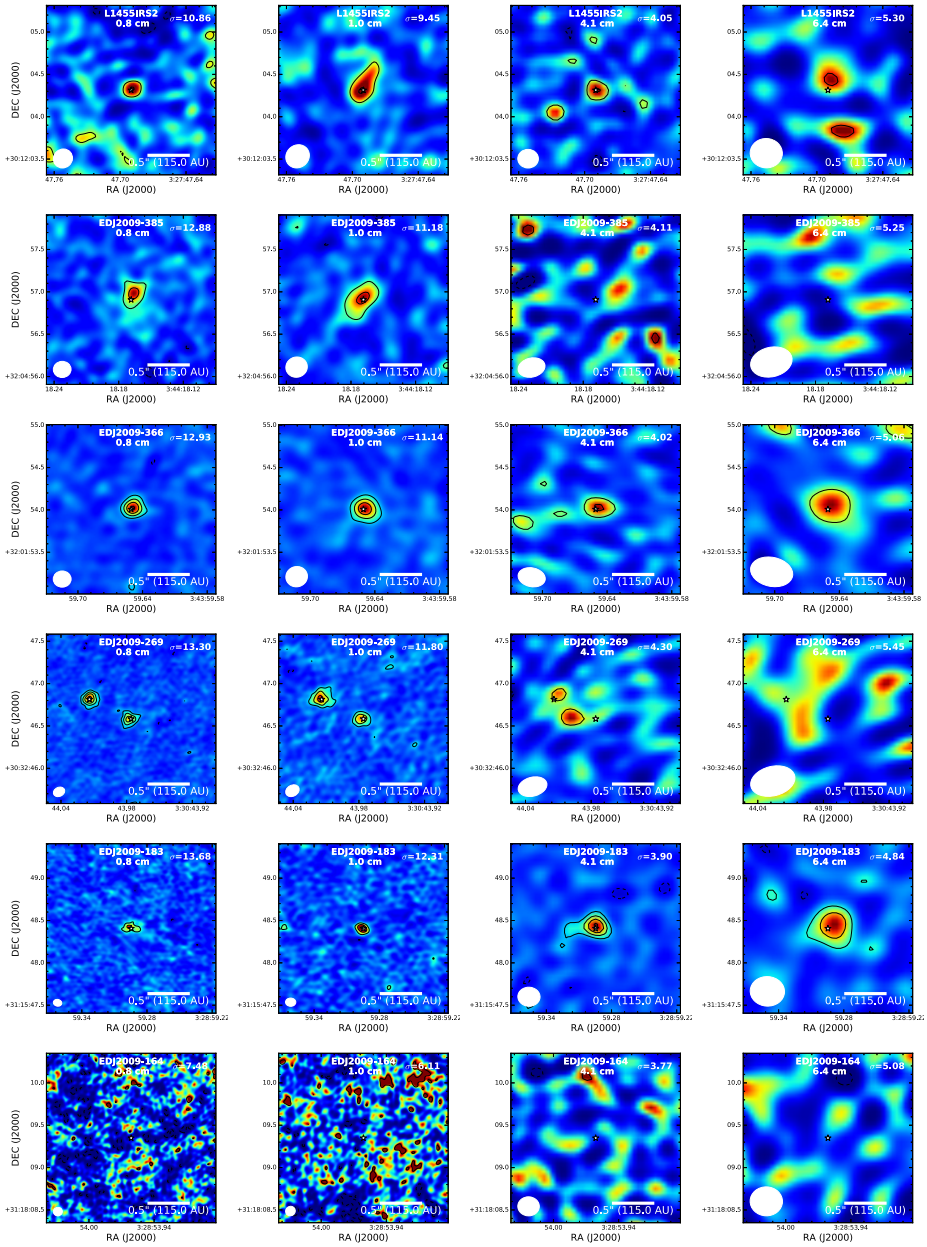


Figure 2.E.6: contd.

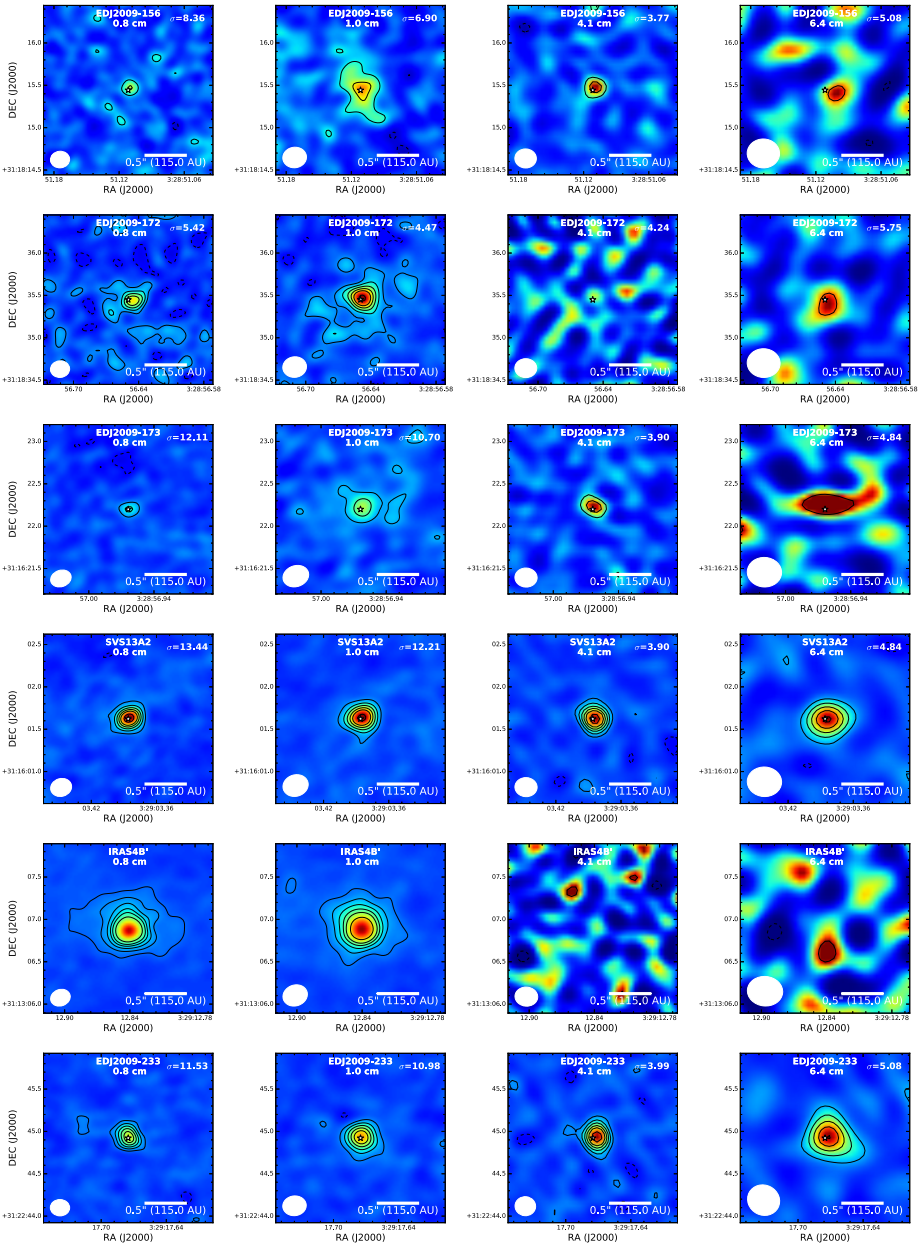


Figure 2.E.6: contd.

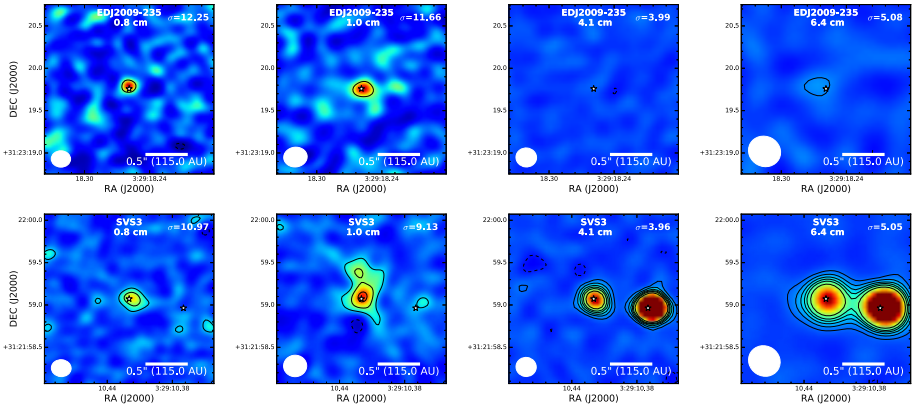
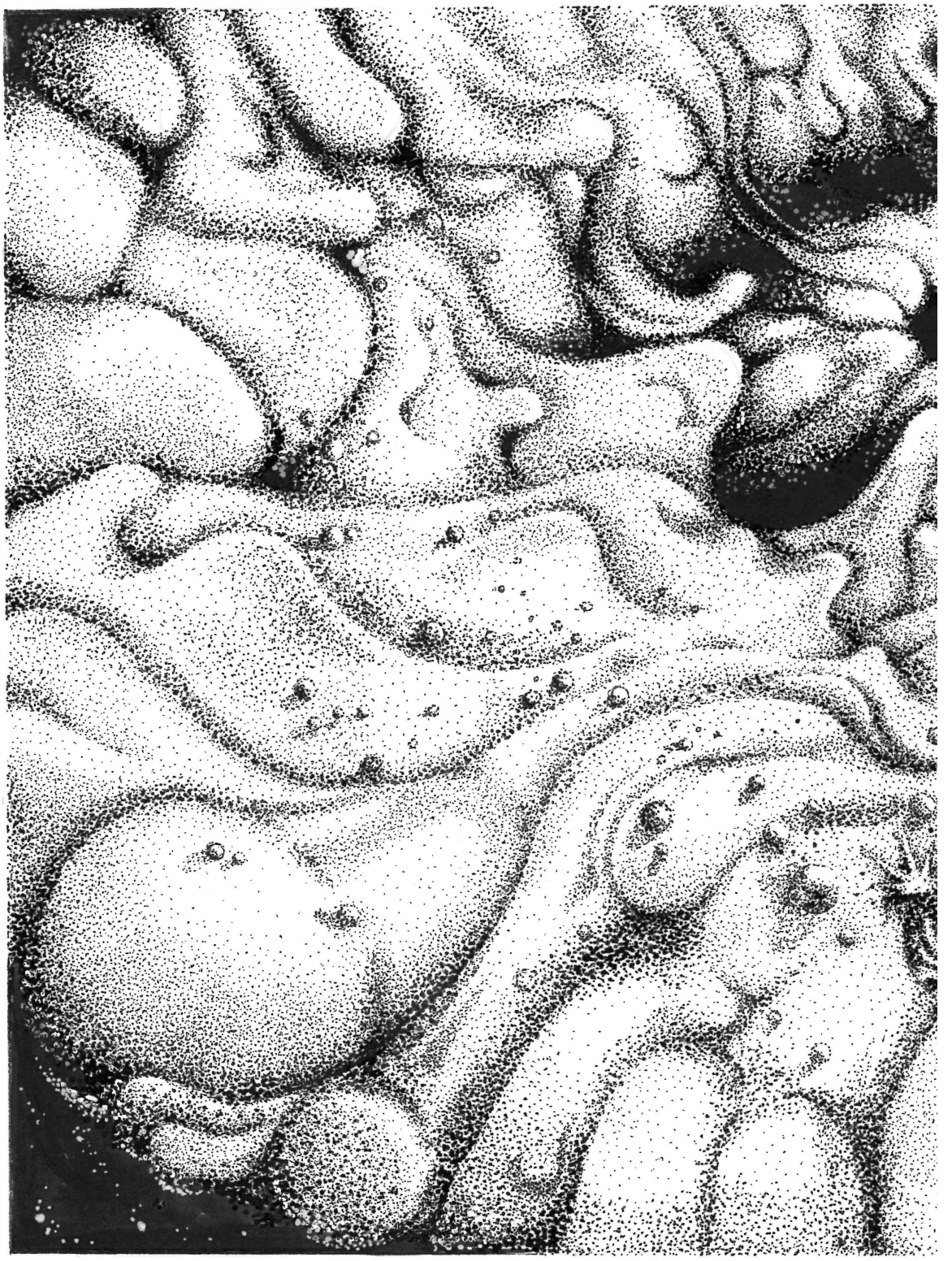
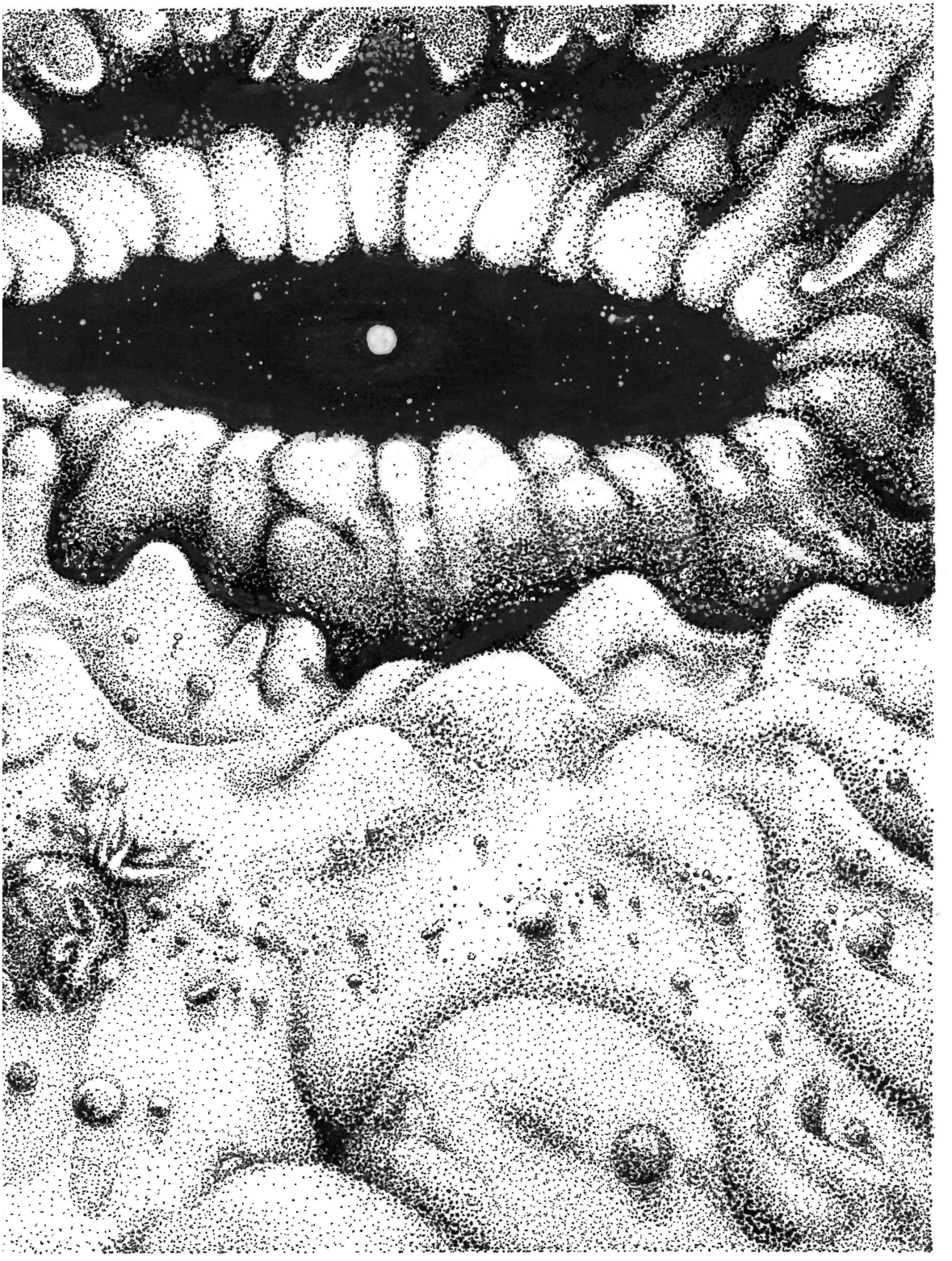


Figure 2.E.6: contd.





3

Dust masses of young disks: constraining the initial solid reservoir for planet formation

Tychoniec Ł., Manara C. F., Rosotti G. P., van Dishoeck E. F., Cridland A. J., Hsieh T., Murillo N. M., Segura-Cox D., van Terwisga S. E., Tobin J. J.,
Published in Astronomy & Astrophysics, 2020.

Abstract

Recent years have seen building evidence that planet formation starts early, in the first ~ 0.5 Myr. Studying the dust masses available in young disks enables us to understand the origin of planetary systems given that mature disks are lacking the solid material necessary to reproduce the observed exoplanetary systems, especially the massive ones.
We aim to determine if disks in the embedded stage of star formation contain enough dust to explain the solid content of the most massive exoplanets.
We use Atacama Large Millimeter/submillimeter Array (ALMA) Band 6 (1.1 – 1.3 mm) continuum observations of embedded disks in the Perseus star-forming region together with Very Large Array (VLA) Ka-band (9 mm) data to provide a robust estimate of dust disk masses from the flux densities measured in the image plane. We find a strong linear correlation between the ALMA and VLA fluxes, demonstrating that emission at both wavelengths is dominated by dust emission. For a subsample of optically thin sources, we find a median spectral index of 2.5 from which we derive the dust opacity index $\beta = 0.5$, suggesting significant dust growth. Comparison with ALMA surveys of Orion shows that the Class I dust disk mass distribution between the two regions is similar, but that the Class 0 disks are more massive in Perseus than those in Orion. Using the DIANA opacity model including large grains, with a dust opacity value of $\kappa_{9\ \mathrm{mm}} = 0.28\ \mathrm{cm^2\ g^{-1}}$, the median dust masses of the embedded disks in Perseus are 158 $M_\oplus$ for Class 0 and 52 $M_\oplus$ for Class I from the VLA fluxes. The lower limits on the median masses from ALMA fluxes are 47 $M_\oplus$ and 12 $M_\oplus$ for Class 0 and Class I, respectively, obtained using the maximum dust opacity value $\kappa_{1.3\mathrm{mm}} = 2.3\ \mathrm{cm^2\ g^{-1}}$. The dust masses of young Class 0 and I disks are larger by at least a factor of ten and three, respectively, compared with dust masses inferred for Class II disks in Lupus and other regions. The dust masses of Class 0 and I disks in Perseus derived from the VLA data are high enough to produce the observed exoplanet systems with efficiencies acceptable by planet formation models: the solid content in observed giant exoplanets can be explained if planet formation starts in Class 0 phase with an efficiency of ~ 15%. A higher efficiency of ~ 30% is necessary if the planet formation is set to start in Class I disks.

3.1 Introduction

The formation of planets is inherently entangled with the formation and evolution of their natal protoplanetary disks. The physical conditions and chemical composition at the onset of planet formation determine the properties of the resulting planetary systems (e.g., Armitage 2011; Öberg et al. 2011; Morbidelli & Raymond 2016). The key question is then: at what stage of disk evolution do planets start to form?

The protoplanetary disks around Class II pre-main sequence stars were considered to be the starting point of the planet formation process. However, submillimeter surveys of those disks reveal that the mass reservoir available in Class II disks is much lower than the masses needed to explain the formation of the observed exoplanetary systems (Andrews & Williams 2007b; Greaves & Rice 2010; Williams 2012; Najita & Kenyon 2014; Manara et al. 2018). Structures observed in the disks (e.g., van der Marel et al. 2013; Andrews et al. 2018; Long et al. 2019) are also evidence that planet formation is already underway in the Class II phase. One of the possible solutions to this conundrum is to move the onset of planet formation to the younger disks surrounding Class 0/I protostars (< 0.5 Myr; Dunham et al. 2014b), where more material is available (Andrews & Williams 2007a; Greaves & Rice 2011; Ansdell et al. 2017).

There is other evidence for early planet formation. The distribution of different types of meteorites in our solar system can be explained by the formation of Jupiter's core in the first million years of the solar system (Kruijer et al. 2014). There is also evidence for dust growth in the earliest stages of disk formation (e.g., Jørgensen et al. 2007; Kwon et al. 2009; Miotello et al. 2014; Harsono et al. 2018; Hsieh et al. 2019a). Another indication is provided by young sources with structures suggestive of ongoing planet formation (e.g., ALMA Partnership et al. 2015; Sheehan & Eisner 2018). These all suggest that planet formation starts early in disks surrounding much younger Class 0 and Class I protostars rather than in Class II disks.

This begs the question: what is the amount of material available for planet formation in Class 0/I disks? Greaves & Rice (2011), in a study of a small sample of Class 0 disks known at the time, found that 20 - 2000 $M_\oplus$ dust mass is available in Class 0 disks around low-mass stars; they concluded that this is sufficient to form the most massive exoplanet systems found to date. An analysis of a sample of Class I disks in Taurus (Andrews et al. 2013) combined with information about the occurrence of exoplanets led Najita & Kenyon (2014) to conclude that Class I disks can explain the population of exoplanetary systems, contrary to Class II disks in the same region. A study of a larger sample of young disks extending to Class 0 protostars is needed to put constraints on planet formation timescales and efficiency.

In the first complete survey of Class 0/I protostars in a single cloud, Perseus, Tychoniec et al. (2018b) used Very Large Array (VLA) 9 mm observations at 75 au resolution to show that there is a declining trend in the dust masses from Class 0 to Class I disks. The median masses for the Class 0 and Class I phase (~250 and ~100 $M_\oplus$, respectively) are explained by a significant fraction of the dust being converted into larger bodies already in the Class 0 phase. Moreover, they compared the results for Class 0/I disks in Perseus with Atacama Large Millimeter/submillimeter Array (ALMA) observations of several Class II regions which have mean dust masses in the range 5-15 $M_\oplus$ (Ansdell et al. 2017). This suggests that dust masses in the Class 0/I disks are an order of magnitude higher that those for Class II disks. Note, however, that the adopted dust mass absorption coefficient (κ_ν - dust opacity) varies in these studies.

ALMA observations by Tobin et al. (2020) in the Orion Molecular Cloud, based on the largest sample of protostars observed in a single region at sub-millimeter wavelengths (379

detections), found much lower mean dust masses for Class 0 and I disks than those in Perseus, 26 and 15 $M_\oplus$, respectively. Very low Class I mean dust disk mass (4 $M_\oplus$) were also reported in the Ophiuchus star-forming region (Williams et al. 2019). Also in this case, different opacities assumed in those studies could contribute to the difference between the median masses measured.

Comparison of the VLA observations for Perseus with other embedded disks surveys using ALMA is difficult because of the different wavelength range of observations. The VLA obsercvations at 9 mm can have a significant free-free emission contribution, which could result in overestimating the actual flux coming from the dust (e.g., Choi 2009); although Tychoniec et al. (2018b) applied the correction for a free-free contribution using information from the C-band (4.1 and 6.4 cm) flux densities. On the other hand, the dust emission at those long wavelengths is less likely to be optically thick than that in the ALMA wavelength range (Dunham et al. 2014c). The way forward is to use observations of young disks with VLA and ALMA in the same star-forming region, offering a direct comparison of dust disk masses and determining if the difference in observing wavelengths can be the reason for the described differences. Therefore, in this work we present ALMA observations of protostars in Perseus and compare them with our previous VLA data.

This work aims to compare the solid masses of the embedded (Class 0/I) disks with the masses of the exoplanetary systems observed to date to ultimately infer an efficiency of the planet formation. In Section 2, we describe the ALMA observations and data analysis. In Section 3, the integrated fluxes at 1 mm and 9 mm are compared, and dust masses are calculated based on those fluxes and then compared with other young and more mature dust disks observed with ALMA. In Section 4, we put the inferred masses in the context of known exoplanetary systems masses and planet formation models.

3.2 Observations and analysis

3.2.1 Observations

In this paper we analyze ALMA Band 6 continuum observations of 44 protostars in the Perseus molecular cloud. The data were obtained in September 2018 with a Cycle 5 program (2017.1.01693.S, PI: T. Hsieh). The absolute flux and bandpass calibrator was J0237+2848, and the phase calibrator was J0336+3218. Continuum images and spectral lines observed in this project are presented in Hsieh et al. (2019b). The continuum bandwidth was ~ 1.85 GHz centered at 267.99 GHz (1.1 mm). The absolute flux calibration uncertainty is on the order of $\sim 30\%$. The synthesized beam of the continuum observations in natural weighting is $0''.45 \times 0''.30$. The average spatial resolution of observations ($0''.38$) corresponds to 110 au (diameter) at the distance to Perseus (293±22 pc; Ortiz-León et al. 2018). The typical rms value of the continuum images is ~ 0.1 mJy beam^{-1}.

Additional data on 8 disks were obtained in a Cycle 5 program (2017.1.01078.S, PI: D. Segura-Cox). The continuum bandwidth was centered at 233.51 GHz (1.3 mm) with a total bandwidth of 2 GHz. The average synthesized beam of $0''.41 \times 0''.28$ provides spatial resolution corresponding to 100 au at the distance of Perseus. The rms value of the images is $\sim$ 0.05 mJy beam^{-1}. The absolute flux and bandpass calibrator was J0510+1800 and the phase calibrator was J0336+3218. The accuracy of the flux calibration is on the order of $\sim 10\%$. The measurement sets were self-calibrated and cleaned with the robust parameter 0.5.

We also use the flux densities of 25 disks published in Tobin et al. (2018) which were observed at 1.3 mm with a resolution of $0''.27 \times 0''.16$ and sensitivity of 0.14 mJy beam^{-1}. The

flux and disk masses in Tobin et al. (2018) are measured using a Gaussian fit in the image domain to the compact component in the system without subtraction of an envelope component. Altogether we compile a sample of 77 Class 0 and Class I disks in Perseus observed with ALMA. In the following, when referring to ALMA data, we use 1 mm observations for short, but anywhere the wavelength is used to calculate properties of the source (e.g., disk mass) the exact value of the observed wavelength is used.

The VLA observations come from the VLA Nascent Disks and Multiplicity Survey (VANDAM) (Tobin et al. 2015a, 2016; Tychoniec et al. 2018c). The sample for the VANDAM survey was prepared based on unbiased infrared and submillimeter surveys of protostars in Perseus (Enoch et al. 2009; Evans et al. 2009; Sadavoy et al. 2014). Fluxes at 9.1 mm (Ka-band), obtained with 0.25″resolution from 100 Class 0 and I disks (including upper limits) were reported in Tobin et al. (2016). Tychoniec et al. (2018c) applied a correction for free-free emission, based on C-band (4.1 and 6.4 cm) observations. In that work, all sources with a Ka-band spectral index suggestive of emission not coming from dust ($\alpha \ll 2$) were marked as upper limits, and we use the same criteria here. We use the 9 mm fluxes corrected for the free-free emission for further analysis.

3.2.2 Gaussian fitting

Pre-ALMA surveys of embedded sources have found that disk masses are typically only a small fraction of the total envelope mass in the Class 0 phase (1-10%), becoming more prominent as the system evolves in the Class I phase (up to 60%, e.g., Jørgensen et al. 2009). In the much smaller ALMA beam, the envelope contamination is reduced (e.g., Crapsi et al. 2008), but still needs to be corrected for (Tobin et al. 2020). Here both components, disk and envelope, are represented by Gaussians.

The CASA (McMullin et al. 2007) v. 5.4.0 *imfit* task was used to fit Gaussian profiles to the sources. After providing the initial guess, all parameters: position, flux, and shape of the Gaussian, were set free during the fit. All sources were inspected by eye to assess the number of necessary Gaussian components. In case of a single source without a noticeable contribution from the envelope, a single compact Gaussian with the size of the synthesized beam was provided as input to the *imfit* task (Fig. 3.7a). In cases where a contribution of the envelope by eye was significant, an additional broad Gaussian with a size of 3″was added to the initial guess parameters of the fitting (Fig. 3.7b). In two cases (Per-emb-4 and SVS13A2) it was necessary to fix the size of the Gaussian to the synthesized beam size for the fit to converge (Fig. 3.7c). Two binary systems with separations below our resolution (Per-emb-2 and Per-emb-5) are treated as single systems with a common disk.

The flux density of the compact Gaussian is assumed to be that of the embedded disk. It is called 'disk' here, even though no evidence for a Keplerian rotation pattern yet exists. We report the measured fluxes of the embedded disks in Table 3.1.

The broad component is used only to force the *imfit* task to not fit extended emission without constraining the compact Gaussian size which would in turn overestimate the flux of the compact emission. It was necessary to add an envelope component to 31 sources out of 51 targets, specifically 20 Class 0 and 11 Class I sources. We assessed remaining 6 Class 0 sources and 20 Class I sources as not having significant contribution from their envelope.

The envelope flux remaining after subtracting the model of the disk component is measured as the flux in the area of the size of the FWHM of the disk in the residual image. This ratio of the envelope residual flux to the disk flux ranges from less than 1% to usually below 30%. In one case the source is dominated by the envelope emission (Per-emb-51; Fig. 3.7d),

but after the envelope component subtraction the residual flux is only ∼ 6% of that of the disk (Table 3.1). The two sources with high values of the ratio - Per-emb-22-B and Per-emb-27B are heavily affected by the nearby binary component so the value is not reliable.

We stress that the remaining envelope fraction is not incorporated in the flux density of the disk component, and it is presented to show that fitting the envelope component is needed to exclude the contamination of the envelope from the disk. Fig. 3.7 shows that residuals are significantly reduced after removing the envelope contribution, and that without fitting the extended component some of this emission could contaminate the flux coming from the disk.

3.3 Dust disk masses

3.3.1 Comparison of the integrated fluxes between 1 and 9 mm

Measurements of the continuum emission at different wavelengths allow us to analyze the properties of the emitting material. First, it is important to verify that the fluxes at both 1 mm (ALMA) and 9 mm (VLA) have their origin in the same physical process. This is to confirm that the correction for contamination of the VLA observations by the free-free emission is accurate. In order to do so, we investigate the correlation between the flux densities at both wavelengths and the spectral index of the emission for each source.

The flux densities from the ALMA 1.1-1.3 mm observations are presented in Table 3.1. In Fig. 3.1 we compare the measurements with the VLA 9.1 mm observations (Tobin et al. 2016; Tychoniec et al. 2018b). There is a clear correlation with a close-to-linear slope (1.15 ± 0.10) obtained with the *lmfit* Python function. The fitting was performed excluding upper limits. The value of the slope indicates that all sources have a similar spectral index between ALMA and VLA wavelengths. Thus, the mechanism responsible for emission at both wavelength ranges is the same. Since it is generally accepted that the ALMA 1 mm emission is dominated by dust thermal emission, we can conclude that this is also the case for the 9 mm VLA observations. The sources with resolved emission at 9 mm can be modelled successfully with the disk (Segura-Cox et al. 2016).

The nature of this emission can be also investigated with the value of the spectral index between the two wavelengths. In the Rayleigh-Jeans approximation, the flux density F_ν changes with frequency $F_\nu \sim \nu^\alpha$, where α is the spectral index. The dust emissivity index β defines the dependence of the dust opacity on the frequency $\kappa_\nu \sim \nu^\beta$. From the observed spectral index, the emissivity index can be derived accordingly:

$$\beta = (\alpha - 2)(1 + \Delta) \tag{3.1}$$

where Δ is the ratio of optically thick to optically thin emission (Beckwith et al. 1990; Lommen et al. 2007). It is often assumed that emission at millimeter wavelengths is optically thin, in which case $\Delta = 0$ and then $\beta = \alpha - 2$.

The spectral index between the ALMA and VLA fluxes is calculated as

$$\alpha_{\mathrm{VLA/ALMA}} = \frac{\ln(F_{1\ \mathrm{mm}}/F_{9\ \mathrm{mm}})}{\ln(9\ \mathrm{mm}/1\ \mathrm{mm})}. \tag{3.2}$$

The mean spectral index obtained between ALMA and VLA is $\alpha \sim 2.4$, with a standard deviation for the sample of 0.5. This indicates that $\beta = 0.4 \pm 0.5$, which is lower than the typical ISM value, i.e. ∼1.8 for small grains (Draine 2006). The index is also lower than 1, the value typically used for protoplanetary disks, specifically in our previous study of embedded

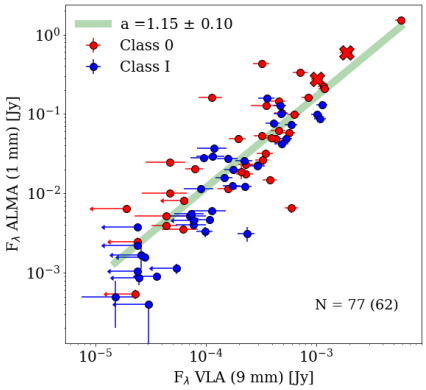


Figure 3.1: ALMA (1.1 and 1.3 mm) integrated fluxes plotted against VLA integrated fluxes at 9.1 mm. A total of 77 sources are plotted but only the 62 sources that are not upper limits are included in fitting the linear function. The best fit to the data is shown with the green line and has a slope of 1.15 ± 0.1. The Class 0 sources are shown in red and Class I sources in blue. Crosses mark sources that are unresolved binaries.

disks in Perseus (Tychoniec et al. 2018b). If emission is optically thin, the low value of β can point to dust growth as is commonly seen in Class II disks (e.g., Natta & Testi 2004; Ricci et al. 2010; Testi et al. 2014). There are other effects that could alter the value of the dust spectral index such as dust porosity (Kataoka et al. 2014), and grain composition (Demyk et al. 2017a,b) but to explain $\beta < 1$ some grain growth is required (Ysard et al. 2019).

While the VLA 9 mm flux is unlikely to be optically thick, the ALMA 1 mm emission from young disks can be opaque. Optically thick emission at 1 mm would result in a lower spectral index value. If the indices obtained between 1 and 9 mm $\alpha_{\rm VLA/ALMA}$ are consistent with the Ka-band intraband indices $\alpha_{\rm VLA}$, it can be assumed that the emission at 1 mm is optically thin so that it is possible to measure the spectral index in a robust way. We calculate the VLA intraband spectral index, determined between the two sidebands of the Ka-band observations as follows:

$$\alpha_{\rm VLA} = \frac{\ln(F_{8\ \rm mm}/F_{10\ \rm mm})}{\ln(10\ \rm mm/8\ mm)}. \tag{3.3}$$

Fig. 3.9 shows the range of the $\alpha_{\rm VLA/ALMA}$ and $\alpha_{\rm VLA}$ values measured. For 23 sources out of 77 we found the $\alpha_{\rm VLA/ALMA}$ - $\alpha_{\rm VLA} \leq 0.4$, and therefore in reasonable agreement (see Fig. 3.8). For those sources, the emission at both 1 mm and 9 mm wavelengths is most likely optically thin, so the spectral index should provide information about the grain size. The mean spectral index of those sources is 2.5, which means that $\beta \sim 0.5$. This value confirms that significant dust growth is occurring in the observed disks. The spectral index calculated for the selected optically thin sample (0.5) is similar to that calculated for the full sample (0.4). We therefore proceed with assuming a value of $\beta = 0.5$ for the further analysis, as an average value, which does not exclude that the 1 mm emission is optically thick. It is also likely that the spectral index varies with the radius of the disk due to optically thick emission close to the protostar and due to the grain growth further out (Pinilla et al. 2012; van Terwisga et al. 2018), as well as a grain size that depends on radius (Tazzari et al. 2016). Our observed emission is largely unresolved and the measured spectral index is an average of those effects.

The emission at shorter wavelengths is more likely to be optically thick. With at least

marginally resolved disks, we can obtain an estimate of the dust optical depth, because the extent of the emission allows to approximate the disk radius. We use the major axis deconvolved from the beam as the diameter of the disk. Then, we obtain optical depth as $\tau \sim \kappa_\nu \Sigma$, where κ_ν is dust opacity used to calculate the mass and Σ is averaged surface density. Fig. 3.10 presents a distribution of calculated optical depths. For all the disks with available major axis value, we get $\tau < 0.4$ and in vast majortiy of cases < 0.1.

Summarizing, we have identified dust thermal emission as the dominating physical process responsible for the emission at both 1 mm and 9 mm. What is more, from the sample of sources for which the emission is most likely optically thin, we calculate a spectral index value of 2.5, suggestive of significant grain growth already at these young stages.

3.3.2 Disk mass measurements

The continuum flux at millimeter wavelengths is commonly used as a proxy of the dust mass of the emitting region. Here we utilize the collected fluxes for the continuum flux in Perseus with VLA and ALMA to calculate the masses of the embedded disks. The key assumptions used in the calculation, temperature and dust opacity (dust mass absorption coefficient), are discussed. Then we proceed to compare the results with other disk surveys both at Class 0/I and at Class II phases.

From the integrated disk fluxes, the dust mass of the disk is calculated following the equation from Hildebrand (1983):

$$M = \frac{D^2 F_\nu}{\kappa_\nu B_\nu(T_{\rm dust})} \tag{3.4}$$

where D is the distance to the source, B_ν is the Planck function for a temperature $T_{\rm dust}$ and κ_ν is the dust opacity with the assumption of optically thin emission. Temperature of the dust is set to 30 K, typical for dust in dense protostellar envelopes (Whitney et al. 2003), and disks are assumed to be isothermal. The same temperature is set for Class 0 and Class I disks. If the decrease of the temperature of dust from Class 0 to Class I is significant, the mass difference diminishes (e.g., Andersen et al. 2019). We consider two cases for the values of κ_ν at 1.3 and 9 mm.

First, since our aim is to compare the results with the Class II disk masses in the literature, most notably the Lupus star-forming region, we use $\kappa_{1.3\ \rm mm} = 2.3\ \rm cm^2\ g^{-1}$ as used in the determination of masses in Ansdell et al. (2016). Fig. 3.2 (top panel) shows the cumulative distribution function (CDF) for Class II disks in Lupus and Class 0 and I disks in Perseus, all observed with ALMA. The CDF plot is prepared using the survival analysis with the *lifelines* package for Python (Davidson-Pilon 2017). The CDF plot describes the probability of finding the element of the sample above a certain value. Uncertainty of the cumulative distribution is inversely proportional to the size of the sample and 1σ of the confidence interval is indicated as a vertical spread on the CDF plot. It takes into account the upper limits of the measurement, and the median is only reliable if the sample is complete. While the VLA observations sample is complete, the ALMA sample of disks is not, as we assemble $\sim$ 80% of the total sample. Therefore the VLA median values and distributions are more reliable.

The median dust mass for young disks in Perseus measured with ALMA at 1 mm with the adopted opacity of $\kappa_{1.3\ \rm mm} = 2.3\ \rm cm^2\ g^{-1}$ is 47 $M_\oplus$ and 12 $M_\oplus$ for Class 0 and Class I disks, respectively (Fig. 3.2, top panel). The median is taken from the value corresponding to the 0.5 probability on the CDF plot. The opacity value used here is likely close to the maximum

value of the opacity at 1.3 mm (Draine 2006). In an analysis of dust opacity value at 1.3 mm, Panić et al. (2008) find a range between 0.1 and 2 cm^2 g^{-1}. Therefore, the dust masses obtained with $\kappa_{1.3\ mm}$ = 2.3 cm^2 g^{-1} from Ansdell et al. (2016) should be considered as a lower limit to the disk masses in Perseus. Only if the grain composition is significantly different from the typical assumption, in particular if dust has a significant fraction of amorphous carbon, will the actual masses of the dust be lower by a factor of a few (Birnstiel et al. 2018), even when compared with the $\kappa_{1.3\ mm}$ = 2.3 cm^2 g^{-1} that we assume to provide a lower limit on the dust disk mass.

Regardless of the uncertainties, there is a clear evolutionary trend from Class 0 to Class II with disk masses decreasing with evolutionary phase. The median dust masses for disks in Perseus measured with ALMA of 47 $M_\oplus$ and 12 $M_\oplus$ for Class 0 and Class I disks, respectively, are significantly higher than for Class II disks in Lupus which have a median mass of 3 $M_\oplus$. We note that this value differs from the 15 $M_\oplus$ value reported in Ansdell et al. (2016), since in that work the standard mean is calculated, contrary to the median taken from the CDF plot. Also, distances to Lupus disks have been updated with *Gaia* DR2 distances (Gaia Collaboration et al. 2018). It should be noted that the dust temperature used in Ansdell et al. (2016) was 20 K, while we use 30 K, but the opacity value adopted to calculate the masses is the same. A lower temperature results in an increase of the total mass, based on Equation 4. Therefore if the temperature would be set to 20 K for the Perseus disks, the difference between Class 0/I and Class II disks would be even higher. Class 0/I disks are, however, expected to be warmer than Class II disks (Harsono et al. 2015a; van 't Hoff et al. 2020).

As an alternative method, considering that ALMA fluxes can be optically thick, we use the VLA flux densities to estimate the disk masses. Here we adopt κ_{9mm} = 0.28 cm^2 g^{-1} as provided by dust models of the DIANA project (Woitke et al. 2016) that consider large grains up to 1 cm; we recall that significant grain growth is indicated in our data by the empirically measured value of β = 0.5. In Tychoniec et al. (2018b), a value of κ_{9mm} = 0.13 cm^2 g^{-1} was used, scaled from $\kappa_{1.3mm}$ = 0.9 cm^2 g^{-1} of Ossenkopf & Henning (1994) using β = 1. If β = 0.5 is instead used to scale the opacity $\kappa_{1.3mm}$ to 9 mm, the value is consistent with that of DIANA.

The median masses measured from the 9 mm observations are 158 $M_\oplus$ for Class 0 and 52 $M_\oplus$ for Class I (Fig. 3.2, bottom panel). Those masses are lower than the estimate provided in Tychoniec et al. (2018b) by a factor of two, which stems from the different opacity values used. Additionally the values quoted in Tychoniec et al. (2018b) are regular medians, taken from the sample of detected disks and the distance to the Perseus star-forming region has been revised from 235 to 293 pc (Ortiz-León et al. 2018) which increases the estimate of the mass.

An important difference between the ALMA and VLA samples is that the VLA sample is complete, as it targeted all known protostars in Perseus (Tobin et al. 2016). Additionally, it is likely that the VLA flux densities are coming from optically thin emission, whereas the ALMA flux densities can become optically thick in the inner regions. We also use a refined model of the dust opacity of the DIANA project (Woitke et al. 2016) including large grains. Therefore, the median masses reported with VLA (158 $M_\oplus$ and 52 $M_\oplus$ for Class 0 and Class I, respectively) can be considered more robust.

3.3.3 ALMA Class 0/I disk masses for different star-forming regions

Recent ALMA observations of Orion and Ophiuchus reveal masses of embedded Class 0/I dust disks that are somewhat lower than those obtained for Perseus with the VLA (Williams et al. 2019; Tobin et al. 2020). Here we collect available ALMA observations for Perseus that

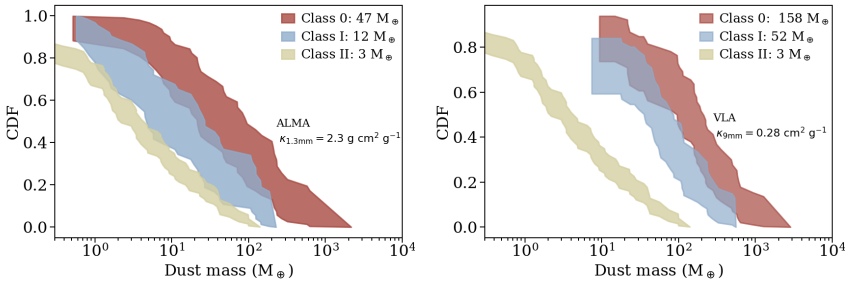


Figure 3.2: Cumulative distribution plots of the dust disk masses. *Top:* Masses of the Perseus Class 0 and I disks measured with ALMA at 1 mm compared with the Lupus Class II disks measured with ALMA (Ansdell et al. 2016). The opacity value of $\kappa_{1.3\mathrm{mm}} = 2.3\ \mathrm{cm}^2\ \mathrm{g}^{-1}$ is used to calculate the masses. The ALMA sample consist of 77 sources (38 Class 0 and 39 Class I) and the Lupus sample consist of 69 sources. *Bottom:* Masses of the Perseus Class 0 and I disks measured with VLA at 9 mm (red and blue, respectively), compared with the Lupus Class II disks measured with ALMA (Ansdell et al. 2016). The opacity value of $\kappa_{9\mathrm{mm}} = 0.28\ \mathrm{cm}^2\ \mathrm{g}^{-1}$ is used to calculate the VLA masses. The VLA sample consist of 100 sources (49 Class 0 and 51 Class I). Medians are indicated in the labels.

use the same techniques as other embedded surveys. Such analysis can reveal the inherent differences between the different protostellar regions.

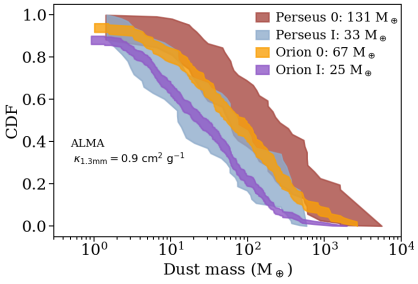


Figure 3.3: Cumulative distribution plots for Perseus disk masses calculated from ALMA flux densities, and Orion disk masses from Tobin et al. (2020), both calculated with the same opacity assumptions of $\kappa_{1.3\mathrm{mm}} = 0.9\ \mathrm{cm}^2\ \mathrm{g}^{-1}$. The Perseus sample consist of 77 sources (38 Class 0 and 39 Class I), the Orion sample consist of 415 sources (133 Class 0 and 282). Medians are indicated in the labels.

In Fig. 3.3 we show the cumulative distribution of disks observed with ALMA for Orion (Tobin et al. 2020) and for Perseus. The Orion disks were targeted within the VANDAM survey of Orion protostars where 328 protostars were observed with ALMA Band 7 (0.87 mm) at 0.″1 (40 au) resolution. The sample in Tobin et al. (2020) is divided into Class 0, Class I and Flat spectrum sources. We incorporate the Flat Spectrum sources into Class I in the comparison. An opacity value of $\kappa_{0.87\mathrm{mm}} = 1.84\ \mathrm{cm}^2\ \mathrm{g}^{-1}$ (Ossenkopf & Henning 1994) has been assumed to calculate the masses in the Orion survey. We use the same reference for opacity at 1.3 mm wavelengths, $\kappa_{1.3\mathrm{mm}} = 0.9\ \mathrm{cm}^2\ \mathrm{g}^{-1}$, to calculate the masses from ALMA flux densities in Perseus to compare with the Orion sample. The median for Class 0 dust disk masses is still significantly lower in Orion, 67 $M_\oplus$ versus 131 $M_\oplus$ in Perseus, but is remarkably similar

for Class I: 25 $M_\oplus$ versus 33 $M_\oplus$. Thus, using ALMA-measured flux densities and the same opacity assumption as Tobin et al. (2020), we find that there are some inherent differences between the population of Class 0 disks in Perseus and Orion. Note that values calculated here are different than reported in Tobin et al. (2020) because the temperature of the dust was scaled with the luminosity in that work, while we use a constant T = 30 K for a consistent comparison with our sample.

Differences in sound speed or initial core rotation can result in different disk masses (e.g., Terebey et al. 1984; Visser et al. 2009). The initial composition of grains could also affect the dust spectral index. The Orion Molecular Complex seems to show a higher fraction of the amorphous pyroxene than the typical ISM (Poteet 2012). It is likely that such factors are resulting in different observed masses between Orion and Perseus. Tobin et al. (2020) noted that the 9 mm flux density distribution is similar between Perseus and Orion.

The low Class I median masses reported in Ophiuchus (Williams et al. 2019, median mass 3.8 $M_\oplus$) are puzzling as it suggests that the problem of missing dust mass for planet formation extends from Class II to Class I disks. In our data, the median Class I disk mass median is 11 $M_\oplus$ for the same opacity assumption as in Williams et al. (2019), a factor of 3 higher. The Ophiuchus sample does not include the entire population of Class I disks in Ophiuchus and may be contaminated with more evolved sources due to the high foreground extinction (van Kempen et al. 2009b; McClure et al. 2010). For this reason, we will not include it in the further analysis. Despite those caveats it is possible that the population of young disks in Ophiuchus is less massive than in Perseus and Orion.

3.4 Exoplanetary systems and young disks - a comparison of their solid content

Surveys of protoplanetary (Class II) disks around pre-main sequence stars reveal that dust masses of most disks are not sufficient to explain the inferred solid masses of exoplanetary systems (Williams 2012; Najita & Kenyon 2014; Ansdell et al. 2017; Manara et al. 2018). On the other hand, the results from the younger (Class 0/I) star-forming regions show that the dust reservoir available in younger disks is much higher than in the Class II phase (Tychoniec et al. 2018b; Tobin et al. 2020). Here, we aim to determine if the amount of dust available at the onset of planet formation (Class 0/I disks) agrees with the masses of the exoplanet systems observed for reasonable efficiencies of the planet formation process. Simply stated: are the masses of the embedded disks high enough to produce the observed population of the most massive exoplanet systems, or does the problem of the missing mass extend even to the youngest disks?

In this analysis we focus on the Perseus sample, the only complete sample that is available for Class 0/I protostars in a low-mass star-forming region. As such it guarantees that there is no bias towards the more massive disks. Perseus, however, may not be a representative star-forming region for the environment of our own Solar System (Adams 2010). Also, because it is difficult to estimate the stellar mass of the Class 0/I sources, making a comparison of planets and disks around similar stellar types is challenging. Therefore, we include as well a comparison with the Orion disks. The Orion star-forming region contains more luminous protostars than Perseus; thus it might be more representative of the initial mass function. The other limitation is that we analyze mostly unresolved disks, hence the radial dust distribution in the disk is unknown.

3.4.1 Exoplanet sample selection

The exoplanet systems masses were obtained from the exoplanet.eu database (Schneider et al. 2011). From the catalog (updated 28.04.2020) we obtained 2074 exoplanets with provided value for the total mass, either a true mass, or a lower limit to the mass ($M \times sin(i)$). We do not filter for detection method, mass measurement method, or stellar type of the host star. The mass estimation method for the majority of planets with information on a mass detection method provided is a radial velocity method, which introduces a strong bias toward more massive exoplanets. Indeed 1373 of the exoplanets in our analysis have a total (gas+dust) masses above 0.3 Jupiter masses (M_J). There are 1062 systems with more than one planet where at least one is > 0.3 M_J, and 173 systems with a single > 0.3 M_J planet.

Gaseous planets are expected to be less frequent than the rocky low-mass planets (e.g., Mayor et al. 2011). It is estimated that only 17-19% of planetary systems would contain a planet more massive than 0.3 M_J within 20 au orbit (Cumming et al. 2008). Therefore, we use only systems containing at least one planet with a total mass of 0.3 M_J and normalize it to 18% of the total population. This is done by setting the 18% value of the CDF plot at the estimated solid fraction of the gaseous planet of 0.3 M_J, which is 27.8 $M_\oplus$. We assume that 82% of the systems have masses below that value. By doing so, we focus on the sample of gas giants and their solid material content.

In this work, we focus on a reliably estimated solid mass and its cumulative distribution for the most massive exoplanetary systems. By comparing their CDF to the total dust mass distribution from surveys of young disks we can answer the pivotal question: do the Class 0/I disks contain enough solids to explain the masses of those systems.

Our study focuses on the dust masses of disks. In order to compare the solid content between the disks and exoplanets, we calculate the solid content in exoplanets using the formula from Thorngren et al. (2016) for estimating the solid content in gaseous planets. This study is based on structural and thermal planetary evolution models relating the metallicity of a gas giant with the total mass of the planet. Importantly, the metals in those gas giants are assumed to be located not only in the core but also in the envelope of a planet. We combined the masses of planets orbiting the same star to retrieve the total dust mass of the system, resulting in 1235 systems in the analysis.

3.4.2 Comparison of young disk dust masses with the solids in exoplanetary systems

In Fig. 3.4 (top panel) we compare the sample of exoplanetary systems with dust masses of young Class 0 and Class I disks in Perseus with our best estimate of embedded disk dust masses in Perseus, i.e., with the complete VLA survey, using the DIANA opacities. In Fig. 3.4 (bottom panel) we show efficiency of planet formation for a given bin of the disk and exoplanet distributions. The efficiency is calculated as a ratio of the total mass of the exoplanetary systems at the certain fraction of the cumulative distribution plot divided by the corresponding dust mass of the disk at the same value of the CDF plot. This calculation provides information on how much total dust disk mass will be converted to planets.

In order to reproduce the population of exoplanets with the top 18% most massive disks in Perseus, the efficiency of planet formation would have to be on the order of 15% for Class 0 and 34% for Class I (Fig. 3.4). The average efficiency is measured by taking the mass at 10% of the cumulative distribution plot (CDF plot is not well sampled for disk masses, and the 10% value is the closest to the mean of the sample with data available). The Class 0/I disk masses in Perseus calculated from the VLA data at 9 mm for the refined value of the dust

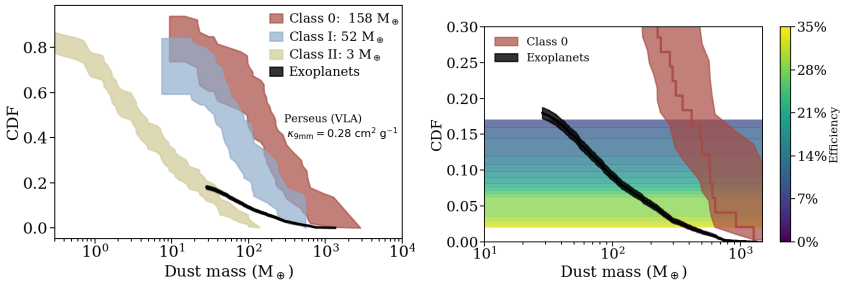


Figure 3.4: Cumulative distribution function of dust disk masses and solid content of exoplanets. *Top:* Cumulative distribution function of dust masses for Class 0 (red) and Class I (blue) disks in Perseus and Class II disks (yellow) in Lupus measured with ALMA (Ansdell et al. 2016). In black, the masses of the exoplanet systems are normalized to the fraction of the gaseous planets (Cumming et al. 2008). Perseus disk masses calculated with $\kappa_{9\mathrm{mm}} = 0.28$ cm^2 g^{-1} from the VLA fluxes. Medians are indicated in the labels. *Bottom:* Zoom-in to the ranges where exoplanets are present. The color scale shows the efficiency needed for the planet formation for a given bin of the distribution.

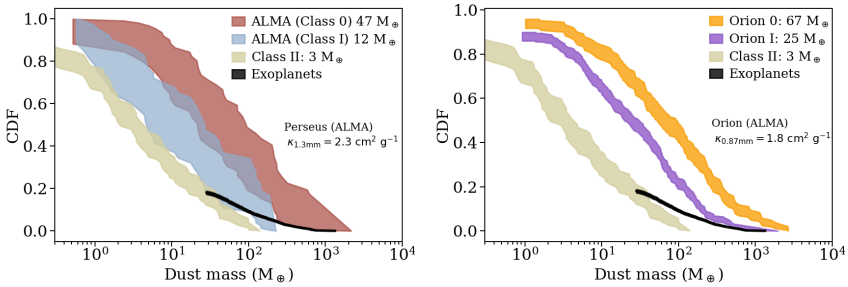


Figure 3.5: Cumulative distribution function of dust masses for Class 0 and Class I disks in Perseus and Orion and Class II disks in Lupus measured with ALMA *Top:* Perseus disk masses calculated with $\kappa_{1.3\mathrm{mm}} = 2.3$ cm^2 g^{-1} from the ALMA fluxes. *Bottom:* Orion disk masses calculated with the $\kappa_{0.89\mathrm{mm}} = 1.3$ cm^2 g^{-1} (Tobin et al. 2020). Medians are indicated in the labels.

opacity suggest that on average there is enough mass available at those early phases to form the giant planet systems that we observe.

In Fig. 3.4 (bottom panel), instead of the average value of the efficiency we attempt to measure the efficiency per each percentage level of the disk masses on the cumulative distribution plot . We note that this analysis has a higher uncertainty than the average value as the distribution of the exoplanets is uncertain. With known masses of a large number of giant planets and expected occurrences of such systems (Cumming et al. 2008) we notice that the most massive exoplanets require efficiencies $\sim 30\%$, stretching the requirements of some of the planet formation models (see Section 4.3). It is also possible that some of the most massive exoplanets or brown dwarfs present in the database do not follow the core accretion formation mechanisms, and excluding them would lower the requirement on efficiency.

If the underlying initial mass function of stars in Perseus is not representative of the stellar initial mass function, it could be that such exo-systems were produced from more

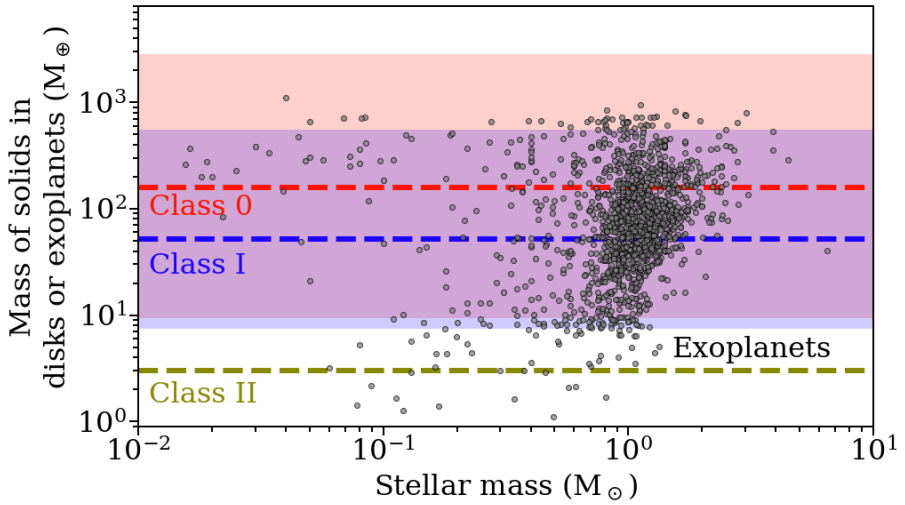


Figure 3.6: Plot showing the distribution of masses of exoplanetary systems obtained from the exoplanet.eu catalog (Schneider et al. 2011), for the planets around main-sequence stars with the measured masses. Shaded areas mark the range of our best estimation of the dust disk masses in Perseus: Class 0 (red) and Class I (blue) calculated from the VLA fluxes with the opacity value of $\kappa_{9\mathrm{mm}} = 0.28$ cm^2 g^{-1}. Medians of the distributions, 158 and 52 $M_\oplus$, for Class 0 and I, respectively, are indicated with the dashed lines. The median mass of the Class II disks in Lupus, 3 $M_\oplus$ (Ansdell et al. 2016) is showed in yellow. The masses of the solids in exoplanetary systems are plotted against the stellar mass of the host star. All planets with available information on the mass are included in this plot, without introducing the 0.3 M_J threshold.

massive disks than observed here. Another possibility is that young disks at the Class 0/I phase are still being replenished with material accreting from the envelope (Hsieh et al. 2019b), making the effective material available for planet formation higher. It is also possible that the most massive systems are indeed producing the planets most efficiently.

In Fig. 3.5 (top panel) the disk masses from the ALMA fluxes in Perseus using the opacity value from Ansdell et al. (2016) are presented. We remind that this is likely the maximum value of the dust opacity at those wavelengths (Panić et al. 2008) and therefore the masses are lower limits. In the bottom panel of Fig. 3.5, the Orion Class 0/I disk masses measured with ALMA 0.87 mm observations (Tobin et al. 2020) are used.

The comparison of the exoplanet sample with the disk masses for the maximum value of the opacity used with the ALMA data (i.e., lower limit to the disk mass, Fig. 3.5, top panel) shows that if those opacities were the correct ones, the efficiency of forming planets in the Class 0 phase would be on the order of 33%. The efficiency of the Class I phase would be on the order of 72%. It is in line with our expectations that for our most conservative estimates of disk mass, the efficiencies required for giant planet formation are high, whereas for our best estimate of the dust masses in the young disks, we achieve an average efficiency in agreement with models (see Section 4.3). It is also clear that use of dust opacities that result in an order of magnitude lower disk masses (Birnstiel et al. 2018) do not provide dust masses that would be compatible with such models. The Orion sample, which contains more luminous protostars and could be more representative of the IMF than Perseus, has comparable disk

dust masses in Class I and much lower disk masses in Class 0. The efficiencies required to produce the exoplanet population from the Orion disks dust content, as measured with ALMA, are comparable with those measured for Perseus with VLA observations (Fig. 3.5 bottom panel): 16% and 45% for Class 0 and Class I, respectively.

Fig. 3.6 presents a different visualization of the distribution of exoplanet systems dust masses compared to the range of disk masses observed in Class 0 and Class I disks in Perseus. The conclusions of our work show that for the complete sample of disks in Perseus and with a large sample of known exoplanets, there is enough solid material in Class 0 stage to explain the solid content in observed exoplanetary systems. This conclusion is consistent with Najita & Kenyon (2014) and Greaves & Rice (2011) but now with much more robust statistics.

In recent years several studies, specifically with the use of microlensing observations, estimate that nearly all stars can have at least 10 $M_{\oplus}$ planet (Cassan et al. 2012; Suzuki et al. 2016). Very few cases and irreproducibility of microlensing observations suggest caution with extrapolating the results to all systems. It should be kept in mind that large population of wide-orbit planets could pose a challenge to efficiency of planet formation even in Class 0/I stage (Najita & Kenyon 2014).

Actual timescales for the different phases of low-mass star formation are uncertain. Based on a statistical analysis of a population of protostars, it is estimated that the Class 0 evolutionary phase lasts for ~0.1 Myr since the beginning of the collapse, and the Class I phase ends when the protostar is ~ 0.5 Myr old (Dunham et al. 2014a). More recent estimates of the half-lifes of the protostellar phases give Class 0 half-life values of ~ 0.05 Myr and ~ 0.08 Myr for Class I (Kristensen & Dunham 2018). Therefore our results indicate the start of the planet formation begins less than 0.1 Myr after the beginning of the cloud collapse. This is consistent with the ages of the oldest meteorites in our Solar system (Connelly et al. 2012).

3.4.3 The context of planet formation models

It is of worth to put our empirical constraints on the solid mass reservoir in the context of planet formation models. Broadly speaking, planets can either form bottom-up through the assembly of smaller building blocks, in the so-called *core accretion* scenario, or top-down in the *gravitational instability* scenario, via direct gravitational collapse of the disk material. In the latter case (see Kratter & Lodato 2016 for a review), planets need not contain rocky cores and we may therefore have over-estimated the solid mass locked in planets. In addition, in this view planets form at the very beginning of the disk lifetime when the disk is gravitationally unstable, possibly at even earlier stages than we probe here. If this is the case, our observations do not put constraints on the mass budget required for planet formation since planets would already be formed in the disks we are considering.

Our results are instead relevant for the core accretion scenario. In this case, two large families of models can be defined, differing in the type of building block: planetesimal accretion (e.g., Pollack et al. 1996) and pebble accretion (Ormel & Klahr 2010; Lambrechts & Johansen 2012).

If planets grow by accreting planetesimals, it should be kept in mind that our observations are sensitive only to the dust. Therefore, the efficiency we have defined in this paper should be intended as the product of two efficiencies: the efficiency of converting dust into planetesimals and the efficiency of converting planetesimals into planets. The latter is relatively well constrained from theory and observations. Indeed, the accretion of planetesimals is highly efficient in numerical models (e.g., Alibert et al. 2013) and nearly all planetesimals are accreted into planets over Myr timescales. Observationally, constraints on the mass in

planetesimals that are not locked into planets is set by the debris disk population (Sibthorpe et al. 2018). For Sun-like stars, the median planetesimal mass[1] is 3 $M_\oplus$, i.e. much smaller than the solid content of giant planets. In this context, the Solar System could be an exception because attempts at explaining its complex history (such as the well known Nice model, Tsiganis et al. 2005) require instead a much more massive (20-30 $M_\oplus$) population of planetesimals past the orbits of Uranus and Neptune that later evolved into the current Kuiper Belt. Even so, this mass is comparable to the mass in the cores of the giant planets, implying an efficiency of planet conversion from planetesimals $\gtrsim 50\%$.

Using this value, our observations place empirical constraints on the planetesimal formation efficiency. To satisfy our measurement of a total efficiency of $\sim 10\%$, a planetesimal formation efficiency of $\sim 20\%$ would be needed. There is considerable uncertainty in planetesimal formation models (e.g., Drążkowska & Dullemond 2014, 2018; Lenz et al. 2019), but such an efficiency can in principle be reached by most of the expected conditions in the protoplanetary disks (see Fig. 9 of Lenz et al. 2019 and Table 1 of Drążkowska & Dullemond 2014). Thus, it is possible to explain the observed population of giant planets with the initial dust masses we report in this paper.

If instead planets grow by accreting pebbles, the growth rates can be significantly higher than in planetesimal accretion, but the formation efficiency is lower because most pebbles drift past the forming planets without being accreted (Ormel & Klahr 2010; Ormel 2017). The efficiency of $\sim 10\%$ reported here is among the highest that can be reached by pebble accretion (Ormel 2017) and it favours models where the disk is characterised by low turbulence ($\alpha < 10^{-3}$). Assuming such a value for the turbulence, Bitsch et al. (2019) finds that in pebble accretion models that form giant planets the total planet formation efficiency is 5-15%, in line with our findings. It is also suggestive that in their models giant planet formation requires initial dust masses larger than 200 – 300 $M_\oplus$: note how this condition is satisfied for $\sim 20\%$ of the Class 0 dust mass distribution. Therefore, the mass constraints derived in this paper from the VLA data are also consistent with pebble accretion, provided that the turbulence in the disk is sufficiently low.

3.5 Conclusions

This work collects available ALMA and VLA data of a complete sample of Perseus young disks in the Class 0/I phase to provide robust estimates of the disk dust masses at the early phases of star and planet formation. The refined values are used to compare the inferred disk masses with the exoplanetary systems to obtain constraints on when exoplanets start to form.

A linear correlation is found between the fluxes obtained with VLA and ALMA, supporting the fact that thermal dust emission is responsible for the emission at both wavelengths. The value of the dust spectral index measured with ALMA and VLA observations is $\beta = 0.5$, lower than the commonly used value of $\beta = 1$, pointing to significant grain growth occurring already in the Class 0 and I phases. Therefore, compared with our previous study (Tychoniec et al. 2018b) we recalculated the masses with the new dust opacity value that account for large grains. The best estimate of the median initial reservoir of dust mass available for planet formation in Perseus is 158 $M_\oplus$ and 52 $M_\oplus$ for Class 0 and Class I disks, respectively, derived from the VLA data.

[1] As discussed in Wyatt et al. (2007), this value is degenerate with the maximum planetesimal size; here we have assumed a diameter of 1000 km, and we note that the mass would be even lower if using smaller planetesimals.

Comparison of ALMA observations in Orion and Perseus shows that while disk masses in Class I disks agree well, Class 0 disks are more massive in Perseus than in Orion. This suggests that initial cloud conditions may lead to different masses of disks in the early phases.

Dust masses of disks measured with the VLA for Perseus are compared with the observed exoplanet systems. If we assume that planet formation starts with the dust mass reservoir equal to the dust mass of Class I disks in Perseus, efficiency of $\sim 30\%$ is required to explain the currently observed systems with giant exoplanets. Lower efficiencies of $\sim 15\%$ on average are needed if the Class 0 disks are assumed as the starting point. We find strong evidence that there is enough dust mass in young disks to make planet formation possible already in the first ~ 0.5 Myr of star formation. Given that low efficiencies are more in line with theoretical core accretion models, our results are most consistent with significant accumulation of material in larger bodies occurring already at the Class 0 phase.

Acknowledgements: ŁT and EvD thank Dr. Yao Liu for discussions on dust opacities. ŁT thanks Leon Trapman for discussions that helped in the presentation of results. G.R. acknowledges support from the Netherlands Organisation for Scientific Research (NWO, program number 016.Veni.192.233). JT acknowledges support from grant AST-1814762 from the National Science Foundation. The National Radio Astronomy Observatory is a facility of the National Science Foundation operated under cooperative agreement by Associated Universities, Inc. This paper makes use of the following ALMA data: ADS/JAO.ALMA#2017.1.01693.S, ADS/JAO.ALMA#2017.1.01078.S, ADS/JAO.ALMA#2015.1.00041.S,
and ADS/JAO.ALMA#2013.1.00031.S. ALMA is a partnership of ESO (representing its member states), NSF (USA) and NINS (Japan), together with NRC (Canada), MOST and ASIAA (Taiwan), and KASI (Republic of Korea), in cooperation with the Republic of Chile. The Joint ALMA Observatory is operated by ESO, AUI/NRAO and NAOJ. Astrochemistry in Leiden is supported by the Netherlands Research School for Astronomy (NOVA), by a Royal Netherlands Academy of Arts and Sciences (KNAW) professor prize, and by the European Union A-ERC grant 291141 CHEMPLAN. This project has received funding from the European Union's Horizon 2020 research and innovation programme under the Marie Skłodowska-Curie grant agreement No 823823 (DUSTBUSTERS). This work was partly supported by the Deutsche Forschungs-Gemeinschaft (DFG, German Research Foundation) - Ref no. FOR 2634/1 TE 1024/1-1. This research made use of Astropy, a community-developed core Python package for Astronomy (Astropy Collaboration et al. 2013), http://astropy.org); Matplotlib library (Hunter 2007); NASA's Astrophysics Data System.

Table 3.1: Measured properties of the disks in Perseus molecular cloud

Source name	F_λ mJy	Size $''$	Deconvolved size $''$	Envelope %	Residual %	Ext. fit
Per-emb-1	57.5 ± 0.6	0.48 × 0.34	0.27 × 0.16	11	<1	yes
Per-emb-2	593.4 ± 13.3	1.24 × 0.86	1.16 × 0.79	20	<1	yes
Per-emb-3	53.0 ± 0.3	0.53 × 0.36	0.27 × 0.16	4	<1	yes
Per-emb-4	0.5 ± 0.1	[a] 0.47 × 0.31	–	<1	<1	no
Per-emb-5	276.8 ± 1.5	0.59 × 0.40	0.37 × 0.25	3	<1	yes
Per-emb-6	11.4 ± 0.2	0.50 × 0.34	0.20 × 0.13	4	<1	yes
Per-emb-7	2.5 ± 0.3	0.83 × 0.59	0.75 × 0.41	47	<1	yes
Per-emb-9	10.0 ± 0.3	0.66 × 0.45	0.48 × 0.32	27	<1	yes
Per-emb-10	22.5 ± 0.2	0.50 × 0.34	0.18 × 0.12	4	<1	yes
Per-emb-11-A	160.3 ± 0.8	0.52 × 0.42	0.32 × 0.30	4	<1	yes
Per-emb-11-B	5.1 ± 0.5	0.41 × 0.28	–	<1	<1	no
Per-emb-11-C	3.5 ± 0.2	0.48 × 0.35	0.25 × 0.21	26	<1	yes
Per-emb-14	98.8 ± 0.6	0.62 × 0.36	0.42 × 0.17	3	<1	yes
Per-emb-15	6.5 ± 0.3	0.54 × 0.42	0.29 × 0.27	19	<1	yes
Per-emb-19	17.7 ± 0.2	0.50 × 0.34	0.18 × 0.14	2	<1	yes
Per-emb-20	8.1 ± 0.3	0.68 × 0.50	0.50 × 0.38	29	<1	yes
Per-emb-22-A	49.0 ± 1.1	0.66 × 0.43	0.49 × 0.27	28	1	yes
Per-emb-22-B	24.7 ± 1.1	0.66 × 0.41	0.49 × 0.23	[b] 60	[b] 2	yes
Per-emb-24	3.9 ± 0.3	0.60 × 0.40	0.39 × 0.24	1	1	no
Per-emb-25	126.6 ± 0.8	0.57 × 0.36	0.33 × 0.18	<1	<1	no
Per-emb-27-A	222.4 ± 3.7	0.47 × 0.44	–	13	1	yes
Per-emb-27-B	23.3 ± 3.5	0.44 × 0.44	–	[b] 224	[b] 56	yes
Per-emb-29	127.6 ± 1.7	0.52 × 0.37	0.23 × 0.19	11	<1	yes
Per-emb-30	48.4 ± 0.3	0.49 × 0.35	0.18 × 0.13	3	<1	yes
Per-emb-31	1.1 ± 0.2	0.43 × 0.34	–	17	<1	yes
Per-emb-34	12.4 ± 0.2	0.52 × 0.36	0.24 × 0.18	6	<1	yes
Per-emb-35-B	19.9 ± 0.3	0.50 × 0.33	0.19 × 0.11	11	<1	yes
Per-emb-35-A	27.8 ± 0.3	0.50 × 0.34	0.20 × 0.14	7	<1	yes
Per-emb-38	27.7 ± 0.2	0.52 × 0.38	0.27 × 0.16	<1	<1	no
Per-emb-39	0.9 ± 0.2	0.67 × 0.34	0.48 × 0.09	20	1	yes
Per-emb-41	11.3 ± 0.2	0.47 × 0.34	0.11 × 0.10	<1	<1	no
Per-emb-45	1.0 ± 0.1	0.45 × 0.34	–	9	<1	yes
Per-emb-46	6.0 ± 0.2	0.58 × 0.38	0.35 × 0.22	2	1	no
Per-emb-49-A	22.1 ± 0.2	0.49 × 0.35	0.18 × 0.13	2	<1	yes
Per-emb-49-B	4.7 ± 0.2	0.50 × 0.30	–	46	<1	yes
Per-emb-50	86.4 ± 0.2	0.46 × 0.29	0.22 × 0.07	<1	<1	no
Per-emb-51	1.7 ± 0.6	0.48 × 0.43	0.29 × 0.10	262	5	yes
Per-emb-52	5.2 ± 0.2	0.52 × 0.34	0.23 × 0.13	<1	<1	no
Per-emb-53	29.5 ± 0.4	0.54 × 0.42	0.39 × 0.34	<1	<1	no
Per-emb-54	3.1 ± 0.6	0.59 × 0.50	0.39 × 0.36	<1	<1	no
Per-emb-58	4.6 ± 0.2	0.51 × 0.36	0.22 × 0.16	<1	<1	no
Per-emb-59	1.6 ± 0.1	0.47 × 0.32	–	<1	<1	no
Per-emb-62	77.0 ± 0.1	0.44 × 0.33	0.19 × 0.13	<1	<1	no
Per-emb-63-B	3.8 ± 0.2	0.53 × 0.35	0.26 × 0.16	<1	<1	no
Per-emb-63-C	2.2 ± 0.2	0.50 × 0.31	–	<1	<1	no
Per-emb-63-A	25.8 ± 0.2	0.50 × 0.36	0.18 × 0.17	<1	<1	no
Per-emb-64	42.4 ± 0.3	0.51 × 0.34	0.20 × 0.13	<1	<1	no
Per-emb-65	37.1 ± 0.2	0.53 × 0.39	0.26 × 0.23	<1	<1	no
B1-bS	330.4 ± 2.6	0.60 × 0.52	0.42 × 0.39	7	<1	yes
SVS13C	62.1 ± 0.9	0.46 × 0.38	0.29 × 0.09	<1	<1	no
SVS13B	207.3 ± 5.9	0.57 × 0.47	0.37 × 0.31	20	<1	yes
SVS13A2	18.8 ± 3.8	[a] 0.46 × 0.31	–	<1	<1	no

Notes. F_λ- integrated flux density at the wavelength of the observations: 1.1 mm for sources in the Hsieh et al. (2019b), 1.3 mm for sources in the 2017.1.01078.S dataset (PI: D. Segura-Cox), uncertainty is provided by the *imfit* task in CASA; Size - FWHM of the 2D Gaussian fit to the disk component; Deconvolved size - the size of the emission deconvolved from the beam, provided by *imfit* task in CASA, where no value is provided, the size of the emission is too close to the synthesized beam size; Envelope - flux remaining in the ellipse of the size of the disk, after removing the model of the disk from the image as a fraction of the disk flux; Residual - flux remaining in the ellipse of the size of the disk, after removing both the disk model and the broad envelope model, as a fraction of the disk flux; Ext. fit - flag indicating if the second, broad Gaussian component was used in the fit. [a] FWHM of the Gaussian fixed before fitting. [b] Value not reliable due to a close companion.

Table 3.2: Masses of the embedded disks in Perseus

Source name	Class	$M_{\rm dust}$@ 9 mm $M_\oplus$	$M_{\rm dust}$ @ 1 mm $M_\oplus$	α VLA/ALMA	α VLA	robust	Dataset
Per-emb-1	0	279.6 ± 50.0	82.5 ± 1.2	2.4	1.9	n	Segura-Cox
Per-emb-2	0	927.4 ± 175.6	573.6 ± 18.2	2.8	2.9	y	Hsieh
Per-emb-3	0	157.8 ± 32.7	51.2 ± 0.4	2.4	1.5	n	Hsieh
Per-emb-4	0	<11.3 ± 7.2	0.5 ± 0.1	1.5	—	n	Hsieh
Per-emb-5	0	502.3 ± 86.3	267.6 ± 2.1	2.7	2.7	y	Hsieh
Per-emb-6	0	78.5 ± 21.5	11.0 ± 0.2	2.0	1.7	y	Hsieh
Per-emb-7	0	<11.8 ± 7.2	2.4 ± 0.4	2.2	—	n	Hsieh
Per-emb-8	0	237.9 ± 47.5	147.6 ± 5.5	2.7	3.0	y	Tobin
Per-emb-9	0	23.1 ± 14.4	9.7 ± 0.4	2.6	3.3	n	Hsieh
Per-emb-10	0	143.4 ± 30.7	21.7 ± 0.3	2.1	1.5	n	Hsieh
Per-emb-11-A	0	413.5 ± 73.1	230.2 ± 1.6	2.7	2.4	y	Segura-Cox
Per-emb-11-B	0	21.7 ± 14.9	7.4 ± 1.1	2.4	1.7	n	Segura-Cox
Per-emb-11-C	0	30.5 ± 15.4	5.1 ± 0.4	2.1	3.2	n	Segura-Cox
Per-emb-12-A	0	2853.9 ± 437.0	2159.5 ± 59.3	2.8	3.0	y	Tobin
Per-emb-12-B	0	158.1 ± 38.4	623.6 ± 16.0	3.7	3.2	n	Tobin
Per-emb-13	0	1271.3 ± 207.6	—	—	2.7	n	—
Per-emb-14	0	311.2 ± 58.6	95.5 ± 0.9	2.4	2.4	y	Hsieh
Per-emb-15	0	<9.3 ± 6.6	6.3 ± 0.4	2.8	—	n	Hsieh
Per-emb-16	0	<34.9 ± 18.1	—	—	—	n	—
Per-emb-17-A	0	160.1 ± 32.4	37.5 ± 1.0	2.2	1.9	y	Tobin
Per-emb-17-B	0	39.3 ± 10.4	29.3 ± 1.0	2.8	2.6	y	Tobin
Per-emb-18	0	224.8 ± 47.1	208.5 ± 2.8	2.9	1.5	n	Tobin
Per-emb-19	0	112.3 ± 27.7	17.1 ± 0.2	2.1	1.1	n	Hsieh
Per-emb-20	0	<31.1 ± 15.5	7.8 ± 0.4	2.3	—	n	Hsieh
Per-emb-21	0	211.9 ± 41.1	70.8 ± 1.0	2.4	2.5	y	Tobin
Per-emb-22-A	0	96.4 ± 24.1	47.3 ± 1.5	2.6	1.0	n	Hsieh
Per-emb-22-B	0	23.1 ± 13.0	23.9 ± 1.5	3.0	3.4	n	Hsieh
Per-emb-23	0	37.2 ± 15.0	—	—	3.8	n	—
Per-emb-24	0	21.5 ± 7.9	3.8 ± 0.3	2.2	3.0	n	Hsieh
Per-emb-25	0	172.6 ± 65.4	122.4 ± 1.1	2.8	1.7	n	Hsieh
Per-emb-26	0	636.1 ± 102.5	—	—	2.2	n	—
Per-emb-27-A	0	570.1 ± 90.4	215.0 ± 5.1	2.5	1.9	n	Hsieh
Per-emb-27-B	0	113.6 ± 24.4	22.5 ± 4.8	2.2	1.9	y	Hsieh
Per-emb-28	0/I	23.5 ± 16.6	—	—	4.4	n	—
Per-emb-29	0/I	233.5 ± 43.5	123.3 ± 2.4	2.7	1.8	n	Hsieh
Per-emb-30	0/I	263.5 ± 47.7	46.8 ± 0.4	2.2	2.1	y	Hsieh
Per-emb-31	0/I	<26.5 ± 14.9	1.1 ± 0.2	1.5	—	n	Hsieh
Per-emb-32-A	0/I	18.2 ± 8.1	—	—	0.9	n	—
Per-emb-32-B	0/I	30.0 ± 10.5	—	—	3.6	n	—
Per-emb-33-A	0	294.0 ± 57.6	9.3 ± 1.6	1.2	2.3	n	Tobin
Per-emb-33-B	0	170.6 ± 39.4	45.8 ± 2.8	2.3	1.2	n	Tobin
Per-emb-33-C	0	55.8 ± 19.0	234.1 ± 3.7	3.7	2.0	n	Tobin
Per-emb-34	I	85.6 ± 22.5	12.0 ± 0.3	2.0	1.2	n	Hsieh
Per-emb-35-B	I	86.8 ± 20.6	19.3 ± 0.4	2.3	1.3	n	Hsieh
Per-emb-35-A	I	47.0 ± 15.7	26.8 ± 0.4	2.7	3.2	n	Hsieh
Per-emb-36-A	I	555.9 ± 90.4	185.5 ± 1.8	2.4	2.5	y	Tobin
Per-emb-36-B	I	110.6 ± 23.3	17.7 ± 1.4	2.0	2.2	y	Tobin
Per-emb-37	0	95.4 ± 23.9	—	—	1.7	n	—
Per-emb-38	I	78.7 ± 23.6	26.7 ± 0.3	2.5	1.9	n	Hsieh
Per-emb-39	I	<12.3 ± 7.3	0.8 ± 0.2	1.7	—	n	Hsieh
Per-emb-40-A	I	72.9 ± 18.0	22.8 ± 0.6	2.4	2.3	y	Tobin
Per-emb-40-B	I	<17.6 ± 8.7	1.3 ± 0.2	1.7	—	n	Tobin
Per-emb-41	I	44.2 ± 18.8	11.0 ± 0.3	2.3	0.9	n	Hsieh
Per-emb-42	I	116.5 ± 29.0	—	—	1.7	n	—
Per-emb-43	I	<11.8 ± 7.2	—	—	—	n	—
Per-emb-44-A	0/I	497.7 ± 80.8	142.2 ± 2.2	2.3	2.3	y	Tobin
Per-emb-44-B	0/I	176.7 ± 41.7	227.1 ± 3.7	3.1	1.7	n	Tobin
Per-emb-45	I	<11.8 ± 7.2	1.0 ± 0.2	1.8	—	n	Hsieh
Per-emb-46	I	55.5 ± 26.6	5.8 ± 0.3	1.9	0.8	n	Hsieh
Per-emb-47	I	106.5 ± 28.3	—	—	2.2	n	—
Per-emb-48-A	I	37.9 ± 16.5	5.7 ± 0.8	2.0	0.7	n	Tobin
Per-emb-48-B	I	<14.9 ± 10.5	<0.6 ± 0.8	1.3	—	n	Tobin
Per-emb-49-A	I	145.2 ± 31.0	21.4 ± 0.3	2.1	0.6	n	Hsieh
Per-emb-49-B	I	<53.0 ± 16.5	4.5 ± 0.3	1.8	—	n	Hsieh
Per-emb-50	I	535.2 ± 91.0	124.1 ± 0.4	2.2	2.1	y	Segura-Cox
Per-emb-51	I	<12.8 ± 8.1	1.6 ± 0.8	2.0	—	n	Hsieh
Per-emb-52	I	35.4 ± 19.6	5.0 ± 0.3	2.0	1.0	n	Hsieh
Per-emb-53	I	56.6 ± 22.6	42.3 ± 0.8	2.8	1.1	n	Segura-Cox

Table 3.2: continued.

Source name	Class	$M_{\rm dust}$@ 9 mm $M_\oplus$	$M_{\rm dust}$ @ 1 mm $M_\oplus$	α VLA/ALMA	α VLA	robust	Dataset
Per-emb-54	I	115.5 ± 28.2	3.0 ± 0.9	1.2	1.0	y	Hsieh
Per-emb-55-A	I	48.7 ± 11.8	4.7 ± 1.0	1.8	3.6	n	Tobin
Per-emb-55-B	I	7.4 ± 5.2	0.7 ± 0.6	1.8	4.4	n	Tobin
Per-emb-56	I	45.7 ± 16.9	–	–	3.7	n	–
Per-emb-57	I	67.9 ± 22.8	–	–	0.6	n	–
Per-emb-58	I	<37.9 ± 17.9	4.4 ± 0.2	2.0	–	n	Hsieh
Per-emb-59	I	<13.8 ± 8.2	1.5 ± 0.2	1.9	–	n	Hsieh
Per-emb-60	I	<13.3 ± 8.1	–	–	–	n	–
Per-emb-61	I	52.1 ± 23.4	–	–	2.6	n	–
Per-emb-62	I	200.8 ± 41.6	110.5 ± 0.2	2.7	2.2	n	Segura-Cox
Per-emb-63-B	I	<11.8 ± 8.3	3.6 ± 0.3	2.4	–	n	Hsieh
Per-emb-63-C	I	<11.8 ± 8.3	2.1 ± 0.2	2.2	–	n	Hsieh
Per-emb-63-A	I	109.7 ± 27.3	24.9 ± 0.3	2.3	2.0	y	Hsieh
Per-emb-64	I	240.9 ± 48.0	40.9 ± 0.4	2.1	1.8	y	Hsieh
Per-emb-65	I	58.5 ± 25.0	35.9 ± 0.3	2.8	1.1	n	Hsieh
Per-emb-66	I	<13.3 ± 8.1	–	–	–	n	–
Per-bolo-58	0	<12.8 ± 8.1	–	–	–	n	–
Per-bolo-45	0	<12.3 ± 7.3	–	–	–	n	–
L1451-MMS	0	97.3 ± 22.8	–	–	2.2	n	–
L1448IRS2E	0	<14.7 ± 9.0	–	–	–	n	–
B1-bN	0	483.8 ± 85.1	–	–	2.5	n	–
B1-bS	0	354.0 ± 76.5	319.4 ± 3.5	2.9	2.1	n	Hsieh
L1448IRS1-A	I	292.7 ± 53.2	105.4 ± 1.8	2.5	2.2	y	Tobin
L1448IRS1-B	I	36.4 ± 15.6	7.9 ± 1.4	2.2	3.7	n	Tobin
L1448NW-A	0	194.5 ± 38.6	71.5 ± 1.0	2.5	1.7	n	Tobin
L1448NW-B	0	187.9 ± 39.1	21.3 ± 0.4	1.9	1.7	y	Tobin
L1448IRS3A	I	235.1 ± 47.8	145.0 ± 5.1	2.7	0.7	n	Tobin
SVS13C	0	223.9 ± 48.4	89.3 ± 1.9	2.5	1.4	n	Segura-Cox
SVS13B	0	581.1 ± 98.2	200.3 ± 8.1	2.5	2.3	y	Hsieh
IRAS03363+3207	I?	326.3 ± 58.0	–	–	2.4	n	–
IRAS4B'	0	603.2 ± 115.2	–	–	2.6	n	–
SVS13A2	0?	102.6 ± 27.7	18.2 ± 5.2	2.2	1.4	n	Hsieh

Notes. Class - Evolutionary class of the source. In the analysis, borderline sources (0/I) are treated as Class 0. Dataset: Tobin - (Tobin et al. 2018) (1.3 mm), Segura-Cox - 2017.1.01078.S (1.3 mm), Hsieh - (Hsieh et al. 2019b) (1.1 mm). $\alpha_{\rm VLA/ALMA}$ - spectral indices obtained between 1 and 9 mm, $\alpha_{\rm VLA}$ - Ka-band intraband indices. Robust - if 'y', sources with consistent spectral indices betweem VLA/ALMA and VLA Ka-band.

Appendix

3.A Additional plots

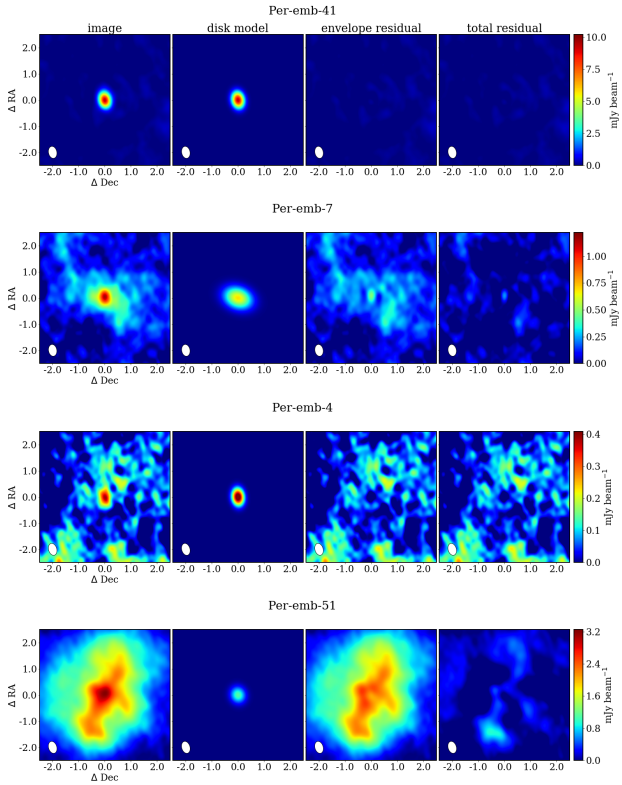


Figure 3.7: From left to right: observed 1.1 mm ALMA continuum images of the targeted protostars; an image of the disk model for the source resulting from the Gaussian fitting, in cases where the envelope component is fitted, only the disk component is shown; the residual image after subtracting the disk model from the image; the residual image after subtracting both disk and envelope models. From top to bottom, cases that occur in the Gaussian fitting procedure are presented: Per-emb-41, single source, without a noticeable contribution from the envelope; Per-emb-7, contribution of the envelope, as assessed by eye, is significant, an additional broad Gaussian with size of 3″was added to the input parameters; Per-emb-54, the central compact component was faint compared to the noise level, it was necessary to fix the size of the Gaussian to the synthesized beam size for the fit to converge. Per-emb-51, the central component has a very small flux compared to the envelope.

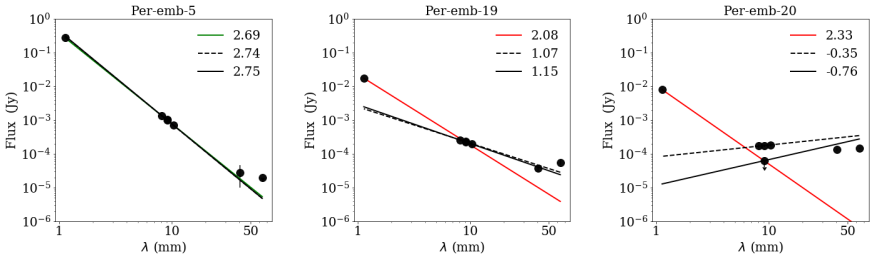


Figure 3.8: Examples of fitting the spectral index to the fluxes from VLA (8 mm - 6.4 cm) and ALMA observations (1 mm). *Left:* Per-emb-5 has an intra-band Ka-band spectral index in agreement with the spectral index between 1 mm and 9 mm wavelengths. *Center:* For Per-emb-19 Ka-band spectral index is too low to be explained only by dust emission, some free-free contamination cannot be excluded. *Right:* In Per-emb-20, negative spectral index at Ka-band shows that emission is heavily contaminated by other effects, in such cases the Ka-band flux is treated as an upper limit of the dust emission.

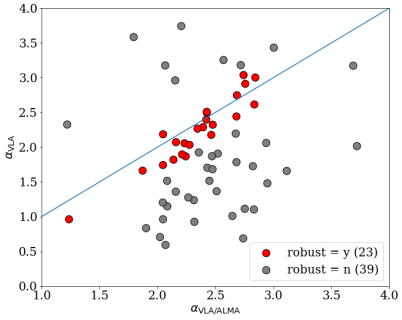


Figure 3.9: Plot showing spectral indices obtained between 1 and 9 mm $\alpha_{\mathrm{VLA/ALMA}}$ and Ka-band intra-band indices α_{VLA}, only for sources with both values provided. Red points are the sources with consistent spectral indices betweem VLA/ALMA and VLA Ka-band.

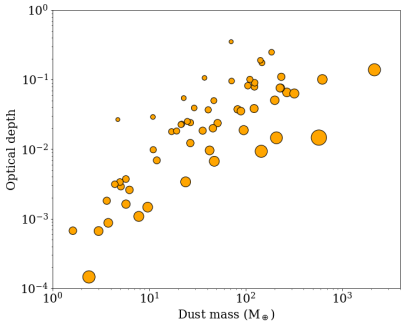
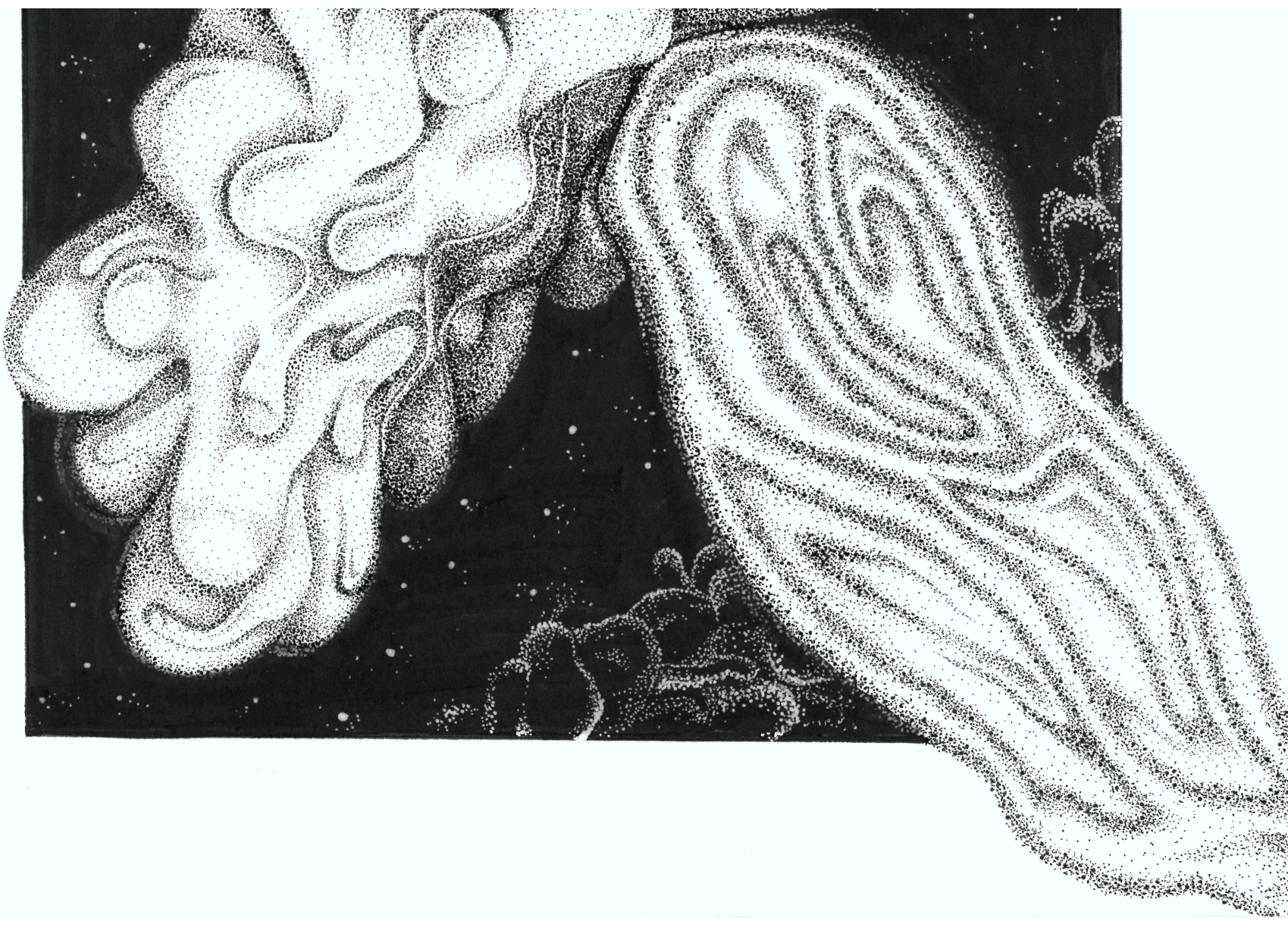


Figure 3.10: Plot showing optical depth as a function of the disk dust masses. Size of the circle is proportional to the disk size of the source.





4

Chemical and kinematic structure of extremely high-velocity molecular jets in the Serpens Main star-forming region

Tychoniec Ł., Hull C. L. H., Kristensen L. E., Le Gouellec V. J. M., van Dishoeck E. F.
Published in Astronomy & Astrophysics, 2019.

Abstract

Outflows are one of the first signposts of ongoing star formation. The fastest molecular component of protostellar outflows, extremely high-velocity (EHV) molecular jets, are still puzzling since they are seen only rarely. As they originate deep inside the embedded protostar-disk system, they provide vital information about the outflow-launching process in the earliest stages.

The first aim is to analyze the interaction between the EHV jet and the slow outflow by comparing their outflow force content. The second aim is to analyze the chemical composition of the different outflow velocity components and to reveal the spatial location of molecules. The Atacama Large Millimeter/submillimeter Array (ALMA) 3 mm (Band 3) and 1.3 mm (Band 6) observations of five outflow sources at 0.″3 − 0.″6 (130 − 260 au) resolution in the Serpens Main cloud are presented. Observations of CO, SiO, H_2CO, and HCN reveal the kinematic and chemical structure of those flows. The following three velocity components are distinguished: the slow and the fast wing, and the EHV jet. Out of five sources, three have the EHV component. The comparison of outflow forces reveals that only the EHV jet in the youngest source, Ser-emb 8 (N), has enough momentum to power the slow outflow. The SiO abundance is generally enhanced with velocity, while HCN is present in the slow and the fast wing, but disappears in the EHV jet. For Ser-emb 8 (N), HCN and SiO show a bow-shock shaped structure surrounding one of the EHV peaks, thus suggesting sideways ejection creating secondary shocks upon interaction with the surroundings. Also, the SiO abundance in the EHV gas decreases with distance from this protostar, whereas it increases in the fast wing. H_2CO is mostly associated with low-velocity gas, but, surprisingly, it also appears in one of the bullets in the Ser-emb 8 (N) EHV jet. No complex organic molecules are found to be associated with the outflows. The high detection rate suggests that the presence of the EHV jet may be more common than previously expected. The EHV jet alone does not contain enough outflow force to explain the entirety of the outflowing gas. The origin and temporal evolution of the abundances of SiO, HCN, and H_2CO through high-temperature chemistry are discussed. The data are consistent with a low C/O ratio in the EHV gas versus a high C/O ratio in the fast and slow wings.

4.1 Introduction

Spectacular outflows are one of the crucial signposts of ongoing star formation. Outflows are invoked to release angular momentum, enabling a continuous flow of matter onto the disk and the young star (e.g., Frank et al. 2014). Their feedback from small to large scales can have a profound impact on the evolution of both the protostar and the entire parent star-forming region (e.g., Arce & Sargent 2006; Plunkett et al. 2013). Thus, probing the youngest and most powerful outflow sources is crucial for understanding the interactions between the outflows and their surroundings.

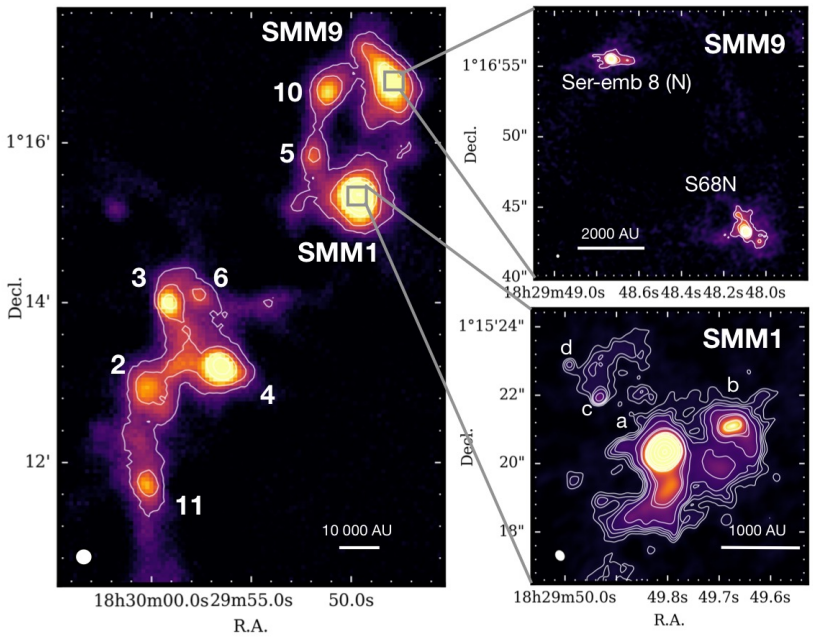


Figure 4.1: Left: JCMT/SCUBA 850-μm map of Serpens Main region with numbers corresponding to SMM sources as classified by Davis et al. (1999). Contours are [3, 6, 12, 20, 40] × 0.50 mJy arcsec^{-2}. Beam of the JCMT observations of 14 ″ is indicated in the bottom-left corner. Right: ALMA 1.3 mm continuum of targeted protostars. For SMM9, field contours are [3, 6, 9, 12] × 0.53 mJy beam^{-1} and for SMM1 field contours are [3, 4, 5, 6, 9, 15, 40, 50] × 0.62 mJy beam^{-1}. Synthesized beams of the ALMA observations are 0.″35 × 0.″33 for the SMM9 field and 0.″36 × 0.″30 for the SMM1 field.

While the molecular emission from a typical protostellar outflow usually appears as slow and wide-angle entrained gas, there is a peculiar group of sources with high-velocity collimated molecular emission. The extremely high-velocity (EHV) molecular jets ($v > 30$ km s^{-1}) are found toward the youngest protostars (e.g., Bachiller et al. 1990; Bachiller 1996) in the Class 0 stage (André et al. 1993). They were first detected as spectral features, high-velocity peaks detached from the low-velocity outflow wings (Bachiller et al. 1990), and subsequently spatially resolved as discrete bullets embedded in a cocoon of low-velocity gas (e.g., Santiago-García et al. 2009; Hirano et al. 2010). These "bullets" are thought to arise from the variability

of the outflow activity, which is possibly related to the variability of the accretion processes itself (Raga et al. 1993). In the deeply embedded stage, EHV molecular jets have been observed at submillimeter wavelengths (e.g., Bachiller et al. 1994; Tafalla et al. 2004), as well as in far-infrared (IR) observations (Kristensen et al. 2012; Mottram et al. 2014). They appear to be quite rare. In a survey of 29 protostars with *Herschel Space Observatory*/Heterodyne Instrument for the Far-Infrared (HIFI), water bullets were detected in only four sources, all of them being Class 0 (Kristensen et al. 2012). Thus, EHV jets are thought to be associated exclusively with very young sources.

Apart from the spatial and spectral characteristics of the EHV jets relative to low-velocity outflows, it appears that their chemical composition is significantly different from that of the slow outflow. In observations with the IRAM-30m of two young outflows with EHV jet components, Tafalla et al. (2010) show that the molecular jets are more oxygen-rich compared to the slow and the fast wing component of the molecular outflow. The molecular jets are prominently seen in species, such as SiO (see also Guilloteau et al. 1992), SO, CH_3OH, and H_2CO, whereas emission from molecules like HCN and CS, which tend to be present in the slow and the fast wing, is missing at the highest velocities. These led Tafalla et al. (2010) to define three distinct velocity components: the slow and the fast wing, and the EHV jet (see Sect. 4.3.2). These studies presented spectrally resolved line profiles of different molecules, but their spatial location remains unclear. To date, only CO and SiO have been studied at high spatial resolution within the EHV jets (e.g., Lee et al. 2008; Santiago-García et al. 2009; Hirano et al. 2010; Codella et al. 2014; Hull et al. 2016). It is still not well understood what the spatial distribution of other molecules is in the different kinematic components of the outflow.

Additional important information on molecular jets and outflows comes from observations with the HIFI instrument (de Graauw et al. 2010) on board *Herschel* (Pilbratt et al. 2010) on scales of 12″ – 40″. Many water and high-J CO transitions probing warm shocked gas show complex line profiles that can be decomposed in two main velocity components. The kinematic and chemical signatures of those components are universal for all protostars, from low to high mass (Kristensen et al. 2012; Mottram et al. 2014; San José-García et al. 2016): a broad component (FWHM > 20 km s^{-1}), and an offset component (20 > FWHM > 5 km s^{-1}), which is usually blue-shifted with respect to the systemic velocity up to a few km s^{-1}. The CO excitation temperatures in the broad component are typically 300 K in the broad component and 700 K in the offset component. EHV bullets are also seen in HIFI line profiles as discrete peaks that are detached from the main line profile; however, as noted above, these only appear in a few sources. The spatial origin of those components can potentially be revealed with spectrally and spatially resolved Atacama Large Millimeter/submillimeter Array (ALMA) observations of low-J CO and other molecules. ALMA's high spatial resolution is needed since the water analysis suggests that its emission originates from structures that are only a few hundred au in size. This is much smaller than the region encompassed by the HIFI beam at distances of nearby star-forming regions (Mottram et al. 2014).

Here we target three protostars in the Serpens Main region at a distance of 436 pc (Ortiz-León et al. 2017), namely, the Serpens SMM1 (hereafter referred to as SMM1), S68N, and Ser-emb 8 (N) protostellar systems. SMM1 is directly between a low and intermediate mass protostar (100 $L_\odot$; Kristensen et al. 2012), and it is known to host a massive disk-like structure (Hogerheijde et al. 1999; Enoch et al. 2010). The SMM1 source was discovered as a multiple system in the continuum observations (Choi 2009) as confirmed by the observations of the atomic jet (Dionatos et al. 2014). More recently, resolving the system with ALMA unveiled a total of five protostellar components (Hull et al. 2017) within a 2000 au radius, three of which

Table 4.1: Targeted protostars

Name	Other names	R.A. (J2000)	Decl. (J2000)	L_{bol} ($L_\odot$)	T_{bol} (K)	M_{env} ($M_\odot$)	Ref.
Serpens SMM1	S68FIRS1 (1), Ser-emb 6 (5)	18:29:49.765	+1:15:20.506	109	39	58	(4)
S68N	Ser-emb 8 (5), SMM9 (2)	18:29:48.087	+1:16:43.260	6	58	10	(5)
Ser-emb 8 (N)	S68Nb (6), S68Nc (3)	18:29:48.731	+1:16:55.495	—	—	—	—

(1) McMullin et al. 1994, (2) Davis et al. 1999, (3) Dionatos et al. 2010, (4) Kristensen et al. 2012, (5) Enoch et al. 2009, (6) (Maury et al. 2019).

show outflows (labeled a, b, and d in Fig. 4.1). S68N and Ser-emb 8 (N) are deeply embedded protostars separated by 5000 au (Fig. 4.1b), and both power outflows (Hull et al. 2014). The chemical structure of Serpens Main on cloud scale has been studied in detail by McMullin et al. (1994, 2000) and Kristensen et al. (2010). A summary of the sources is provided in Table 4.1.

ALMA observations of CO 2 – 1 and SiO 5 – 4 reveal EHV jets toward the SMM1-a and SMM1-b sources in CO, which are both asymmetric, and only redshifted emission is detected at high velocities. SMM1-b additionally shows EHV emission in SiO (Hull et al. 2016, 2017).

In this paper we use ALMA to resolve, both spectrally and spatially, the emission from different molecules. This allow us not only to distinguish different kinematic components of the outflows and jets from protostars but also to link them to the specific physical components of the system, such as entrained gas, outflow cavity walls, or the protostellar jet.

4.2 Observations

ALMA observations of four molecular transitions, CO 2 – 1, SiO 5 – 4, H_2CO $3_{03} - 2_{02}$ in Band 6 (ALMA project 2013.1.00726.S; PI: C. Hull) and HCN 1 – 0 observed in Band 3 (ALMA project 2016.1.00710.S; PI: C. Hull) are presented. The synthesized beam of the observations is between $\sim 0\farcs3$ and $\sim 0\farcs6$, corresponding to 130 – 260 au at the distance to Serpens Main. The largest recoverable scale in the data is $\sim 5''$ and $\sim 12''$ (2150 and 4960 au) for Band 3 and Band 6, respectively. The spectral resolution of the observations differs between the spectral windows, ranging from 0.04 – 0.3 km s^{-1}. For both bands, only 12-m array data were used. The Band 6 data were obtained in two configurations (C43-1 and C43-4 with resolutions of $1\farcs1$ and $0\farcs3$, respectively), and the final images were produced from the combined datasets.

After obtaining the C43-4 configuration data, it became apparent that SiO and H_2CO emission is present at velocities extending further than the spectral setup. To capture the emission at high-velocities, the spectral configuration for SiO and H_2CO was changed for the compact C43-1 configuration. Thus the SiO and H_2CO emission at the highest velocities (> 40 km s^{-1} for SiO and > 25 km s^{-1} for H_2CO in both the redshifted and blueshifted direction with respect to the systemic velocity of 8.5 km s^{-1}) are only available at lower spatial resolution.

Continuum images were obtained from the dedicated broadband spectral windows and line-free channels. Self-calibration on continuum data was performed, and solutions were transferred to the emission line measurement sets. The line data were then continuum subtracted. The imaging was performed with the Common Astronomy Software Application (CASA) v. 5.1.0 (McMullin et al. 2007) *tclean* task with masked regions selected by hand for each line. Data were imaged with Briggs weighting = 0.5 and re-binned to 0.5 km s^{-1}. Due to the large extent and complicated structure of the emission lines, the multiscale option in *tclean* was used for the lines, and the scales were manually adjusted for each line. Information about the observations is summarized in Table 4.4.

4.3 Results

4.3.1 Images of outflows

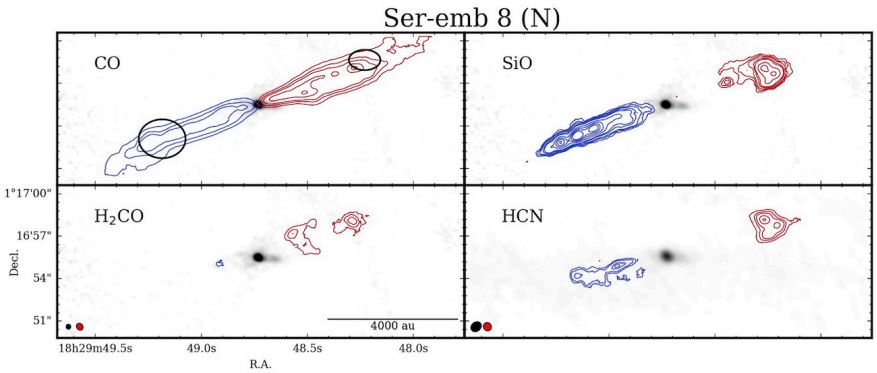


Figure 4.2: Integrated intensity maps of CO 2 − 1, SiO 5 − 4, H_2CO $3_{03} - 2_{02}$, and HCN 1 − 0 overlaid on the Band 6 (Band 3 for HCN) continuum in grayscale for Ser-emb 8 (N). The emission is integrated from the inner boundary of the slow wing component to the outer boundary of the EHV component as listed in Table 4.2 for the red and blueshifted emission. The exceptions are SiO and H_2CO maps where only the channels obtained at high spatial resolution are plotted (< 26 km s^{-1} for H_2CO and < 40 km s^{-1} for SiO). The synthesized beam size of the continuum images is 0.″35 × 0.″33 for Band 6 and 0.″79 × 0.″64 for Band 3; for spectral lines it is 0.″53 × 0.″45 (CO), 0.″55 × 0.″45 (SiO), 0.″53 × 0.″44 (H_2CO), and 0.″60 × 0.″56 (HCN). The beam size of the Band 6 spectral line is presented in the bottom-left corner of the H_2CO map and in HCN map for Band 3. Contour levels are [3, 6, 9, 15, 20, 40, 60, 80, 100] for CO, SiO, H_2CO, and redshifted HCN, and [2, 3, 5, 6, 12] for blueshifted HCN, which were multiplied by rms value of moment 0 maps. The rms values for the blueshifted and redshifted side of the outflow in K km s^{-1} is as follows: CO [19.7, 14.4], SiO [2.2, 2.5], H_2CO [2.8, 2.1], and HCN [9.3, 12.2]. Black ellipses indicate regions from which spectra were extracted for Fig. 4.4 and 4.16.

The highest resolution and sensitivity observations of the S68N and Ser-emb 8 (N) molecular outflows taken to date are presented here. For SMM1, H_2CO, and HCN, emission is shown in addition to the CO and SiO outflow presented in previous papers (Hull et al. 2016, 2017).

Figures 4.2 and 4.3 show the integrated emission maps of CO, SiO, H_2CO, and HCN for all five sources. Various other molecules were detected as well in the ALMA observations (e.g., DCO^+, $C^{18}O$, and complex organic molecules; Tychoniec et al. 2018a). Those molecules either trace the cold quiescent envelope or the warm inner envelope, but they do not show the outflow components; thus, they are not further discussed here.

Ser-emb 8 (N) (Fig. 4.2) shows a relatively symmetric outflow morphology in CO. It has a very small opening angle of 25°, which was measured as an angle between the outflow cavity walls seen at the low-velocity CO.

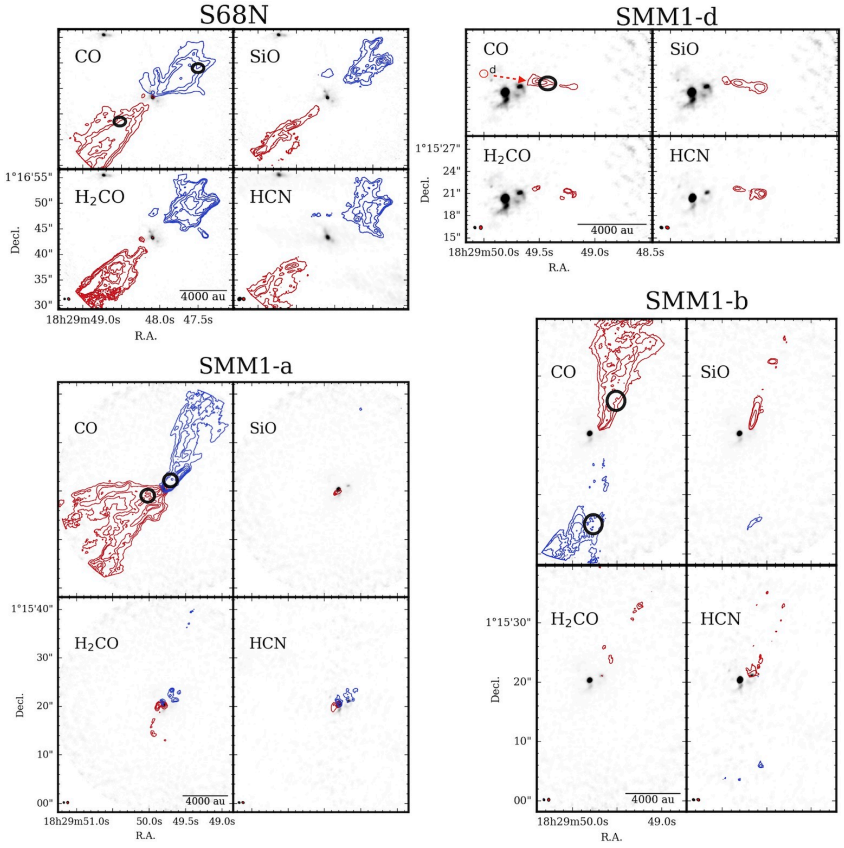


Figure 4.3: Similar to Fig. 4.2, but for remaining sources. S68N: Contour levels are [3, 6, 9, 15, 20, 40, 60, 80, 100] for CO and HCN; [3, 8, 15, 30, 45] for SiO; and [3, 5, 9, 15, 20, 40] for H_2CO, which were multiplied by the rms value of moment 0 maps. The rms values for the blueshifted and redshifted side of the outflow, in K km s^{-1}: CO [19.5, 14.1], SiO [1.6, 1.9], H_2CO [3.2, 2.0], and HCN [9.4, 12.7]. SMM1-a: Contour levels are [3, 6, 9, 15, 20, 40, 60, 80, 100] for all molecules, which were multiplied by the rms value of moment 0 maps. The rms values for the blueshifted and redshifted side of the outflow, in K km s^{-1}: CO [20.2, 20.6], SiO [3.6, 4.0], H_2CO [2.0, 2.9], and HCN [7.5, 11.5]. SMM1-b: Contour levels are [3, 6, 9, 15, 20, 40, 60, 80, 100] for CO, [3, 9, 36] for SiO, and [3, 5] for H_2CO and HCN, which were multiplied by the rms value of moment 0 maps. The rms values for the blueshifted and redshifted side of the outflow, in K km s^{-1}: CO [18.7, 20.3], SiO [3.6, 4.0], H_2CO [1.9, 2.9], and HCN [7.4, 11.5]. SMM1-d: Only redshifted moment 0 map is presented as no blueshifted component has been detected toward this source. Contour levels are [3, 6, 9, 15, 20, 40, 60, 80, 100] for CO and HCN, [3, 12, 36] for SiO, and [2, 3] for H_2CO, which were multiplied by the rms value of moment 0 maps. The rms values in K km s^{-1} are: CO [20.1], SiO [3.3], H_2CO [2.7], and HCN [9.1]. Black ellipses indicate regions from which spectra were extracted for Fig. 4.16.

SiO emission toward this source traces both the central, most collimated part of the outflow, and the bow-shock structure at the redshifted part of the outflow, which are also clearly seen in the HCN. The structure is not so clear on the blueshifted side, although HCN is mostly present off of the main axis of the outflow there, while there is no clear evidence for a blueshifted bow-shock from SiO emission. H_2CO is enhanced at the bow-shock position in the redshifted part of the outflow.

S68N has an outflow with a wide opening angle of 50°, although the cavity walls do not seem well defined for this source (Fig. 4.3). The morphology of the outflow is similar in all molecules, but it can be noticed that peaks of the SiO emission generally appear in regions with weaker CO emission. There seems to be a narrow on-axis ridge on the redshifted side of the S68N outflow where both SiO and HCN emission peaks. This is in contrast to H_2CO, which emits mostly off-axis.

The SMM1-a outflow has an asymmetric structure in CO, which is comprised of misaligned blue- and redshifted lobes with respect to each other (30° difference in position angles) and the following different opening angles: 65° and 35° for red and blueshifted sides, respectively (Fig. 4.3). Other molecules are seen close to the protostar rather than throughout the full extent of the outflow, for example, SiO is only found very close to the protostar and only on the redshifted side, furthermore, H_2CO and HCN are seen tracing the innermost regions of the outflow with irregular morphologies.

SMM1-b has an outflow with consistent position angles on both sides, but the redshifted part is much brighter in both CO and SiO (Fig. 4.3). The CO outflow has a moderate opening angle of 45°; the blueshifted part of the SiO emission is only detected several thousands of au away from the source as a clump of emission. This is very different from the bright, highly-collimated structures with several well-defined bullets on the redshifted side of the jet. HCN and H_2CO are only faintly detected toward SMM1-b at low-velocities.

The SMM1-d outflow has a peculiar morphology (Fig. 4.3); the redshifted side is seen in three distinct clumps starting as far as 3000 au away from the SMM1-d protostar (Hull et al. 2017), while no blueshifted side is observed. The CO emission peaks at the nearest clump while the SiO, HCN, and H_2CO peak in the most distant one.

4.3.2 Velocity regimes

The high spectral resolution and high sensitivity observations of ALMA allow for the analysis of the different velocity components present in the outflows. Tafalla et al. (2010) define three velocity components in molecular outflows as follows: the slow wing is seen as a typical Gaussian profile and the fast wing shows up as a broad component added to this profile; and the transition between the two is smooth. The EHV component appears as a discrete peak at high velocities and is clearly separated from the wing profile.

To define boundaries between the velocity regimes, especially to distinguish the slow from the fast wing, the examination of multiple molecules is needed. We note that $C^{18}O$ spectra within the Band 6 observations have been used to set constraints on possible contamination by the envelope emission in the outflow measurements, even though most of the envelope emission should be resolved out. Spectra of $C^{18}O$ of regions outside the outflow positions were used to assess, with the naked eye, the velocity at which $C^{18}O$ is still significant. Those values are set as the inner velocity limit for the slow wing.

Tafalla et al. (2010) identify the transition between slow and fast wing by a decrease of intensity of H_2CO emission and an enhancement of SiO and HCN, relative to CO; where possible, the same criteria are used here. Defining the EHV regime is more straightforward as it

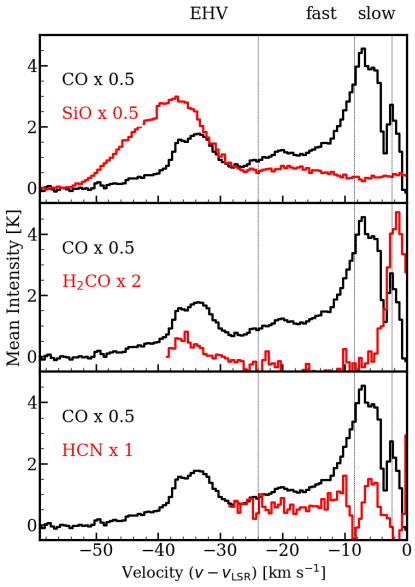


Figure 4.4: Spectra of CO (black) and SiO, H_2CO, and HCN (red) for selected part of blueshifted part of Ser-emb 8 (N) outflow, indicated in Fig. 4.2. The dashed lines show boundaries between different velocity components. Full set of spectra for the other sources is shown in the Appendix (Fig. 4.16).

is the beginning of the increasing CO and SiO flux at high velocities. Figure 4.4 shows spectra used to define the velocity regimes in Ser-emb 8 (N). Table 4.2 summarizes the velocity borders defined for each source.

Out of the five outflow sources observed, the EHV component is detected toward three sources. This is remarkable, as it is considered to be a rare phenomenon. The new detection of the Ser-emb 8 (N) high-velocity molecular jet, along with further analysis of EHV jets toward SMM1-a and SMM1-b (Hull et al. 2016, 2017), is presented here.

Figure 4.5 shows intensity maps of CO (2 – 1) integrated over velocity regimes defined in the previous section. Ser-emb 8 (N) has a high degree of symmetry between red and blueshifted emission at high velocities, with several peaks of emission, occurring at similar distances from the protostar on both sides. Three main clumps of EHV emission can be

Table 4.2: Boundary velocities of different components

Source	blue			red		
	EHV ($km\,s^{-1}$)	fast ($km\,s^{-1}$)	slow ($km\,s^{-1}$)	slow ($km\,s^{-1}$)	fast $km\,s^{-1}$	EHV ($km\,s^{-1}$)
SMM1-a	–	[-35,-8]	[-8, -1.5]	[2, 12]	[12, 50]	[50, 80]
SMM1-b	[-36, -29]	[-29, -8.5]	[-8.5, -2]	[2, 9]	[9, 25]	[25, 56]
SMM1-d	–	–	–	[2, 7]	[7, 29]	–
S68N	–	[-22, -14]	[-14, -2]	[2,5, 12]	[12, 25]	–
Ser-emb 8(N)	[-62,-24]	[-24, -8.5]	[-8.5, -2.5]	[2.5, 13.5]	[13.5, 35]	[35, 58]

Notes. Velocities are given after subtracting the systemic velocity of the cloud v_{lsr} = 8.5 km s^{-1}.

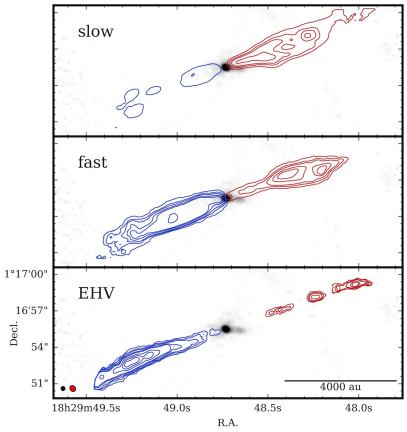


Figure 4.5: Integrated intensity maps of CO for different velocity regimes overlaid on Band 6 continuum in grayscale for Ser-emb 8 (N). The emission is integrated over the velocities listed in Table 4.2. The synthesized beams of the CO (red) and continuum (black) are showed in bottom-left corner of EHV plot with sizes 0.″35 × 0.″33 and 0.″55 × 0.″45 for continuum and CO, respectively. The contours are [3, 6, 9, 15, 20, 40, 60, 80, 100] times the rms value. The rms values for each velocity channel, which are blueshifted and redshifted in K km s^{-1}, are slow [18.3, 13.7], fast [3.1, 4.5], EHV [1.7, 1.4].

distinguished at 1500, 4000, and 6000 au away from the central protostar, although each of those clumps can be split into a more complex structure.

A similar bullet-like structure is observed toward the SMM1-b source in its redshifted jet, with bullets at roughly 1000, 3000, 5000, and 7000 au. The redshifted bullets seem to have only a single blueshifted counterpart - the furthermost EHV component at ∼ 7000 au (Fig. 4.18).

The EHV component from SMM1-a is very different from that of the first two jets described. It resembles a continuous stream emerging very close to the protostar, rather than forming discrete bullets. Hints of redshifted EHV emission that are further away are present as far as 7000 au from the protostar, although they are significantly off-axis compared with the stream that is close to the protostar; this may suggest precession, as discussed by Hull et al. (2016). No corresponding blueshifted EHV emission is seen toward this source, which is in contrast to the slow and fast wing gas (Fig. 4.17).

S68N shows no signs of the EHV component. (Fig. 4.20). In the case of the SMM1-d outflow (Fig. 4.19), it is difficult to assign the velocity components described above because almost all emission is confined to the low-velocity stream. SiO and HCN seem to follow CO in the spectral profile, and no enhancement is seen at higher velocities, but the CO profile appears broad and therefore slow and fast wing components are assigned. EHV emission is not present toward this source.

4.3.3 Chemical abundances in velocity components

Probing the composition of the wind at different velocities can shed light on physical conditions within the outflows, since a change in velocity also triggers a change in temperature and density. Moreover, a contrast between the chemical composition of wing and jet compo-

nents can also point to a different physical origin of the outflowing gas (Tafalla et al. 2010), and thus help us to understand the mechanism of the EHV jet formation and its interaction with entrained and quiescent gas.

Analysis method

The emission from each pixel inside a region defined by hand was summed in order to measure the abundances in each flow. The region was defined based on the extent of the low-velocity CO emission for the red and blueshifted parts of the outflow separately. These regions were then consistently used for all molecules and all velocity regimes. We calculated an integrated intensity of every pixel within the region, with the integration going from fixed $v_{\rm in}$ to $v_{\rm out}$ specified for each velocity regime (see Table 4.2).

Assuming that the emission is optically thin, the column density of the molecule in each pixel is computed as:

$$\frac{N_u}{g_u} = \frac{\beta \nu^2 \int T(v) dv}{A_{ul}} \ , \tag{4.1}$$

where $\beta = 8\pi k/hc^2$, ν is frequency, A_{ul} is the Einstein coefficient of a transition, g_u is the degeneracy of the transition, and $T(v)$ is an intensity of the emission in Kelvin in a single channel of velocity, v, with dv being a width of a channel. For a given excitation temperature, the column density of the molecule in a pixel is then:

$$N_{\rm tot} = N_u \times Q(T) \left[g_u e^{-E_u/kT} \right] , \tag{4.2}$$

where $Q(T)$ is the partition function at the assumed excitation temperature. Since only a single transition of each molecule was observed, it is not possible to derive an excitation temperature from these data. The CO excitation temperature is set to 75 K, based on statistics of excitation temperatures for low-mass protostars (Yıldız et al. 2015; van Kempen et al. 2009), which show that the bulk of the low-J CO emission can be fit with this value.

The assessment of excitation temperatures for other molecules is not straightforward. Tafalla et al. (2010) performed an LTE analysis of all molecules included in this work for several transitions and obtained a very low values of $T_{\rm ex}$ of $\sim$ 7 K. However, their analysis was performed using low-energy transitions. Nisini et al. (2007) show, based on SiO observations for a broader range of $E_{\rm up}$, that the conditions in the outflow may exhibit much higher kinetic temperatures. Their work shows an increase in temperature (up to 500 K) and density (up to 10^6 cm^{-3}) for the high-velocity jet, which is consistent with the values derived from CO *Herschel* data (Karska et al. 2018). For SiO, H_2CO, and HCN we ran RADEX (van der Tak et al. 2007) calculations to constrain excitation temperatures under the conditions expected in the protostellar outflow ($n_{H2} = 10^4 - 10^6$ cm^{-3}; $T_{kin} = 75 - 700$ K; $\Delta v = 10$ km s^{-1}). The extreme excitation temperatures found this way (low and high, see the column $T_{\rm ex}$ in Table 4.3) are used to calculate the column densities and associated uncertainties for those molecules. The excitation temperatures of the SiO, H_2CO, and HCN are lower than the expected kinetic temperatures as the critical density of the transitions are high, see column $n_{\rm crit}$ in Table 4.3. The low critical density of the CO transition justifies the assumption that its excitation temperature is equal to the kinetic temperature.

Optically thin emission is assumed for all the molecules. SiO emission has been suggested to be optically thick for the outflowing gas (Lee et al. 2008; Cabrit et al. 2012). Our calculations with RADEX show that within the conditions expected in the outflows, the SiO 5–4 emission reaches $\tau \sim 0.1$ only for high gas densities $n_{H2} = 10^6$ cm^{-3} at low temperatures $T_{kin} = 75$ K for the column densities inferred here (Section 4.3.3; Tables 4.5-4.9. High optical depths are only

Table 4.3: Outflow molecules

Molecule	J_U - J_L	Frequency [GHz]	n^a_{crit} [cm^3]	E_{up} [K]	T_{ex} [K]	SMM1 Beam	SMM1 RMS [mJy/bm]	Emb8 Beam	Emb8 RMS [mJy/bm]
CO	2-1	230.538	2.7 x 10^3	16.6	75 – 700	0.″53x0.″43	3.2	0.″54x0.″45	2.5
SiO	5-4	217.104	1.7 x 10^6	31.3	9 – 47	0.″54x0.″43	4.8	0.″55x0.″45	3.5
H_2CO	$3_{(0,3)}$-$2_{(0,2)}$	218.222	4.7 x 10^5	21.0	8 – 46	0.″54x0.″42	4.1	0.″54x0.″45	3.4
HCN	1-0	88.631	2.3 x 10^5	4.3	12 – 41	0.″54x0.″41	2.3	0.″60x0.″56	3.5

[a] Critical densities from (Jansen 1995) calculated in the optically thin limit for T_{kin}

found with our RADEX calculations for much narrower linewidths, but all the lines observed within our sample are broad.

The H_2CO can become optically thick for high T_{kin} = 700 K; regardless of gas density. Therefore if the emission comes from the highest velocity material, the abundance of H_2CO may be underestimated. For the column densities we infer that HCN 1–0 emission seems to be optically thick regardless of the conditions in the shock, and thus abundances of this molecule should be treated as lower limits.

For CO, our RADEX calculations show that $\tau \sim 0.3$ for the low-velocity gas with $T_{kin} \sim 75$ K. Dunham et al. (2014a) suggest that CO lines can become optically thick at low velocities (< 2km s^{-1}). By excluding channels at the lowest velocities using $C^{18}O$ as a tracer of the dense gas, we mostly probe the optically thin gas as the opacity rapidly decreases with velocity for CO wings (Yıldız et al. 2015; van der Marel et al. 2013; Zhang et al. 2016).

Column densities and abundances

After calculating the column density in each pixel, the average of the column density within the pre-defined region was calculated from only those pixels with a signal above 3 σ. Calculated values for each molecule are summarized in Tables 4.5-4.9, where the boundary values calculated for the minimum and maximum T_{ex} are reported.

Abundances shown in Fig. 4.6 and 4.7 were obtained from the column density calculated for a mean temperature between the two extreme T_{ex} reported for each molecule in Table 4.3. To obtain the abundance with respect to CO, this column density was divided by the column density of CO calculated for T = 75 K. The CO column density was measured only in the region in which the emission from both molecules is above 3σ.

Figure 4.6 shows that the molecular abundances relative to CO change with velocity for each source. SiO increases in relative abundance from the slow to the fast wing for the redshifted SMM1-b outflow and both sides of the Ser-emb 8 (N) outflow. For the blueshifted Ser-emb 8 (N) flow, the abundance continues to rise toward the EHV regime, while it remains relatively constant for redshifted SMM1-b and Ser-emb 8 (N). H_2CO is primarily associated with low-velocity gas, and it disappears in the fast wing for all sources. The only outflow to have EHV H_2CO emission is the blueshifted part of the Ser-emb 8 (N) outflow, where H_2CO reappears in the EHV jet with a relative abundance to CO around two times higher than in the slow gas. HCN is present in most of the outflows in both the slow and fast wing, but it is never present in the EHV gas.

Even within the same velocity regime, the emission may come from different spatial regions, thus the analysis of the abundances over the entire outflow introduces additional uncertainties. Therefore, for the clearest case of the EHV jet, Ser-emb 8 (N), we also measured the molecular abundances along the different positions of the outflow in order to probe local abundances.

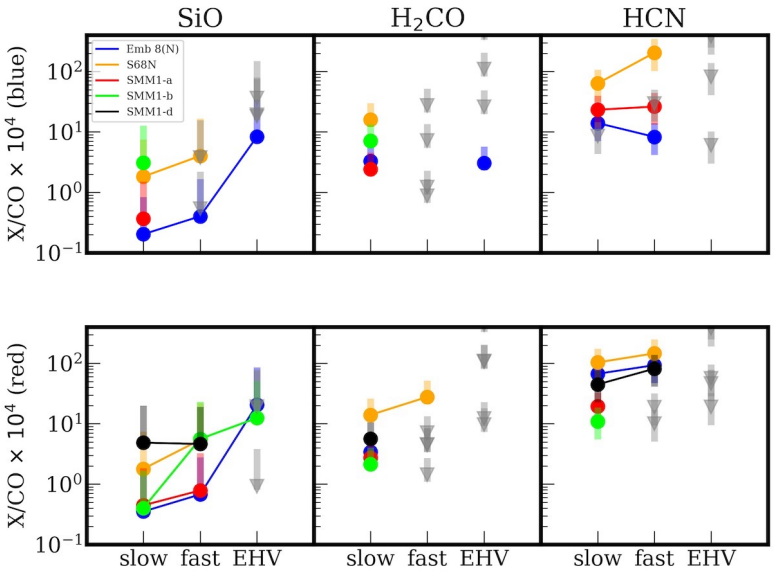


Figure 4.6: Molecular abundances with respect to CO scaled by 10^4 for blueshifted (top) and redshifted (bottom) part of outflow for all sources. Gray triangles represent upper limits. Points on the plot show values calculated for the mean T_{ex} of the range defined for each molecule, see Table 4.3. Error bars represent the column densities calculated for minimum and maximum values of the excitation temperature. To obtain the abundance of the given molecule, the column density was divided by the CO column density (for T_{ex} = 75 K.) measured in the region in which the emission from the molecule was above 3σ. The HCN emission is likely optically thick and therefore the abundance should be treated as a lower limit.

Figure 4.7 shows molecular abundances measured at three different positions on both sides of the Ser-emb 8 (N) outflow with regions defined appropriately to capture all of the lower-resolution SiO emission at the position. A remarkably similar behavior of SiO relative to CO can be noted on both sides of the outflow. For the fast wing gas, SiO abundance increases with distance from the protostar up to the bullet at 4000 au and then it disappears. In the EHV gas, the highest SiO abundance is observed close to the protostar, and then it drops with distance to the protostar by more than an order of magnitude.

The furthermost region, associated with the CO bullet, is depleted in all of the molecules except CO. The intermediate region at 4000 au appears as the most abundant in molecules, with HCN and SiO increasing for the slow and the fast wing. The H_2CO abundance is similar in the regions where it is detected.

To highlight the variations in the abundance ratios, maps of the SiO to CO ratio in the blueshifted part of the Ser-emb 8(N) are shown in Fig. 4.8. Only the blueshifted part is shown as an example since the significant part of the redshifted EHV jet in SiO has been observed only at lower spatial resolution. It is clear that for the fast wing, the SiO/CO ratio peaks at a significant distance from the protostar (3000 au; corresponding to dynamical age of 500 years for a 30 km s^{-1} outflow). In the EHV jet, the SiO/CO ratio peaks at a similar distance

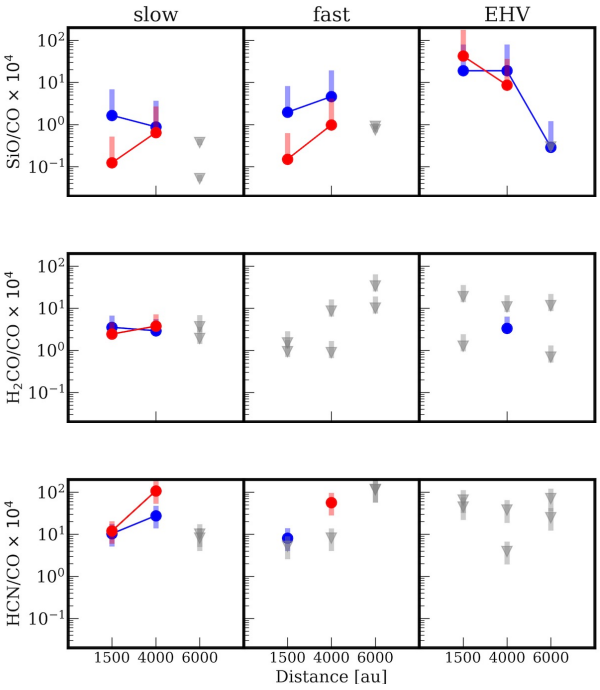


Figure 4.7: Molecular abundances with respect to CO scaled by 10^4 for Ser-emb 8 (N). The distance from the protostar is on the x-axis. Panels from left to right are for the slow wing, the fast wing, and the EHV component. The abundances measured for three different regions along the outflow are shown for blueshifted and redshifted parts of the outflow separately. Abundances are measured in the same manner as in Fig. 4.6. The HCN emission is likely optically thick and therefore the abundance should be treated as a lower limit.

as in the fast wing and then decreases.

4.3.4 Outflow force

Detection of the extremely high-velocity molecular jets provides a unique opportunity to probe the fastest and the most collimated part of the outflowing material. Quantifying the distribution of kinetic energy and mass among the different velocity components sheds light on their kinematic relationship, specifically determining if the jet is the driving force of the slow outflow.

The mass of the gas must be derived from the number of molecules (see Sect. 4.3.3). The area of the pixel, times the total number of molecules within pixel $N_{tot,}$ times the ratio of $H_2/CO = 1.2 \times 10^4$ (Frerking et al. 1982) with a molecular weight $\mu = 2.8$ that takes helium into account (Kauffmann et al. 2008), times the mass of the hydrogen atom m_H gives the amount of gas mass in a pixel (Yıldız et al. 2015):

$$M = \mu m_H A \frac{H_2}{CO} N_{tot} \ . \tag{4.3}$$

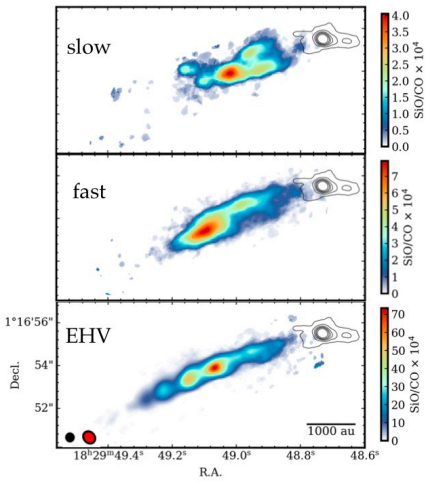


Figure 4.8: Maps of SiO/CO ratio for blueshifted part of Ser-emb 8(N) outflow for each velocity component. For the EHV component, only the channels for which SiO emission was obtained at high spatial resolution are taken into account (< 40 km s^{-1}). The synthesized beams of the CO (red) and continuum (black) are shown in the bottom-left corner of EHV plot with sizes 0.″35 × 0.″33 and 0.″55 × 0.″45 for continuum and CO, respectively. The black contours show 1.3 mm continuum emission.

The momentum of the outflowing material can then be defined accordingly:

$$P = M \times v_{\rm max} \ . \tag{4.4}$$

We define the distance from the protostar to the edge of the integration region as $R_{\rm lobe}$. It is important to note that the area of the ALMA observations in all cases, except for SMM1-d and Ser-emb 8 (N), does not cover the full extent of the outflows, as evident in single dish observations (Dionatos et al. 2010; Yıldız et al. 2015). For that reason, parameters like outflow mass or momentum do not provide information about the overall gas mass and kinetic energy content in the flow, but they are rather local values or lower limits to those; the outflow force, on the other hand, is dependent on $R_{\rm lobe}$ and can be treated as a more general value under the assumption that the outflow force content does not significantly vary at larger scales (van der Marel et al. 2013).

The contribution of the different velocity components to the overall outflow force was computed for each side of the flow separately. In order to calculate the outflow mass loss rate, $\dot{M}$, it is convenient to make a velocity-weighted calculation per pixel since this is more sensitive to the velocity changes than using a single v_{max} for the total outflow; this is method M7, as described in van der Marel et al. (2013). According to this method, the Equation 4.1 changes as follows:

$$\left\langle \frac{N_u}{g_u} \right\rangle_v = \frac{\beta v^2 \int T(v) v dv}{A_{ul}} \ , \tag{4.5}$$

and the resulting velocity-weighted column density can be used to calculate the momentum in the same way as the column density is used to calculate the mass. Finally, the outflow

force in a pixel is given by:

$$F_{\rm out} = \frac{\dot{M}}{R_{\rm lobe}} v_{\rm max} \ . \tag{4.6}$$

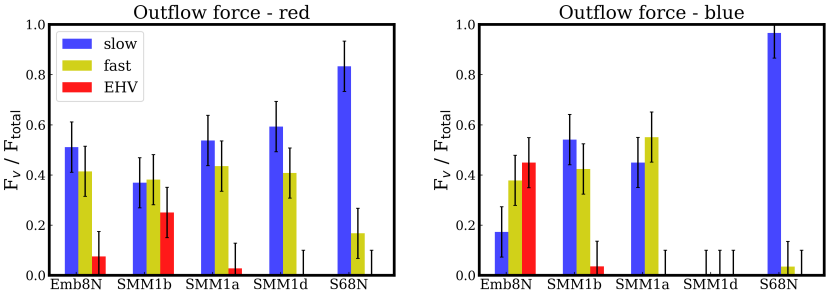


Figure 4.9: Fraction of outflow force in each velocity regime for blueshifted (top) and redshifted (bottom) sides of outflow for all sources. Approximate errors of 10% are shown, resulting from uncertainty in the borders between the velocity regimes.

Calculated values are presented in Tables C6-C10. As the choice of the velocity borders is done with the naked eye, it introduces uncertainty in the measurement of the outflow properties per velocity regime. Changing the velocity border by 5 km s^{-1} between the fast wing and the EHV jet typically results in a change of ~ 2–10% in the outflow properties.

Figure 4.9 shows the outflow force in each velocity regime relative to the total value. It shows that the contribution of the EHV jets to the total outflow force is between 5–40 % of the total outflow force. The fraction of the fast wing component is similar for all outflows with a detected EHV jet (30–50 %). The slow wing dominates the S68N outflow.

Inclination can introduce a significant uncertainty into the outflow parameters. For method M7, which has been adopted here to calculate the outflow force, Downes & Cabrit (2007) provide a multiplication factor that should be used to account for inclination (Table 6 in their paper); values of the correction factor range between 1.2 – 7.1. This correction largely affects the absolute values of the outflow forces; however, the relative ratios between the velocity components should not be affected (Eq. 9 in van der Marel et al. 2013)

Although the outflows probed here often extend to much larger scales than those probed by ALMA, the outflow force should be a conserved property. Yıldız et al. (2015) probed the outflow force of the SMM1 outflow in CO 3 – 2 and CO 6 – 5. They measured 1.5 and 8.7×10^{-4} M$_\odot$ yr^{-1} km s^{-1} for the blueshifted and redshifted emission, respectively, for CO 6–5 and 6.7 and 23×10^{-4} M$_\odot$ yr^{-1} km s^{-1} for CO 3 – 2 using the same M7 method, assuming a source inclination of 50°. From ALMA CO 2 – 1 (slow + fast wing), we obtain 1.4 and 11 $\times 10^{-4}$ M$_\odot$ yr^{-1} km s^{-1} for blueshifted and reshifted parts of the outflow, respectively. Our results are thus consistent with single-dish data within the typical uncertainties of a factor of a few even though no inclination correction was applied to ALMA observations. The inclination correction applied by Yıldız et al. (2015) is based on Table 6 of Downes & Cabrit (2007), and it resulted in an increase of the outflow force by a factor of 4.4. Based on the similarity of the outflow force results between ALMA and single-dish data, it appears that the observations obtained with the C43-1 configuration with a largest angular scale of 12″ were sufficient to recover the bulk of the flux from those outflows. It is, however, plausible that some of the emission has been resolved out, especially at low-velocities (see comparisons

between the interferometric and single dish observations Yıldız et al. 2015; Tafalla et al. 2017). The similarity of the obtained outflow force values could be coincidental and related to the increased sensitivity of the ALMA observations.

4.4 Discussion

4.4.1 Jet and wind kinematics. The driving force of outflows.

The exact origin of the large-scale outflows from protostars is still unclear. It is suggested that the narrow, highly-collimated jet from the protostar or the inner disk could power the entirety of the outflow (Raga & Cabrit 1993). However, models with jet bow-shocks that power the slow outflow fail to reproduce all of the observed kinematic features of the slow gas (Lee et al. 2002). Resolving the kinematic structure of the EHV bullets suggests, however, that a significant fraction of the momentum of the jet is ejected sideways, impacting the surrounding envelope (Santiago-García et al. 2009; Tafalla et al. 2017).

Directly studying the relationship between the outflow and jet is difficult, since the atomic and ionized jet is invisible in the same wavelength regime as the colder molecular outflows. Thus, studying protostars in their earliest stages of formation, when the jet is still mostly molecular, gives a unique opportunity to study the relation between the outflow and the jet. Our ALMA observations allow us to study three remarkable outflows with EHV jet components within one cloud. Moreover, it is often difficult to study outflows at high resolution since they propagate to vast distances very rapidly. Only a few of them have been studied to their full extent with ALMA (e.g., Arce et al. 2013). While it appears that the SMM1-a,b, and S68N outflows have indeed already propagated to tens of thousands of au (Dionatos et al. 2010; Yıldız et al. 2015), it is plausible that Ser-emb 8 (N) outflow is not as apparent from the observations with a larger field of view (Dionatos et al. 2010; Hull et al. 2014) . This source thus provides an opportunity to study the full extent of the outflow.

The relation between the different components here is quantified by measuring the outflow force in three velocity components: slow and fast wing, and in the EHV jet. From Fig. 4.9 it is apparent that only for the blueshifted jet of Ser-emb 8 (N) is the EHV contribution (45%) to the total outflow force higher than that of the slow and fast wing components. The contribution of the EHV components to the outflow force in the other two sources is smaller than the contribution from the wing. Based on these findings, it seems that the force contained in the jet is generally not enough to power the total observed outflowing gas.

One of the explanations for the missing force is that the jet becomes atomic as the source evolves. Thus, measurements of the molecular component alone can underestimate the total mass of the gas. Such a scenario is supported by the observations of atomic oxygen from *Herschel* (van Kempen et al. 2010; Nisini et al. 2015). For a small sample of protostars, Nisini et al. (2015) show that the atomic jet becomes an important dynamical agent in more evolved sources (late Class 0/ Class I), while younger outflows have a significant fraction of the jet in the form of molecular gas. Typical mass-loss rates in the jet derived from atomic oxygen for the Class 0 sources targeted by Nisini et al. (2015) are between $1–10 \times 10^{-7}$ $M_\odot$ yr^{-1} whereas for the one Class I source HH46 they find $2–8 \times 10^{-6}$ $M_\odot$ yr^{-1} , which shows that the atomic jet becomes more important at the later stages of protostellar evolution.

The mass-loss rates of the molecular jets presented here are 7.0, 3.9, and 15.0 $\times 10^{-7}$ $M_\odot$ yr^{-1} for Ser-emb 8 (N), SMM1-a, and SMM1-b, respectively. The atomic jet of SMM1-a has been probed in [O I] (Mottram et al. 2017) and [Fe II] (Dionatos et al. 2014). From these tracers, both authors find a consistent mass flux of $2–4 \times 10^{-7}$ $M_\odot$ yr^{-1}, which is smaller than our

molecular value by a factor of two. The total mass-loss of the slow and fast wing combined for SMM1-a is 1.4×10^{-5} $M_\odot$ yr^{-1}. While these results are consistent with the SMM1-a jet that is mostly molecular, as is expected for a young Class 0 source, it appears that the jet cannot be solely responsible for driving the outflow, even when the atomic component is taken into account.

Another explanation for the missing force in the molecular jet could be that the excitation temperature of the gas in the jet has been underestimated. Observations of high-J CO and SiO suggest that excitation conditions change at higher velocities, with density and gas temperature rapidly rising (Nisini et al. 2007; Lefloch et al. 2015; Kristensen et al. 2017). The assumed temperature here is 75 K, which is reasonable for a slow wing (Yıldız et al. 2015; van Kempen et al. 2016). However, if the jet has different excitation conditions with higher temperatures, the CO mass of the gas is underestimated. To test this possibility, we compare the change in relative contribution to the total outflow force for two other sets of temperatures. In one example we increased the temperature of the fast wing to 250 K, and the EHV temperature to 300 K — this is the temperature of the warm component identified with PACS observations (Karska et al. 2013, 2018; Kristensen et al. 2017; Dionatos et al. 2013). In the second case we used 250 K for the fast wing again, and increased the temperature of the EHV component to 700 K, which was fit as the temperature of the hot component in PACS. In Fig. 4.10 results of this comparison are presented for three cases for SMM1-a. The fraction of the EHV contribution to the total outflow force increases from 3% to 10%. A significant increase is seen in the fast wing with a change from 44% to 62% . For the case of SMM1-a, it does not change the general picture of the EHV jet that contributes only a small fraction of the outflow force.

Fig. 4.11 shows how the outflow force contributions change for all of the sources in the redshifted outflow if the temperature is changed to 75 K, 250 K, and 700 K, for the slow wing, the fast wing, and the EHV jet, respectively. The SMM1-b EHV jet now contributes the majority of the outflow force, while for Ser-emb 8 (N), the fast wing becomes the primary component. This indicates that if the temperature of the gas in the jet is higher than assumed for the slow wing (75 K), the total mass of the gas and hence other properties derived from it can be significantly higher.

Nonetheless, the example of Ser-emb 8 (N) shows that young outflows that have not propagated to larger distances yet and, therefore, have a smaller number of shocks along the jet, can have a significant fraction of the outflow force in the EHV gas. Likely, older sources like SMM1-a that are more affected by precession have a more complicated jet-outflow relation and thus the interpretation is less straightforward.

While the SMM1-d outflow also lacks EHV emission, the contribution of the fast wing to the total outflow force is substantial (~40%). Other characteristics of this source – for example, its bullet-like structure and lack of the well-defined cavity walls in CO – suggest a peculiar nature of the outflow, and thus its lack of EHV emission cannot be attributed to the more evolved nature of the outflow.

For both SMM1-d and S68N, there is potentially another reason why the EHV component is not detected: inclination. While for S68N we do not see a clear bullet-like structure, for SMM1-d it might well be that the bullets are seen moving at very high velocities, but in the plane of the sky. This is consistent with the fact that we see a significant blueshifted component on the redshifted side of the flow, which is consistent with the sideways expansion.

We can see an evolution of the outflow force distribution among the different velocity components, which cannot only be attributed to the chemical changes in the jet. One way

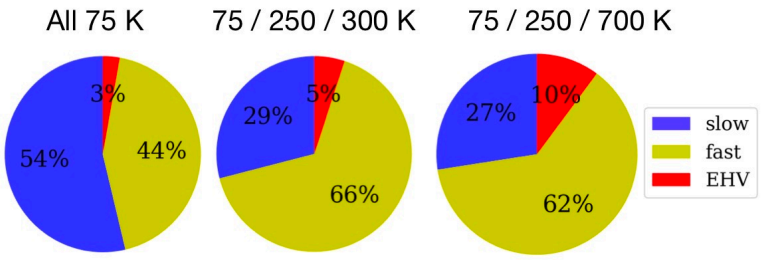


Figure 4.10: Fraction of outflow force in three different components (slow, fast, EHV) of redshifted SMM1-a outflow for three different CO excitation temperatures used to calculate outflow force. On the left plot all of the components have 75 K; in the middle plot, slow wing has 75 K, fast wing has 250 K, and EHV jet has 300 K; on the right plot, slow wing has 75 K, fast wing has 250 K, and EHV jet has 700 K. The slow wing is yellow

to explain this is that a significant amount of outflow force is deposited in the fast and the slow wind very early in the protostellar evolution. Additional launching mechanisms like a wide-angle wind could also contribute to the bulk force released from the protostellar system.

4.4.2 Relations with temperature and velocity components from HIFI

Understanding the far-infrared (FIR) emission from outflows is crucial to quantify and describe cooling processes around young protostars, as the majority of cooling occurs in this regime (Ceccarelli et al. 1996; Karska et al. 2013, 2018). The *Herschel Space Observatory* provides new insights into the kinematics via FIR line profiles from the HIFI instrument (e.g., Tafalla et al. 2013; Kristensen et al. 2013; Mottram et al. 2014).

Specifically, observations with HIFI of large numbers of low-mass protostars have shown that the high-J CO line profiles of shocked, outflowing gas can be decomposed universally into two velocity components. Subsequent radiative transfer modeling has linked these velocity components to the physical components of the protostellar system (Kristensen et al. 2017). Unfortunately, the spatial information from *Herschel* is limited, and single-dish low-J CO data show a different distribution from that of the high-J lines, as the low-J CO observations are sensitive to more extended emission (Santangelo et al. 2012; Tafalla et al. 2013). ALMA data are sensitive to small scale emission, and thus offer the opportunity to relate the spatially unresolved components of the HIFI emission (estimated to arise on a few hundred au scales, Mottram et al. 2014) with ALMA observations of low-J lines, allowing us to unveil the physical origin of the emission observed with HIFI.

Here we compare the ALMA observations of CO 2 – 1 toward Serpens SMM1 with *Herschel*/HIFI observations including CO 16 – 15, CO 10 – 9, and several water transitions (Yıldız et al. 2013; Kristensen et al. 2012; Kristensen et al. 2013; Mottram et al. 2014). Interferometric observations resolve the SMM1 system into at least five protostars with three active outflows; this can help to disentangle the various components of the system blended into one HIFI beam of typically 20″. Fig. 4.15 shows three examples of comparisons between HIFI and ALMA spectral profiles.

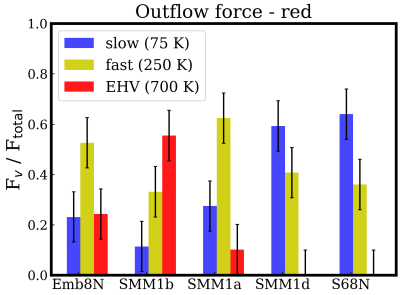


Figure 4.11: Fraction of outflow force in each velocity regime, for redshifted side of outflow for all sources. Approximate errors of 10% are shown, resulting from uncertainty in the borders between the velocity regimes. The excitation temperatures used to calculate the outflow force are: 75 K for the slow wing, 250 K for the fast wing, and 700 K for the EHV jet.

There are some similarities between the HIFI velocity components for the SMM1 system and the ALMA low-J CO spectra. The offset HIFI component is seen in the SMM1-a spectra and is spatially linked to the ridge of the blueshifted emission of the SMM1-a outflow. The broad component appears similar to the fast wing CO 2 – 1 component and is present at both SMM1-a and SMM1-b outflows. The EHV bullet seen in water transitions from HIFI can be associated spatially with ALMA CO SMM1-b bullets, but it peaks at higher velocities than the SMM1-b jet. While it is impossible to spatially resolve the location of the water emission, this result suggests that water is formed in the higher velocity shock than CO or SiO. A detailed discussion of the comparison of ALMA observations with *Herschel* data is presented in the Appendix 4.A.

4.4.3 The case of Ser-emb 8 (N): a pristine outflow-jet system

Many characteristics of Ser-emb 8 (N), such as its narrow opening angle of 25° and the high contribution of the molecular jet to the total force of the outflow, show that it is likely the youngest of the sources in the sample and therefore the best example of a pristine molecular jet and outflow system. It is also likely that we see most of the outflow within the ALMA field of view. This is in contrast to SMM1-a and b, which are known to extend to much larger scales (Davis et al. 1999; Dionatos et al. 2010). If so, the most distant bullet at 4500 au would have a dynamical age of only 350 years for a velocity of 60 km s^{-1}. In this section, we explore the spatial distribution of the analyzed velocity components of other molecules of the Ser-emb 8 (N) outflow. Figure 4.12 shows the spatial distribution of the fast and EHV velocity components for the CO, SiO, H_2CO, and HCN.

One thing that is immediately apparent is the very similar shape of the SiO and HCN emission, which both form a redshifted bow-shock in the fast velocity component.

On the blueshifted side, the shape of emission does not resemble a bow-shock, but both HCN and SiO appear mostly off the jet axis. The SiO and HCN bow-shock on the red side (Figs. 4.12d,e) surrounds one of the EHV bullets seen in CO (Figs. 4.12a). The weak blueshifted emission on the redshifted side of the outflow seen in SiO and HCN (velocities from −5 to −2 km s^{-1} with respect to the source velocity) is consistent with the sideways expansion of the gas due to interaction with the internal shock in the EHV bullet (Tafalla et al. 2017). This suggests a relation between EHV jets with the fast wing. Sideways ejections of

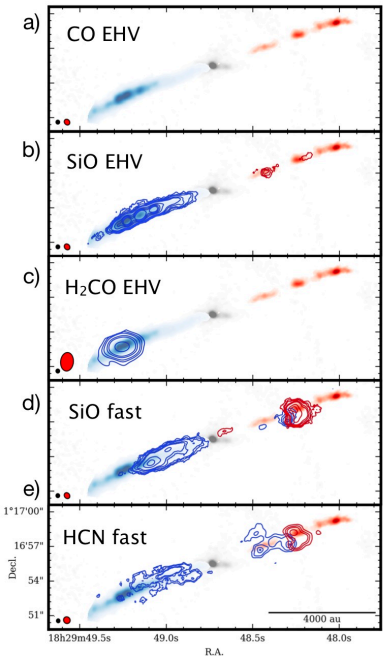


Figure 4.12: Schematic view of spatial distribution of different molecules and their relation with different velocity components in Ser-emb 8 (N) outflow. a) In colorscale the CO moment 0 map is shown integrated over the EHV velocities, also overlaid on the following plots; b) contours are SiO EHV emission captured at high spatial resolution, i.e., below 40 km s^{-1}; c) H_2CO EHV emission (available only at low spatial resolution - synthesized beam is 1.″65 × 1.″13); d) SiO fast wing emission; e) HCN fast wing emission. The synthesized beams of continuum (black) and contour map (red) is shown in bottom-left corner.

the EHV gas can create slow shocks along the cavity walls. *Herschel* line profiles show that when the source exhibits EHV emission, the broad component is always present (Kristensen et al. 2012). The nearly identical shape of the SiO and HCN emission in the fast wing can be related to the same physical process that is responsible for the production of the SiO and HCN gas, as both species are enhanced in shocks (Schilke et al. 1997; Pineau des Forêts et al. 1990).

The most distant EHV bullet at 6000 au – corresponding to the dynamical age of 500 yrs – is seen mostly in CO with SiO emission that is much fainter compared with the "younger" bullets. It is possible that grains have started to reform, causing the SiO depletion from the gas. The decrease in the SiO emission can, however, also be caused by the change in the excitation conditions along the jet: the density and the temperature of the gas likely decrease in the more distant bullets (Nisini et al. 2007).

H_2CO is seen in only one bullet on the blueshifted side of Ser-emb 8 (N). This H_2CO bullet is coincident with the CO peak of intensity along the jet at ~ 4000 au. Thus, the presence of H_2CO can be related to the total density of the gas at that position - CO formation in the EHV jet is enhanced with density (Glassgold et al. 1991).

4.4.4 Chemistry of the velocity components

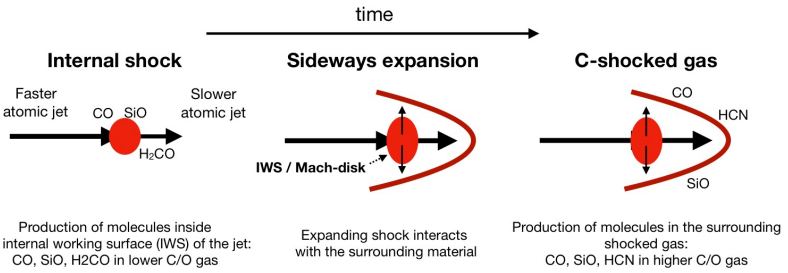


Figure 4.13: Cartoon presenting interaction between molecular bullet and surrounding material. From the left to right a time evolution is shown starting with an internal shock within the molecular jet where atomic gas produces molecules inside a high-density internal working surface. As the bullet expands both forward and sideways it creates a shock with the surrounding ambient material; in the shocked gas, molecules are formed. The molecules observed in the EHV bullet are produced in lower C/O gas originating from the inner Mach disk, while the molecules from the shocked gas are formed from ambient gas with higher C/O ratio.

The first extensive chemical survey of the molecular jets revealed differences in the chemical composition of the slow and fast components and the EHV jet (Tafalla et al. 2010), the main conclusion being that the EHV component has more oxygen-containing molecules than the slow and the fast wing gas, which are carbon-rich (abbreviated as a higher C/O ratio). The high-resolution interferometric observations presented here are consistent with these single-dish studies: SiO abundances are enhanced with velocities up to those of the EHV jet for Ser-emb 8 (N) and redshifted SMM1-b. H_2CO appears in one EHV bullet of Ser-emb 8(N). The HCN is present in the slow and the fast wing, but it does not appear in the EHV jet. Unique to our analysis is the ability to not only study the spectra but also relate the abundances with different spatial and velocity components of the outflow.

The spatial distribution of molecules can indeed provide essential clues about the relation between different velocity components. The bow-shock structure in the redshifted part of the Ser-emb 8(N) outflow (fast wing, Fig. 4.12) is co-spatial with a gas bullet moving at much higher velocities. The interaction between the EHV jet and the ambient gas, and the origin of the chemical composition of the fast wing component and the jet, is described in Fig. 4.13. If the jet indeed has a low C/O ratio (Tafalla et al. 2010), the production of oxygen-bearing molecules takes place in the internal working surface of the jet. Then, the (sideways) expanding internal shock interacts with the surrounding ambient material (with a higher C/O ratio) where the production of other species, such as HCN, can take place.

Our results can also be compared with interferometric studies of the prototypical chemically rich outflow L1157 (e.g., Gueth et al. 1996; Arce et al. 2008; Codella et al. 2009, 2017), which is also known to have a molecular jet (Podio et al. 2016). The L1157 data show a chemical evolution with time along the outflow, while the jet impacts current shocked gas.

SiO

SiO is enhanced consistently for Ser-emb 8 (N) from the slow to the fast wing and then to the EHV jet, where it peaks in abundance. The enhancement of SiO in supersonic gas

is commonly explained by sputtering and grain destruction, and the subsequent formation of the SiO in the gas phase through reactions of Si with OH in the shocked gas (Schilke et al. 1997; Gusdorf et al. 2008a,b). If the high-velocity jet is ejected in an atomic state thus containing ample atomic Si, SiO molecules can also be efficiently formed in the internal shocks in the jet that triggers the density enhancement (Glassgold et al. 1991; Tafalla et al. 2010).

There are differences among the SiO velocity profiles of the various sources. Ser-emb 8 (N) and SMM1-b, the two sources with the EHV emission, show weak emission at low velocities, with SiO emission peaking at high velocities. Such offsets in the peak of the emission can be caused by shock enhancement of the SiO abundance,which is consistent with models described above. S68N and SMM1-d, on the other hand, have SiO profiles that peak close to the systemic velocity and then decrease with velocity.

Nisini et al. (2007) see a similar dichotomy with the profiles for two protostellar outflows: L1448-mm, the prototypical EHV source, and L1157-mm, a classic example of the chemically rich outflow, with EHV bullets detected by Tafalla et al. (2015) and Podio et al. (2016). These authors attribute this difference to the temporal evolution of the outflow, where young shocks show offset peak profiles, while wing profiles peaking at low velocities correspond to the gas after the passage of a shock, where gas slowed down but retained its enhanced SiO abundance (Jiménez-Serra et al. 2009). It is possible that this temporal evolution can be observed within one outflow. The SiO abundance along the Ser-emb 8 (N) outflow decreases with the distance from the source for the EHV jet. On the other hand, the fast wing abundance increases with the distance from the source up to $\sim$ 4000 au and then decreases toward the most distant CO bullet. This can be interpreted as the SiO being produced in the EHV gas and then consistently slowing down as the shell of the internal shock is expanding.

The similarity of the HCN and SiO emission in the bow shock of the Ser-emb 8(N) poses a challenge to this scheme. Their similar spatial and kinematic structure in the fast wing would suggest a similar origin; however, HCN is not seen in the EHV gas, and therefore its formation in the jet is unlikely. An alternative explanation for the SiO emission in the fast wing is a C−shock along the cavity walls. Fig. 4.13 presents a schematic of this scenario. The formation of the SiO in the C−shocked gas is a process with a timescale of > 100 yr (Gusdorf et al. 2008a), which would explain an enhancement at some distance from the protostar. If the EHV SiO emission arises from the production in the dense atomic jet gas (Glassgold et al. 1991), this process would occur much faster, explaining the high EHV SiO abundance close to the protostar (Hirano et al. 2010; Podio et al. 2016). The observed H_2O line with HIFI, which appears faster than the EHV jet toward SMM1-b, can thus be interpreted as having been formed even earlier, that is, in the fastest component of the internal working surface of the jet.

H_2CO

Tafalla et al. (2010) detected H_2CO in EHV gas for the first time in only one source in their study of two EHV jets. In the case of L1448-mm, H_2CO is also accompanied by CH_3OH emission. In the slow wing, the H_2CO abundance swiftly decreases with increasing velocity, which is likely to be easily destroyed in shocks, similar to CH_3OH (Suutarinen et al. 2014). It is then remarkable that we see the H_2CO in the high-velocity bullet of Ser-emb 8(N) (see Fig. 4.12c). More recently, several transitions of H_2CO have been detected in the high-velocity component of the IRAS 2A outflow, while CH_3OH has only been seen at low velocities (Santangelo et al. 2015). Figure 4.14 compares CO and H_2CO spectra integrated toward the H_2CO bullet for Ser-emb 8 (N).

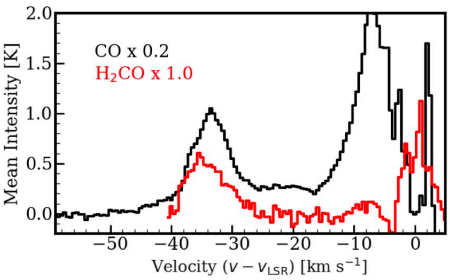


Figure 4.14: Spectra of CO (black) and H_2CO (red) of Ser-emb 8 (N) integrated on region where H_2CO high-velocity emission is present.

Surprisingly, H_2CO is seen in only one particular EHV bullet in the blueshifed jet of Ser-emb 8 (N). It is located at the peak of CO EHV emission but ahead of the SiO peak emission. The presence of the EHV H_2CO emission for one of the three sources, and exclusively on one side of the emission, is puzzling. Two main explanations can be considered. One is the hydrogenation of CO on the reformed post-shock grains and then the subsequent release from the grains (e.g., Watanabe et al. 2004; Chuang et al. 2016). Within the bandwidth of the ALMA observations, many complex organic molecules are detected toward the protostars SMM1-a and S68N, with their location indicating an origin in the warm inner envelopes of the protostars (Tychoniec et al. 2018a). Those molecules are not detected toward the position of the H_2CO EHV bullet. If the release from the ices were a mechanism that is responsible for the H_2CO emission at high velocities, one would expect the presence of other ice mantle components in the gas-phase. This is not seen in the case of this high-velocity bullet. Releasing H_2CO from the ices is usually associated with lower outflow velocities; toward the L1157 outflow, H_2CO is present in the shell of low-to-intermediate velocity gas. It is argued that the release of H_2CO from the ices can trigger formation of the complex organic molecules in the gas-phase (Codella et al. 2017). Again, this is not seen here.

An alternative explanation for the H_2CO emission in the high-velocity jet is gas-phase formation, mainly through the $CH_3 + O$ reaction (Dalgarno et al. 1973; Millar & Williams 1975) with CH_3 abundance enhanced due to the high temperature. In particular, the C + $H_2 \rightarrow$ CH + H reaction has a barrier of ~12000 K, with subsequent reactions of CH and CH_2 with H_2 leading to CH_3 having only somewhat smaller barriers (Agúndez et al. 2008; Bast et al. 2013). In this case, the abundance of the H_2CO increases from the slow wing to the EHV component by at least a factor of two; therefore, the mechanisms responsible for the production and excitation of H_2CO can be more efficient at higher velocities where temperatures are higher. A high abundance of atomic oxygen in the jet can further facilitate the reaction. This scenario would require the presence of some free atomic C in the jet, which would form H_2CO but not HCN before all of the carbon is locked up in CO.

HCN

HCN traces the most energetic outflows associated with young, Class 0 sources (Jørgensen et al. 2004; Walker-Smith et al. 2014). High temperatures and densities of the shocked gas are responsible for HCN production. The enhancement of the HCN emission in shocks arises

due to the H_2 + CN → HCN + H reaction (Bruderer et al. 2009; Visser et al. 2018), which has an activation barrier of 960 K (Baulch et al. 2005). Both models and observations suggest that orders of magnitude increase in HCN abundance for gas temperatures above 200 K (Boonman et al. 2001; Lahuis et al. 2007).

We see HCN present in the slow and the fast wing, but it is depleted in the EHV jet. However, it appears that the presence of the fast HCN and SiO strongly depends on the presence of the EHV jet, as both HCN and SiO are observed in the bow shock in which the EHV bullet is embedded. It appears that, as an EHV bullet is present and as it ejects gas sideways at locations where it can interact with the cavity wall, both HCN and SiO are produced in these lower velocity *C*–type shocks. This interpretation is straightforward only for Ser-emb 8 (N); it is much harder to interpret the HCN in SMM1, as no HCN emission is observed toward SMM1-b and very little in SMM1-a.

Tafalla et al. (2010) argue that HCN enhancement in the fast wing and depletion in the EHV jet is related to the atomic carbon abundance in the gas phase, specifically to a much lower C/O ratio in the EHV gas, which leads to the efficient formation of CO and SiO, but not HCN. It is unlikely that the gas in the EHV jet is colder than in the fast wing, so a temperature difference can not explain the lack of HCN in the EHV gas. Therefore our results support different chemical compositions of the EHV gas compared with the slow and the fast wings.

4.5 Summary

In this work, we use ALMA to study extremely high-velocity molecular jets in the Serpens Main region. The relationship between the fast jet and slow outflow is studied, in an attempt to unveil the chemical composition of the different velocity components. The conclusions are as follows.

Out of five observed outflows, three show the extremely high-velocity jet component. The high-sensitivity ALMA observations reveal that the EHV component in outflows from protostars is more frequent than previously thought.

The comparison of outflow forces between the slow outflow and EHV jet reveals that the observed force in the molecular jet is not sufficient to power the slow outflow in 3/5 sources. The most narrow and compact outflow (i.e., likely very young) in Ser-emb 8 (N) drives the jet with the highest EHV contribution of outflow force relative to the total energetic content of the flow. These results suggest an evolutionary sequence of the molecular emission from protostellar outflows where the EHV component is present in the youngest sources. The EHV and the fast wing components then subsequently disappear as the protostellar system evolves. Even after accounting for the atomic component, we conclude that the outflow force in the jet component is not sufficient to carry the entirety of the flow for all observed sources. This shows that a large fraction of the outflow force could already have been deposited in the fast and the slow wind, or that another launching mechanism (i.e., a wide-angle wind) is also at play; however, the latter option cannot explain the bow-shock structures we observe in the fast wing component of Ser-emb 8(N).

The spatial distribution of the different molecular species is revealed in 0.″4 ALMA observations; we focus in particular on the newly reported EHV jet from Ser-emb 8 (N). The fast wing SiO and HCN emission on the redshifted side of this outflow resembles bow-shocks that surround the EHV bullet, which indicates a relationship between the fast wing and the sideways ejections of the EHV jet.

The chemical composition of the velocity components of the outflow has been probed. The SiO abundance is enhanced from the slow to fast gas; the HCN is present from slow

to fast wing but disappears in the EHV jet; and H_2CO is only seen in the slow gas and in one EHV bullet exclusively in the blueshifted part of the Ser-emb 8 (N) jet. These results are in agreement with the single-dish results from Tafalla et al. (2010) where the EHV jet has a lower C/O ratio than the entrained slow and fast gas. Consistent velocity profiles of both molecules suggest that gas-phase formation is a plausible explanation for H_2CO emission in the EHV jet. The HCN presence at the bow-shock (fast wing) is consistent with an increased temperature in the *C*–shocked region compared with the lower velocity gas. HCN depletion in the EHV gas can be associated with the lower C/O ratio in that gas.

The decrease in the SiO abundance in the EHV gas with distance from the protostar, combined with an increase in the fast wing, suggests that SiO produced in the EHV gas is slowed down, but remains abundant at lower velocities. The production of SiO and HCN in C-shocks (fast wing) after some time from the passage of the shock front, as expected by the models, provides an alternative explanation to an apparent temporal evolution of the abundances. We compare ALMA observations with the *Herschel*/HIFI velocity profiles of high-*J* CO and water, specifically by comparing the offset and broad components seen universally in the HIFI observations (Mottram et al. 2014; Kristensen et al. 2017) with the slow wing, the fast wing, and the EHV jets explored with ALMA CO 2 – 1 line profiles. The spatial location of the HIFI profiles is revealed; the fast wing has a similar profile to the HIFI broad component and EHV features are seen in both HIFI water emission and in ALMA spectra. However, the water EHV bullet peaks at higher velocities and is therefore formed first in the internal working surface of the jet.

Acknowledgements: The authors are grateful to the referee for comments that helped to improve the manuscript. ŁT would like to thank Benoît Tabone for stimulating discussions. This paper makes use of the following ALMA data: ADS/JAO.ALMA#2013.1.00726.S and ADS/JAO.ALMA#2016.1.00710.S. ALMA is a partnership of ESO (representing its member states), NSF (USA) and NINS (Japan), together with NRC (Canada), MOST and ASIAA (Taiwan), and KASI (Republic of Korea), in cooperation with the Republic of Chile. The Joint ALMA Observatory is operated by ESO, AUI/NRAO and NAOJ. Astrochemistry in Leiden is supported by the Netherlands Research School for Astronomy (NOVA), by a Royal Netherlands Academy of Arts and Sciences (KNAW) professor prize, and by the European Union A-ERC grant 291141 CHEMPLAN. The research of L.E.K. is supported by a research grant (19127) from VILLUM FONDEN. C.L.H.H. acknowledges the support of both the NAOJ Fellowship as well as JSPS KAKENHI grant 18K13586. This research made use of Astropy, a community-developed core Python package for Astronomy (Astropy Collaboration et al. 2013), http://astropy.org); Matplotlib library (Hunter 2007); NASA's Astrophysics Data System.

Appendix

4.A Relations with temperature and velocity components from HIFI

The comparison of ALMA CO 2–1 observations with HIFI high–J CO and H_2O line profiles is presented in Fig. 4.15. The HIFI CO 16–15 spectrum is plotted alongside three ALMA spectra in Fig. 4.15a„ one of which is averaged over the HIFI beam (13″) for CO 16 – 15, and two of which are averaged over the region dedicated to SMM1-a and SMM1-b but limited to the borders of the HIFI beam. The HIFI spectra are shown with the Gaussian offset component overlaid based on the fit from Kristensen et al. (2013).

The offset component for SMM1 is seen in all water transitions targeted by Mottram et al. (2014), and in CO 16 – 15 (Kristensen et al. 2013). At the same time, CO 10 – 9 does not show a clear offset component (Yıldız et al. 2013). This suggests high temperatures in the offset component, and indeed the offset profile has been linked to the hot gas component (700 K) as seen in the rotational diagrams from PACS observations (Karska et al. 2013; Green et al. 2013; Kristensen et al. 2017). Radiative transfer modeling of the physical conditions for this component (Kristensen et al. 2013) suggests that this emission comes from a small emitting area (~100 AU; 0″.25) with high densities (10^6-10^7 cm^{-3}).

Hints about the spatial origin of the offset component can be seen with ALMA: the offset component is likely associated with the prominent blueshifted emission from SMM1-a close to the source (Fig. 4.15a). This particular position has also been associated with a series of blueshifted water maser emissions (van Kempen et al. 2009) and a bright spot of ion emission in the near-IR (Dionatos et al. 2014). In Fig. 4.15b, the H_2O $1_{11} - 0_{00}$ spectrum is plotted with ALMA spectra: one is averaged over the HIFI beam (20″) for H_2O H_2O $1_{11} - 0_{00}$, and two are averaged over the region dedicated to SMM1-a and SMM1-b, but they are limited to the borders of the HIFI beam. The HIFI spectrum is shown with the broad Gaussian component that is overlaid based on the Mottram et al. (2014) fit. The redshifted broad component is seen mostly in the lower energy levels of water in the HIFI data (Mottram et al. 2014). It is explained by emission tracing warm (300 K) gas from the outflow cavity shocks, where the protostellar wind interacts with the outflow cavity walls (Kristensen et al. 2013; Mottram et al. 2014). It is also proposed that this component can trace the protostellar wind itself (Panoglou et al. 2012; Yvart et al. 2016). Figure 4.15b shows that ALMA CO 2 – 1 for SMM1-a and SMM1-b has a very similar line profile to the H_2O $1_{11} - 1_{00}$ in the fast wing component. Spatially, the emission is widespread, coming from both sources.

It is worth noting that the broad component is much more prominent in the redshifted part of the HIFI spectra; similarly, the EHV jets are associated only with the redshifted jets for both SMM1-a and b. This shows that the presence of the jet could be linked to the presence of the broad component, and possibly part of the component arises as the high-velocity jet material ejected sideways interacts with the outflow cavity walls.

The broad component from the HIFI water emission seems coincident spectrally with the fast wing component in CO 2–1. The chemical signatures of the fast wing, such as abundance enhancement of the SiO and the presence of HCN, can then be linked to the outflow cavity shocks. In Fig. 4.15c, the H_2O $3_{12} - 3_{03}$ spectrum is plotted with ALMA spectra: one is averaged over the HIFI beam (20″) for H_2O $3_{12} - 3_{03}$, and two are averaged over the region dedicated to SMM1-a and SMM1-b, but they are limited to the borders of the HIFI beam. The EHV bullets seen prominently in CO 2 – 1 are not bright in the HIFI spectra. Although

no EHV detection for this source with HIFI has been claimed, it seems that there is a faint emission in the two most energetic transitions observed by Mottram et al. (2014): 3_{12}-3_{03} and $3_{12} - 2_{21}$, which suggests that the water bullets might be associated with high temperatures, although due to higher frequency of the transitions and thus a smaller beam, less dilution can play a role at the same time. H_2O (3_{12}-3_{03}) shows a peak at 55 km s^{-1} while the $3_{12} - 2_{21}$ shows a tentative detection at 72 km s^{-1}.

At the same time CO 16-15 and 10-9 show no EHV emission, which suggests that the temperatures are not high enough to populate those levels. Even if the temperatures reach 700 K, the bullets are very compact and the filling factor is too small.

Fig. 4.15c shows that H_2O 3_{12}-3_{03} spectral EHV feature peaks outside the EHV peak for both SMM1-a and SMM1-b. The CO 2 – 1 emission at the peak velocities of the water bullet shows that the emission could be associated with both jets. Spectra show that the water EHV feature peaks just as the SMM1-b CO 2 – 1 feature decreases. It is possible that the water feature is associated with the jet at higher temperatures, where CO 2 – 1 emission is weak.

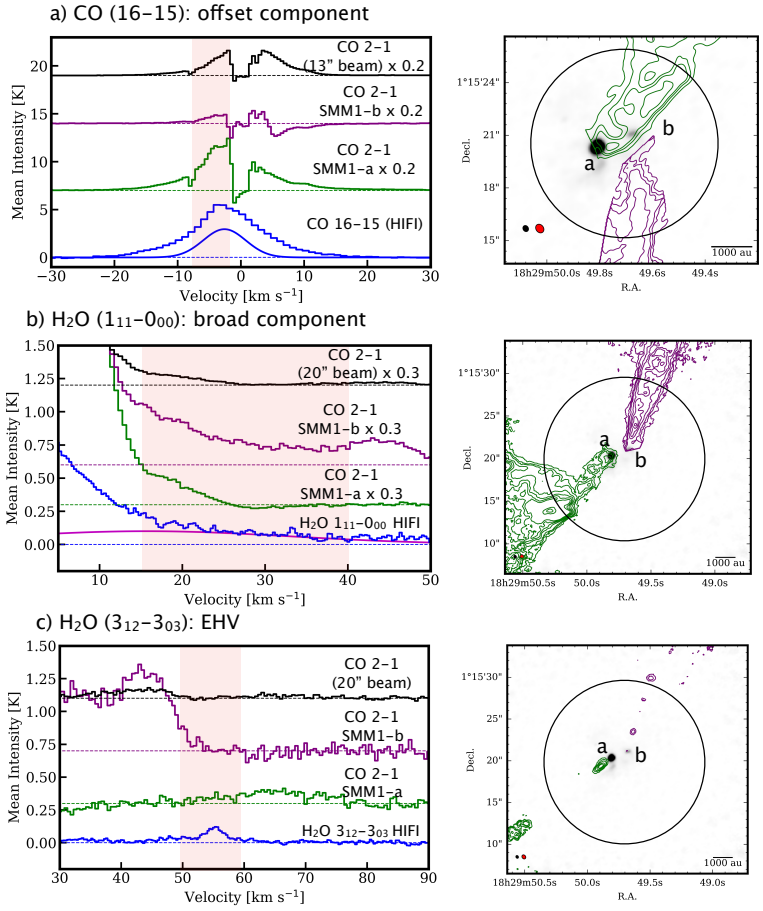


Figure 4.15: Comparison of CO 2 – 1 emission from SMM1 system with HIFI observations. Left: Spectra from HIFI (blue), ALMA integrated with HIFI beam (black), ALMA spectra integrated with regions drawn to capture all emission from SMM1-a (purple) and SMM1-b (green) within HIFI beam. The velocity range from which the moment 0 map on the right was produced is indicated with the red shade. The Gaussian profiles for the relevant velocity components that were fit to the HIFI profiles for CO 16-15 (Kristensen et al. 2012) and H_2O (Mottram et al. 2014) are shown. Right: moment 0 maps made by integrating the emission from range indicated by the red, shaded box on the left. Colors correspond to the spectra with SMM1-a outflow in green and SMM1-b outflow in purple. HIFI beam is plotted as a black circle. The beam size of the ALMA Band 6 spectral line (red) and continuum (black) is presented in the bottom-left corner of images.

4.B Additional figures

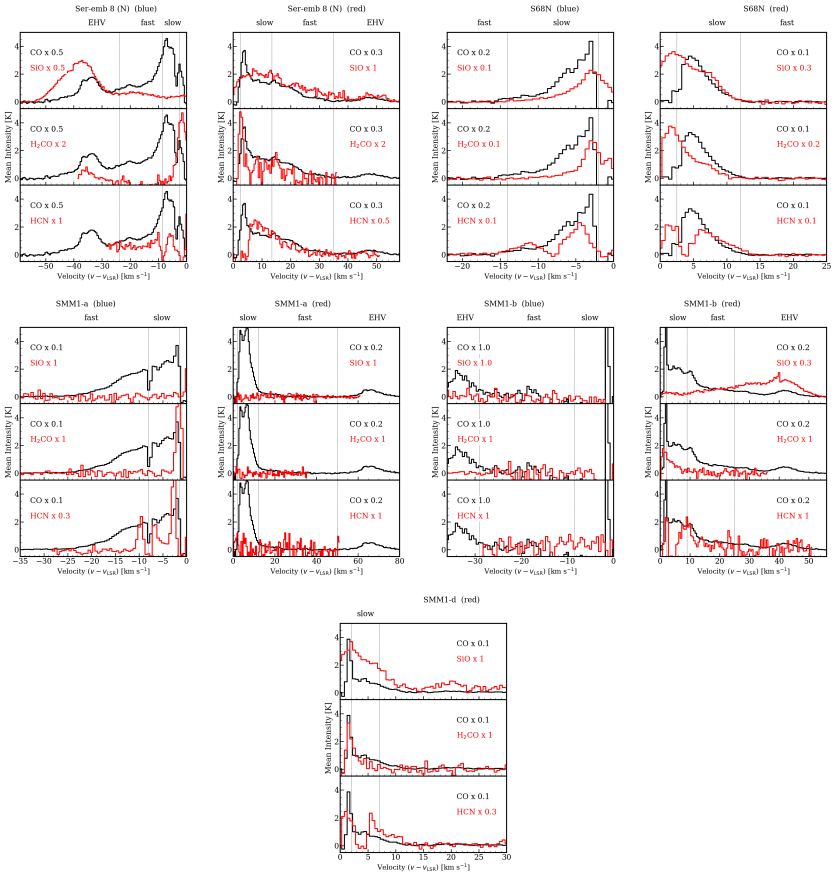


Figure 4.16: Spectra of CO in black, and different molecules as annotated in top-right corner in red. Spectra extracted from selected part of the outflow to highlight the key velocity components indicated in Figs. 4.2 and 4.3. Vertical dashed lines represent boundaries between different velocity regimes: slow wing, fast wing, and extremely high velocity.

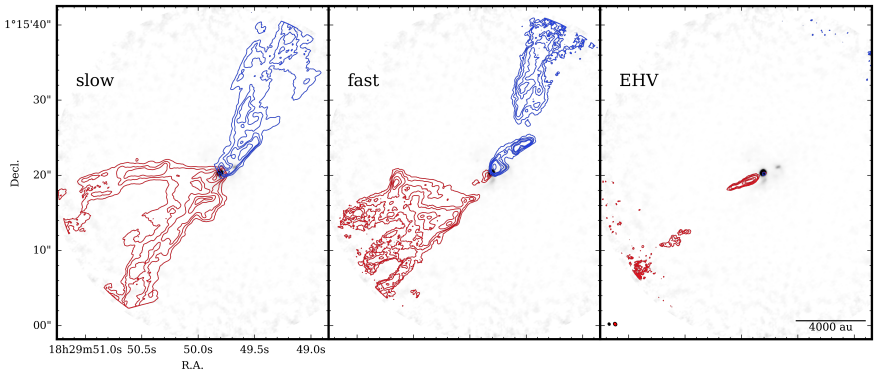


Figure 4.17: Integrated intensity maps of CO for different velocity regimes overlaid on Band 6 continuum in grayscale for SMM1-a. The emission is integrated over the velocities listed in Table 4.2. The synthesized beam of the CO (red) and continuum (black) is presented in bottom-left corner of EHV plot. The synthesized beam size of the continuum images is 0.″35 × 0.″33 and 0.″55 × 0.″45 for CO map. The contours are [3, 6, 9, 15, 20, 40] times the rms value. The rms values for each velocity channel, which are blueshifted and redshifted in K km s^{-1}, are slow [18.8, 20.5], fast[5.8, 7.2], EHV [2.0, 2.8].

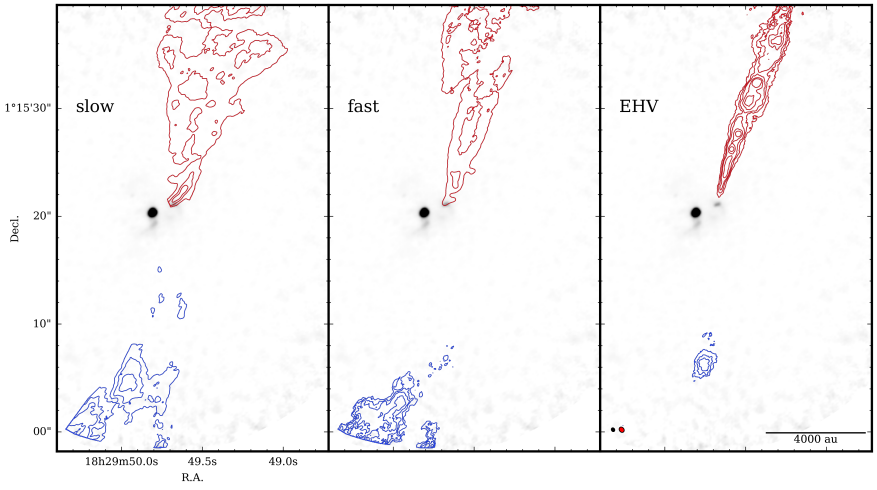


Figure 4.18: Same as Fig. 4.17, but for SMM1-b. The rms values for each velocity channel, which are blueshifted and redshifted in K km s^{-1}, are slow [17.5, 21.0], fast [5.3, 12.6], EHV [2.1, 3.7].

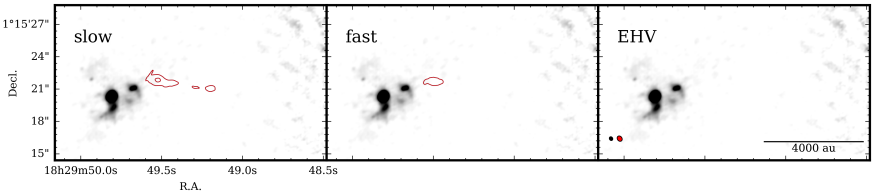


Figure 4.19: Same as Fig. 4.17, but for SMM1-d. The rms values for each velocity channel, which are redshifted in K km s^{-1} [20.7],[15.72]. No blueshifted and no EHV emission is detected toward this source.

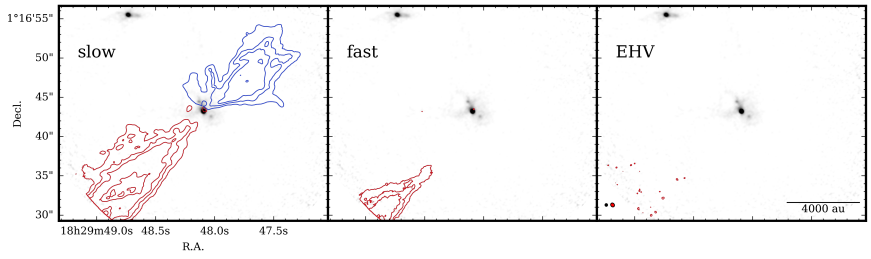


Figure 4.20: Same as Fig. 4.17, but for S68N. The rms values for each velocity channel, which are blueshifted and redshifted in K km s^{-1}, are slow [19.2, 13.8], fast [-, 4.7]. No EHV emission is detected toward this source.

4.C Tables

Details of the observations used in this paper are listed in Table 4.4 The calculated abundances of each molecule are shown in Tables 4.5-4.9. For each molecule we calculated column density for the minimum and maximum expected T_{ex} as listed in Table 4.3. We assume that values have 20% uncertainty, which arise from calibration, arbitrary defining velocity regimes, and other factors. Tables 4.10-4.14. present the outflow forces that are not corrected for inclination (see main text). Their absolute values are therefore uncertain by factors of a few.

Table 4.4: Specifications of observations

Configuration	λ	Max. Baseline	Date	Calibration[a]	Bandpass	Phase	Flux
Band 6 (C43-1)	1.3 mm	378 m	06/04/2015	4.2.2 - m	J1733-1304	J1751+0939	Titan
Band 6 (C43-4)	1.3 mm	1250 m	18/08/2014	4.3.1 - p	J1751+0939	J1751+0939	J1751+096
Band 3 (C43-5)	3 mm	2500 m	04/10/2016	4.7.38335 - p	J1751+0939	J1838+0404	J1838+0404

Notes. [(a)] Version of CASA used for calibration (m - manual calibration, p - pipeline calibration)

Table 4.5: Column densities of targeted molecules per velocity regime for Ser-emb 8 (N)

Ser-emb 8 (N)	CO cm^{-2}	SiO cm^{-2}	H_2CO cm^{-2}	HCN cm^{-2}
red				
slow	6e+16 – 4e+17	1e+13 – 3e+12	3e+13 – 5e+13	> 2e+14 – 6e+14
fast	3e+16 – 2e+17	1e+13 – 4e+12	< 7e+12 – 1e+13	> 2e+14 – 4e+14
EHV	6e+15 – 4e+16	2e+13 – 6e+12	< 7e+12 – 1e+13	< 2e+13 – 4e+13
blue				
slow	4e+16 – 3e+17	4e+12 – 1e+12	1e+13 – 3e+13	> 4e+13 – 1e+14
fast	4e+16 – 3e+17	1e+13 – 3e+12	< 7e+12 – 1e+13	> 2e+13 – 5e+13
EHV	3e+16 – 2e+17	8e+13 – 2e+13	1e+13 – 2e+13	< 2e+13 – 4e+13

Table 4.6: Column densities of targeted molecules per velocity regime for S68N

S68N	CO cm^{-2}	SiO cm^{-2}	H_2CO cm^{-2}	HCN cm^{-2}
red				
slow	7e+16 – 5e+17	8e+13 – 2e+13	1e+14 – 2e+14	> 1e+14 – 3e+14
fast	1e+16 – 1e+17	3e+13 – 9e+12	7e+12 – 1e+13	> 5e+13 – 1e+14
EHV	< 8e+14 – 5e+15	< 5e+12 – 1e+12	< 7e+12 – 1e+13	< 2e+13 – 4e+13
blue				
slow	8e+16 – 6e+17	8e+13 – 2e+13	1e+14 – 2e+14	> 2e+14 – 4e+14
fast	5e+15 – 3e+16	1e+13 – 4e+12	< 7e+12 – 1e+13	> 2e+13 – 6e+13
EHV	< 8e+14 – 5e+15	< 5e+12 – 1e+12	< 7e+12 – 1e+13	< 2e+13 – 4e+13

Table 4.7: Column densities of targeted molecules per velocity regime for SMM1-a

SMM1-a	CO cm^{-2}	SiO cm^{-2}	H_2CO cm^{-2}	HCN cm^{-2}
red				
slow	9e+16 – 6e+17	4e+13 – 1e+13	4e+13 – 8e+13	> 1e+14 – 4e+14
fast	4e+16 – 3e+17	6e+12 – 2e+12	< 8e+12 – 2e+13	< 2e+13 – 6e+13
EHV	8e+15 – 5e+16	< 2e+12 – 4e+11	< 8e+12 – 2e+13	< 2e+13 – 6e+13
blue				
slow	8e+16 – 5e+17	1e+13 – 4e+12	3e+13 – 5e+13	> 7e+13 – 2e+14
fast	4e+16 – 3e+17	< 6e+12 – 2e+12	< 2e+12 – 4e+12	> 3e+13 – 7e+13
EHV	< 9e+14 – 6e+15	< 6e+12 – 2e+12	< 2e+12 – 4e+12	< 2e+13 – 6e+13

Table 4.8: Column densities of targeted molecules per velocity regime for SMM1-b

SMM1-b	CO cm^{-2}	SiO cm^{-2}	H_2CO cm^{-2}	HCN cm^{-2}
red				
slow	7e+16 – 5e+17	1e+13 – 4e+12	2e+13 – 3e+13	> 4e+13 – 1e+14
fast	3e+16 – 2e+17	1e+14 – 3e+13	< 8e+12 – 2e+13	< 2e+13 – 6e+13
EHV	2e+16 – 2e+17	1e+14 – 3e+13	< 8e+12 – 2e+13	< 2e+13 – 6e+13
blue				
slow	6e+16 – 4e+17	4e+13 – 1e+13	1e+13 – 2e+13	< 2e+13 – 6e+13
fast	2e+16 – 2e+17	< 6e+12 – 2e+12	< 2e+12 – 4e+12	< 2e+13 – 6e+13
EHV	5e+15 – 4e+16	< 6e+12 – 2e+12	< 2e+12 – 4e+12	< 2e+13 – 6e+13

Table 4.9: Column densities of targeted molecules per velocity regime for SMM1-d

SMM1-d	CO cm^{-2}	SiO cm^{-2}	H_2CO cm^{-2}	HCN cm^{-2}
red				
slow	2e+16 – 2e+17	7e+13 – 2e+13	2e+13 – 4e+13	> 8e+13 – 2e+14
fast	1e+16 – 9e+16	4e+13 – 1e+13	< 8e+12 – 2e+13	> 8e+13 – 2e+14
EHV	< 9e+14 – 6e+15	< 6e+12 – 2e+12	< 8e+12 – 2e+13	< 2e+13 – 6e+13
blue				
slow	< 9e+14 – 6e+15	< 6e+12 – 2e+12	< 8e+12 – 2e+13	< 2e+13 – 6e+13
fast	< 9e+14 – 6e+15	< 6e+12 – 2e+12	< 8e+12 – 2e+13	< 2e+13 – 6e+13
EHV	< 9e+14 – 6e+15	< 6e+12 – 2e+12	< 8e+12 – 2e+13	< 2e+13 – 6e+13

Table 4.10: Outflow properties per velocity regime for Ser-emb 8 (N)

Ser-emb 8 (N)	M $M_\odot$	$\dot{M}$ $M_\odot\ yr^{-1}$	P $M_\odot\ km\ s^{-1}$	F_{out} $M_\odot\ km\ s^{-1}\ yr^{-1}$
red				
slow	2.4e-06	5.1e-07	2.1e-02	2.9e-05
fast	7.3e-07	4.1e-07	1.7e-02	2.4e-05
EHV	5.2e-08	7.4e-08	3.1e-03	4.3e-06
blue				
slow	1.3e-06	2.4e-07	1.0e-02	1.4e-05
fast	1.2e-06	5.3e-07	2.2e-02	3.1e-05
EHV	6.2e-07	6.3e-07	2.6e-02	3.7e-05

Table 4.11: Outflow properties per velocity regime for S68N

S68N	M $M_\odot$	$\dot{M}$ $M_\odot\,yr^{-1}$	P $M_\odot\,km\,s^{-1}$	F_{out} $M_\odot\,km\,s^{-1}\,yr^{-1}$
red				
slow	1.1e-05	2.4e-06	1.0e-01	5.9e-05
fast	1.1e-06	4.8e-07	2.0e-02	1.2e-05
EHV	—	—	—	—
blue				
slow	1.2e-05	2.6e-06	1.1e-01	5.8e-05
fast	1.7e-07	9.4e-08	3.9e-03	2.1e-06
EHV	—	—	—	—

Table 4.12: Outflow properties per velocity regime for SMM1-a

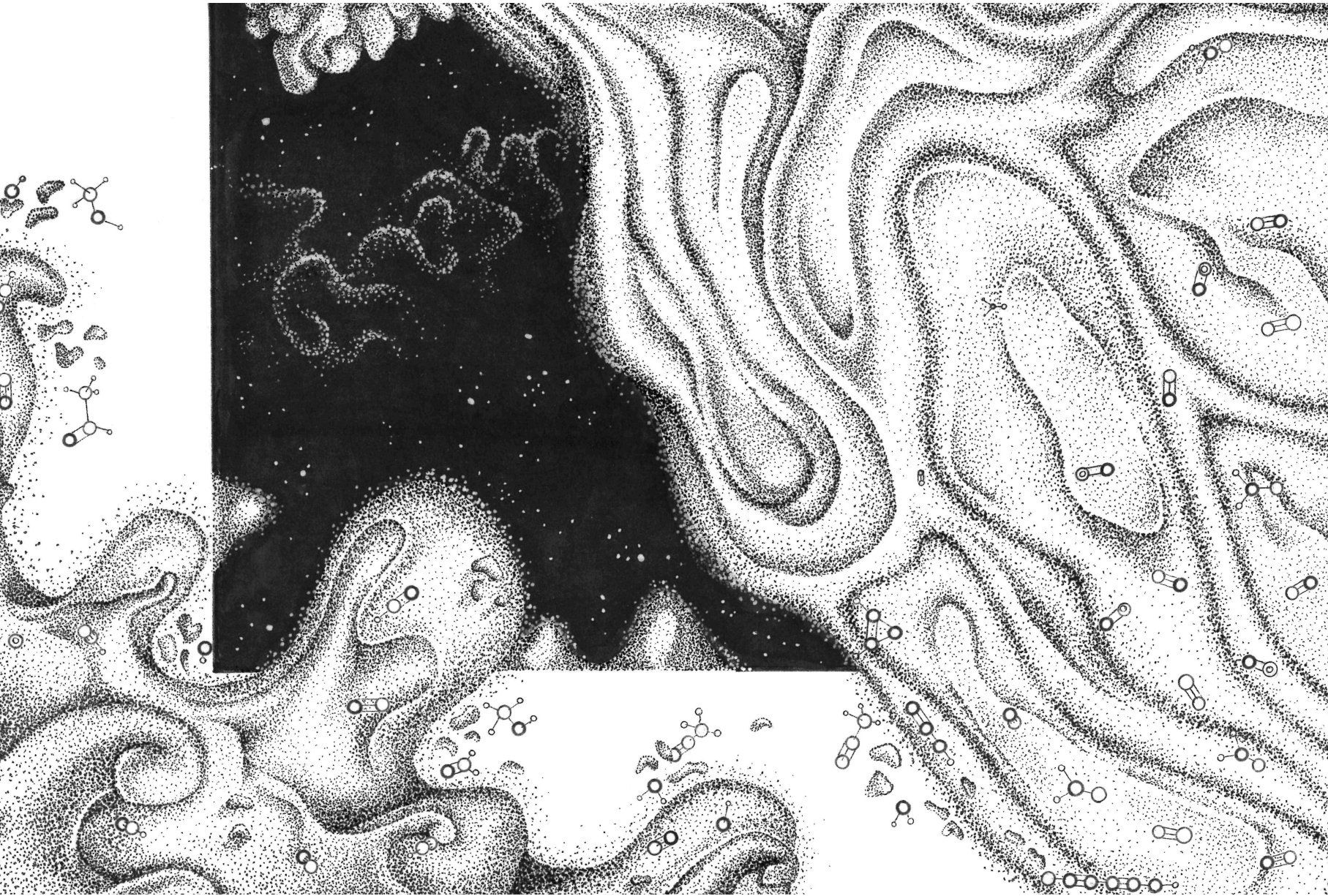
SMM1-a	M $M_\odot$	$\dot{M}$ $M_\odot\,yr^{-1}$	P $M_\odot\,km\,s^{-1}$	F_{out} $M_\odot\,km\,s^{-1}\,yr^{-1}$
red				
slow	2.6e-05	7.6e-06	3.5e-01	6.1e-04
fast	7.2e-06	6.2e-06	2.9e-01	4.9e-04
EHV	2.2e-07	3.9e-07	1.8e-02	3.1e-05
blue				
slow	1.4e-05	1.8e-06	8.7e-02	6.4e-05
fast	4.5e-06	2.2e-06	1.1e-01	7.8e-05
EHV	—	—	—	—

Table 4.13: Outflow properties per velocity regime for SMM1-b

SMM1-b	M $M_\odot$	$\dot{M}$ $M_\odot\,yr^{-1}$	P $M_\odot\,km\,s^{-1}$	F_{out} $M_\odot\,km\,s^{-1}\,yr^{-1}$
red				
slow	1.2e-05	2.2e-06	9.1e-02	1.2e-04
fast	4.4e-06	2.2e-06	9.4e-02	1.2e-04
EHV	1.5e-06	1.5e-06	6.2e-02	8.2e-05
blue				
slow	5.9e-06	1.1e-06	4.4e-02	3.8e-05
fast	1.6e-06	8.3e-07	3.5e-02	3.0e-05
EHV	7.0e-08	7.0e-08	2.9e-03	2.5e-06

Table 4.14: Outflow properties per velocity regime for SMM1-d

SMM1-d	M $M_\odot$	$\dot{M}$ $M_\odot\,yr^{-1}$	P $M_\odot\,km\,s^{-1}$	F_{out} $M_\odot\,km\,s^{-1}\,yr^{-1}$
red				
slow	5.6e-07	1.5e-07	6.3e-03	4.5e-06
fast	2.5e-07	1.0e-07	4.3e-03	3.1e-06
EHV	—	—	—	—
blue				
slow	—	—	—	—
fast	—	—	—	—
EHV	—	—	—	—



5

Which molecule traces what: chemical diagnostics of protostellar sources

Tychoniec Ł., van Dishoeck E. F., van 't Hoff M. L. R., van Gelder M. L., Tabone B., Chen Y., Harsono D., Hull C. L. H., Hogerheijde M. R., Murillo N. M., Tobin J. J.
Submitted to Astronomy & Astrophysics.

Abstract

The physical and chemical conditions in Class 0/I protostars are fundamental in unlocking the protostellar accretion process and its impact on planet formation. The aim is to determine which physical components are traced by different molecules at sub-arcsecond scales (<100 – 400 au). We use a suite of Atacama Large Millimeter/submillimeter Array (ALMA) datasets in Band 6 (1 mm), Band 5 (1.8 mm) and Band 3 (3 mm) at spatial resolutions 0.″5 – 3″for 16 protostellar sources. For a subset of sources, Atacama Compact Array (ACA) data at Band 6 with a spatial resolution of 6″ are added. The availability of both low- and high-excitation lines, as well as data on small and larger scales, are important to unravel the full picture. The quiescent protostellar envelope is well traced by $C^{18}O$, DCO^+ and N_2D^+, with the freeze-out of CO governing the chemistry at envelope scales. Molecular outflows are seen in classical shock tracers like SiO and SO, but ice-mantle products such as CH_3OH and HNCO released with the shock are also observed. The molecular jet is a key component of the system, only present at the very early stages, and prominent not only in SiO and SO but also occasionally in H_2CO. The cavity walls show tracers of UV-irradiation such as hydrocarbons C_2H and c-C_3H_2 as well as CN. The hot inner envelope, apart from showing emission from complex organic molecules (COMs), also presents compact emission from small molecules like H_2S, SO, OCS and $H^{13}CN$, most likely related to ice sublimation and high-temperature chemistry. Sub-arcsecond millimeter-wave observations allow to identify those (simple) molecules that best trace each of the physical components of a protostellar system. COMs are found both in the hot inner envelope (high excitation lines) and in the outflows (lower-excitation lines) with comparable abundances. COMs can coexist with hydrocarbons in the same protostellar sources, but their origin is different. In near future, mid-IR observations with JWST–MIRI will provide complementary information about the hottest gas and the ice mantle content, at unprecedented sensitivity and at resolutions comparable to ALMA for the same sources.

5.1 Introduction

The formation of Sun-like stars is set in motion by the collapse of a cold, dense cloud. Many different physical processes take place in the protostellar stage – first few 10^5 yrs that are critical to the subsequent evolution of the star and its planetary system (Lada 1987). The mass of the star and that of its circumstellar disk are determined during this embedded phase (Hueso & Guillot 2005) and the first steps of planet formation must take place then (Greaves & Rice 2010; Williams 2012; ALMA Partnership et al. 2015; Manara et al. 2018; Harsono et al. 2018; Tobin et al. 2020; Tychoniec et al. 2018b; Tychoniec et al. 2020; Segura-Cox et al. 2020). At the same time, on larger scales, the collapsing envelope is dispersed by the energetic action of bipolar jets and winds emanating from the star-disk system which create outflows of entrained gas and dust.

Until recently, studies of low-mass protostars have suffered from low spatial resolution to disentangle these different physical components. The combination of the low temperatures (< 300 K) and high visual extinction (A_V >100) shifts the radiative processes in protostellar systems to peak in the far-infrared and submillimeter regimes. The longer the wavelength, the larger apertures are required to provide high-resolution observations. In previous lower-resolution observations, continuum emission has been readily detected, but tracing mostly the centrally-concentrated envelope, unable to disentangle the embedded disk (Hogerheijde et al. 1998; Shirley et al. 2000; Chandler & Richer 2000; Enoch et al. 2009; van Kempen et al. 2009b). Rotational transitions of molecules are a powerful tool to probe other components of the system and can be used to infer densities, temperatures, UV fields, chemical abundances and kinematics (van Dishoeck & Blake 1998; Evans 1999), but existing data often lacked sensitivity.

The advent of submillimeter interferometry opened the possibility to study protostellar systems at much smaller scales than with single-dish observations. Observations of star-forming regions with first interferometric arrays such as the Very Large Array (VLA) (e.g., Jackson et al. 1988), Owens Valley Radio Observatory (OVRO) (e.g., Chandler & Carlstrom 1996; Langer et al. 1996; Hogerheijde et al. 1999), IRAM-Plateau de Bure (IRAM-PdBI) (e.g Schilke et al. 1992; Wilner et al. 2000; Bottinelli et al. 2004), Submillimeter Array (SMA (e.g., Jørgensen et al. 2005, 2009) and others, mapped the continuum and molecular emission at few arcsecond scales, disentangling different pieces of the physical structure of the protostellar systems.

With the Atacama Large Millimeter/submillimeter Array (ALMA), it is possible to image many lines on the relevant physical scales with achievable observing times at sub-arcsecond resolution. Impressive ALMA studies of individual low-mass protostars have been presented, focusing both on simple species (< 6 atoms) and complex molecules (> 6 atoms) (e.g., Sakai et al. 2014a; Jørgensen et al. 2016; López-Sepulcre et al. 2017; Lee et al. 2019a; Codella et al. 2018; Lee et al. 2019b; Manigand et al. 2020; van Gelder et al. 2020; Bianchi et al. 2020), but larger comparative studies are still lacking. Here we present ALMA data of 16 protostellar sources covering rotational transitions of various molecules; we use these data to build a complete picture of what types of molecules trace which physical structures in protostars.

This work presents ALMA 12m-array observations of 16 protostellar sources, 10 Class 0 and 6 Class I protostars, on scales of the Solar System, ~100 au. For 5 Class 0 and 1 Class I sources, observations on protostellar envelope scales of ~2000 au are provided with the 7m Atacama Compact Array (ACA).

Class 0 sources are defined by their strong excess of submillimeter luminosity and very low bolometric temperatures <70 K (André et al. 1993; Chen et al. 1995). These sources

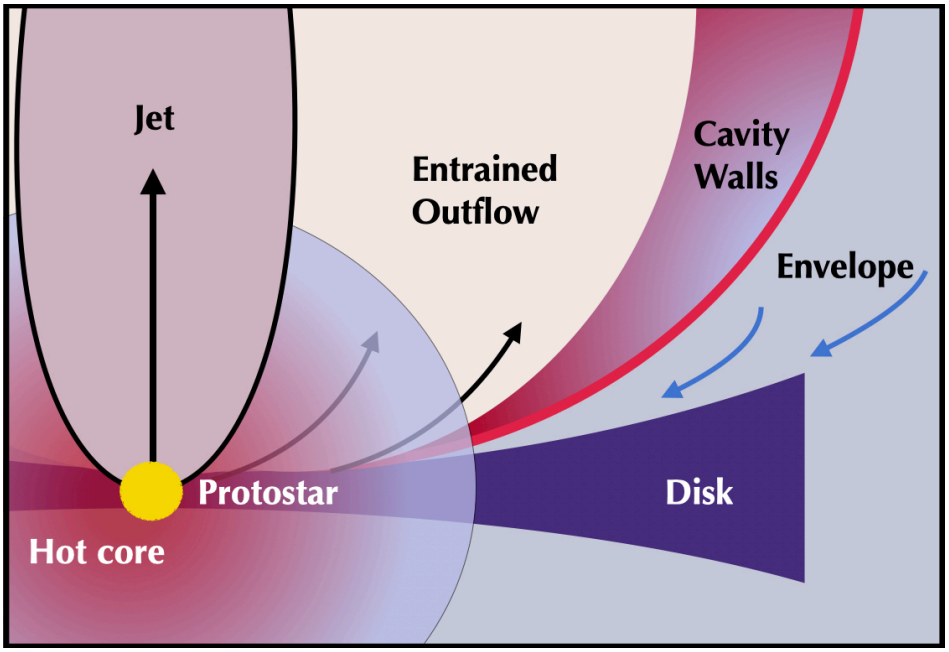


Figure 5.1: Cartoon illustrating the physical components of a protostellar system. Arrows indicate the direction of material in motion; the protostellar jet emerges from the innermost region of the protostellar-disk system. The size of the envelope with respect to the disk can vary depending on the disk size and temperature profile of the system.

are associated with powerful outflows, and the envelope mass dominates the mass of the entire system. Class I sources are defined by having an infrared spectral index indicating strong reddening (Lada 1987) with bolometric temperatures of 70–650 K (Chen et al. 1995). Those systems have already converted most of their envelope mass into disk and protostar (Crapsi et al. 2008; van Kempen et al. 2009b; Maury et al. 2011). For the typical envelope masses of sources presented here and average disk masses found by Tychoniec et al. (2020), the $M_{\rm disk}/M_{\rm env} \simeq 1\%$ for Class 0 and $\simeq 20\%$ for Class I, with values up to 75–98% in cases of rotationally supported disks (Jørgensen et al. 2009).

The targeted protostars are well-known objects located in different star-forming regions. They span a range of properties within the low-mass regime; the probed range of $L_{\rm bol}$, $T_{\rm bol}$ and $M_{\rm env}$ is presented in Fig. 5.2; those properties are provided by a suite of observations across the infrared and submillimeter spectrum (McMullin et al. 1994; Davis et al. 1999; Enoch et al. 2009; Dionatos et al. 2010; Kristensen et al. 2012; Maury et al. 2019).

Many of our sources are included in upcoming *James Webb Space Telescope* (JWST) observations with the Mid-Infrared Instrument (MIRI) (Wright et al. 2015). MIRI will provide unprecedented resolution and sensitivity in the mid-infrared (mid–IR) (5–28 μm) regime. Such mid-IR data at 0.2–0.7″ resolution will unveil the origin of the hot gas in outflows and cavity walls, as well as inner disk emission (if not too extincted) and outer envelope ice-mantle content in absorption spectra. A major limitation of MIRI is its spectral resolving power ($\lambda/\Delta\lambda \sim 3000$; $\Delta v \sim 100$ km s^{-1}) which does not reveal kinematic information of the processes in protostellar systems. MIRI is also not able to penetrate the most highly extincted

Table 5.1: Targeted protostellar systems

Source name	R.A. (J2000)	Decl. (J2000)	d (pc)	Class	L_{bol} ($L_\odot$)	T_{bol} (K)	M_{env} ($M_\odot$)	Ref.
Serpens SMM1	18:29:49.8	+01:15:20.5	439	0	109	39	58	(1)
Serpens S68N	18:29:48.1	+01:16:43.3	439	0	6	58	10	(2)
Ser-emb 8 (N)	18:29:48.7	+01:16:55.5	439	0	—	—	—	—
Serpens SMM3	18:29:59.2	+01:14:00.3	439	0	28	38	13	(1)
BHR 71	12:01:36.3	-65:08:53.0	200	0	15	44	2.7	(1)
IRAS 4B	03:29:12.0	+31 13 08.1	293	0	7	28	4.7	(1)
Per-emb-25	03:26:37.5	+30:15:27.8	293	0/I	1.9	61	2.0	(2)
B1-c	03:33:17.9	+31:09:31.8	293	0	5	48	15	(2)
HH211-mm	03:43:56.8	+32:00:50.2	293	0	2.8	27	19	(2)
L1448-mm	03:25:38.9	+30:44:05.3	293	0	13	47	15	(2)
L1527 IRS	04:39:53.9	+26:03:09.5	140	0/I	1.6	79	0.12	(3)
B5-IRS1	03:47:41.6	+32:51:43.7	293	I	7	181	3.5	(2)
TMC1	04:41:12.7	+25:46:34.8	140	I	0.9	101	0.14	(1)
IRAS 04302	04:33:16.5	+22:53:20.4	140	I	0.7	300	0.05	(1)
L1489 IRS	04:04:43.0	+26:18:57.0	140	I	3.8	200	0.2	(1)
TMC1A	04:39:34.9	+25:41:45.0	140	I	2.7	118	0.2	(1)

(1) Kristensen et al. 2012, (2) Enoch et al. 2009, (3) Green et al. 2013

inner envelope regions of Class 0 sources. This is why ALMA and JWST data are highly complementary. ALMA observes at comparable spatial resolution, but with spectral resolution at <1 km s^{-1}. ALMA also images colder gas and dust with emission lines and continuum radiation.

This work presents one of the largest combinations of high-resolution ALMA observations of Class 0/I protostars to date at three different ALMA frequency bands. Covering a broad range of protostellar properties within the low-mass regime, the aim is to identify and describe key molecular tracers of future Sun-like stars and what physical components of star-forming sources they correspond to. This work is organized as follows. In Section 2, the observations used in this work are presented, Sections 3–6 discuss molecular tracers of each of the physical components presented in Fig. 5.1. The focus is on a qualitative description, rather than quantitative analyses for which source specific models and more rotational transitions of a given molecule would be needed. Section 7 discusses various new insights from our work on the Class 0/I protostars. We summarize our work in Section 8.

5.2 Physical components of a protostellar system

The different components of protostellar systems vary significantly in their physical conditions, such as density and temperature, molecular enrichment, and dynamics. We divide the protostellar system in key physical components that are illustrated in Fig. 5.1. Our current knowledge about them is described briefly below to set the scene for the interpretation of our data.

Envelope. The envelope surrounding a protostar is the material that fuels the accretion process onto the star and disk. The physical conditions in the outer envelope on scales of a few 1000 au are reminiscent of those of starless cores with heavy freeze-out, and their chemical composition is directly inherited from the cloud out of which the star is being born (Caselli & Ceccarelli 2012). Systematic motions such as infall or expansion can occur but otherwise they are characterized by low turbulence and narrow (FWHM < 0.5 - 1 km s^{-1}) line profiles indicative of quiescent gas (Jørgensen et al. 2002).

Observations with sub-arcsecond interferometers are challenging because most of the envelope material is resolved out at high resolution. Single-dish studies have been very

useful in probing the entirety of the envelope emission and pointing to the importance of molecular tracers and line ratios in understanding the physics on large scales (~ 10^4 au) (e.g., Blake et al. 1994; van Dishoeck et al. 1995; Ceccarelli et al. 2000; Jørgensen et al. 2002; Maret et al. 2004; Jørgensen et al. 2004b; Sakai et al. 2008; Emprechtinger et al. 2009; Carney et al. 2016; Higuchi et al. 2018; Murillo et al. 2018). Additionally, interferometric studies at few arcsecond resolution can characterize the envelope, without losing much information on large-scale emission (e.g., Brinch et al. 2007; Chen et al. 2007; Jørgensen et al. 2007, 2009; Tobin et al. 2011, 2013).

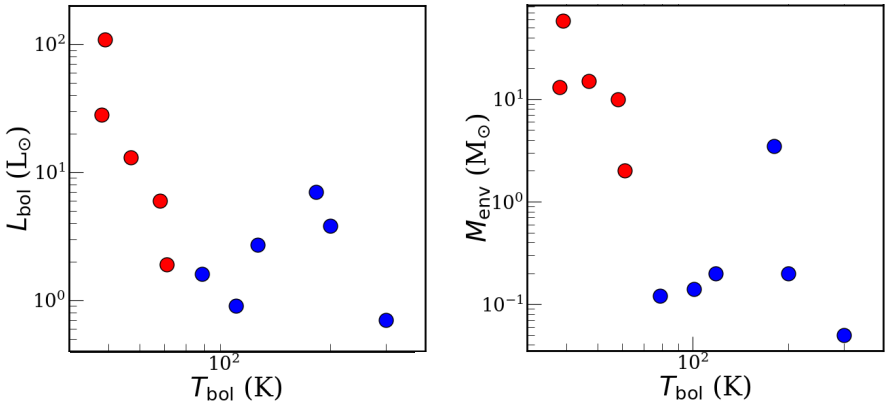


Figure 5.2: Key properties of the targeted protostars. Class 0 protostars are showed in red and Class I protostars in blue. The figures show bolometric luminosity (left) and envelope mass (right) versus bolometric temperature of protostars. The values are provided in Table 5.1 with references.

Warm inner envelope. In the innermost part of the envelope on scales of the disk, temperatures rise above 100 K, so any water and complex organic molecules (COMs) contained in ices are released from the grains back into the gas where they are readily observed at submillimeter wavelengths. This region with its unique chemical richness is called the hot core, or to distinguish it from its high-mass counterpart, hot corino (Herbst & van Dishoeck 2009).

Jets and outflows. As the material is accreting from the envelope onto the disk and protostar, excess angular momentum is released by means of collimated high-velocity jets which originate from the innermost star-disk interface regions of the protostellar system. In the earliest stages when the mass loss is at its peak, the densities are high enough to form molecules in the internal shocks in the jet (Bachiller & Gomez-Gonzalez 1992; Tafalla et al. 2010). The composition of the jet undergoes significant chemical evolution throughout the protostellar lifetime, with the molecular component being most prominent in the early stages (Nisini et al. 2015). Much slower (<20 km s^{-1}) and less collimated gas moving away from the protostar is called an outflow. It consists mostly of envelope material entrained by the jet and any wide-angle wind launched from the disk (Bjerkeli et al. 2016). Temperatures in shocked regions are much higher than in the surrounding envelope, up to a few thousand K, and sputtering of grain cores and ice mantles can further result in unique chemical signatures

like SiO and other molecules (e.g., Arce et al. 2008).

Outflow cavity walls. These are the narrow zones in between the cold dense quiescent envelope material and the lower-density warm cone where outflows are propagating at large velocities. Cavity walls are exposed to UV radiation from the accreting star-disk boundary layer, which can escape through the outflow cavity without being extincted (Spaans et al. 1995). This creates conditions similar to those found in Photon Dominated Regions (PDRs), which occur throughout the interstellar medium near sources of intense UV radiation (Hollenbach & Tielens 1997). In units of the interstellar radiation field (ISRF, Draine 1978), typical values of 10^2–10^3 are found on scales of $\sim$ 1000 au (van Kempen et al. 2009a; Yıldız et al. 2012; Benz et al. 2016; Karska et al. 2018).

Young disk. In the inner envelope, a protoplanetary disk starts to form as the natural outcome of a rotating collapsing core (Ulrich 1976; Cassen & Moosman 1981; Terebey et al. 1984). A young disk should be rotating in Keplerian motion. At early stages it is difficult to identify whether the so-called embedded disk is rotationally supported, since any molecular emission from the disk is entangled with that from the envelope. In recent years several embedded disks have been identified to have Keplerian rotational structure on scales of ~100 au (Tobin et al. 2012; Murillo et al. 2013; Ohashi et al. 2014; Codella et al. 2014; Yen et al. 2017). Molecular tracers in young disks, apart from providing the kinematic information, can probe their temperature structure as well (van 't Hoff et al. 2018b). Hydrodynamical models of disk formation also predict an accretion shock as envelope material falls onto the disk (Neufeld & Hollenbach 1994; Li et al. 2011) . Some molecules, notably SO and SO_2, are proposed as tracers of such shocks (Yen et al. 2014; Sakai et al. 2014b, 2017; Artur de la Villarmois et al. 2019).

5.3 Observations

5.3.1 Datasets

Six different ALMA 12m datasets at Band 3, 5, and 6 are used in this work to cover 14 out of 16 sources. The spatial resolution of all ALMA 12m datasets is comparable (0.″3–0.″6), except for 2017.1.01174.S, where Band 3 observations are obtained at 3″. Additionally for 6 out of 16 sources in Band 6, ACA observations with 7m antennas were obtained at 6″resolution. The combined data provide a representative survey of low-mass protostars. While it does not provide a uniform observational setting for all protostars, our study presents an overview of different molecular tracers at a range of crucial spatial scales: sub-arcsecond (0.″3–0.″6) datasets provide the necessary resolution to disentangle protostellar envelope and disk component; supplemented ACA observations at 6″allow to include larger scales and inform about the components that could be resolved out by high-resolution observations.

The observations presented here are collected across several ALMA projects, and are summarized in Table 5.4. The spatial resolution allows to observe protostellar systems at solar-system scales; Band 5 and 6 observations provide a resolution of ~0.″5, which corresponds to a 70–220 au diameter for sources in our sample. Thus, regions down to 35-110 au radius in the inner envelope are probed. The Band 3 data achieve moderate resolution of ~3″which provides information on intermediate envelope scales of 500–1500 au. The ACA observations of six sources at 6″ resolution probe envelope scales of 800–2000 au. The datasets were pipeline calibrated and not self-calibrated except for 2013.1.00726.S and 2016.1.00710.S; calibrator sources and details are presented in Table 5.4.

The 2017.1.01350.S dataset (PI: Ł. Tychoniec) targets the SMM3 and TMC1 protostars in

Band 6 (1.3 mm) with ALMA 12m antennas at 0.″4 resolution, covering 13 spectral windows. Additionally for SMM3, TMC1, IRAS 4B, BHR71, Per-emb-25, and B1-c, ACA observations with 7m dishes were obtained in Band 6 at 6″with the same spectral settings as the 12m observations. The 2017.1.01174.S dataset (PI: E. van Dishoeck) targeted B1-c and S68N in Band 3 (3 mm) with ALMA 12m at 3″and B1-c, S68N, and SMM3 in Band 6 (1.3 mm) with ALMA 12m at 0.4″resolution.

The 2017.1.013781.S dataset (PI: M. van 't Hoff) targeted L448-mm, B1-c, B5-IRS1, and HH211 in Band 5 (2 mm) with ALMA 12m antennas at 0.″4 resolution. The 2017.1.01413.S dataset (PI: M. van 't Hoff) targeted IRAS-04302, L1527, L1489, TMC1, and TMC1A in Band 6 (1.3 mm) with ALMA 12m at 0.″3 resolution. The images created from all the datasets mentioned above are the result of an automated pipeline CLEAN algorithm run with automasking with the CASA software (McMullin et al. 2007). The version of CASA used for each specific dataset is specified in Table 5.4.

The 2013.1.00726.S dataset (PI: C. Hull) targets SMM1, S68N, and Ser-Emb8N in Band 6 with 0.″3 resolution in Band 6 (1.3 mm) with ALMA 12m antennas. The images presented from this dataset were produced with a manual CLEAN algorithm, with a single mask covering the entire outflow. See Hull et al. (2016); Tychoniec et al. (2019) for calibration and CLEAN algorithm details. For the same sources, Band 3 (3 mm) images were generated with manual CLEAN (dataset 2016.1.00710.S; PI: C. Hull).

5.3.2 Spectral setup of the observations

A collection of different datasets using different ALMA Bands implies varying spectral and spatial resolution as well as spectral coverage across the analysis. This is the reason that throughout this paper the sources shown in the figures differ when presenting detections and maps of different molecules. In all cases, when the molecule is discussed, only those sources where the given transition has been targeted are discussed. All non-detections are explicitly stated. Table 5.5 provides a list of targeted molecular transitions, with sources that have a particular line covered and detected or not detected.

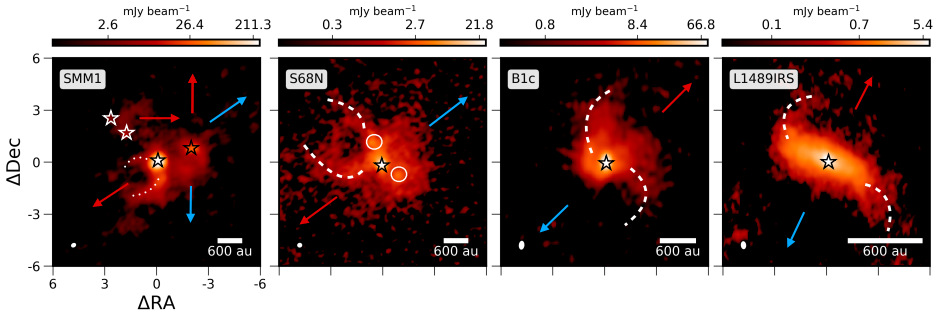


Figure 5.3: Continuum emission at 1.3 mm of four example protostellar systems obtained with ALMA at 0.″5 resolution. Symbols of stars point to confirmed protostellar sources, circles show condensations of continuum emission, without confirmed protostellar nature, dotted lines show outflow cavity walls, and dashed lines show streams of envelope material. Arrows indicate outflow directions.

The ALMA observations presented here target different spectral setups across Band 3, 5,

and 6. Observations of protostellar systems require a variety of tracers to probe the strongly varying physical scales and conditions. In particular, Band 3 grants access to lines at very low excitation that enable tracing more extended material. Dust is less optically thick in Band 3 compared with Band 6 which potentially allows to peek inside the densest inner regions.

Cold outer envelopes with temperatures < 20 K are probed with low $E_{\rm up}$ transitions. Additionally, non-thermal processes such as sputtering of material from the grains in the outflow, will also be seen in low $E_{\rm up}$ due to their lower critical densities. On the other hand, thermal desorption from grains in the innermost regions are best probed with lines with high $E_{\rm up}$. With the large span of frequencies of the observations, different transitions of the same molecule can be detected and used to trace different components of the system (e.g., a HNCO line at $E_{\rm up}$ at 15 K is available in Band 3 and lines at 70 and 125 K are covered in Band 6).

5.4 Protostellar envelope

In this section, we present molecules that trace the bulk of the protostellar envelope, which has a typical radius on the order of a few 1000 au (Jørgensen et al. 2002; Kristensen et al. 2012). Thus, the sub-arcsecond ALMA 12m array observations tend to resolve-out the envelope emission (Jørgensen et al. 2004a). For instance, the maximum recoverable scale (MRS) of ALMA Band 6 observations at 0.″4 presented here is 5″, which is between 600–2000 au diameter depending on distance to the source. For that reason, we discuss in this section mainly the ALMA-ACA observations obtained at lower spatial resolution (6″; 750–2500 au) for six sources in our datasets; Class 0 sources: B1-c, BHR71, Per-emb-25, SMM3, and IRAS 4B, and Class I source TMC1. The ACA can zoom-in on what was previously contained in a single-dish beam of 15–20″, while the MRS of ACA (30″) enables us to preserve sensitivity to large-scale emission. The MRS of all observations presented here are reported in Table 5.4.

5.4.1 Continuum emission from protostars

Figure 5.3 presents continuum emission maps toward four example protostars obtained with ALMA at ∼ 0.″5. The examples illustrate most characteristic features observed in the continuum maps. The continuum images for all sources are presented in Fig. 5.17.

The continuum emission observed at millimeter wavelengths (1.3 - 3 mm in our observations) traces thermal dust emission from the inner envelope and the embedded disk. In Class 0 sources the central continuum peak is usually unresolved, showing that the embedded disk is typically compact with $R_{\rm disk}$ <100 au (e.g., B1-c, Fig. 5.3). The example of SMM3 (Fig. 5.17) shows a large resolved dust structure perpendicular to the outflow, but its classification as a disk is not certain. The fact that we do not observe large Class 0 disks is consistent with observations (e.g., Tobin et al. 2018; Maury et al. 2019; Tobin et al. 2020) and predictions of analytical models (Visser et al. 2009; Visser & Dullemond 2010; Harsono et al. 2015b; Machida et al. 2016).

The extended emission in Class 0 sources indicates that there is a significant amount of envelope material surrounding the protostar. In the case of the SMM1 system, presented in Fig. 5.3 (left), the continuum clumps outside the central emission are components of multiple protostellar systems, marked with stars, confirmed by the presence of individual molecular outflows (Hull et al. 2016, 2017). Binary components are also seen in TMC1 and IRAS 4B (Fig. 5.17). In the case of S68N presented in Fig. 5.3, two emission peaks that stand out of

the diffuse envelope emission are marked with circles, but their protostellar nature is not confirmed.

Cavity walls are pronounced in several sources indicating a young age of these objects where the molecular jets are freshly escaping through the envelope pushing its contents to the cavity walls, see Fig. 5.3 for the case of SMM1 (dotted line). Similar structures can be seen for Emb8N, HH211 and SMM3 (Fig.5.17). In S68N, B1-c, and L1489 IRS, dashed lines highlight streamers of envelope material infalling onto the protostar, commonly observed in continuum and line observations of young systems (Alves et al. 2020; Hull et al. 2020) (Fig. 5.3).

In more evolved Class I sources, the continuum emission is dominated by the disk; there are examples of a large, resolved disk (L1489 IRS, Fig. 5.3), while others are more compact (e.g., TMC1, TMC1A, Fig. 5.17). Keplerian rotation, which can be observed only through observations of molecular gas, has so far been confirmed in L1527, TMC1, IRAS-04302, L1489 and TMC1A (Tobin et al. 2012; Harsono et al. 2014).

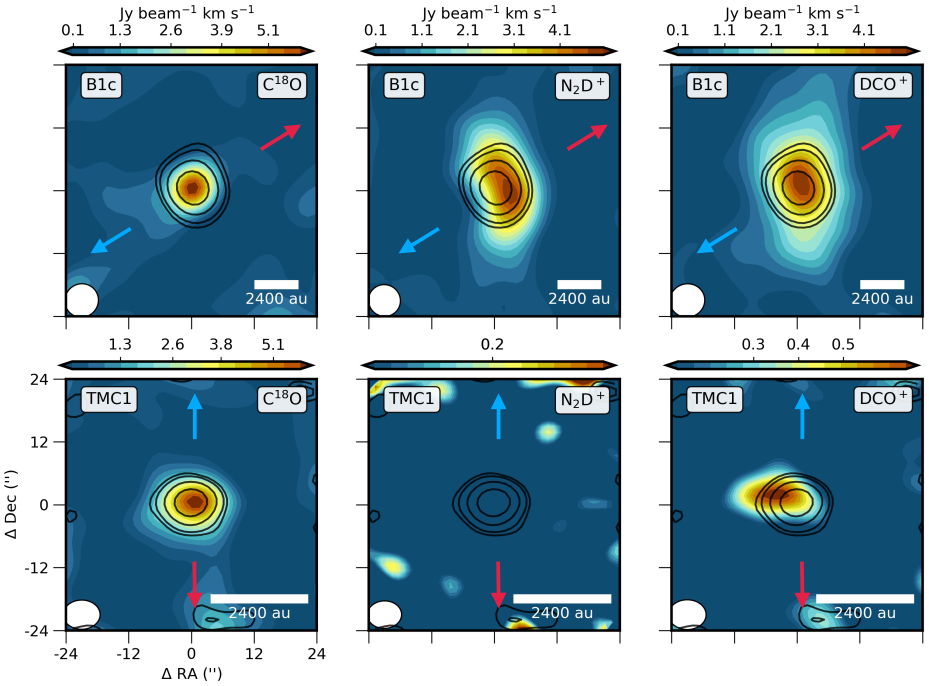


Figure 5.4: Maps of key envelope tracers toward B1-c (Class 0, top) and TMC1 (Class I, bottom) obtained with ACA. Contours represent continuum emission at 1.3 mm observed with ACA. Note different distances to B1-c and TMC1 resulting in different spatial resolutions of the maps. *Left:* $C^{18}O$ 2 – 1 *Middle:* N_2D^+ 3 – 2. *Right:* DCO^+ 3 – 2. All moment 0 maps are integrated from -2.5 to 2.5 km s^{-1} w.r.t v_{sys}.

5.4.2 Molecular lines

$C^{18}O$

In Fig. 5.4 typical envelope tracers $C^{18}O$ 2–1 (E_{up} = 16 K), DCO^+ 3–2 (E_{up} = 21 K), and N_2D^+ 3–2 (E_{up} = 22 K), observed at 6″resolution with the ACA, are presented toward example Class 0 and Class I sources – B1-c and TMC1, respectively. The emission from the presented molecules exhibits similar behaviour for all Class 0 sources, therefore B1-c serves as a representative case; TMC1 is the only Class I source in the sample with 7m observations available. The maps for all sources for which these molecules have been targeted can be found in Appendix A.2. All envelope tracers presented here are characterized by narrow line profiles with FWHM $\sim$ 1 km s^{-1}.

The $C^{18}O$ emission peak coincides with the continuum peak for our six sources and appears to be compact, less than 1000 au diameter for B1-c and TMC1. For B1-c and all Class 0 sources (Fig. 5.18), low-level extended $C^{18}O$ emission is seen along the outflow direction. For the only Class I source targeted with the ACA, emission is marginally resolved in the direction perpendicular to the outflow.

$C^{18}O$ is a good tracer of high column density material, however, it becomes less abundant as soon as the dust temperature drops below the CO freeze-out temperature ($\sim$ 20–25 K). There is also a density threshold: CO freeze-out only occurs at densities above $\sim$ 10^4–10^5 cm^{-3}, because at lower densities the timescales for freeze-out are longer than the lifetime of the core (Caselli et al. 1999; Jørgensen et al. 2005).

For 4 out of 6 sources presented at 6″resolution, Kristensen et al. (2012) performed modeling of the SED and sub-mm spatial extent using the DUSTY code (Ivezic & Elitzur 1997). The results provide, among other properties, a temperature structure throughout the envelope and the radius at which the temperature drops below 10 K, which is considered as the border between envelope and the parent cloud. Kristensen et al. (2012) obtained radii of 3800, 5000, 6700, and 9900 au for IRAS4B, TMC1, SMM3, and BHR71, respectively. The compact $C^{18}O$ emission observed on-source and its non-detection over the full expected extent of the protostellar envelope can be explained by CO freeze-out occurring already within the inner 1800 – 2500 au radius, which is the spatial resolution of our observations for Class 0 sources. This upper limit on the CO snowline is consistent with CO snowlines typically observed and modeled toward other Class 0 protostars (Jørgensen et al. 2004b; Anderl et al. 2016; Hsieh et al. 2019b).

Equation 1 from Frimann et al. (2017) allows to calculate the expected CO snow line for the current luminosity of the example sources B1-c and TMC1 presented in Fig. 5.4 in the absence of an outburst. For B1-c the snowline is expected to be at 200–400 au radius depending on the assumptions of the sublimation temperature (smaller radii for 21 K and larger for 28 K), while the TMC1 CO snowline is expected to be at 100–200 au. For the most luminous source with $C^{18}O$ 7m observations available, the expected radius is at 400–750 au. Therefore clearly in all cases the expected CO snowline is well within the 7m beam.

In high-resolution studies, the CO emission is often seen at greater distances than expected from the current luminosities of those protostars. This is attributed to accretion bursts of material which increase their luminosities resulting in a shift of the observed CO emission radius up to a few times its expected value (but usually still within a 1000 au radius) (Jørgensen et al. 2015; Frimann et al. 2017; Hsieh et al. 2019b). Therefore, we cannot say anything about past accretion burst based on these data.

N_2D^+ and DCO^+

In our observations N_2D^+ is seen extended in the direction perpendicular to the core rotation axis, which is typically the same as the outflow rotation axis, toward B1-c (Fig. 5.4) and other Class 0 sources except IRAS 4B (Fig.5.19). In the case of IRAS 4B the emission from this molecule appears dominated by large-scale emission from the filament detected toward this source, connecting it with IRAS 4A (Sakai et al. 2012). The peak of the N_2D^+ emission is significantly shifted from the continuum peak in all cases, with a significant decrease in the inner regions in some cases (see BHR 71 in Fig. 5.19). Similar extended N_2D^+ emission in other Class 0 sources was seen by Tobin et al. (2013) based on lower resolution OVRO data. For TMC1 the N_2D^+ molecule is not detected.

The DCO^+ emission is seen extended in a similar fashion to what is observed for N_2D^+. However, contrary to N_2D^+, DCO^+ is brightest on the continuum peak for all sources except TMC1 and Per-emb-25. For these two sources, the emission peak is offset by 1000–2000 au from the continuum source in the direction perpendicular to the outflow.

Both DCO^+ and N_2D^+ are considered cold gas tracers. N_2D^+ is efficiently destroyed by CO in the gas-phase, therefore freeze-out of CO results in N_2D^+ being retained in the gas-phase at larger radii of the envelope, where temperatures are lower. This behaviour has been demonstrated in several other protostellar sources by Tobin et al. (2011, 2013).

Both DCO^+ and N_2D^+ are produced through reactions with H_2D^+. At cold temperatures the H_2D^+ abundance is enhanced through the $H_3^+ + HD \rightarrow H_2D^+ + H_2$ reaction, which is exothermic by 230 K. As the reverse reaction is endothermic, low temperatures increase H_2D^+. Additionally, both H_3^+ and H_2D^+ are enhanced in gas where CO has been depleted. However, the CO molecule is still needed for the production of DCO^+ through the H_2D^+ + CO reaction. Therefore, DCO^+ is expected to be most abundant around the CO snowline (Jørgensen et al. 2004b; Mathews et al. 2013). Warmer production routes through CH_2D^+ + CO are also possible (Wootten 1987; Favre et al. 2015; Carney et al. 2018).

The difference between DCO^+ and N_2D^+ chemistry is reflected in the morphology of the emission observed toward our sample. As DCO^+ requires gas-phase CO for its formation, it peaks close to the CO snowline, which is within the resolution of our observations (~1800–2500 au radius), while N_2D^+ is only located where CO is not present in the gas phase. Therefore we observe a significant decrease of N_2D^+ in the inner envelope. If the warm production of DCO^+ is triggered in the inner regions, this will additionally produce DCO^+ within the beam of our observations, hence DCO^+ does not decrease in the inner envelope. The extent of the DCO^+ and N_2D^+ emission in each source is comparable, ranging from ~ 5000 au in B1-c and BHR71 to 1500 au in TMC1, suggesting that their outside radii trace the region where CO becomes present again in the gas phase due to the low density.

The morphology of the emission from cold gas tracers such as DCO^+ and N_2D^+ is sensitive to the density and temperature profile of the system, which can be affected by system geometry (i.e., outflow opening angle, disk flaring angle, flattening of the envelope). DCO^+ has been shown to increase its abundance in the cold shadows of a large embedded disk (Murillo et al. 2015).

In the Class I source, DCO^+ is present on much smaller scales (< 2000 au radius) than in Class 0 sources and no N_2D+ is seen. Emission from those molecules is consistent with a picture of a dissipating envelope in Class I sources, resulting in less dense, warmer gas surrounding the protostar. TMC1 has an order of magnitude lower envelope mass compared to the Class 0 sources (Table 5.1; Kristensen et al. 2012). This causes the extent of the cold and dense region to shrink, preventing N_2D^+ from being detected, and limiting the extent of DCO^+ emission. The dense gas toward TMC1 is clearly present only in the flattened structure

surrounding the binary system, likely forming a young, embedded disk. In fact this source is suggested to have a rotationally-supported circumbinary disk (Harsono et al. 2014; van't Hoff et al. 2020). The geometry of the disk can create favourable conditions for the DCO^+ enhancement in the cold shadows of the disk.

Other relevant molecules that trace the quiescent envelope material but are not presented here are HCO^+ and $H^{13}CO^+$ (Hogerheijde et al. 1997; Jørgensen et al. 2007; Hsieh et al. 2019b, van 't Hoff et al. in prep.). These molecules have been shown to probe the material outside of the water snowline (Jørgensen et al. 2013; van 't Hoff et al. 2018a). As water sublimates at temperatures $\sim$ 100 K, much higher than CO, HCO^+ can be seen throughout the envelope, except for the warmest inner regions. N_2H^+ is tracing the envelope material and CO snowline and has been shown to peak closer to the central protostar than N_2D^+ (Tobin et al. 2013). Their ratio can potentially be used as an evolutionary tracer of protostars (Emprechtinger et al. 2009).

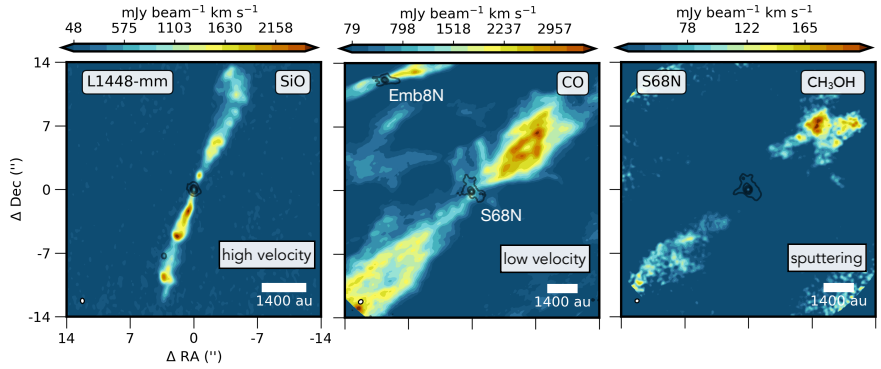


Figure 5.5: Maps of three different components of the outflow. Moment 0 maps are presented in color scale with continuum emission at 1.3 mm in black contours, both obtained with ALMA 12m observations. *Left:* An extremely high-velocity (EHV) molecular jet illustrated with the SiO (4–3) map for L1448-mm integrated from -70 to -50 and from 50 to 70 km s^{-1} w.r.t v_{sys}. *Middle:* Low-velocity outflow illustrated with the CO 2–1 map for S68N integrated from -15 to -3 and from 3 to 15 km s^{-1} w.r.t v_{sys}. *Right:* Ice mantle content released with shock sputtering presented with the CH_3OH ($2_{1,0} - 1_{0,0}$) map for S68N integrated from -8 to -1 and from 1 to 8 km s^{-1} w.r.t v_{sys}. The CO outflow from Ser-emb-8N is present at the edge of the map.

In summary, the quiescent envelope material is traced by dense and/or cold gas tracers. Chemical interactions result in N_2D^+ tracing the outer envelope where CO is frozen-out, whereas DCO^+ is seen both in the outer envelope as well as in the inner regions, tracing the unresolved CO snowline. $C^{18}O$ is a good tracer of dense ($n > 10^5$ cm^{-3}) and warm ($T > 30$ K) regions in the inner 2000 au radius of the protostellar systems. The protostellar evolution from Class 0 to Class I is evident as the envelope becomes less dense and more warm and the protostellar luminosity can heat up dust and gas more easily.

5.5 Outflows and jets

Outflowing material from protostellar systems is best analyzed with kinematic information. In the following section, we will discuss three different components of protostellar outflows

observed with the ALMA 12m array: 1) the high-velocity jet (>30 km s^{-1}), 2) the low-velocity entrained outflow (<30 km s^{-1}), 3) the gas that results from the interaction with the outflow – ice sputtering products at velocities close to that of ambient material, but with linewidths significantly broader (up to 15 km s^{-1}) than the quiescent envelope tracers. The three components are presented in Fig. 5.5 with examples of S68N, a representative case of a prominent outflow and ice sputtering, and L1448-mm, a source with a prototypical high-velocity jet.

5.5.1 Extremely high-velocity jet

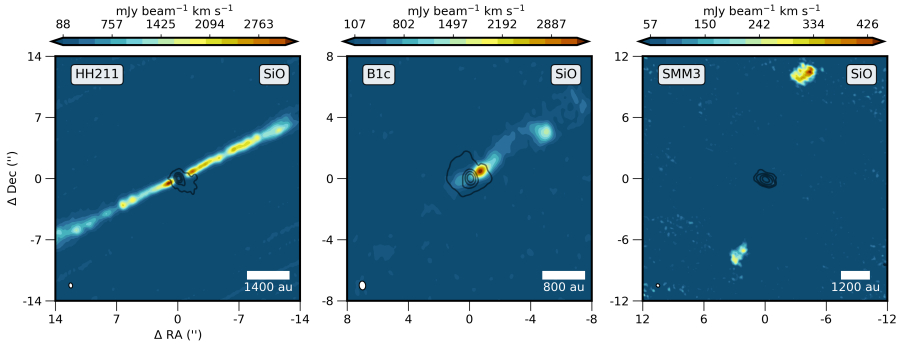


Figure 5.6: Maps of the EHV jets observed in SiO. Moment 0 maps are presented in color scale with continuum emission at 1.3 mm presented in black contours, both obtained with 12m observations. SiO 4–3 map of HH211 integrated from -20 to -10 and from 10 to 20 km s^{-1} w.r.t v_{sys}; B1-c ntegrated from -70 to -40 and from 40 to 70 km s^{-1} w.r.t v_{sys}; SMM3 integrated from -60 to -40 and from 20 to 35 km s^{-1} w.r.t v_{sys}.

Figure 5.6 presents the extremely high-velocity (EHV) molecular jet component for HH211, B1c, and SMM3 observed in SiO with the ALMA 12m array; the L1448-mm EHV is shown in Fig. 5.5. The latter and HH211 are well-known EHV sources (Guilloteau et al. 1992; Lee et al. 2007) while SMM3 and B1-c are new detections of the jet component. HH211 shows SiO emission at low-velocities because the outflow is almost in the plane of the sky, but the high velocities are evident from the large proper motion movements of the bullets (~115 km s^{-1}; Lee et al. 2015). CO, H_2CO, and SiO in the EHV jets of Emb8N and SMM1 are presented in detail in Hull et al. (2016) and Tychoniec et al. (2019). Altogether, these detections in 6 out of 7 Class 0 sources targeted at high-resolution, strengthen the conclusion that EHV jets are more common than previously thought in Class 0 sources.

In the case of L1448-mm and HH211, there are several molecular bullets along the jet axis with velocities up to 100 km s^{-1}, while both B1c and SMM3 show a much simpler structure with two bullets detected on one side in the former and a single pair of symmetrically placed bullets observed in the latter case. B1-c actually has a pair of bullets ~ 200 au from the continuum peak, with the other bullet at 2500 au only seen in the redshifted part of the jet. The emission in SiO and SO appears very similar (Fig. 5.22, Fig. 5.23). There are no other molecules tracing the high-velocity component toward this source. H_2CO and ^{12}CO are not targeted with our ALMA 12m datasets toward B1-c. The SMM3 jet has two distinct high-velocity bullets at ~ 3200 au from the source which appear similar in CO, SiO and SO (see

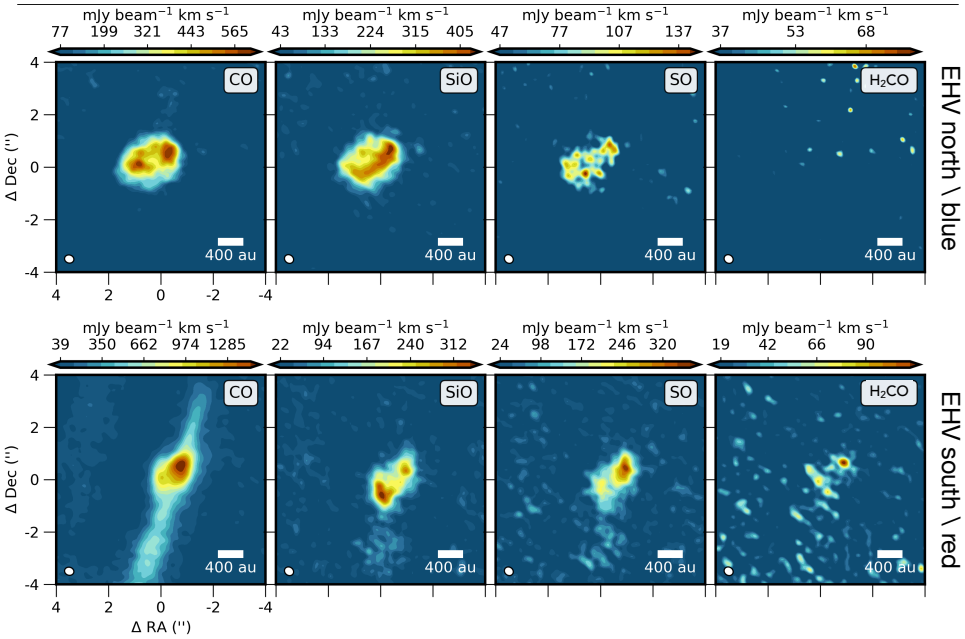


Figure 5.7: Zoom-in on molecular bullets from the SMM3 jet (see Fig. 5.6). CO, SiO, SO, and H_2CO molecular transitions are presented. *Top:* Norther/blueshifted bullet. Moment 0 maps are integrated from -60 to -40 km s^{-1} w.r.t v_{sys}. The map center is offset from the SMM3 continuum center by (−3.″7, +10.″3). *Bottom:* Southern/redshifted bullet. Moment 0 maps are integrated from 20 to 40 km s^{-1}. The map center is offset from the SMM3 continuum center by (+2.″7, −7.″).

zoom-in on Fig 5.7). Additionally, the redshifted bullet shows faint, but significant emission from H_2CO. No traces of H_2CO are found in the blueshifted outflow.

These data are particularly interesting as still only few molecules tracing EHV jets have been identified to date (see Lee 2020 for review). Apart from those presented here – CO, SiO, SO, and H_2CO– molecules such as HCO^+ and H_2O have been seen in this high-velocity component (Kristensen et al. 2012; Lee et al. 2014). What is especially important to highlight is the third detection of a H_2CO bullet in SMM3 after IRAS04166 (Tafalla et al. 2010) and Emb8N (Tychoniec et al. 2019). This detection means that either a significant fraction of ice-coated dust is released with the jet, or that the H_2CO is efficiently produced in the jet through gas-phase chemistry.

It is argued that the molecular jet tracers have a very different physical origin than the protostellar outflows. Contrary to the low-velocity outflow, which consists mostly of entrained envelope material, the EHV jet is expected to be directly launched from the innermost region of the system (Tafalla et al. 2010; Lee 2020). The high-velocity jet is comprised of atomic material which readily forms molecules in the high-density clumps (internal working surfaces; Raga et al. 1990; Santiago-García et al. 2009) that are resulting from shocks in the jet, which are produced by the velocity variations of the ejection. This in turn means that by observing the high-velocity bullets, one gains insight on the variability of the accretion process (Raga et al. 1990; Stone & Norman 1993). The new EHV sources B1c and SMM3 show bullet spacings of 1200 au in B1c and 3200 au in SMM3, which can be converted using the terminal velocity of the jets (not corrected for inclination) to the dynamical ages of 80 and

250 years, respectively. If the central mass of the protostar can be estimated this can be used to provide the orbital period of the component causing the variability (Lee 2020).

The fact that the EHV jet tracers are dominated by O-bearing molecules has been associated with a low C/O ratio in the jet material (Tafalla et al. 2010). For high mass-loss rates, molecules are produced efficiently in the jet from the launched atomic material (Glassgold et al. 1991; Raga et al. 2005; Tabone et al. 2020). Additionally the ratio of SiO-to-CO can indicate the presence of dust in the launched material, which can in turn inform about the jet launching radius, i.e., whether it is inside or outside the dust sublimation radius (Tabone et al. 2020). The new detections of high-velocity jets suggest that this process may be occurring in every young Class 0 object. Studying large samples of objects with ALMA and combining with multi-transition observations can unveil the atomic abundances of the inner regions, which are difficult to measure otherwise directly (McClure 2019).

In summary: O-bearing species such as CO, SiO, SO, and H_2CO observed at high velocities are excellent tracers of the chemistry within the protostellar jet. Those molecules most likely formed in the internal working surfaces from the material carried away from the launching region of the jet.

5.5.2 Low-velocity outflow

Figure 5.8 presents low-velocity outflow tracers CO 2–1 (E_{up} = 16 K) for TMC1, SO 5_6–4_5 (E_{up} = 35 K), and SiO 4–3 (E_{up} = 21 K) for B1c. In Fig. 5.21 we present an overview of CO 2–1 emission for five sources obtained with the ALMA 12 m array at 0.″4 resolution. The sources show a variety of emission structures in the low velocity gas (<20 km s^{-1}). In all cases, we do not capture the entirety of the outflows as they extend beyond the primary beam of observations (~ 30″). SMM3 and Emb8N have very narrow outflow opening angles (< 20 degrees), while SMM1, S68N and TMC1 present larger opening angles.

CO emission is especially prominent in the cavity walls, which can be related to both the limb brightening effect as well as higher (column) density of the material in the outflow cavity walls. This is especially highlighted in the Class I source, TMC1, where CO emission is almost exclusively seen in the outflow cavity walls. Even though CO is piling up in this region, it is observed at velocities up to 15 km s^{-1} so it is clearly tracing the entrained material and not the quiescent envelope. The lower envelope density in Class I results in less material to be entrained in the outflow. In SMM1, three CO outflows from SMM1-a, SMM1-b, and SMM1-d are overlapping (Hull et al. 2016; Tychoniec et al. 2019).

The CO molecule traces the bulk of the gas as it is the most abundant molecule detectable in the sub-mm regime. It serves as an indicator of the outflow extent and gas morphology, as it is not affected by chemical processing in shocks. It can also be used to quantify the total mass-loss rates, using the dense cloud abundance ratio of $CO/H_2 \sim 10^{-4}$. A well-known correlation between molecular outflows and protostellar luminosities indicates a strong link between the accretion and ejection processes (Cabrit & Bertout 1992; Bontemps et al. 1996; Mottram et al. 2017). The decrease in accretion and total envelope mass with evolution of the system also results in fainter, less powerful outflows. The weak emission from the Class I source TMC1, which is an order of magnitude lower in intensity with respect to outflows from Class 0 protostars, is consistent with this trend.

In Fig. 5.22, SiO maps are presented: Band 5 SiO 4–3 (E_{up} = 21 K) and Band 6 SiO 5–4 (E_{up} = 31 K) data are shown in velocity ranges corresponding to the low-velocity outflow. In contrast to CO emission, the low-velocity SiO is mostly observed in clumps of emission instead of tracing the entirety of the outflowing gas. Several such clumps can be seen in

the S68N source. In some cases, the clumps are relatively symmetric (Emb8N, B1-c), while monopolar emission is seen in other examples (L1448-mm, SMM1-d). In the case of SMM1-a and SMM1-b, very weak SiO emission at low velocities is observed. SiO emission in outflows is exclusively present in the Class 0 sources, while absent in the Class I sources, TMC1 and B5-IRS1, covered in these data sets.

SiO is a molecule that is enhanced by several orders of magnitude in shocks compared with gas in cold and dense clouds where most of the Si is locked in the grains (e.g., Guilloteau et al. 1992; Dutrey et al. 1997). Shocks release Si atoms from the grains by means of sputtering and grain destruction, leading to subsequent reactions with OH, another product of shocks, forming SiO (Caselli et al. 1997; Schilke et al. 1997; Gusdorf et al. 2008b,a). Thus, SiO is much more prominent in high-velocity gas, where grains are more efficiently destroyed (see Section 4.1), than in low-velocity shocks.

SO is a shock tracer, similarly to SiO. Fig. 5.23 presents SO 5_6–4_5 (E_{up} = 35 K) and SO 6_7–5_6 (E_{up} = 47 K) observations in Band 6. The emitting regions of SO are comparable with those of SiO for the Class 0 sources. The cases of S68N and B1-c show that SO emission also peaks at the source position while SiO is absent there. Thus, SO and SiO do not always follow each other and some SO might be associated with hot core emission (Drozdovskaya et al. 2018). Important differences are observed for TMC1, where SO seems to be associated with the remainder of the envelope or the disk, while the SiO is not detected toward this source, as mentioned above.

SO is enhanced in shocks through reactions of atomic S released from the grains with OH, as well as through H_2S converted to SO with atomic oxygen and OH (Hartquist et al. 1980; Millar & Williams 1993). Shocks could also explain the emission toward TMC1, where weak accretion shocks onto the disk could enhance the SO abundances (Sakai et al. 2014b; Yen et al. 2014; Podio et al. 2015). Overall, there is a clear decrease of both SiO and SO low-velocity emission from Class 0 to Class I. Either the less powerful jet cannot destroy the grains and create conditions for the production of SiO and SO and/or the much less dense envelope and outflow cavity walls do not provide enough dust grains for creating large column densities of those molecules; additionally, the excitation conditions might change significantly with evolution of the protostellar system, hampering the detection of even low-J SO and SiO transitions with critical densities in the 10^5 – 10^6 cm^{-3} range.

HCN 1–0 (E_{up} = 4 K) and $H^{13}CN$ 2–1 (E_{up} = 12 K) maps are presented in Fig. 5.24 and 5.25, respectively. HCN is clearly seen in outflowing material enhanced in similar regions as low-velocity SiO. For Emb8N the HCN emission has been associated with intermediate velocity shock (Tychoniec et al. 2019). In B1-c and L1448-mm weak extended emission along the outflow direction is detected but $H^{13}CN$ strongly peaks on source. In the case of HH211, $H^{13}CN$ is seen only in the outflow, with a geometry consistent with the outflow cavity walls, but with velocity profiles that are consistent with the outflowing material.

HCN is associated with the most energetic outflows (Jørgensen et al. 2004; Walker-Smith et al. 2014) and is enhanced at high temperatures in shocks. $H^{13}CN$ is likely associated with both the hot inner regions (not detected in HCN due to optical thickness of the line) and the low-velocity outflow (Tychoniec et al. 2019; Yang et al. 2020). The geometry of $H^{13}CN$ emission seen in HH211 resembles a cavity wall: it could be a result of CN produced by UV-photodissociation and subsequent production of HCN via the H_2 + CN reaction, which requires high temperatures (Bruderer et al. 2009; Visser et al. 2018). The fact that $H^{13}CN$ is seen at outflow velocities shows that shocks are required to produce HCN, which is likely released at the cavity walls and then dragged with the outflow.

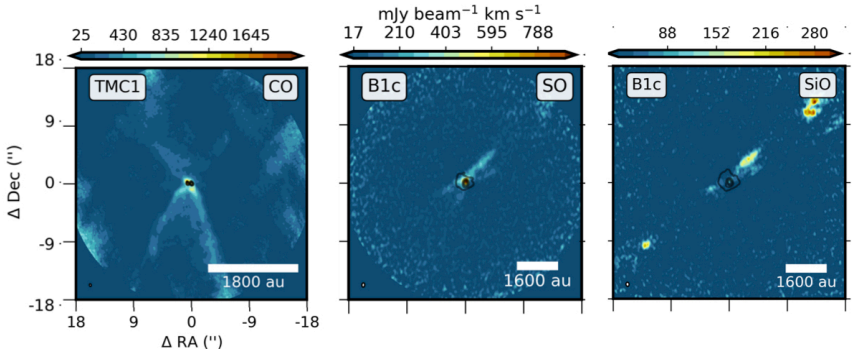


Figure 5.8: Low-velocity outflow in CO, SO, and SiO. Moment 0 maps of CO toward TMC1, SO and SiO map toward B1c are integrated from -10 to 10 km s^{-1} w.r.t v_{sys}.

5.5.3 Shock sputtering products

Ice-mantle tracers are a different class of molecules detected in low-velocity protostellar outflows. They are produced and entrained through interactions between the jet and the envelope. Here we present ALMA 12m array observations in Band 6 at 0.″5 resolution for CO 2 − 1 ($E_{\rm up}$ = 17 K), CH_3OH $2_{1,0} - 1_{0,0}$ ($E_{\rm up}$ = 28 K), and H_2CO $3_{0,3} - 2_{0,2}$ ($E_{\rm up}$ = 21 K) , and in Band 3 at 3″ for CH_3CN $6_1 - 5_1$ ($E_{\rm up}$ = 26 K), CH_3CHO $6_{1,6,0} - 5_{1,5,0}$ ($E_{\rm up}$ = 21 K), and HNCO $5_{0,5} - 5_{0,4}$ ($E_{\rm up}$ = 16 K). Fig. 5.9 compares maps of integrated emission from those molecules with those of CO for S68N. All ice-mantle tracers detected in the outflow are observed in their low-energy transitions.

The shape of the emission of these ice-mantle tracers is somewhat similar. CH_3CN and HNCO are clearly brighter on the redshifted part of the outflow (south-east) and CH_3CHO are brighter in the blueshifted (north-west) side. CH_3OH and H_2CO show an even distribution between the two lobes. The peak intensity for all species occurs at significant distances from the source (~ 5000 au) and in some cases the emission drops below the detection limit closer to the source. This is contrary to the CO emission, which can be traced all the way back to the central source. In all tracers the emission is also detected at the continuum position, however, this emission has a narrow profile and results from thermal sublimation of ices in the hot core of S68N (van Gelder et al. 2020).

The velocities observed for ice-mantle tracers in the outflow are <15 km s^{-1} with respect to the systemic velocity. This is slower than the CO and SiO outflow line wings which have velocities up to 20–30 km s^{-1}. On the other hand, the lines are clearly broader than those of molecular tracers of UV-irradiated regions that trace passively heated gas (see Section 5). The velocities observed for CH_3OH and other ice-mantle tracers are high enough for these molecules to be material near the outflow cavity walls, where ice mantles could be sputtered. These molecules therefore most likely trace low-velocity entrained material with a considerable population of ice-coated grains that are sputtered in the shock (Tielens et al. 1994; Buckle & Fuller 2002; Arce et al. 2008; Jiménez-Serra et al. 2008; Burkhardt et al. 2016). Thermal desorption of molecules from grains is not likely as dust temperatures are below 100 K in the outflow cavity walls at distances of few times 10^3 au for low-mass stars, and at those temperatures most COMs are frozen out on grains. The fact that there is no enhancement of these tracers closer to the source also argues against emission being related to high temperature.

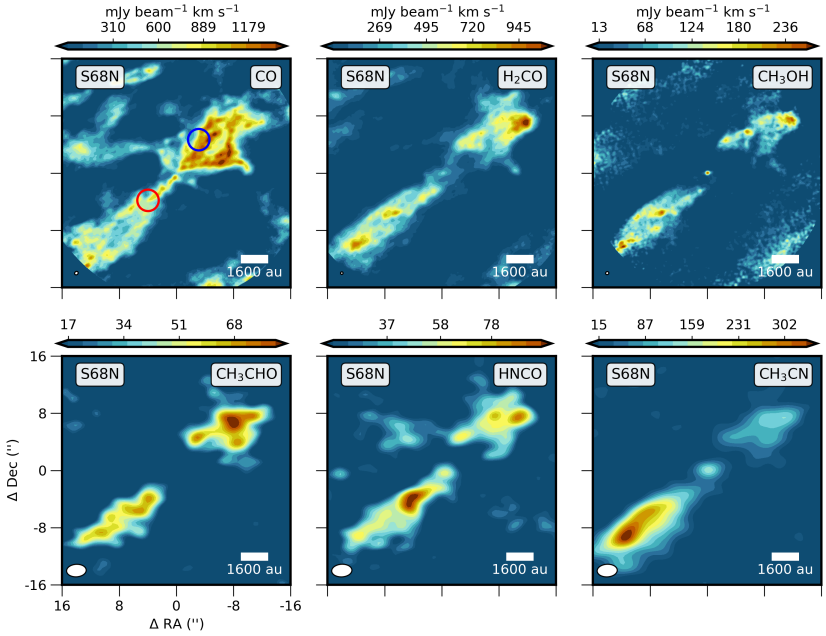


Figure 5.9: Maps of the ice mantle tracers toward the S68N outflow, with the CO low-velocity outflow map for reference. *Top:* CO, H_2CO and CH_3OH moment 0 maps obtained in Band 6 at 0.″5 resolution. Circles show regions from which spectra were obtained for analysis in Section 7.1. *Bottom:* CH_3CHO, HNCO, and CH_3CN moment 0 maps obtained in Band 3 at 2.″5 resolution. The emission is integrated from -10 to -1 km s^{-1} and from 1 to 10 km s^{-1} w.r.t v_{sys}.

The prototypical outflow source with complex organic chemistry – the L1157-B1 shock spot – exhibits emission from many species. Complex molecules such as CH_3OCHO and C_2H_5OH (Arce et al. 2008), H_2CCO, $HCOCH_2OH$, CH_3OCH_3 (Lefloch et al. 2017) and NH_2CHO (Codella et al. 2017) are seen. The abundances of some COMs w.r.t. CH_3OH detected at the B1 position exceed those of 'hot corinos' by a factor of 2 to 10. However, the largest molecules seen in warm inner envelopes of protostars are not detected at L1157-B1 (Lefloch et al. 2017). THe hot core and outflow chemical composition for source S68N are compared in Section 7.1.

The complex structure of H_2CO seen in S68N at low-velocities contrasts with the simple kinematic structure of the high-velocity bullet seen in SMM3 (Section 4.1, Fig. 5.7). The origin of the H_2CO emission for these two sources could be different, with the low-velocity emission arising from the sputtering of ices, whereas the presence of H_2CO in the jet could result from gas-phase production through the reaction of CH_3 with O. Alternatively, if the icy grains were launched with the jet, they could be sputtered in the internal working surfaces at high velocities (Tychoniec et al. 2019).

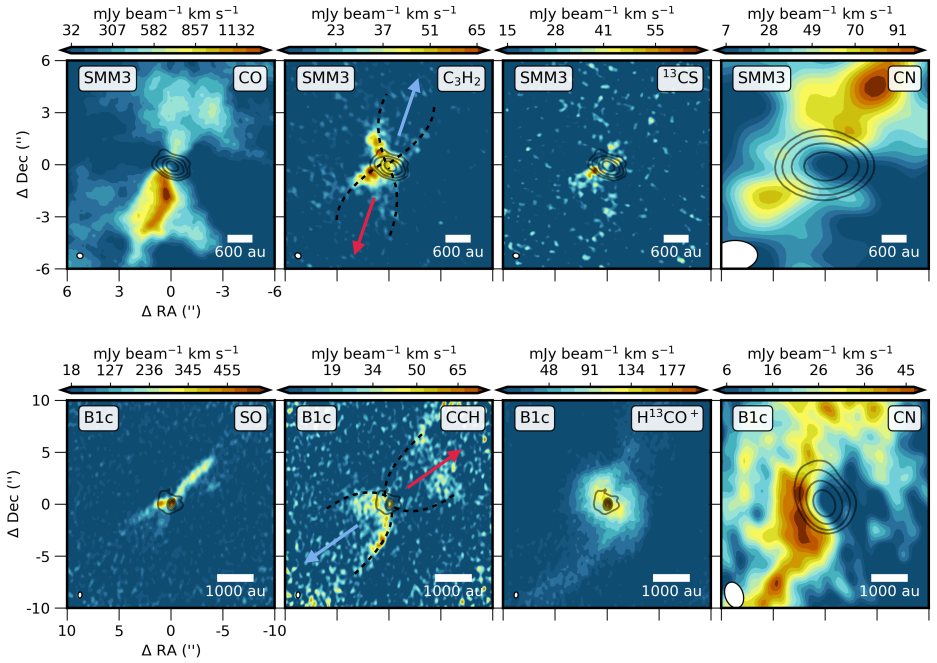


Figure 5.10: Maps of the outflow cavity wall tracers toward SMM3 and B1c, with low-velocity outflow map for reference. *Top:* Moment 0 maps toward SMM3 of CO 2–1, c-C_3H_2 $6_{1,6}$–$5_{0,5}$, and ^{13}CS 5–4 obtained in Band 6 at 0.″5 resolution and CN 1–0 in Band 3 at 3″. *Bottom:* Moment 0 maps toward B1c of SO 6_7–5_6, C_2H $3_{2.5,3}$–$2_{1.5,1}$ and $H^{13}CO^+$ 3–2 obtained at 0.″5 and CN 1–0 at 3″. The emission is integrated from -5 to -1 km s^{-1} and from 1 to 5 km s^{-1} w.r.t v_{lsr}. Outflow directions and delineated cavity walls are showed in C_2H and C_3H_2 maps.

5.6 Outflow cavity walls

In this section, we highlight key molecules detected in the outflow cavity walls. It is challenging to precisely distinguish cavity walls from the outflowing material. The velocity of the gas in the cavity walls should be lower than in the outflow, as the cavity wall contains envelope material at rest but which is passively heated by UV radiation. We first discuss maps of species associated with cavity walls and then their line profiles.

5.6.1 Maps

Figure 5.10 presents integrated emission maps of key tracers discussed in this section for two examples: SMM3 and B1-c. Plots for the remainder sources (S68N, Emb8N, and TMC1) are presented in the Appendix in Fig. 5.26.

Key tracers of the outflow cavity walls are simple unsaturated hydrocarbon molecules: c-C_3H_2 $4_{4,1}$–$3_{3,0}$ ($E_{\rm up}$ = 32 K) for SMM3 and TMC1, and C_2H $3_{2.5,3}$–$2_{1.5,2}$ ($E_{\rm up}$ = 25 K) for S68N, B1-c, and Emb8N, as seen in maps obtained with ALMA Band 6 at 0.″5 resolution.

In Emb8N and SMM3 the emission from C_2H and c-C_3H_2, respectively, is symmetric; it appears similar in extent and shape on both sides of the continuum source. Comparison with CO emission, which traces the bulk of the outflowing gas, indicates that the hydrocarbons

are located in the outflow cavity walls close to the source. For B1-c, the emission from C_2H is U-shaped suggestive of a cavity wall, stronger on the blueshifted side of the outflow, which could be either a projection effect or an asymmetry in the envelope structure. For B1-c no ALMA CO observations exist to compare with the bulk of the outflow at comparable resolution; however, the other outflow tracer, SO, confirms the outflow direction and rough extent of the outflow cavity walls. Moreover, the shape of the cavity walls is consistent with the appearance of the CO 3–2 outflow observed with SMA toward this source at 4″resolution (Stephens et al. 2018).

S68N presents a chaotic structure (Fig. 5.26, top), but C_2H is found elongated in the outflow direction. While it is difficult to identify the cavity wall, the C_2H emission surrounds the CO outflow emission. The C_2H emission toward this source is asymmetric, with stronger emission in the blueshifted part of the outflow. Emission of c-C_3H_2 toward the Class I source TMC1 (Fig. 5.26, bottom) is not directly related to the cavity walls, but is extended perpendicular to the outflow, which suggests that c-C_3H_2 traces the envelope or extended disk material.

Both c-C_3H_2 and C_2H have been prominently observed in PDRs such as the Horsehead Nebula and the Orion Bar tracing the layers of the cloud where UV-radiation photodissociates molecules, which helps to maintain high atomic carbon abundance in the gas-phase that is needed to build these molecules. C_2H is enhanced in the presence of UV radiation at cloud densities (Fuente et al. 1993; Hogerheijde et al. 1995) and c-C_3H_2 usually shows a good correlation with C_2H (Teyssier et al. 2004). Both molecules have efficient formation routes involving C and C^+, although models with only PDR chemistry tend to underpredict their abundances, especially for c-C_3H_2. A proposed additional mechanism is the top-down destruction of PAHs (Teyssier et al. 2004; Pety et al. 2005, 2012; Guzmán et al. 2015); the spatial coincidence of PAH emission bands with hydrocarbons in PDRs is consistent with that interpretation (van der Wiel et al. 2009).

It is instructive to compare the conditions between classic PDRs and outflow cavity walls around low-mass protostars.The G_0 value for Orion Bar is estimated at 2.6×10^4 (Marconi et al. 1998), while the Horsehead Nebula has a much more moderate field of 10^2 (Abergel et al. 2003). The UV radiation field around low-mass protostars measured by various tracers is 10^2–10^3 at $\sim$ 1000 au from the protostar (Benz et al. 2016; Yıldız et al. 2015; Karska et al. 2018), therefore the PDR origin of small hydrocarbons is plausible. The top-down production of hydrocarbons due to PAHs destruction does not appear to be an efficient route here, as PAHs are not commonly observed in low-mass protostellar systems (Geers et al. 2009), and the UV-fields required for this process are above 10^3 (Abergel et al. 2003).

The difference in morphology of hydrocarbons between Class 0 and Class I systems – outflow cavity walls in Class 0 versus rotating disk-like structure in Class I – is most likely related to the evolution of the protostellar systems. Class 0 sources have a dense envelope and the UV radiation can only penetrate the exposed outflow cavity walls, while for Class I it is likely much easier for both the UV radiation from the accreting protostar and the interstellar radiation to reach deeper into the envelope or disk.

Figure 5.10 also shows CN 1–0 ($E_{\rm up}$ = 5 K) observed at 3″resolution in Band 3 for SMM3 and B1-c. Compared with C_2H, CN is tracing similar regions. In S68N CN has a similar extent as C_2H but not over the full extent of the outflow traced by CO. In B1-c, the CN emission has a similar shape of the cavity wall cone as seen in C_2H, but also a significant contribution from larger scales is detected. In all cases the CN emission avoids the central region, which likely results from on-source absorption by the foreground CN molecules.

TMC1 presents a high-resolution example of CN emission (Fig. 5.26). The offset between

CO and CN reveals a physical structure of the inner regions of the protostellar system: the entrained outflow traced with CO appears closer to the jet axis, while CN highlights the border between the outflow cavity wall and quiescent envelope. CN is sensitive to UV radiation, as it can be produced with atomic C and N, whose abundances are enhanced in PDRs, with UV photodissociation of HCN contributing as well (Fuente et al. 1993; Jansen et al. 1995; Walsh et al. 2010; Visser et al. 2018).

$H^{13}CO^+$ emission is presented for B1c (Fig. 5.10) and S68N (Fig. 5.26) observed in Band 6 at 0.″4 resolution. The bulk of the emission from this molecule appears to be related to the cold envelope, however streams of material can be seen in B1-c and S68N. The streams of gas observed in $H^{13}CO^+$ are coincident with the cavity wall observed in C_2H. As $H^{13}CO^+$ is expected to probe the dense envelope, the similarity of the morphology of the traced material between $H^{13}CO^+$ and C_2H and CN shows that the envelope material is UV-irradiated. ^{13}CS observed in Band 6 with the 12m array is detected for SMM3 (Fig. 5.10). Weak emission from this molecule is observed in TMC1. The morphology of ^{13}CS emission is very similar to that of c-C_3H_2.

The ^{13}CS molecule, as a high-density tracer likely traces the material piling up on the cavity walls pushed by the outflow. This emission is usually slow ($\pm$ 2 km s^{-1}) indicating that this is not outflowing gas but rather envelope material on the outflowing cavity walls.

Faint emission of ^{13}CS towards the Class I source TMC1 is consistent with the dissipating envelope as the source evolves, hence no high-density material is seen in the remnant cavity walls, even though they are still highlighted by the CO emission.

5.6.2 Spectral profiles - cavity walls or entrained outflow

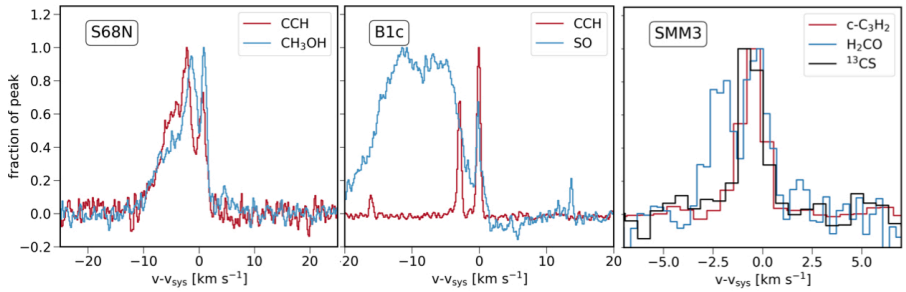


Figure 5.11: Spectra obtained at the cavity wall positions for hydrocarbons (red) and ice-mantle tracers (blue). *Left:* C_2H $3_{2.5,2}$–$2_{1.5,1}$ (E_{up} = 25 K) and CH_3OH $2_{1,0}$–$1_{0,1}$ (E_{up} = 28 K) spectra for S68N, *Middle:* C_2H $3_{2.5,2}$–$2_{1.5,1}$ (E_{up} = 25 K) and SO 6_7–5_6 (E_{up} = 48 K) spectra for B1-c, *Right:* c-C_3H_2 $4_{4,1}$–$3_{3,0}$ (E_{up} = 32 K), H_2CO $3_{2,1}$–$2_{2,0}$ (E_{up} = 68 K), and ^{13}CS 5–4 (E_{up} = 33 K) spectra for SMM3.

In Fig. 5.11 spectra of ice mantle tracers, CH_3OH and H_2CO, and the hydrocarbon molecules, C_2H and C_3H_2 are presented. All spectra are shifted by their source velocity to zero km s^{-1}. In case of S68N, it is seen that C_2H and CH_3OH have very similar line profiles indicating that they trace similar material. The width of $\sim$ 10 km^{-1} suggests that this material is entrained with the outflow. A narrow component appears to be superposed at systemic velocities. Note that fine splitting of C_2H blends the spectra although the other transition at +2 km s^{-1} does

not affect the blueshifted velocity component. In contrast, B1c shows only remarkably narrow C_2H line profiles with a FWHM of ~ 2 km s^{-1}, and SMM3 has similarly narrow c-C_3H_2 and ^{13}CS lines compared with broader H_2CO emission (Fig. 5.11, right) . This is consistent with emission from well-defined cavity walls seen toward those sources.

The case of moderate ~ 10 km s^{-1} velocity material observed toward S68N indicates that the C_2H line does not in all sources trace exclusively the quiescent cavity walls. The profile is consistent with the observed morphology of the line (see Fig. 5.26) – emission is seen up to a few thousand au from the source and its shape does not resemble a cavity wall as clearly as in other sources. The narrow component centered at systemic velocity seen in Fig. 5.11 indicates that while the broad component might be dominating the emission, the UV-irradiated cavity wall also contributes to the emission observed for S68N. S68N could be a very young source, as the chaotic structure of its outflow and envelope indicates (Le Gouellec et al. 2019). The high abundances of freshly released ice-mantle components described in Section 4.3 are consistent with this interpretation (see also Section 7.1). It is also possible that UV radiation produced locally in shocks is causing the enhancement of C_2H emission at higher velocities.

To summarize, we observe the hydrocarbons C_2H and c-C_3H_2, as well as CN, $H^{13}CO^+$ and ^{13}CS in the outflow cavity walls of Class 0 protostars. These tracers show that the outflow cavity walls are regions with enhanced density compared with the rest of the envelope exposed to the protostellar UV radiation, resulting from the interaction of the protostellar outflow with the cavity walls. Some of those molecules also likely have enhanced abundances. C_2H, as the most abundant of the hydrocarbons presented here, is also seen prominently across the envelope at velocities comparable to the low-velocity outflow whereas c-C_3H_2 appears as a clean tracer of the quiescent, UV-irradiated gas in the cavity walls in the Class 0 sources.

5.7 Inner envelope

5.7.1 Compact emission

The inner regions of young protostellar systems are characterized by high temperatures which result in a rich chemistry as molecules that form efficiently in ices on grains in cold clouds sublimate into the gas phase. Complex organic molecules (COMs) detected in these datasets are discussed quantitatively in detail elsewhere, for both O-bearing by van Gelder et al. (2020) and for N-bearing species by Nazari et al. (subm.). In this section we focus on smaller molecules that also trace the innermost hot core regions and therefore are likely abundant in ices. This includes several small S-bearing molecules.

Fig. 5.12 shows emission from H_2CCO, HNCO, t-HCOOH, SO, H_2CS, and $H^{13}CN$ for the Class 0 protostar B1-c, and H_2S and OCS lines for SMM3; all data are observed with the ALMA 12m array at 0.″5.

The SO 6_7–5_6 $E_{\rm up}$ = 48 K line is seen to peak on the central source for B1-c and S68N (Fig. 5.23). SO has already been discussed in the outflow (Section 6), but it is also prominent in the inner envelope. While the spatial resolution does not allow to disentangle the hot corino emission from the small-scale outflow on a few hundred au scale, there is a difference between these two sources and SMM3 and Emb8N. The latter two sources show a substantial decrease in SO intensity towards the continuum peak, i.e., they have prominent SO emission in the outflow, but not from the hot corino. This suggests that sources like B1-c and S68N, which are bright in SO toward the continuum emission peak, have an additional component

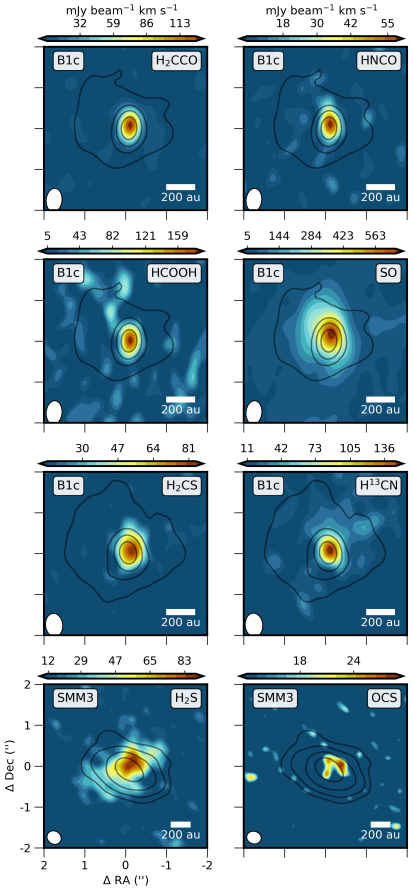


Figure 5.12: Compact emission for B1-c and SMM3 for various molecules tracing the warm inner envelope (hot corino). Moment 0 maps shown in colorscale integrated from -3 to 3 km s^{-1} w.r.t v_{sys}. 1.3 mm continuum presented in contours.

responsible for SO emission. This is highlighted by the narrower lines of SO toward the continuum peak compared with the outflow in S68N (Fig. 5.27). The narrow component, visible in spectra taken on-source, has a width of $\sim$ 5 km s^{-1}. The main component of the spectrum taken in the blueshifted outflow has a similar width but has a more prominent line wing up to 20 km s^{-1}.

Both B1-c and S68N are sources characterized as hot corinos (Bergner et al. 2017; van Gelder et al. 2020), which means that the conditions in their inner regions are favourable for release of molecules from the ice mantles. For the well-studied case of IRAS16293-2422, Drozdovskaya et al. (2018) have also identified a hot core component of SO based on isotopologue data, in addition to an SO component in the large scale outflow. Overall, SO appears to be present in ices.

TMC1 shows SO emission clearly toward both components of the binary system, slightly offset from the central position (Fig. 5.23). There is also a molecular ridge present in SO close

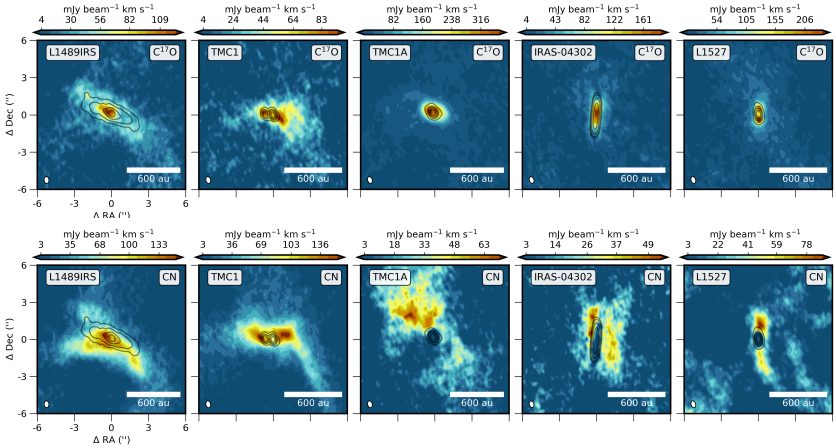


Figure 5.13: Images of Class I disks observed with ALMA 12m in Band 6 (van't Hoff et al. 2020). *Top:* Moment 0 maps of $C^{17}O$ at 0.″4 resolution integrated from -10 to 10 km s^{-1} w.r.t v_{sys}. *Bottom:* Moment 0 maps of CN integrated from -2 to 2 km s^{-1} w.r.t v_{sys}. Continuum contours in black.

to the disk-envelope interface.

This morphology could be an accretion as the accretion shocks are much weaker than shocks that cause the SO emission seen in the outflows (Section 4), the SO is likely released from the icy mantles with the infalling material (Sakai et al. 2014b). Narrow linewidths of SO toward TMC1 seem to rule out the shock scenario, and is more likely associated with emission along the cavity walls (Harsono et al. 2020).

HNCO and $HN^{13}CO$ are detected toward B1-c and S68N peaking on source in higher $E_{\rm up}$ transitions (Nazari et al., subm.). For lines with $E_{\rm up}$ <90 K an extended component is also detected in the outflow. SMM3 and Emb8N have no detections of HNCO on source, but for SMM3 this molecule appears in the outflow. For all Class I sources where the relatively strong HNCO $11_{0,11}-10_{0,10}$ line (A_{ij} = 2×10^{-4} s^{-1}, $E_{\rm up}$=70 K) was targeted, it was not detected.

HNCO emission has been modeled by Hernández-Gómez et al. (2018) and suggested to be a superposition of both warm inner regions of the envelope as well as the colder, outer envelope. Its similar behaviour to sulphur-bearing species, also observed in our work, is proposed to be related to the fact that O_2 and OH are involved in formation of species like SO and HNCO (Rodríguez-Fernández et al. 2010).

OCS is detected toward SMM3 peaking in the center; S68N and SMM1 show centrally peaked $OC^{33}S$ detection, a minor isotopologue signaling a high abundance of OCS. In all cases the emission is moderately resolved; of size ∼ 200 au in case of SMM3 and detected up to 500 au away from source for S68N and SMM1.

H_2S shows strong emission toward SMM3 and is also weakly present in TMC1. For SMM3 the emission is resolved along the outflow direction and perpendicular to the expected disk axis. Those are the only two sources for which H_2S 12m array data were taken. Additionally, the 7m data presented in the Appendix show prominent, centrally peaked H_2S emission for four more sources. H_2S is expected to be the dominant sulphur carrier in ices (Taquet et al. 2020). However, it has not yet been detected in ice absorption spectra to date (Boogert et al. 2015). The weak emission from H_2S in dark clouds has been modeled as a result of the

photodesorption of ices at the outside of the cloud (like in the case of H_2O, Caselli et al. 2012), while chemical desorption is important for grains deeper inside the cloud but outside the water snowline (Navarro-Almaida et al. 2020). These models are consistent with H_2S ice containing most of the sulphur.

H_2CS is detected for B1-c, S68N and L1448-mm through a line with E_{up} = 38 K. Another transition with E_{up} = 46 K is found in Class I disks: IRAS-04302, L1489, and TMC1A. In B1-c, the emission is marginally resolved, while in IRAS-04302 the molecule is clearly seen across the midplane, indicating release at temperatures of at least 20 K (van't Hoff et al. 2020; Podio et al. 2020). Multiple lines of H_2CS are a powerful tool to probe the warm > 100 K, innermost regions of the protostellar systems (van 't Hoff et al. 2020).

H_2CCO is detected for B1-c and S68N. For the lower E_{up} = 100 K transition, the molecule is also detected in the outflow. For Class I sources, the transition at comparable energy is not detected. HCOOH is detected for B1-c and S68N with low-energy transitions that are seen both on source and in the outflow, while the higher energy line (E_{up} = 83 K) is seen only on source. $H^{13}CN$ is detected in B1-c and L1448-mm on source, additionally to the outflow component.

While B1-c and S68N are characterized as hot corinos with many COM lines detected (van Gelder et al. 2020), and L1448-mm has warm water in the inner regions (Codella et al. 2010), SMM3 does not appear to have significant emission from COMs. Moreover, simple molecules associated with the hot core for B1-c, such as SO and H_2CO, are only seen outside of the SMM3 central source. While it is possible that the optically thick continuum prevents a detection of COMs in its inner envelope (De Simone et al. 2020), differences in chemistry or physical structure (e.g., a large cold disk, see Section 6.2) between the SMM3 and the hot corino sources are also possible. The fact that emission from OCS and H_2S is centrally peaked (Fig. 5.12, bottom row) suggests that continuum optical depth is not an issue, although both those species could be a result of grain destruction or ices sputtering, therefore not necessarily coming from the midplane but rather from the surface of a disk-like structure.

5.7.2 Embedded disks

Disks are commonly observed in Class I sources (Harsono et al. 2014; Yen et al. 2017), as the envelope clears out. Fig. 5.13 presents maps of the $C^{17}O$ 2–1 (E_{up} = 16 K) and CN 2–1 (E_{up} =16 K) lines toward Class I disks and L1527-IRS, which is identified as a Class 0/I object, observed with ALMA 12m at 0″.3 resolution. The $C^{17}O$ and H_2CO emission for disks in Taurus using these data are analyzed in detail by van't Hoff et al. (2020). Here we discuss CN in comparison with $C^{17}O$.

$C^{17}O$ is observed concentrated towards the continuum emission for all disks, and is a much cleaner tracer of the disk than any other more abundant CO isotopologues, although even $C^{17}O$ still shows some trace emission from the surrounding envelope. In the case of large edge-on disks like IRAS-04302 and L1527, the vertical structure of the emission can be probed, as well as the radius where CO freeze-out occurs. Overall, Class I disks are warmer than their Class II counterparts with CO freeze-out taking place only in the outermost regions (Harsono et al. 2015a; van 't Hoff et al. 2018a; van't Hoff et al. 2020; Zhang et al. 2020).

We detect CN in all observed Class I disks, although it does not trace the midplane of the disk. In the near edge-on example of IRAS-04302, the CN emission originates from the upper layers of the disks, in the same direction as the outflow, which is perpendicular to the disk in this source. This opens a possibility that the emission is also related to the irradiated residual cavity walls in those sources. TMC1A is a clear example where CN is tracing the

same material as probed by Bjerkeli et al. (2016) in CO, which is attributed to a disk wind. TMC1 and L1527 show CN oriented in the same direction as the disk; in TMC1 there is also a clear filament structure on larger scales irradiated by the UV from the protostar, seen also in other tracers.

In comparison with the $C^{17}O$ emission, which traces the midplane disk, CN thus appears in the upper layers and in the outflow, therefore in most cases the two molecules are mutually exclusive. This picture is consistent with the bulk density traced by CO and the irradiated layers of the disk and envelope exposed to UV traced by CN. Recent observations of a sample of Class I sources including IRAS-04302 by Garufi et al. (2020). is consistent with CN not tracing the disk.

In the younger Class 0 sources characterization of the disk is much more difficult because of the strong envelope emission. Nevertheless, several Keplerian disks have been identified with observations of CO isotopologues like $C^{18}O$ (Tobin et al. 2012; Murillo et al. 2013). Our data allow us to investigate this for the case of SMM3. Fig. 5.28 shows the red and blue-shifted emission from $C^{18}O$ toward SMM3. There is a clear rotational signature in the direction perpendicular to the outflow on scales of a few hundred au. However, to unambiguously identify the disk and its radius, higher spatial and spectral resolution data are necessary.

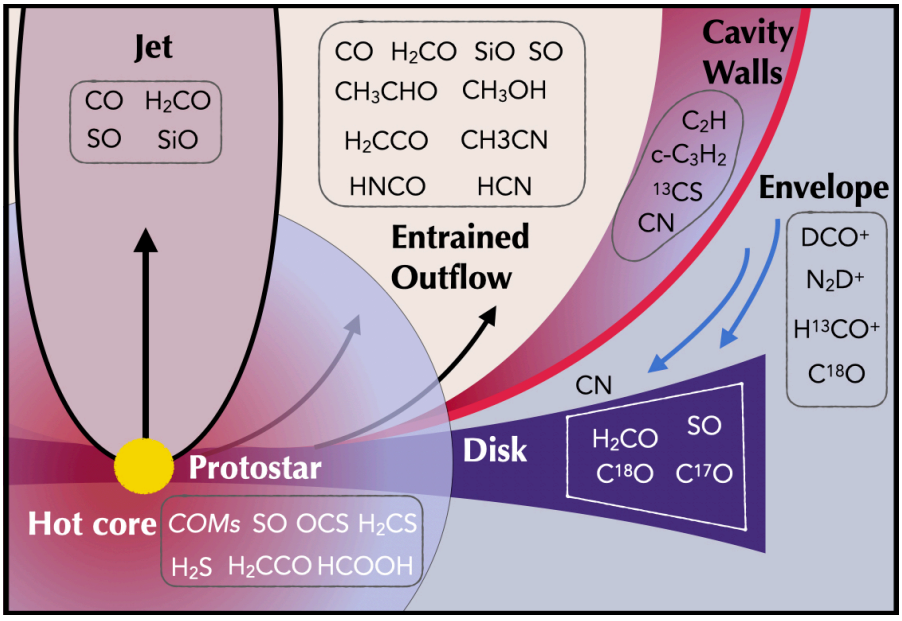


Figure 5.14: Summary cartoon of the key molecular tracers of different components, exclusive to molecules presented in this work.

5.8 Discussion

Figure 5.14 summarizes our findings about which molecule traces which component in Class 0/I protostars. Table 5.5 lists all molecules discussed in this work with indication of the physical component that they trace. Below, we will address several implications of the results.

Table 5.2: Molecular tracers of physical components

Molecule	Envelope	Disk	Hot corino	Outflow	Jet	Cavity
CO	✓	–	–	✓	✓	✓
$C^{18}O$	✓	✓	–	✓	–	✓
^{13}CO	✓	✓	–	✓	–	✓
$C^{17}O$	✓	✓	✓	–	–	✓
$H^{13}CO^+$	✓	–	–	✓	–	✓
H_2CO	✓	✓	✓	✓	✓	–
H_2CS	–	✓	✓	–	–	–
SO	–	✓	✓	✓	✓	–
SiO	–	–	–	✓	✓	–
DCO^+	✓	–	–	–	–	–
N_2D^+	✓	–	–	–	–	–
OCS	–	–	✓	–	–	–
HNCO	–	–	✓	✓	–	–
H_2CCO	–	–	✓	✓	–	–
HCOOH	–	–	✓	✓	–	–
^{13}CS	✓	–	–	–	–	✓
CN	✓	✓	–	–	–	✓
HCN	–	–	–	✓	–	–
$H^{13}CN$	–	–	✓	✓	–	–
C_2H	✓	–	–	✓	–	✓
c-C_3H_2	–	–	–	–	–	✓
CH_3CHO	–	–	✓	✓	–	–
CH_3CN	–	–	✓	✓	–	–
CH_3OCHO	–	–	✓	✓	–	–
CH_3OH	–	–	✓	✓	–	–

5.8.1 COMs in outflow versus hot core

COMs are detected already in the prestellar stage of star formation (Bacmann et al. 2012; Scibelli & Shirley 2020), where they are thought to be efficiently produced on the surfaces of the icy grains. Small amounts can subsequently be released back into the gas through various non-thermal desorption processes, and/or be re-formed by gas-phase reactions. In the inner envelope, temperatures are high enough that thermal desorption of ices is enabled. In the outflow cavity walls, sputtering by shocks can release ices from the grains. COMs in the hot core are detected through high excitation lines while COMs in the outflow are observed primarily through transitions of low E_{up}. Therefore, comparing the observations of molecular complexity in outflows with hot cores can unveil if there is any warm temperature processing of the ices, and whether some molecules also have a gas phase production route.

We therefore calculate abundance ratios between different ice mantle species and methanol at three positions for S68N: one on source, obtained from van Gelder et al. (2020) and Nazari et al. (subm.), and one each in the blueshifted and redshifted part of the outflow. We measure the abundance of the species in a 3″region centered on CH_3OH peak on the blueshifted and redshifted region. The size of the region is based on the spatial resolution of the Band 3 data. The regions are indicated in Fig. 5.9. From these regions we obtain the average brightness temperature which are converted to column density using the same formulation as in Tychoniec et al. (2019). The emission is assumed to be optically thin, and the excitation temperature T_{ex} is taken to be 20 K, typical of subthermally excited molecules with large dipole moments in outflow gas.

The assumption of optically thin emission needs to be verified, especially in the case of CH_3OH which is the most abundant ice species. Since it is the reference molecule for our comparison, by underestimating the column density of methanol, the relative abundance of other molecules can be overestimated. Only a single CH_3OH line is detected in the outflow in our data set, $2_1–1_0$ (E_{up} = 62 K). Escape probability calculations show that even at the lower densities in outflows this CH_3OH line is likely optically thick. No optically thin CH_3OH

isotopologue is detected in the outflow of S68N, therefore we provide an upper limit for the $^{13}CH_3OH$ $5_{2,3}$-$4_{1,3}$ E_{up} =56 K line. The upper limit on this $^{13}CH_3OH$ line translates to an upper limit on the CH_3OH column density that is a factor of 5 higher, assuming ^{12}C / ^{13}C = 70. Thus, our CH_3OH column densities in the outflow could be underestimated by up to a factor of 5. Methanol abundances from the hot corino of S68N reported in van Gelder et al. (2020) are corrected for optical thickness with $^{13}CH_3OH$.

Figure 5.15 compares the abundance ratios of various species with respect to methanol for S68N. First, it is seen that the relative abundances are remarkably similar on both sides of the outflow, well within the uncertainties. That could mean that sputtering is the main reason for the molecules to be released. For gas phase reactions to produce similar abundances, both the conditions and timescales need to be similar on both sides of the outflow. Second, most abundances relative to CH_3OH are found to be comparable to the hot core within our uncertainties and those of van Gelder et al. (2020) and Nazari et al. (subm.), noting that due to lack of optically thin CH_3OH line detected in the outflow, our uncertainties are much larger. The greatest difference is seen for CH_3OCHO, which could be attributed to additional gas-phase formation in the hot core, but because of the large uncertainties with the optically thick CH_3OH this is only tentative result. More transitions, especially optically thin isotopologues of CH_3OH and other complex molecules, are needed to provide a robust conclusion.

For the well-studied L1157 outflow, Codella et al. (2020) find CH_3CHO/CH_3OH is 0.5%. which they find in agreement with ratios in hot cores toward different protostars, but not including L1157 itself. In the case of S68N we uniquely show a comparison between the emission from molecules in the outflows and hot core for the same source. While modeling by Codella et al. (2020) shows that the similar spatial origin of CH_3OH and CH_3CHO does not imply that they are both solely grain sputtering products, an agreement between hot cores and outflows could mean that similar processes are responsible for emission in both regions.

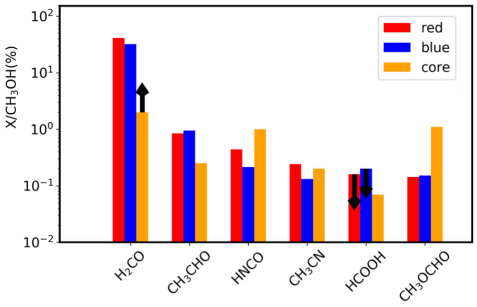


Figure 5.15: Column density ratios of molecules to CH_3OH in S68N. The ratios are shown for a 3″region in both redshifted and blueshifted part of the outflow. The central 0.″5 region with abundance ratios from (van Gelder et al. 2020, Nazari et al. subm.)

It is interesting that the SMM3 outflow shows ice mantle tracers in the outflow but not on the source. Thus, the lack of hot corino emission is likely due to the physical conditions in the inner regions such as a large disk (Section 6.2) or continuum optical depth (De Simone et al. 2020) and not to the lack of complex molecules on the grains. Since methanol is not detected, we cannot provide abundance ratios for this outflow. B1-c - another source with an outflow containing ice mantle products, has methanol lines overlapping with the high-velocity SO outflow, therefore precise abundance measurements are not possible.

JWST will be able to provide information on the ice content due to rich absorption spectra in the mid-IR. The abundances of COMs in the gas-phase provided by ALMA (van Gelder et al. 2020, Nazari et al. subm.) can then be directly compared with the ice content. So far, the ice content observed on cloud scales with *Spitzer* does not show a correlation with the gas content but those data do not probe thermally desorbed ices (Perotti et al. 2020).

5.8.2 Carbon-chains and other hydrocarbons vs COMs

Early observations at low spatial resolution suggested that large carbon-chains such as C_5H, HC_7N, and HC_9N and complex organic molecules are mutually exclusive and therefore the two were proposed to be tracers of two different categories of protostellar sources driven by different chemistry, namely warm carbon-chain chemistry (WCCC) and hot core chemistry (Sakai & Yamamoto 2013). Warm carbon-chain chemistry is thought to occur above the sublimation temperature of CH_4 ~ at 30 K. The proposed difference then lies in the WCCC sources collapsing more rapidly than the hot core sources, which prevents CO to accumulate on the ices, leaving a higher CH_4 ice content. Thus, in WCCC sources, there would be less CO to form more complex organic molecules such as CH_3OH, and an underabundance of COMs is indeed observed. This scenario has been supported by the lower deuteration observed in WCCC sources (Sakai et al. 2009). With ALMA observations at higher resolution and sensitivity, sources harboring both COMs and small hydrocarbons, c-C_3H_2 and C_2H, have now been observed (Imai et al. 2016; Oya et al. 2017).

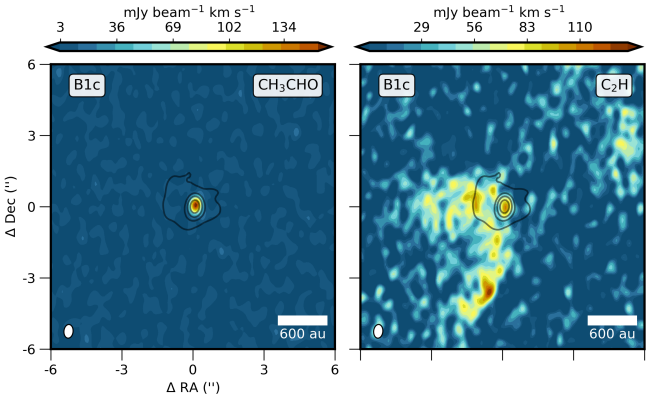


Figure 5.16: Emission maps of an example COM and hydrocarbon toward B1-c. *Left:* CH_3CHO moment 0 map, *Right:* C_2H moment 0 map; both integrated from -2 to 2 km s^{-1} w.r.t v_{sys}.

Our data also show detection of small hydrocarbons and COMs in the same sources (Fig. 5.16). However, our high resolution maps now show those hydrocarbons to originate in the UV irradiated outflow cavity walls (Section 5). Both c-C_3H_2 and C_2H can be solely explained by PDR chemistry (Guzmán et al. 2015; Cuadrado et al. 2015) even in moderate UV fields of low-mass protostars and therefore WCCC chemistry does not need to be invoked for the sources presented in this work. The PDR origin is consistent with our observed geometry at the edges of the cavities, where lower extinction allows the UV radiation from the protostellar accretion to easily reach this region. It also explains confinement of this emission to the inner 2000 au of the envelope, as the UV radiation decreases with distance from the source.

Table 5.3: Summary of evolution of chemical tracers

Component	Class 0	Class I
Envelope	Cold, dense envelope results in cold tracers (DCO^+, N_2H^+)	Envelope dissipates, extent of cold tracers is much smaller
Jet	O-bearing molecules (CO, SiO, SO, H_2CO) are present in high-velocity bullets	Molecular jet disappears, seen only in atomic and ionised gas
Outflow	Ice sputtering (CH_3OH, HNCO) and grain destruction (SO, SiO) tracers are present	Decreased outflow mass and less dense envelope result in no tracers of sputtering and grain destruction, only faint CO remains
Cavity walls	Prominent signs of UV-irradiated cavity walls (CN, C_2H, c-C_3H_2)	No prominent signs of hydrocarbons in cavity walls, CN still present
Hot corino	COMs and simple tracers of ice sublimation and high-temperature chemistry (H_2S, OCS)	Small extent plus disk shadowing results in less complexity, except for outbursting sources
Disk	Warm disk with COMs, dust obscuration	Colder disk molecules, Keplerian rotation seen in H_2CO, $C^{18}O$, CN in the disk surface.

A deep search for larger hydrocarbons like HC_5N in cavity walls could help to understand their origin.

5.8.3 Class 0 vs Class I in different components

There are many processes that take place within the protostellar lifetime of a few 10^5 yr that alter the chemical composition and physical conditions. First, the envelope is dissipating and the radius where key molecules are in the gas-phase is becoming smaller (Jørgensen et al. 2005). With high resolution studies it is possible to now probe different snowlines in unprecedented detail (van 't Hoff et al. 2018a; Hsieh et al. 2019b). There is a clear evolutionary trend observed in temperature – Class 0 disks are generally warmer than Class II disks, with Class I sources in between, which has major impact on the richness of their spectra (van 't Hoff et al. 2020; van't Hoff et al. 2020).

Molecular EHV jets are only present in the Class 0 phase (Nisini et al. 2015) whereas the lower velocity outflows in these stages are rich in ice mantle tracers. The Class I jets are invisible in molecular tracers and their outflows only show primarily CO, with much less contribution from shock tracers such as SO and SiO.

Complex organic molecules are a key tracer of chemistry at early stages. We see them in the outflows only in Class 0 sources. This is likely due to the decrease of the outflow force and mass and envelope density. In the inner regions, the physical conditions such as temperature and density also favour the early stages for the abundances of COMs. In rare cases of rich chemistry in Class I disks, it is usually attributed to accretion outbursts heating up the disk (van 't Hoff et al. 2018c; Lee et al. 2019a).

Cavity walls are seen prominently in the Class 0 sources in molecules whose abundances are sensitive to UV radiation. In Class I sources a flared disk and weak outflow remain. While there is less envelope to attenuate the UV radiation, there is also less material to irradiate, which results in less prominent emission from UV tracers on large scales in Class I. Another example of a transition of molecular appearance between Class 0 and I is SO: this molecule traces primarily the outflow in Class 0 and the disk-envelope interface in Class I. The evolution of molecular composition is summarized in Table 5.3.

5.9 Conclusions

In this work we have presented an overview of the molecular tracers of the physical components in protostellar Class 0 and Class I systems. Fig. 5.14 and Table 5.2 present overview of the results and they are summarized below.

- Envelopes are primarily traced by the dense gas tracers $C^{18}O$ and CO snowline tracers such as DCO^+, N_2D^+, $H^{13}CO^+$. For this component, it is essential to use observations that trace large scales of ~ 5000 au.
- Protostellar outflows are separated into different components. High-velocity molecular jets are traced by O-bearing molecules CO, SiO, SO, and H_2CO. Entrained outflow material can be probed by low-velocity CO, SiO, SO, H_2CO, HCN as well as molecules released from ices by sputtering, such CH_3OH, CH_3CHO, HNCO, H_2CCO, CH_3CN, and CH_3OCHO.
- Outflow cavity walls are pronounced in UV-tracers: C_2H, c-C_3H_2, and CN, and high-density tracers such as ^{13}CS.
- Hot cores, the inner warm envelopes, are probed predominantly by COMs but also by simple products released from ice mantles and produced by high-temperature chemistry such as SO, H_2S, H_2CS, OCS, $H^{13}CN$, HCOOH, and HNCO.
- Embedded disks, which are most clearly seen in Class I sources, can be traced by $C^{17}O$ and H_2CO while their upper layers are also traced by CN. SO may probe envelope accretion streams or shocks onto the disk. CO isotopologues can be used to probe disks in Class 0 sources, however, the confusion with the envelope emission requires a detailed analysis of the kinematics to confirm that a Keplerian disk is present.

Hydrocarbons and COMs are found to routinely co-exist in protostellar sources: the former are present in the UV-irradiated cavity walls and the latter in the hot core and in the outflows. It is plausible that PDR chemistry for the formation of hydrocarbons is sufficient to explain the presence of molecules such as C_2H and c-C_3H_2, and that no warm carbon chain chemistry is required which relies on abundant CH_4 in ices. Observations of more complex carbon chains in cavity walls and envelopes is necessary to understand whether the WCCC plays a role there. *JWST* will be able to probe the CH_4 ice content, which will show if any inherent differences in the ice composition between sources.

Throughout this study, the availability of both low-lying molecular lines to probe the cold extended envelope and outflow, as well as high-excitation lines to trace compact hot cores, has been key for the analysis. The occurrence of the same molecules in different physical components then provides an opportunity to study the processes involved in their formation and excitation. For example, ice mantle tracers sputtered from the grains in outflows give useful insight on the ice composition, whereas comparison with abundances of thermally released COMs in the inner region is a powerful tool to probe whether gas-phase formation routes contribute to complex molecule formation.

JWST-MIRI will provide unprecedented resolution and sensitivity in mid-IR that will allow to probe the emission from hot gas in shocks as well as ice absorption features. This can then be combined with our understanding of the kinematics and spatial origin of molecules revealed by ALMA.

Acknowledgements: This paper makes use of the following ALMA data:
ADS/JAO.ALMA#2017.1.01350.S, ADS/JAO.ALMA#2017.1.1174.S,

ADS/JAO.ALMA#2017.1.1371.S, ADS/JAO.ALMA#2017.1.1413.S,
ADS/JAO.ALMA#2013.1.00726.S, and ADS/JAO.ALMA#2016.1.00710.S. ALMA is a partnership of ESO (representing its member states), NSF (USA) and NINS (Japan), together with NRC (Canada), MOST and ASIAA (Taiwan), and KASI (Republic of Korea), in cooperation with the Republic of Chile. The Joint ALMA Observatory is operated by ESO, AUI/NRAO and NAOJ. Astrochemistry in Leiden is supported by the Netherlands Research School for Astronomy (NOVA), by a Royal Netherlands Academy of Arts and Sciences (KNAW) professor prize, and by the European Union A-ERC grant 291141 CHEMPLAN. This research made use of Astropy, a community-developed core Python package for Astronomy (Astropy Collaboration et al. 2013), http://astropy.org); Matplotlib library (Hunter 2007); NASA's Astrophysics Data System.

Appendix

5.A Continuum images

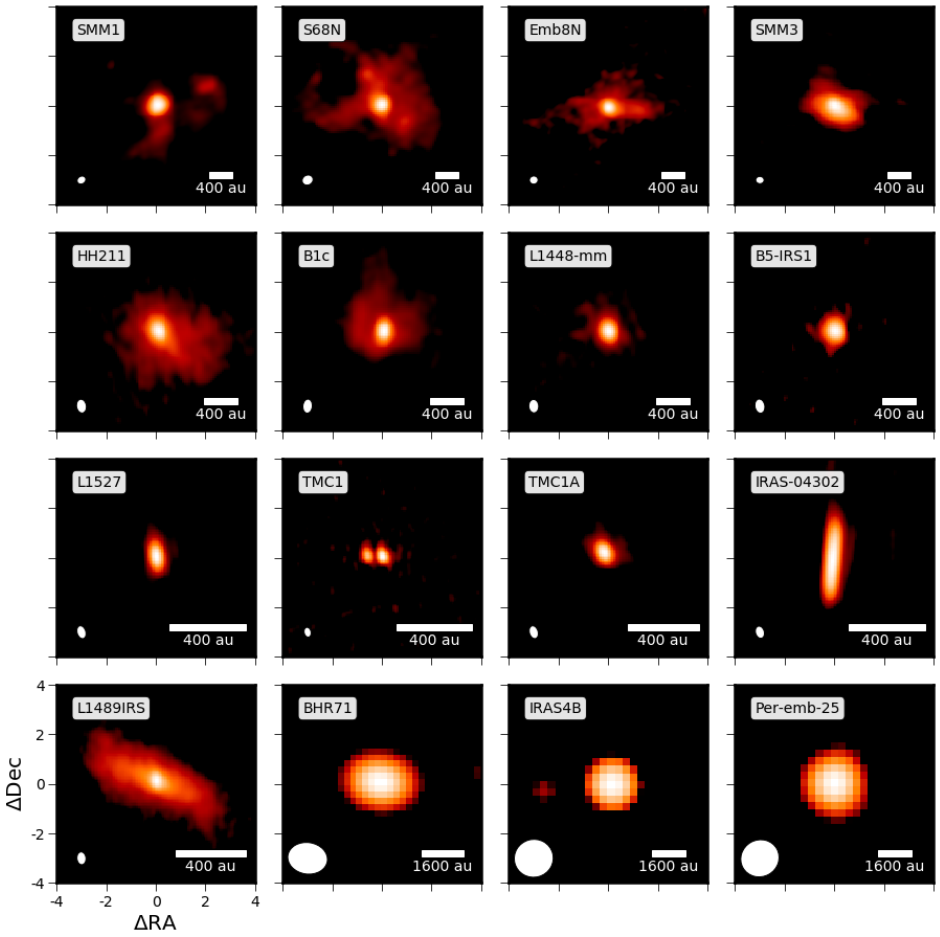


Figure 5.17: Continuum emission from the sources in the sample.

5.B Envelope tracers

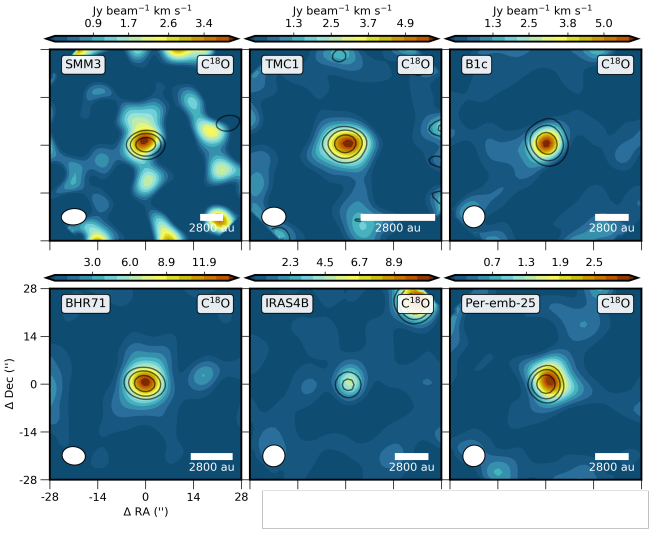


Figure 5.18: Moment maps of $C^{18}O$ at 6″resolution. Contours: continuum, color scale: $C^{18}O$.

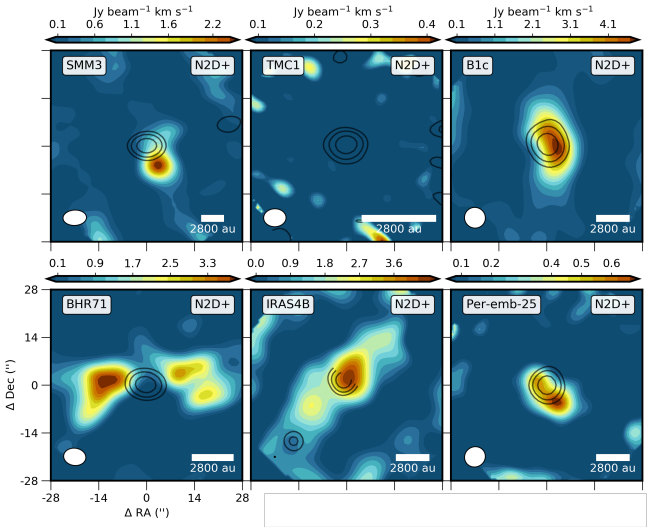


Figure 5.19: Moment maps of N_2D^+ at 6″resolution. Contours: continuum, color scale: moment 0 map integrated from -2 to 2 km s^{-1} w.r.t v_{sys}

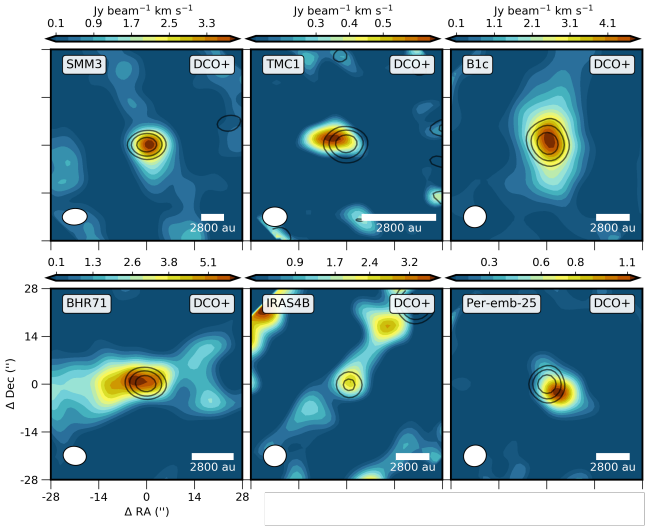


Figure 5.20: Moment maps of DCO^+ at 6″resolution. Contours: continuum, color scale: moment 0 map integrated from -2 to 2 km s^{-1} w.r.t v_{sys}

5.C Outflow

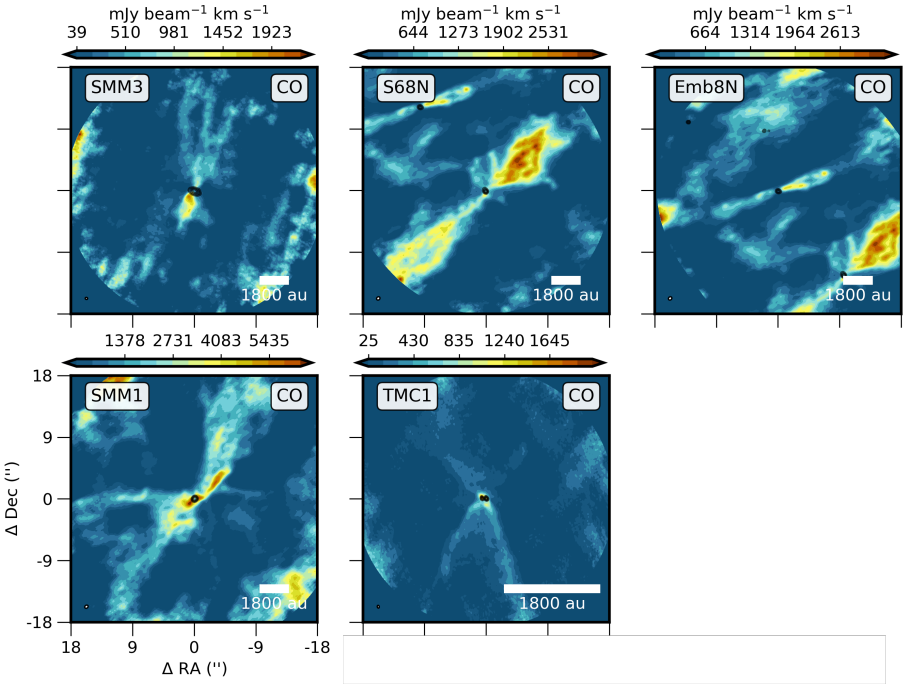


Figure 5.21: Moment maps of low-velocity CO outflow at 0.″4 resolution. Contours: continuum, color scale: moment 0 map integrated from -10 to 10 km s^{-1} w.r.t v_{sys}

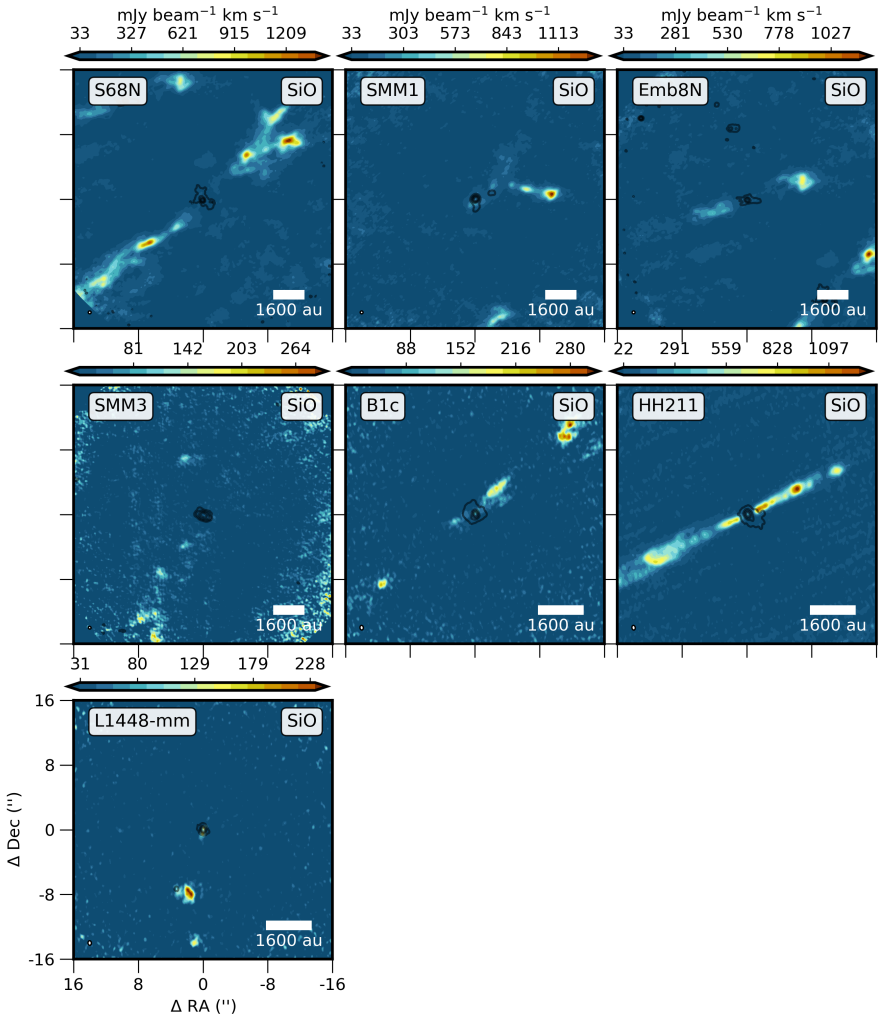


Figure 5.22: Moment maps of low-velocity SiO outflow at 0.″4 resolution. Contours: continuum, color scale: moment 0 map integrated from -15 to 15 km s^{-1} w.r.t v_{sys}

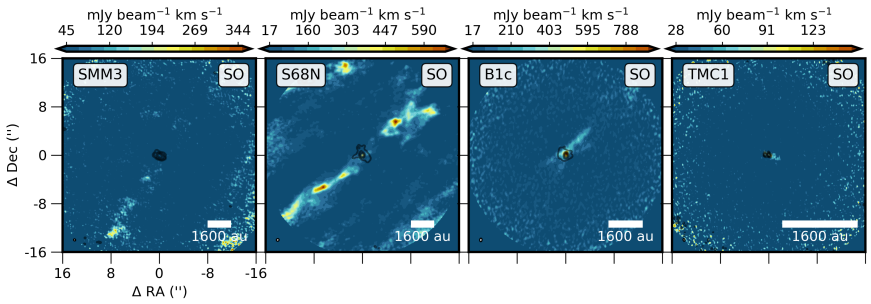


Figure 5.23: Moment maps of low-velocity SO outflow at 0.″4 resolution. Contours: continuum, color scale: moment 0 map integrated from -10 to 10 km s^{-1} w.r.t v_{sys}

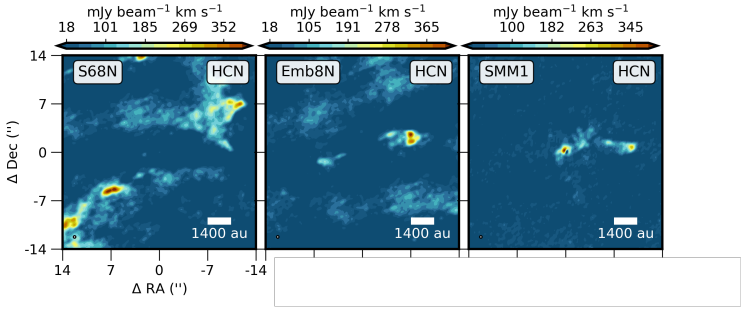


Figure 5.24: Moment maps of HCN at 0.″5 resolution. Color scale: moment 0 map integrated from -15 to 15 km s^{-1} w.r.t v_{sys}

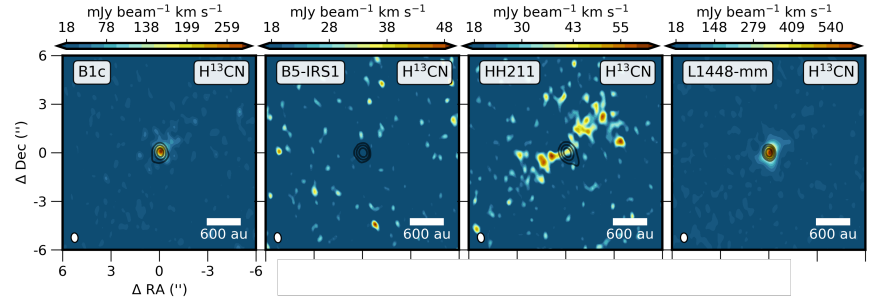


Figure 5.25: Moment maps of H^{13}CN at 0.″4 resolution. Contours: continuum, color scale: moment 0 map integrated from -7 to 7 km s^{-1} w.r.t v_{sys}

5.D Cavity walls

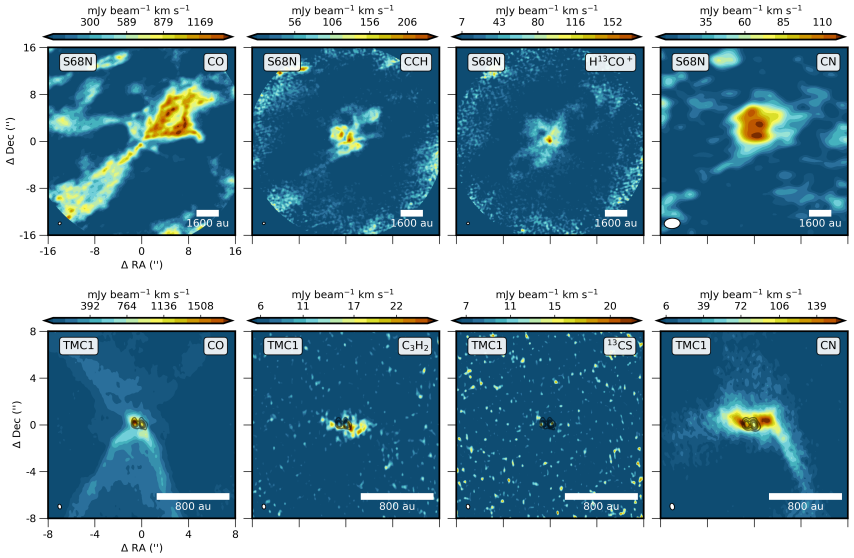


Figure 5.26: Maps of the outflow cavity wall tracers toward S68N and TMC1, with the CO low-velocity outflow map for reference. *Top:* Moment 0 maps toward S68N of CO, C_2H, H_13CO^+ obtained in Band 6 at 0.″5 resolution and CN in Band 3 at 3″. *Bottom:* Moment 0 maps toward TMC1 of CO, c-C_3H_2 and ^{13}CS and CN obtained at 0.″5. The emission is integrated from -5 to -1 km s^{-1} and from 1 to 5 km s^{-1} w.r.t v_{sys}.

5.E Additional plots

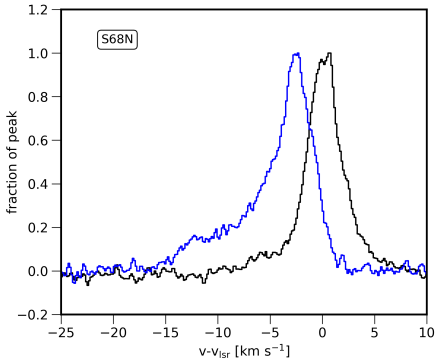


Figure 5.27: Spectra of SO 6_7–5_6 for S68N. Spectra averaged over the 0.″6 diameter circle on positions: central source (black), blueshifted outflow (blue). Both spectra normalized to the peak emission at the position

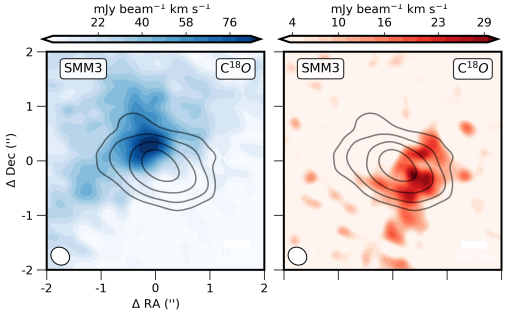


Figure 5.28: Map of the $C^{18}O$ emission toward SMM3. Moment 0 map in colourscale and 1.3 mm continuum in contours. *Left:* Moment 0 map integrated from -3 to -0.5 km s^{-1} w.r.t v_{sys}. *Right:* Moment 0 map integrated from 0.5 to 3 km s^{-1} w.r.t v_{sys}.

5.F Tables

Table 5.4: Specifications of observations

Project ID	Configuration	λ	Res.	MRS	Calibration[a]	Bandpass	Phase	Flux	Targets
2017.1.1350.S	Band 6 (C-4)	1.3 mm	$0\farcs40 \times 0\farcs29$	$5''$	5.4.0-68	J0423-0120	J0336+3218	J0510+1800	SMM3, TMC1
2017.1.1350.S	Band 6 (7m)	1.3 mm	$6\farcs4 \times 6\farcs1$	$25''$	5.4.0-68	J0423-0120	J0336+3218	J0510+1800	SMM3, TMC1, IRAS4B, BHR71, Emb25, B1c
2017.1.1174.S	Band 6 (C-4)	1.3 mm	$0\farcs58 \times 0\farcs39$	$6''$	5.1.1	J1751+0939	J1830+0619	J1751+0939	B1c, S68N, SMM3
2017.1.1174.S	Band 3 (C-2)	3 mm	$2\farcs8 \times 1\farcs8$	$16''$	5.1.1	J0238+1636	J0336+3218	J0238+1636	B1c, S68N
2017.1.1371.S	Band 5 (C-5)	2 mm	$0\farcs6 \times 0\farcs4$	$4''$	5.1.1	J0237+2848	J0336+3218	J0237+2848	L1448, B1c, B5IRS1, HH211
2017.1.1413.S	Band 6 (C-4)	1.3 mm	$0\farcs42 \times 0\farcs28$	$6''$	5.4.0	J0510+1800	J0438+3004	J0510+1800	TMC1, 04302, L1527, TMC1A, L1489
2013.1.00726.S	Band 6 (C-4, C-2)	1.3 mm	$0\farcs45 \times 0\farcs35$	$10''$	4.2.2	J1733-1304	J1751+0939	Titan	SMM1, S68N, Emb8N
2016.1.00710.S	Band 3 (C-5)	3 mm	$0\farcs5 \times 0\farcs4$	$7''$	4.7.38335	J1751+0939	J1838+0404	J1838+0404	SMM1, S68N, Emb8N

Notes. [(a)] Version of CASA used for calibration

Table 5.5: Molecular transitions targeted

Molecule	Transition	Frequency	E_{up}	A_{ij}	Serpens				Perseus				Taurus				
		GHz	K	s^{-1}	S68N	SMM3	SMM1	8N	B1c	L1448	HH211	B5	04302	TMC1	TMC1A	L1527	L1489
CO	2–1	230.5380	16.6	6.91e-07	✓	✓	✓	✓	–	–	–	–	–	✓	–	–	–
$C^{18}O$	2–1	219.5604	15.8	6.01e-07	–	✓	–	–	–	–	–	–	–	✓	–	–	–
^{13}CO	2–1	220.3987	15.9	6.07e-07	✓	✓	✓	✓	–	–	–	–	–	✓	–	–	–
$C^{17}O$	$2_{1.5}$–$1_{1.5}$	224.7147	16.2	4.50e-07	–	–	–	–	–	–	–	–	✓	✓	✓	✓	✓
$H^{13}CO^+$	1–0	86.7543	4.2	3.85e-05	–	–	✓	–	–	–	–	–	–	–	–	–	–
	2–1	173.5067	12.5	3.70e-04	–	–	–	–	✓	✓	✓	✗	–	–	–	–	–
	3–2	260.2553	25.0	1.34e-03	✓	–	–	✓	✓	–	–	–	–	–	–	–	–
H_2CO	$9_{1,8}$–$9_{1,9}$	216.5687	174.0	7.22e-06	–	✗	–	–	–	–	–	–	–	✗	–	–	–
	$3_{0,3}$–$2_{0,2}$	218.2222	21.0	2.82e-04	✗	–	✗	✗	–	–	–	–	–	–	–	–	–
	$3_{2,1}$–$2_{2,0}$	218.7601	68.1	1.58e-04	–	✓	–	–	–	–	–	–	–	✓	–	–	–
	$3_{1,2}$–$2_{1,1}$	225.6978	33.5	2.77e-04	–	–	–	–	–	–	–	–	✓	✓	✓	✓	✓
H_2CS	$5_{1,4}$–$4_{1,3}$	174.3452	38.3	7.32e-05	–	–	–	–	✓	✓	✗	✓	–	–	–	–	–
	$7_{0,7}$–$6_{0,6}$	240.2669	46.1	2.05e-04	–	–	–	–	–	–	–	–	✓	✗	✓	✗	✗
SO	5_6–4_5	219.9494	35.0	1.36e-04	–	✓	–	–	–	–	–	–	–	✓	–	–	–
	6_7–5_6	261.8437	47.6	2.33e-04	✓	–	–	✓	✓	–	–	–	–	–	–	–	–
SiO	4–3	173.6883	20.8	2.61e-04	–	–	–	–	✓	✓	✓	✗	–	–	–	–	–
	5–4	217.1050	31.3	5.21e-04	✓	✓	✓	✓	–	–	–	–	–	✗	–	–	–
DCO^+	3–2	216.1126	20.7	7.61e-04	✓	✓	✓	✓	–	–	–	–	–	✓	–	–	–
N_2D^+	3–2	231.3218	22.2	7.14e-04	–	✓	–	–	–	–	–	–	–	✗	–	–	–
OCS	19–18	231.0610	110.9	3.58e-05	–	✓	–	–	–	–	–	–	–	✗	–	–	–
HNCO	$5_{0,5}$–$4_{0,4}$	109.9058	15.8	1.80e-05	✓	–	–	✗	✓	–	–	–	–	–	–	–	–
	$11_{0,11}$–$10_{0,10}$	241.7741	69.6	2.00e-04	–	–	–	–	–	–	–	–	✗	✗	✗	✗	✓
	$12_{1,12}$–$11_{1,11}$	262.7696	125.3	2.57e-04	✓	–	–	✗	✓	–	–	–	–	–	–	–	–
	$12_{0,12}$–$11_{0,11}$	263.7487	82.3	2.61e-04	✓	–	–	✗	✓	–	–	–	–	–	–	–	–
	$12_{1,12}$–$11_{1,11}$	262.7751	125.1	2.57e-04	✓	–	–	✗	✓	–	–	–	–	–	–	–	–
H_2CCO	$13_{1,13}$–$12_{1,12}$	260.1920	100.5	1.98e-04	✓	–	–	–	✓	–	–	–	–	–	–	–	–
	$13_{2,11}$–$12_{2,10}$	262.7609	140.5	2.01e-04	✓	–	–	✗	✓	–	–	–	–	–	–	–	–
HCOOH	$12_{0,12}$–$11_{0,11}$	262.1036	82.8	1.95e-04	✓	–	–	✗	✓	–	–	–	–	–	–	–	–
	$5_{0,5}$–$4_{0,4}$	111.7468	16.1	1.44e-05	✗	–	–	✗	✓	–	–	–	–	–	–	–	–
	$5_{2,4}$–$4_{2,3}$	112.2871	28.9	1.23e-05	✗	–	–	✗	✓	–	–	–	–	–	–	–	–
^{13}CS	5–4	231.2207	33.3	2.51e-04	✓	✓	✓	✓	–	–	–	–	–	✓	–	–	–
CN	$1_{0,0.5,0.5}$–$0_{0,0.5,1.5}$	113.1442	5.4	1.05e-05	✓	–	–	✓	✓	–	–	–	–	–	–	–	–
	$2_{0,1.5,2.5}$–$1_{0,1.5,2.5}$	226.3599	16.3	1.61e-05	–	–	–	–	–	–	–	–	✗	✓	✓	✓	✓
	$2_{0,1.5,0.5}$–$1_{0,0.5,1.5}$	226.6166	16.3	1.07e-05	–	–	–	–	–	–	–	–	✗	✓	✗	–	✓
	$2_{0,1.5,1.5}$–$1_{0,0.5,1.5}$	226.6322	16.3	4.26e-05	–	–	–	–	–	–	–	–	✓	✓	✓	✓	✓
	$2_{0,1.5,2.5}$–$1_{0,0.5,1.5}$	226.6596	16.3	9.47e-05	–	–	–	–	–	–	–	–	✓	✓	✓	✓	✓
	$2_{0,1.5,0.5}$–$1_{0,0.5,0.5}$	226.6637	16.3	8.46e-05	–	–	–	–	–	–	–	–	✓	✓	✓	✓	✓
	$2_{0,1.5,1.5}$–$1_{0,0.5,0.5}$	226.6793	16.3	5.27e-05	–	–	–	–	–	–	–	–	✓	✓	✓	✓	✓
	$2_{0,2.5,2.5}$–$1_{0,1.5,1.5}$	226.8742	16.3	9.62e-05	–	–	–	–	–	–	–	–	✓	✓	✓	✓	✓
	$2_{0,2.5,3.5}$–$1_{0,1.5,2.5}$	226.8748	16.3	1.14e-04	–	–	–	–	–	–	–	–	✓	✓	✓	✓	✓
	$2_{0,2.5,1.5}$–$1_{0,1.5,0.5}$	226.8759	16.3	8.59e-05	–	–	–	–	–	–	–	–	✓	✓	✓	✓	✓
	$2_{0,2.5,1.5}$–$1_{0,1.5,1.5}$	226.8874	16.3	2.73e-05	–	–	–	–	–	–	–	–	✓	✓	✓	✓	✓

Table 5.5: Continued.

Molecule	Transition	Frequency	E_{up}	A_{ij}	Serpens				Perseus				Taurus				
		GHz	K	s^{-1}	S68N	SMM3	SMM1	8N	B1c	L1448	HH211	B5	04302	TMC1	TMC1A	L1527	L1489
	$2_{0,2.5,2.5}-1_{0,1.5,2.5}$	226.8921	16.3	1.81e-05	–	–	–	–	–	–	–	–	✓	✓	✓	✓	✓
HCN	1_1-0_1	88.6304	4.3	2.43e-05	✓	–	✓	✓	–	–	–	–	–	–	–	–	–
	1_2-0_1	88.6318	4.3	2.43e-05	✓	–	✓	✓	–	–	–	–	–	–	–	–	–
	1_0-0_1	88.6339	4.3	2.43e-05	✓	–	✓	✓	–	–	–	–	–	–	–	–	–
$H^{13}CN$	1_0-0_1	86.3423	4.1	2.22e-05	✓	–	✓	✓	–	–	–	–	–	–	–	–	–
	2_2-1_2	172.6766	12.4	5.34e-05	–	–	–	–	✓	✓	✓	✗	–	–	–	–	–
	2_1-1_2	172.6779	12.4	5.93e-06	–	–	–	–	✓	✓	✓	✓	–	–	–	–	–
	2_2-1_1	172.6780	12.4	1.60e-04	–	–	–	–	✓	✓	✓	✗	–	–	–	–	–
CCH	$3_{2.5,2}-2_{1.5,2}$	262.0788	25.2	6.49e-06	✓	–	–	✗	✓	–	–	–	–	–	–	–	–
	$3_{2.5,3}-2_{1.5,2}$	262.0648	25.2	5.28e-05	✓	–	–	✓	✓	–	–	–	–	–	–	–	–
	$3_{2.5,2}-2_{1.5,1}$	262.0673	25.2	4.83e-05	✓	–	–	✓	✓	–	–	–	–	–	–	–	–
	$3_{3.5,3}-2_{2.5,2}$	262.0064	25.1	5.52e-05	✓	–	–	✓	✓	–	–	–	–	–	–	–	–
	$3_{3.5,4}-2_{2.5,3}$	262.0042	25.1	5.74e-05	✓	–	–	✓	✓	–	–	–	–	–	–	–	–
c-C_3H_2	$7_{4,3}-7_{3,4}$	112.4908	82.6	4.50e-05	✓	✓	–	✓	✓	–	–	–	–	–	–	–	–
	$6_{1,6}-5_{0,5}$	217.8221	38.6	5.93e-04	–	✓	–	–	–	–	–	–	–	✓	–	–	–
	$7_{2,6}-7_{1,7}$	218.7327	61.2	9.82e-05	–	✓	–	–	–	–	–	–	–	✓	–	–	–
	$3_{3,1}-2_{0,2}$	261.8318	19.0	4.66e-05	–	–	–	–	✓	–	–	–	–	–	–	–	–
CH_3CHO	$6_{1,6}-5_{1,5}$	112.2545	21.2	4.50e-05	✓	✓	–	✗	–	–	–	–	–	–	–	–	–
	$9_{4,5}-8_{4,4}$	173.5191	77.7	1.41e-04	–	–	–	–	✓	✓	✗	✗	–	–	–	–	–
	$14_{0,14}-13_{0,13}$	262.9601	95.8	6.20e-04	✓	–	–	–	✓	–	–	–	–	–	–	–	–
	$14_{0,14}-13_{0,13}$	263.0040	95.7	6.20e-04	✓	–	–	–	✓	–	–	–	–	–	–	–	–
CH_3CN	6_0-5_0	110.3835	18.5	1.11e-04	✓	✓	–	✓	✓	–	–	–	–	–	–	–	–
	6_4-5_4	110.3495	132.8	6.17e-05	✓	–	–	–	✓	–	–	–	–	–	–	–	–
	6_3-5_3	110.3644	82.8	8.33e-05	✓	✓	–	✓	✓	–	–	–	–	–	–	–	–
	6_2-5_2	110.3750	47.1	9.87e-05	✓	✓	–	✓	✓	–	–	–	–	–	–	–	–
	6_1-5_1	110.3814	25.7	1.08e-04	✓	✓	–	✓	✓	–	–	–	–	–	–	–	–
CH_3OH	$4_{2,3}-5_{1,4}$	234.6834	60.9	1.85e-05	–	✗	–	–	–	–	–	–	–	✗	–	–	–
	$5_{-1}-4_{-1}$	241.7672	40.4	5.81e-05	–	–	–	–	✓	–	–	–	–	✗	–	–	–
	5_0-4_0	241.7914	34.8	6.05e-05	–	–	–	–	–	–	–	–	–	✗	–	✓	✓
	5_2-4_2	241.9046	57.1	5.03e-05	–	–	–	–	–	–	–	–	–	✗	✓	✓	–
	$2_{1,0}-1_{0,1}$	261.8057	28.0	5.57e-05	✓	–	–	✓	✓	–	–	–	–	–	–	–	–
CH_3OCHO	$9_{5,5}-8_{5,4}$	110.8823	43.2	1.38e-05	✓	–	–	–	✓	–	–	–	–	–	–	–	–
	$10_{0,10}-9_{0,9}$	111.1699	30.2	1.99e-05	✓	✗	–	✗	✓	–	–	–	–	–	–	–	–
	$9_{1,8}-8_{1,7}$	111.6741	28.1	1.98e-05	✓	✗	–	✗	✓	–	–	–	–	–	–	–	–

Notes. ✓- transition detected, ✗- transition not detected, – transition not targeted

Bibliography

Abergel, A., Teyssier, D., Bernard, J. P., et al. 2003, A&A, 410, 577

Adams, F. C. 2010, ARA&A, 48, 47

Agúndez, M., Cernicharo, J., & Goicoechea, J. R. 2008, A&A, 483, 831

Ainsworth, R. E., Scaife, A. M. M., Ray, T. P., et al. 2014, ApJ, 792, L18

Alibert, Y., Carron, F., Fortier, A., et al. 2013, A&A, 558, A109

ALMA Partnership, Brogan, C. L., Pérez, L. M., et al. 2015, ApJ, 808, L3

Alves, F. O., Cleeves, L. I., Girart, J. M., et al. 2020, ApJ, 904, L6

Alves, J., Lombardi, M., & Lada, C. J. 2007, A&A, 462, L17

Ambartsumian, V. A. 1947, The evolution of stars and astrophysics (Izdatel'stvo Akad Nauk Arm SSR, Erevan)

AMI Consortium: Scaife, A. M. M., Buckle, J. V., Ainsworth, R. E., et al. 2012, MNRAS, 420, 3334

AMI Consortium: Scaife, A. M. M., Hatchell, J., Davies, M., et al. 2011, MNRAS, 415, 893

Anderl, S., Maret, S., Cabrit, S., et al. 2016, A&A, 591, A3

Andersen, B. C., Stephens, I. W., Dunham, M. M., et al. 2019, ApJ, 873, 54

André, P., Di Francesco, J., Ward-Thompson, D., et al. 2014, in Protostars and Planets VI, ed. H. Beuther, R. S. Klessen, C. P. Dullemond, & T. Henning, 27

André, P., Men'shchikov, A., Bontemps, S., et al. 2010, A&A, 518, L102

André, P., Ward-Thompson, D., & Barsony, M. 1993, ApJ, 406, 122

Andrews, S. M., Huang, J., Pérez, L. M., et al. 2018, ApJ, 869, L41

Andrews, S. M., Rosenfeld, K. A., Kraus, A. L., & Wilner, D. J. 2013, ApJ, 771, 129

Andrews, S. M. & Williams, J. P. 2005, ApJ, 631, 1134

Andrews, S. M. & Williams, J. P. 2007a, ApJ, 671, 1800

Andrews, S. M. & Williams, J. P. 2007b, ApJ, 659, 705

Andrews, S. M., Wilner, D. J., Hughes, A. M., Qi, C., & Dullemond, C. P. 2009, ApJ, 700, 1502

Anglada, G., Estalella, R., Mauersberger, R., et al. 1995, ApJ, 443, 682

Anglada, G. & Rodríguez, L. F. 2002, Rev. Mexicana Astron. Astrofis., 38, 13

Anglada, G., Rodriguez, L. F., & Torrelles, J. M. 1996, ApJ, 473, L123

Anglada, G., Villuendas, E., Estalella, R., et al. 1998, AJ, 116, 2953

Ansdell, M., Williams, J. P., Manara, C. F., et al. 2017, AJ, 153, 240

Ansdell, M., Williams, J. P., van der Marel, N., et al. 2016, ApJ, 828, 46

Arce, H. G., Mardones, D., Corder, S. A., et al. 2013, ApJ, 774, 39

Arce, H. G., Santiago-García, J., Jørgensen, J. K., Tafalla, M., & Bachiller, R. 2008, ApJ, 681, L21

Arce, H. G. & Sargent, A. I. 2006, ApJ, 646, 1070

Aristotle. 370 B.C., On the Heavens I & II (Liverpool University Press, 1995), 47–169

Armitage, P. J. 2011, ARA&A, 49, 195

Artur de la Villarmois, E., Jørgensen, J. K., Kristensen, L. E., et al. 2019, A&A, 626, A71

Aspin, C., Sandell, G., & Russell, A. P. G. 1994, A&AS, 106, 165

Astropy Collaboration, Robitaille, T. P., Tollerud, E. J., et al. 2013, A&A, 558, A33

Bachiller, R. 1996, ARA&A, 34, 111

Bachiller, R. & Gomez-Gonzalez, J. 1992, A&A Rev., 3, 257

Bachiller, R., Martin-Pintado, J., Tafalla, M., Cernicharo, J., & Lazareff, B. 1990, A&A, 231, 174

Bachiller, R., Tafalla, M., & Cernicharo, J. 1994, ApJ, 425, L93

Bacmann, A., Taquet, V., Faure, A., Kahane, C., & Ceccarelli, C. 2012, A&A, 541, L12

Barenfeld, S. A., Carpenter, J. M., Ricci, L., & Isella, A. 2016, ApJ, 827, 142

Bast, J. E., Lahuis, F., van Dishoeck, E. F., & Tielens, A. G. G. M. 2013, A&A, 551, A118

Baulch, D. L., Bowman, C. T., Cobos, C. J., et al. 2005, Journal of Physical and Chemical Reference Data, 34, 757

Beckwith, S. V. W., Sargent, A. I., Chini, R. S., & Guesten, R. 1990, AJ, 99, 924

Benz, A. O., Bruderer, S., van Dishoeck, E. F., et al. 2016, A&A, 590, A105

Bergner, J. B., Öberg, K. I., Garrod, R. T., & Graninger, D. M. 2017, ApJ, 841, 120

Bianchi, E., Chandler, C. J., Ceccarelli, C., et al. 2020, MNRAS, 498, L87

Birnstiel, T., Dullemond, C. P., Zhu, Z., et al. 2018, ApJ, 869, L45

Bitsch, B., Izidoro, A., Johansen, A., et al. 2019, A&A, 623, A88

Bjerkeli, P., van der Wiel, M. H. D., Harsono, D., Ramsey, J. P., & Jørgensen, J. K. 2016, Nature, 540, 406

Blake, G. A., van Dishoeck, E. F., Jansen, D. J., Groesbeck, T. D., & Mundy, L. G. 1994, ApJ, 428, 680

Bontemps, S., Andre, P., Terebey, S., & Cabrit, S. 1996, A&A, 311, 858

Boogert, A. C. A., Gerakines, P. A., & Whittet, D. C. B. 2015, ARA&A, 53, 541

Boogert, A. C. A., Pontoppidan, K. M., Knez, C., et al. 2008, ApJ, 678, 985

Boonman, A. M. S., Stark, R., van der Tak, F. F. S., et al. 2001, ApJ, 553, L63

Boss, A. P. 1997, Science, 276, 1836

Bottinelli, S., Ceccarelli, C., Lefloch, B., et al. 2004, ApJ, 615, 354

Brinch, C., Crapsi, A., Jørgensen, J. K., Hogerheijde, M. R., & Hill, T. 2007, A&A, 475, 915

Bruderer, S., Benz, A. O., Bourke, T. L., & Doty, S. D. 2009, A&A, 503, L13

Buckle, J. V. & Fuller, G. A. 2002, A&A, 381, 77

Burkhardt, A. M., Dollhopf, N. M., Corby, J. F., et al. 2016, ApJ, 827, 21

Cabrit, S. & Bertout, C. 1992, A&A, 261, 274

Cabrit, S., Codella, C., Gueth, F., & Gusdorf, A. 2012, A&A, 548, L2

Cameron, A. G. W. 1978, Moon and Planets, 18, 5

Carney, M. T., Fedele, D., Hogerheijde, M. R., et al. 2018, A&A, 614, A106

Carney, M. T., Yıldız, U. A., Mottram, J. C., et al. 2016, A&A, 586, A44

Carrasco-González, C., Rodríguez, L. F., Anglada, G., et al. 2010, Science, 330, 1209

Caselli, P. & Ceccarelli, C. 2012, A&A Rev., 20, 56

Caselli, P., Hartquist, T. W., & Havnes, O. 1997, A&A, 322, 296

Caselli, P., Keto, E., Bergin, E. A., et al. 2012, ApJ, 759, L37

Caselli, P., Walmsley, C. M., Tafalla, M., Dore, L., & Myers, P. C. 1999, ApJ, 523, L165

Cassan, A., Kubas, D., Beaulieu, J. P., et al. 2012, Nature, 481, 167

Cassen, P. & Moosman, A. 1981, Icarus, 48, 353

Ceccarelli, C., Castets, A., Caux, E., et al. 2000, A&A, 355, 1129

Ceccarelli, C., Hollenbach, D. J., & Tielens, A. G. G. M. 1996, ApJ, 471, 400

Chandler, C. J. & Carlstrom, J. E. 1996, ApJ, 466, 338

Chandler, C. J. & Richer, J. S. 2000, ApJ, 530, 851

Chen, H., Myers, P. C., Ladd, E. F., & Wood, D. O. S. 1995, ApJ, 445, 377

Chen, X., Arce, H. G., Zhang, Q., et al. 2010, ApJ, 715, 1344

Chen, X., Launhardt, R., & Henning, T. 2007, ApJ, 669, 1058

Chiang, H.-F., Looney, L. W., & Tobin, J. J. 2012, ApJ, 756, 168

Choi, M. 2009, ApJ, 705, 1730

Chuang, K.-J., Fedoseev, G., Ioppolo, S., van Dishoeck, E. F., & Linnartz, H. 2016, MNRAS, 455, 1702

Codella, C., Benedettini, M., Beltrán, M. T., et al. 2009, A&A, 507, L25

Codella, C., Bianchi, E., Tabone, B., et al. 2018, A&A, 617, A10

Codella, C., Cabrit, S., Gueth, F., et al. 2014, A&A, 568, L5

Codella, C., Ceccarelli, C., Bianchi, E., et al. 2020, A&A, 635, A17

Codella, C., Ceccarelli, C., Caselli, P., et al. 2017, A&A, 605, L3

Codella, C., Ceccarelli, C., Nisini, B., et al. 2010, A&A, 522, L1

Condon, J. J. 1984, ApJ, 287, 461

Condon, J. J., Cotton, W. D., Greisen, E. W., et al. 1998, AJ, 115, 1693

Connelley, M. S., Reipurth, B., & Tokunaga, A. T. 2008, AJ, 135, 2496

Connelly, J. N., Bizzarro, M., Krot, A. N., et al. 2012, Science, 338, 651

Copernicus, N. 1543, De revolutionibus orbium coelestium (Johnson Reprint Corporation, New York, 1965)

Cox, E. G., Harris, R. J., Looney, L. W., et al. 2015, ApJ, 814, L28

Crapsi, A., van Dishoeck, E. F., Hogerheijde, M. R., Pontoppidan, K. M., & Dullemond, C. P. 2008, A&A, 486, 245

Cridland, A. J., Eistrup, C., & van Dishoeck, E. F. 2019, A&A, 627, A127

Cuadrado, S., Goicoechea, J. R., Pilleri, P., et al. 2015, A&A, 575, A82

Cumming, A., Butler, R. P., Marcy, G. W., et al. 2008, PASP, 120, 531

Curiel, S., Rodríguez, L. F., Bohigas, J., et al. 1989, ApL&C, 27, 299

Curiel, S., Rodríguez, L. F., Moran, J. M., & Canto, J. 1993, ApJ, 415, 191

Cutri, R. M., Skrutskie, M. F., van Dyk, S., et al. 2003, yCat, 2246

Dalgarno, A., Oppenheimer, M., & Black, J. H. 1973, Nature Physical Science, 245, 100

Davidson-Pilon, C. 2017, CamDavidsonPilon/lifelines: 0.11.1

Davis, C. J., Matthews, H. E., Ray, T. P., Dent, W. R. F., & Richer, J. S. 1999, MNRAS, 309, 141

Davis, C. J., Scholz, P., Lucas, P., Smith, M. D., & Adamson, A. 2008, MNRAS, 387, 954

Dawson, R. I. & Johnson, J. A. 2018, ARA&A, 56, 175

de Graauw, T., Helmich, F. P., Phillips, T. G., et al. 2010, A&A, 518, L6

De Simone, M., Ceccarelli, C., Codella, C., et al. 2020, ApJ, 896, L3

Demyk, K., Meny, C., Leroux, H., et al. 2017a, A&A, 606, A50

Demyk, K., Meny, C., Lu, X. H., et al. 2017b, A&A, 600, A123

Dionatos, O. & Güdel, M. 2017, A&A, 597, A64

Dionatos, O., Jørgensen, J. K., Green, J. D., et al. 2013, A&A, 558, A88

Dionatos, O., Jørgensen, J. K., Teixeira, P. S., Güdel, M., & Bergin, E. 2014, A&A, 563, A28

Dionatos, O., Nisini, B., Codella, C., & Giannini, T. 2010, A&A, 523, A29

Downes, T. P. & Cabrit, S. 2007, A&A, 471, 873

Draine, B. T. 1978, ApJS, 36, 595

Draine, B. T. 2006, ApJ, 636, 1114

Draine, B. T., Roberge, W. G., & Dalgarno, A. 1983, ApJ, 264, 485

Drążkowska, J. & Dullemond, C. P. 2014, A&A, 572, A78

Drążkowska, J. & Dullemond, C. P. 2018, A&A, 614, A62

Drozdovskaya, M. N., van Dishoeck, E. F., Jørgensen, J. K., et al. 2018, MNRAS, 476, 4949

Dunham, M. M., Arce, H. G., Mardones, D., et al. 2014a, ApJ, 783, 29

Dunham, M. M., Stutz, A. M., Allen, L. E., et al. 2014b, in Protostars and Planets VI (Tucson, AZ: Univ. Arizona Press), 195–218

Dunham, M. M., Vorobyov, E. I., & Arce, H. G. 2014c, MNRAS, 444, 887

Dutrey, A., Guilloteau, S., & Bachiller, R. 1997, A&A, 325, 758

Dzib, S. A., Loinard, L., Mioduszewski, A. J., et al. 2013, ApJ, 775, 63

Dzib, S. A., Loinard, L., Rodríguez, L. F., et al. 2015, ApJ, 801, 91

Eiroa, C., Torrelles, J. M., Curiel, S., & Djupvik, A. A. 2005, AJ, 130, 643

Eistrup, C., Walsh, C., & van Dishoeck, E. F. 2018, A&A, 613, A14

Emprechtinger, M., Caselli, P., Volgenau, N. H., Stutzki, J., & Wiedner, M. C. 2009, A&A, 493, 89

Enoch, M. L., Corder, S., Duchêne, G., et al. 2011, ApJS, 195, 21

Enoch, M. L., Evans, II, N. J., Sargent, A. I., & Glenn, J. 2009, ApJ, 692, 973

Enoch, M. L., Lee, J.-E., Harvey, P., Dunham, M. M., & Schnee, S. 2010, ApJ, 722, L33

Enoch, M. L., Young, K. E., Glenn, J., et al. 2006, ApJ, 638, 293

Evans, Neal J., I. 1999, ARA&A, 37, 311

Evans, II, N. J., Dunham, M. M., Jørgensen, J. K., et al. 2009, ApJS, 181, 321

Favre, C., Bergin, E. A., Cleeves, L. I., et al. 2015, ApJ, 802, L23

Ferreira, J. 1997, A&A, 319, 340

Ferreira, J., Dougados, C., & Cabrit, S. 2006, A&A, 453, 785

Fischer, W. J., Megeath, S. T., Furlan, E., et al. 2017, ApJ, 840, 69

Forbrich, J., Osten, R. A., & Wolk, S. J. 2011, ApJ, 736, 25

Frank, A., Ray, T. P., Cabrit, S., et al. 2014, in Protostars and Planets VI, ed. H. Beuther, R. S. Klessen, C. P. Dullemond, & T. Henning (Tucson, AZ: Univ. Arizona Press), 451–474

Frerking, M. A., Langer, W. D., & Wilson, R. W. 1982, ApJ, 262, 590

Frimann, S., Jørgensen, J. K., Dunham, M. M., et al. 2017, A&A, 602, A120

Fuente, A., Martin-Pintado, J., Cernicharo, J., & Bachiller, R. 1993, A&A, 276, 473

Furuya, R. S., Kitamura, Y., Wootten, A., Claussen, M. J., & Kawabe, R. 2003, ApJS, 144, 71

Gaia Collaboration, Brown, A. G. A., Vallenari, A., et al. 2018, A&A, 616, A1

Galván-Madrid, R., Rodríguez, L. F., Liu, H. B., et al. 2015, ApJ, 806, L32

Garufi, A., Podio, L., Codella, C., et al. 2020, arXiv e-prints, arXiv:2012.07667

Geers, V. C., van Dishoeck, E. F., Pontoppidan, K. M., et al. 2009, A&A, 495, 837

Gerin, M., Pety, J., Fuente, A., et al. 2015, A&A, 577, L2

Getman, K. V., Feigelson, E. D., Townsley, L., et al. 2002, ApJ, 575, 354

Ghavamian, P. & Hartigan, P. 1998, ApJ, 501, 687

Girart, J. M., Curiel, S., Rodríguez, L. F., & Cantó, J. 2002, Rev. Mexicana Astron. Astrofis., 38, 169

Glassgold, A. E., Mamon, G. A., & Huggins, P. J. 1991, ApJ, 373, 254

Goldreich, P., Lithwick, Y., & Sari, R. 2004, ApJ, 614, 497

Goodman, A. A., Barranco, J. A., Wilner, D. J., & Heyer, M. H. 1998, ApJ, 504, 223

Greaves, J. S. & Rice, W. K. M. 2010, MNRAS, 407, 1981

Greaves, J. S. & Rice, W. K. M. 2011, MNRAS, 412, L88

Green, J. D., Evans, II, N. J., Jørgensen, J. K., et al. 2013, ApJ, 770, 123

Greene, T. P., Wilking, B. A., Andre, P., Young, E. T., & Lada, C. J. 1994, ApJ, 434, 614

Gueth, F., Guilloteau, S., & Bachiller, R. 1996, A&A, 307, 891

Guilloteau, S., Bachiller, R., Fuente, A., & Lucas, R. 1992, A&A, 265, L49

Gusdorf, A., Cabrit, S., Flower, D. R., & Pineau des Forêts, G. 2008a, A&A, 482, 809

Gusdorf, A., Pineau des Forêts, G., Cabrit, S., & Flower, D. R. 2008b, A&A, 490, 695

Guzmán, V. V., Pety, J., Goicoechea, J. R., et al. 2015, ApJ, 800, L33

Hacar, A., Tafalla, M., Kauffmann, J., & Kovács, A. 2013, A&A, 554, A55

Hancock, P. J., Murphy, T., Gaensler, B. M., Hopkins, A., & Curran, J. R. 2012, MNRAS, 422, 1812

Harsono, D., Bjerkeli, P., van der Wiel, M. H. D., et al. 2018, Nature Astronomy, 2, 646

Harsono, D., Bruderer, S., & van Dishoeck, E. F. 2015a, A&A, 582, A41

Harsono, D., Jørgensen, J. K., van Dishoeck, E. F., et al. 2014, A&A, 562, A77

Harsono, D., van der Wiel, M., Bjerkeli, P., et al. 2020, arXiv e-prints, arXiv:2010.13722

Harsono, D., van Dishoeck, E. F., Bruderer, S., Li, Z. Y., & Jørgensen, J. K. 2015b, A&A, 577, A22

Hartquist, T. W., Dalgarno, A., & Oppenheimer, M. 1980, ApJ, 236, 182

Hatchell, J., Fuller, G. A., & Richer, J. S. 2007, A&A, 472, 187

Hatchell, J., Fuller, G. A., Richer, J. S., Harries, T. J., & Ladd, E. F. 2007, A&A, 468, 1009

Herbig, G. H. 1950, ApJ, 111, 11

Herbst, E. & van Dishoeck, E. F. 2009, Annual Review of Astronomy and Astrophysics, 47, 427

Herczeg, G. J., Karska, A., Bruderer, S., et al. 2012, A&A, 540, A84

Hernández-Gómez, A., Sahnoun, E., Caux, E., et al. 2018, Monthly Notices of the Royal Astronomical Society, 483, 2014–2030

Higuchi, A. E., Sakai, N., Watanabe, Y., et al. 2018, ApJS, 236, 52

Hildebrand, R. H. 1983, QJRAS, 24, 267

Hirano, N., Ho, P. P. T., Liu, S.-Y., et al. 2010, ApJ, 717, 58

Hirano, N., Kamazaki, T., Mikami, H., Ohashi, N., & Umemoto, T. 1999, in Proceedings of Star Formation 1999, ed. T. Nakamoto (Nobeyama Radio Observatory), 181–182

Hirota, T., Honma, M., Imai, H., et al. 2011, PASJ, 63, 1

Hogerheijde, M. R., Bergin, E. A., Brinch, C., et al. 2011, Science, 334, 338

Hogerheijde, M. R., Jansen, D. J., & van Dishoeck, E. F. 1995, A&A, 294, 792

Hogerheijde, M. R., van Dishoeck, E. F., Blake, G. A., & van Langevelde, H. J. 1997, ApJ, 489, 293

Hogerheijde, M. R., van Dishoeck, E. F., Blake, G. A., & van Langevelde, H. J. 1998, ApJ, 502, 315

Hogerheijde, M. R., van Dishoeck, E. F., Salverda, J. M., & Blake, G. A. 1999, ApJ, 513, 350

Hollenbach, D. & McKee, C. F. 1989, ApJ, 342, 306

Hollenbach, D. J. & Tielens, A. G. G. M. 1997, ARA&A, 35, 179

Hsieh, T.-H., Hirano, N., Belloche, A., et al. 2019a, ApJ, 871, 100

Hsieh, T.-H., Murillo, N. M., Belloche, A., et al. 2019b, ApJ, 884, 149

Huang, J., Andrews, S. M., Dullemond, C. P., et al. 2018, ApJ, 869, L42

Hubble, E. 1929, Proceedings of the National Academy of Science, 15, 168

Hueso, R. & Guillot, T. 2005, A&A, 442, 703

Hull, C. L. H., Girart, J. M., Kristensen, L. E., et al. 2016, ApJ, 823, L27

Hull, C. L. H., Girart, J. M., Tychoniec, Ł., et al. 2017, ApJ, 847, 92

Hull, C. L. H., Le Gouellec, V. J. M., Girart, J. M., Tobin, J. J., & Bourke, T. L. 2020, ApJ, 892, 152

Hull, C. L. H., Plambeck, R. L., Kwon, W., et al. 2014, ApJS, 213, 13

Hunter, J. D. 2007, Computer Science and Engineering, 9, 90

Imai, M., Sakai, N., Oya, Y., et al. 2016, ApJ, 830, L37

Isobe, T., Feigelson, E. D., & Nelson, P. I. 1986, ApJ, 306, 490

Ivezic, Z. & Elitzur, M. 1997, MNRAS, 287, 799

Jackson, J. M., Ho, P. T. P., & Haschick, A. D. 1988, ApJ, 333, L73

Jansen, D. J. 1995, PhD thesis, Leiden Observatory, Leiden University, The Netherlands

Jansen, D. J., Spaans, M., Hogerheijde, M. R., & van Dishoeck, E. F. 1995, A&A, 303, 541

Jeans, J. H. 1928, Astronomy and cosmogony (The University Press, Cambridge)

Jiménez-Serra, I., Caselli, P., Martín-Pintado, J., & Hartquist, T. W. 2008, A&A, 482, 549

Jiménez-Serra, I., Martín-Pintado, J., Caselli, P., Viti, S., & Rodríguez-Franco, A. 2009, ApJ, 695, 149

Johansen, A. & Lambrechts, M. 2017, Annual Review of Earth and Planetary Sciences, 45, 359

Jørgensen, J. K., Hogerheijde, M. R., Blake, G. A., et al. 2004, A&A, 415, 1021

Jørgensen, J. K., Hogerheijde, M. R., van Dishoeck, E. F., Blake, G. A., & Schöier, F. L. 2004a, A&A, 413, 993

Jørgensen, J. K., Johnstone, D., Kirk, H., & Myers, P. C. 2007, ApJ, 656, 293

Jørgensen, J. K., Schöier, F. L., & van Dishoeck, E. F. 2002, A&A, 389, 908

Jørgensen, J. K., Schöier, F. L., & van Dishoeck, E. F. 2004b, A&A, 416, 603

Jørgensen, J. K., Schöier, F. L., & van Dishoeck, E. F. 2005, A&A, 435, 177

Jørgensen, J. K., van der Wiel, M. H. D., Coutens, A., et al. 2016, A&A, 595, A117

Jørgensen, J. K., van Dishoeck, E. F., Visser, R., et al. 2009, A&A, 507, 861

Jørgensen, J. K., Visser, R., Sakai, N., et al. 2013, ApJ, 779, L22

Jørgensen, J. K., Visser, R., Williams, J. P., & Bergin, E. A. 2015, A&A, 579, A23

Kant, I. 1755, Allgemeine Naturgeschichte und Theorie des Himmels, Kant im Original (Harald Fischer Verlag, 1984)

Karska, A., Herczeg, G. J., van Dishoeck, E. F., et al. 2013, A&A, 552, A141

Karska, A., Herpin, F., Bruderer, S., et al. 2014a, A&A, 562, A45

Karska, A., Kaufman, M. J., Kristensen, L. E., et al. 2018, ApJS, 235, 30

Karska, A., Kristensen, L. E., van Dishoeck, E. F., et al. 2014b, A&A, 572, A9

Kataoka, A., Okuzumi, S., Tanaka, H., & Nomura, H. 2014, A&A, 568, A42

Kauffmann, J., Bertoldi, F., Bourke, T. L., Evans, II, N. J., & Lee, C. W. 2008, A&A, 487, 993

Kawabe, R., Ishiguro, M., Omodaka, T., Kitamura, Y., & Miyama, S. M. 1993, ApJ, 404, L63

Kirk, H., Johnstone, D., & Tafalla, M. 2007, ApJ, 668, 1042

Kratter, K. & Lodato, G. 2016, ARA&A, 54, 271

Kristensen, L. E. & Dunham, M. M. 2018, A&A, 618, A158

Kristensen, L. E., van Dishoeck, E. F., Benz, A. O., et al. 2013, A&A, 557, A23

Kristensen, L. E., van Dishoeck, E. F., Bergin, E. A., et al. 2012, A&A, 542, A8

Kristensen, L. E., van Dishoeck, E. F., Mottram, J. C., et al. 2017, A&A, 605, A93

Kristensen, L. E., van Dishoeck, E. F., van Kempen, T. A., et al. 2010, A&A, 516, A57

Kruijer, T. S., Touboul, M., Fischer-Gödde, M., et al. 2014, Science, 344, 1150

Krumholz, M. R., Bate, M. R., Arce, H. G., et al. 2014, in Protostars and Planets VI, ed. H. Beuther, R. S. Klessen, C. P. Dullemond, & T. Henning, 243

Kuiper, G. P. 1951, Proceedings of the National Academy of Science, 37, 1

Kukarkin, B. V., Kholopov, P. N., Pskovsky, Y. P., et al. 1971, in General Catalogue of Variable Stars, 3rd ed. (Moscow: Akademiia Nauk)

Kwon, W., Looney, L. W., Mundy, L. G., Chiang, H.-F., & Kemball, A. J. 2009, ApJ, 696, 841

Kwon, W., Looney, L. W., Mundy, L. G., & Welch, W. J. 2015, ApJ, 808, 102

Lada, C. J. 1987, in IAU Symposium, Vol. 115, Star Forming Regions, ed. M. Peimbert & J. Jugaku, 1–17

Lada, C. J. & Lada, E. A. 2003, ARA&A, 41, 57

Lada, C. J. & Wilking, B. A. 1984, ApJ, 287, 610

Ladd, E. F., Myers, P. C., & Goodman, A. A. 1994, ApJ, 433, 117

Lahuis, F., Spoon, H. W. W., Tielens, A. G. G. M., et al. 2007, ApJ, 659, 296

Lambrechts, M. & Johansen, A. 2012, A&A, 544, A32

Langer, W. D., Velusamy, T., & Xie, T. 1996, ApJ, 468, L41

Laplace, P.-S. 1796, Exposition du systeme du monde (De l'Imprimerie du Cercle-Social Paris, Microopaque. New York)

Larson, R. B. 1969, MNRAS, 145, 271

Le Gouellec, V. J. M., Hull, C. L. H., Maury, A. J., et al. 2019, ApJ, 885, 106

Lee, C.-F. 2020, A&A Rev., 28, 1

Lee, C.-F., Codella, C., Li, Z.-Y., & Liu, S.-Y. 2019a, ApJ, 876, 63

Lee, C.-F., Hirano, N., Zhang, Q., et al. 2014, ApJ, 786, 114

Lee, C.-F., Hirano, N., Zhang, Q., et al. 2015, The Astrophysical Journal, 805, 186

Lee, C.-F., Ho, P. T. P., Bourke, T. L., et al. 2008, ApJ, 685, 1026

Lee, C.-F., Ho, P. T. P., Li, Z.-Y., et al. 2017, Nature Astronomy, 1, 0152

Lee, C.-F., Ho, P. T. P., Palau, A., et al. 2007, The Astrophysical Journal, 670, 1188

Lee, C.-F., Mundy, L. G., Stone, J. M., & Ostriker, E. C. 2002, ApJ, 576, 294

Lee, J.-E., Lee, S., Baek, G., et al. 2019b, Nature Astronomy, 3, 314

Lefloch, B., Ceccarelli, C., Codella, C., et al. 2017, MNRAS, 469, L73

Lefloch, B., Gusdorf, A., Codella, C., et al. 2015, A&A, 581, A4

Lenz, C. T., Klahr, H., & Birnstiel, T. 2019, ApJ, 874, 36

Li, Z.-Y., Krasnopolsky, R., & Shang, H. 2011, ApJ, 738, 180

Lissauer, J. J. 1993, ARA&A, 31, 129

Lommen, D., Wright, C. M., Maddison, S. T., et al. 2007, A&A, 462, 211

Long, F., Herczeg, G. J., Harsono, D., et al. 2019, ApJ, 882, 49

Looney, L. W., Mundy, L. G., & Welch, W. J. 2000, ApJ, 529, 477

López-Sepulcre, A., Sakai, N., Neri, R., et al. 2017, A&A, 606, A121

Luhman, K. L., Rieke, G. H., Lada, C. J., & Lada, E. A. 1998, ApJ, 508, 347

Machida, M. N. 2014, ApJ, 796, L17

Machida, M. N., Matsumoto, T., & Inutsuka, S.-i. 2016, MNRAS, 463, 4246

Madhusudhan, N. 2012, ApJ, 758, 36

Madhusudhan, N. 2019, ARA&A, 57, 617

Manara, C. F., Morbidelli, A., & Guillot, T. 2018, A&A, 618, L3

Manigand, S., Jørgensen, J. K., Calcutt, H., et al. 2020, A&A, 635, A48

Manoj, P., Green, J. D., Megeath, S. T., et al. 2016, ApJ, 831, 69

Manoj, P., Watson, D. M., Neufeld, D. A., et al. 2013, ApJ, 763, 83

Marconi, A., Testi, L., Natta, A., & Walmsley, C. M. 1998, A&A, 330, 696

Maret, S., Ceccarelli, C., Caux, E., et al. 2004, A&A, 416, 577

Maret, S., Ceccarelli, C., Tielens, A. G. G. M., et al. 2005, A&A, 442, 527

Markwardt, C. B. 2009, in ASPC, Vol. 411, Astronomical Data Analysis Software and Systems XVIII, ed. D. A. Bohlender, D. Durand, & P. Dowler, 251

Mathews, G. S., Klaassen, P. D., Juhász, A., et al. 2013, A&A, 557, A132

Maury, A. J., André, P., Men'shchikov, A., Könyves, V., & Bontemps, S. 2011, A&A, 535, A77

Maury, A. J., André, P., Testi, L., et al. 2019, A&A, 621, A76

Mayor, M., Marmier, M., Lovis, C., et al. 2011, arXiv e-prints, arXiv:1109.2497

Mayor, M. & Queloz, D. 1995, Nature, 378, 355

McClure, M. K. 2019, A&A, 632, A32

McClure, M. K., Furlan, E., Manoj, P., et al. 2010, ApJS, 188, 75

McKee, C. F. & Ostriker, E. C. 2007, ARA&A, 45, 565

McMullin, J. P., Mundy, L. G., Blake, G. A., et al. 2000, ApJ, 536, 845

McMullin, J. P., Mundy, L. G., Wilking, B. A., Hezel, T., & Blake, G. A. 1994, ApJ, 424, 222

McMullin, J. P., Waters, B., Schiebel, D., Young, W., & Golap, K. 2007, in ASPC, Vol. 376, Astronomical Data Analysis Software and Systems XVI, ed. R. A. Shaw, F. Hill, & D. J. Bell, 127

Mellon, R. R. & Li, Z.-Y. 2008, ApJ, 681, 1356

Millar, T. J. & Williams, D. A. 1975, MNRAS, 170, 51P

Millar, T. J. & Williams, D. A. 1993, Dust and chemistry in astronomy (The Graduate Series in Astronomy, Bristol: IOP Publishing)

Miotello, A., Testi, L., Lodato, G., et al. 2014, A&A, 567, A32

Mizuno, H. 1980, Progress of Theoretical Physics, 64, 544

Morata, O., Palau, A., González, R. F., et al. 2015, ApJ, 807, 55

Morbidelli, A. & Raymond, S. N. 2016, Journal of Geophysical Research (Planets), 121, 1962

Mottram, J. C., Kristensen, L. E., van Dishoeck, E. F., et al. 2014, A&A, 572, A21

Mottram, J. C., van Dishoeck, E. F., Kristensen, L. E., et al. 2017, A&A, 600, A99

Mousis, O., Marboeuf, U., Lunine, J. I., et al. 2009, ApJ, 696, 1348

Murillo, N. M., Bruderer, S., van Dishoeck, E. F., et al. 2015, A&A, 579, A114

Murillo, N. M., Lai, S.-P., Bruderer, S., Harsono, D., & van Dishoeck, E. F. 2013, A&A, 560, A103

Murillo, N. M., van Dishoeck, E. F., Tobin, J. J., & Fedele, D. 2016, A&A, 592, A56

Murillo, N. M., van Dishoeck, E. F., Tobin, J. J., Mottram, J. C., & Karska, A. 2018, A&A, 620, A30

Myers, P. C. & Ladd, E. F. 1993, ApJ, 413, L47

Najita, J. R. & Kenyon, S. J. 2014, MNRAS, 445, 3315

Natta, A., Grinin, V., & Mannings, V. 2000, in Protostars and Planets IV, ed. V. Mannings, A. Boss, & R. S. Samantha (Tucson, AZ: Univ. Arizona Press), 559–588

Natta, A. & Testi, L. 2004, in Astronomical Society of the Pacific Conference Series, Vol. 323, Star Formation in the Interstellar Medium: In Honor of David Hollenbach, ed. D. Johnstone, F. C. Adams, D. N. C. Lin, D. A. Neufeeld, & E. C. Ostriker, 279

Navarro-Almaida, D., Le Gal, R., Fuente, A., et al. 2020, A&A, 637, A39

Neufeld, D. A. & Dalgarno, A. 1989, ApJ, 340, 869

Neufeld, D. A. & Hollenbach, D. J. 1994, ApJ, 428, 170

Neufeld, D. A. & Kaufman, M. J. 1993, ApJ, 418, 263

Nisini, B., Codella, C., Giannini, T., et al. 2007, A&A, 462, 163

Nisini, B., Giannini, T., & Lorenzetti, D. 2002, ApJ, 574, 246

Nisini, B., Santangelo, G., Giannini, T., et al. 2015, ApJ, 801, 121

Notsu, S., Eistrup, C., Walsh, C., & Nomura, H. 2020, MNRAS, 499, 2229

Öberg, K. I., Murray-Clay, R., & Bergin, E. A. 2011, ApJ, 743, L16

Offner, S. S. R. & Arce, H. G. 2014, ApJ, 784, 61

Ohashi, N., Saigo, K., Aso, Y., et al. 2014, ApJ, 796, 131

Opik, E. 1922, ApJ, 55, 406

Ormel, C. W. 2017, Astrophysics and Space Science Library, Vol. 445, The Emerging Paradigm of Pebble Accretion (Springer International Publishing AG, 2017), 197

Ormel, C. W. & Klahr, H. H. 2010, A&A, 520, A43

Ortiz-León, G. N., Loinard, L., Dzib, S. A., et al. 2018, ApJ, 865, 73

Ortiz-León, G. N., Loinard, L., Kounkel, M. A., et al. 2017, ApJ, 834, 141

Ossenkopf, V. & Henning, T. 1994, A&A, 291, 943

Oya, Y., Sakai, N., Watanabe, Y., et al. 2017, ApJ, 837, 174

Padovani, M., Hennebelle, P., & Galli, D. 2013, A&A, 560, A114

Padovani, M., Marcowith, A., Hennebelle, P., & Ferrière, K. 2016, A&A, 590, A8

Panagia, N. & Felli, M. 1975, A&A, 39, 1

Panić, O., Hogerheijde, M. R., Wilner, D., & Qi, C. 2008, A&A, 491, 219

Panoglou, D., Cabrit, S., Pineau des Forêts, G., et al. 2012, A&A, 538, A2

Pascucci, I., Testi, L., Herczeg, G. J., et al. 2016, ApJ, 831, 125

Pech, G., Loinard, L., Dzib, S. A., et al. 2016, ApJ, 818, 116

Perley, R. A. & Butler, B. J. 2017, ApJS, 230, 7

Perotti, G., Rocha, W. R. M., Jørgensen, J. K., et al. 2020, A&A, 643, A48

Pety, J., Gratier, P., Guzmán, V., et al. 2012, A&A, 548, A68

Pety, J., Teyssier, D., Fossé, D., et al. 2005, A&A, 435, 885

Pezzuto, S., Elia, D., Schisano, E., et al. 2012, A&A, 547, A54

Pilbratt, G. L., Riedinger, J. R., Passvogel, T., et al. 2010, A&A, 518, L1

Pineau des Forêts, G., Roueff, E., & Flower, D. R. 1990, MNRAS, 244, 668

Pineda, J. E., Arce, H. G., Schnee, S., et al. 2011, ApJ, 743, 201

Pinilla, P., Birnstiel, T., Ricci, L., et al. 2012, A&A, 538, A114

Plunkett, A. L., Arce, H. G., Corder, S. A., et al. 2013, ApJ, 774, 22

Plunkett, A. L., Arce, H. G., Mardones, D., et al. 2015, Nature, 527, 70

Podio, L., Codella, C., Gueth, F., et al. 2015, A&A, 581, A85

Podio, L., Codella, C., Gueth, F., et al. 2016, A&A, 593, L4

Podio, L., Garufi, A., Codella, C., et al. 2020, A&A, 642, L7

Poglitsch, A., Waelkens, C., Geis, N., et al. 2010, A&A, 518, L2

Pollack, J. B., Hubickyj, O., Bodenheimer, P., et al. 1996, Icarus, 124, 62

Poteet, C. A. 2012, PhD thesis, The University of Toledo

Preibisch, T. 1997, A&A, 324, 690

Preibisch, T., Stanke, T., & Zinnecker, H. 2003, A&A, 409, 147

Preibisch, T. & Zinnecker, H. 2001, AJ, 122, 866

Ptolemei. 120, Almagest (Princeton University Press , 1999)

Pudritz, R. E. & Norman, C. A. 1983, ApJ, 274, 677

Raga, A. & Cabrit, S. 1993, A&A, 278, 267

Raga, A. C., Canto, J., Binette, L., & Calvet, N. 1990, ApJ, 364, 601

Raga, A. C., Canto, J., Calvet, N., Rodriguez, L. F., & Torrelles, J. M. 1993, A&A, 276, 539

Raga, A. C., Williams, D. A., & Lim, A. J. 2005, Rev. Mexicana Astron. Astrofis., 41, 137

Raghavan, D., McAlister, H. A., Henry, T. J., et al. 2010, ApJS, 190, 1

Reipurth, B., Rodríguez, L. F., Anglada, G., & Bally, J. 2004, AJ, 127, 1736

Reynolds, S. P. 1986, ApJ, 304, 713

Ricci, L., Testi, L., Natta, A., & Brooks, K. J. 2010, A&A, 521, A66

Robitaille, T. & Bressert, E. 2012, APLpy: Astronomical Plotting Library in Python, Astrophysics Source Code Library

Robitaille, T. P., Whitney, B. A., Indebetouw, R., Wood, K., & Denzmore, P. 2006, ApJS, 167, 256

Rodríguez, L. F., Anglada, G., & Curiel, S. 1997, ApJ, 480, L125

Rodríguez, L. F., Anglada, G., & Curiel, S. 1999, ApJS, 125, 427

Rodríguez, L. F., Curiel, S., Moran, J. M., et al. 1989a, ApJ, 346, L85

Rodríguez, L. F., Marti, J., Canto, J., Moran, J. M., & Curiel, S. 1993, Rev. Mexicana Astron. Astrofis., 25, 23

Rodríguez, L. F., Myers, P. C., Cruz-Gonzalez, I., & Terebey, S. 1989b, ApJ, 347, 461

Rodríguez, L. F., Porras, A., Claussen, M. J., et al. 2003, ApJ, 586, L137

Rodríguez, L. F. & Reipurth, B. 1989, Rev. Mexicana Astron. Astrofis., 17, 59

Rodríguez, L. F. & Reipurth, B. 1998, Rev. Mexicana Astron. Astrofis., 34, 13

Rodríguez, L. F., Zapata, L. A., & Palau, A. 2014, ApJ, 790, 80

Rodríguez, L. F., Zapata, L. A., & Palau, A. 2017, AJ, 153, 209

Rodríguez-Fernández, N. J., Tafalla, M., Gueth, F., & Bachiller, R. 2010, A&A, 516, A98

Rybicki, G. B. & Lightman, A. P. 1979, Radiative processes in astrophysics (New York: Wiley-Interscience)

Sadavoy, S. I., Di Francesco, J., André, P., et al. 2014, ApJ, 787, L18

Sakai, N., Ceccarelli, C., Bottinelli, S., Sakai, T., & Yamamoto, S. 2012, ApJ, 754, 70

Sakai, N., Oya, Y., Higuchi, A. E., et al. 2017, MNRAS, 467, L76

Sakai, N., Oya, Y., Sakai, T., et al. 2014a, ApJ, 791, L38

Sakai, N., Sakai, T., Hirota, T., Burton, M., & Yamamoto, S. 2009, ApJ, 697, 769

Sakai, N., Sakai, T., Hirota, T., et al. 2014b, Nature, 507, 78

Sakai, N., Sakai, T., Hirota, T., & Yamamoto, S. 2008, ApJ, 672, 371

Sakai, N. & Yamamoto, S. 2013, Chemical Reviews, 113, 8981

San José-García, I., Mottram, J. C., Kristensen, L. E., et al. 2013, A&A, 553, A125

San José-García, I., Mottram, J. C., van Dishoeck, E. F., et al. 2016, A&A, 585, A103

Santangelo, G., Codella, C., Cabrit, S., et al. 2015, A&A, 584, A126

Santangelo, G., Nisini, B., Giannini, T., et al. 2012, A&A, 538, A45

Santiago-García, J., Tafalla, M., Johnstone, D., & Bachiller, R. 2009, A&A, 495, 169

Schilke, P., Walmsley, C. M., Pineau des Forêts, G., & Flower, D. R. 1997, A&A, 321, 293

Schilke, P., Walmsley, C. M., Pineau Des Forets, G., et al. 1992, A&A, 256, 595

Schnee, S., Di Francesco, J., Enoch, M., et al. 2012, ApJ, 745, 18

Schneider, J., Dedieu, C., Le Sidaner, P., Savalle, R., & Zolotukhin, I. 2011, A&A, 532, A79

Scibelli, S. & Shirley, Y. 2020, ApJ, 891, 73

Segura-Cox, D. M., Harris, R. J., Tobin, J. J., et al. 2016, ApJ, 817, L14

Segura-Cox, D. M., Schmiedeke, A., Pineda, J. E., et al. 2020, Nature, 586, 228

Sheehan, P. D. & Eisner, J. A. 2017, ApJ, 851, 45

Sheehan, P. D. & Eisner, J. A. 2018, ApJ, 857, 18

Sheehan, P. D., Tobin, J. J., Federman, S., Megeath, S. T., & Looney, L. W. 2020, ApJ, 902, 141

Shirley, Y. L., Claussen, M. J., Bourke, T. L., Young, C. H., & Blake, G. A. 2007, ApJ, 667, 329

Shirley, Y. L., Evans, Neal J., I., Rawlings, J. M. C., & Gregersen, E. M. 2000, ApJS, 131, 249

Shu, F., Najita, J., Ostriker, E., et al. 1994, ApJ, 429, 781

Shu, F. H., Adams, F. C., & Lizano, S. 1987, ARA&A, 25, 23

Shu, F. H., Najita, J. R., Shang, H., & Li, Z. Y. 2000, in Protostars and Planets IV, ed. V. Mannings, A. P. Boss, & S. S. Russell, 789–814

Sibthorpe, B., Kennedy, G. M., Wyatt, M. C., et al. 2018, MNRAS, 475, 3046

Snell, R. L., Loren, R. B., & Plambeck, R. L. 1980, ApJ, 239, L17

Spaans, M., Hogerheijde, M. R., Mundy, L. G., & van Dishoeck, E. F. 1995, ApJ, 455, L167

Stephens, I. W., Dunham, M. M., Myers, P. C., et al. 2018, ApJS, 237, 22

Stevenson, D. J. & Lunine, J. I. 1988, Icarus, 75, 146

Stone, J. M. & Norman, M. L. 1993, ApJ, 413, 210

Strom, S. E., Vrba, F. J., & Strom, K. M. 1976, AJ, 81, 314

Suutarinen, A. N., Kristensen, L. E., Mottram, J. C., Fraser, H. J., & van Dishoeck, E. F. 2014, MNRAS, 440, 1844

Suzuki, D., Bennett, D. P., Sumi, T., et al. 2016, ApJ, 833, 145

Swedenborg, E. 1734, Prodromus philosophiae ratiocinantis de infinito et causa finali creationis (Hekel)

Tabone, B., Godard, B., Pineau des Forêts, G., Cabrit, S., & van Dishoeck, E. F. 2020, A&A, 636, A60

Tafalla, M., Bachiller, R., Lefloch, B., et al. 2015, A&A, 573, L2

Tafalla, M. & Hacar, A. 2015, A&A, 574, A104

Tafalla, M., Liseau, R., Nisini, B., et al. 2013, A&A, 551, A116

Tafalla, M., Santiago, J., Johnstone, D., & Bachiller, R. 2004, A&A, 423, L21

Tafalla, M., Santiago-García, J., Hacar, A., & Bachiller, R. 2010, A&A, 522, A91

Tafalla, M., Su, Y.-N., Shang, H., et al. 2017, A&A, 597, A119

Taquet, V., Codella, C., De Simone, M., et al. 2020, A&A, 637, A63

Tazzari, M., Testi, L., Ercolano, B., et al. 2016, A&A, 588, A53

Terebey, S., Shu, F. H., & Cassen, P. 1984, ApJ, 286, 529

Testi, L., Birnstiel, T., Ricci, L., et al. 2014, in Protostars and Planets VI, ed. H. Beuther, R. S. Klessen, C. P. Dullemond, & T. Henning (Tucson, AZ: Univ. Arizona Press), 339–361

Teyssier, D., Fossé, D., Gerin, M., et al. 2004, A&A, 417, 135

Thorngren, D. P., Fortney, J. J., Murray-Clay, R. A., & Lopez, E. D. 2016, ApJ, 831, 64

Tielens, A., McKee, C., Seab, C., & Hollenbach, D. 1994, The physics of grain-grain collisions and gas-grain sputtering in interstellar shocks., 431: 321–340

Tobin, J. J., Bergin, E. A., Hartmann, L., et al. 2013, ApJ, 765, 18

Tobin, J. J., Dunham, M. M., Looney, L. W., et al. 2015a, ApJ, 798, 61

Tobin, J. J., Hartmann, L., Chiang, H.-F., et al. 2011, ApJ, 740, 45

Tobin, J. J., Hartmann, L., Chiang, H.-F., et al. 2012, Nature, 492, 83

Tobin, J. J., Looney, L. W., Li, Z.-Y., et al. 2016, ApJ, 818, 73

Tobin, J. J., Looney, L. W., Li, Z.-Y., et al. 2018, ApJ, 867, 43

Tobin, J. J., Looney, L. W., Wilner, D. J., et al. 2015b, ApJ, 805, 125

Tobin, J. J., Sheehan, P. D., Megeath, S. T., et al. 2020, ApJ, 890, 130

Tsiganis, K., Gomes, R., Morbidelli, A., & Levison, H. F. 2005, Nature, 435, 459

Tychoniec, Ł., Hull, C. L. H., Kristensen, L. E., et al. 2019, A&A, 632, A101

Tychoniec, Ł., Hull, C. L. H., Tobin, J. J., & van Dishoeck, E. F. 2018a, in IAU Symposium, Vol. 332, IAU Symposium, ed. M. Cunningham, T. Millar, & Y. Aikawa, 249–253

Tychoniec, Ł., Manara, C. F., Rosotti, G. P., et al. 2020, A&A, 640, A19

Tychoniec, Ł., Tobin, J. J., Karska, A., et al. 2018b, ApJS, 238, 19

Tychoniec, Ł., Tobin, J. J., Karska, A., et al. 2018c, ApJ, 852, 18

Ulrich, R. K. 1976, ApJ, 210, 377

van der Marel, N., Kristensen, L. E., Visser, R., et al. 2013, A&A, 556, A76

van der Marel, N., van Dishoeck, E. F., Bruderer, S., et al. 2013, Science, 340, 1199

van der Tak, F. F. S., Black, J. H., Schöier, F. L., Jansen, D. J., & van Dishoeck, E. F. 2007, A&A, 468, 627

van der Wiel, M. H. D., van der Tak, F. F. S., Ossenkopf, V., et al. 2009, A&A, 498, 161

van Dishoeck, E. F. & Blake, G. A. 1998, ARA&A, 36, 317

van Dishoeck, E. F., Blake, G. A., Jansen, D. J., & Groesbeck, T. D. 1995, ApJ, 447, 760

van Dishoeck, E. F. & Hogerheijde, M. R. 1999, in NATO Advanced Study Institute (ASI) Series C, Vol. 540, The Origin of Stars and Planetary Systems, ed. C. J. Lada & N. D. Kylafis, 97

van Dishoeck, E. F., Kristensen, L. E., Benz, A. O., et al. 2011, PASP, 123, 138

van Gelder, M. L., Tabone, B., Tychoniec, Ł., et al. 2020, A&A, 639, A87

van Kempen, T. A., Hogerheijde, M. R., van Dishoeck, E. F., et al. 2016, A&A, 587, A17

van Kempen, T. A., Kristensen, L. E., Herczeg, G. J., et al. 2010, A&A, 518, L121

van Kempen, T. A., van Dishoeck, E. F., Güsten, R., et al. 2009a, A&A, 507, 1425

van Kempen, T. A., van Dishoeck, E. F., Salter, D. M., et al. 2009b, A&A, 498, 167

van Kempen, T. A., Wilner, D., & Gurwell, M. 2009, ApJ, 706, L22

van 't Hoff, M. L. R., Persson, M. V., Harsono, D., et al. 2018a, A&A, 613, A29

van 't Hoff, M. L. R., Tobin, J. J., Harsono, D., & van Dishoeck, E. F. 2018b, A&A, 615, A83

van 't Hoff, M. L. R., Tobin, J. J., Trapman, L., et al. 2018c, ApJ, 864, L23

van 't Hoff, M. L. R., van Dishoeck, E. F., Jørgensen, J. K., & Calcutt, H. 2020, A&A, 633, A7

van Terwisga, S. E., van Dishoeck, E. F., Ansdell, M., et al. 2018, A&A, 616, A88

van't Hoff, M. L. R., Harsono, D., Tobin, J. J., et al. 2020, ApJ, 901, 166

Visser, R., Bruderer, S., Cazzoletti, P., et al. 2018, A&A, 615, A75

Visser, R. & Dullemond, C. P. 2010, A&A, 519, A28

Visser, R., van Dishoeck, E. F., & Black, J. H. 2009, A&A, 503, 323

Walker-Smith, S. L., Richer, J. S., Buckle, J. V., Hatchell, J., & Drabek-Maunder, E. 2014, MNRAS, 440, 3568

Walsh, C., Millar, T. J., & Nomura, H. 2010, ApJ, 722, 1607

Wampfler, S. F., Bruderer, S., Karska, A., et al. 2013, A&A, 552, A56

Ward-Thompson, D., André, P., Crutcher, R., et al. 2007, in Protostars and Planets V, ed. B. Reipurth, D. Jewitt, & K. Keil, 33

Watanabe, N., Nagaoka, A., Shiraki, T., & Kouchi, A. 2004, ApJ, 616, 638

Weintraub, D. A., Sandell, G., & Duncan, W. D. 1989, ApJ, 340, L69

Whitney, B. A., Wood, K., Bjorkman, J. E., & Cohen, M. 2003, ApJ, 598, 1079

Wilking, B. A., Meyer, M. R., Greene, T. P., Mikhail, A., & Carlson, G. 2004, AJ, 127, 1131

Williams, J. P. 2012, Meteoritics and Planetary Science, 47, 1915

Williams, J. P., Cieza, L., Hales, A., et al. 2019, ApJ, 875, L9

Williams, J. P. & Cieza, L. A. 2011, ARA&A, 49, 67

Wilner, D. J., Myers, P. C., Mardones, D., & Tafalla, M. 2000, ApJ, 544, L69

Winn, J. N. & Fabrycky, D. C. 2015, ARA&A, 53, 409

Winston, E., Megeath, S. T., Wolk, S. J., et al. 2010, AJ, 140, 266

Woitke, P., Min, M., Pinte, C., et al. 2016, A&A, 586, A103

Wolszczan, A. & Frail, D. A. 1992, Nature, 355, 145

Wootten, A. 1987, in IAU Symposium, Vol. 120, Astrochemistry, ed. M. S. Vardya & S. P. Tarafdar, 311–319

Wright, G. S., Wright, D., Goodson, G. B., et al. 2015, PASP, 127, 595

Wu, Y., Wei, Y., Zhao, M., et al. 2004, A&A, 426, 503

Wyatt, M. C., Smith, R., Su, K. Y. L., et al. 2007, ApJ, 663, 365

Yang, Y.-L., Evans, Neal J., I., Smith, A., et al. 2020, ApJ, 891, 61

Yen, H.-W., Koch, P. M., Takakuwa, S., et al. 2017, ApJ, 834, 178

Yen, H.-W., Takakuwa, S., Ohashi, N., et al. 2014, ApJ, 793, 1

Yıldız, U. A., Kristensen, L. E., van Dishoeck, E. F., et al. 2012, A&A, 542, A86

Yıldız, U. A., Kristensen, L. E., van Dishoeck, E. F., et al. 2015, A&A, 576, A109

Yıldız, U. A., Kristensen, L. E., van Dishoeck, E. F., et al. 2013, A&A, 556, A89

Youdin, A. N. & Goodman, J. 2005, ApJ, 620, 459

Young, C. H., Jørgensen, J. K., Shirley, Y. L., et al. 2004, ApJS, 154, 396

Young, K. E., Young, C. H., Lai, S.-P., Dunham, M. M., & Evans, II, N. J. 2015, ApJ, 150, 40

Ysard, N., Koehler, M., Jimenez-Serra, I., Jones, A. P., & Verstraete, L. 2019, A&A, 631, A88

Yvart, W., Cabrit, S., Pineau des Forêts, G., & Ferreira, J. 2016, A&A, 585, A74

Zhang, K., Schwarz, K. R., & Bergin, E. A. 2020, ApJ, 891, L17

Zhang, Y., Arce, H. G., Mardones, D., et al. 2016, ApJ, 832, 158

Nederlandse samenvatting

Hoe worden sterren en planeten gevormd?

De nieuwsgierigheid naar hoe de Aarde, planeten en de Zon zijn gevormd geeft een constante drang naar nieuwe astronomische ontdekkingen. Het is geen verrassing dat we met elke nieuwe technologische ontwikkeling - beginnende bij een simpele handtelescoop ontwikkeld door Lippershey en gebruikt door Galileo, tot de Very Large Telescope met een diameter van 8 meter en de 66 radio antennes van de Atacama Large Millimeter/submillimeter Array - proberen te leren over onze herkomst door naar de hemel te kijken. De ontdekkingen van de afgelopen 30 jaar hebben laten zien dat ons zonnestelsel slechts één voorbeeld is van de vele planetenstelsels rondom andere sterren, met meer dan 4000 planeten die tot op heden ontdekt zijn. Om uit te vinden hoe deze planeten gevormd worden is het niet genoeg om alleen planeten waar te nemen die al geboren zijn, maar is het ook essentieel om onze telescopen te richten op de geboorteplaatsen van sterren en planeten: moleculaire wolken.



Figuur 1: *Links: Spitzer* samengestelde afbeelding van het NGC1333 stervormingscomplex in de Perseus moleculaire wolk. Kleuren representeren verschillende golflengtes van de waarnemingen: 3.6 μm (blauw), 4.5 μm (groen), 5.8 μm (oranje), 8.0 μm (rood). Auteursrechten figuur: NASA/JPL-Caltech/R. A. Gutermuth (Harvard-Smithsonian CfA). *Rechts:* Afbeelding van hetzelfde gebied in het optisch in een blauwe, groene en rode filter. Auteursrechten figuur: Robert Franke.

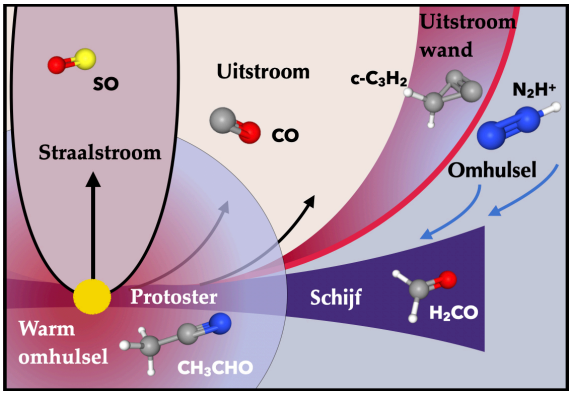
Er is de afgelopen jaren genoeg bewijs gevonden dat de vorming van planeten heel snel van start gaat op een kosmische tijdsschaal. In dit proefschrift zal ik bewijs leveren dat het vormen van planeten al in de eerste 100 000 jaar na het begin van stervormingsproces moet beginnen. Dit is slechts een oogwenk vergeleken met de leeftijd van onze Zon: 4.6 miljard jaar. Dit heeft belangrijke implicaties: om te begrijpen wat het planeetvormingsproces beïnvloed en onder welke condities ze vormen moeten we zeer jonge sterren waarnemen. De condities in dit soort systemen zijn alles behalve kalm en rustig: krachtige supersonische straalstromen worden gelanceerd vanuit de ster en schijf, en de temperatuur is hoog doordat een hoop gas nog steeds op de ster valt. De chemische compositie wordt hevig beïnvloed door deze omgeving. Een voorbeeld van een jong stervormingsgebied is de Perseus moleculaire wolk, met een van de meeste spectaculaire wolken, NGC1333, uitgebeeld in Fig. 1.

Als we de herkomst van complexe organische moleculen en prebiotische moleculen op Aarde willen ontdekken moeten de eerste 100 000 jaar van de stervormingscyclus bestuderen. Deze fase, waarin de ster geboren wordt, heet de protostellaire fase en is de focus van dit proefschrift.

Waarnemingen van jonge sterren

Jonge sterren zijn diep gelegen in de stoffige wolken waaruit ze worden gevormd. Dit betekent dat zelfs de meest krachtige optische telescopen niet goed geschikt zijn om ze te observeren door de zware extinctie. Een andere factor die waarnemingen van jonge sterren niet eenvoudiger maakt is dat de geboorteplaatsen van sterren koud zijn. De aard van licht (elektromagnetische golven) is zo dat de Zon met een oppervlakte temperatuur van 5400 K helder schijnt in het optische bereik. Daarentegen kan licht van protosterren gekarakteriseerd worden met een temperatuur van 30 - 500 K, wat betekent dat ze het meeste licht uitstralen op langere golflengtes dan de Zon - in het infrarood en submillimeter regime van het elektromagnetische spectrum. Daarom worden in dit proefschrift observatoria gebruikt die werken bij submillimeter en centimeter golflengtes zoals de Atacama Large Millimeter/submillimeter Array (ALMA) en Very Large Array (VLA). Dit zijn interferometrische faciliteiten, hetgeen betekent dat ze het signaal van meerdere antennes combineren om tot een resolutie te komen die equivalent is aan die van een enkelvoudige schotel met een even grote diameter als de afstand tussen de antennes.

Thermische straling van koud stof rondom protosterren manifesteert zich breedbandig, over een groot golflengtebereik. Spectroscopie, aan de andere kant, focusseert zich op discrete pieken en dalen in het licht en is een uniek hulpmiddel om de chemie en fysica in zulke gebieden te bestuderen. Het submillimeter bereik is rijk aan moleculaire rotatie spectraallijnen die informatie geven over de abondanties van moleculen en de energie die ze bezitten. Wat cruciaal is, is dat verschillende moleculen te vinden zijn onder verschillende fysische condities. Met deze kennis kunnen we een protostellair systeem ontleden in meerdere componenten en moleculen daarmee associëren (zie Fig. 2). In dit proefschrift worden continuüm waarnemingen gebruikt om de thermische straling van stof in protoplanetaire schijven en de omhullende wolk van jonge protosterren te bestuderen, en spectroscopie om de moleculaire emissie van het gas in verschillende delen van het protostellaire systeem te analyseren.



Figuur 2: Cartoon die de verschillende fysische componenten van een protostellair systeem illustreert. Pijlen geven de richting van bewegend materiaal weer; de protostellaire straalstroom verrijst in het binnenste gebied van het systeem, maar niet exclusief vanuit de protoster zelf. Voorbeelden van moleculen die goed geassocieerd kunnen worden met de verschillende componenten zijn uitgelicht. Molecuul figuren zijn afkomstig uit: https://pubchem.ncbi.nlm.nih.gov/.

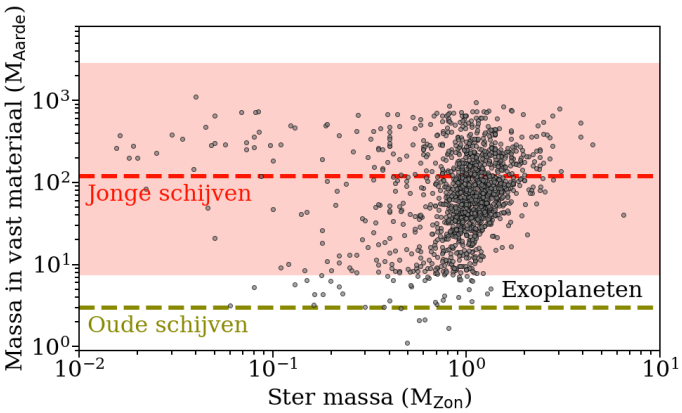
Protostellaire straalstromen en schijven

In dit proefschrift ligt de focus op het karakteriseren van de verschillende componenten van protostellaire systemen, in het bijzonder de straalstromen en schijven. Straalstromen bestaan uit gas dat met hoge snelheid (tientallen tot honderden kilometers per seconde) vanuit het binnenste gedeelte van het protostellaire systeem worden gelanceerd. Tijdens de ineenstorting van de wolk gaat het materiaal sneller ronddraaien doordat impulsmoment behouden is. Een deel van deze overmaat aan rotatie-energie komt vrij in hoge-snelheid straalstromen. Omdat de snelheden waarmee deze straalstromen zich bewegen zeer supersonisch zijn, ontstaan er schokken met het omringend materiaal die tot gevolg hebben dat de condities zoals temperatuur en dichtheid drastisch veranderen. Straalstromen zijn omringd door een langzamere en bredere lage-snelheid uitstroom. Deze bestaat voornamelijk uit materiaal uit de omhullende wolk dat wordt meegesleurd door de straalstroom. Het bestuderen van jonge straalstromen kan informatie geven over de compositie van het gelanceerde materiaal in het binnenste deel van de schijf en de impact die schokken kunnen hebben op de chemische compositie van het gehele systeem.

Het sneller ronddraaien van materiaal in de ineenstortende wolk zorgt ervoor dat het materiaal dicht bij de ster wordt platgedrukt tot een schijfachtige structuur. In die schijven wordt het proces van planeetvorming geïnitieerd door het botsen en samenvoegen van kleine stofdeeltjes. Deze stofdeeltjes zijn gecoat met een laag ijs dat voornamelijk, maar niet alleen, bestaat uit water. Andere moleculen zoals CO (koolmonoxide) kunnen ook vanuit het gas bevriezen op de stofdeeltjes en daar omgezet naar moleculen zoals CH_3OH (methanol) en H_2CO (formaldehyde).

Als de samenstelling van deze ijzen bekend is weten wat het bouwmateriaal van de kernen van planeten is. Of een molecuul zich in de gasfase of in het ijs bevindt is afhankelijk van de temperatuur: water bevriest op de stofdeeltjes beneden 100 K en CO beneden 20 K. De temperatuur van de schijf neemt af met toenemende afstand tot de protoster en de laag

waarbuiten een bepaald molecuul zich vooral in het ijs bevindt wordt de ijslijn genoemd. Deze ijslijnen spelen een belangrijke rol bij het vormen van planeten aangezien ze kunnen zorgen voor een opeenstapeling van stofdeeltjes, maar ook omdat ze de chemische samenstelling van de bouwstenen van planeten effectief kunnen veranderen. Gemeten massa's van oudere schijven laten zien dat, als de omliggende wolk verdwenen is, er niet genoeg massa is om planeten te maken. Betekent dit dat planeten al eerder beginnen te vormen? Er zijn meerdere bewijzen hiervoor: meteorieten in ons zonnestelsel zijn onderverdeeld in twee categorieën tussen het binnenste en buitenste deel, alsof een zware planeet vroeg gevormd was en deze twee categorieën gescheiden hield. Tevens is waargenomen dat stofdeeltjes snel groeien in schijven.



Figuur 3: Figuur die de distributie van massa's van de rotsachtige kernen van exoplanetaire systemen rondom hoofdreekssterren met een gemeten massa (gehaald van exoplanet.eu) laat zien. Het rood gearceerde gebied laat het bereik zien van beste schatting van stofschijfmassa's in de Perseus moleculaire wolk, met de mediaan weergegeven als de rood gestreepte lijn. De mediaan van de stofmassa's van oudere schijven is weergegeven als de geel gestreepte zijn.

Dit proefschrift

Dit proefschrift presenteert waarnemingen die de vroegste stadia van ster- en planeetvorming karakteriseren. In Hoofdstuk 2 gebruiken we observaties met de VLA op 4 en 6.4 cm van 100 protosterren in de Perseus moleculaire wolk om de geïoniseerde straalstroom component te bestuderen. We laten zien dat eigenschappen van de geïoniseerde straalstroom gelinkt zijn aan de stellaire eigenschappen. Voor deze grote groep bronnen gebruiken we de informatie over de straalstroom om de metingen van schijfmassa's op lagere golflengtes te corrigeren voor deze component. Dit maakte het voor het eerst mogelijk om de massa van jonge schijven te meten en te vergelijken met die van oudere schijven, en leidde tot de volgende vraag: is er genoeg massa beschikbaar in de jongste schijven om planeten te vormen?

We vervolgen deze vraag in Hoofdstuk 3 waar we waarnemingen van ALMA en VLA combineren om het stof in jonge schijven te karakteriseren. Door het vergelijken van de stofmassa's van jonge schijven met exoplanetaire systemen laten we zien dat gasreuzen gevormd kunnen (en moeten) worden in de vroegste stadia. Dit resultaat is uitgelicht in Fig. 3:

waargenomen rotsachtige kernen van exoplaneten hebben veel grotere massa's dan oude stofschijven, maar de massa's zijn vergelijkbaar met die van jongere schijven.

In Hoofdstuk 4 onderzoeken we de chemische compositie van de hoge-snelheid straalstromen afkomstig van meerdere protosterren in de Serpens moleculaire wolk. We bevestigen dat de C/O ratio van de straalstroom lager is dan die van de omhullende wolk; dit laat zien dat het bestuderen van jonge straalstromen potentieel cruciaal kan zijn om de binnenste regio's van de schijf te kunnen bestuderen. Hoofdstuk 5 geeft een overzicht van welke moleculen voorkomen in welke fysische componenten van protostellaire systemen. ALMA waarnemingen van een tiental protosterren maakt het mogelijk om de verschillende componenten te onderscheiden. Dit kan ook gebruikt worden om de temperatuur (bijvoorbeeld door DC^+O^+ en N_2D^+ voor koud gas) of de oorsprong van hoog-energetische straling (C_2H en CN als producten van UV-gedomineerde chemie) te bepalen.

Dit proefschrift kan als volgt worden samengevat: planeetvorming begint vroeg, in de eerste 0.1 miljoen jaar van het leven van de ster, in zeer jonge schijven. Het karakteriseren van deze jonge systemen is essentieel voor het begrijpen van de condities van planeetvorming. Interferometrische waarnemingen van moleculen op schalen van het zonnestelsel zijn ongelooflijk behulpzaam om deze condities te beschrijven. Moleculaire straalstromen, waarvan we laten zien dat ze heel gebruikelijk zijn in jonge systemen, kunnen bijzonder belangrijk zijn om uit te vinden wat er zich afspeelt in de binnenste gebieden van jonge systemen.

Toekomstperspectief

Waarnemers van jonge protostellaire systemen gaan een mooie toekomst tegemoet: ALMA is nu op volle snelheid en laat al zijn fantastische capaciteiten zien die ons in staat stellen om jonge protosterren en hun schijven op te lossen op schalen van het zonnestelsel. ALMA is in het bijzonder geschikt om jonge straalstromen te karakteriseren die ook het geheim van de chemische samenstelling van de binnenste delen van de schijf in zich dragen. Een revolutie is aanstaande met de JWST telescoop, de grootste schotel die ooit gelanceerd wordt in de ruimte. In het bijzonder zal het MIRI instrument protosterren karakteriseren met vergelijkbare resolutie als ALMA in het 5-28 micron golflengtebereik, wat onbereikbaar is vanaf de grond, en daarmee zowel het hete gas als de ijscompositie onthullen. Gecombineerd met informatie van ALMA over de condities, samenstelling en bewegingen van het koudere gas hebben we binnenkort de duidelijkste blik ooit op het begin van het planeetvormingsproces.

English summary

How are stars and planets made?

The curiosity about the origin of the Earth, our planets and the Sun is a constant drive for new astronomical discoveries. Thus, it is no surprise that with each new achievement of technology – starting from a simple hand telescope invented by Lippershey and used by Galileo, to 8-m diameter Very Large Telescopes and 66 radio antennas of the Atacama Large Millimeter/submillimeter Array –we try to learn about our origins by staring into the sky. The discoveries over the past 30 years show that our Solar System is only one example of many planetary systems orbiting other stars, with more than 4000 planets discovered to date. To understand how such planets are made it is not sufficient to observe planets that are already born, but it is essential to point our telescopes to the stellar and planetary nurseries: molecular clouds.



Figure 1: *Left: Spitzer* composite image of NGC1333 star-forming region in Perseus molecular cloud. Colors correspond to different wavelengths of observations: 3.6 μm (blue), 4.5 μm (green), 5.8 μm (orange), 8.0 μm (red). Credit: NASA/JPL-Caltech/R. A. Gutermuth (Harvard-Smithsonian CfA). *Right:* Optical light image in blue, green, and red filters of the same region. Credit: Robert Franke.

In recent years plenty of evidence has emerged that planet formation takes place very fast on a cosmic time-scale. In this thesis, I provide evidence that planets must start to form already in the first 100 000 years after star formation begins, a blink of an eye compared to the age of our Sun – 4.6 billion years. This has important implications: to understand what

affects planet formation and under which conditions planets are forming, we need to observe very young stars. The conditions in those systems are anything but calm and quiet: powerful supersonic jets are launched from the star and the disk, the temperature is high due to a lot of gas still infalling onto the disk, and the chemical composition of the gas is heavily affected by the range of conditions. An example of such a young star-forming region is the Perseus molecular cloud, with one of its most spectacular clouds NGC1333 presented in Fig. 1.

If we want to get to the bottom of the origin of complex organic and prebiotic molecules on Earth, we need to probe what happens in first 100 000 years of the star-formation cycle. This phase of stellar birth is called the protostellar stage and is the focus of this thesis.

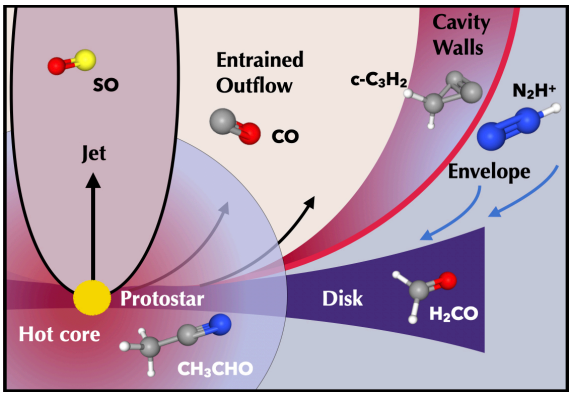


Figure 2: Cartoon illustrating the physical components of a protostellar system. Arrows indicate the direction of material in motion; the protostellar jet emerges from the innermost region of the system, but not exclusively from the protostar itself. Example molecules that are a good tracers of the corresponding components are presented. Molecule images from: https://pubchem.ncbi.nlm.nih.gov/.

Observations of young stars

Young stars are deeply embedded in the dusty clouds that they are made of. This means that optical telescopes, even the most powerful ones, are not well suited to observe them due to heavy extinction. Another factor that does not make observations any easier is that stellar nurseries are cold environments. The nature of light (electromagnetic waves) is such that our Sun with a surface temperature of 5400 K shines brightly in the visible range. On the other hand, radiation from protostellar systems can be characterized with temperatures of 30 – 500 K, which means they emit mostly at longer wavelengths than the Sun – in the infrared and submillimeter regime of the electromagnetic spectrum. This is why this thesis employs submillimeter and centimeter wavelength observatories, such as the Atacama Large Millimeter/submillimeter Array (ALMA) and Very Large Array (VLA). These interferometric facilities combine the signal from each of the separate antennas to achieve a resolution that is equivalent to that of a single-dish telescope with a diameter similar to the largest distance between the antennas.

Thermal emission from cold dust surrounding protostars is manifested by broad-band radiation across wavelengths. Spectroscopy, on the other hand, focuses on discrete peaks and troughs in light and is a unique tool to probe the chemistry and physics in such young

regions. The submillimeter range is rich in molecular rotational lines, which inform about the abundances of molecules and energies that they contain. What is crucial, is that different molecules trace different physical conditions. Using this knowledge we can dissect a protostellar system and associate molecules with individual components (Fig. 2). This thesis uses continuum observations to probe thermal emission from small dust particles in protoplanetary disks and envelopes around young stars, and spectroscopy to trace gaseous molecules in different parts of protostellar systems.

Protostellar jets and disks

This thesis focuses on characterizing different components of protostellar systems, most notably their jets and disks. Jets consist of gas at high velocities (ranging from tens to hundreds kilometers per second) released from the inner regions of the protostellar system. As the cloud core collapses, the material spins faster due to the conservation of the angular momentum, and some excess of this rotational energy is released in high-velocity jets. Because the velocities at which the jet moves are highly supersonic, they create shocks with the surrounding medium, which means that the conditions such as density and temperature change dramatically. Jets are surrounded by slower and wider, low-velocity outflows, comprised predominantly of material that is entrained from the envelope with the jet. Studying young jets can reveal information about the composition of the launched material and impact that the shocks can have on the chemical composition of the whole system.

The spin-up of the infalling envelope results in flattening of the material surrounding a star into a disk-shaped structure. In those disks, the first seeds of planets are created as the dust grains collide and coagulate. The dust grains are coated by ices, not only water, which is the main component of the ice. Other molecules such as CO (carbon monoxide) can also freeze-out from the gas-phase onto the grains and be converted to species like CH_3OH (methanol) and H_2CO (formaldehyde). Knowing the composition of those ices means knowing what provides the building blocks of the cores and atmopsheres of planets. Whether the molecule will be present in the gas phase or in the ice, depends on the temperature: water freezes onto the grains below 100 K and CO below 20 K. The temperature of the disk decreases with distance from the protostar, and the layer beyond which a certain molecule is present predominantly in the ice is called the iceline. Icelines play an important role in planet formation as they can facilitate the pile-up of material, but they also effectively change the composition of the building blocks of planets.

Measured dust masses of mature disks show that when envelope has dissipated they do not have enough mass to make the solid cores of planets. Does that mean that planets start to form early? There are several evidences for that: meteorites seen in our Solar System are divided in two classes between inner and outer part as if a massive planet formed and separated them very early on. Also, dust grains have been observed to grow very quickly in disks.

This thesis

This thesis presents observational efforts to characterize the earliest stages of star and planet formation. In Chapter 2 we use VLA observations at 4 and 6.4 cm of 100 protostars in the Perseus molecular cloud to study the ionized jet component and show that the ionized jet properties are connected to the stellar properties. For the observed large sample of sources,

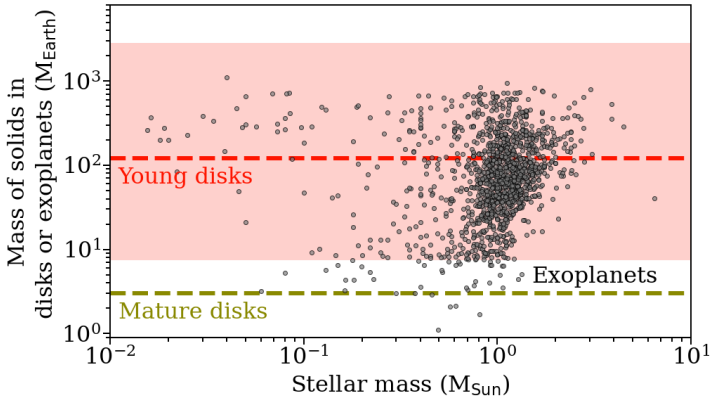


Figure 3: Plot showing the distribution of masses in solids of exoplanetary systems for planets around main sequence stars with the measured stellar masses (taken from exoplanet.eu). The shaded red area marks the range of the best estimate of dust disk masses in the Perseus molecular cloud with median mass indicated with the dashed line. The median dust mass of mature disks is shown in yellow.

we use information on the jet fluxes to correct the measurements of disk masses at shorter wavelengths. This allowed to compare dust masses of young disks with those of older disks for the first time and opened a question: is there enough solid material to make planets in the youngest disks?

We follow up on that question in Chapter 3, in which we combine observations of ALMA and VLA to characterize the dust in young disks. By comparing the dust masses of young disks with exoplanetary systems we show that the solid cores of gas giants can be formed in the earliest stages. This result is highlighted in Figure 3: observed exoplanets have masses in solids that are well above those of the mature disks, but are within the range of the dust masses of young disks.

In Chapter 4 we probe the chemical composition of high-velocity jets towards several protostars in the Serpens molecular cloud. We confirm that the C/O ratio of the jet is lower than that of the surrounding envelope; this shows that studying young jets can potentially be crucial to probe the inner regions of disks.

Chapter 5 provides an overview of the chemical tracers of different physical components of protostellar systems. ALMA observations of a dozen protostars enable to dissect these different components. This can also be used to measure the temperature (e.g., DCO^+ and N_2D^+ are a cold gas tracers) or nature of the energetic radiation (C_2H and CN as products of UV dominated chemistry).

This thesis can be summarized as follows: Planet formation starts early, in the first 0.1 Myr of stellar life in very young disks. Characterization of those young systems is essential for understanding the conditions of planet formation. Interferometric observations of molecules at Solar System scales are incredibly useful to describe those conditions. Molecular jets, which we show to be very common in young systems, can be particularly important to inform about the innermost regions of young disks.

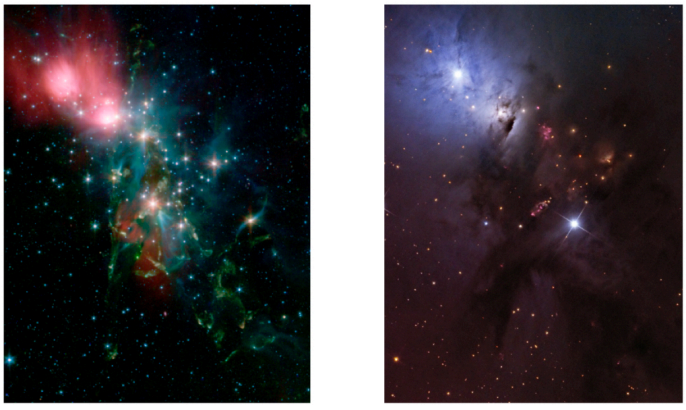
Future outlook

Observers of young protostellar systems are in for an exciting future: ALMA is now at full speed revealing its amazing capabilities, able to resolve young protostars and their disks at Solar System scales. It is especially well suited to provide good characterization of young protostellar jets, which hold the mystery of the chemical composition of the inner regions of disks. A revolution is imminent with the JWST telescope, the largest dish ever launched to space. Especially the MIRI instrument will characterize protostars at similar resolution to ALMA, in the 5-28 micron range unreachable from the ground, and will reveal hot gas as well as ice mantle composition. Combined with ALMA information on the physics and chemistry of colder gas and kinematics of the individual components, we will soon have the clearest view ever on the onset of planet formation.

Podsumowanie w języku polskim

Jak powstają gwiazdy i planety

Ciekawość na temat pochodzenia Ziemi, planet i Słońca jest nieustanną motywacją do dokonywania nowych odkryć astronomicznychnowych odkryć astronomicznych. Nic dziwnego, że z każdym nowym osiągnięciem technologicznym — począwszy od prostego teleskopu ręcznego wynalezionego przez Lippersheya i używanego przez Galileusza, po Very Large Telescope (VLT) o średnicy 8 m i 66 anten radiowych składających się na Atacama Large Millimeter / submillimeter Array (ALMA) — staramy się dowiedzieć się czegoś o powstaniu naszego świata patrząc w niebo. Odkrycia dokonane w ciągu ostatnich 30 lat pokazują, że nasz Układ Słoneczny jest tylko jednym z wielu układów planetarnych. Do dziś odkryto już ponad cztery tysiące planet orbitujących wokół mniej lub bardziej odległych gwiazd. Aby zrozumieć, jak powstają te planety, nie wystarczy obserwować tylko te, które już uformowanych, ale konieczne jest skierowanie naszych teleskopów na obszary, w których właśnie teraz powstają nowe gwiazdy i planety: na obłoki molekularne.



Rysunek 1: *Z lewej:* Obserwacje teleskopu *Spitzer* w podczerwieni regionu gwiazdotwórczego NGC1333 w Perseuszu. Obraz kolorowy powstały po złożeniu filtrów podczerwonych: 3.6 μm (niebieski), 4.5 μm (zielony), 5.8 μm (pomarańczowy), 8.0 μm (czerwony). Źródło: NASA/JPL-Caltech/R. A. Gutermuth (Harvard-Smithsonian CfA). *Z prawej:* Obraz w świetle widzialnym w filtrach niebieskim, zielonym, i czerwonym tego samego regionu. Źródło: Robert Franke.

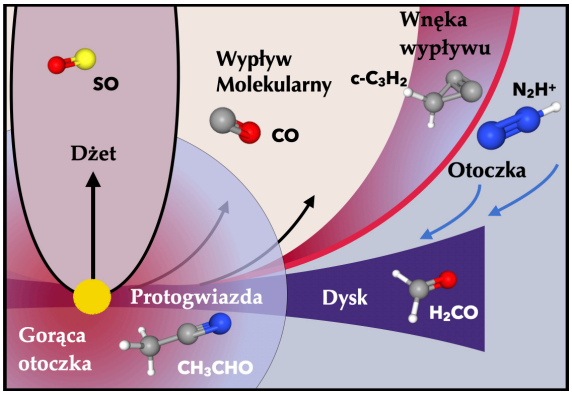
W ostatnich latach pojawiło się wiele dowodów na to, że formowanie planet zaczyna się błyskawicznie w kosmicznej skali czasu. W tej pracy dostarczam dowodów na to, że planety muszą zacząć się formować już w ciągu pierwszych 100 tysięcy lat po rozpoczęciu zapadania się pod wpływem grawitacji, obłoku z którego powstanie gwiazda i jej układ planetarny. To mgnienie oka w porównaniu z wiekiem naszego Słońca, które ma 4.6 miliarda lat. To odkrycie ma fundamentalne konsekwencje: aby zrozumieć, co wpływa na tworzenie się planet i w jakich warunkach powstają, musimy obserwować bardzo młode, jeszcze powstające gwiazdy. Warunki w młodych obłokach molekularnych wcale nie są spokojne: z gwiazdy i dysku protoplanetarnego wyrzucane są potężne naddźwiękowe dżety, temperatura jest wysoka z powodu dużej ilości materii opadającej na dysk. Przykładem takiego młodego regionu gwiazdotwórczego jest obłok molekularny Perseusza, z jednym z jego najbardziej spektakularnych obłoków NGC1333 przedstawionym na Rysunku 1.

Jeśli chcemy dotrzeć do sedna pochodzenia molekuł, których mieszanka sprawiła, że Ziemia eksplodowała życiem, musimy zbadać, co dzieje się w ciągu pierwszych 100 tysięcy lat cyklu formowania się gwiazd. Ta faza narodzin gwiazd nazywana jest fazą protogwiazdową i jest przedmiotem tej pracy doktorskiej.

Obserwacje powstających gwiazd

Młode gwiazdy są głęboko ukryte w obłokach gazowo-pyłowych, z których powstają. Oznacza to, że teleskopy optyczne, nawet te najpotężniejsze, nie nadają się do ich obserwacji z powodu silnej ekstynkcji - światło widzialne produkowane przez te obiekty jest pochłonięte. Innym czynnikiem, który nie ułatwia obserwacji, jest to, że rejony gwiazdotwórcze to zimne środowiska. Natura światła (fali elektromagnetycznej) sprawia, że nasze Słońce o temperaturze powierzchni 5400 K, świeci jasno w zakresie widzialnym, natomiast protogwiazdy charakteryzuje się temperaturą 30-500 K, co oznacza, że emitują one głównie fale o większej długości niż Słońce, a więc w podczerwieni i submilimetrowym zakresie widma elektromagnetycznego. Z tego powodu niniejsza praca wykorzystuje obserwatoria fal submilimetrowych i centymetrowych, takie jak Atacama Large Millimeter / submillimeter Array (ALMA) i Very Large Array (VLA). Są to interferometry, co oznacza, że łączą sygnał z każdej z oddzielnych anten, aby uzyskać rozdzielczość, która jest równoważna rozdzielczości teleskopu z jedną anteną o średnicy równej odległości między antenami.

Każdy obiekt posiadający temperaturę, a więc także zimny pył otaczający protogwiazdy, emituje szerokopasmowym promieniowaniem o różnych długościach fal, taką emisję nazywamy kontinuum. Spektroskopia natomiast skupia się na liniach widmowych - wierzchołkach i spadkach w intensywności światła i jest wyjątkowym narzędziem do badania składu chemicznego i warunków fizycznych w tak młodych regionach. Zakres submilimetrowy jest bogaty w linie rotacyjne molekuł. Przejścia rotacyjne informuje o ilości cząsteczek emitujących światło i energii, którą posiadają. Kluczowe jest to, że różne molekuły śledzą różne warunki fizyczne. Dzięki temu możemy wyizolować poszczególne elementy układu protogwiezdnego (Rysunek 2). Niniejsza praca wykorzystuje obserwacje kontinuum do badania emisji termicznej pyłu w dyskach protoplanetarnych oraz spektroskopię do śledzenia gazowej emisji molekularnej.



Rysunek 2: Ilustracja komponentów składających się na system protogwiazdowy. Strzałki wskazują kierunki przemieszczania się gazu. Przedstawiono przykłady cząsteczek molekularnych, które są optymalne do obserwacji odpowiednich komponentów. Grafiki cząsteczek z https://pubchem.ncbi.nlm.nih.gov/.

Dżety i dyski protogwiazdowe

Ta praca koncentruje się na scharakteryzowaniu głównych elementów układów protogwiazdowych, w szczególności ich dżetów i dysków. Dżety składają się z gazu o dużych prędkościach (od kilkudziesięciu do setek kilometrów na sekundę) wyrzucanego z wewnętrznych obszarów układu protogwiazdowego. Gdy chmura protogwiezdna zapada się, materiał wiruje szybciej z powodu zasady zachowania momentu pędu. Nadmiar tej energii obrotowej jest uwalniany w wypływach gazu o dużej prędkości, znacznie powyżej lokalnej prędkości dźwięku. Te wyrzuty materii nazywane dżetami, wchodzą w interakcje z otoczką gazowo-pyłową wokół młodej gwiazdy tworząc fale uderzeniową. Oznacza to, że warunki takie jak gęstość i temperatura zmieniają się diametralnie. Dżety są otoczone wolniejszymi i szerszymi wypływami o małej prędkości, składającymi się głównie z materiału, który jest unoszony z otoczki przez dżet. Badanie młodych dżetów może ujawnić informacje o składzie wyrzucanego materiału i wpływie, jaki szoki mogą mieć na procesy chemiczny całego układu.

Rotacja opadającego obłoku powoduje spłaszczenie materii otaczającej gwiazdę w strukturę w kształcie dysku. W tych dyskach powstają pierwsze zalążki planet, gdy ziarna pyłu zderzają się i łączą ze sobą. Ziarna pyłu są pokryte zamarzniętym materiałem, głównie wodą. Inne cząsteczki, takie jak CO (tlenek węgla), mogą również osiadać z fazy gazowej na ziarna pyłu i zostać przekształcone w związki takie jak CH_3OH (metanol) i H_2CO (formaldehyd). Znajo-

mość składu tego lodu na powierzcni pyłu pozwala zdobyć informację o tym, jakie molekuły wchodzą w skład tworzących się planet. To, czy cząsteczka będzie obecna w fazie gazowej, czy w lodzie, zależy od temperatury: woda zamarza na ziarnach poniżej 100 K, a tlenek węgla poniżej 20 K. Temperatura dysku spada wraz z odległością od protogwiazdy. Granica, poza którą pewna cząsteczka występuje głównie w stanie stałym, nazywana jest linią lodu. Te linie odgrywają ważną rolę w formowaniu się planet, ponieważ mogą ułatwiać gromadzenie się materii, ale także znacząco zmieniają skład gazu i pyłu, z którego powstają planety. Masy dojrzałych dysków protoplanetarnych, starszych niż milion lat, pokazują, że po rozproszeniu obłoku molekularnego nie mają one dość materiału, aby móc tworzyć planety. Czy to oznacza, że planety zaczynają się formować wcześniej? Jest na to kilka dowodów: meteoryty widziane w naszym Układzie Słonecznym są podzielone na dwie klasy między wewnętrzną a zewnętrzną częścią układu, tak jakby masywna planeta (prawdopodobnie Jowisz) uformowała się i oddzieliła je bardzo wcześnie. Dzięki obserwacjom sieci ALMA zaobserwowano również bardzo szybki wzrost rozmiaru ziaren pyłu w młodych dyskach.

Główne wyniki i ich implikacje

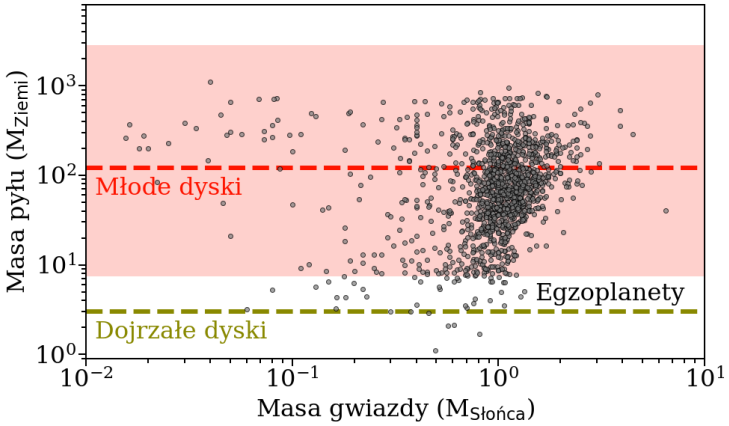
Ta praca przedstawia obserwacje astronomiczne mające na celu scharakteryzowanie najwcześniejszych etapów formowania się gwiazd i planet. W Rozdziale 2 wykorzystaliśmy obserwacje 100 protogwiazd w Perseuszu interferometrem VLA na 4 i 6.4 cm, w celu zbadania zjonizowanych dżetów pochodzących od protogwiazd. Pokazaliśmy, że parametry zjonizowanego dżetu są powiązane z innymi kluczowymi właściwościami gwiazd. Dzięki dużej liczbie zaobserwowanych obiektów, byliśmy w stanie wykorzystać informacje o radiowych dżetach, aby skorygować pomiary mas dysków na krótszych długościach fal. Pozwoliło to po raz pierwszy porównać masy młodych dysków ze starszymi oraz sprowokowało nową zagadkę: czy w najmłodszych dyskach jest wystarczająco dużo materiału do tworzenia się planet?

Na to pytanie odpowiadamy w Rozdziale 3, w którym łączymy obserwacje ALMA i VLA, aby scharakteryzować pył w młodych dyskach. Porównując masy młodych dysków z układami egzoplanetarnymi, pokazujemy, że planety gazowe mogą powstawać na najwcześniejszych etapach. Wynik ten jest pokazany na Rysunku 3: obserwowane egzoplanety mają masy znacznie większe od mas dojrzałych dysków, ale mieszczą się w zakresie mas młodych dysków.

W Rozdziale 4 badamy skład chemiczny dżetów molekularnych z protogwiazd w obłoku molekularnym w gwiazdozbiorze Węża. Potwierdzamy poprzednie badania pokazujące, że stosunek obfitości atomów węgla do atomów tlenu w dżecie jest niższy niż ten w otaczającej powłoce. Badanie młodych dżetów może mieć zatem kluczowe znaczenie dla zbadania wewnętrznych obszarów dysków i zmian, które zachodzą w jego składzie. Rozdział 5 zawiera przegląd chemicznych wskaźników fizycznych komponentów protogwiazd. Obserwacje siecią ALMA kilkunastu protogwiazd umożliwiają systematyczną analizę róznych elementów tworzących układ protogwiezdny. Obserwacje molekuł można użyć do pomiaru temperatury (np. DCO^+ i N_2D^+ to wskaźniki zimnego gazu) lub rodzaju promieniowania (C_2H i CN jako produkty przemian chemicznych zdominowanych przez promieniowanie UV).

Tę pracę doktorską można podsumować następująco: Powstawanie planet rozpoczyna się bardzo wcześnie, w pierwszych 100 tysiącach lat od początków systemu gwiezdnego w bardzo młodych dyskach otaczających protogwiazdy. Charakterystyka tych młodych systemów jest niezbędna do zrozumienia warunków powstawania planet. Obserwacje interfero-

metryczne molekuł w skalach porównywalnych z Układem Słonecznym są niezwykle przydatne do opisywania tych warunków. Dżety molekularne, które, jak pokazujemy, są bardzo powszechne w młodych układach, mogą być szczególnie ważne w pozyskiwaniu informacji o wewnętrznych rejonach układów, z których powstają planety.



Rysunek 3: Wykres przedstawiający rozkład mas układów egzoplanetarnych dla planet wokół gwiazd ciągu głównego (źródło: exoplanet.eu). Zacieniowany na czerwono obszar oznacza zakres oszacowania mas dysków w obłoku molekularnym w Perseuszu z medianą masy zaznaczoną linią przerywaną. Mediana masy dojrzałych dysków jest pokazana na żółto.

Przyszłość badań powstających gwiazd i planet

Obserwatorzy młodych systemów protogwiazdowych mają przed sobą ekscytująca przyszłość: ALMA działa na pełnych obrotach ujawniając swoje niesamowite możliwości obserwując młode protogwiazdy, ich dyski i dżety, w skali porównywalnej do rozmiarów Układu Słonecznego. ALMA szczególnie dobrze nadaje się do charakteryzowania młodych dżetów protogwiazdowych, które skrywają tajemnicę składu wewnętrznych obszarów dysków. Kolejna rewolucja nadchodzi dzięki teleskopowi Jamesa Webba (JWST), największemu teleskopowi kosmicznemu, jaki kiedykolwiek zbudowano, a który zostanie wystrzelony w kosmos w 2021 roku. Szczególnie Mid-InfraRed Instrument (MIRI) będzie obserwował protogwiazdy w podobnej rozdzielczości przestrzennej co ALMA lecz w zakresie 5-28 μm, który jest nieosiągalny, lub znacząco ograniczony dla obserwatoriów na Ziemi. Te obserwacje ujawnią skład zarówno gorącego gazu jak i chłodnego lodu zamarzniętego na powierzchni pyłu. W połączeniu z informacjami z sieci ALMA na temat chłodniejszego gazu, wkrótce będziemy mieli najbardziej przejrzysty obraz początków powstawania gwiazd i planet.

Publications

Refereed first-author publications:

4. *Dust masses of young disks: constraining the initial solid reservoir for planet formation.* **Tychoniec Ł.**, Manara C. F., Rosotti G. P., van Dishoeck E. F., Cridland A. J., Hsieh T., Murillo N. M., Segura-Cox D., van Terwisga S. E., Tobin J. J., 2020, A&A, 640, 19.

3. *Chemical and kinematic structure of extremely high-velocity molecular jets in the Serpens Main star-forming region.* **Tychoniec Ł.**, Hull C. L. H., Kristensen L. E., Le Gouellec V. J. M., van Dishoeck E. F., 2019, A&A, 632, 101

2. *The VLA nascent disk and multiplicity survey of Perseus protostars (VANDAM). IV. Free-free emission from protostars: links to infrared properties, outflow tracers, and protostellar disk masses.* **Tychoniec Ł.**, Tobin J.J., Karska A., Chandler C., Dunham M. M., Harris R. J., Kratter K. M., Li Z., Looney, L. W., Melis C., Pérez L. M., Sadavoy S. I., Segura-Cox, D., van Dishoeck E. F., 2018, ApJS, 238, 19.

1. *The VLA nascent disk and multiplicity survey of Perseus protostars (VANDAM). III. Extended radio emission from protostars in Perseus.* **Tychoniec Ł.**, Tobin J.J., Karska A., Chandler C., Dunham M. M., Li Z., Looney L. W., Segura-Cox D., Harris R. J., Melis C., Sadavoy S. I., 2018, ApJ, 852, 18.

Other refereed publications:

10. *Complex organic molecules in low-mass protostars on Solar System scales. I. Oxygen-bearing species.* van Gelder M. L., Tabone B., **Tychoniec Ł.**, van Dishoeck E. F., Beuther H., Boogert A. C. A., Caratti o Garatti A., Klaassen P. D., Linnartz H., Müller H. S. P., Taquet V., 2020, A&A, 639, 87.

9. *The VLA/ALMA nascent disk and multiplicity (VANDAM) survey of Orion protostars. II. A statistical characterization of Class 0 and Class I protostellar disks.* Tobin J. J., Sheehan P. D., Megeath S. T., Díaz-Rodríguez A. K., Offner S. S. R., Murillo N. M., van 't Hoff M. L. R., van Dishoeck E. F., Osorio M., Anglada G., Furlan E., Stutz A. M., Reynolds N., Karnath N., Fischer W. J., Persson M., Looney L. W., Li Z., Stephens I., Chandler C. J., Cox E., Dunham M. M., **Tychoniec Ł.**, Kama M., Kratter K., Kounkel M., Mazur B., Maud L., Patel L., Perez L., Sadavoy S., Segura-Cox D., Sharma R., Stephenson B., Watson D. M., Wyrowski F., 2020, ApJ, 890, 130.

8. *The VLA/ALMA nascent disk and multiplicity (VANDAM) survey of Orion protostars I. Identifying and characterizing the protostellar content of the OMC2-FIR4 and OMC2-FIR3 regions.* Tobin J. J., Megeath S. T., van 't Hoff M.L.R., Diaz-Rodriguez, A. K., Reynolds N., Osorio

M., Anglada G., Furlan E., Karnath N., Offner S. S. R., Sheehan P. D., Sadavoy, S. I., Stutz A. M., Fischer W. J., Kama M., Persson M., Di Francesco J., Looney L. W., Watson D. M., Li Z., Stephens I., Chandler C. J., Cox E., Dunham M. M., Kratter K., Kounkel M., Mazur B., Murillo N. M., Patel L., Perez L., Segura-Cox D., Sharma R., **Tychoniec Ł.**, Wyrowski F., 2019, ApJ, 886, 6.

7. *Characterizing magnetic field morphologies in three Serpens protostellar cores with ALMA.* Le Gouellec V. J. M., Hull C. L. H., Maury A. J., Girart J. M., **Tychoniec Ł.**, Kristensen L. E., Li Z., Louvet F., Cortes P. C., 2019, ApJ, 885, 106.

6. *The mass evolution of protostellar disks and envelopes in the Perseus molecular cloud.* Andersen B. C., Stephens I. W., Dunham M. W., Pokhrel R., Jørgensen J. K., Frimann S., Segura-Cox D., Myers P. C., Bourke T. L., Tobin J. J. **Tychoniec Ł.**, 2019, ApJ, 873, 54.

5. *The Herschel-PACS legacy of low-mass protostars: the properties of warm and hot gas components and their origin in far-UV illuminated shocks.* Karska A., Kaufman M. J., Kristensen L. E., van Dishoeck E. F., Herczeg G. J., Mottram J. C., **Tychoniec Ł.**, Lindberg J. E., Evans N. J. II, Green J. D., Yang Y., Gusdorf A., Itrich D., Siódmiak N., 2018, ApJS, 235, 30.

4. *ALMA observations of dust polarization and molecular line emission from the Class 0 protostellar source Serpens SMM1.* Hull C. L. H., Girart J. M., **Tychoniec Ł.**, Rao R., Cortés P. C., Pokhrel R., Zhang Q., Houde M., Dunham M. M., Kristensen L. E., Lai S., Li Z., Plambeck R. L., 2017, ApJ, 847, 92.

3. *Against the biases in spins and shapes of asteroids.* Marciniak A., Pilcher F., Oszkiewicz D., Santana-Ros T., Urakawa S., Fauvaud S., Kankiewicz P., **Tychoniec Ł.**, Fauvaud M., Hirsch R., Horbowicz J., Kamiński K., Konstanciak I., Kosturkiewicz E., Murawiecka M., Nadolny J., Nishiyama K., Okumura S., Polińska M., Richard F., Sakamoto T., Sobkowiak K., Stachowski G., Trela P., 2015,Planetary and Space Science, 118, 256.

2. *High-resolution 8 mm and 1 cm polarization of IRAS 4A from the VLA nascent disk and multiplicity (VANDAM) survey.* Cox, E. G., Harris, R. J., Looney, L. W., Segura-Cox, Dominique M., Tobin J. J., Li Z., **Tychoniec Ł.**, Chandler C. J., Dunham M. M., Kratter K., Melis C., Perez L. M., Sadavoy S. I., 2015, ApJ, 814, L28.

1. *Far-infrared CO and H_2O emission in intermediate-mass protostars.* Matuszak, M., Karska, A., Kristensen, L. E., Herczeg G. J., **Tychoniec Ł.**, van Kempen T. A., Fuente, A., 2015, A&A, 578, 20.

Non-refereed publications:

1. Chemical and kinematic complexity of the very young star-forming region Serpens Main observed with ALMA. **Tychoniec Ł.**, Hull C. L. H., Tobin J. J., van Dishoeck E. F., 2018, Astrochemistry VII: Through the Cosmos from Galaxies to Planets, in Proceedings of the International Astronomical Union, IAU Symposium, Volume 332, pp. 249-253.

Curriculum Vitae

I was born in the city of Nowogard in north-west Poland, on 25th of January 1992, to Jolanta and Edward Tychoniec. From my dad I inherited a passion for stargazing, from my mom a curiosity for math and science; from both of them an appreciation for a spiritually-oriented life. My ridiculously successful older sister Agata, set a path that for me seemed natural to follow: that of a constant drive for new challenges. My younger brother Krzyś, taught me most that I know about patience, selfless love and compassion, qualities that I later appreciated as essential for a human being.

I was blessed with a house and high-school environment that allowed me to explore my interest and opportunities. Mrs. Aldona Kopycińska helped me to get an early start at peculiarities of European Union law system, Mrs. Marta Maziarz and Mrs. Izabella Koladyńska saw my inclination to delve into philoshopical discussions, and patiently convinced me to explore this path. Ft. Marek Gajowiecki sparked in me an enthusiasm not only in rock music and Dark Tower series, but also in theology. Those efforts allowed me to become a finalist of both Theology and Philosophy Olympiad in 2010. It all seemed that a path of a true humanist is right in front of me. Therefore I enrolled for a B.A. in International Relationships at Adam Mickiewicz University (AMU) in Poznań. However, this path has proven not to be fertile, and after one year I decided to explore my lifelong passion for astronomy, one of the most philosophical of sciences, in a more professional way – I started a BSc and further on a MSc in Astronomy at Astronomical Observatory in AMU in Poznań.

Years 2011-2016 that I spent on studying astronomy were exciting as I first got to experience professional observations in Borówiec Observatory on the outskirts of Poznań, and collaborate in a first scientific project on studying asteroids of the Solar System with Dr. Anna Marciniak. One of my career defining moments was when I met Dr. Agata Karska during the 1st year of my master studies, as she offered me to work on a project studying young massive stars with the Herschel Space Observatory. An exploration of the origin of stars and planets with a space telescope, was extremely exciting for me and I jumped on this with all enthusiasm I had, however this would not happen without an all-important nudge by my colleague Monika Matuszak. This resulted in my first international collaboration with Dr. Antoine Gusdorf at Observatoire de Paris. In the break between first and second year of my masters I participated in the Leiden/ESA Astrophysics Program for Summer Students in Leiden working with Dr. John Tobin on Very Large Array observations of young protostars in the Perseus molecular cloud. This has also become a topic of my master thesis I finished in Poznań under supervison of Dr. Karska and Dr. Tobin. During my studies I also became a

proficient barista (a professional coffee maker) in Brisman Kawowy Bar in Poznań. Working with a coffee legend Mateusz Gaca, who led me to become a 5th Polish Barista in 2015, and future World Barista Champion Agnieszka Rojewska, was a unique experience, and I was on a brink of choosing a career path of a professional barista. However, the determination of Dr. Karska, and also financial support from stipends of Polish Ministry of Higher Education and AMU, allowed me to fully focus on scientific research.

I was admitted to the PhD program in Leiden Observatory in Netherlands to work with Prof. dr. Ewine van Dishoeck on star and planet formation in 2016. One of my first tasks was to assist in preparation of the first scientific observations of star-forming regions on the James Webb Space Telescope (JWST). Although it was not meant for me to witness the excitement of a JWST launch and first data delivery during my PhD, I learned plenty about infrared astronomy and experienced working in a large collaboration within MIRI European Consortium.

My first research projects were a continuation of VLA studies of radio jets in Perseus that I started during my masters. My first paper explored the ionized component of the jet, finding exciting evidence for cosmic rays production in protostars. A second paper, aside from providing a very extended survey dataset on radio emission from protostars, also opened a path that determined my next main interest: planet-forming disks. We used the data to provide an updated estimate of protostellar disk masses. This chapter, without a doubt inspired by sharing an office with disk expert Dr. Sierk van Terwisga, resulted in an exciting outcome: disks in young systems are more massive than their mature counterparts, and the planets could form very early. This work prompted a collaboration with Dr. Carlo Manara, Dr. Giovanni Rosotti, and Dr. Alex Cridland on the relation between the disk masses and exoplanets. This comparison showed that planets must form early, and it delivered for me a first press release. My PhD was also revolving around Atacama Large Millimeter/submillimeter Array (ALMA). Through a collaboration with Dr. Charles Hull and Dr. Lars Kristensen we explored the nature of young protostellar jets in Serpens. This also triggered a lot of fruitful discussion with Dr. Benoit Tabone and helped to put in motion a final work on the molecular tracers of physical components of the protostellar systems with Dr. Merel van 't Hoff and Martijn van Gelder.

During the first three years of my graduate program I was a Teaching Assistant for Galaxies and Cosmology, course led by Dr. Jacqueline Hodge. I also had the privilege to supervise together with my colleague Martijn van Gelder, two master students: Micha Heilman and Yuan Chen. As the excitement for the JWST launch heated up I was an expert speaker at the JWST MasterClass in Toruń and at the Dutch JWST day. On my final year I co-ran with Dr. Alex Cridland a Star Formation and Disk Coffee meeting. I had opportunity to present my research in Puerto Varas in Chile, Pasadena in California, USA, and many virtual conferences during pandemic times.

I will continue my career as a Research Fellow at the European Southern Observatory in Garching, Germany, pursuing ALMA studies of young protostellar systems, while getting experience at using Very Large Telescopes at Paranal, and eagerly awaiting launch of the JWST in the fall of 2021.

Acknowledgements

As this journey called PhD comes to an end, I want to take this opportunity to acknowledge everyone who helped me to get here. In all honesty, this was an outcome that didn't seem very likely for me many times across this endeavor. I can admit that if it wasn't for all the people who believed in me when I didn't, and who constantly put their money on me against all odds, I wouldn't make it. Thank you! Dziękuję! Below I will try to thank some of you in person, but I am grateful to everyone who even briefly lifted me up along the way.

Moving to a different country can be a challenge, which was made a lot nicer, thanks to two awesome flatmates who helped me to settle in, Andrej and Iva, I will always think fondly about our year at Lasserstraat! You both without a blink dragged me into your social circle, which resulted in many parties, new friendships and I didn't have time to feel alone during my first year. Andrej, I still miss your cooking!

At the very beginning, support from Agata Karska and John Tobin was essential for me to choose the path of a professional astronomer. Agata, thank you for betting on me early on, investing your time and resources so I can get a fast-track into high-level research. Antoine Gusdorf, thanks for being my first foreign collaborator and showing me that doing science can't be so scary. John, I will be always indebted for trusting me with the impressive VANDAM dataset, and for your support over the years. Chat, Lars, Carlo, Migo, Henrik, Valentin, Giovanni, Tien-Hao, Nadia, Tyler, Mario, Yao-Lun, Dominique, Tom, thank you for various scientific and non-scientific discussions and advice. Leiden/ESA Astrophysics Program for Summer Students (LEAPS) was a life-changing event for me not only for scientific reasons, which cemented my dedication to star-formation and to interferometry but also for a social life, which made me feel that I can fit in in an international environment. Thanks, LEAPS 2015, both organizers and fellow students!

The two Dutchies who became my main resort for science questions, life problems, shared difficulties, board games, and late-night drinks. Arthur, I never stopped being impressed with your knowledge and intelligence, thank you for your tireless help with 'easy' questions. Merel, your kind heart and compassion dragged me through the hard parts of this journey, thanks for the company during all the ALMA deadlines and all the insights on disks and chemistry. Thank you both for being fantastic traveling companions, through Chile, California, and Sweden! I'm sure this is not over yet!

I was very lucky to be a part of a large, diverse, and friendly research group. Sierk, your knowledge is beyond the limit, I greatly enjoyed our discussions on countless topics, thanks for your help with statistics and setting first steps in the disk territory. Christian, my fellow coffee geek, we ran a small revolution in the observatory and had some nice coffee-hunting excursions, it was great fun! Danna, you were one of the first friends I made in the Netherlands, I was lucky to have you around! Alex, thanks for timeless geek-outs at

the borrels, and for insights during my exoplanetary endeavor. Pooneh, I wish we shared more time in and outside the observatory, your positive attitude is so contagious. Benoît, I was so excited to welcome another outflow aficionado in the group, thank you for being a fun and always an enthusiastic companion. Martijn, thank you for your help and support, co-supervision of students together was a great adventure! Thanks also for being a helpful and patient neighbor, whenever I lost my keys. Giovanni, thank you for your insights and mentoring. Niels, till the next borrel. Daniel, thank you for your patience in answering all the questions to an ALMA beginner. Anna, I'm looking forward to our Paranal reunion. Nadia, thanks for all the practical insights on how to do better science, Alice, I'm still waiting for a karaoke duel, and good luck with the new band, Leon, Margot, Kirstin, Shota, thanks for countless coffee breaks, Jeroen, thanks for all the jokes and lunch discussions, Gleb, I always enjoyed your visits at 504.

Thanks to Stefano, Yao, Lisa, Paolo, the Garching crew, usually on the other side of the screen. Vianney, Melissa, Ko-Ju, Maria, thank you! Alvaro, Luke, Liz, Yanette, Andres, Michiel, and all the helpful staff at Allegro, thank you for your patient help. My second home for those years was room 504: Anna, Maria, Erik, Sierk, Michał, Danna. Thank you! Yuan and Micha, thank you for being such great students on my first steps as a supervisor.

My unexpected friends, my wedding witnesses: Dario, Lydia, Michał (Dario and the Slavs). Dario, you are such a star, a fun personality, a great friend, for good and bad, your energy was always lifting me up! Lydia, thank you for being such a caring, helpful, attentive friend. You were invaluable support during hardships. Michał, thanks for supporting me in so many ways, especially as a Sunday-mass companion, and always an uplifting presence at the office.

Sterrewacht is much bigger than a research group and I especially appreciate people with whom I could share Friday borrels, King's Birthdays, Leiden Ontzet, and countless other parties. Kirsty, what are the odds?! Mantas, greatest micro-parties at your place. Eleonora, Fran, Gwen, Leindert, Marta, Matus, Alex, Marina, Sarah, Jerry, Jordy, Maria Cristina, Turgay, Dilovan, Nico, Anna, Fraser, Sanjana, Gabriela, Volkert, and many others, thanks for being around!

Chiel, thanks for getting me into squash! Lisanne, thank you for supporting us during our wedding. Chummy crew: Jaap and Corrie, I can't express enough how important your lovely coffee house was during this PhD, kind of a safe haven from which I always left with a little bit more enthusiasm to fight another day. Dario and the Monkeys: Hiddo and Dario, thanks for bringing me back to my old hobby of playing guitar, I had fun exploring my 'rock & roll' side. Dario, I am so glad we fulfilled our goal and played at the BBQ!

I was always looking forward to coming back to Poland, especially to Poznań, however, 2020 brought me a surprise and I had to stay there for 4 months: Oskar, Patryk, thank you for letting me in and for sharing a home office, through games of LoL, board games and morning coffees. Thank you to all with whom we managed to get in touch, despite the distance Uran and Agata, Kamila and Max, Michu, Marika i Jan, all people at Brisman Coffee, Krycha, Dawid, Grześ i Madzia, Szopen, Mery, I was always excited to see you all!

I am also indebted to a fantastic crew of people who studied with me in Poznań. Thanks for accompanying me through the ups and downs of a student's life! Izabella, I'm so glad our friendship lasts, please don't stop sending memes my way. Monika, thank you for pushing me into 'real' astronomy, Mateusz, thanks for the board games, Przemek, I still laugh when I think about our first observing trip to Suhora.

I am grateful to those who supported me in my early years and encouraged me to follow my dreams: Mom and Dad, thank you for sharing the passion for stargazing and math, my

sister Agata, thanks for teaching me what ambition and hard work mean, my brother Krzyś for teaching me so much so early in my life. Szymon, my young godson, for helping me rediscover my child's passion for the cosmos. Staś, welcome to the world! Can't wait to spam you with astronomy books!

I left this to the very end but in many ways, it is the most important paragraph: Marta, my wife. When we met, I told you that in a few months I need to leave abroad to do a PhD in astronomy, but you didn't run away. We made a bold and somewhat crazy choice to spend the next four years 1000 kilometers apart. Not only we made it, but our relationship thrived and I was delighted to say 'I do' to you a month before the end of my time in Leiden. It is impossible to overstate your role in getting this thesis done, with your unconditional support, your confidence in me, and your patience. Having you designing this beautiful cover is my honor. I'm so excited to start our new life in Germany! Kocham Cię!